TABLE OF CONTENTS

List of Appendices

List of Figures

1 ATTENDEES

1.1 FARA Attendees

Jennifer Farmer	MS Chief Executive Officer
Ron Bartek	President and Co-founder
Barbara Tate, PhD	Chief Scientific Officer
Joy Cavagnaro, PhD	Scientific Advisory Board Member
David Lynch, MD, PhD	Scientific Advisory Board Member
Massimo Pandolfo, MD	Scientific Advisory Board Member
Helene Puccio, PhD	Scientific Advisory Board Member
Maritza McIntyre, PhD	Consultant
Pat Ritschel	Director
Brigid Brennan, Esq	Director
Alex Fielding	Director
Ruth Acton	Treasurer
Shandra Trantham	FARA Patient Ambassador

1.2 Industry Attendees

AavantiBio	Jessie Hanrahan, MS, MPH, PhD, Chief Regulatory Officer; Chris Wright, MD, PhD, Chief Medical Officer
Astellas	Diane Barnes-Glait, Senior Director, Regulatory Affairs; Jill Woloszynek, Director, Gene Therapy Program Management
CRISPR	Laurie Kelliher, Executive Director of Regulatory Affairs; Hari Padmanabhan, Ph.D., Principal Scientist
FA212	Tom Hamilton, Co-Founder; Thomas Brenninkmeijer, MBA, Co-Founder
Lacerta	Darin Falk, Ph.D. Chief Scientific Officer; Edgar Rodriguez, Ph.D. Chief Executive Officer
Lexeo	Jay Barth, Chief Medical Officer; Richie Khanna, VP and Head of Nonclinical Development
LifeEdit	Kathryn Woodburn, Ph.D., SVP Preclinical Development; Sally Kim, Ph.D., Scientist I, Preclinical Development
Neurocrine	Stephen Perry, Ph.D., Executive Director of Research; Amanda Richter, MS RAC, Executive Director of Regulatory Strategy

Novartis	Evgenia Dimova, NS & MSD, Global Therapeutic Area Lead, NS & MSD; Michelle L Krishnan, MD PhD, Executive Medical Director, NIBR Translational Medicine
Pfizer	Laurence Whiteley, DVM Nonclinical Safety/Pharmacology; Nicole Parker, PhD Regulatory
Prime Medicine	Eric Zheng. PhD, Principal Scientist, Neuromuscular Diseases; Fubao Wang, PD, SVP, Regulatory Affairs
PTC	Matt Klein, MD, MS, FACS, Chief Operating Officer; Bert Yao, MD, PhD, MHS, Vice President Clinical Developmen
Takeda	Gabriele Proetzel, PhD, Senior Director, External Neuroscience Innovation, Neuroscience Drug Discovery Unit; Edwin Addai, PharmD, RPh, Sr. Mgr. Regulatory Strategy
Tune	Luis Sanchez-Perez, PhD, Director of Preclinical Translation; Mike P. Hefferan, PhD, Director, Head of In vivo Pharmacology
Vesigen	Wendy Zhao, PhD, Principal Scientist; Joe Nabhan, PhD, Chief Scientific Officer

2 GOALS OF THE MEETING

Gene therapy and gene editing (GT/GE) approaches represent promising developments in the search for effective treatments for Friedreich Ataxia (FA) because of their potential to directly address the cause of FA - frataxin (FXN) deficiency. These therapeutic approaches have different development challenges and carry different risk-benefit considerations from those of small molecule therapeutics. For FA, these specific challenges include achieving appropriate frataxin expression in target tissues, recognizing the limitations of preclinical models, and identifying relevant FA biomarkers and outcome assessments. The goals of this meeting are to discuss proposed preclinical and clinical development strategies for addressing the above challenges with FDA to obtain feedback on their suitability or input on areas needing refinement.

This meeting will be a success if FDA, FARA, and sponsors achieve a mutual understanding of FA patient perspectives on unmet medical needs and risk/benefit considerations and the acceptable approaches for addressing the challenges common to FA GT/GE developers. The information contained in this document is not intended to be regulatory consulting advice or to impose a specific development strategy on any sponsor developing a GT/GE treatment for FA. Instead, all information, content, and materials within this document are for general informational purposes only. Information in the document may not constitute the most up-to-date information. Not all approaches have been addressed here. For example, different targets for gene editing have not been proposed or discussed within this document.

3 MEETING DISCUSSION TOPICS

1. Special considerations for gene therapy or gene editing development programs for FA. FARA would like FDA's feedback about:
    a. FARA would like FDA to better understand the patient perspective on potential benefit of selected tissue targeted GT/GE vs potential risk of only receiving one lifetime treatment with a viral vector.
    b. Emerging data indicates that FXN overexpression via construct design or dose selection may impact safety. Thus, FARA suggests that FXN expression levels should be determined relative to wild type in preclinical models, length of toxicity studies should be considered, and assessment of tissues with higher frataxin levels should include histology. In addition, current thinking is that transduction/editing efficiency is relevant to interpreting expression and total protein in the target tissue and might be more relevant than total protein FXN level alone for dose selection. FARA would like FDA feedback on our current proposed strategy to evaluate for FXN expression for safety, toxicity, and optimizing dose selection.
    c. It is feasible to assess FXN expression and protein levels in blood, skin, and buccal cells and while these are not disease relevant or specific targets for therapy, they can provide information relevant to safety, dose, and activity/efficacy for some programs. Does FDA agree that interpretation of meaningfulness of changes in frataxin levels in these tissues should be based on context of use? For example, in programs where disease relevant tissues can be accessed (e.g., heart and skeletal muscle) measuring FXN expression and protein levels is highly relevant as pharmacodynamic /activity biomarkers.
    d. Dorsal Root Ganglia (DRG) toxicity has been observed with AAV9 based vectors. However, DRGs do not develop fully in FA and standard methods to assess function cannot be used. Thus, there may be no method to assess potential for AAV related toxicity in FA. As such, FARA suggests that evidence from toxicity studies of mild toxicity without a functional correlate should not be a sole factor that impedes clinical translation. Can FDA provide comment?
2. Cardiac-focused therapeutic approaches: Section 8 describes the cardiac disease natural history and correlates of cardiac disease severity; strengths and weaknesses of preclinical models; available proof of concept data from *in vitro* and *in vivo* GT/GE studies; and correlation of efficacy and safety of FXN gene transfer to dose and FXN expression levels. Suggested preclinical data to support first in human (FIH) studies, inclusion criteria for FIH studies in adults and transition to pediatric patients, and outcome measures likely to predict clinical benefit are also discussed. FARA has proposed an example development plan for cardiac-focused GT or GE products in included in Appendix 3 for discussion.
    a. Preclinical: Can FDA comment on utility of the proposed preclinical models to support IND enabling studies?
        i. A well-validated cardiac-specific mouse model (Mck knock out mouse) that closely mimics human disease has been used for demonstrating proof-of-concept (POC). The treatment effect can be observed even when symptoms are advanced and pre-symptomatic treatment prevents disease. In addition, studies in this model

have informed percent transduction required for benefit, and consequences of over expression or frataxin toxicity. These learnings not only inform approaches for the preclinical program in cardiac disease but are also informative when considering other target tissues.

ii. Knock out models cannot be used to evaluate GE approaches. Considering the lack of humanized mouse models with repeat expansion and a functional cardiac phenotype to support GE, can FDA comment on suggested plan to use weight of evidence from multiple model systems?

b. Clinical development: FARA would like FDA to comment on the example proposal that suggests an approach to patient selection, clinical outcome assessments, and biomarkers for consideration. Given the inability to assess functional cardiac outcome with certainty in less than 5 years, does FDA agree that weight of evidence across well-validated cardiac biomarkers could provide evidence of efficacy?

c. Risk/benefit: Regarding the cardiac aspects of the disease, does the FDA need any additional information on patient perspective on risk/benefit of GT/GE for cardiac disease or appropriate population for these treatments?

3. Nervous system-focused therapeutic approaches: Section 9 describes the neurological natural history and relevant CNS/PNS targets for GT/GE to treat the neurologic components for FA; strengths and weaknesses of preclinical models; available proof of concept from *in vitro* and *in vivo* GT/GE studies and suggested preclinical data to support FIH studies. Considerations for clinical development, such as need for pediatric inclusion, concerns about unilateral intraparenchymal injection, the use of the mFARS as an approval endpoint, and use of natural history data in clinical trial design and as comparator are also discussed. An example development plan for nervous system-focused GT or GE products in included in Appendix 3 for discussion purposes. FARA would like FDA's comments on:

   a. Preclinical: Can FDA comment on whether there are any concerns regarding the proposed preclinical models to support IND enabling studies for GT of CNS manifestation of FA?

      i. In the absence of animal models that authentically recapitulates clinical symptoms, could demonstration of increase of frataxin and percent transduction in a target tissue in vivo sufficient for clinical translation? The data would be supplemented with effects on biological activity in vitro and/or in vivo models where functional improvement can be demonstrated in FA relevant target tissues (non-related tissues may still show dysfunction).

      ii. Considering the lack of humanized mouse models with repeat expansions and a behavioral phenotype to support GE, can FDA comment on suggested plan to include in vitro evidence of increased frataxin expression and functional correction after gene editing plus characterization of nervous system gene editing efficiency in an animal model?

   b. Clinical development: Anatomical targets will dictate patient selection, biomarkers, and clinical assessments.

      i. Studies in adults with later stage disease may appropriately assess safety/toxicity but benefit may be limited because of frank neurodegeneration. Because stage of

disease impacts what can be assessed, translation to early stage, younger populations is not direct but essential. Therefore, does the FDA agree with the plan to initiate pediatric studies early in development if supported by safety in adults, and some evidence of benefit in preclinical models?

ii. Given the abundance of neurological natural history data, FARA believes these data are informative for designing trials, providing outcome assessments, and providing a comparator arm for clinical trials, or at least to supplement placebo, e.g., employing Bayesian approaches to reduce size of placebo group in trial design. Can FDA comment on the proposed utility of natural history data?

c. Risk/benefit: Treatment of neurological manifestations are highly relevant, specific patient preferences related to design and conduct of trials include limiting the size and duration of placebo groups. In programs where route of administration is intra-parenchymal to the dentate nucleus, unilateral intra-parenchymal administration presents greater risk than bilateral administration.

i. In FDA draft Guidance for Industry on Human Gene Therapy for Neurodegenerative Disease, "…*FDA recommends that the sponsor utilize a staged approach: initiating the early-phase study with unilateral administration*". Can FDA comment on FARA's request that FDA not recommend unilateral administration, especially in the case of intraparenchymal administration to the dentate nucleus in FA?

4. Vision-focused therapeutic approaches: Section 10 describes the prevalence of vision loss, symptomology and target tissues, progression, and milestones in FA; strengths and weaknesses of preclinical models; available proof of concept from *in vitro* and *in vivo* GT/GE studies, inclusion criteria and relevant clinical outcome assessments. An example development plan for vision-focused GT or GE products is included in Appendix 3 for discussion purposes. FARA would like FDA's comments on:

a. Preclinical: Particularly considering the lack of efficacy models with relevant cell-type pathology or a vision phenotype to support GT/GE, can FDA comment on proposed plan to use a weight of evidence approach using multiple available models to evaluate proof of concept and extrapolate doses?

b. Clinical development: Does the FDA agree with the proposed strategy for patient selection, biomarkers, and clinical assessments?

i. FDA guidance on Human Gene Therapy for Retinal Disorders GT states that the rate of photoreceptor loss is an acceptable endpoint for retinal disorders. However, since photoreceptors are not the relevant retinal cell type in FA, would FDA consider RNFL loss to be an acceptable endpoint in FA?

ii. FARA suggests natural history data can be informative for trial design including patient selection, outcome measures and as a supplement to placebo to reduce number of participants in placebo arm. Does FDA have a comment?

c. Risk/Benefit: FARA is aware that vision loss in FA may be under appreciated. Does FDA need any additional information on the impact of vision on quality of life for individuals with FA, and/or patient perspective on risk/benefit of treating vision loss?

4 OVERVIEW OF FA

FA is a debilitating, life-shortening, progressive, degenerative, multisystem disorder that affects approximately 1 in every 50,000 people in Caucasian populations of Europe, North America, South America, the Middle East, South Asia (Indian subcontinent) and North Africa. The incidence is very low in other ethnic groups [Labuda 2000, Cissé 2021]. Although rare, it is the most common form of inherited ataxia [Lynch 2021b]. FA is an autosomal recessive disease caused by mutations in the *FXN* gene [Campuzano 1996]. In most cases, it is caused by biallelic expanded GAA triplet repeats in intron 1 of the *FXN* gene (Figure 1). In about 4% of cases, patients have a triplet repeat expansion on one allele and a loss of function mutation on the other allele [Delatycki 2019, Galea 2016]. Diagnosis is typically made by genetic testing, which detects about 99% of all cases. About 75% of patients are diagnosed between 6 and 20 years of age, while about 22% are diagnosed after 21 years of age.

Figure 1 Cartoon of the *FXN* Gene: Normal and Friedreich Ataxia Allele

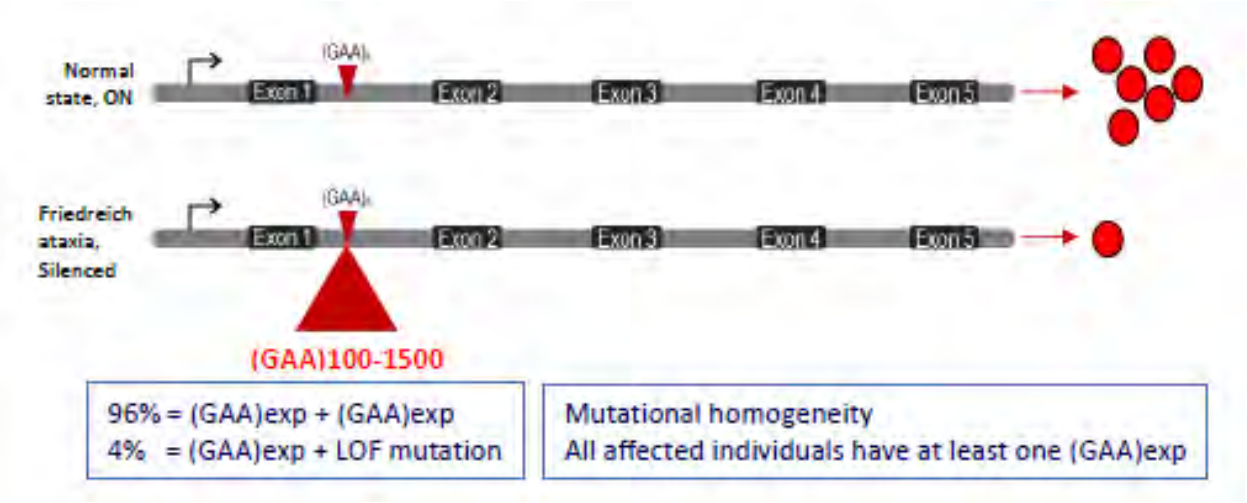

Loss of balance and coordination is the most common presenting symptom, typically beginning between the ages of 5 and 15 years with progression of symptoms leading to loss of ambulation and independence of all activities of daily living. Adult or late-onset FA is less common and occurs after the age of 25 [Geschwind 1997]. Adult onset FA is characterized by slower progression and less risk for cardiac disease Patients with loss of function mutations may have slightly different disease course than those with two expanded repeats, especially regarding vision loss, diabetes, and cardiomyopathy [Cossee 1999, McCormack 2000, Galea 2016].

FA is multisystemic, affecting the central and peripheral nervous systems leading to dysfunction truncal and limb ataxia, loss of coordination of muscle movements, dysarthria, dysphagia, and loss of vision and hearing. FA also affected the heart, skeletal muscle, skeleton (scoliosis, pes cavus), and endocrine system (diabetes, bones). While neurological features of the disease are fully penetrant, affecting 100% of those diagnosed, other systems are not affected in all patients. Two thirds of patients develop cardiomyopathy, more than half develop severe scoliosis and 10-40% develop diabetes [Greeley 2014]. The mean age at death is 36-37 years, due to cardiac

complications in approximate 60% of individuals and other causes result from long-term neurological disease, such as infections, falls, and stroke [Tsou 2011].

Frequently, the first symptom identified is ataxia - loss of coordination and balance - but, in some cases, cardiomyopathy or scoliosis may precede onset of neurological disease [Regner 2012, Reetz 2016]. Symptoms such as vision impairment, hearing loss, swallowing difficulties and urinary disturbances are generally more prominent in late-stage disease. On careful examination, however, signs of these problems are often detectable in patients early in disease course. By end-stage disease, almost all patients have at least some myocardial involvement [Lynch 2021b]. Depression was diagnosed in 14% of patients with FA in a European study compared to the general population prevalence rate of about 8.5% in Europe [Reetz 2018]. FA patients also have a higher incidence than unaffected people of certain other diseases, such as ulcerative colitis, Crohn's disease, inflammatory bowel disease and growth hormone deficiency [Shinnick 2016]. However, incidence of such conditions is still low in the FA population.

The progressive loss of coordination and motor control leads to motor incapacitation and the full-time use of a wheelchair, typically within 10-15 years of diagnosis. Most young people diagnosed with FA require mobility aids such as a cane, walker, or wheelchair by their teens or early 20s. While subtle differences in cognition can be detected, most individuals with FA are cognitively intact and often remarkably well informed and engaged in the research and advocacy community. There are no approved therapies for FA.

Figure 2 Typical Onset FA Progression

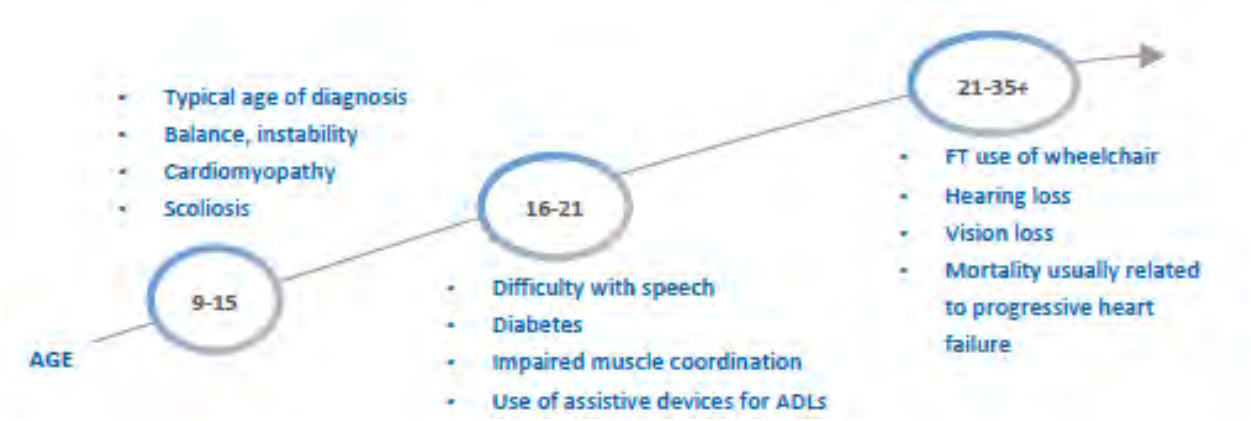

Features of disease severity, such as age of onset, cardiomyopathy, diabetes, and premature death correlate with the length of the shorter of the two alleles [Durr 1996, Koeppen 2011]. See Figure 3, below.

Figure 3 Correlation between Age of Onset (left panel) or Age of Death (right panel) and GAA Repeat Length

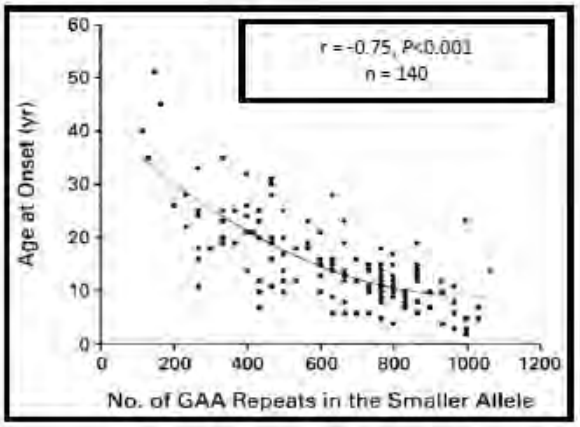

[Durr 1996]

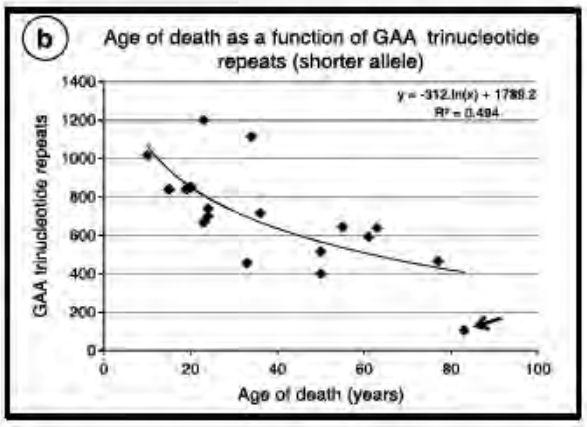

[Koeppen 2011]

FA is a disease of frataxin protein deficiency. The GAA repeat expansion causes epigenetic silencing of the FXN gene [Saveliev 2003, Herman 2006]. In this recessive disorder, carriers have one allele with an expansion of the repeats and one allele with a normal number of repeats, resulting in approximately half of the protein expression found in non-carriers. Carriers have no discernable phenotype. Therefore, restoring frataxin levels to 50% of normal should restore normal cellular function and less protein may provide clinical benefit.

The primary function of frataxin appears to be a crucial role as an activator of the biogenesis of iron-sulfur (Fe-S) clusters within the mitochondria [Muhlenhoff 2002, Gerber 2003, Fox 2015, Fox 2019, Maio 2020]. Fe-S clusters are prosthetic groups for enzymes with various functions (Fe-S proteins) found in all cellular compartments. In mitochondria, Fe-S proteins are involved in oxidative phosphorylation, the Krebs cycle, and cofactor biosynthesis. In the cytosol, Fe-S proteins participate in several metabolic processes and include a major regulator of iron metabolism, IRP1. In the nucleus, several factors in DNA replication and repair are Fe-S proteins. Mitochondrial Fe-S cluster biogenesis is essential also for the assembly of extra-mitochondrial Fe-S clusters, so, though frataxin is a mitochondrial protein, its deficiency affects many cellular processes in all compartments.

Frataxin deficient cells upregulate iron import into the mitochondria, possibly as a homeostatic response to low Fe-S clusters [Martelli 2015]. While the resulting increased mitochondrial iron helps sustaining Fe-S cluster biogenesis, iron also accumulates in the organelles because of its inefficient utilization [Babcock 1997]. Iron in mitochondria reacts with reactive oxygen species (ROS), whose levels are also increased by low frataxin because of respiratory chain dysfunction, generating oxidative stress, leading to damaged mitochondrial membranes, compromised mitochondrial function, and cell death [Delatycki 2019].

Figure 4 Pathophysiology of FA; Consequences of FXN and FE-S Cluster Deficiency

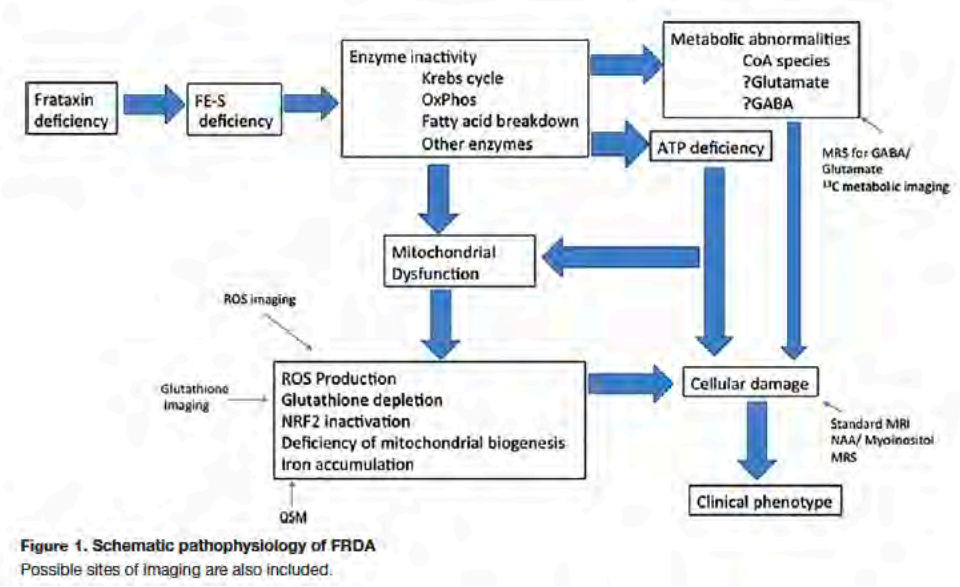

[Lynch 2021]

Cellular changes downstream of the direct consequences of frataxin loss contribute to the pathophysiology. These include a down regulation of factors promoting the expression of genes that counter oxidative stress and stimulate mitochondrial biogenesis. These include nuclear factor erythroid 2-related factor 2 (NRF2), a transcription factor that regulates the expression of genes that counter oxidative stress [La Rosa 2020a, Chiang 2020] and peroxisome proliferator-activated receptor gamma (PPARγ)/PPARγ coactivator 1 alpha (PGC-1α) [Marmolino 2010]. In mouse models and cellular models derived from human FA patient cells, iron accumulation and deposition within the mitochondria can activate ferroptosis, an iron-dependent cell death which thus may also occur in patients [La Rosa 2020c, Turchi 2020]. Reductions in Fe-S cluster-containing DNA repair enzymes may be responsible for the increased genomic DNA damage and mitochondrial mutational load that have been observed in FA cells [Haugen 2010, Bhalla 2016]. Evidence of upregulation of the integrated stress response and inflammation are seen in tissues especially impacted in FA, including the heart, spinal cord, specific brain nuclei, as well as skeletal muscle [Vásquez-Trincado 2021, Vásquez-Trincado 2022]. Cellular stress may be secondary to compromised mitochondrial function. Inflammation may also reflect a response to cell death [Apolloni 2022]. These insights into the function of frataxin and the downstream consequences of low frataxin levels suggest potential therapeutic targets and potential biomarkers [Zesiewicz 2020].

5 INTRODUCTION TO THE FRIEDREICH'S ATAXIA RESEARCH ALLIANCE (FARA)

The Friedreich's Ataxia Research Alliance (FARA) was founded by patient families and FA scientists to fund and facilitate research with the goal of achieving meaningful treatments for FA. A founding principle of FARA is a collaborative approach to research, which has accelerated what we understand about FA; such knowledge is being applied to the discovery and development of treatment approaches. This briefing document represents a collaborative effort between FARA, leading academic researchers, and those drug developers focused on bringing gene therapy/editing approaches into the clinic for the treatment of FA. Insights and potential solutions to some of the challenges in developing these promising therapeutics will be widely shared.

During the meeting we will share the patient's perspective on participation in the development of gene therapy/gene editing clinical trials. In 2017, FARA hosted an externally led, patient-focused drug development meeting. The meeting drew over 400 FA patients and caregivers, about 25 FDA officials, and a similar number of representatives from pharmaceutical companies. FA patients, and their families, friends, and caregivers, discussed their perspectives on living with the disease: what symptoms patients experience, how it affects their lives, what concerns them about the disease, their opinions on current and future treatment options, and experiences with research studies and clinical trials. The entire report from the meeting can be found here - https://www.curefa.org/patient-focused-drug-development. The global FA community, including medical professionals and patient families, has been involved in efforts to become educated about the differences between small/large molecule therapeutics and GT/GE. FARA has helped to fund the Australian Friedreich Ataxia Stem Cell and Gene Therapy Consortium, which prepares patients, families, clinicians, and clinical research sites for gene therapy trials for FA. This Consortium is engaging all sites within the global Collaborative Clinical Research Network in Friedreich Ataxia (CCRN in FA). Activities have included patient and family surveys on knowledge of and concerns about gene therapy; symposia and collaborative meetings for researchers and clinicians to share and discuss the state of the art of gene therapy; and establishment of processes and procedures needed to help make these sites gene therapy ready. In addition, FARA, in collaboration with Salem Oaks, developed a five-part interactive educational series on the basics of gene therapy, the risk-benefit equation, decision making, and informed consent. These educational materials are available on FARA's website, https://www.curefa.org/trial. This document and at our meeting we will share the valuable insights FARA has gained from these initiatives as we approach clinical trials with GT/GE.

FARA has also been instrumental in funding basic, translational, and clinical research. FARA funds both investigator-initiated research through a competitive grant program as well as FARA-directed research that addresses areas of unmet need and/or creates research resources (e.g., animal and cell models) for the community. Over the past 20 years, many preclinical models have been developed to contribute to the basic understanding of FA as well as to demonstrate efficacy of putative therapeutic approaches. Through collaborations with the Jackson Laboratory (JAX), Brunel University (UK), Erasme University (Belgium), the Murdoch Children's Research Institute (Australia), IGBMC (France), and the University of California Los Angeles, Weill-Cornell, the University of Alabama, and the University of Florida (USA) many mouse models of

FA have been developed. FARA has also partnered with The Jackson Laboratory (JAX) to centralize and expedite sharing of models developed in academic labs, and to create new models. The variety of these mouse models has proven to be important because no single FA mouse model has been developed that can be used for proof of concept in evaluating all GT/GE approaches. Appendix 2 contains a table of all the mouse models (with a descriptions, phenotypes, relevance, and utility) that are available for preclinical evaluation of potential GT/GE approaches.

For several years FARA's Scientific Advisory Board has debated the utility of creating a model in a higher animal species. About a year ago FARA launched an effort to create a rat model. This effort continues but creating a rat model carrying expanded GAA repeats within the rat Fxn gene has proved challenging as it is very difficult to generate a template for homologous recombination with very long GAA repeats.

The current clinical pipeline, including GT/GE programs, rests on the foundation of the basic understanding of frataxin deficiency in FA that has emerged from decades of research, much of which was funded by FARA. These insights have resulted in the knowledge that some normal transcript and normal protein is made in every FA patient and the level of frataxin protein is negatively correlated with severity of disease. Restoration of frataxin levels ameliorates relevant phenotypic features in all models. Increasing production of or supplementing frataxin in humans is highly likely to be therapeutic.

FARA established a longitudinal natural history study which began in 2003, the Friedreich Ataxia Clinical Outcome Measure Study (FA-COMS). Today, more than 1250 participants are enrolled and there are 15 participating CCRN in FA clinical sites: the Children's Hospital of Philadelphia/University of Pennsylvania, University of California Los Angeles, Emory University, University of South Florida, University of Florida, University of Iowa, Ohio State University, University of Colorado, St. Jude Children's Research Hospital, University of Rochester, the Hospital for Sick Children, Centre Hospitalier de l'Université de Montréal, Murdoch Children's Research Institute, University of Auckland, and the All India Institute for Medical Sciences. This natural history study has contributed significantly to our understanding of the disease course and the development of outcome measures and biomarkers. It has also established the infrastructure for conducting more than 10 FA clinical trials and generated more than 30 scientific publications. Data from FA-COMS, along with data from five clinical trials, are available through the Critical Path Institute (C-Path) in the Friedreich's Ataxia Integrated Clinical Database (FA-ICD). These data have also been integrated into C-Path's new Rare Disease Cures Accelerator-Data and Analytics Platform (RDCA-DAP). Access to these data helps to catalyze and accelerate FA research and drug development. For example, qualified researchers and drug developers have used the data to design efficient and robust clinical trials. Borrowing from the natural history and clinical trial data available in FA-ICD can be an external source used in a Bayesian adaptive design. Borrowing data from these studies via informative prior distributions can improve efficiency of the trial, reducing placebo group size. Use of the data in this way is consistent with the 2019 FDA guidance "*Adaptive Designs for Clinical Trials of Drugs and Biological*". Please see Appendix 1 for a detailed discussion of the natural history study and clinical trial data in FA-ICD.

The natural history study, FA-COMS, has been instrumental for informing clinical development for many therapeutic approaches, including the development of endpoints and biomarkers. FA-COMS has been primarily focused on monitoring and measuring the neurological symptoms of FA with some data collected on cardiac disease, vision changes, scoliosis, diabetes and other medical conditions and medications. The Friedreich's Ataxia Rating Scale (FARS) was developed to include neurologic signs and functional assessments reflecting specific neural substrates that are affected in FA [Subramony 2005]. Alongside the neurological exam the concept of measuring FA disease severity also provides other instruments, such as a Functional Disease Staging (FA-FDS), scored 0 to 6 assessing overall mobility (e.g., 5 being non-ambulatory), an activities of daily living scale (FA-ADL, scored 0 to36), the Timed 25-foot walk (T25FW), and the 9-whole peg board test (9HPT).

The FARS has high ICC values for most of its components and has demonstrated good interrater reliability. Components of the FARS neurologic examination correlate well with ADL and FDS scores, demonstrating construct validity of the scale as a measure of FA. The first publication demonstrating utility of the FARS score in the natural history study in its complete version was in 2006 [Lynch 2006]. Psychometric properties [Rummey 2019], the assessment of loss of ambulation and clinical relevance [Rummey 2020a], as well as longitudinal progression [Patel 2016] in the FACOMS study have been subject to extensive evaluation and have led to modification of the scale. Removing items of limited functional significance improved the measure, creating the modified FARS or mFARS [Rummey 2019] and subsequent studies have demonstrated the test-retest reliability of the mFARS [Rummey 2020b].

Using FA-COMS data, Rummey et al propose clinical trial enrichment strategies using a stratification paradigm for patients based on time to loss of ambulation (LoA) [Rummey 2020a]. A sequence of a unique pattern of function loss, specifically stance/balance items in subscale E of the mFARS exam, predicts future risk of LoA and can be used to rank patients in their individual progression. These data also suggest that a change in the rate of progression to LoA has potential use as an outcome measure in clinical trials.

In summary, FARA sits at a unique interface between patients/ families and the research /drug development communities. We appreciate the opportunity to share our hard-won knowledge and to suggest solutions to support scientifically sound and efficient strategies for developing gene and gene editing therapies for FA.

6 PREVIOUS THERAPEUTIC TRIALS AND CLINICAL OUTCOMES

There is currently no approved treatment for FA. Several drug candidates have been tested in Phase 1, 2 and 3 clinical trials, but most have not reached their primary endpoints. The majority of these drug candidates address the impact of mitochondrial dysfunction by blocking the downstream consequences, including low energy production (idebenone) [Lynch 2010, Meier 2012, Lagedrost 2011], high levels of ROS leading to oxidative stress (EGb-761; Oxigon, [Rodríguez 2020]), lipid peroxidation and ferroptosis (deuterated polyunsaturated fatty acids, aka RT001, [Zesiewicz 2018] PTC 743 [Lynch 2012]), high mitochondrial iron levels (Deferiprone, [Greeley 2014]), or inflammation (methylprednisolone, [Tsou 2011]). None of these approaches provided sustained significant clinical benefit.

The peroxisome proliferator-activated receptor gamma (PPARγ)/PPARγ coactivator 1 alpha (PGC-1α) pathway is dysregulated when frataxin levels are low [Coppola 2009, Marmolino 2010]. This may be because PPARγ plays a key role in mitochondrial function and biogenesis, fatty acid storage, energy metabolism, and antioxidant defense. A proof-of-concept trial with pioglitazone, a well-known PPARγ was completed in 2013 but the results have not been published. In December 2020, Minoryx Therapeutics reported results of a Phase 2 clinical trial of their compound leriglitazone, an orally bioavailable selective PPAR gamma agonist that is one of the metabolites of pioglitazone. Treatment with leriglitazone resulted in PPARγ engagement as assessed by the relevant biomarker (adiponectin). Results of the trial show modulation of the frataxin pathway and restoration of the bioenergetics deficits in FA patients.

One potential treatment addressing the consequences of loss of frataxin is omaveloxolone, a potent activator of nuclear factor erythroid 2-related factor (Nrf2) [Reisman 2019]. FA cells have impaired Nrf2 signaling and decreased levels of Nrf2-mediated endogenous antioxidants, making the cells particularly vulnerable to oxidative stress [La Rosa 2020b, La Rosa 2020a, Chiang 2020]. Omaveloxolone activates Nrf2 in FA cells and improves mitochondrial function [Abeti 2018]. In clinical trials, omaveloxolone significantly improved neurological function relative to the placebo control group and was well tolerated [Lynch 2021a, Lynch 2019]. Reata Pharmaceuticals has filed an NDA for omaveloxolone for the treatment of FA. From the current clinical data, it is not clear if Nrf2 activation can address all the deficits resulting from frataxin loss in all subgroups of FA patients, in all affected, and when it might be most efficacious during the course of the disease. Additionally, this therapeutic does not address the root cause of FA, low levels of the essential protein, frataxin. The function of frataxin is not fully understood and may include functions not addressed by activating Nrf2. Although this may become the first approved therapeutic in FA, the need to find additional effective therapies for FA remains.

In the omaveloxolone pivotal trial, mFARS was used as the primary endpoint. The MOXIe study, a safety and efficacy study of omaveloxolone in FA, measured changes from baseline in mFARS scores in omaveloxolone and placebo patients, demonstrating that omaveloxolone significantly improved neurological function compared to placebo [Lynch 2021a]. In the planned Phase 2/3 study of vatiquinone (aka PTC 743) the primary endpoint is a change from baseline in the mFARS score (https://www.clinicaltrials.gov/ct2/show/record/NCT04577352 ?term= Vatiquinone+%28PTC743%29&draw=2&rank=3). The MOXIe trial provided important

validation of mFARS in clinical development programs; additional ongoing trials will provide further support for this endpoint [Rummey 2019].

Between 2009-2020, over a dozen small molecule library screens and several siRNA screens have been carried out to identify targets or pathways that can effectively increase frataxin levels. Drug candidates reported to increase frataxin levels include interferon gamma, calcitriol, resveratrol, and kinase inhibitors. However, more recent studies suggest that modest increases in frataxin can be seen in cell models treated with a variety of compounds with no clear mechanistic link. Instead, data appears to be emerging that these small, acute increases in frataxin may be a stress response, rather than specific target-driven increases that would be sustained and therapeutic. Additional small and large molecule approaches with the potential to either increase frataxin levels or replace frataxin in function continue to be evaluated.

Because FA is a complex, multi-system disease, it is likely that multiple complementary therapies and a diversity of approaches may be needed to treat all manifestations of FA throughout the course of the disease. The community is actively engaged in supporting clinical development through providing funds for basic research and leading patient engagement meeting with sponsors and participation in trials. Adding gene therapies and gene editing approaches to the armamentarium is key to fully treating this devastating disease.

Figure 5 Pipeline of Potential Therapeutics Programs Known to FARA

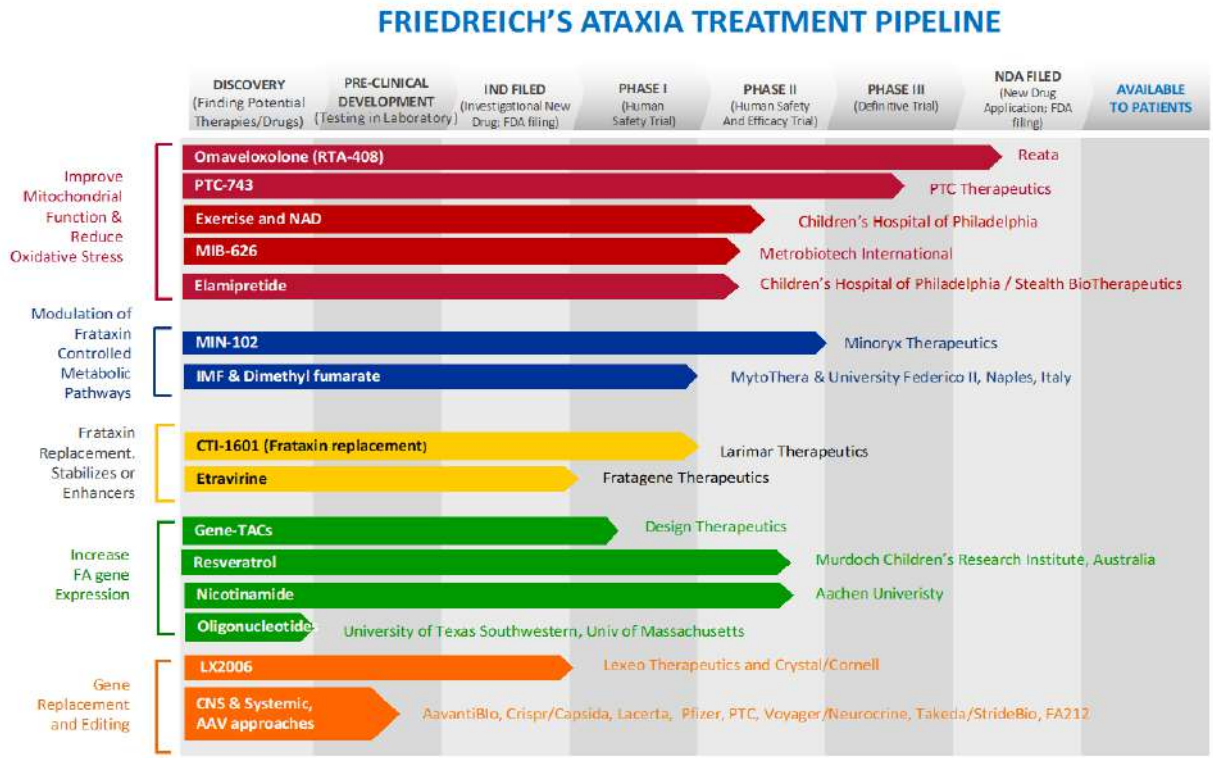

7 RATIONALE FOR GENE THERAPY AND GENE EDITING APPROACHES FOR FA

The root cause of FA is low levels of frataxin. As reviewed above, to date, the search for frataxin mimetics or substitutes has not been successful. However, heterologous frataxin gene expression via gene therapy or de-repression of the frataxin gene to enable endogenous gene expression via gene editing are likely to provide a profound therapeutic benefit, provided the gene therapy or gene editing therapeutics can reach enough cells in the target tissues before such tissues have developed irreversible damage. Phenotypic correction of cardiac and neurological symptoms in conditional knockout models after AAV-mediated gene transfer has been reported in peer-reviewed journals [Perdomini 2014, Piguet 2018, Gerard 2014, Salami 2020]. At the 2022 American Society for Gene & Cell Therapy Annual Meeting seven different groups presented their research efforts to develop and characterize the efficacy and safety of AAV gene therapy and *ex vivo* gene editing, demonstrating the interest in and promise of these modalities. There are, however, special considerations related to the development of cardiac, neuronal, and ocular gene therapy or gene editing therapeutic approaches in FA.

Homologous recombination and nuclease-mediated excision of the expanded GAA repeats in iPSC derived FA neurons significantly increased frataxin expression, normalized gene expression changes, and reversed disease-associated phenotypes [Li 2015, Lai 2019]. One study showed successful CRISPR-Cas9 editing of the GAA expansion in vivo following delivery by electroporation in the Tibialis anterior of the YG8R mouse [Ouellet 2017].

One important concern is the finding that supraphysiologic levels of frataxin result in cardiomyocyte and hepatocyte dysfunction and death after AAV-mediated frataxin gene transfer in murine frataxin knockout models and wild type mice [Belbellaa 2020, Huichalaf 2022]. In an unpublished study reviewed at the 2022 ASGCT meeting, Hinderer et al reported cardiac and neurological toxicity after AAV-meditated frataxin gene transfer in non-human primates [Hinderer 2022]. The observations in Belbellaa and Huichalaf suggest that the frataxin overexpression-associated toxicity threshold may differ by organ and that capsid serotype and expression cassette design may influence the vector biodistribution and frataxin expression levels. Furthermore, expression levels differ between wild type vs. transgenic models treated with the same vector and dose [Belbellaa 2020, Huichalaf 2022]. Consequences of frataxin toxicity also appears to develop over time so the duration of toxicity studies should account for this. Taken together, these data indicate that the preclinical data packages to support a clinical trial should include determination of the level of frataxin protein expressed with the proposed gene delivery construct or after gene editing relative to levels of protein in wild type cells. Additionally, we propose that the impact of the protein expression on cellular function and survival should also be assessed to ensure that the proposed therapeutic maintains frataxin levels below the threshold for toxicity.

An understanding of the relevant measures of FXN expression after GT/GE for assessment of efficacy and dose selection is unclear. Frataxin is an intracellular protein which exerts most of its biological activity within the mitochondria. Belbellaa et al [Belbellaa 2019] demonstrated a direct relationship between the percentage of cardiomyocytes transduced with the rescue of Fe-S enzyme activity, iron metabolism and mitochondria homeostasis, with no cross-correction

between transduced and un-transduced cardiomyocytes. Thus, only FA cells that are transduced or edited resulting in increased frataxin levels below the toxic threshold will achieve restored function. Belbellaa et al [Belbellaa 2019] also demonstrated that full rescue of cardiac function and hypertrophy was achieved with vector doses resulting in transduction of ~50% of cardiomyocytes, while meaningful therapeutic effect was achieved with transduction efficiencies as low as 30-40%. We propose that the preclinical development for GT/GE products should include an assessment of the percentage of cells transduced/edited in the target tissue as well as an assessment of the degree of functional rescue achieved in that tissue. For GT, additional important data would include an assessment of whether this percentage of correction is significantly different across impacted tissue in preclinical models when the proposed clinical vector and promoter is used. However, this may not be possible to assess with a GE approach, as the final clinical construct may not be able to edit in the preclinical model because of differences in the sequence between clinical population and the preclinical model. Since construct design or gene editing approaches can result in varied levels of FXN expression in the transduced/edited cells, the percentage of corrected cells in a target tissue/organ is a more relevant correlate of efficacy than total frataxin protein levels in a tissue lysate.

In FA patients the FXN coding sequence remains intact, leading to the production of a normal FXN protein, albeit at low levels. Previous work suggest that epigenetic mechanisms contribute to silencing of the frataxin gene. Therefore, epigenetic editing may result in increased transcription of FXN mRNA and consequential protein synthesis. This mechanism would potentially avoid the FXN overexpression induced toxicity. Epigenetic therapy approaches focusing on the recruitment of transcription factors that allow for chromatin remodeling, and RNA polymerase recruitment and initiation are novel alternative approaches, utilizing the native exons devoid of mutations.

The clinical relevance of frataxin measurement as a biomarker in blood or CSF samples as indicators of bioactivity and target organ transduction/editing has not been demonstrated. Human full length frataxin (210 amino acids, MW 23,135 Da) has an N-terminal mitochondrial targeting sequence which facilitates translocation to the mitochondria. The protein is proteolytically cleaved by mitochondrial processing peptidase in a two-step process to first produce an intermediate form (aa 42-210, MW 18,826 Da) and then to produce mature frataxin (81-210, MW 14,268) [Schmucker 2008]. A form of extra mitochondrial frataxin is also found that appears to be a splice variant [Guo 2018]. This form is called isoform E because it is found in long lived erythrocytes. Isoform E lacks a mitochondrial targeting sequence. Sensitive quantitative methodology to measure all frataxin isoforms in blood have been developed [Wang 2022]. The assay, based on stable isotope dilution coupled with immunoprecipitation (IP) and two-dimensional-nano-ultrahigh performance liquid chromatography/ parallel reaction monitoring/high resolution mass spectrometry (2D-nano-UHPLC-PRM/HRMS), may also be useful for other tissues. Mature frataxin, isoform E, and total frataxin levels inversely correlate with GAA repeat length in those patients with two expanded alleles. There is also a direct correlation with frataxin levels and age of onset of the disease. However, changes in frataxin levels in target organs (heart, brain) achieved via GT or GE are not likely to be reflected in blood levels as frataxin is not secreted. Frataxin is not abundant in CSF, but sensitive assays can detect very low levels. It is unclear how to interpret changes in CSF frataxin levels measured after GT or GE. Therefore, we suggest that it would be necessary to demonstrate the relationship between

frataxin levels in an accessible compartment relative to target tissues prior to using frataxin levels as a target engagement biomarker.

Complete knock out of the frataxin gene is embryonic lethal. However, mouse models that knock out one allele in most tissues while selectively knocking out both alleles in tissue specific manner have proven useful in studying the disease and in profiling potential therapeutics. For example, versions of the FXN $^{flox/null}$::MCK-Cre that is compound heterozygous at the frataxin locus and hemizygous for MCK-Cre have a profound cardiac phenotype of hypertrophy, myocardial degeneration, fibrosis, and shortened life span [Puccio 2001]. A second cardiac tissue specific knock out mouse (Fxn KO/Fxn LoxP αMyhc-Cre; [Salami 2020] has a mild phenotype, with normal heart function at rest, but exhibits a cardiac phenotype when stressed. In the more severe model, gene therapy studies have provided data on the percentage of transduced cardiomyocytes that resulted in phenotypic correction and increased survival, information that can inform dose selection for human gene therapy trials. Unfortunately, tissue selective knock outs of frataxin in the CNS or the eye do not reflect human disease anatomically and therefore, extrapolation from preclinical PoC models to human for efficacy dose setting is less reliable. A weight of evidence approach, taking into consideration *in vitro* efficacy, *in vivo* efficacy and model limitations is proposed as the best solution when the models do not authentically represent the human disease. Obviously, knock out models are not useful for assessing GE approaches.

Finally, FA impacts multiple tissues, including the heart, peripheral nervous system, and the central nervous system. Current gene delivery methods will require multiple routes of administration to target brain, heart, and eye, but immune responses to AAV capsids may preclude ability to redose to address compartments not targeted by the first of vector administration. FA patients are weighing the benefit/risk of treating specific disease manifestations or tissues against the current limitations of one-time treatment due to immune response with re-administration or exposure to AAV. For some, a more rapid progression of cardiac disease would justify a cardiac specific approach that has little or no chance of treating CNS manifestations of FA. For others, maintaining neurological function is the highest consideration, because the cardiac changes may be mild and stable.

When considering development of GT/GE that would be simultaneously delivered product to more than one tissue (e.g., IV to treat heart and IT to treat brain), the available preclinical models do not provide an opportunity to simultaneously evaluate efficacy in multiple tissues. Therefore, it will be necessary to leverage multiple model systems, both *in vitro* and *in vivo*, to assess potential for therapeutic benefit.

8 CARDIOMYOPATHY IN FA

Cardiac abnormalities are a major concern for FA patients and the leading cause of early mortality. Mouse models alone or in combination with *in vitro* cellular models can allow assessment of potential therapeutic benefit of GT/GE. Clinical measures and GAA repeat length predict those most likely to progress to heart failure and a weight of evidence of stabilization/improvement in cardiac structural and functional biomarkers, coupled with patient reported outcomes (PROs), evidence of cardiomyocyte transduction and/or restoration of mitochondrial function could provide evidence of therapeutic activity that would predict clinical benefit.

8.1 Clinical Phenotype Description and Progression

In FA, hypertrophic cardiomyopathy is present in most patients at the time of diagnosis [Hanson 2019]. Echocardiographic findings include left ventricular (LV) hypertrophy with generally preserved systolic function early in disease; outflow tract obstruction (as is more often seen in non-FA hypertrophic cardiomyopathy) is notably absent in most FA patients. High-sensitivity troponin T/troponin I plasma concentrations are detectable and higher in FA patients than healthy controls [Legrand 2020b], although only rarely in association with coronary artery disease. The LV hypertrophy may increase initially, but for some an eventual decrease in LV wall thickness along with LV dilation and dysfunction occur. Cardiac magnetic resonance imaging (cMRI) findings include significant concentric left ventricular remodeling and focal myocardial fibrosis in 50% of patients [Legrand 2022]. Nonspecific ECG abnormalities are almost always present [Schadt 2012, Salih 1990, Alboliras 1986, Harding 1983], and supraventricular ectopy is common [Mejia 2021, Ribai 2007]. Arrythmias are also common in FA. Supraventricular arrythmias are also common [Pousset 2015] and may contribute to mortality. Patients sometimes receive implantable defibrillators and pacemakers. Cardiac disease is more severe in those patients with early onset of neurological symptoms and longer GAA repeat length. However, cardiac disease and severity of neurologic disease do not show any relationship if GAA length or age of onset is accounted for [Pousset 2015].

Unfortunately, these insights into how biomarkers and other measures change with disease progression have been gleaned from small cohort studies or cross-sectional analyses of patients at different time points post diagnosis. There is currently a lack of detailed longitudinal data on these measures in a large patient group. FARA has begun a three-year retrospective natural history study via a multi-center, collaborative project, led by Kim Lin, MD, Medical Director of Cardiomyopathy at Children's Hospital of Philadelphia, to collect cardiac and other relevant data from several clinician scientists who treat a significant number of FA patients and have at least 5 years of prior data. Echo images will be re-read at a single site to standardize methodology, and additional cardiac data will be collected whenever available to better characterize the cardiac phenotype in FA. These retrospective data will be analyzed to better describe the natural history of cardiac disease in FA and to identify predictors of adverse cardiac outcomes in FA. However, until this three-year study is completed, extrapolations from smaller studies and cross-sectional analyses provide the best predictors of the course of cardiac disease in FA.

Assessment of cardiac health in FA is also confounded by the neurological aspects of the disease. The commonly used classification system, the New York Heart Association (NYHA) Functional Classification, is based on assessing limitations during physical activity. Balance and coordination issues limit the ability to perform physical tasks, including walking or other types of exercise. Even early-stage patients have lower limb ataxia and weakness that interferes with assessment of cardiac function by cardiopulmonary exercise testing (CPET) using the classic cycle ergometer. However, recent studies demonstrate that upper arm ergometry is an equally effective and safe non-invasive method to assess cardiovascular performance and exercise tolerance in FA [Pane 2022]. Using CPET, FA patients had elevated ventilatory flow/exhaled volume of carbon dioxide and an abnormal left ventricular diastolic filling.

The patients most likely to benefit long-term from heart-directed GT/GE are those that have progressive cardiomyopathy but have not yet experienced excessive cardiac dilation and fibrosis. In adults, longer GAA repeats in the shorter allele, with the presence of decreased left ventricular ejection fraction predict worsening of cardiac function over 12-24 months [Pousset 2015, Legrand 2020b]. Hypertrophic cardiomyopathy is found in many children with FA prior to adolescence, but the time course of progression to later stage disease (fibrosis, loss of systolic function) is unpredictable. Children with very long repeats may experience rapid decline in cardiac function; there is a rare and severe form of FA where young children present with severe cardiomyopathy prior to the onset of neurological symptoms. Children have received cardiac transplants who were later diagnosed with FA [McCormick 2017]. Thus, although GT/GE therapeutics may be beneficial in adults, in whom trials would be more straightforward due to a better likelihood of measurable disease progression, enrolling children is also essential to preserve as much cardiac function as possible.

Several heart transplants (HT) have been performed in FA patients. McCormick et al. [McCormick 2017] reported three cases with favorable long-term follow up. In one of these cases, FA was diagnosed after HT. Several other reports of successful HT in FA include at least twelve patients, two of whom were emergency HT due to cardiac arrest [Segovia 2001, Valero 2022]. Thus, FA patients would likely be good candidates for GT/GE treatment prior to progression to severe heart failure requiring a transplant.

8.2 Patient Perspective

At the externally led Patient-Focused Drug Development (PFDD) meeting hosted by FARA in June 2017, patients and parents of FA children expressed that while a cure for FA is needed, short of a cure they would find a slowing or stopping of disease progression to be very valuable. Treatment of individual symptoms, particularly cardiomyopathy, is meaningful as it is a major concern related to disease progression. The figure below (Figure 6) reports on the survey question, *As disease progresses, development or progression of which of the following symptoms worries you the most? [Respondents could select up to 3 symptoms]. There were 142 responses.*

Figure 6 Survey Responses

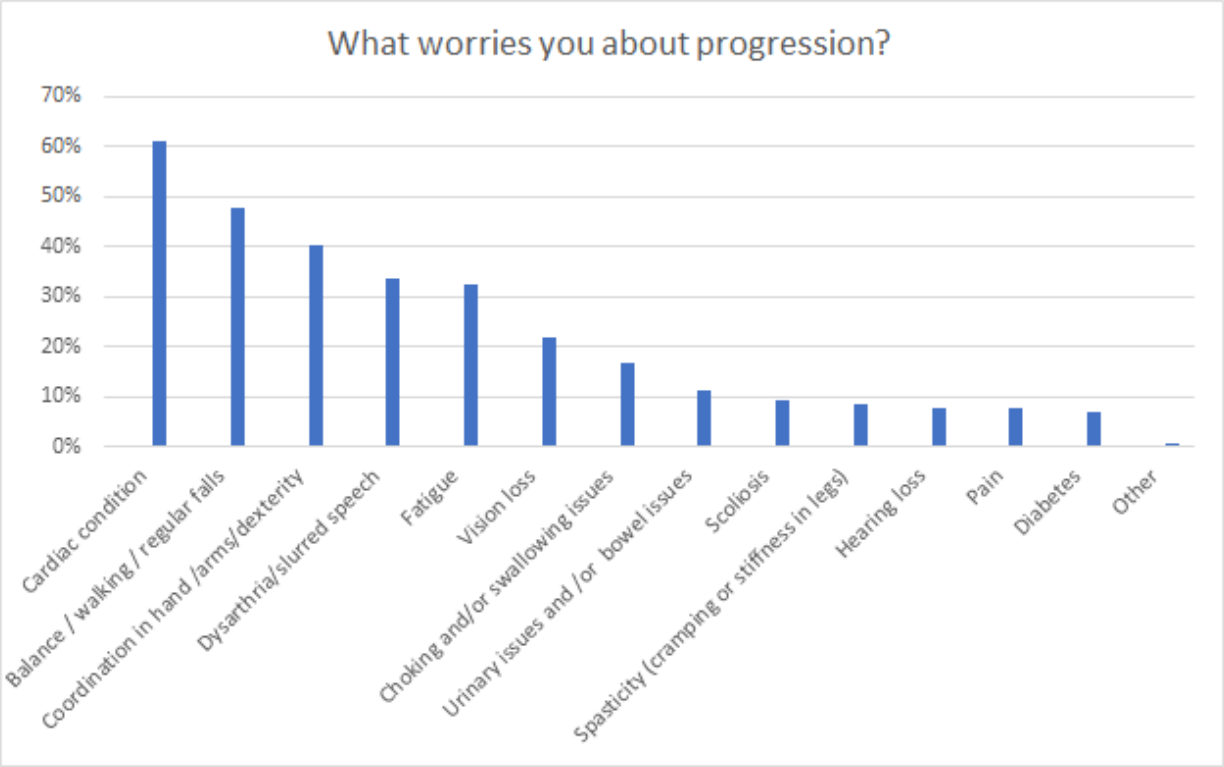

See below quotes from patients and parents.

> *"The cardiomyopathy is the biggest stress. It is an unknown – how will it progress? That is what kills."*

> *"My heart is on the losing side of this battle. A premature death, that you hear in all the literature, is becoming apparent. I'm not scared of it, but I'm sure my family worries every single day."*

Cardiac dysfunction is the eventual cause of death for approximately 60% of FA patients [Tsou 2011, Hewer 1968]. In addition, cardiomyopathy may contribute to fatigue, which significantly impacts quality of life.

> *"One of my biggest problems is dilated cardiomyopathy. This makes it very hard staying active for any long period, especially if I am in a hot and humid environment."*

> *"She doubts her ability to swim laps for swim team and keep up with lacrosse teammates during basic drills, due to her inconsistent heartbeat."* Mother of a newly diagnosed 5th grader.

In summary, in most patients, cardiac abnormality is present early in disease as cardiac hypertrophy. The rate of progression is variable but cardiac complications are the most common cause of early mortality. Treating cardiac disease is meaningful to patients, especially those who

are symptomatic or present with predictive markers associated with higher likelihood of adverse cardiac outcomes. Fatigue is major symptom of FA (majority of patients report as one of the most important symptoms for treatment/impact on daily activities and quality of life) for which cardiac dysfunction may be one of several contributing factors.

8.3 Tissue Pathology and Target Cells

Low levels of frataxin in the FA heart is associated with iron deposits within the cardiac tissue and extensive loss of contractile fibers with replacement by fibrosis. Cardiomyocytes are damaged in the disease, displaying hypertrophy, apoptosis, and fibrosis. Enlarged cardiomyocytes seen in autopsy tissue are also detectable in FA patients by MRI measurement of cardiomyocyte intracellular lifetime water (τ_{ic}) [Koeppen 2015, Ramirez 2015, Crombie 2017, Takazaki 2021]. In addition, cultured cardiomyocytes derived from patient iPSCs exhibit a lipid metabolism defect as well as transcriptome changes characteristic of hypertrophic cardiomyopathy [Li 2019].

More recent data suggests that the vascular endothelium and autonomic neurons in the heart may also contribute to the pathophysiology of cardiac disease in FA. Evidence of diseased vasculature and autonomic dysfunction are seen in FA and could contribute to cardiomyocyte necrosis, fibrosis, and arrhythmias [Culley 2021, Lees 2022]. In advanced stages of disease, fibrosis, and the presences of inflammatory infiltrates, considered secondary to vascular damage, are observed [Koeppen 2015].

8.4 Animal and Cellular Models for Proof of Concept

The *Mck* mouse model (FXN $^{flox/null}$::MCK-Cre) is compound heterozygous at the frataxin locus and hemizygous for the muscle creatine kinase (*Mck*) promoter, to create a cardiac and muscle specific frataxin knock out. These mice display histological evidence of cardiac hypertrophy, myocardial degeneration, necrosis and in later stages, fibrosis [Puccio 2001]. Mitochondria in the heart are abnormal, with membrane disruption and iron deposits. There are deficits in respiratory chain complexes I–III and aconitase and succinate dehydrogenase activities in cardiac tissue from these mice. *Mck* mice show progressive body weight loss and die at approximately 11 weeks of age [Puccio 2001] with an increasing heart to body weight ratio reflective of cardiomyopathy. Of note, the skeletal muscle does not show any histological or biochemical defect, which might be due to the early mortality from cardiac disease. While the *Mck* mouse replicates the pathophysiological and biochemical features of the cardiac disease in humans, the time course for development of these is very rapid compared to the human. This may be because the mouse is a complete knock out, while all FA patients produce at least some frataxin.

As discussed above, gene therapy rescues the cardiac phenotype of the *Mck* mouse. Full rescue of cardiac function was achieved with an AAAVrh10.CAG-hFXN-HA vector administered IV, at both pre-symptomatic (3 weeks) and symptomatic (7 weeks) time-points. Dose ranging studies coupled with assessment of cardiac transduction, provided a correlation of percent cardiac transduction with functional rescue [Perdomini 2014]. At the 2022 ASGCT meeting various academic and industry groups also reported on efficacy and safety in the *Mck* model with AAV vectors based on AAV9 [Perez 2022, Huichalaf 2022], AAV7 [Hamm 2022], AAV8 [Chang 2022], and rh10 [Zuluaga 2022, Belbellaa 2020].

Subsequent studies have demonstrated that strong overexpression of frataxin protein induces a toxicity related to frataxin function in iron-sulfur cluster biogenesis [Belbellaa 2020, Huichalaf 2022]. Dose levels resulting in cardiac toxicity varied with construct design and FXN expression levels [Belbellaa 2020]. In Huichalaf et al [Huichalaf 2022] an AAV9.CAG.hFXN construct resulted in cardiac toxicity at all doses tested and was associated with dramatic weight loss and only partial transient improvement in cardiac function. Additionally, unlike Belbellaa et al [Belbellaa 2020] dose dependent hepatocyte toxicity was observed in the AAV9.CAG.hFXN treated *Mck* mice. In the heart of knock out mice, the level of frataxin mRNA associated with toxicity was 50 to over 700-fold higher than the levels in wild type (WT) animals [Huichalaf 2022], whereas protein levels greater than 20-fold over WT were found to be toxic [Belbellaa 2020]. Protein levels less than 9-fold above WT were not associated with toxicity. However, these levels were not generalizable to all tissues as liver appeared to tolerate much higher levels of frataxin without evidence of toxicity. These two studies also suggested that WT animals are less sensitive to frataxin induced toxicity in the heart when compared to cardiac knock out models, underscoring the need to include safety assessments in the preclinical proof of concept and efficacy studies for GT/GE products. Hinderer et al [Hinderer 2022] reported delayed cardiac toxicity in non-human primates with an unspecified AAV vector, highlighting the importance of long-term studies to assess toxicity associated with *FXN* overexpression.

A second mouse model, the αMyhc cardiac-specific knock out, expresses 50% lower levels of frataxin relative to wild-type cardiomyocytes and activity of the mitochondrial complex II/complex IV respiratory chain is reduced by ~56% [Salami 2020]. The cardiac function of αMyhc mice is normal at rest but exhibits a reduced stress response, with lowered ejection fraction and fractional shortening after dobutamine challenge. Salami et al [Salami 2020] demonstrated that AAVrh10.CAG.hFXN-HA restored the ability to respond to chemically induced stress in αMyhc mice to WT. Additionally, treated αMyhc mice had restored exercise tolerance on a treadmill test compared to untreated mice.

While Salami et al did not include assessments for cardiotoxicity, these studies used the same vector AAVrh10.CAG.hFXN-HA as [Belbellaa 2020] at a dose orders of magnitude below those associated with toxicity. This study provides additional proof of concept for the potential of AAVrh10-mediated FXN gene therapy. However, while the degree of FXN knockout in the MCK model is more extreme than found in FA patients, the reduction in the αMyhc mice is only to levels found in heterozygous carriers, possibly compromising the utility of the model for dose selection for the clinic [Salami 2020].

While conditional knock out mouse models are useful in evaluating frataxin replacement strategies including gene therapy, they cannot be used to evaluate gene editing approaches, as they do not harbor GAA repeats. Mouse models with the human frataxin gene including expanded GAA repeats provide the opportunity to assess editing efficiency and increases in frataxin message and protein. The YG8 or Pook series of mice harbor one or two copies of the human FXN locus transgene (YAC construct) randomly inserted, on a mouse frataxin knock-out background [Pook 2001, Al-Mahdawi 2004, Al-Mahdawi 2006, Clark 2007, Al-Mahdawi 2008, Anjomani Virmouni 2014, Anjomani Virmouni 2015]. Jackson labs carries the Fxn null::YG8s(GAA)>800 mice – a human FXN YAC transgenic mouse model harboring a global null allele of mouse frataxin (Fxn null) and the human FXN YAC transgene small repeat YG8s (contracted integration to a single copy of the human FXN gene) with >800 GAA trinucleotide

sequence repeats. Jackson Labs also carries YG8sR that are similar but carry shorter repeats [Anjomani Virmouni 2015]. The repeat numbers in these mice, especially the longer repeats, show intergenerational and somatic instability [Anjomani Virmouni 2015, Al-Mahdawi 2004]. Since the YG8sR mice harbor the entire human FXN gene and a large GAA tract, they represent the best FA model to test therapeutic approaches aimed at excising the expanded GAA repeats. However, unpublished reports have suggested possible copy number variations within the transgene, which would make measuring editing efficiency challenging. Confirmation of the presence of the target sequence and assessment of copy number of the transgene with multiple probes should be performed within the mouse colony that will be used for such studies.

Despite the long repeats and the lower frataxin levels in the YG8 series mice, these mouse models do not have a robust cardiac phenotype that reproduces the profound pathology seen in human FA. They develop mild, late-onset biochemical changes (iron deposition, mitochondrial enzyme changes) that do not impact life span. Therefore, with the caveats cited above, the repeat expansion mice can be useful models for demonstrating editing of cardiomyocytes that results in increases in mRNA and protein to levels equivalent to human carrier levels and to correlate dose to editing efficiency. We propose that gene editing approaches can use the data from the *in vivo* mouse studies rescuing phenotype by gene replacement approaches to estimate the target percent cardiac cell to be corrected for functional improvement.

Cellular models can be used to establish the functional rescue of FA-induced changes in cardiomyocytes. Multiple academic labs have published protocols for iPSC-derived FA cardiomyocytes and a range of phenotypes such as morphological differences, abnormal calcium handling and abnormal mitochondria have been reported (see the *in vitro* model table in Appendix 2 for details and references). iPSC-derived FA cardiomyocytes exhibit molecular defects characteristic of cardiomyopathy that can be corrected by genome editing of the expanded GAA repeats. Excision of the expanded GAA repeat from cardiomyocytes derived iPSCs resulted in upregulated frataxin expression, reduced pathological lipid accumulation, and reversed gene expression signatures [Li 2015]. We further propose that gene editing approaches can use the data from *in vivo* mouse studies rescuing phenotype by gene replacement approaches to estimate the target the percent of cardiac cell to be corrected for functional improvement. A gene editing drug product will include gene editing payload in an AAV vector capable of transducing cardiomyocytes. The ability of gene editing strategy to achieve a therapeutic level of gene editing needs to be evaluated in NHPs since the transduction profile of AAV capsids can vary substantially between different species. This study can be performed using surrogate NHP gRNAs or gRNAs that target both NHP and human sequences.

8.5 Proposed Approach to Establish Preclinical Proof of Concept

For a cardiac focused approach Mck and αMyhc mouse models can be used to demonstrate proof of concept for FXN gene replacement and can be used to determine the minimal effective transduction efficiency required for rescue of phenotype, confirm that FXN expression levels are below the toxic threshold, and identify the relevant dose ranges. With the caveats outlined above, the YG8s(GAA)>800 mice may be used to assess editing efficiency *in vivo and* confirm restoration of frataxin mRNA and protein expression at non-toxic levels; however, phenotypical rescue needs to be evaluated in *in vitro* FA derived iPSC cardiomyocytes. We propose that these preclinical data, coupled with safety toxicology studies designed to assess both acute and late-

emerging toxicity, should be sufficient to support IND clearance of the GT/GE product. An example of one potential preclinical data package to support development of a GT/GE therapeutic for the heart is included in Appendix 3.

8.6 Clinical Trial Considerations

8.6.1 Diagnosis/Patient Stratification

Most FA patients have cardiomyopathy at the time of diagnosis, but we do not understand what factors contribute to progression to heart failure within a decade in some while others remain stable over an even longer period. In retrospective studies, echocardiography using standard of care protocols has identified markers that are associated with poor outcomes. These include left ventricular ejection fraction (LVEF) and left ventricular wall thickness, particularly when the ejection fraction is below 40%. Higher and stable LVEF predict lower risk of mortality while lower and declining LVEF predict higher risk of mortality over ten years [Legrand 2021], which suggests a paradigm for patient selection in clinical trials focused on cardiac aspects of FA. Longitudinal strain may also be useful in predicting poor outcome, especially in patients with LVEF greater than 40% [St John Sutton 2014]. A 16-year observational study demonstrated that using length of GAA repeat in addition to echocardiographic measures of septal wall thickness and LVEF together were predictors of patients at a higher risk of systolic dysfunction [Legrand 2020a].

In FA, cMRI detects changes in left ventricular modeling, fibrosis, and cardiomyocyte size, all of which may be useful diagnostic measures to determine disease severity. Other cardiac assessments include abnormal repolarization frequently found in electrocardiograms [Legrand 2020a] and atrial or ventricular ectopic burden as measured by Holter monitoring [Mejia 2021].

Cardiac troponins are unlikely to be a useful biomarker for staging or following disease progression in all FA patients. Some patients have higher cardiac troponins as in other cardiac diseases such as ischemia and other forms of cardiomyopathy [Weidemann 2015] but such values occur in some patients without structural evidence of heart disease [Friedman 2013]. In addition, a longitudinal study did not detect a change in high-sensitivity troponin T plasma concentrations over one 1 year [Legrand 2022] suggesting this may not be a sensitive biomarker of short-term disease progression.

Finally, cardiomyocytes derived from FA iPSCs have measurable defects consistent with clinical observations. A positive correlation between frataxin expression and contractility was observed in iPSC derived cardiomyocytes which was rescued by frataxin protein expression by lentiviral transduction [Wong 2019]. Frataxin deficiency in cardiomyocytes is also associated with mitochondrial damage, metabolic dysfunction, and DNA damage [Lees 2022, Culley 2021], which are also expected to be reversed with restoration of frataxin levels. Therefore, levels of frataxin in cardiac tissue, measured by direct biopsy of tissue, may provide useful information to stage patients, and monitor progression.

8.6.2 Biomarkers/Clinical Outcome Assessments

Unlike the progression of the neurological aspects of FA, the rate of progression to a major cardiac event is unpredictable. Use of time to a significant cardiac event as an outcome measure would require very large and long clinical trials ill-suited for this rare disease. Instead, a constellation of quantifiable clinical measures and biomarkers including stable ejection fraction, a reduction in LV hypertrophy without an increase in fibrosis or cardiac dilation as measured by echocardiography or cMRI, cardiopulmonary exercise test performance, and decreases in cardiomyocyte size as assessed by cMRI represent the best markers of changes in the course of the disease.

Repeated echocardiographic assessments of left ventricular ejection fraction (LVEF) and left ventricular wall thickness over 12-18 months may provide evidence of therapeutic impact. Although the clinical manifestation of changes in echo measurements may not be easily demonstrated, stable readings over time, especially in a high-risk group with low LVEF at baseline, is likely to represent a meaningful impact on disease progression.

Cardiovascular performance and exercise tolerance as measured by upper arm or recumbent leg ergometry over time provides another biomarker of cardiac and global function. FA patients have decreased performance as measured by CPET; maintenance of performance or improvements would indicate changes in disease trajectory. Recumbent leg cycle ergometry is feasible and reliable in a subset of FA individuals, leading to its incorporation as an outcome measure in several FA clinical trials including the Reata sponsored trial of omaveloxolone (https://www.clinicaltrials.gov/ct2/show/study/NCT02255435 , the Retrotope sponsored trial of RT001 (https://www.clinicaltrials.gov/ct2/show/results/NCT04102501) and the ongoing NIH sponsored trial at the Children's Hospital of Philadelphia titled NAD+ and Exercise in FA (ExRx in FA) (https://clinicaltrials.gov/ct2/show/NCT04192136).

MRI-based ^{31}Phosphorus magnetic resonance spectroscopy (^{31}P-MRS) has been used to detected dysfunctional bioenergetics in individuals with FA. The myocardial phosphocreatine (PCr) to ATP ratio is reduced to around 60% of normal, consistent with a decrease in mitochondrial energy production even in individuals who had not yet developed overt hypertrophy or contractile dysfunction [Lodi 2001]. Increases in PCr/ATP may represent a functional improvement in bioenergetics, although the degree of change associated with clinically meaningful change has not been established.

IV administration gene therapy is likely to result in transduction of skeletal muscle as well as cardiac muscle. Therefore, it may be possible to assess biochemical changes in muscle (NAD+, enzyme activity) to confirm that GT/GE increases frataxin leads to improved mitochondrial function in muscle, if supported by preclinical data assessing the transduction efficiency of skeletal vs heart muscle. Additional biomarkers in peripheral tissue have been suggested by recent work [O'Connell 2022]. Using a multi-platform approach of mass spec and NMR on plasma samples, a metabolic perturbation, especially related to 1 carbon metabolism, was found to be characteristic of FA. Similar metabolic alterations have also been seen in preclinical mouse models which were corrected by GT (Puccio personal communication).

Left ventricular hypertrophy and concentric remodeling are associated at the tissue level with an expansion of the extracellular volume (ECV) and an increase in cardiomyocyte size as measured by cardiac magnetic resonance (cMRI). A recent study CMR study demonstrated that left ventricular mass, extracellular volume, and intracellular lifetime water (τic), a measure of cardiomyocyte size, were all larger in FA patients [Takazaki 2021]. Serial CMR measures of these markers may be useful in tracking disease progression and potentially therapeutic benefit.

Monitoring an increase in frataxin levels in cardiac tissue pre and post GT/GE represents a meaningful target engagement biomarker. It may also be possible to assess cellular changes that represent recovery of mitochondrial function in cardiac biopsy tissue after treatment. A previous clinical trial (Deferoxamine, Jerry Kaplan, personal communication) took cardiac biopsies from FA patients which were well tolerated in this population. Declines in the procedural risk of cardiac biopsy and the value in assessing target tissue transduction/editing make the risk benefit ratio favorable, especially when the procedure is performed at medical referral centers with necessary technical expertise. A major complication rate of <1% for endomyocardial biopsy, especially at experienced, tertiary, high volume centers is generally cited [Fowles 1982]. In addition, the procedure does not require general anesthesia, which can represent a risk for FA patients. Overall, participants in FA trials have been willing to undergo cardiac, skeletal muscle and skin biopsies when such procedures are performed without general anesthesia and are important for evaluating efficacy of an intervention.

8.7 Proposed Clinical Development Strategy

In FA, there is no single functional clinical measure associated with cardiomyopathy or heart failure, partly because of the physical limitations from the neurological aspects of the disease. However, there are a series of biomarkers (imagining, biochemical measures in heart, blood, and skeletal tissue) that can be assessed that are reasonably likely to be associated with improvement or decreased risk for progression of cardiac disease or heart failure. Of note, FA patients are willing to undergo cardiac biopsy to directly assess pharmacodynamic biomarkers such as frataxin mRNA and protein, and mitochondrial or metabolic markers. An example of one potential clinical development plan for a GT/GE therapeutic for the heart is included in Appendix 3.

8.8 Risk Benefit

Patients and their families are aware that the cause of pre-mature mortality in the majority of FA patients is cardiac disease [Tsou 2011] and fatigue, which may be related to cardiomyopathy, has a significant negative impact on daily function. Although patients understand that systemic GT/GE to treat the heart may limit the ability to be treated for neurological symptoms, those with unstable cardiac disease or at high risk for adverse cardiac outcomes may prioritize treating the heart over treating the CNS. Patients expect treatment effect at the dose they receive, and it would be unacceptable to them to receive a non-efficacious dose that prevents them from future treatment because of immune response.

Patients have the expectation that GT/GE doses they would receive in a clinical trial would have the potential for clinical benefit, especially if the delivery mechanism was likely to exclude the patient from future trials. Thus, even the lowest dose in a trial should be optimized to provide

benefit. Patients are also aware that overexpression of frataxin can lead to toxicity and, unlike small molecule treatments, that GT/GE is irreversible. We have discussed this important difference in FARA led community education meetings. Patients are likely to carefully consider the data supporting dose selection before enrolling in GT/GE trials. Those opting to choose GT/GE for heart will also weigh the impact on participation in future trials if they also may have access to omaveloxolone as well as future non-GT/GE approaches to address neurological aspects of the disease.

While nearly all FA patients do develop cardiomyopathy, those with the longest repeat length and earliest onset of symptoms are at the highest risk to develop the most severe heart conditions. Research to date has demonstrated that longer GAA repeat, greater left ventricular dilation and septal wall thickness are predictors of a drop in ejection fraction, with LVEF as the only independent predictor of mortality [Legrand 2021]. Adults with overt cardiomyopathy have a greater likelihood of easily measurable benefit from GT/GE directed to the heart. Younger patients with severe disease should be considered eligible as quickly as possible, as they are most likely to be at greatest risk from mortality due to heart failure and therefore to receive the greatest benefit from therapy.

In the past, patients have volunteered to provide skin, muscle, and cardiac biopsies for research studies, demonstrating patient understanding of need to assess biomarkers in multiple tissues. In focus group discussions, patients have expressed willingness to undergo minimally invasive procedures, such as cardiac biopsy, if it would provide them more direct knowledge about therapeutic impact/success of the intervention. Patients understand the need to measure baseline levels of frataxin and to subsequently sample to detect changes in frataxin levels, mitochondrial function, and cellular health post treatment. As cardiac biopsies were performed as part of a previous clinical trial with no reported AEs (Deferoxamine trial, Jerry Kaplan, personal communication) the patient community is familiar with the procedure and accepts the risk. In addition, the major complication rate is <1% for endomyocardial biopsy, especially at experienced, tertiary, high volume centers [Fowles 1982].

9 BRAIN AND SPINAL CORD ASPECTS OF FA

Neurological symptoms are universally present in FA and include ataxic gait and loss of balance, incoordination of upper limbs, dysarthria, dysphagia, and oculomotor abnormalities. These symptoms progress and profoundly impact quality of life. However, there are developmental components of the disease that are unlikely to be readily reversed with treatment of adults or older children. These include developmental abnormalities of the primary proprioceptive neurons in the dorsal root ganglia (DRG) as well as early, even pre-diagnosis progressive degeneration, making the proprioceptive system an unlikely candidate for a therapeutic target. Cellular models derived from patient iPSCs, including neurons and DRG organoids, are useful *in vitro* tools for assessing efficacy. *In vivo,* mouse models provide a tool to assess both efficacy and frataxin related toxicity to establish starting doses in clinical trials. Clinical outcome assessment and biomarkers can stage disease, document progression, and be informative endpoints for clinical trials.

9.1 Clinical Phenotype Description and Progression

In 95% of individuals, the first symptoms of FA are abnormal gait and stance. This is most likely due to proprioceptive dysfunction, which usually precedes cerebellar symptoms but is often mild and compensated for by visual control. There is also an early absence of deep tendon reflexes, which may also be the consequence of primary proprioceptive neuron pathology, impairing transmission of sensory information from muscle spindles. FA is also characterized by a profound deficit in joint position and vibratory sense in extremities. The deficits in the proprioceptive system may largely be due to developmental issues versus progressive degeneration [Lynch 2021b]. Upper limb dysmetria is almost always present in patients at the time of diagnosis even under visual control, indicating the onset of cerebellar ataxia. Progressive cerebellar pathology leads to worsening gait, limb and truncal ataxia. Lower extremity weakness and spasticity develops with progression to loss of ambulation and wheelchair dependency [Lynch 2021b]. In advanced disease, upper limb function becomes severely impaired due to pyramidal pathology adding to cerebellar ataxia [Naeije 2021].

Speech is often characterized by mild dysphonia which progresses to dysarthria in later stage disease [Vogel 2017]. Swallowing difficulties (dysphagia) are also common in FA and correlate with disease duration and severity [Keage 2017, Keage 2019].

Oculomotor dysfunction is present and characterized by brainstem-cerebellar circuit disruption. Major findings include saccadic movement dysmetria, fixation instability with square-wave jerks, deficits in tracking and vestibular abnormalities [Rojas 2020, Rojas 2021].

A recent meta-analysis concluded that FA patients have measurable deficits in language, attention, executive function, memory, visuospatial perception, emotion recognition and social cognitive abilities. However, these cognitive deficits are considered relatively subtle and do not cause obvious functional impairment as FA patients achieve advanced degrees, are employed, marry, and raised children. The spectrum of cognitive impairments and correlation with disease severity and cerebellar structural parameters suggest a cerebellar role in the pathophysiology of FA cognitive impairments [Naeije 2022].

Finally, other clinical findings include hearing difficulties when background noise is present although major hearing loss is uncommon. Depression is common but it is unclear if this is a disease-specific symptom or a reaction to the diagnosis and its challenges [Lynch 2021b].

9.2 Patient Perspective

Issues with balance and walking are prominent in FA, with nearly 90% of patients responding to a survey conducted by FARA (Externally Led Patient Focused Drug Development Meeting, 2017) reporting these symptoms. Patients explained that these symptoms had a profoundly negative impact on their lives; a mother described her son's experience with the loss of balance caused by FA, and how this affects his ability to socialize with other children:

> *"… the worst part is the loss of ability to walk. He is left behind…. It is hard to see him getting to where the other kids are, but by then the kids are going somewhere else. He just wants to fit in."*

Manual dexterity is also impacted in the disease, limiting educational and employment opportunities, as well as negatively affecting activities of daily living. Patients report frustration trying to button their clothes, dress, eat and apply make-up. Parents talk about how messy eating and drinking has become for children with FA.

> *"I can't type, which means that I can't get my PhD, which means I can't get my ideal job," explained one patient.*

Slurring of speech, or dysarthria, another major symptom, is cited by many as an important aspect of disease progression, particularly in later stage patients. Hearing impairment compounds communication difficulties, further isolating FA patients. Below is a graphic representation of survey data from the 2017 Externally led patient-focused drug development (PFDD) meeting. The report from this meeting is known as the FA-Voice of the Patients https://www.curefa.org/pdf/news/FA-Voice-of-the-Patient.pdf

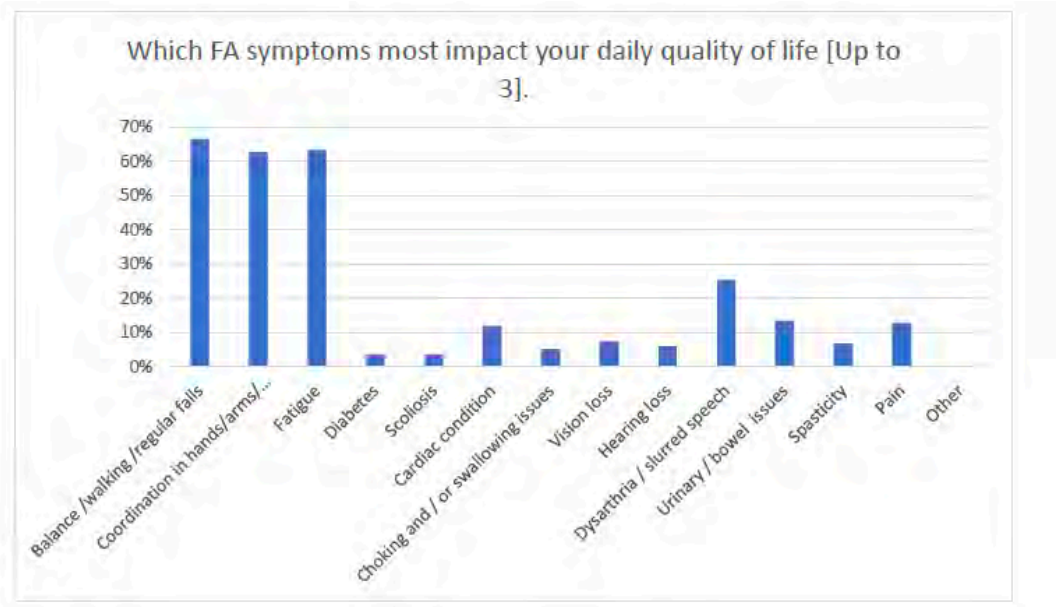

The neurological impairments of FA significantly impact quality of life. As shown in the survey data below, from the PFDD, activities requiring nervous system function are among the top most important activities for most patients.

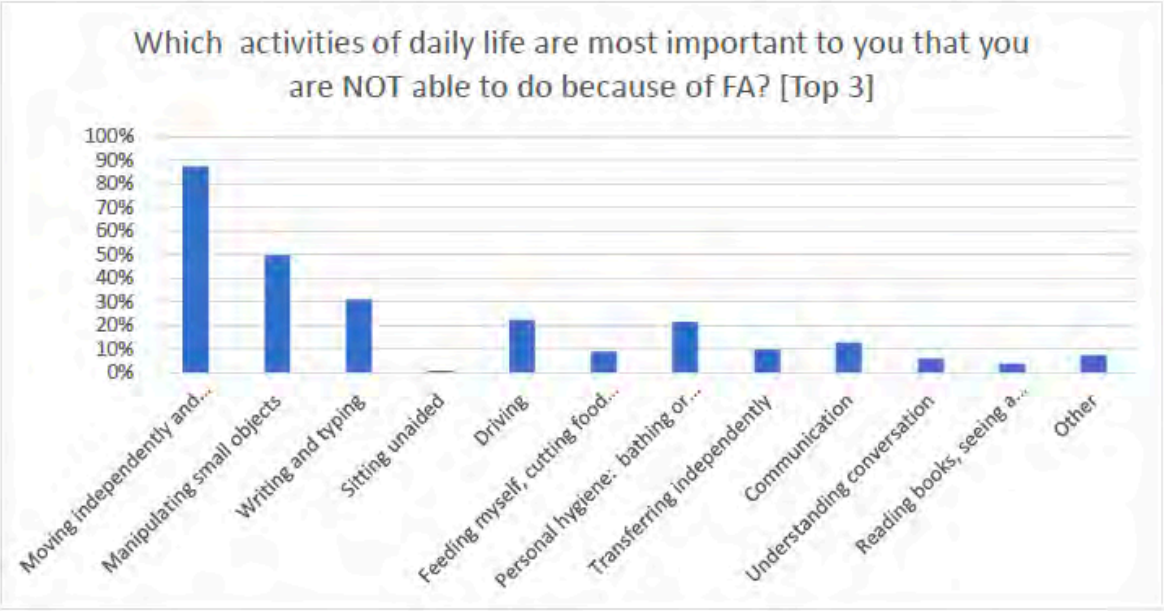

9.3 Tissue Pathology and Target Cells

DRG, dorsal roots (DR), DR entry zones (DREZ), and sensory nerves are affected. The DRG show hypoplasia of both large and small neurons, with evidence of failure to develop normally. There is likely inadequate development of the boundary cap cells, with failure to form a barrier to allow DRG neurons to grow into the spinal cord as well as to prevent CNS glia infiltration. There is also evidence of an ongoing disease process beyond the developmental period, with infiltration of satellite cells and macrophages into the DRG [Harding 2020]. While large proprioceptors are mostly developmentally affected, clinical studies showed progressive impairment in mechanoreceptors, at least until patients become non-ambulatory [Creigh 2019]. Nociceptors can be affected causing neuropathic pain with evidence of small fiber neuropathy [Nolano 2001].

Histological studies demonstrate peripheral sensory nerve hypoplasia with superimposed degeneration of predominantly large sensory nerve axons and associated mechanoreceptors, including Meissner's corpuscles [Koeppen 2013]. These findings reflect the DRG pathology mostly affecting large proprioceptive and mechanoreceptive neurons. The neurophysiological correlate of this pathology is the early loss of sensory action potentials (SAP) and somatosensory evoked potentials (SSEP) in FA, which are non-measurable in most patients [Naeije 2019].

Because the neurons of the DRG may fail to develop normally and may also undergo degeneration very early in FA [Koeppen 2017a], such neurons likely cannot be rescued by GT/GE therapeutic treatment in non-ambulatory adults. In addition, following reports of damage to the DRG due to immune response to viral vectors (especially AAV) or transgene expression [Hordeaux 2020], it would be difficult to monitor for such adverse events in FA because the

already severely compromised function and structure of DRG prevents the use of commonly utilized clinical and electrophysiological parameters.

9.3.1 Spinal Cord

Hypoplasia of the DRG neurons impacts the dorsal columns, as the DRG are the source of the myelinated fibers in the dorsal columns. Axons of the dorsal nuclei of Clarke that travel in the ipsilateral dorsal spinocerebellar tracts also do not develop properly [Koeppen 2017b]. The lack of fibers in the dorsal columns and dorsal spinocerebellar tracts are found in all FA patients. Motor neurons of the spinal cord (lower motor neurons, LNM) are much less impacted in FA, a few clinical signs suggest some LNM involvement such as modest intrinsic hand muscle atrophy and early pes cavus found in typical FA patients. The lack of deep tendon reflexes in FA is likely due to loss of the sensory arm of the monosynaptic stretch reflex arc rather than loss of motor neurons [Harding 2020].

The spinal cord also shows reduced volume, low cross-sectional area, and increased eccentricity (flattening) when imaged by MRI. These changes are evident in all vertebral levels, with most pronounced abnormalities in the upper cervical and upper thoracic sections [Dogan 2019, Rezende 2019, Chevis 2013]. At symptom onset, the spinal cord white matter integrity and thickness are reduced compared to controls and show progressive declines over 1-2 years [Pierre-Gilles Henry 2017, Christophe Lenglet 2018].

Neurophysiological testing also implicates neuronal loss in the corticospinal motor pathways. Motor evoked potentials (MEPs) which require functional integrity of the motor pathways from brain through spinal cord to muscle, are delayed with decreased amplitude which progressively worsen over time. MEP abnormalities can be detected in children with FA, suggesting they are an early manifestation of the disease [Kessler 2019], but they also worsen over time, indicating a progressive degenerative process affecting the pyramidal tracts that can be monitored by measuring MEPs.

9.3.2 Cerebellum

The dentate nucleus (DN) progressively degenerates in FA. The perceived onset of neurological symptoms corresponds to the appearance of cerebellar ataxia and degeneration of the DN [Pandolfo 2020]. Many of the clinical assessments that are part of the FA clinical exam reflect cerebellum dysfunction, and progressive loss of function parallels active degeneration in the DN [Harding 2020]. The atrophy of the DN (as measured by structural MRI) correlates with disease duration but not with age of onset or length of GAA repeats. Neuropathological and imaging studies suggest that the DN are normal before the onset of overt symptoms but atrophy soon after the appearance of cerebellar ataxia [Koeppen 2011]. The DN axonal projections form the dentato-thalamic pathway connecting the cerebellum to neocortical regions via the thalamus, including those regulating motor control but also cognitive and affective processes. Loss of white matter detectable with diffusion MRI is consistent with the atrophy of dentato-thalamic fibers [Selvadurai 2020]. The loss of the large projection neurons from the DN and subsequent neurological dysfunction implicates the DN as a target for GT/GE approaches [Harding 2020]. Progressive increases in iron content as measured by in vivo magnetic resonance imaging including quantitative susceptibility mapping are also evident in the DN [Ward 2019].

The remaining cerebellar cortex is overall preserved at a cellular level in FA, except for degeneration of axonal terminals of the Purkinje cells in the DN, most likely due to the loss of their synaptic targets [Koeppen 2011]. Late in disease progression, imaging detects mild thinning of the primary motor and somatosensory cortices. Other areas appear to be spared [Harding 2021].

In summary, the major anatomical sites that undergo progressive degeneration are likely the dentate nucleus of the cerebellum (the output nucleus) and the corticospinal tract. Volumetric changes in the dentate region and brainstem are evident in structural MRI studies early in the disease and show a linear relationship with disease duration but not age of onset or GAA repeat length [Harding 2020]. Cellular loss in the dentate and corticospinal tracts results in progressive ataxia and later spasticity. Therefore, approaches leading to delivery of the GT/GE therapeutic to the DN is desirable. Currently available GT/GE vectors poorly target these CNS structures when systemically administered. For these reason, multiple routes of administration are being proposed to reach the key targets for FA GT/GE. Intrathecal (IT) administration has been proposed, but studies in animal models, including non-human primates (NHP) have shown disappointing results in terms of CNS biodistribution for commonly used AAV capsids such as AAV9 [Meseck 2022]. More central administration into the CSF via cisterna magna is being explored, but it seems also to have limitations.

FA is a bilateral disease, unlike for example, Parkinson Disease (PD). The projections from the DN to thalamus to motor cortex cross over to the contralateral side so treating one side only would affect motor symptoms only in the contralateral hemibody, which is unlikely to improve and may even worsen the symptomology of FA. The Draft FDA Guidance on Gene Therapy for Neurodegenerative Diseases (2021) recommends that early clinical trials involving invasive surgical procedures, such as would be required for intraparenchymal injection into targeted brain regions, initially involve unilateral injection to establish the safety of the procedure prior to proceeding to bilateral therapeutic injection. However, we recommend that the FDA reconsider this guidance for intraparenchymal injections targeting the DN in FA. The safety of the delivery procedure and potential local and neurologic toxicity can be assessed in non-clinical safety studies in large animal models.

As the axons from the DN form the dentato-thalamic pathway connecting the cerebellum with many neocortical areas, the thalamus may be a target to consider. Bi-directional axonal transport from thalamus, if possible, with the chosen vector, may result in good coverage of cortical and cerebellar targets due to broad connectivity of thalamic projection neurons and their afferents, providing a manner to spread vector far beyond the specific injection site [Naidoo 2018]. Rescue of thalamic neurons may positively impact motor control as well as perceptual and cognitive processes [Harding 2020].

There may be benefit to GT/GE treatment even after the disease has progressed, as ataxia continues to worsen after onset, suggesting an ongoing degeneration. With the current understanding of the major targets of disease however, the consequences of limiting GT/GE delivery to the DN (such as via intraparenchymal administration) are unclear. Both the DN and the corticospinal tract degenerate over time. The macroscopic progression of degeneration in the DN and corticospinal tracts appears to be independent of each other. Speech impairments in late

stages of FA are likely to be due to DN degeneration. There is some concern that pyramidal symptoms may become more prominent if only the DN were rescued in late-stage patients.

Figure 7 Site of Cell Loss and Dysfunction in the Nervous System in FA (courtesy of D Lynch)

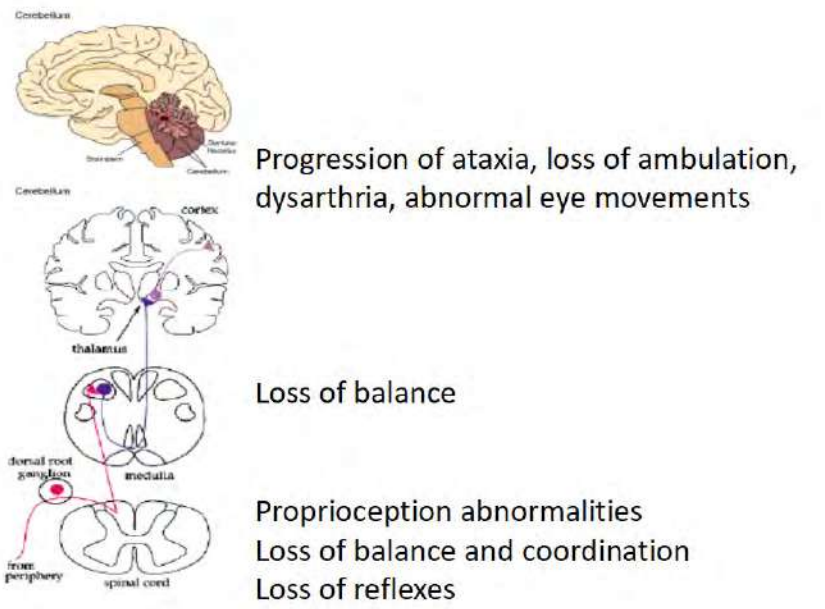

9.4 Animal and Cellular Models for Proof of Concept

While cerebellar changes can be detected in some of the FXN KO/transgenic mice (KIKO; YG8) none fully recapitulate the cerebellar pathology in humans and behavioral phenotypes of these models are not robust. YG8n models have very late onset and mild phenotype, with some reports that the phenotypes are only detectable on some genetic backgrounds or when two copies of transgene are present (personal communication Cat Lutz, JAX). To establish a model that recapitulates the sensory ataxia and neuropathy associated with FA, Piguet et al [Piguet 2018] generated a conditional mouse model specifically targeting complete *FXN* deletion to parvalbumin positive neurons. Consistent with the loss of *FXN* in proprioceptive neurons of the DRG, cerebellar Purkinje cells and deep nuclei the Pvalb cKO mice recapitulated the neurobehavioral phenotypes of FA including early onset of sensory deficits followed by development of cerebellar ataxia. However, unlike in FA, the disease course was rapid, and the mice died within 20 weeks from epileptic seizures, a feature not found in FA patients and likely related in part to the loss of frataxin in cortical neurons. Pathological changes included progressive degeneration and loss of lumbar DRG, Purkinje cells, and sciatic nerve.

Systemic delivery of AAV9-CAG-FXN-HA in early symptomatic Pvalb cKO mice resulted in rapid improvement in coordination and prevented lumbar DRG and sciatic nerve degeneration [Piguet 2018]. Systemic AAV delivery resulted in poor transduction of spinal cord and cerebellum and did not prevent the development of tremors, which necessitated sacrifice at 17.5 weeks. To explore the potential for disease modification in more advanced disease, 7.5-week-old

mice received simultaneous IV delivery of AAV9.CAG-FXN-HA and intracerebral injection of AAVrh10.CAG-FXN-HA to the striatum and cerebellar white matter, resulting in higher brain transduction compared to IV delivery alone. Rapid, complete rescue of the sensory neuropathy was observed with evidence of prevention of lumbar DRG loss and sciatic nerve regeneration. Combined IV and intracerebral treatment did not prevent the development of tremors and animals were sacrificed at 18.5 weeks. Histology at 18 weeks showed significant prevention of Purkinje cell loss compared to untreated Pvalb cKO mice, with evidence of partial correction likely reflecting the incomplete and non-homogenous transduction of the cerebellum. Piguet (2018) did not conduct dose ranging studies and thus data is not available to predict the percentage of cells that must be transduced for phenotypic rescue.

Although more severe than human disease, the Pvalb cKO mouse model has many brain and spinal cord targets that are relevant to for FA. Thus, the model can be used to demonstrate that the putative therapeutic construct is biologically active and to characterize the biodistribution of the vector in the DRG, brain and spinal cord via the intended route of administration. However, while the Pvalb cKO model demonstrates cerebellar dysfunction, the exact cells responsible for the phenotype may not authentically model the disease [Piguet 2018]. Therefore, preclinical PoC studies are likely to demonstrate some benefit in the model, but not complete rescue. Furthermore, due to the incomplete rescue of the phenotype necessitating euthanasia, the model may not be useful for assessment of potential toxicity associated with frataxin overexpression. We suggest that rescue of the sensorimotor and cerebellar phenotype would be sufficient preclinical PoC, which may be strengthen with *in vitro* efficacy data and safety studies in an appropriate large animal species to support initiation of an IND in adult FA patients. Demonstration of safety and potentially evidence of biological activity or effectiveness would provide a basis for beginning studies in pediatric patients.

A knock down model has also been developed [Chandran 2017]. This inducible mouse model uses a genomic integration of a single copy shRNA transgene (doxycycline-inducible) in the rosa26 locus to control modulation of Fxn levels. Systemic knockdown of Fxn in adult mice led to decreased aconitase activity in the heart, with changes in heart wall thickness, DRG pathology and loss of cerebellar Purkinje neurons and large DN principal neurons, weight loss and reduced survival. Restoration of near wildtype FXN levels restores some but not all aspects of the phenotype; restoration appears to correlate better with stopping doxycycline administration than with restoration of frataxin levels [Mercado-Ayón 2022]. To date this model has not been reported to be used to test the efficacy of AAV-mediated frataxin gene transfer.

Gene editing approaches targeting the GAA expansion region require models in which this expansion in the context of the human frataxin gene is replicated. The available models include the YG8R, YG8Rs800, and Sarsero models; however, unpublished reports suggest a possible copy number variations within the transgene, which would make measuring editing efficiency challenging. Confirmation of the presence of the target sequence and assessment of copy number of the transgene with multiple probes should be performed within the mouse colony. In addition, none of these have a robust neurologic phenotype, although the YG8 series have been reported to have mild neurological/coordination phenotype and lower body weight [Al-Mahdawi 2006, Anjomani Virmouni 2015, Villa 2021] (also Anjomani-Virmouni, Puccio and Lutz personal communication). Nevertheless, these models may be used to assess editing efficiency in the nervous system and the correlation of editing efficiency to dose.

The ability of gene editing to rescue an FA phenotype could be demonstrated in iPSC derived FA patient neurons. These are likely to be sensory neurons and DRG organoids, as protocols to derived deep cerebellar nuclei neurons from iPSCs are not well established. In addition, because there is a detectable, functional loss of retinal ganglion cells (RGCs) in FA and RGC are a type of central nervous system (CNS) neuron, there is a rationale for extrapolating from the percent transduction necessary for rescue the RGC in a retinal explant from a repeat mouse model and use this to estimate the percentage transduction necessary to rescue other areas of the CNS, for example to DN or thalamus.

Combined with *in vivo* data confirming the ability to target the gene editing machinery to the intended neurologic targets by the intended ROA and safety studies, this *in vitro* POC should support initiation of clinical trials in adult patients. Evidence of safety and possible preliminary evidence of efficacy would support initiation of clinical trials in pediatric FA patients.

9.5 Proposed Approach to Establish Preclinical Proof of Concept for Approaches Aimed at the Neurological Features of FA

Cellular models and conditional knock out mouse models can be used to demonstrate proof of concept for gene replacement. The *in vivo* models can be used to model minimal effective transduction required for rescue of phenotype, confirm that FXN expression levels are below the toxic threshold, and identify the relevant dose ranges. The repeat expansion mice can be used to demonstrate editing efficiency *in vivo* and establish restoration of frataxin mRNA and protein expression; however, phenotypical rescue for GE needs to be evaluated in *in vitro* FA derived iPSC neurons. These preclinical data, coupled with safety toxicology studies designed to assess both acute and late-emerging toxicity is sufficient to support IND clearance of the GT/GE product. A proposed plan for a preclinical package to support development of GT/GE therapeutics for the nervous system is included in Appendix 3.

9.6 Clinical Trial Considerations

9.6.1 Diagnosis/Patient Selection Strategies

All FA patients display neurological features of the disease. After symptoms develop, diagnosis is typically made by sub-specialists, usually pediatric neurologists, cardiologists, or orthopedic surgeons rather than primary care physicians, genetic counselors, or genetic specialists. Confirmation is by a positive genetic test for biallelic mutations. Targeted testing directly assesses the length of the GAA repeat in FXN. This test alone will be diagnostic in 96% of patients while 4% of patients will require FXN sequencing, identifying one expanded allele and one normal allele by GAA repeat sizing [Rodden 2021]. However, the diagnostic journey can be long, and therefore young children are slightly underrepresented in the patient registry.

Due to the slowly progressive nature of the disease, with many patients living more than three decades, it may be challenging to translate efficacy across those with later stage disease to early-stage disease. For example, in later stage, non-ambulatory individuals where significant neurodegeneration is present, it may be more difficult to demonstrate a clinical benefit as a return of function, although slowing disease progression could be assessed. Changes in speech or swallowing may represent later stage functional outcomes, however, these are rarely

significantly abnormal in younger or earlier stage patients. In younger patients, including children, there is the potential to slow or block neurodegeneration, thus, starting studies in a population where it is possible to fully evaluate clinical benefit is important to allow rapid translation to development in pediatric population. Changes in gait and balance as well as upper limb function are most robust in earlier ambulatory individuals. While starting populations for Phase I trials might include non-ambulatory or later stage adults, we suggest that transition to earlier stage young adult and pediatric ambulatory patients early in development is needed for a more complete evaluation of efficacy potential.

The stage of disease, and hence the anatomical targets and concurrent symptomology, may be a factor in determining route of administration. In trials involving dual routes of administration that aim to address both CNS and cardiac manifestations of FA, the target patient population is likely to exhibit overt neurological symptoms but no clinical symptoms of cardiac disease. Efficacy would slow progression of neurological disease as assessed by mFARS, measures of speech, upper limb function, or walking tests, while cardiac assessments may consist of biomarkers not clinical signs. We suggest it is reasonable to predict that these cardiac biomarkers changes reflect decreased chances of progression to a major cardiac event.

The size of the GAA repeats on the shorter allele partially predicts disease phenotype. Therefore, stratifying or enriching by the size of the GAA repeat will reduce variability within the trial cohort. However, repeat lengths greater than 700 GAA repeats do not seem to contribute to clinical or pathological variation, suggesting a ceiling effect [Rodden 2022].

9.6.2 Routes of Administration

Systemic delivery could be used to target the peripheral nervous system (as well as cardiac and skeletal muscle). However, as previously discussed, it is not likely to address CNS components of the disease, requiring direct administration via intrathecal (IT), intracerebroventricular (ICV) or intraparenchymal (IP) routes. In preclinical models, the IT injection route primarily transduced the cerebellar cortex and the spinal cord, which may indicate this route will not achieve sufficient transduction of the deep cerebellar nuclei [Naidoo 2018]. ICV administration also only transduces superficial layers of the brain and thus may also fail to reach deep cerebellar nuclei [Naidoo 2018]. Intraparenchymal injection might be required to achieve sufficient transduction of the DN or other deep areas of the brain. However, there is also a concern that limiting GT/GE to only the DN would not address all the neuronal symptoms and may contribute to a change in the phenotype of FA to be more similar to hereditary spastic paraparesis. Based on these concerns, therefore, we suggest that characterizing the degree of transduction of the deep cerebellar nuclei, cerebellar Purkinje cells, and spinal cord after GT/GE delivery via the intended ROA should be provided by sponsors.

9.6.3 Biomarkers/Clinical Outcome Assessments

Meissner corpuscle (MC) imaging using *in vivo* reflectance confocal microscopy (RCM) of skin is a noninvasive way to quantify MC density and has been used in other diseases as a sensitive measure of sensory polyneuropathies. Preliminary data from a prospective, cross-sectional study in FA indicate decreases in skin nerve densities over time [Creigh 2019]. In addition, quantitative sensory testing (QST) thresholds including touch, vibration, and cooling thresholds, were found

to be higher in FA vs controls [Creigh 2019]. These measures may be used to track improvements in peripheral nerves post GT/GE treatment.

Motor evoked potentials (MEPs) measure integrity and function of the corticospinal tracts and results of studies of MEPs show correlations with clinical features of FA [Naeije 2021]. Ideally, MEPs would be used to detect dysfunction prior to substantial axonal degeneration, although it may be possible to detect disease stabilization using this biomarker.

Anatomical biomarkers that detect structural changes may be helpful to stage disease but measures of atrophy reflecting cell death are unlikely to change upon treatment. Disease duration and severity correlate with volume deficits in the dentate nucleus region, brainstem, and superior/inferior cerebellar peduncles [Harding 2021]. Cerebral white matter abnormalities, particularly in corticospinal pathways are seen at intermediate stages of disease. Cerebellar and cerebral gray matter loss, principally targeting motor and sensory systems, preferentially manifests later in the disease course [Selvadurai 2021].

Instead, functional abnormalities in affected tissues represent dynamic measures that reflect underlying disease. Functional MRI studies have demonstrated hypo and hyper activation in different cerebral and cerebellar brain regions. Although most studies to date were cross sectional designs, the data suggest that progressive changes occur in cerebral-cerebellar circuitry [Vavla 2021] and stabilization of fMRI signal may be a useful measure of changes in rate of progression. Magnetic resonance spectroscopy (MRS), which can be used to image biochemical changes immediately downstream of FXN, can also be useful to detect increased oxidative stress, reactive oxygen species and restored glutathione levels, as well as changes in GABA levels in selected brain regions in FA, and therefore may be useful biomarkers of biological activity of therapeutic approaches.

Imaging markers provide sensitive biomarkers of pharmacodynamic response in affected neurological tissues which are otherwise difficult to assess. Neuroimaging measures of the brain and spinal cord provide promising biomarkers for tracking FA progression and potentially treatment effects. FARA and a consortium of academic and industry partners are currently conducting a multi-site, multimodal, and longitudinal neuroimaging natural history study designed to identify sensitive, clinical trial-ready biomarkers for FA. The study, called TRACK-FA, aims to develop an FA neuroimaging dataset from brain and spinal cord that is suitable for assessing the potential value of neuroimaging biomarkers and providing a basis for instituting them in clinical trials. Data read outs are expected in late 2023.

Smaller studies have suggested that imaging markers can be used to detect disease progression and potential therapeutic effect. Neuroinflammation has been detected in the cerebellum and brainstem using PET imaging [Khan 2021] which may be reversed by some therapeutic approaches. Quantitative susceptibility mapping (QSM) shows increased magnetic susceptibility (suggestive of increased iron content) in the cerebellar dentate nucleus in Friedreich's ataxia [Harding 2016, Ward 2019]. Minoryx reported that leriglitazone prevented an accumulation of iron in the brain of FA patients, as assessed by QSM (https://www.minoryx.com/media/minoryx%E2%80%99s_clinical_candidate_leriglitazone_shows_clinical_benefit_in_a_proof_of_concept_phase_2_study_in_friedreichs_ataxia/).

9.6.4 Clinical Outcome Assessments

Clinical trials and natural history studies in FA have used clinical rating scales as primary outcome measures. In Europe, the Scale for Assessment and Rating of Ataxia (SARA) has been used in the European Friedreich Ataxia Consortium for Translation Studies (EFACTS) natural history study and in the phase 2 leriglitazone trial. The SARA is a simple scale designed to assess ataxia severity regardless of its etiology [Reetz 2015, Reetz 2016, Reetz 2021]. The modified Friedreich Ataxia Rating Scale (mFARS), utilized in FA-COMS, is instead derived from a FA-specific, exam-based neurological rating scale (FARSn). The mFARS omits items of limited functional significance in the original FARS neurological scale, focusing on the assessment of ataxia, which improved the features of the measures. The mFARS has been used as an outcome measure in clinical trials, including the pivotal trial for omaveloxolone. Extensive testing has demonstrated its validity in measuring disease progression as well as excellent test-retest reliability [Rummey 2019; Rummey 2021]. A correlation-based psychometric analysis of the original neurologic FARSn score justifies the overall validity of the scale. Thus, published studies provide the basis of the application of the mFARS in clinical trials.

Figure 8 Components of the mFARS Scale

Figure 1 Measurement model of the neurologic examination of the FARSn and the modified FARS (mFARS)

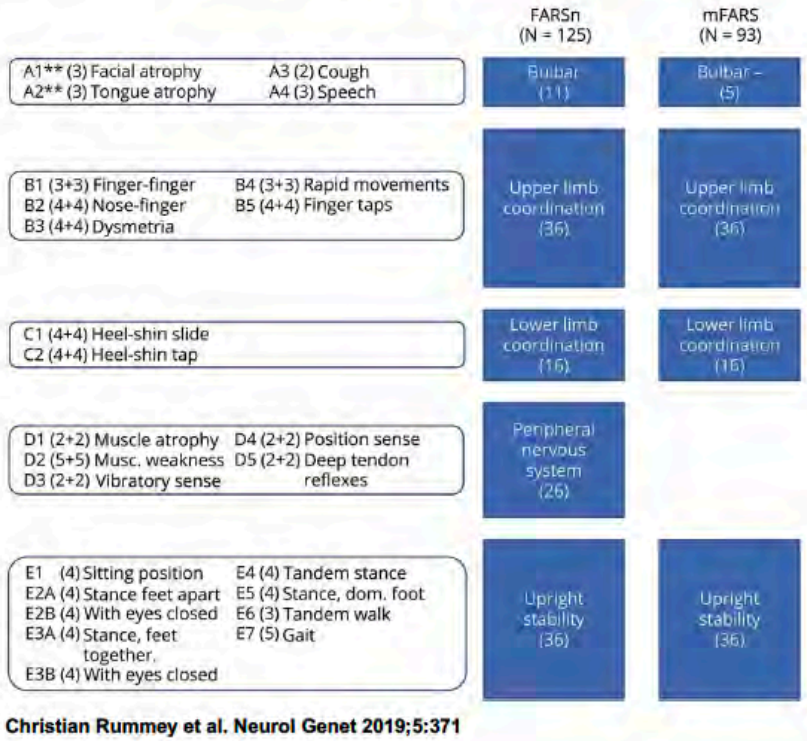

Christian Rummey et al. Neurol Genet 2019;5:371

Timed walk tests have been used in natural history and as secondary endpoints in trials of FA therapeutics. The T25-FW is a quantitative mobility and leg function performance test. The

patient is directed to one end of a clearly marked 25-foot course and is instructed to walk 25 feet as quickly as possible, but safely. The time is calculated from the initiation of the instruction to start and ends when the patient has reached the 25-foot mark. The task is immediately administered again by having the patient walk back the same distance. Patients may use assistive devices when doing this task. The 6 Minute Walk Test is a sub-maximal exercise test used to assess aerobic capacity and endurance and often used in trials for other neuromuscular diseases. The distance covered over a time of 6 minutes is used as the outcome by which to compare changes in performance capacity. This test is not used in FA due to ataxia which makes completion of 6-minute walk very difficult (high risk of falls). However, a one-minute walk test determining distance covered over time has been used in the pediatric natural history study, FA-CHILD, and as an exploratory outcome in a few trials.

In FA, speech disturbances progress throughout the course of the disease. Initially, mild dysphonia characterized by hoarseness (combined roughness and breathiness), increased strain, and altered pitch variability (increased in vowel productions) is present. In fact, a combination of perceptual and acoustic measures of dysphonia was effective in categorizing FA versus control participants, with >80% overall accuracy [Vogel 2017]. Eventually, the speech disturbances of FA progress to dysarthria, a result of continued central and peripheral neurodegeneration. Therefore, speech disturbances may be responsive to GT/GE administration to the neurological system and used as a measure of clinical efficacy.

Assessments of upper limb activities that are meaningful and relevant to specific capabilities have also been developed. Upper limb function remains important both to individuals with mild and severe symptoms of ataxia. The nine-hole pegboard test (9HPT) has been used in natural history studies and clinical trials, capturing the time it takes to put all nine pegs in the holes and remove them back to the start tray. This test has been used widely in Multiple Sclerosis trials to evaluate functional neurologic performance. The Ataxia Instrumented Measure-Spoon (AIM-S), which consists of a spoon equipped with a BioKin wireless motion capture device, and algorithms that analyze these signals, have been used to measure ataxia of the upper limb [Nguyen 2019, Nguyen 2020b, Nguyen 2020a, Corben 2021]. The AIM-S was studied in a prospective longitudinal FA study to evaluate the capacity to detect change in upper limb function over 48 weeks. The results of the study suggest that the AIM-S is a more accurate, less variable measure of upper limb function in FA than existing measures [Corben 2021].

New patient reported outcome measures (PROs) for patients with FA have recently been developed, including the Friedreich's Ataxia Health Index (FA-HI), measures symptomatic burden using the perspective of the patient and the Friedreich's Ataxia Caregiver Reported Health Index (FACR-HI), which measures symptomatic burden in younger children with FA and is completed by caregivers. These instruments are currently under evaluation in a longitudinal study to complete the validation process, satisfy the FDA guidance criteria for their use in drug-labeling claims, as well as to optimize the responsiveness of the instruments and prepare them for global use as relevant markers of symptomatic disease burden. Activities of daily living have also been assessed in natural history and clinical trials by the FA-ADL, an FA validated ADL questionnaire. In the EFACTS study this measure has shown a size effect comparable to the neurological rating scale, [Reetz 2015, Reetz 2016, Reetz 2021, Pandolfo 2020] while it was less sensitive to progression and noisier in FA-COMS, possibly depending on how it was administered and the larger number of children in FA-COMS. Time to disease milestones such

as balance function or loss of ambulation are also potentially relevant measures [Rummey 2020a]

9.7 Proposed Clinical Development Strategy

All FA patients display neurological features of the disease although it may be more difficult to demonstrate functional improvement in later stage patients. Imaging biomarkers may be useful to establish pharmacodynamic response of target engagement. Functional outcomes/symptoms that are directly linked to neurodegeneration of specific brain regions, including dysarthria and ataxia, can be measured by clinical assessments. The modified Friedreich Ataxia Rating Scale (mFARS) is a disease specific, exam-based neurological rating scale that has been used as an outcome measure in clinical trials, including the pivotal trial for omaveloxolone. An example of a development plan to support GT/GE approaches for the nervous system is included in Appendix 3.

9.8 Risk Benefit

Patients understand that reversal of neurological deficits may not be possible; however, it is meaningful to halt progression of neurological function and retain upper limb function in non-ambulatory patients or to preserve ambulation despite persistence of ataxia, as shown in the graph below shows survey data from the PFDD. Note that many patients expressed that slowing progression would be of significant value.

> "*Life would be wonderful if we were able to stop this tireless race against time and sustain life as it is today.*"

> *"Short of a cure, being able to objectively slow or stop progression would be invaluable to me. I want to plan my life, with confidence; to be able to rely on my current abilities in the future, and without the fear of devastating complications…"*

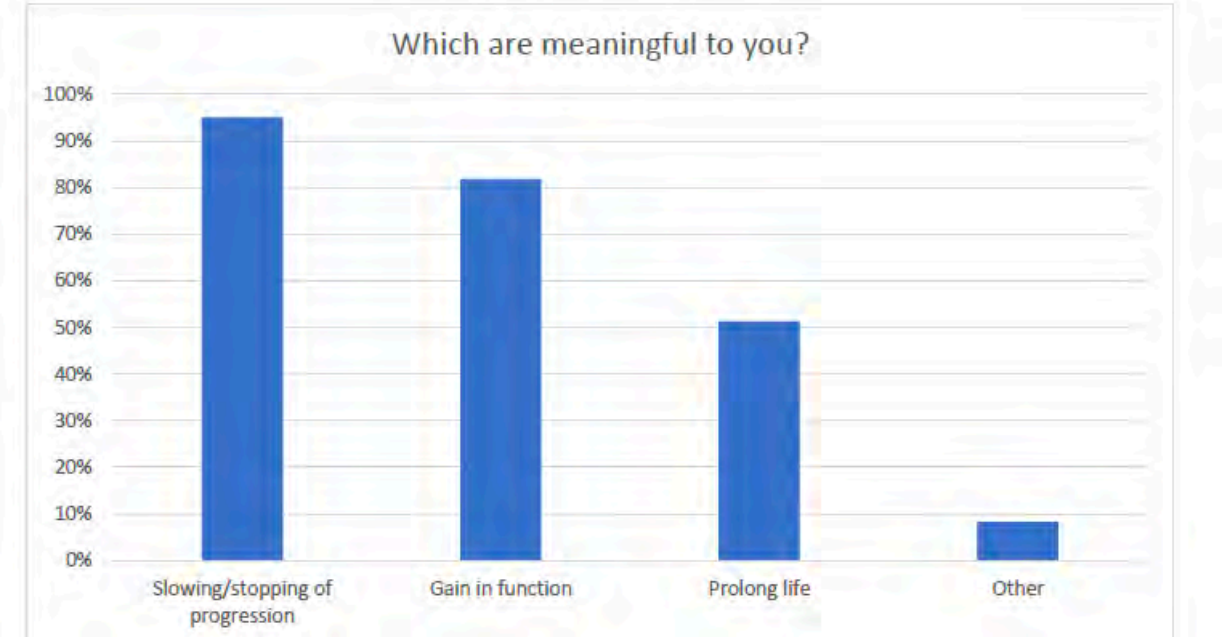

Patients will weigh the benefit of GT/GE treatment of neurological symptoms against the risk that this would prevent GT/GE treatment of the heart and for some, the risk of ineligibility for further GT/GE treatment does not out weight the near-term benefit of treating neurological symptoms. Recent data suggests that patients receiving intraparenchymal administration of viral vectors may generate an immune response [Hwu 2022] and thus would not be able to receive additional viral vectors for GT/GE for other target tissues with currently available immune suppression strategies.

Because of an increased risk for FA patients for perioperative cardiovascular complications including unpredictable severe heart failure and death, there is reluctance to undergo surgical procedures. Therefore, sham surgeries present a high risk with no prospect of benefit that may be unacceptable to most patients. In addition, unilateral intraparenchymal administration of GT/GE may worsen neurological symptoms, especially in the complex nuclei of the cerebellum. Patients may also weigh the risk presented by surgical procedures to administer GT/GE.

In a development program where both cardiac and neurological aspects of FA are targeted, the patient population most likely to benefit from CNS gene delivery/editing would likely be young, whereas the likelihood of seeing an effect on cardiac function in a reasonable timeframe is greater in an older FA population. In adults the ideal result is rescue of the DN and cortico-spinal tracts. Although children may have more cells remaining in target tissues, the target is not absent in adults until very late-stage disease. Late onset FA patients are likely to have more cells remaining in cerebellar nuclei but may also have cerebellar deficits that are less likely to be rescued by DN injections.

Patients accept that GT/GE may not treat all aspects of the disease or may vary in degree of disease modification depending on the age of administration, as has been seen with onasemnogene abeparvovec [Hjartarson 2022]. Patients also understand that the current delivery mechanisms (viral vectors) may limit patients to a single GT/GE treatment and thus will weigh treatment of one brain region or system vs the another.

Because there appears to be both developmental and degenerative neuronal cell loss of large neurons in the DRG, and AAV toxicity has been reported to be mainly to large neurons, FA patients have less concern about AAV driven toxicity of the DRG.

10 VISION LOSS IN FA

Vision loss is a devastating aspect of FA, with clinically significant vision loss primarily in later stages of disease. However, early signs of vision abnormalities and thinning of the retinal fiber layer are often present in late childhood and can be readily assessed by biomarkers and clinical measures. Current mouse models are not authentic representations of the human disease but could be used in combination with human iPSC derived retinal cells or organoids to demonstrate increased frataxin levels/function, biodistribution to target ocular structures, and set starting doses. It may be possible to demonstrate gene editing in NHP, as they possess GAA repeats, though small in number. Stabilization /improvement in visual acuity, with support from stabilization of OCT biomarkers, and PROS would provide evidence of therapeutic benefit.

10.1 Clinical Phenotype Description and Progression

Vision impairment is detectable in FA by the late teens/early 20's as sub-clinical changes in optical coherence tomography (OCT; [Seyer 2013, Dag 2014]) and low- contrast letter acuity (LCLA; [Seyer 2013]). Clinically, individuals initially observe loss of peripheral vision and contrast sensitivity with usually modest loss of acuity (See Figure 9, below). Clinical outcome assessments of high and low contrast letter acuity and vision patient reported outcomes are yearly assessed in the FA-COMS study, thus there are longitudinal natural history data that inform the clinical progression and relevance in FA. These data are also informative in clinical trial design.

Figure 9 Vision Changes Over Time as Assessed in FA-COMS

Mean± SD		Year 1	Year 2	Year 3	Year 4	Year 5
Overall	Total Vision Acuity	-1.38 ± 16.78	-1.08 ± 19.98	-6.75 ± 18.44	-8.50 ± 21.57	-10.97 ± 22.40
Age <16 @ BL	Total Vision Acuity	1.13 ± 19.49	4.79 ± 24.57	-4.94 ± 24.20	-5.07 ± 25.59	-7.36 ± 27.74
Age 16-40 @ BL	Total Vision Acuity	-3.98 ± 15.42	-4.55 ± 15.71	-7.43 ± 15.58	-10.79 ± 20.04	-12.58 ± 20.30
Age >40 @ BL	Total Vision Acuity	0.00 ± 12.92	-1.70 ± 19.57	-8.12 ± 13.47	-8.38 ± 17.61	-13.33 ± 14.40

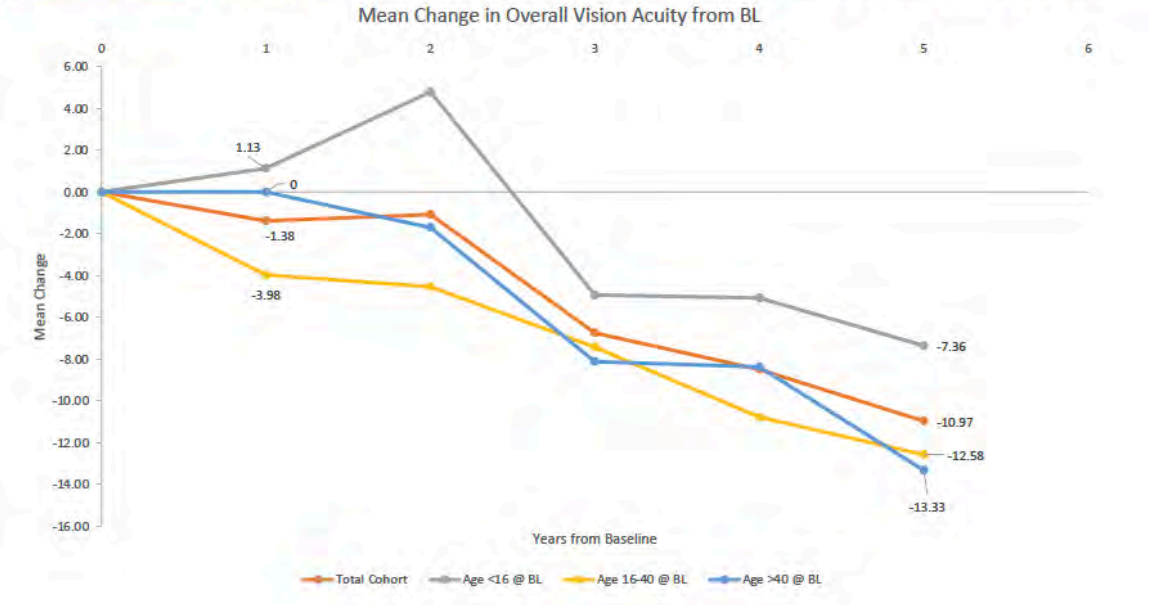

As the disease progresses, vision loss is slow and inexorable, progressing from loss of acuity ultimately to blindness in some individuals. Even early in disease progression, a vision-dependent component of ataxia is present, meaning compromised vision has broader impact on QoL through the importance of visual functioning in minimizing sensory ataxia [Lynch 2021b].

10.2 Patient Perspective

The vision loss due to FA, especially during later stages of disease progression, has a profoundly negative impact on quality of life. Even in earlier stages of the disease, compromised vision may have broad impact, as the developing ataxia is vision-dependent for movement and spatial awareness. Once ambulation is lost, compromised vision further impacts the ability to go to school or work, or care for oneself, and leads to increased isolation. This is particularly true when combined with auditory and somatosensory dysfunction. Thus, maintaining vision is critical to maintaining independence.

As part of FARA's Externally Led Patient Focused Drug Development Meeting held in June 2017, patients offered the following comments regarding loss of vision:

> *"Without vision you have nothing – isolation from the world is complete"*
>
> *"I am most worried about losing my vision because of FA. I feel if I lose my vision, I will lose my remaining link to the world. It would take even more of my independence away…"*
>
> *"By losing their vision I fear it will take away the last of life's enjoyments for them both. Saving the vision of these young people will be a life-line for them, and an answer to an ongoing prayer for me."* (Mary, mother of two young adults with FA)

Afsharian et al (2020) [Afsharian 2020] used the 25-Item National Eye Institute Visual Functioning Questionnaire (NEI-VFQ-25) to assess vision specific quality of life in Friedreich ataxia patients (n=99). Subscores of the NEI-VFQ-25 that were most affected in FA included general health, general vision, distance vision, and peripheral vision. In addition, quality of life was lower in patients with the most advanced disease, indicating that vision loss most impacts those at a later stage of disease. Thus, addressing vision loss will provide significant improvement in quality of life, especially in later stage patients.

10.3 Tissue Pathology and Target Cells

FA patients develop an optic neuropathy distinct from ophthalmological changes seen in other mitochondrial diseases. Postmortem histological evaluation of eyes from FRDA patients demonstrated varying degrees of retinal ganglion cell (RGC) loss, thinning of the retinal nerve fiber layer and optic nerve atrophy, while the retinal pigment epithelium (RPE) is preserved [Crombie 2015]. Given that the RPE supports the health of the RGC, it is encouraging that the RPE is intact, but also suggests that RGC loss is frank neurodegeneration, analogous to the loss of somatosensory ganglion cells. However, the papillo-macular bundle is preserved, and early changes in visual acuity include loss of low contrast vision and loss of peripheral components of the visual field [Fortuna 2009]. Still, some patients over time progress to central visual loss or have precipitous loss of central vision earlier in their disease course.

Figure 10 Histological Images of FA Human Eyes

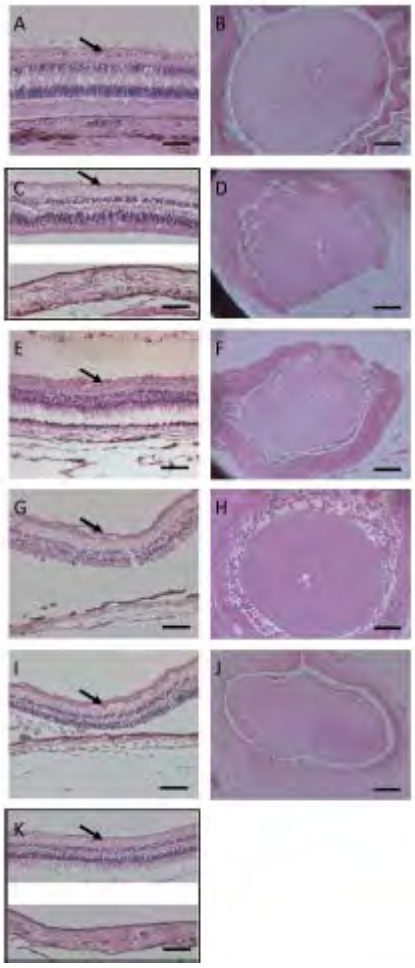

[Crombie 2015].
Left column is retinal sections, right column is optic nerve sections. A, B - FA patient with normal retina and optic nerve. Remaining images are paired images from FA patients with retinal and optic nerve degeneration.

The degree of RGC loss appears to be greater in patients with high GAA triple repeat expansion or compound heterozygotes and severe clinical presentation [Fortuna 2009, Crombie 2015]. Retinal nerve fiber layer thinning assessed by OCT appears to be a useful measure of the pathological progression of RGC loss [Thomas-Black 2019].

Associated with RGC loss, FA patients often have degeneration of the optic nerve (the downstream axons of RGCs) and to a lesser degree optic radiations (the geniculocalcarine tract [Rojas 2021]), which can be assessed using diffusion weighted imaging [Fortuna 2009]. Data collected by DWI and compared to OCT measurements in the same individual suggest that degeneration in the anterior and posterior visual pathways are independent events [Fortuna 2009]. The clinical phenomena (particularly visual fields) match the degeneration of the optic nerve more than loss of optic radiations.

10.4 Cellular and Animal Models for Proof of Concept for Approaches Aimed at the Vision Loss in FA

Three-dimensional iPSCs-derived retina-like tissues called retinal organoids contain all major retina-specific cell types: amacrine, bipolar, horizontal, retinal ganglion cells, Müller glia, as well as rod and cone photoreceptors [Cowan 2020]. These systems have the added advantage of using human cells derived from patients with the disease-causing mutation, for example, in the case of FA, the GAA repeat in the frataxin gene. In the absence of an animal model with high fidelity to the human disease, iPSC-derived cells or organoids play an important role in developing preclinical data to both demonstrate efficacy and to assess safety in the target cells.

The mouse models that have most often been used to study other aspects of FA do not recapitulate the pathology of the eye found in human FA patients. A mouse model with a *Fxn* knock out and a human transgene with a GAA expansion in the first intron has been reported to have progressive retinal degeneration [Crombie 2015]. However, upon close histological examination, the degeneration is confined to the outer retina with photoreceptor loss and thinning of the RPE and no loss of RGC. The thinning of the RPE was also seen in a transgenic control without a FXN deficiency, suggesting this change may be due to the insertion site rather than to loss of FXN. A conditional knock down mouse model (FRDA kd, [Chandran 2017]) also showed disruption of photoreceptors and vacuoles in RPE. These findings in the mouse models differ significantly from human FA patients, in which preservation of the RPE and loss of RGC is seen [Crombie 2015]. In addition, changes in the visual system occur later in the progression of the disease; this later onset is not reflected in the mouse models. Additionally, frataxin protein and mRNA expression in the retina have not been determined in these mouse models. For these reasons, the use of such models may be limited and the exact cell types that are rescued in these mouse models does not represent the cells damaged in the human condition.

New mouse models that may better approximate the human disease are under development. A mRX-Cre mouse that constitutively expresses Cre in all retinal cell types, together with heterozygous Fxn knock-out (B6(Cg)-Fxnem2.1Lutzy/J) and Fxn floxed mice C57BL/6J-Fxnem2Lutzy/J mice have been used to generate a conditional, retina-only frataxin knockout mice (mRx-Fxn KO mice; [Gupte 2022]). The mouse has early, progressive degeneration of the retina as measured by OCT and functional impairment as measured by electroretinogram (ERG). An optimized FXN construct delivered via intravitreal injection increased the level of frataxin in the retina and significantly preserved retinal structure. While this mouse model can therefore be used to demonstrate the efficacy of the GT/GE approach to increase frataxin levels in the retina, it does not faithfully replicate the human disease. The progression of retinal dystrophy in the mRx-FXN KO mice is rapid and involves the entire retina. FARA continues to fund the Boye lab to generate an RGC-specific FXN knockout mouse as this provides a model with frataxin knock out in the cells that undergo degeneration in the human patient.

Non-human primates or pigs can be used to establish adequate distribution of product to target cells, as well as assessment of potential toxicity. It may also be possible to use the NHP to assess *in vivo* editing efficiency. Nonhuman primates have consecutive GAA repeats that are less than 10. Although the GAA repeat number is much lower than what FA patients typically carry, the gene editing product can target the sequences that encompass the GAA repeats regardless of the repeat size, which results in excision of the GAA repeats. Therefore, nonhuman primates can be

served as an *in vivo* model to evaluate the activity of the GE product (e.g., excision frequency), if it has previously established that editing is not dependent on the length of the GAA repeat.

10.5 Proposed Approach to Establish Preclinical Proof of Concept for an Ocular Focused Therapy

Cellular models such as retinal ganglion cells or organoids, derived from FA iPSCs, are useful to demonstrate restoration of frataxin levels although they may be limited in demonstrating functional rescue and a direct one to one correlation with transduction *in vivo* is not expected. Knock out and expansion mouse model do not authentically replicate degeneration in the retinal cells that degenerate in FA. Therefore, their use may be limited to demonstration of vector distribution and transduction efficacy or to characterize the gene editing efficiency and targeting of the RGC. Nonhuman primates can be used to demonstrate vector distribution and transduction efficacy or to characterize the gene editing or replacement efficiency and targeting of the RGCs. An example of a preclinical data package to support development of the GT/GE approach for the vision loss found in FA is included in Appendix 3.

10.6 Clinical Trial Considerations

10.6.1 Diagnosis/Patient Stratification

Cerebellar damage is reflected in ocular motor abnormalities including fixation instability, saccadic dysmetria, and disrupted pursuit. These changes limit the usefulness of, for example, visual field tests, which are irreproducible due to neurological impairments. Although high contrast visual acuity is rarely impacted early, low-contrast letter acuity, the perception of gray letters on a white or retro illuminated background, is reduced in FA and progressively worsens in most patients [Hamedani 2018, Seyer 2013, Afsharian 2020]. Earlier age of onset, higher GAA repeat number and worsening clinical status are associated with greater visual impairment.

Individuals with high contrast visual acuity levels of 20/32 to 20/800, consistent in FA with retinal nerve fiber layer (RNFL) of 60 microns or less, are appropriate patients to receive GT/GE treatment for FA optic neuropathy. LCLA is abnormal in earlier stage disease, but progression may be slow. Children have no overt visual phenotype as the detectable changes in LCLA do not clearly impact quality of life.

Optical coherence tomography (OCT) demonstrates RNFL thickness in FA that continues to decrease over time [Noval 2012, Seyer 2013, Dag 2014]. In FA, thickness of the layer correlates with visual acuity and contrast sensitivity [Noval 2012]. Age of onset of disease and neurological status also correlate with RNFL thickness suggesting that OCT can be used to stratify patients into groups more likely to show progressive vision loss [Fortuna 2009].

10.6.2 Biomarkers/Clinical Outcome Assessments

In FA, high contrast visual acuity provides a measure of visual function, although it becomes abnormal mainly in later stage disease and changes at approximately 2-3 letters (1/2 line) per year. Thus, while measurable and specific, high contrast acuity changes only slowly over time. OCT is a useful measure of change as it is precise and reproducible, detects significant retinal thinning, and although not a measure of function, changes in OCT correlate with low contrast

sensitivity [Rojas 2020]. Loss of RNFL is 1 micron per year with a reproducibility is +- 1 micron and thus RNFL measurements could be a relevant endpoint in clinical trials.

While the central visual field is spared early in the disease, there is a general and concentric reduction in visual field sensitivity at later stages of the disease [Rojas 2020]. In the FA-COMS longitudinal study, low contrast acuity testing demonstrated a linear progression of decline, and the rate of progression was greater in those with larger number of GAA repeats [Hamedani 2018]. Thus, OCT and low contrast acuity testing represents useful measures of visual function in FA. The FA-COMS data can be informative for trial design including patient selection, outcome measures and as a supplement to placebo to reduce number of participants in placebo arm.

Patient reported outcome measures of vision-specific quality of life have been tested in FA. The 25-item National Eye Institute Visual Functioning Questionnaire (NEI-VFQ-25) and the 10-Item Neuro-Ophthalmic Supplement have been used to assess the impact of eye disease due to FA on quality of life [Afsharian 2020]. FA patients scored lower on these tests compared to published control groups. Worse quality of life scores were associated with greater clinical and visual dysfunction and with longer disease duration.

10.7 Proposed Clinical Development Strategy

An appropriate FA population for treatment is patients can be defined with high contrast visual acuity scores. Because photoreceptors are not lost in FA, rate of photoreceptor loss, an acceptable endpoint in the FDA guidance on GT for retinal disorders, cannot be used in FA. However, rate of RNFL loss is an analogous endpoint relevant to FA that can be measured by OCT. NEI -VFQ-25 can be used as a patient-reported measure of vision-specific quality of life in patients with FA. An example clinical development plan to support GT/GE therapeutic for vision in FA is included in Appendix 3.

10.8 Risk/Benefit

Patients have expressed the desire to preserve their remaining vision and to stop the relentless progression of loss. Those likely to choose participation in a GT/GE trial directed at vision loss are early or typical onset FA patients in their 20's and 30's. Often these patients are non-ambulatory by this age but may continue to drive and are often employed. Loss of vision has a profoundly negative impact on quality of life for these patients, including losing the ability to read or use a computer, effectively shutting them off from the world. Patients would find it meaningful to stop further progression.

Patients who experience vision impairment at an earlier stage of disease progression will weigh the risk of being unable to participate in other GT trials targeting other tissues against the benefit of GT/GE to address vision loss.

Patients have concerns about a placebo control group in a trial aimed at the optic neuropathy of FA, as patients with visual impairment are likely to continue to lose remaining vision during the conduct of the trial. There is parallel disease in each eye, suggesting both eyes should be treated. Use of the FA-COMS natural history study data on the visual system to supplement and therefore reduce the size of a placebo group would be desired.

11 REFERENCES

Abeti R, Baccaro A, Esteras N, et al. Novel Nrf2-Inducer Prevents Mitochondrial Defects and Oxidative Stress in Friedreich's Ataxia Models. Front Cell Neurosci. 2018 Jul 17;12:188.

Afsharian P, Nolan-Kenney R, Lynch A, et al. Correlation of Visual Quality of Life With Clinical and Visual Status in Friedreich Ataxia. J Neuroophthalmol. 2020 Jun;40(2):213-217.

Al-Mahdawi S, Pinto RM, Ismail O, et al. The Friedreich ataxia GAA repeat expansion mutation induces comparable epigenetic changes in human and transgenic mouse brain and heart tissues. Hum Mol Genet. 2008 Mar 1;17(5):735-46.

Al-Mahdawi S, Pinto RM, Ruddle P, et al. GAA repeat instability in Friedreich ataxia YAC transgenic mice. Genomics. 2004 Aug;84(2):301-10.

Al-Mahdawi S, Pinto RM, Varshney D, et al. GAA repeat expansion mutation mouse models of Friedreich ataxia exhibit oxidative stress leading to progressive neuronal and cardiac pathology. Genomics. 2006 Nov;88(5):580-90.

Alboliras ET, Shub C, Gomez MR, et al. Spectrum of cardiac involvement in Friedreich's ataxia: clinical, electrocardiographic and echocardiographic observations. Am J Cardiol. 1986 Sep 1;58(6):518-24.

Anjomani Virmouni S, Ezzatizadeh V, Sandi C, et al. A novel GAA-repeat-expansion-based mouse model of Friedreich's ataxia. Dis Model Mech. 2015 Mar;8(3):225-35.

Anjomani Virmouni S, Sandi C, Al-Mahdawi S, et al. Cellular, molecular and functional characterisation of YAC transgenic mouse models of Friedreich ataxia. PLoS One. 2014 Sep 8;9(9):e107416.

Apolloni S, Milani M, D'Ambrosi N. Neuroinflammation in Friedreich's Ataxia. Int J Mol Sci. 2022 Jun 4;23(11):6297.

Babcock M, de Silva D, Oaks R, et al. Regulation of mitochondrial iron accumulation by Yfh1p, a putative homolog of frataxin. Science. 1997 Jun 13;276(5319):1709-12.

Belbellaa B, Reutenauer L, Messaddeq N, et al. High Levels of Frataxin Overexpression Lead to Mitochondrial and Cardiac Toxicity in Mouse Models. Mol Ther Methods Clin Dev. 2020 Sep 1;19:120-138.

Belbellaa B, Reutenauer L, Monassier L, et al. Correction of half the cardiomyocytes fully rescue Friedreich ataxia mitochondrial cardiomyopathy through cell-autonomous mechanisms. Hum Mol Genet. 2019 Apr 15;28(8):1274-1285.

Bhalla A, Khodadadi-Jamayran A, Li Y, et al. Deep sequencing of mitochondrial genomes reveals increased mutation load in Friedreich's ataxia. Ann Clin Transl Neurol. 2016 Jun 14;3(7):523-36.

Capuzano V, Montermini L, Moltò M, et al. Friedreich's ataxia: autosomal recessive disease caused by an intronic GAA triplet repeat expansion. Science. 1996 Mar 8;271(5254):1423-7.

Chandran V, Gao K, Swarup R, et al. Inducible and reversible phenotypes in a novel mouse model of Friedreich's Ataxia. Elife. 2017 Dec 19;6:e30054.

Chang J, Ryan M, Purushothaman P, et al. Evaluation of Novel AAV Gene Replacement Therapy in Mouse Model of Friedreich's Ataxia. Mol Ther. 2022 30;1-592.

Chevis C, da Silva C, D'Abreu A, et al. Spinal cord atrophy correlates with disability in Friedreich's ataxia. Cerebellum. 2013 Feb;12(1):43-7.

Chiang S, Huang M, Park K, et al. Antioxidant defense mechanisms and its dysfunctional regulation in the mitochondrial disease, Friedreich's ataxia. Free Radic Biol Med. 2020 Nov 1;159:177-188.

Lenglet C, Deelchand J, Eberly L, et al. Longitudinal MRS, MRI and DTI in the Spinal Cord in Friedreich's Ataxia: 36-month Follow-up. 2018 FARA Meeting on Biomarkers and Outcome Measures. Tampa, FL.

Cissé C, Cissé L, Ba H, et al. Friedreich ataxia in a family from Mali, West Africa/Friedreich ataxia in a Malian family. Clin Case Rep. 2021 Mar 24;9(5):e04065.

Clark R, De Biase I, Malykhina A, et al. The GAA triplet-repeat is unstable in the context of the human FXN locus and displays age-dependent expansions in cerebellum and DRG in a transgenic mouse model. Hum Genet. 2007 Jan;120(5):633-40.

Coppola G, Marmolino D, Lu D, et al. Functional genomic analysis of frataxin deficiency reveals tissue-specific alterations and identifies the PPARgamma pathway as a therapeutic target in Friedreich's ataxia. Hum Mol Genet. 2009 Jul 1;18(13):2452-61.

Corben L, Nguyen K, Pathirana P, et al. Developing an Instrumented Measure of Upper Limb Function in Friedreich Ataxia. Cerebellum. 2021 Jun;20(3):430-438.

Cossee M, Durr A, Schmitt M, et al. Friedreich's ataxia: point mutations and clinical presentation of compound heterozygotes. Ann Neurol. 1999 Feb;45(2):200-6.

Cowan C, Renner M, De Gennaro M, et al. Cell Types of the Human Retina and Its Organoids at Single-Cell Resolution. Cell. 2020 Sep 17;182(6):1623-1640.e34.

Creigh P, Mountain J, Sowden J, et al. Measuring peripheral nerve involvement in Friedreich's ataxia. Ann Clin Transl Neurol. 2019 Sep;6(9):1718-1727.

Crombie D, Curl C, Raaijmakers A, et al. Friedreich's ataxia induced pluripotent stem cell-derived cardiomyocytes display electrophysiological abnormalities and calcium handling deficiency. Aging (Albany NY). 2017 May 30;9(5):1440-1452.

Crombie D, Van Bergen N, Davidson K, et al. Characterization of the retinal pigment epithelium in Friedreich ataxia. Biochem Biophys Rep. 2015 Sep 11;4:141-147.

Culley M, Zhao J, Tai Y, et al. Frataxin deficiency promotes endothelial senescence in pulmonary hypertension. J Clin Invest. 2021 Jun 1;131(11):e136459.

Dag E, Ornek N, Ornek K, et al. Optical coherence tomography and visual field findings in patients with Friedreich ataxia. J Neuroophthalmol. 2014 Jun;34(2):118-21.

Delatycki M and Bidichandani S. Friedreich ataxia- pathogenesis and implications for therapies. Neurobiol Dis. 2019 Dec;132:104606.

Dogan I, Romanzetti S, Didszun C, et al. Structural characteristics of the central nervous system in Friedreich ataxia: an in vivo spinal cord and brain MRI study. J Neurol Neurosurg Psychiatry. 2019 May;90(5):615-617.

Durr A, Cossee M, Agid Y, et al. Clinical and genetic abnormalities in patients with Friedreich's ataxia. N Engl J Med. 1996 Oct 17;335(16):1169-75.

Fortuna F, Barboni P, Liguori R, et al. Visual system involvement in patients with Friedreich's ataxia. Brain. 2009 Jan;132(Pt 1):116-23.

Fowles R and Mason J. Endomyocardial biopsy. Ann Intern Med. 1982 Dec;97(6):885-94.

Fox N, Das D, Chakrabarti M, et al. Frataxin Accelerates [2Fe-2S] Cluster Formation on the Human Fe-S Assembly Complex. Biochemistry. 2015 Jun 30;54(25):3880-9.

Fox N, Yu X, Feng X, et al. Structure of the human frataxin-bound iron-sulfur cluster assembly complex provides insight into its activation mechanism. Nat Commun. 2019 May 17;10(1):2210.

Friedman L, Schadt K, Regner S, et al. Elevation of serum cardiac troponin I in a cross-sectional cohort of asymptomatic subjects with Friedreich ataxia. Int J Cardiol. 2013 Aug 20;167(4):1622-4.

Galea C, Huq A, Lockhart P, et al. Compound heterozygous FXN mutations and clinical outcome in friedreich ataxia. Ann Neurol. 2016 Mar;79(3):485-95.

Gerard C, Xiao X, Filali M, et al. An AAV9 coding for frataxin clearly improved the symptoms and prolonged the life of Friedreich ataxia mouse models. Mol Ther Methods Clin Dev. 2014 Oct 8;1:14044.

Gerber J, Muhlenhoff U, Lill R. An interaction between frataxin and Isu1/Nfs1 that is crucial for Fe/S cluster synthesis on Isu1. EMBO Rep. 2003 Sep;4(9):906-11.

Geschwind D, Perlman S, Grody W, et al. Friedreich's ataxia GAA repeat expansion in patients with recessive or sporadic ataxia. Neurology. 1997 Oct;49(4):1004-9.

Greeley N, Regner S, Willi S, et al. Cross-sectional analysis of glucose metabolism in Friedreich ataxia. J Neurol Sci. 2014 Jul 15;342(1-2):29-35.

Guo L, Wang Q, Weng L, et al. Characterization of a new N-terminally acetylated extra-mitochondrial isoform of frataxin in human erythrocytes. Sci Rep. 2018 Nov 19;8(1):17043.

Gupte S, Calabro K, Fajardo D, et al. Development of an AAV-Based Gene Therapy for the Ocular Phenotype of Friedreich's Ataxia. Mol Ther. 2022 30, 1-592.

Hamedani A, Hauser L, Perlman S, et al. Longitudinal analysis of contrast acuity in Friedreich ataxia. Neurol Genet. 2018 Jul 23;4(4):e250.

Hamm M, Goodwin M, McParland T, et al. Biodistribution and Activity of a Novel AAV-hFXN Expression Vector in the MCK Mouse Model of Friedreich's Ataxia. Mol Ther. 2022 30, 1-592.

Hanson E, Sheldon M, Pacheco B, et al. Heart disease in Friedreich's ataxia. World J Cardiol. 2019 Jan 26;11(1):1-12.

Harding A and Hewer R. The heart disease of Friedreich's ataxia: a clinical and electrocardiographic study of 115 patients, with an analysis of serial electrocardiographic changes in 30 cases. Q J Med. 1983 Autumn;52(208):489-502.

Harding I, Chopra S, Arrigoni F, et al. Brain Structure and Degeneration Staging in Friedreich Ataxia: Magnetic Resonance Imaging Volumetrics from the ENIGMA-Ataxia Working Group. Ann Neurol. 2021 Oct;90(4):570-583.

Harding I, Lynch D, Koeppen A, et al. Central Nervous System Therapeutic Targets in Friedreich Ataxia. Hum Gene Ther. 2020 Dec;31(23-24):1226-1236.

Harding I, Raniga P, Delatycki M, et al. Tissue atrophy and elevated iron concentration in the extrapyramidal motor system in Friedreich ataxia: the IMAGE-FRDA study. J Neurol Neurosurg Psychiatry. 2016 Nov;87(11):1261-1263.

Haugen A, Di Prospero N, Parker J, et al. Altered gene expression and DNA damage in peripheral blood cells from Friedreich's ataxia patients: cellular model of pathology. PLoS Genet. 2010 Jan 15;6(1):e1000812.

Herman D, Jenssen K, Burnett R, et al. Histone deacetylase inhibitors reverse gene silencing in Friedreich's ataxia. Nat Chem Biol. 2006 Oct;2(10):551-8.

Hewer R. Study of fatal cases of Friedreich's ataxia. Br Med J. 1968 Sep 14;3(5619):649-52.

Hinderer C, Miller R, Dyer C, et al. Toxicity of Frataxin Overexpression in Nonhuman Primates Treated with Intravenous and MRI-Guided Intracerebellar Infusion of an AAV Vector. Mol Ther. 2022 30, 1-592.

Hjartarson H, Nathorst-Böös K, Sejersen T. Disease Modifying Therapies for the Management of Children with Spinal Muscular Atrophy (5q SMA): An Update on the Emerging Evidence. Drug Des Devel Ther. 2022 Jun 16;16:1865-1883.

Hordeaux J, Buza E, Dyer C, et al. Adeno-Associated Virus-Induced Dorsal Root Ganglion Pathology. Hum Gene Ther. 2020 Aug;31(15-16):808-818.

Huichalaf C, Perfitt T, Kuperman A, et al. In vivo overexpression of frataxin causes toxicity mediated by iron-sulfur cluster deficiency. Mol Ther Methods Clin Dev. 2022 Feb 7;24:367-378.

Hwu W, Muramatsu S, Gidoni-Ben-Zeev B. Reduced Immunogenicity of Intraparenchymal Delivery of Adeno-Associated Virus Serotype 2 Vectors: Brief Overview. Curr Gene Ther. 2022;22(3):185-190.

Keage M, Delatycki M, Dyer J, et al. Changes detected in swallowing function in Friedreich ataxia over 12 months. Neuromuscul Disord. 2019 Oct;29(10):786-793.

Keage M, Delatycki M, Gupta I, et al. Dysphagia in Friedreich Ataxia. Dysphagia. 2017 Oct;32(5):626-635.

Kessler S, Andersen K, Schmidt A, et al. Motor Evoked Potential Input Output Measures and FRDA Disease Burden. 2019 International Ataxia Research Conference. Washington DC.

Khan W, Corben L, Bilal H, et al. Neuroinflammation in the Cerebellum and Brainstem in Friedreich Ataxia: An [18F]-FEMPA PET Study. Mov Disord. 2022 Jan;37(1):218-224.

Koeppen A. Friedreich's ataxia: pathology, pathogenesis, and molecular genetics. J Neurol Sci. 2011 Apr 15;303(1-2):1-12.

Koeppen A, Becker A, Qian J, et al. Friedreich Ataxia: Hypoplasia of Spinal Cord and Dorsal Root Ganglia. J Neuropathol Exp Neurol. 2017a Feb 1;76(2):101-108.

Koeppen A, Becker A, Qian J, et al. Friedreich Ataxia: Developmental Failure of the Dorsal Root Entry Zone. J Neuropathol Exp Neurol. 2017b Nov 1;76(11):969-977.

Koeppen A, Davis A, Morral J. The cerebellar component of Friedreich's ataxia. Acta Neuropathol. 2011 Sep;122(3):323-30.

Koeppen A and Mazurkiewicz J. Friedreich ataxia: neuropathology revised. J Neuropathol Exp Neurol. 2013 Feb;72(2):78-90.

Koeppen A, Ramirez R, Becker A, et al. The pathogenesis of cardiomyopathy in Friedreich ataxia. PLoS One. 2015 Mar 4;10(3):e0116396.

La Rosa P, Bertini E, Piemonte F. The NRF2 Signaling Network Defines Clinical Biomarkers and Therapeutic Opportunity in Friedreich's Ataxia. Int J Mol Sci. 2020a Jan 30;21(3):916.

La Rosa P, Petrillo S, Bertini E, et al. Oxidative Stress in DNA Repeat Expansion Disorders: A Focus on NRF2 Signaling Involvement. Biomolecules. 2020b May 1;10(5):702.

La Rosa P, Petrillo S, Fiorenza M, et al. Ferroptosis in Friedreich's Ataxia: A Metal-Induced Neurodegenerative Disease. Biomolecules. 2020c Nov 13;10(11):1551.

Labuda M, Labuda D, Miranda C, et al. Unique origin and specific ethnic distribution of the Friedreich ataxia GAA expansion. Neurology. 2000 Jun 27;54(12):2322-4.

Lagedrost S, Sutton M, Cohen M, et al. Idebenone in Friedreich ataxia cardiomyopathy-results from a 6-month phase III study (IONIA). Am Heart J. 2011 Mar;161(3):639-645.e1.

Lai J, Nachun D, Petrosyan L, et al. Transcriptional profiling of isogenic Friedreich ataxia neurons and effect of an HDAC inhibitor on disease signatures. J Biol Chem. 2019 Feb 8;294(6):1846-1859.

Lees J, Napierala M, Pébay A, et al. Cellular pathophysiology of Friedreich's ataxia cardiomyopathy. Int J Cardiol. 2022 Jan 1;346:71-78.

Legrand L, Diallo A, Monin ML, et al. Predictors of Left Ventricular Dysfunction in Friedreich's Ataxia in a 16-Year Observational Study. Am J Cardiovasc Drugs. 2020a Apr;20(2):209-216.

Legrand L, Heuze C, Diallo A, et al. Prognostic value of longitudinal strain and ejection fraction in Friedreich's ataxia. Int J Cardiol. 2021 May 1;330:259-265.

Legrand L, Maupain C, Monin ML, et al. Significance of NT-proBNP and High-sensitivity Troponin in Friedreich Ataxia. J Clin Med. 2020b May 28;9(6):1630.

Legrand L, Maupain C, Monin ML, et al. Significance of NT-proBNP and High-sensitivity Troponin in Friedreich Ataxia. J Clin Med. 2020c May 28;9(6):1630.

Li J, Rozwadowska N, Clark A, et al. Excision of the expanded GAA repeats corrects cardiomyopathy phenotypes of iPSC-derived Friedreich's ataxia cardiomyocytes. Stem Cell Res. 2019 Oct;40:101529.

Li Y, Polak U, Bhalla A, et al. Excision of Expanded GAA Repeats Alleviates the Molecular Phenotype of Friedreich's Ataxia. Mol Ther. 2015 Jun;23(6):1055-1065.

Lodi R, Rajagopalan B, Blamire A, et al. Cardiac energetics are abnormal in Friedreich ataxia patients in the absence of cardiac dysfunction and hypertrophy: an in vivo 31P magnetic resonance spectroscopy study. Cardiovasc Res. 2001 Oct;52(1):111-9.

Lynch D, Chin M, Delatycki M, et al. Safety and Efficacy of Omaveloxolone in Friedreich Ataxia (MOXIe Study). Ann Neurol. 2021a Feb;89(2):212-225.

Lynch D and Farmer G. Mitochondrial and metabolic dysfunction in Friedreich ataxia: update on pathophysiological relevance and clinical interventions. Neuronal Signal. 2021c May 17;5(2):NS20200093.

Lynch D, Farmer J, Hauser L, et al. Safety, pharmacodynamics, and potential benefit of omaveloxolone in Friedreich ataxia. Ann Clin Transl Neurol. 2018 Nov 10;6(1):15-26.

Lynch D, Farmer J, Tsou A, et al. Measuring Friedreich ataxia: complementary features of examination and performance measures. Neurology. 2006 Jun 13;66(11):1711-6.

Lynch D, Perlman S, Meier T. A phase 3, double-blind, placebo-controlled trial of idebenone in friedreich ataxia. Arch Neurol. 2010 Aug;67(8):941-7.

Lynch D, Schadt K, Kichula E, et al. Friedreich Ataxia: Multidisciplinary Clinical Care. J Multidiscip Healthc. 2021b Jun 28;14:1645-1658.

Lynch D, Willi S, Wilson R, et al. A0001 in Friedreich ataxia: biochemical characterization and effects in a clinical trial. Mov Disord. 2012 Jul;27(8):1026-33.

Maio N, Jain A, Rouault T. Mammalian iron-sulfur cluster biogenesis: Recent insights into the roles of frataxin, acyl carrier protein and ATPase-mediated transfer to recipient proteins. Curr Opin Chem Biol. 2020 Apr;55:34-44.

Marmolino D, Manto M, Acquaviva F, et al. PGC-1alpha down-regulation affects the antioxidant response in Friedreich's ataxia. PLoS One. 2010 Apr 7;5(4):e10025.

Martelli A, Schmucker S, Reutenauer L, et al. Iron regulatory protein 1 sustains mitochondrial iron loading and function in frataxin deficiency. Cell Metab. 2015 Feb 3;21(2):311-323.

McCormack M, Guttmann R, Schumann M, et al. Frataxin point mutations in two patients with Friedreich's ataxia and unusual clinical features. J Neurol Neurosurg Psychiatry. 2000 May;68(5):661-4.

McCormick A, Shinnick J, Schadt K, et al. Cardiac transplantation in Friedreich Ataxia: Extended follow-up. J Neurol Sci. 2017 Apr 15;375:471-473.

Meier T, Perlman S, Rummey C, et al. Assessment of neurological efficacy of idebenone in pediatric patients with Friedreich's ataxia: data from a 6-month controlled study followed by a 12-month open-label extension study. J Neurol. 2012 Feb;259(2):284-91.

Mejia E, Lynch A, Hearle P, et al. Ectopic Burden via Holter Monitors in Friedreich Ataxia. Pediatr Neurol. 2021 Apr;117:29-33.

Mercado-Ayón E, Warren N, Halawani S, et al. Cerebellar Pathology in an Inducible Mouse Model of Friedreich Ataxia. Front Neurosci. 2022 Mar 24;16:819569.

Meseck E, Guibinga G, Wang S, et al. Intrathecal sc-AAV9-CB-GFP: Systemic Distribution Predominates Following Single-Dose Administration in Cynomolgus Macaques. Toxicol Pathol. 2022 Jun;50(4):415-431.

Mühlenhoff U, Richhardt N, Ristow M, et al. The yeast frataxin homolog Yfh1p plays a specific role in the maturation of cellular Fe/S proteins. Hum Mol Genet. 2002 Aug 15;11(17):2025-36.

Naeije G, Rovai A, Pandolfo M, et al. Hand Dexterity and Pyramidal Dysfunction in Friedreich Ataxia, A Finger Tapping Study. Mov Disord Clin Pract. 2020 Dec 21;8(1):85-91.

Naeije G, Schulz J, Corben L. The cognitive profile of Friedreich ataxia: a systematic review and meta-analysis. BMC Neurol. 2022 Mar 17;22(1):97.

Naeije G, Wens V, Bourguignon M, et al. Altered neocortical tactile but preserved auditory early change detection responses in Friedreich ataxia. Clin Neurophysiol. 2019 Aug;130(8):1299-1310.

Naidoo J, Stanek L, Ohno K, et al. Extensive Transduction and Enhanced Spread of a Modified AAV2 Capsid in the Non-human Primate CNS. Mol Ther. 2018 Oct 3;26(10):2418-2430.

Nguyen K, Corben L, Pathirana P, et al. An Instrumented Measurement Scheme for the Assessment of Upper Limb Function in Individuals with Friedreich Ataxia. Annu Int Conf IEEE Eng Med Biol Soc. 2019 Jul;2019:317-320.

Nguyen K, Corben L, Pathirana P, et al. Assessment of Disease Progression in Friedreich Ataxia using an Instrumented Self Feeding Activity. Annu Int Conf IEEE Eng Med Biol Soc. 2020a Jul;2020:3827-3830.

Nguyen K, Corben L, Pathirana P, et al. The Assessment of Upper Limb Functionality in Friedreich Ataxia via Self-Feeding Activity. IEEE Trans Neural Syst Rehabil Eng. 2020b Apr;28(4):924-933.

Nolano M, Provitera V, Crisci C, et al. Small fibers involvement in Friedreich's ataxia. Ann Neurol. 2001 Jul;50(1):17-25.

Noval S, Contreras I, Sanz-Gallego I, et al. Ophthalmic features of Friedreich ataxia. Eye (Lond). 2012 Feb;26(2):315-20.

O'Connell T, Logsdon D, Payne R. Metabolomics analysis reveals dysregulation in one carbon metabolism in Friedreich Ataxia. Mol Genet Metab. 2022 Aug;136(4):306-314.

Ouellet D, Cherif K, Rousseau J, et al. Deletion of the GAA repeats from the human frataxin gene using the CRISPR-Cas9 system in YG8R-derived cells and mouse models of Friedreich ataxia. Gene Ther. 2017 May;24(5):265-274.

Pandolfo M. Neurologic outcomes in Friedreich ataxia: Study of a single-site cohort. Neurol Genet. 2020 Mar 20;6(3):e415.

Pane C, Salzano A, Trinchillo A, et al. Safety and feasibility of upper limb cardiopulmonary exercise test in Friedreich ataxia. Eur J Prev Cardiol. 2022 Mar 25;29(3):445-451.

Patel M, Isaacs C, Seyer L, et al. Progression of Friedreich ataxia: quantitative characterization over 5 years. Ann Clin Transl Neurol. 2016 Jul 25;3(9):684-94.

Perdomini M, Belbellaa B, Monassier L, et al. Prevention and reversal of severe mitochondrial cardiomyopathy by gene therapy in a mouse model of Friedreich's ataxia. Nat Med. 2014 May;20(5):542-7.

Perez B, Wheeler J, Deiulio A, et al. Prevention of Cardiac Disease Features Observed in a Conditional Knockout Mouse Model of Friedreich's Ataxia Treated with a Novel AAV FXN Gene Therapy (AVB-202). Mol Ther. 2022 30, 1-592.

Pierre-Gilles H, Deelchand J, Eberly L, et al. Longitudinal MRS, MRI and DTI in the Spinal Cord in Friedreich's Ataxia: 24-month follow-up. 2017 International Ataxia Research Conference. Pisa, Italy.

Piguet F, Montigny C, Vaucamps N, et al. Rapid and Complete Reversal of Sensory Ataxia by Gene Therapy in a Novel Model of Friedreich Ataxia. Mol Ther. 2018 Aug 1;26(8):1940-1952.

Pook M, Al-Mahdawi S, Carroll C, et al. Rescue of the Friedreich's ataxia knockout mouse by human YAC transgenesis. Neurogenetics. 2001 Oct;3(4):185-93.

Pousset F, Legrand L, Monin ML, et al. A 22-Year Follow-up Study of Long-term Cardiac Outcome and Predictors of Survival in Friedreich Ataxia. JAMA Neurol. 2015 Nov;72(11):1334-41.

Puccio H, Simon D, Cossée M, et al. Mouse models for Friedreich ataxia exhibit cardiomyopathy, sensory nerve defect and Fe-S enzyme deficiency followed by intramitochondrial iron deposits. Nat Genet. 2001 Feb;27(2):181-6.

Rodríguez L, Lapeña T, Calap-Quintana P, et al. Antioxidant Therapies and Oxidative Stress in Friedreich´s Ataxia: The Right Path or Just a Diversion? Antioxidants (Basel). 2020 Jul 24;9(8):664.

Ramirez R, Becker A, Mazurkiewicz J, et al. Pathology of Intercalated Discs in Friedreich Cardiomyopathy. J Am Coll Cardiol. 2015 Oct 13;66(15):1739-40.

Reetz K, Dogan I, Costa A, et al. Biological and clinical characteristics of the European Friedreich's Ataxia Consortium for Translational Studies (EFACTS) cohort: a cross-sectional analysis of baseline data. Lancet Neurol. 2015 Feb;14(2):174-82.

Reetz K, Dogan I, Hilgers RD, et al. Progression characteristics of the European Friedreich's Ataxia Consortium for Translational Studies (EFACTS): a 2 year cohort study. Lancet Neurol. 2016 Dec;15(13):1346-1354.

Reetz K, Dogan I, Hilgers RD, et al. Progression characteristics of the European Friedreich's Ataxia Consortium for Translational Studies (EFACTS): a 4-year cohort study. Lancet Neurol. 2021 May;20(5):362-372.

Reetz K, Dogan I, Hohenfeld C, et al. Nonataxia symptoms in Friedreich Ataxia: Report from the Registry of the European Friedreich's Ataxia Consortium for Translational Studies (EFACTS). Neurology. 2018 Sep 4;91(10):e917-e930.

Regner S, Wilcox N, Friedman L, et al. Friedreich ataxia clinical outcome measures: natural history evaluation in 410 participants. J Child Neurol. 2012 Sep;27(9):1152-8.

Reisman S, Gahir S, Lee CY, et al. Pharmacokinetics and pharmacodynamics of the novel Nrf2 activator omaveloxolone in primates. Drug Des Devel Ther. 2019 Apr 17;13:1259-1270.

Rezende T, Martinez A, Faber I, et al. Developmental and neurodegenerative damage in Friedreich's ataxia. Eur J Neurol. 2019 Mar;26(3):483-489.

Ribaï P, Pousset F, Tanguy ML, et al. Neurological, cardiological, and oculomotor progression in 104 patients with Friedreich ataxia during long-term follow-up. Arch Neurol. 2007 Apr;64(4):558-64.

Rodden L and Lynch D. Designing phase II clinical trials in Friedreich ataxia. Expert Opin Emerg Drugs. 2021 Dec;26(4):415-423.

Rodden L, Rummey C, Dong Y, et al. Clinical Evidence for Variegated Silencing in Patients With Friedreich Ataxia. Neurol Genet. 2022 May 17;8(3):e683.

Rojas P, de Hoz R, Cadena M, et al. Neuro-Ophthalmological Findings in Friedreich's Ataxia. J Pers Med. 2021 Jul 23;11(8):708.

Rojas P, Ramírez A, de Hoz R, et al. Ocular Involvement in Friedreich Ataxia Patients and its Relationship with Neurological Disability, a Follow-up Study. Diagnostics (Basel). 2020 Jan 29;10(2):75.

Rummey C, Corben L, Delatycki M, et al. Psychometric properties of the Friedreich Ataxia Rating Scale. Neurol Genet. 2019 Oct 29;5(6):371.

Rummey C, Farmer J, Lynch D. Predictors of loss of ambulation in Friedreich's ataxia. EClinicalMedicine. 2020a Jan 8;18:100213.

Rummey C, Zesiewicz T, Perez-Lloret S, et al. Test-retest reliability of the Friedreich's ataxia rating scale. Ann Clin Transl Neurol. 2020b Sep;7(9):1708-1712.

Salami C, Jackson K, Jose C, et al. Stress-Induced Mouse Model of the Cardiac Manifestations of Friedreich's Ataxia Corrected by AAV-mediated Gene Therapy. Hum Gene Ther. 2020 Aug;31(15-16):819-827.

Salih M, Ahlsten G, Stålberg E, et al. Friedreich's ataxia in 13 children: presentation and evolution with neurophysiologic, electrocardiographic, and echocardiographic features. J Child Neurol. 1990 Oct;5(4):321-6.

Saveliev A, Everett C, Sharpe T, et al. DNA triplet repeats mediate heterochromatin-protein-1-sensitive variegated gene silencing. Nature. 2003 Apr 24;422(6934):909-13.

Schadt K, Friedman L, Regner S, et al. Cross-sectional analysis of electrocardiograms in a large heterogeneous cohort of Friedreich ataxia subjects. J Child Neurol. 2012 Sep;27(9):1187-92.

Schmucker S, Argentiti M, Carelle-Calmels N, et al. The in vivo mitochondrial two-step maturation of human frataxin. Hum Mol Genet. 2008 Nov 15;17(22):3521-31.

Segovia J, Alonso-Pulpon L, Burgos R, et al. Heart transplantation in Friedreich's ataxia and other neuromuscular diseases. J Heart Lung Transplant. 2001 Feb;20(2):169.

Selvadurai L, Corben L, Delatycki M, et al. Multiple mechanisms underpin cerebral and cerebellar white matter deficits in Friedreich ataxia: The IMAGE-FRDA study. Hum Brain Mapp. 2020 May;41(7):1920-1933.

Selvadurai L, Georgiou-Karistianis N, Shishegar R, et al. Longitudinal structural brain changes in Friedreich ataxia depend on disease severity: the IMAGE-FRDA study. J Neurol. 2021 Nov;268(11):4178-4189.

Seyer L, Galetta K, Wilson J, et al. Analysis of the visual system in Friedreich ataxia. J Neurol. 2013 Sep;260(9):2362-9.

Shinnick J, Schadt K, Strawser C, et al. Comorbid Medical Conditions in Friedreich Ataxia: Association With Inflammatory Bowel Disease and Growth Hormone Deficiency. J Child Neurol. 2016 Aug;31(9):1161-5.

St John Sutton M, Ky B, Regner S, et al. Longitudinal strain in Friedreich Ataxia: a potential marker for early left ventricular dysfunction. Echocardiography. 2014;31(1):50-7.

Subramony S, May W, Lynch D, et al. Measuring Friedreich ataxia: Interrater reliability of a neurologic rating scale. Neurology. 2005 Apr 12;64(7):1261-2.

Takazaki K, Quinaglia T, Venacio T, et al. Pre-clinical left ventricular myocardial remodeling in patients with Friedreich's ataxia: A cardiac MRI study. PLoS One. 2021 Mar 26;16(3):e0246633.

Thomas-Black G, Parkinson M, Bremner F, et al. Peripapillary retinal nerve fibre layer thickness in Friedreich's ataxia: a biomarker for trials? Brain. 2019 Jun 1;142(6):e23.

Tsou A, Paulsen E, Lagedrost S, et al. Mortality in Friedreich ataxia. J Neurol Sci. 2011 Aug 15;307(1-2):46-9.

Turchi R, Faraonio R, Lettieri-Barbato D, et al. An Overview of the Ferroptosis Hallmarks in Friedreich's Ataxia. Biomolecules. 2020 Oct 28;10(11):1489.

Valero M, Muñoz-Blanco J, Sanchez A, et al. Should Advanced Friedreich's Ataxia Be a Contraindication for Heart Transplantation? A Case Report of a Successful Procedure in a 58-Year-Old Patient. J Cardiovasc Dev Dis. 2022 Mar 9;9(3):80.

Vavla M, Arrigoni F, Peruzzo D, et al. Functional MRI Studies in Friedreich's Ataxia: A Systematic Review. Front Neurol. 2022 Mar 10;12:802496.

Villa C, Legato M, Umbach A, et al. Treatment with ROS detoxifying gold quantum clusters alleviates the functional decline in a mouse model of Friedreich ataxia. Sci Transl Med. 2021 Aug 18;13(607):eabe1633.

Vogel A, Wardrop M, Folker J, et al. Voice in Friedreich Ataxia. J Voice. 2017 Mar;31(2):243.e9-243.e19.

Vásquez-Trincado C, Dunn J, Han J, et al. Frataxin deficiency lowers lean mass and triggers the integrated stress response in skeletal muscle. JCI Insight. 2022 May 9;7(9):e155201.

Vásquez-Trincado C, Patel M, Sivaramakrishnan A, et al. Adaptation of the heart to Frataxin depletion: Evidence that integrated stress response can predominate over mTORC1 activation. Hum Mol Genet. 2021 Sep 22;ddab216.

Wang Q, Laboureur L, Weng L, et al. Simultaneous Quantification of Mitochondrial Mature Frataxin and Extra-Mitochondrial Frataxin Isoform E in Friedreich's Ataxia Blood. Front Neurosci. 2022 Apr 28;16:874768.

Ward P, Harding I, Close T, et al. Longitudinal evaluation of iron concentration and atrophy in the dentate nuclei in friedreich ataxia. Mov Disord. 2019 Mar;34(3):335-343.

Weidemann F, Liu D, Hu K, et al. The cardiomyopathy in Friedreich's ataxia - New biomarker for staging cardiac involvement. Int J Cardiol. 2015 Sep 1;194:50-7.

Wong A, Wong G, Shen M, et al. Correlation between frataxin expression and contractility revealed by in vitro Friedreich's ataxia cardiac tissue models engineered from human pluripotent stem cells. Stem Cell Res Ther. 2019 Jul 8;10(1):203.

Zesiewicz T, Heerinckx F, De Jager R, et al. Randomized, clinical trial of RT001: Early signals of efficacy in Friedreich's ataxia. Mov Disord. 2018 Jul;33(6):1000-1005.

Zesiewicz T, Hancock J, Ghanekar S, et al. Emerging therapies in Friedreich's Ataxia. Expert Rev Neurother. 2020 Dec;20(12):1215-1228.

Zuluaga C, Gertz M, Yost-Bido M, et al. Identification of the Therapeutically Beneficial Intravenous Dose of AAVrh.10hFXN to Treat the Cardiac Manifestations of Friedreichs's Ataxia. Mol Ther. 2022 30, 1-592.

12 APPENDICES

Appendix 1 FA Natural History Study

This Appendix will provide background and an overview to the largest (and only) natural history study of Friedreich ataxia being conducted in the United States with data accessible to the research community.

FA-Clinical Outcome Measures Study (FA-COMS) – A natural history study of Friedreich Ataxia being conducted by the Collaborative Clinical Research Network in FA (CCRN in FA).

FA-COMS is a multicenter natural history study that aims to understand the clinical symptoms, progression, and long-term outcomes for individuals with FA. FA-CPOMS also serves to expand the network of clinical research centers in FA and provides a framework for facilitating therapeutic interventions. In addition, FA-COMS has led the development of clinical outcome assessments being used in clinical trials, genetic modifier studies, and biomarker studies including frataxin protein level assessments.

Initiated by a core group of clinical researchers and supported by FARA (Friedreich's Ataxia Research Alliance), this natural history study is the largest, most diverse source of longitudinal clinical data in FA. Enrollment started in 2003 at six sites in the United States and has continued ever since while continuously adding new sites. Today, more than 1250 participants have contributed more than 6000 clinical visits at 16 sites worldwide (The Children's Hospital of Philadelphia/University of Pennsylvania, University of California Los Angeles, Emory University, University of South Florida, University of Florida, University of Iowa, The Ohio State University, University of Colorado, St. Jude Children's Research Hospital, University of Rochester, the Hospital for Sick Children, Centre Hospitalier de l'Université de Montréal, Murdoch Children's Research Institute, University of Auckland, and the All India Institute for Medical Sciences).

The initial study protocol remains minimally altered today, ensuring continuity in longitudinal collection of data. There are study specific case report forms, standard operating procedures, training protocols for new sites and staff, quarterly investigator and coordinator meetings, and use of an electronic data capture system, all of which ensure high quality data collection and uniform study performance across sites.

Table 1: Demographic and follow-up characteristics by Onset Group.

Onset Group	0-7y (early)	8-14y (typical)	15-24y (intermediate)	>24y (late)	Overall
N (% of overall)	324 (29)	438 (39)	234 (21)	119 (11)	1115
Sex (m, %)	53	49	48	40	49
Age of Onset (AOO) [y]	5 [4, 6]	11 [9, 13]	18 [16, 20]	32 [28, 40]	11 [7, 16]

GAA1[1]	790 [700, 896]	704 [600, 820]	500 [376, 630]	250 [136, 360]	690 [500, 800]
GAA2[1]	980 [875, 1099]	917.0 [800, 1020]	869.0 [730, 1018]	866.0 [627, 1000]	926.5 [800, 1034]
Point Mutations (%)	8.6	3.7	4.3	2.5	5.1
Time Since Diagnosis [y]	2.4 [0.9, 9.2]	3.7 [1.1, 12.3]	5.6 [1.7, 12.6]	6.4 [3.0, 11.8]	4.2 [1.1, 11.5]
Age [y]	12 [9, 19]	19 [15, 27]	30 [24, 39]	49 [43, 57]	21 [14, 34]
Age at last visit [y]	18 [14, 25]	24 [19, 33]	35 [29, 44]	53 [47, 63]	27 [19, 39]
Ambulatory at enrollment (%)	71	65	75	78	70
Ambulatory at last visit (%)	43	45	54	66	49
Follow-Up [y]	5 [3, 9]	5 [3, 9]	6 [3, 10]	6 [3, 10]	5 [3, 10]
Patients without follow- up (%)	20	22	24	29	23

Data are % or median [IQR];

1Excluding point mutations (n=57) and participants with missing repeat length information (n=58).

From Rummey et al Neurology 20220

FARA has partnered with the University of Rochester Clinical Trial Coordination Center (CTCC), to provide a range of management and database services for FA-COMS. The CTCC specializes in the development, management, and conduct of clinical research studies and provides a full range of research and clinical trial management support services that facilitate the conduct of clinical research from study conceptualization through data analysis, publication, and FDA approval. Over the past 30 years, the CTCC has managed the conduct of more than 130 clinical research studies with 45 sponsors (government, industry and private) that enrolled over 40,000 research participants in US, Canada, Europe, New Zealand, and Australia. The CTCC specifically ensures that FA-COMS data is captured into a 21 CFR part 11 compliant electronic data capture system (eDC) for management of the database. The CTCC has over 60 SOPs that they follow to meet regulatory requirements. The CTCC is responsible for oversight of the study database, training staff on data entry, query management, reporting, development new CRFs, coordinating study amendments and IRB updates and approvals.

In FA-COMS, each site follows a protocol inclusive of demographic and medical history, neurological rating scale, clinical and functional assessments, patient reported outcome measures, collection of event-based outcomes, and collection of blood and cheek swab samples. A schedule of activities for visits for children and adults enrolled in FA-COMS is included at the end of this document. The primary clinical outcome assessment is the Friedreich's Ataxia Rating Scale (FARS-Neuro, from which the mFARS is derived), administered alongside the Functional Disability Staging (FDS), Activities of Daily Living (ADL), Timed 25-foot walk (T25FW), 9 Hole Peg Test (9HPT) and Low Contrast Letter Acuity (LCLA). Each of these is discussed in detail below. The complete list of publications from the FA-COMS study is included at the end of this document.

Neurological Exam Rating Scale: FA-COMS uses Friedreich's Ataxia Rating Scale (FARS), the most commonly used neurological rating scale in FA clinical trials. It includes assessments of neurological signs and symptoms that specifically reflect neural substrates affected in the disease. Alternative scales, such as the Scale for the Assessment and Rating of Ataxia (SARA) are more commonly used in Europe and other countries. Both the FARS and the SARA score have been used in large natural history studies, and progression in various populations has been extensively characterized.

The US Food and Drug Administration (FDA) has worked with the FA community to consider the use of the FARS as an approvable endpoint in later stage clinical trials which has led to the modified FARS (mFARS) score, consisting of the specific neurological subscales and items that focus on clinically relevant function, meaningful to individuals with FA. Based on data and experience from FA-COMS, this mFARS is used as the primary outcome in clinical trials, and it has gained some acceptance with the FDA for that purpose.

The FARS score was first published in its complete version in 2006 (Lynch et al. 2006). FARS and mFARS data collected as part of FA-COMS allowed cross sectional and longitudinal analyses confirming the sensitivity, reproducibility, test-retest reliability, and functional significance of changes in the scales and subscales. The most advanced, modified version (mFARS) assesses functions from 4 domains with 18 items yielding a maximum score of 93 (see Figure 1). Data from the natural history study provides the basis of publications on e.g., the psychometric properties (Rummey et al. 2019), the assessment of loss of ambulation and clinical relevance (Rummey, Farmer and Lynch 2020), as well as longitudinal progression (Patel et al. 2016).

Figure 1: Subscales of mFARS

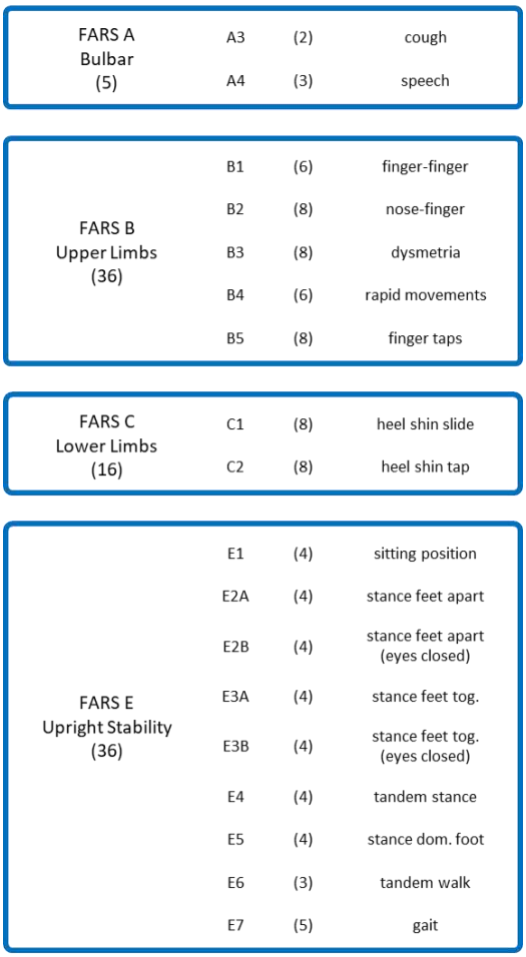

FARS A Bulbar (5)	A3	(2)	cough
	A4	(3)	speech
FARS B Upper Limbs (36)	B1	(6)	finger-finger
	B2	(8)	nose-finger
	B3	(8)	dysmetria
	B4	(6)	rapid movements
	B5	(8)	finger taps
FARS C Lower Limbs (16)	C1	(8)	heel shin slide
	C2	(8)	heel shin tap
FARS E Upright Stability (36)	E1	(4)	sitting position
	E2A	(4)	stance feet apart
	E2B	(4)	stance feet apart (eyes closed)
	E3A	(4)	stance feet tog.
	E3B	(4)	stance feet tog. (eyes closed)
	E4	(4)	tandem stance
	E5	(4)	stance dom. foot
	E6	(3)	tandem walk
	E7	(5)	gait

Functional Disability Staging and Activities of Daily Living: Alongside the FARS, two other measures for FA were created and tested to further quantify function outcomes and impact of disease. These have also been used in natural history studies and clinical trials. The Functional Disability Staging (FDS) scale is a clinician graded scale (0-6) that describes the severity of ataxia and impact on mobility. The Activities of Daily Living (ADL) scale is a patient reported outcome measure that assesses impact of disease symptoms in 9 domains, scoring 0-36 with higher scores being associated with more impairment or inability to perform ADLs.

Functional Assessments: Several functional assessments have been evaluated over time in FA. Specifically, the T25FW, 9HPT, and LCLA were selected based on their development and utility in multiple sclerosis (Cutter et al. 1999, Balcer et al. 2017). All 3 have been collected as part of the annual evaluation since FA-COMS was initiated. In smaller, sub-studies additional assessments have been evaluated including gait using the gaitrite system and a one-minute walk test, balance using the Berg Balance Scale (BBS) and Biodex balance system, upper limb function using Ataxia Instrumented Measurements (AIMS – spoon and cup), hearing using the

LiSNS, vision using Ocular Coherence Tomography (OCT), and speech using the RedenLab speech battery. Most recently, there have been a few exploratory studies of digital, continuous monitoring devices, such as accelerometers, to evaluate utility in the clinic and at home.

Additional Sample and Data Collection

Once a year, study participants are asked to provide a cheek swab and/or blood sample for a variety of different measures including frataxin protein level assessments and other biomarker tests. There is also a one-time optional sample collection offered to study participants for DNA analyses from whole blood and/or a cheek swab. Study participants are asked to provide electrocardiogram (EKG), 24hr-Holter, and echocardiogram data if it has been collected by their cardiologist, and additional data is captured for specific events, if they have occurred, such as cardiac adverse events, scoliosis surgery, pulmonary function tests, pregnancy, and mortality.

FA-COMS and the CCRNs have also been used as a testing ground for new biomarkers and clinical outcome assessments (Seyer et al. 2013, Hamedani et al. 2018, Rummey et al. 2019, Regner et al. 2012). Blood samples collected from FA-COMS participants have been used to evaluate various assays for frataxin protein assessments along with other blood biomarkers.

The FA-CHILD study

Overall, the FA-COMS initially recruited an over-representation of adults with FA, both newly diagnosed as well as with established diagnoses. Therefore, the CCRN investigators and FARA partnered with several initiatives to enroll more pediatric participants. One of those initiatives included an FDA-funded grant allowing the enrollment of 100 children into a separate natural history with more frequent visits (every six months), called the FA-CHILD study. See Table 2 for the demographic of FA-CHILD. This study administers a broader set of assessments, potentially more sensitive in children. A schedule of activities for visits for FA-CHILD is included at the end of this document. In practice, FA-CHILD is run alongside FA-COMS and its participants are enrolled in FA-COMS as well. The study still has a separate database in the same 21 CFR part 11 compliant eDC system as FA-COMS with management and oversight by University of Rochester CTCC.

A total of 108 participants were enrolled across 3 sites; all visits will be completed by September 2022 with data analysis to follow. Initial results will be presented at the ICAR conference in November 2022.

The baseline demographics of FA-CHILD indicate that most enrollees are early onset, severely affected patients. Approximately ten percent of participants have a point mutation and are heterozygous for the repeat. See table below for detailed demographic.

Table 2: Demographics of the FA-CHILD study

	Overall
n	108
Sex = m	50 (46)
Age of Onset	7.0 [5.0, 9.0]
Repeat Length (short)*	766.0 [670.0, 866.0]
Point Mutations	10 (9)
Age	13.9 [12.0, 16.0]
Follow Up (visits)	4.0 [3.0, 4.0]
Non-Ambulatory [FDS>4]	16 (15)
mFARS	40.2 (15.1)
Upright Stability Score (FARS E)	23.4 (7.1)

The cohort in this study provides a representative group for investigation of the change over time in clinical measures and biomarkers in younger FA patients. All participants enrolled will continue to be followed through FA-COMS. FA-CHILD data will also be made available to the research community through the FA-ICD and the RDCA-DAP housed with C-Path. The ongoing characterization will be useful in planning of future therapeutic interventions trials in younger patients.

Access to FA-COMS data

FA-COMS was designed to catalyze and accelerate FA research and drug development. Therefore, the data from the study has been made available to the research community

through the Friedreich's Ataxia Integrated Clinical Database (FA-ICD), which is also part of the Rare Disease Accelerator-Data and Analytics Platform (RDCA-DAP) established by C-Path, with funding from FDA. Through FA-ICD, FARA supported an effort to establish a database containing FA patient-level de-identified data standardized to CDISC from the natural history studies and from sponsor supported interventional clinical trials (see Figure 2 below). Access to these data is open to qualified external researchers. In addition, a collaborative initiative of FARA and C-Path scientists at C-Path is working to further increase knowledge and understanding of the mFARS, other clinical outcome assessments, along with models of disease progression to share with regulatory authorities.

FIGURE 2: Data sets in the Friedreich's Ataxia Integrated Clinical Database (FA-ICD).

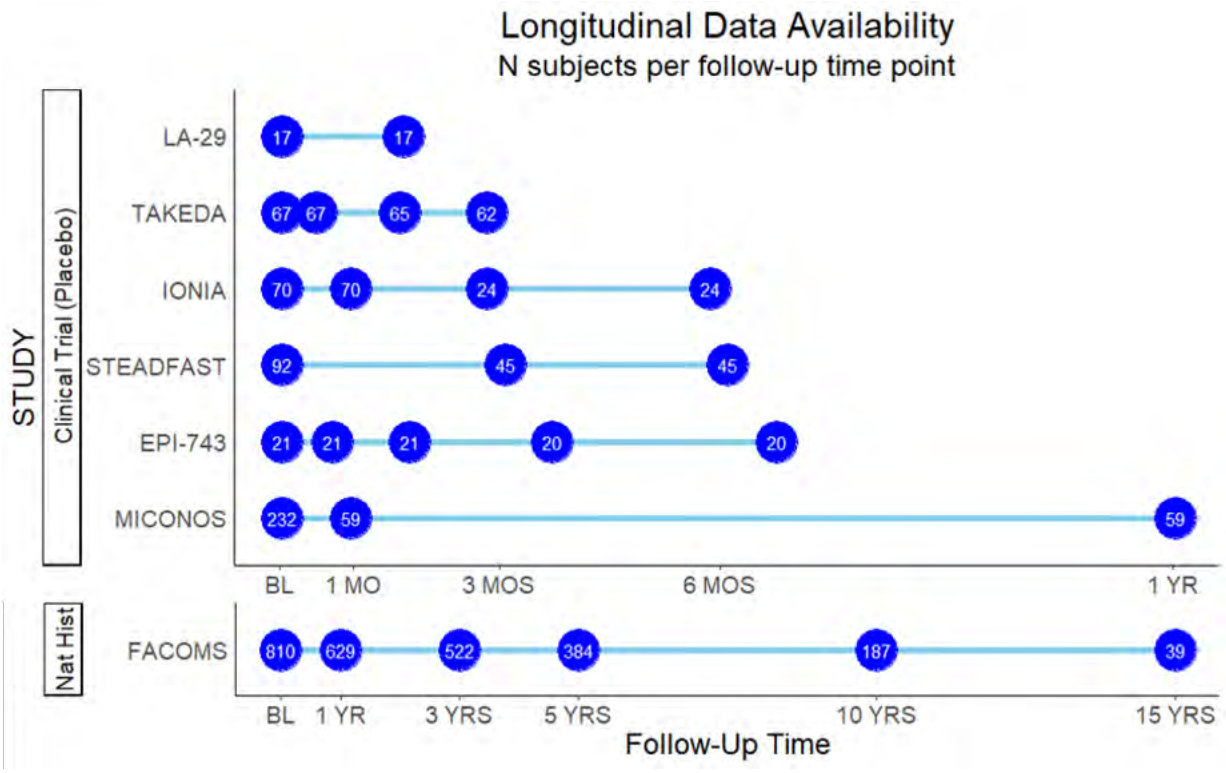

The numbers in the blue circles indicate the number of participants at each visit for each study.

Cited References

Balcer, L. J., J. Raynowska, R. Nolan, S. L. Galetta, R. Kapoor, R. Benedict, G. Phillips, N. LaRocca, L. Hudson, R. Rudick & M. S. O. A. Consortium (2017) Validity of low-contrast letter acuity as a visual performance outcome measure for multiple sclerosis. *Mult Scler,* 23**,** 734-747.

Cutter, G. R., M. L. Baier, R. A. Rudick, D. L. Cookfair, J. S. Fischer, J. Petkau, K. Syndulko, B. G. Weinshenker, J. P. Antel, C. Confavreux, G. W. Ellison, F. Lublin, A. E. Miller, S. M. Rao, S.

Reingold, A. Thompson & E. Willoughby (1999) Development of a multiple sclerosis functional composite as a clinical trial outcome measure. *Brain,* 122 (Pt 5)**,** 871-82.

Hamedani, A. G., L. A. Hauser, S. Perlman, K. Mathews, G. R. Wilmot, T. Zesiewicz, S. H. Subramony, T. Ashizawa, M. B. Delatycki, A. Brocht & D. R. Lynch (2018) Longitudinal analysis of contrast acuity in Friedreich ataxia. *Neurol Genet,* 4**,** e250.

Lynch, D. R., J. M. Farmer, A. Y. Tsou, S. Perlman, S. H. Subramony, C. M. Gomez, T. Ashizawa, G. R. Wilmot, R. B. Wilson & L. J. Balcer (2006) Measuring Friedreich ataxia: complementary features of examination and performance measures. *Neurology,* 66**,** 1711-6.

Patel, M., C. J. Isaacs, L. Seyer, K. Brigatti, S. Gelbard, C. Strawser, D. Foerster, J. Shinnick, K. Schadt, E. M. Yiu, M. B. Delatycki, S. Perlman, G. R. Wilmot, T. Zesiewicz, K. Mathews, C. M. Gomez, G. Yoon, S. H. Subramony, A. Brocht, J. Farmer & D. R. Lynch (2016) Progression of Friedreich ataxia: quantitative characterization over 5 years. *Ann Clin Transl Neurol,* 3**,** 684-94.

Regner, S. R., N. S. Wilcox, L. S. Friedman, L. A. Seyer, K. A. Schadt, K. W. Brigatti, S. Perlman, M. Delatycki, G. R. Wilmot, C. M. Gomez, K. O. Bushara, K. D. Mathews, S. H. Subramony, T. Ashizawa, B. Ravina, A. Brocht, J. M. Farmer & D. R. Lynch (2012) Friedreich ataxia clinical outcome measures: natural history evaluation in 410 participants. *J Child Neurol,* 27**,** 1152-8.

Rummey, C., L. A. Corben, M. B. Delatycki, S. H. Subramony, K. Bushara, C. M. Gomez, J. C. Hoyle, G. Yoon, B. Ravina, K. D. Mathews, G. Wilmot, T. Zesiewicz, S. Perlman, J. M. Farmer & D. R. Lynch (2019) Psychometric properties of the Friedreich Ataxia Rating Scale. *Neurol Genet,* 5**,** 371.

Rummey, C., J. M. Farmer & D. R. Lynch (2020) Predictors of loss of ambulation in Friedreich's ataxia. *EClinicalMedicine,* 18**,** 100213.

Seyer, L. A., K. Galetta, J. Wilson, R. Sakai, S. Perlman, K. Mathews, G. R. Wilmot, C. M. Gomez, B. Ravina, T. Zesiewicz, K. O. Bushara, S. H. Subramony, T. Ashizawa, M. B. Delatycki, A. Brocht, L. J. Balcer & D. R. Lynch (2013) Analysis of the visual system in Friedreich ataxia. *J Neurol,* 260**,** 2362-9.

FA-COMS Publications

2022

Natural History of Friedreich's Ataxia: Heterogeneity of Neurological Progression and Consequences for Clinical Trial Design Neurology. 2022. Jul 11;10.1212/WNL.0000000000200913.

Friedreich's Ataxia related Diabetes: Epidemiology and management practices. Diabetes Res Clin Pract. 2022 Apr;186:109828. doi: 10.1016/j.diabres.2022.109828. Epub 2022 Mar 14.

2021

Scoliosis in Friedreich's ataxia: longitudinal characterization in a large heterogeneous cohort Ann Clin Transl Neurol. 2021 Jun;8(6):1239-1250. doi: 10.1002/acn3.51352. Epub 2021 May 5.

2020

Test-retest reliability of the Friedreich's ataxia rating scale
Ann Clin Transl Neurol. 2020 Sep;7(9):1708-1712. doi: 10.1002/acn3.51118. Epub 2020 Aug 11.

Predictors of loss of ambulation in Friedreich's ataxia
EClinicalMedicine. 2020 Jan 8;18:100213. doi: 10.1016/j.eclinm.2019.11.006. eCollection 2020 Jan.

Correlation of Visual Quality of Life With Clinical and Visual Status in Friedreich Ataxia
J Neuroophthalmol. 2020 Jan 17. doi: 10.1097/WNO.0000000000000878. [Epub ahead of print]

2019

Psychometric properties of the Friedreich Ataxia Rating Scale
Neurol Genet. 2019 Oct 29;5(6):371. doi: 10.1212/NXG.0000000000000371. eCollection 2019 Dec.

Health related quality of life in Friedreich Ataxia in a large heterogeneous cohort
J Neurol Sci. 2020 Mar 15;410:116642. doi: 10.1016/j.jns.2019.116642. Epub 2019 Dec 24.

2018

Longitudinal analysis of contrast acuity in Friedreich ataxia
Neurol Genet. 2018 Jul 23;4(4):e250. doi: 10.1212/NXG.0000000000000250. eCollection 2018 Aug.

Impact of Mobility Device Use on Quality of Life in Children With Friedreich Ataxia
J Child Neurol. 2018 May;33(6):397-404. doi: 10.1177/0883073818764941. Epub 2018 Apr 2.

Peripheral blood gene expression reveals an inflammatory transcriptomic signature in Friedreich's ataxia patients
Hum Mol Genet. 2018 Sep 1;27(17):2965-2977. doi: 10.1093/hmg/ddy198.

2017

Impact of diabetes in the Friedreich ataxia clinical outcome measures study
Ann Clin Transl Neurol. 2017 Jul 26;4(9):622-631. doi: 10.1002/acn3.439. eCollection 2017 Sep.

2016

Comorbid Medical Conditions in Friedreich Ataxia: Association With Inflammatory Bowel Disease and Growth Hormone Deficiency
J Child Neurol. 2016 Aug;31(9):1161-5. doi: 10.1177/0883073816643408. Epub 2016 Apr 12.

Progression of Friedreich ataxia: quantitative characterization over 5 years
Ann Clin Transl Neurol. 2016 Jul 25;3(9):684-94. doi: 10.1002/acn3.332. eCollection 2016 Sep.

Geographic and Sociodemographic Features of Friedreich Ataxia: Implications for Clinical Research.
Journal of Rare Disorders. 2016. Vol 4, Issue 1

2015

Frataxin levels in peripheral tissue in Friedreich ataxia
Ann Clin Transl Neurol. 2015 Aug;2(8):831-42. doi: 10.1002/acn3.225. Epub 2015 Jul 1.

2014

Consensus clinical management guidelines for Friedreich ataxia
Orphanet J Rare Dis. 2014 Nov 30;9:184. doi: 10.1186/s13023-014-0184-7.

2013

Analysis of the visual system in Friedreich ataxia
J Neurol. 2013 Sep;260(9):2362-9. doi: 10.1007/s00415-013-6978-z. Epub 2013 Jun 18.

Rating disease progression of Friedreich's ataxia by the International Cooperative Ataxia Rating Scale: analysis of a 603-patient database
Brain, Volume 136, Issue 1, January 2013, Pages 259–268

Common data elements for clinical research in Friedreich's ataxia
Mov Disord. 2013 Feb;28(2):190-5. doi: 10.1002/mds.25201. Epub 2012 Dec 12.

2012

Friedreich ataxia clinical outcome measures: natural history evaluation in 410 participants
J Child Neurol. 2012 Sep;27(9):1152-8. doi: 10.1177/0883073812448462. Epub 2012 Jun 29.

Cross-Sectional Analysis of Electrocardiograms in a Large Heterogeneous Cohort of Friedreich Ataxia Subjects
J Child Neurol. 2012 Sep;27(9):1187-92. doi: 10.1177/0883073812448461. Epub 2012 Jun 29.

Analysis of echocardiograms in a large heterogeneous cohort of patients with friedreich ataxia
Am J Cardiol. 2012 Feb 1;109(3):401-5. doi: 10.1016/j.amjcard.2011.09.025. Epub 2011 Nov 10.

FXN methylation predicts expression and clinical outcome in Friedreich ataxia
Ann Neurol. 2012 Apr;71(4):487-97. doi: 10.1002/ana.22671.

2010

Health-related quality of life in children with Friedreich ataxia
Pediatr Neurol. 2010 May;42(5):335-7. doi: 10.1016/j.pediatrneurol.2010.01.002.

Measuring the rate of progression in Friedreich ataxia: implications for clinical trial design
Mov Disord. 2010 Mar 15;25(4):426-32. doi: 10.1002/mds.22912.

2008

Health related quality of life measures in Friedreich Ataxia
J Neurol Sci. 2008 Sep 15;272(1-2):123-8. doi: 10.1016/j.jns.2008.05.009. Epub 2008 Jun 20.

Antioxidant use in Friedreich ataxia
J Neurol Sci. 2008 Apr 15;267(1-2):174-6. Epub 2007 Nov 7.

2006

Measuring Friedreich ataxia: complementary features of examination and performance measures
Neurology. 2006 Jun 13;66(11):1711-6.

2005

Measuring Friedreich ataxia: Interrater reliability of a neurologic rating scale
Neurology. 2005 Apr 12;64(7):1261-2.

Performance measures in Friedreich ataxia: potential utility as clinical outcome tools
Mov Disord. 2005 Jul;20(7):777-82.

FA - COMS
SCHEDULE OF CRF COMPLETION AND STUDY ACTIVITIES

Form X - Required O - Optional	LEVEL	Adult only			**Adult only- Telehealth**			Children only			**Children only- Telehealth**			Both Adult and Child
		BL - Adult	**ODD Visit** - Adult (V01,V03,V05,V07,V09,V11, etc.)	**EVEN Visit** - Adult (V02,V04,V06,V08,V10,V12,V14, etc.)	**BL** - Adult	**ODD Visit** - Adult (V01,V03,V05,V07,V09,V11, etc.)	**EVEN Visit** - Adult (V02,V04,V06,V08,V10,V12,V14, etc.)	**BL** - Child	**ODD Visit** - Child (V01,V03,V05,V07,V09,V11, etc.)	**EVEN Visit** - Child (V02,V04,V06,V08,V10,V12,V14, etc.)	**BL** - Child	**ODD Visit** - Child (V01,V03,V05,V07,V09,V11, etc.)	**EVEN Visit** - Child (V02,V04,V06,V08,V10,V12,V14, etc.)	**FNL** - Adult/Child
[1]Informed Consent Log	80	X[1]	X[1]	X[1]	X[1]	X[1]	X[1]	X[1]	X[1]	X[1]	X[1]	X[1]	X[1]	
Concomitant Medication Log	88	X	X	X	X	X	X	X	X	X	X	X	X	
Current Medical Conditions Log	11	X	X	X	X	X	X	X	X	X	X	X	X	
Family Participation Log[2]	66	O[2]	O[2]	O[2]	O[2]	O[2]	O[2]	O[2]	O[2]	O[2]	O[2]	O[2]	O[2]	
Randomization (only done once at Baseline)		X												
Visit Form		X	X	X	X	X	X	X	X	X	X	X	X	
Inclusion Exclusion	70	X			X			X			X			
Demographics	02	X			X			X			X			
Characteristics Form	03	X	X	X	X	X	X	X	X	X	X	X	X	
[3]DNA Sample Consent	04	X[3]	O[3]	O[3]				X[3]	O[3]	O[3]				
[3]DNA Sample Collection Form	06	X[3]	O[3]	O[3]				X[3]	O[3]	O[3]				
[1]CTCC Unique ID	05	X[1]			X[1]			X[1]			X[1]			
[3]RNA Sample Consent	21	X[3]	O[3]	O[3]				X[3]	O[3]	O[3]				
[3]RNA Sample Collection Form	23	X[3]	O[3]	O[3]				X[3]	O[3]	O[3]				
FA Medical History Abbreviated	07	X			X			X			X			
FA Symptoms Review	09	X	X	X	X	X	X	X	X	X	X	X	X	
[4]9HPT	14	X[4]	X[4]	X[4]				X[4]	X[4]	X[4]				
[4]T25FW	16	X[4]	X[4]	X[4]				X[4]	X[4]	X[4]				
[4]Vision - Low Contrast Letter Acuity	20	X[4]	X[4]	X[4]				X[4]	X[4]	X[4]				
Functional Staging For Ataxia	22	X	X	X	X	X	X	X	X	X	X	X	X	
Vital Signs	24	X	X	X	X[13]	X[13]	X[13]	X	X	X	X[13]	X[13]	X[13]	
Neurological Examination	26	X	X	X	X[12]	X[12]	X[12]	X	X	X	X[12]	X[12]	X[12]	
[5]Electrocardiogram	28	X[5]	X[5]	X[5]	X[5]	X[5]	X[5]	X[5]	X[5]	X[5]	X[5]	X[5]	X[5]	
[5]Echocardiogram	30	X[5]	X[5]	X[5]	X[5]	X[5]	X[5]	X[5]	X[5]	X[5]	X[5]	X[5]	X[5]	
Activities of Daily Living	32	X	X	X	X	X	X	X	X	X	X	X	X	
[6]Health Status Questionnaire (SF-36)	36	X[6]	X[6]	X[6]	X[6]	X[6]	X[6]							
[6]Modified Fatigue Impact Scale (MFIS)	38	X[6]		X[6]	X[6]		X[6]							
[6]MOS Pain Effects Scale (PES)	42	X[6]		X[6]	X[6]		X[6]							
[6]Bladder Control Scale (BLCS)	44	X[6]		X[6]	X[6]		X[6]							
[6]Bowel Control Scale (BWCS)	46	X[6]		X[6]	X[6]		X[6]							
[6]Impact of Visual Impairment Scale (IVIS)	48	X[6]		X[6]	X[6]		X[6]							
PedsQL - Child Report (8-12)								X	X	X	X	X	X	
PedsQL - Parent Report for Children (8-12)								X	X	X	X	X	X	
PedsQL - Teen Report (13-18)								X	X	X	X	X	X	
PedsQL - Parent Report for Teens (13-18)								X	X	X	X	X	X	
[6]Visual Functioning Questionnaire - 25	72	X[6]	X[6]	X[6]	X[6]	X[6]	X[6]	X[6]	X[6]	X[6]	X[6]	X[6]	X[6]	
[6]NEI VFQ 25 Supplement - 10 items	76	X[6]	X[6]	X[6]	X[6]	X[6]	X[6]	X[6]	X[6]	X[6]	X[6]	X[6]	X[6]	
Redenlab Speech Test	86	X	X	X				X	X	X				
Visit Status	84	X	X	X	X	X	X	X	X	X	X	X	X	

FA - COMS
SCHEDULE OF CRF COMPLETION AND STUDY ACTIVITIES

		Adult only			**Adult only- Telehealth**			Children only			**Children only- Telehealth**			Both Adult and Child
[7]Conclusion of Study Participation	52													X[7]
[15]Mortality Form	56													O[15]
[16]Pregnancy Outcome Form	25	O[14]	O[14]	O[14]	O[14]	O[14]	O[14]	O	O	O	O[14]	O[14]	O[14]	
[8]Subject Site Transfer Form	50	O[8]	O[8]	O[8]	O[8]	O[8]	O[8]	O[8]	O[8]	O[8]	O[8]	O[8]	O[8]	
Cardiac Procedures Form	27	O[14]	O[14]	O[14]	O[14]	O[14]	O[14]	O[14]	O[14]	O[14]	O[14]	O[14]	O[14]	
[9]Pulmonary Function Testing/Spirometry	60	O[9,14]	O[9,14]	O[9,14]	O[9,14]	O[9,14]	O[9,14]	O[9,14]	O[9,14]	O[9,14]	O[9,14]	O[9,14]	O[9,14]	
[10]Holter Monitoring Form	62	O[10,14]	O[10,14]	O[10,14]	O[10,14]	O[10,14]	O[10,14]	O[10,14]	O[10,14]	O[10,14]	O[10,14]	O[10,14]	O[10,14]	
[11]Scoliosis Surgery Form	64	O[11,14]	O[11,14]	O[11,14]	O[11,14]	O[11,14]	O[11,14]	O[11,14]	O[11,14]	O[11,14]	O[11,14]	O[11,14]	O[11,14]	

[1]For active subjects, obtain at next visit post Amendment approval and consent.

NOTE: Investigator Signature Form is no longer being used

NOTE: Investigator Signature Form is no longer being used

[2]Family Participation Log - Optional only complete if other family members are enrolled in FACOMS. Review of family history is recommended at every vist.

[3]Collect DNA/RNA at Baseline or at next visit if not previously collected.

[4]Site 296 Excluded.

[5]When multiple EKG and ECHO exams were conducted during the year, record results from the one closest to annual visit.

[6]Adults only assessments.

[7]Conclusion of Study Participation if question 3 = 06 Death, fill out Mortality Form.

[8]Subject Site Transfer Form Follow training slides on what is needed to transfer a subject. New Site fills out this page. This page is only filled out if a subject transfers.

[9]Pulmonary Function Testing/Spirometry if question 13 on Scoliosis is Yes, this page will need to be filled out.

[10]Holter Monitoring Form if question 5 on Cardiac is Yes; if question 12 on Scoliosis is Yes; if question 7c.10 on FA Symptom Review is Yes, fill out Holter Monitoring Form.

[11]Scoliosis Surgery Form if question 10a.3 on FA Symptom Review is Yes, fill out Scoliosis Surgery Form.

[12] Neurological Exam - A telehealth (audio/video) Section A can be completed, Sections BCD are not completed and Section E can be completed depending on patient.

[13]Vitals data can be pulled from Medicals Records up to 3 months prior for a Telehealth Visit.

[14]Assessment data can be pulled from Medical Records.

[15]Mortatity Form is only filled out when a subject has passed on and should be done with the Conclusion of Study Participation.

[16]Pregnancy Form is only filled if subject has been pregnant.

FACHILD (17-014390)
Schedule of Activities (SOA)

VISIT #	Level #	BASELINE (01)	V02	V03	V04	V05	V06	**Telehealth Visit**	FNL
MONTH		MONTH 0	MONTH 6	MONTH 12	MONTH 18	MONTH 24	MONTH 36		
Assessment/CRF									
Informed Consent Log	**02**	**X**							
Inclusion/Exclusion	**04**	**X**							
Randomization		**X**							
CTCC Unique ID	**06**	**X**							
Change of Status Questionnaire	**08**	**X**							
FA Medical History (Abbreviated)	**10**	**X**							
Demographics	**12**	**X**							
Vital Signs	**14**	**X**	**X**	**X**	**X**	**X**	**X**	**X**[1]	
Neurological Exam (FARS)	**16**	**X**	**X**	**X**	**X**	**X**	**X**	**X**[2]	
T25-FW	**18**	**X**	**X**	**X**	**X**	**X**	**X**		
Extended Time Walks	**20**	**X**	**X**	**X**	**X**	**X**	**X**		
Timed Up and Go	**22**	**X**	**X**	**X**	**X**	**X**	**X**	**X**[3]	
9HPT	**24**	**X**	**X**	**X**	**X**	**X**	**X**		
Frataxin, Buccal Cells	**26**	**X**	**X**	**X**	**X**	**X**	**X**		
FA Functional Staging For Ataxia	**28**	**X**	**X**	**X**	**X**	**X**	**X**	**X**	
FA Symptoms Review	**30**	**X**	**X**	**X**	**X**	**X**	**X**	**X**	
Activities of Daily Living	**32**	**X**	**X**	**X**	**X**	**X**	**X**	**X**	
Peds-QL Child 8-12	**34**	**X**	**X**	**X**	**X**	**X**	**X**	**X**	
Peds-QL Parent-Child 8-12	**36**	**X**	**X**	**X**	**X**	**X**	**X**	**X**	
Peds-QL Teen 13-18	**38**	**X**	**X**	**X**	**X**	**X**	**X**	**X**	
Peds-QL Parent-Teen 13-18	**40**	**X**	**X**	**X**	**X**	**X**	**X**	**X**	
BBS	**42**	**X**	**X**	**X**	**X**	**X**	**X**	**X**[3]	
[4]MRI CrCEST - - CHOP Only	**44**		**X**		**X**	**X**	**X**		
[4]MEP - - CHOP Only	**46**		**X**		**X**	**X**	**X**		
Visit Status Page	**48**	**X**	**X**	**X**	**X**	**X**	**X**	**X**	
Conclusion of Study Participation	**52**								**X**
Current Medical Conditions Log	**56**	**X**	**X**	**X**	**X**	**X**	**X**	**X**	
Concomitant Medication Log	**60**	**X**	**X**	**X**	**X**	**X**	**X**	**X**	**X**
Site Subject Transfer	**58**	**X (When needed)**							

[1]Vitals data can be pulled from Medical Records up to 3 month prior for a Telehealth Visit.

[2]Neurological Exam - A Telehealth (audio/video) Section A can be completed, Sections B, C, D are not completed and Section E Can be completed depending on patient.

[3]Complete if site is comfortable completing remotely.

[4]MEP and MRI are a sub study, complete if data is available for visit.

4/28/2021

Appendix 2 In Vitro Models, In Vivo Models

Table of cellular models useful for the development of FA therapeutics

Type	Species	FA Phenotype	Correlation with human disease	Strengths	Weaknesses	Potential utility in gene/cell therapy development	Availability	References
Adult fibroblasts, FA and control	Human	Impaired growth on BHB. Sensitivity to ferroptosis inducers and oxidative stress.		Robust and reproducible phenotypes.	Non relevant cells	Confirm restoration of FXN levels post GT/GE. Possibly assess functional change.	https://www.utsouthwestern.edu/labs/napieralla/cell-line/	https://pubmed.ncbi.nlm.nih.gov/30635474/ https://pubmed.ncbi.nlm.nih.gov/29568068/
iPSCs, FA, controls, and isogenic controls	Human	Decreased frataxin expression, epigenetic changes		Can be differentiated into relevant cell types.		Suitable for differentation into relevant cell types	https://www.utsouthwestern.edu/labs/napieralla/cell-line/	https://www.ncbi.nlm.nih.gov/pmc/articles/PMC6392065/
iPSC cardiomyocytes	Human	Increased cell size, impaired contraction, lower beating rate, abnormal calcium handling. Abnormal/dysfunctional mitochondria.Iron accumulation, mtDNA depletion, impaired ATP production, lipid droplet accumulation.	Hypertrophy, iron deposition, arrhythmia. Disorganized mitochondria.	Represents affected tissue. Several phenotypes described.	Variable differentiation	Confirm restoration of FXN levels post GT/GE. Possibly assess functional change. Potentially useful for a potency assay.	Academic labs/CROs	https://pubmed.ncbi.nlm.nih.gov/31286988/ https://pubmed.ncbi.nlm.nih.gov/31446150/ https://pubmed.ncbi.nlm.nih.gov/23136396/ https://pubmed.ncbi.nlm.nih.gov/24327207/ https://pubmed.ncbi.nlm.nih.gov/28562313/
iPSC cortical neurons	Human	Some reports of reduced mitochondrial membrane potential and calcium handling abnormalities.	Mitochondrial impairment	More robust and reproducible protocols for differentiation than other cell types. Can be maintained for several weeks in culture to favor maturation.	Not the specific neuronal types affected in FA, mixed population, can be variable from line to line, maturation in vitro is still hard to achieve, not consistent phenotypes.	Possibly potency assay, but robust readout needs to be established. Confirm GT/GE in neurons.	Academic labs/CROs	https://pubmed.ncbi.nlm.nih.gov/30552117/
iPSC primary sensory neurons	Human	Altered cytoskeletal organization, axon guidance, synaptic plasticity; alteration in the pattern of tonic firing, changes in metabolism.	Altered development of proprioceptive DRG neurons	Represents affected tissue. Highly enriched cultures for proprioceptive neurons can be obtained.	Phenotypes need validation, maturation in vitro is still hard to achieve.	Possibly useful for potency assay or assessment of gene delivery. POC for gene editing	Academic labs	https://pubmed.ncbi.nlm.nih.gov/23136396/ https://pubmed.ncbi.nlm.nih.gov/33362470/
Organoids - cardiac	Human	Contractility defects, altered electrophysiological properties.		Mimics tissue complexity, could achieve better maturation in vitro.	Variable cell populations, maturation in vitro must be assessed.	Comfirm gene delivery/editing in different cell types, test promoters.	Academic labs/CROs	https://pubmed.ncbi.nlm.nih.gov/32385372/ https://pubmed.ncbi.nlm.nih.gov/30552117/ https://pubmed.ncbi.nlm.nih.gov/31286988/
Organoids - neurospheres	Human			Mimics tissue complexity, could achieve better maturation in vitro.	Variable cell population, maturation in vitro must be assessed.	Confirm gene delivery/editing in different cell types, test promoters.	Academic labs	
Organoids - DRG	Human	Decreased survival, decreased axonal spreading. Some biochemical features of FRDA like oxidative stress, mitochondrial fragmentation.	Decreased survival, oxidative stress.	Mimics tissue complexity, could achieve better maturation in vitro.	Variable cell populations, maturation in vitro must be assessed.	Confirm gene delivery/editing in different cell types, test promoters.	Academic lab	https://pubmed.ncbi.nlm.nih.gov/32826895/

Lymphoblastoid cells, FA and control	Human				Non relevant cells .No phenotype described	Ex-vivo gene editing POC.	http://ccr.coriell.org/Sections/Search/Search.aspx?PgId=165&q=frda	https://pubmed.ncbi.nlm.nih.gov/26896803/
MEFs from G127V mouse	Mouse	Early senescence.		Robust phenotype.	Non relevant cell type No GAA repeat or expansion. Non human cells	Potency assay	Academic lab	https://pubmed.ncbi.nlm.nih.gov/32586831/
Inducible frataxin knockout in Immortalized MEFs	Mouse	Decreased doubling time, loss of aconitase activity and increased ROS production.	Biochemical signatures of disease.	Time resolved KO of frataxin.	Non relevant cell type. No GAA repeat or expansion. Non human cells.	Potency assay	Academic lab	https://pubmed.ncbi.nlm.nih.gov/27106929/
DRG embryonic neurons from conditional KO mouse	Mouse	Decreased size, altered metabolism, Fe-S cluster deficit.	Altered function of proprioceptive DRG neurons.	Time resolved KO of frataxin, robust reproducible phenotype, 96 well compatible.	Phenotypes need validation. No GAA repeat or expansions. Non human cells	Possibly useful for potency assay, confirming gene delivery	Academic lab	https://pubmed.ncbi.nlm.nih.gov/31586352/
Point Mutation in human frataxin (I154F, G130V) in knockout immortalized MEFs	Mouse	Decreased growth, loss of Fe-S cluster activity, increase mitochondrial iron, increased ROS production.	Biochemical signatures of disease.	Robust and reproducible phenotype.	Non relevant cell type. No GAA repeats or expansion. Non human cells.	Possibly useful for potency assay	Academic lab	https://pubmed-ncbi-nlm-nih-gov.proxy.insermbiblio.inist.fr/19629184/

Preclinical models: This table summarizes the characterization of mouse (and one rat) models that have been used in FA research. Additional information on models referred to in the briefing document can be found here.													
Name	**Species**	**Genotype**	**Brief description**	**Phenotype (molecular)**	**Phenotype (histopathological)**	**Phenotype (behavioral and pathology)**	**Correlation with human disease**	**Progression**	**Strengths**	**Weaknesses**	**Potential utility in gene/cell therapy development**	**Availability**	**References**
YG8R/YG8sR	mouse	Fxn (KO)/Fxn(KO); YAC-FXN (200GAA) KI	One (YG8sR) or two copies (YG8R) of human FXN locus transgene (YAC construct) randomly inserted, on a mouse frataxin knock-out background.	Reduced levels of frataxin (30% of FXN mRNA in brain, 60% in heart). Epigenetic silencing, repeat instability, impairment in mitochondrial function, decreased aconitase activity, sign of oxidative stress, changes in Ca2+ signaling.	Large vacuoles in neurons in the DRG, iron deposition in cardiomyocytes. Disrupted purkinje layer	Some coordination deficits and progressive decrease in locomotor activity, decreased grip strength and increase in weight. No overt cardiac phenotype.		Coordination deficits and progressive decrease in locomotor activity, decreased grip strength starting at 6-12mo. Iron deposition in the heart at 18mo.	Recapitulates epigenetic silencing, repeat instability. Useful for POC for human FXN locus for gene editing. Shows some molecular/biochemical phenotype.	Very late onset and mild phenotype. There are reports that the phenotypes are detectable only on some genetic backgrounds. Two copies of transgene present.	Can be useful for gene editing approaches. It is important to be aware of the copy number. The original model YG8R has two copies of the FXN gene. TheYG8sR has a single copy of FXN.	JAX	https://pubmed.ncbi.nlm.nih.gov/16919418/ https://pubmed.ncbi.nlm.nih.gov/25198290/ https://pubmed.ncbi.nlm.nih.gov/25681319/
YG8sR800	mouse	Fxn (KO)/Fxn(KO); YAC-FXN (800GAA) KI	One copy of human FXN locus transgene (YAC construct) randomly inserted, on a mouse frataxin knock-out background.	Reduced levels of frataxin mRNA to 10-15% of WT		Unpublished ongoing characterization from JAX and others. To date, mild neurological/coordination phenotype, lower body weight, no overt cardiac phenotype, no difference in glucose tolerance test.		Mild neurological/coordination phenotype starting 6 months of age		Very late onset and mild phenotype - very variable from one lab to another	Useful for gene-editing approaches	JAX	Unpublished
Sarsero model	Mouse	Fxn (KO)/Fxn(KO); BAC-FXN (500GAA) KI GAA repeats have interruption	One copy of human FXN locus transgene (BAC construct) randomly inserted on a mouse frataxin knock-out background.	Originally reported to have very low levels of frataxin, especially in the heart .		No phenotype.				Very little, unpublished characterization. Reported to have GAA interruptions.	Potentially useful for gene-editing approaches.	JAX	https://pubmed.ncbi.nlm.nih.gov/15170226/
Ckm-Cre	Mouse	Fxn KO/Fxn loxP; Ckm-CRE	Cardiac and muscle specific Fxn KO (muscle creatin kinase expression of CRE recombinase).	Fxn loss in cardiac and muscle tissue. Defects in ISC-enzyme activities - complexes I, II and III of the respiratory chain and aconitase decrease in SDH dysregulation of transferrin receptor 1, ferritins, and ferroportin 1.	Iron deposits in the heart. Thickening of the walls of the left ventricle, myocardial degeneration with cytoplasmic vacuolization in the myocytes, hypertrophic cell. Evidence of necrosis as well as post-necrotic fibrosis, lipid droplets, proliferation of mitochondria.	Cardiac hypertrophy. Dilated cardiomyopathy. Weight loss.	Progressive hypertrophic cardiomyopathy that develops into dilated-like cardiomyopathy, fibrosis present.	Biochemical phenotype detected at 4-10 weeks (no diff at 2 weeks). Cardiac hypertrophy starting at 5 weeks. Weight loss and iron accumulation starting at 7 weeks. Fe-S enzyme deficiencies is the earlier phenotype (4 weeks) and occur in parallel to pathology. Death at 14 weeks.	Severe phenotype, however, it models human cardiomyopathy and can be rescued by frataxin delivery. Well-characterized and stable phenotype overtime. Robust and reproducible in many different laboratories.	Complete frataxin loss in a subset of cells not representing the human disease. Severely affected, not useful to test muscle dysfunction. Developmental component dependent on timing of expression of Ckm.	Cardiac gene therapy.	JAX	https://pubmed.ncbi.nlm.nih.gov/11175786/ https://pubmed.ncbi.nlm.nih.gov/24705334/ https://pubmed.ncbi.nlm.nih.gov/30544254/

Pvalb-Cre	Mouse	Fxn KO/Fxn loxP; Pvalb-CRE	Parvalbumin neuron specific Fxn KO.	Fxn loss in DRG, cerebellar Purkinje cell, deep nuclei, interneurons in the brain, spinal cord. Mitochondrial and cell degeneration. SDH activity by histoenzymatic staining shows low SDH in DRG and PCs.	Vacuoles in the DRG in 1.5% of neurons at 7.5 weeks with no neuronal loss observed, demonstrating that the loss of somatosensory response is not a consequence of neuronal loss. reduction of 30% of large myelinated neurons at 21.5 weeks (proprioceptors and mechanoceptors) seen only in lumbar and not in cervical or thoracic abnormal localization and loss of PCs starting at 10.5 weeks. No iron accumulation. Sign of astrogliosis in granular and PC layer.	Gait abnormality general coordination defects ataxic gait. Sensory ataxia and neuropathy. Cerebellar ataxia after the onset of the PNS pathology. H-wave response (sensorimotor reflex) was significantly affected at 6.5 weeks of age tremors.		Normal growth until 21.5 weeks. Gait abnormality as early as 3.5 weeks of age on the notched-bar test. General coordination defects measured at 8.5 weeks of age on the wire-hanging test and on the rotarod. Incoordination progress over time with complete incapacity by 13.5 weeks. Mice die at 21 weeks due to epileptic seizures (possibly due to frataxin loss in cortical interneurons).	Cerebellar ataxia and PNS pathology. Can be rescued by frataxin delivery.	Complete frataxin loss in a subset of cells not representing the human disease. Some characteristics such as tremor and seizures not seen in patients.	CNS gene therapy approaches to evaluate rescue of DRG and some cerebellum related phenotypes. However, the efficacy of the gene therapy approach will depend on the ability of capsid/construct to deliver and express in pvalb positive cells.	JAX	https://pubmed.ncbi.nlm.nih.gov/29853274/
FRDA-KD	Mouse	Genomic integration of a single copy shRNA transgene (doxycycline-inducible) in the rosa26 locus.	DOX inducible Fxn knock down by RNAi in all tissues.	Frataxin reduction in all tissues with a different extent of reduction depending on the dox doses. 90% KD in most tissues with regimen outlined in paper. Reversible silencing if dox is removed. Decreased aconitase activity in the heart. Loss of cerebellar Purkinje neurons and large DN principal neurons.	Ventricular and posterior wall thickening in heart. Increased myocardial iron, fibrosis, some enlarged and disorganized mitochondria. DRG pathology with condensed mitochondria, neuronal degeneration. Reduction of axonal size and myelin thickness in spinal cord. No alteration of number of PCs and CGCs. Disruption of photoreceptors in the retina and degeneration RPE cells.	Weight loss and reduced survival. Decreased locomotor activity/motor impairment, ataxic gait, lower grip strength. Cataracts and cardiac arrythmia.	Ataxia, hypertrophic cardiomyopathy.	Weight loss and reduced survival ratio (<90%) at 25 weeks with dox. Ataxia and locomotor activity decrease seen at 12weeks. Arrythmia seen at 12 weeks. Cardiac hypertrophy seen at 24 wks. Long QT interval phenotype occurs before left ventricular wall thickening. Levels of the climbing fiber-specific glutamatergic synaptic marker VGLUT2 decline starting at 4 weeks after dox induction, whereas levels of the parallel fiber-specific synaptic marker VGLUT1 are reduced by 18-weeks.	Recapitulates several aspect of disease, very low frataxin in all tissues (instead of complete loss).	Lack of developmental component. Effect of DOX unknown. Difficulties with reproducibility across labs.	Can be useful for GT approaches, but complete reversibility of the phenotypes is not achievable.	Only available through academic lab.	https://pubmed.ncbi.nlm.nih.gov/29257745/
													https://pubmed.ncbi.nlm.nih.gov/35401081/
mRX FXNKO	Mouse	Fxn KO/Fxn LoxP mRX-Cre	Retina specific Fxn KO	Retina specific Fxn KO.	Degeneration of all retinal layers.	Progressive loss of retinal function, as observed via electroretinogram (ERG).	RGC degeneration, thinning of retinal nerve fiber layer (RNFL).	Rx expressed between day E7.5 and 8, degeneration starts at p14 and progresses at day p30 and p60.		Severe phenotype, rapidly progressive - affects all retinal cell-types which is not what is seen in human condition.	Possible utility in POC for ocular gene therapy approach.	Academic lab/unpublished.	Unpublished
αMyhc	Mouse	Fxn KO/Fxn LoxP αMyhc-Cre	Cardiac specific Fxn KO. Cre recombinase is driven by αMyhc promoter, leading to 50% decrease of frataxin in cardiac tissue.	Cardiac specific KO. 50% lower levels of FXN protein in heart at 24w. No change of frataxin levels in skeletal muscle. Reduced complex II activity in the heart.	Hearts of αMyhc mice had decreased levels of FXN and activity of the mitochondrial complex II/complex IV respiratory chain.	At rest, no difference in ejection fraction and fractional shortening, no difference in LV mass. Inability to respond to dobutamine stress. Exercise induced stress, reduced ability to maintain the same pace on a treadmill as wild-type.			Milder phenotype than Mck, closer to human disease.	Not all cells in heart tissue seem to have reduced frataxin, not clear which cells in the cardiac tissue have Fxn KO. The phenotype is driven by the properties of the specific promoter that might not be relevant to affected cells in FA.	Cardiac gene therapy, shows improvement with systemic AAV10 gene therapy.		https://pubmed.ncbi.nlm.nih.gov/32646255/
G127V	Mouse	Homozygous for G127V mutation in Fxn	Homozygous for G127V mutation in Fxn	Fxn point mutation. Dramatic decrease of Fxn protein without affecting transcript synthesis or splicing.		Failure to thrive phenotype in homozygous animals and a substantially reduced number of offspring. Some sex specific phenotypes (preliminary, unpublished).	Most common non-GAA repeat expansion mutation in FA; 3-5% of mutations.		Might possibly recapitulate neurodevelopmental defect.		Possibly useful to address neurodevelopmental defect and early intervention with gene therapy.	Academic lab/unpublished	Unpublished

I151F	Mouse	Homozygous for I151F mutation in Fxn	Homozygous for I151F mutation in Fxn	Homozygous mice are viable. Very low frataxin levels in all tissues. Decreased content of components of OXPHOS complexes I and II, decreased aconitase activity, and alterations in the antioxidant defenses.	Histopathological characterization is needed.	Smaller size, progressive neurological deficit after 23 weeks of age.					Neurobehavioral phenotype at 20 weeks could be use useful but no histopathology data available to correlate with phenotype. Possibly useful to address neurodevelopmental defect and early intervention with gene therapy.	Academic lab	https://pubmed.ncbi.nlm.nih.gov/35038030/
KIKO	Mouse	Fxn (230GAA)/Fxn (KO) A cloned BamHI/BglII fragment from intron 1 of the frataxin gene, containing a (GAA)230 repeat and a flanking sequence of 350 bp upstream and 250 bp downstream	Mouse with one allele that is KO for Fxn and one allele that carries 230 GAA in the first intron of the mouse Fxn.	25-30% of WT FXN. No repeat instability. Deficits in mitochondrial biogenesis and respiratory chain complexes. Dysregulated cerebellar circuit. Rduced IRP1 expression. Increased oxidative stress, hyperlipidemia, reduced energy expenditure and insulin sensitivity, and elevated plasma leptin (T2D-like signatures). Brown adipose tissue dysfunction.	Disrupted mitochondrial ultrastructure and lipid accumulation in brown adipose tissue. No iron deposit in heart	Mild neurobehavioral deficits, exercise intolerance, and glucose intolerance.	Some features of T2D	Neurobehavioral phenotypes starts at >8 months of age.	Many published studies, some behavioral, biochemical and histopathological findings that correlate with the human disease.	Very mild and very late onset behavioral phenotype.	Some utility for gene editing approaches targeting regions proximal to the repeats.	JAX	https://pubmed.ncbi.nlm.nih.gov/11852098/
													https://pubmed.ncbi.nlm.nih.gov/11852098/
													https://pubmed.ncbi.nlm.nih.gov/29125827/
													https://pubmed.ncbi.nlm.nih.gov/27575947/
													https://pubmed.ncbi.nlm.nih.gov/29259026/
													https://pubmed.ncbi.nlm.nih.gov/32269244/
													https://pubmed.ncbi.nlm.nih.gov/31974344/
NSE-Cre	Mouse	Fxn KO/Fxn LoxP NSE-Cre	Fxn KO in cells expressing the neuron specific enolase promoter.	Fxn loss in neuronal and non-neuronal tissue (heart and low in liver and kidney).	Degeneration and necrosis in the dentate nucleus of the cerebellum and the brainstem, brain cortex (particularly frontal cortex). Thickening of the walls of the left ventricle, myocardial degeneration with cytoplasmic vacuolization in the myocytes and neurons.	Low birth weight. Progressive neurological phenotype including ataxia, hunched stance and loss of proprioception. Cardiac hypertrophy. Absence of H band response.		Life expectancy (24±9 d. Average onset of ataxia at 12 days accompanied by progressive loss of proprioception.	Degeneration of cerebellum (dentate).	Severely affected, low life expectancy.	We do not recommend using this model for GT/GE POC studies. The phenotype is not consistent with the human disease, spongiform degeneration of the frontal cortex and liver disease contribute to several phenotypes not relevant to FA.	Academic lab	https://pubmed.ncbi.nlm.nih.gov/11175786/
Ckm-CRE	Rat	Fxn KO/Fxn loxP; Ckm-CRE	Cardiac specific KO of rat Fxn									RRRC soon	Unpublished

Appendix 3 FARA Proposed Development Plans

FARA Example Development Path for GT/GE Products to Treat FA Heart Disease

For discussion purposes, an outline is provided here by FARA that represents one example of a possible development plan. This is meant to be illustrative and help facilitate discussion, this is not meant to suggest or imply specific requirements for development. Each product being developed would need to be considered individually by the sponsor and Agency.

Nonclinical Development

In vitro and *in vivo* model systems of FA can be used to inform programs directed to treating the heart. Although more severe, the Ckm-Cre mouse model exhibits many of the hallmarks of progressive FA cardiomyopathy. AAV-mediated gene therapy has been shown to modify the cardiac phenotype in both asymptomatic and symptomatic Ckm-Cre mice in a dose-dependent fashion. The Ckm-CRE model is well characterized and widely available to researchers. The milder αMyhc, in which FXN k/o is limited to the heart resulting in 50% lower levels of FXN vs WT mice, has been used to support an active clinical trial in adults with FA. This mouse model was generated by an academic laboratory and its availability for widespread use is unknown.

Gene editing approaches targeting the GAA expansion region require models in which this expansion is replicated. These would include one of the humanized GAA based models. The two recommended models are YG8s200 or YG8Rs800. While these models exhibit differing degrees of FXN mRNA reduction, neither display a cardiac phenotype or robust biochemical changes and they may have copy number variations within the transgene, making measuring editing efficiency challenging.

- In vitro: iPSC-derived cardiomyocytes could be used to support *in vitro* preclinical data, especially in cases where in vivo evidence of efficacy cannot be generated due to lack of phenotype in disease models. Supportive data could:
    - Confirm increased frataxin levels after GT/GE
    - Potentially demonstrate biological activity through functional/phenotypic correction (e.g., electrophysiology, Fe-S cluster deficit (SDH and aconitase), mitochondrial function (e.g., O2 consumption, membrane potential, lipid accumulation)
    - Enable a comparison of FXN expression levels in transduced cardiomyocytes derived from FA vs WT iPSCs or isogenic controls.
- In vivo:
    - Gene therapy:
        - A preclinical program in which the FXN gene transfer vector has been shown to demonstrate efficacy in the CKM-cre model while expressing frataxin (FXN) at non-toxic levels should provide strong proof of concept to support a clinical trial. Correlation of percent transduced cells to efficacious doses could be used, in addition to safety data, to identify clinically relevant doses.
        - Appropriate species for use in definitive toxicology studies will depend on the understanding of vector biodistribution and transduction with the AAV capsid serotype selected, route of administration, and available information about preliminary safety information (e.g., FXN toxicity/DRG toxicity) from *in vitro* and *in vivo* proof of concept studies.

- For systemic delivery, the need for a large animal model for toxicology studies would be informed by the understanding of the translation of cardiac transduction efficiency from mouse to a larger animal. Higher expression of GT product at the same dose has been reported in *fxn* k/o mice vs WT. This may necessitate adjustment of doses for toxicity studies in WT to compensate for lower expression. The translation to humans is not clear but may be addressable in human iPSCs derived cardiomyocytes.
- The degree of frataxin overexpression-driven toxicity appears to develop over time and is detectable by histopathological evaluation. Therefore, we recommend at least six-month long tox studies with histological endpoints.
- High dose vector delivery IV may necessitate studies in NHP to assess toxicity in different organ systems including liver and DRG, as there are reports of toxicity after high dose IV AAV gene therapy. Mild to moderate histological changes in the DRG with no clinical correlates we believe should not stop program progression.
- Because DRG toxicity has also been observed in multiple species, NHP studies may not be needed for IV gene therapy with a capsid serotype for which extensive biodistribution knowledge with the ROA is known (e.g., AAV9). The sponsor should provide a rationale for the selected species with consideration of most sensitive species.
- In FA, significant developmental and degeneration changes are present prior to diagnosis and hence prior to GT/GE treatment. It may be difficult to assess any clinical impact of GT/GE to the DRG in FA because of these prior changes. However, the sponsor should describe mechanisms employed (vector design, dose limitations) to avoid overexpression in the DRG.
- Intracardiac gene delivery methods requiring specialized delivery devices will require large animal models capable of assessing the safety of the delivery method as well as the vector. The adult pig has been used to support intracardiac gene therapies, allowing for use of the identical catheters intended for clinical use. The similarity in the size of the porcine heart to human heart should facilitate understanding of the dose related impact on transduction efficiency.

- Gene Editing:
  - *In vitro* evidence of increased frataxin expression and functional correction after gene editing, with characterization of the persistence of edited cardiomyocytes and tissue specificity, with additional safety and distribution studies, may be sufficient to support a clinical trial and dose selection.
  - A preclinical package for a GE product ideally includes data demonstrating successful targeting of the GAA expansion region currently in the YG8s200 or

YGRs800 model, resulting in increased FXN mRNA and/or protein. However, unpublished reports suggest variability in copy number of the transgene in these models, which may preclude this.

- Safety studies would include examination of potential off-target editing events and genomic integrity. Due to the genomic sequence variations among species, these assessments would be conducted *in vitro* using multiple donors as well as in silico analysis.
- The appropriate species for *in vivo* safety assessments would take into consideration the method for delivery of the GE components (e.g., viral vectors, lipid nanoparticles) and ROA. AAV-based GE component delivery should take into consideration the known AAV-related toxicities and dose.

Clinical Development

- Patients that would be well suited for enrollment in GT/GE clinical trials include adults with longer GAA repeats, early age of onset and documented ***decreased left ventricular EF*** in patient history, since these criteria predict worsening of cardiac function over a time, allowing for an assessment of biological effect, as well as safety, within a timeframe amendable to therapeutic development.
- A constellation of increased LVWT with evidence of fibrosis, changes in strain, and impaired perfusion reserve are likely useful for monitoring safety and efficacy.
- Translation to children with longer GAA repeats, early age of onset, and signs of cardiac involvement to prevent rapid cardiac decline or prevent progression of cardiac disease could begin after demonstration of safety and identification of biologically active doses in adults.
- Improvement in cardiomyocyte expression of frataxin, Fe-S cluster deficit and possible histopathology, by cardiac biopsy, could identify biologically relevant doses.
- In the absence of short term, direct clinical efficacy endpoints, stabilized or improved cardiac structure and function, as measured by echocardiogram, cMRI (stabilization or reduction in fibrosis) or other functional imaging (MRS or PET) and cardiopulmonary exercise testing, could be considered reasonable predictors of clinical benefit in FA patients. Coupled with positive patient reported outcomes, a weight of evidence approach could support accelerated or full approval of GT/GE products. These measures would also reflect changes in cardiac function related to safety of the therapy.
- IV delivery (depending on capsid and dose) may transduce other disease relevant target tissues such as skeletal muscle, pancreas, or dorsal root ganglion. However, the extent of transduction may not be sufficient to demonstrate clinical benefit. It may be possible to consider muscle biopsies to assess frataxin levels and downstream biochemical improvements, if supported by preclinical data, to support dose selection in early-stage trials. It may be important to consider safety and exploratory efficacy assessments if pre-clinical studies indicate transduction of additional disease relevant target tissues.

FARA Example Development Path for GT/GE Products to Treat FA Brain, Spinal Cord, and Peripheral Nervous System

For discussion purposes, an outline is provided here by FARA that represents one example of a possible development plan. This is meant to be illustrative and help facilitate discussion. This is not meant to suggest or imply specific requirements for development. Each product being developed would need to be considered individually by the sponsor and Agency.

Nonclinical Development

In vitro and *in vivo* model systems of FA can be used to inform programs directed to treating the nervous system. Although more severe than the human disease, the Pvalb-cKO mouse model has many brain and spinal cord targets that are similar to human. AAV-mediated gene therapy has been shown to modify the neurological phenotype in both asymptomatic and symptomatic Pvalb-cKO mice.

Gene editing approaches targeting the GAA expansion region require *in vivo* models in which this expansion is replicated. The potential models include the YG8s200, YG8Rs800, and Sarsero models. While these models exhibit differing degrees of FXN mRNA reduction, none display a robust neurological phenotype and unpublished reports suggest the possible copy number variations within the transgene, which would make measuring editing efficiency challenging.

- *In vitro*: FA iPSC-derived neurons could be used to support *in vivo* preclinical data, especially in cases where *in vivo* evidence of efficacy cannot be generated due to lack of phenotype in disease models. Possible cell models include FA iPSC-derived cortical neurons, sensory neurons and/or DRG (Dorsal Root Ganglia) organoids. Protocols to derive deep cerebellar nuclei neurons from iPSCs are not well established and therefore it would be difficult to attempt to use this cell type.
    - Confirm increased frataxin levels after GT/GE.
    - If possible, demonstrate biological activity through functional/phenotypic correction (e.g., transcriptional gene expression profile and/or proteomic phenotype and/or functional or biochemical change related to cellular function or survival).
- *In vivo*:
    - Gene therapy:
        - A preclinical package demonstrating efficacy in the disease related target tissue and associated phenotype in the Pvalb-cKO model with a gene therapy vector expressing FXN at non-toxic levels would provide strong proof of concept to support a clinical trial. Correlation of percent transduced cells to efficacious doses could be used, in addition to safety data, to identify clinically relevant doses.
        - As there are various and evolving options for capsid and ROA, an assessment of distribution with ROA and capsid should be included in the package, e.g., demonstration in NHP of bilateral distribution to the dentate nuclei should be achieved by any putative therapeutic approach.
        - It is important that large animal studies demonstrating biodistribution, transduction of desired targets, frataxin expression and safety to establish minimal effective dose and NOAEL are included in the data package.

        - Rationale for minimal % transduction is difficult to achieve in FA models because some aspects of the phenotype appear to be unrelated to loss of frataxin. It may require a best estimate from other neurological diseases – 20% would be minimal – closer to 50% desirable. Also, in FA, treating an already atrophic target complicates assessment for desired transduction.
    - Appropriate species for use in definitive toxicology studies will depend on the understanding of vector biodistribution and transduction with the AAV capsid serotype selected, route of administration, and available preliminary safety information (e.g., FXN toxicity/DRG toxicity) from *in vitro* and *in vivo* proof of concept studies.
        - Systemic delivery could be used to target the peripheral nervous system (as well as cardiac and skeletal muscle). However, with the currently available vectors, it is not likely to address central nervous system components of the disease.
        - Routes of administration may include intrathecal (IT), intracerebroventricular (ICV) or intraparenchymal (IP). It will be necessary to confirm that it is possible to reach deep cerebellar nuclei via proposed CNS route.
        - Gene delivery methods requiring specialized delivery devices will require large animal models capable of assessing the safety of the delivery method as well as the vector.
- Gene Editing:
    - Coupled with *in vitro* evidence of increased frataxin expression and functional correction after gene editing, characterization of nervous system gene editing efficiency in an animal model could provide sufficient proof of concept to support a clinical trial and dose selection.
    - A preclinical package for a GE product would include data demonstrating successful targeting of the GAA expansion region in the YG8s200, YGRs800 or Sarsero model, resulting in increased FXN mRNA and/or protein. However, confirmation of the presence of the target sequence and assessment of copy number of the transgene with multiple probes should be performed within the mouse colony. Characterization of the persistence of edited target neurons and the tissue specificity or inducibility/inhibition of expression of the GE is suggested.
    - It may be possible to use a combination of murine and large animal models to assess editing efficiency in the CNS and the impact of dose.
    - Safety studies should include examination of potential off-target editing events and genomic integrity. Due to the genomic sequence variations among species, these assessments would be conducted *in vitro* using multiple donors as well as in silico analysis.
    - The appropriate species for *in vivo* safety assessments should take into consideration the method for delivery of the GE components (e.g., viral vectors,

lipid nanoparticles) and ROA. AAV-based GE component delivery should take into consideration the known AAV-related toxicities and dose.

Clinical Development

- Patients who are ambulatory or those that are non-ambulatory but retain upper limb function.
    - Translation to children is imperative when treating the brain and spinal cord.
        - After demonstration of safety and identification of biologically active doses in adults, translation to children should be considered
        - A defined criteria and demonstration of prospect of benefit in adults would support transition from adult to pediatric patients
- Route of administration – consideration of ROA should include the possibility that not all neuronal symptoms will be addressed
    - Especially in dual routes of administration studies that aim to address both CNS and cardiac manifestations of FA, patients are likely to have no clinical symptoms of cardiac disease but overt neurological symptoms. Efficacy would slow progression of neurological disease as assessed by clinical measures while cardiac assessments may consist of biomarkers not clinical signs.
- Unilateral treatment of DN could have adverse consequences as FA is a symmetrical disease (unlike PD that is more asymmetrical); we would not recommend unilateral administration of the DN in FA.
- Imaging biomarkers, such as QSM of iron in the dentate, might be useful to establish proof of mechanism.
- The extensive natural history data available from a well conducted study that captures long-term neurological outcomes and function across the spectrum of the disease should be considered, especially as part of a Bayesian adaptive design. The data in FA-ICD from previous trials and the FA-COMS can be borrowed via informative prior distributions to improve the efficacy of a trial. Depending on the target population and the clinical outcome measures selected as endpoints, natural history data could be used as a comparator arm and/or as a supplement to placebo to reduce the size of placebo group in clinical trials.
- Many of the clinical outcome assessments performed in the natural history study are now used in interventional trials, including, for example, functional endpoints/symptoms that are directly linked to DN such as dysarthria and ataxia. The modified Friedreich Ataxia Rating Scale (mFARS), a disease specific, exam-based neurological rating scale has also been used as an outcome measure in clinical trials, including the pivotal trial for omaveloxolone.

FARA Example Development Path for Gene Therapy/Gene Editing (GT/GE) Products to Treat Friedreich Ataxia (FA) Vision Impairment

For discussion purposes, an outline is provided here by FARA that represents one example of a possible development plan. This is meant to be illustrative and help facilitate discussion. This is not meant to suggest or imply specific requirements for development. Each product being developed would need to be considered individually by the sponsor and Agency.

Nonclinical Development

In vitro and *in vivo* model systems of FA can be used to inform programs directed to treating the visual system. The effectiveness of the GT and GE product should be evaluated through the conduct o*f in vitro studies* using patient derived induced pluripotent stem cell (iPSC) cells. Although there are currently no robust preclinical models of the FA related visual loss, the existing models have low frataxin expression in relevant target tissues, which could be used to evaluate aspects of putative GT/GE products.

Gene editing approaches targeting the GAA expansion region require *in vivo* models in which this expansion is replicated. The potential models include the YG8s200, YG8Rs800, and Sarsero models. While these models exhibit differing degrees of FXN mRNA reduction, none display a robust neurological phenotype and they may have copy number variations within the transgene, making measuring editing efficiency challenging.

- *In vitro*: iPSC-derived retinal cells/organoid cultures could be used to support *in vivo* preclinical data, especially in cases where *in vivo* evidence of efficacy cannot be generated due to lack of phenotype in disease models.
    - Confirm GT increases frataxin levels
    - Although there are no published data indicating that biochemical or functional changes are induced by frataxin deficiency in iPSC derived retinal ganglion cells (RGCs), if such changes can be identified, demonstrate correction.
    - iPSC derived central nervous system (CNS) neurons are an appropriate model system for retinal ganglion cells as these are a type of CNS neuron.
- *In vivo*:
    - Gene therapy:
        - Non-human primate (NHP) or pigs are appropriate models to establish percent transduction of retinal ganglion cells for dose setting.
        - A preclinical package could include data from the retinal specific frataxin (Fxn) knock out mouse model (mRX-CRE mouse), with administration of GT prior to onset of symptoms to allow full expression of the transgene prior to significant degeneration. We note that rescue after GT may be limited if cell types in addition to RGC are not also rescued by treatment.
        - As there are various and evolving options for capsid and ROA, an assessment of distribution with ROA and capsid should be included in the package.
        - It is important that large animal studies demonstrating biodistribution, transduction of desired targets, frataxin expression and safety to establish minimal effective dose and NOAEL are included in the data package.
        - Appropriate species for use in definitive toxicology studies will depend on the understanding of vector biodistribution and transduction with the AAV capsid

serotype selected, route of administration, and available preliminary safety information (e.g., FXN toxicity) from *in vitro* and *in vivo* proof of concept studies.

- *In vivo:*
    - Gene Editing:
        - *In vitro* evidence of increased frataxin expression and functional correction after gene editing, with characterization of the persistence of edited retinal cells and appropriate safety and distribution studies could provide sufficient proof of concept to support a clinical trial and dose selection.
        - A preclinical package for a GE product ideally includes data demonstrating successful targeting of the GAA expansion region currently in the YG8s200 or YGRs800 model, resulting in increased FXN mRNA and/or protein. However, the variability in the copy number of the transgene in these models may preclude this.
        - It may also be possible to establish editing efficiency in NHP if data demonstrated no difference in efficiency due to repeat length.
        - Safety studies should include examination of potential off-target editing events and genomic integrity. Due to the genomic sequence variations among species, these assessments would be conducted *in vitro* using multiple donors as well as *in silico* analysis. There are no specific concerns about frataxin gene editing relative to editing of other genes.
        - The appropriate species for *in vivo* safety assessments should take into consideration the method for delivery of the GE components (e.g., viral vectors, lipid nanoparticles) and route of administration (ROA). AAV-based GE component delivery should take into consideration the known AAV-related toxicities and dose.

<u>Clinical Development</u>

- Symptomatic Retinal ganglion cell (RGC) degeneration does not occur until early adulthood in almost all FA patients, although evidence of developmental failure may predict later degeneration.
    - The appropriate population for treatment is patients with high contrast visual acuity levels of 20/32 to 20/800, which equals a retinal nerve fiber layer (RNFL) of 60 microns or less.
    - In earlier stage disease, low contrast letter acuity (LCLA) is impacted and could be used to identify patients for treatment. Children do not have clinical disease.
- Using published data on relative quality of life (QOL) change regarding a single line of loss as a comparator, patients would receive clinically meaningful benefit from preservation of seven high contrast letters (1 1/2 lines of visual acuity).
- Rate of photoreceptor loss, an acceptable endpoint in the FDA guidance on GT for retinal disorders, cannot be used in FA. RNFL though could play an analogous role.
    - In FA, loss of RNFL is 1 micron per year, reproducibility is +/- 1 micron
- National Eye Institute Visual Functional Questionnaire 25 (NEI -VFQ-25) can be used as a patient-reported measure of vision-specific quality of life in patients with FA.

    - The visual impairment scale (IVIS) is sensitive to later disease and can play a complimentary role
- In FA there is parallel disease in each eye, indicating treatment should be bilateral. Ongoing natural history studies include yearly optical coherence tomography (OCT) measures for comparison, providing an opportunity to reduce the size of a placebo group in interventional trials.

Appendix 4 Selected References

Human Molecular Genetics, 2019, Vol. 28, No. 8 1274–1285

doi: 10.1093/hmg/ddy427
Advance Access Publication Date: 13 December 2018
General Article

GENERAL ARTICLE

Correction of half the cardiomyocytes fully rescue Friedreich ataxia mitochondrial cardiomyopathy through cell-autonomous mechanisms

Brahim Belbellaa[1,2,3,4,*,†], Laurence Reutenauer[1,2,3,4], Laurent Monassier[5] and Hélène Puccio[1,2,3,4,*]

[1]Institut de Génétique et de Biologie Moléculaire et Cellulaire (IGBMC), Department of Translational Medicine and Neurogenetics, 67404 Illkirch, France, [2]Institut National de la Santé et de la Recherche Médicale, U1258, 67404 Illkirch, France, [3]Centre National de la Recherche Scientifique, UMR7104, 67404 Illkirch, France, [4]Université de Strasbourg, 67404 Illkirch, France and [5]Faculté de Médecine, Laboratoire de Neurobiologie et Pharmacologie Cardiovasculaire, 67085 Strasbourg, France

*To whom correspondence should be addressed at: Hélène Puccio, 1 Rue Laurent Fries BP10142, 67404 Illkirch, France. Tel: +33 388653264; Fax: +33 388653200; Email: hpuccio@igbmc.fr and Brahim Belbellaa, Tel: +16 506657018; Fax: +1 650-329-8151; Email: BBelbellaa@adverum.com

Abstract

Friedreich ataxia (FA) is currently an incurable inherited mitochondrial neurodegenerative disease caused by reduced levels of frataxin. Cardiac failure constitutes the main cause of premature death in FA. While adeno-associated virus-mediated cardiac gene therapy was shown to fully reverse the cardiac and mitochondrial phenotype in mouse models, this was achieved at high dose of vector resulting in the transduction of almost all cardiomyocytes, a dose and biodistribution that is unlikely to be replicated in clinic. The purpose of this study was to define the minimum vector biodistribution corresponding to the therapeutic threshold, at different stages of the disease progression. Correlative analysis of vector cardiac biodistribution, survival, cardiac function and biochemical hallmarks of the disease revealed that full rescue of the cardiac function was achieved when only half of the cardiomyocytes were transduced. In addition, meaningful therapeutic effect was achieved with as little as 30% transduction coverage. This therapeutic effect was mediated through cell-autonomous mechanisms for mitochondria homeostasis, although a significant increase in survival of uncorrected neighboring cells was observed. Overall, this study identifies the biodistribution thresholds and the underlying mechanisms conditioning the success of cardiac gene therapy in Friedreich ataxia and provides guidelines for the development of the clinical administration paradigm.

Introduction

Friedreich ataxia (FA) is a rare neurodegenerative disease characterized by spinocerebellar and sensory ataxia associated with cardiac hypertrophy and diabetes (1). Cardiac dysfunction is a major medical concern in FA as it is responsible for 59% of premature death of patients (2). Moreover, cardiac anomalies have been shown to be prevalent in 85% of pediatric FA patients (3). FA is mainly caused by a guanine-adenine-adenine repeat $(GAA)_n$ expansion within the first intron of the frataxin gene (*FXN*) (4). The GAA expansion causes the

†Current address: 1035 O'Brien Drive, Menlo Park, California 94025, USA.

Received: October 17, 2018. **Revised:** December 6, 2018. **Accepted:** December 7, 2018

heterochromatinization of the locus leading to reduced transcription (4). FXN is a highly conserved mitochondrial protein regulating the biosynthesis of iron–sulfur clusters (Fe-S) (5). Fe-S clusters are prosthetic groups crucial for many biological functions, including the mitochondrial respiratory chain and iron metabolism (6). The consequence of frataxin deficiency are Fe-S cluster deficit, impairment of Fe-S enzymes such as succinate dehydrogenase (SDH), mitochondrial dysfunction and iron overload, leading to cellular dysfunction and death (7). Several therapeutics approaches targeting the secondary consequences of FXN deficiency such as iron chelators, antioxidants and activators of the mitochondria biogenesis have been evaluated without much success in clinic (8). More promising therapeutic approaches aiming at increasing steady-state FXN levels are also being developed by modifying the locus through epigenetic modulation, stabilizing the protein, protein replacement or gene therapy (9–18). Previously, we have demonstrated the therapeutic efficiency of adeno-associated virus (AAV)-mediated cardiac FXN gene transfer to prevent and rapidly reverse the cardiac phenotype in the *Mck* model, a conditional knock-out model that recapitulates most features of the FA cardiomyopathy (7,19). This was achieved following a single high-dose intravenous injection of AAVrh10 vector, resulting in transduction of >90% of the cardiomyocytes and high expression level of FXN protein (up to 24-fold the endogenous level). While free from functional toxicity in the mouse studies, high level of FXN overexpression is probably not required since asymptomatic carriers express around half of the normal endogenous level. It is also not desirable for long-term clinical safety that can hardly be assessed in small animal model. Furthermore, despite major progress in AAV vector production (20), engineering of new AAV serotype with optimized cardiotropism and neurotropism (21) and more efficient delivery procedure in large animal model (22), it is unlikely to achieve full transduction coverage of the heart in clinical setting. To advance this promising therapeutic strategy towards the clinic, it is therefore crucial to identify the therapeutic thresholds for the vector biodistribution and expression in the heart.

Here, the primary objective was to assess the level of cardiac function rescue following the administration of decreasing doses of the AAVrh10.CAG-hFXN-HA vector in the FA *Mck* model. The study was carried out at two different time points, upon early and advanced cardiac dysfunction, to investigate the effect of disease progression on the therapeutic outcome. Secondary objectives were to characterize the vector pharmacokinetic and pharmacodynamics in the heart. Through correlation and regression analyses, we have defined the minimal cardiac biodistribution, i.e. vector copies number (VCN) per cell and percentage of cardiomyocytes rescued, to correct completely or partially the cardiac function. Furthermore, we have demonstrated the lack of cross-correction between treated and untreated neighboring cells, in particular for the rescue of Fe-S cluster enzyme activity, mitochondria proliferation and iron metabolism. Finally, plasmatic concentration of GDF15, recently shown to be associated with the integrated mitochondrial stress response (23,24), increased in *MCK* mice with disease progression and was rescued following gene therapy proportionally to the vector heart biodistribution. Overall, these findings provide a comprehensive framework for the successful preclinical development of FA cardiac gene therapy in mouse, as well as quantifiable therapeutic thresholds for the design of appropriate therapeutic vector and cardiac delivery protocol in large animal model.

Results

Correction of cardiac dysfunction in a dose-dependent manner, both when treated upon early cardiac dysfunction or heart failure

To determine the lowest therapeutic dose of AAVrh10-CAG-hFXN-HA upon early or late cardiac dysfunction, *Mck* mice were injected, at either 5 or 7 weeks of age, with decreasing doses of vector. Following the first doses evaluation at 5 weeks (5.4×10^{13} to 1×10^{12} vg/kg), 7 weeks *Mck* mice were treated subsequently with a more narrowed and relevant dose range (2.5×10^{13} to 2.5×10^{12} vg/kg).

At 5 weeks, the left ventricle (LV) systolic function is modestly impaired, while at 7 weeks the LV is substantially dilated and hypertrophied leading to one-third of the normal cardiac blood output (CO) (7). In the proof-of-concept study (19), a single IV injection of 5.4×10^{13} vg/kg at 7 weeks was sufficient to fully reverse the cardiac phenotype by 14 weeks of age. Here, mice were treated with one of six doses, ranging from the 5×10^{13} vg/kg down to 1×10^{12} vg/kg, decreasing by 2 to 2.5-fold increments. Mice treated at 5 and 7 weeks were monitored until 12.5 and 15.5 weeks of age, i.e. 7 and 8 weeks post-injection, respectively. These endpoints were selected because they are well beyond the median survival of untreated *Mck* mice (9.5 weeks), but allow histological and molecular analyses of the lowest dose group, whose survival was poorly improved (Figs 1A and 2A). As the phenotype of untreated *Mck* mice is very robust and reproducible, historical data were plotted for echocardiography, survival and body weight (BW). Echocardiography evaluations prior to treatment confirmed the same phenotype in animals of the present studies as in historical data (Supplementary Material, Tables S1 and S2).

When treated at 5 weeks, all mice injected with 5×10^{13} and 2.5×10^{13} vg/kg, as well as four out of five mice treated at 1×10^{13} vg/kg, survived up to 12.5 weeks and showed normal BW and echocardiography parameters (Fig. 1A–E and Supplementary Material, Table S1). Lower dose groups only showed partial or no rescue, in a dose-dependent manner. Nonetheless, meaningful therapeutic effects were also achieved at 5×10^{12} vg/kg. At this dose, the cardiac function and hypertrophy were stabilized, while the incidence and severity of heart failure-associated comorbidities, including arrhythmia, hydrothorax and muscle wasting, were decreased. Altogether, these results indicate that 1×10^{13} vg/kg corresponded to the pivotal therapeutic dose between partial and complete functional rescue. Noteworthy, the heterogeneity of the therapeutic outcome among each dose group was low in the two highest dose groups but increased substantially in the lower dose groups, as illustrated by the LV shortening fraction (SF) (Supplementary Material, Fig. S1B). As demonstrated below, this was in line with the vector biodistribution and its relative heterogeneity among each dose group, especially when approaching the therapeutic thresholds.

On the other hand, *Mck* mice treated at 7 weeks of age, presenting with severe LV dilatation and heart failure, showed a full therapeutic rescue only when treated with 2.5×10^{13} vg/kg (Fig. 2C–E and Supplementary Material, Table S2). Five out of six mice treated at this dose were normalized for cardiac function, BW growth and survival. The remaining mouse in this dose group displayed subnormal but stabilized cardiac function and compensated hypertrophy. As expected, mice treated with lower doses showed decreasing survival and poorer therapeutic rescue. Strikingly, all mice treated with 1×10^{13} vg/kg survived up to 15 weeks, i.e. increased lifespan by 57%, despite presenting

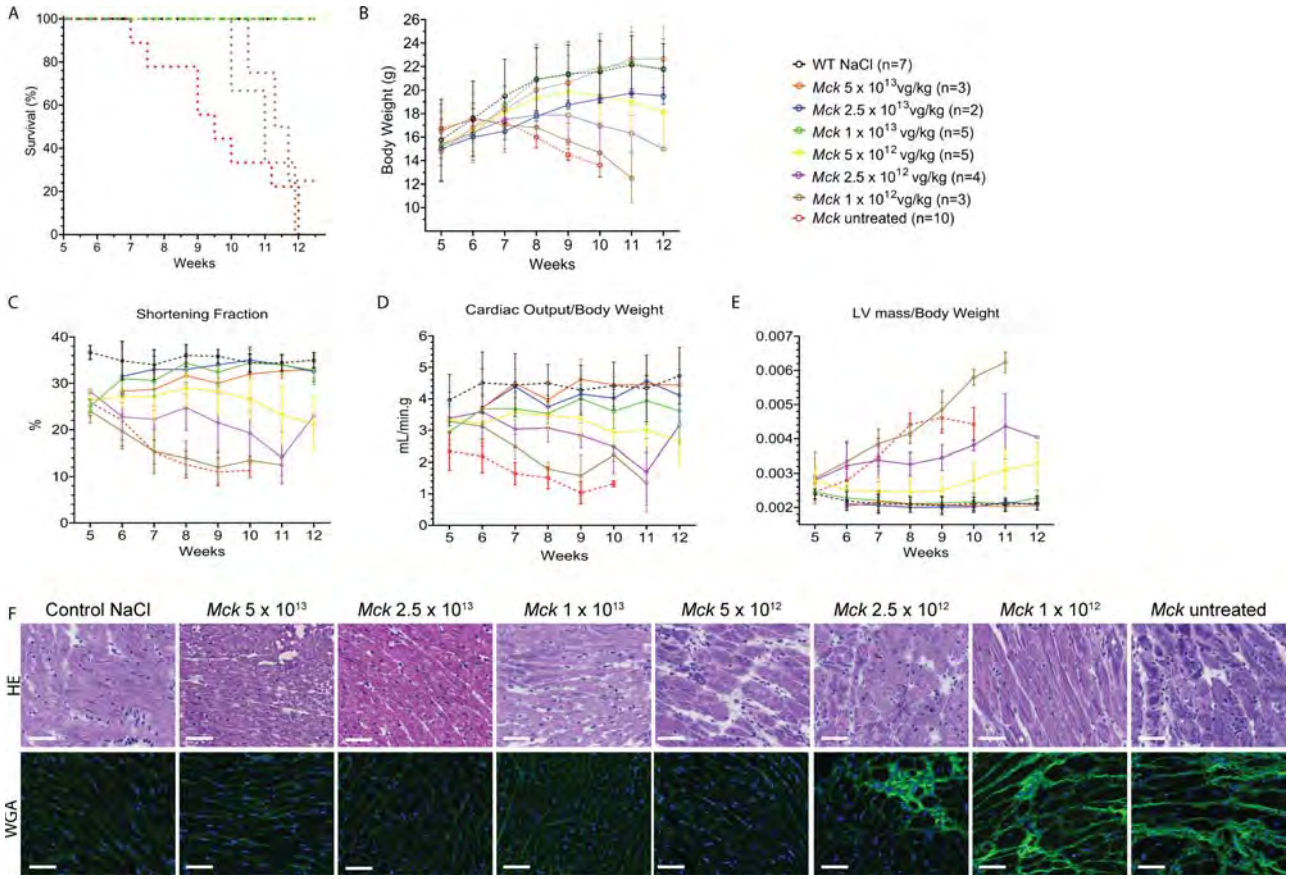

Figure 1. Dose-dependent rescue of survival, cardiac function, hypertrophy and fibrosis in *Mck* mice treated at 5 weeks of age, at early stage of cardiac dysfunction. (**A**) Survival of *Mck* mice treated with decreasing doses of AAVrh10.CAG-hFXN-HA vector from 5×10^{13} down to 1×10^{12} vg/kg at 5 weeks of age. Control mice were treated with vehicle (NaCl). For untreated *Mck* mice, historical data were plotted. Compared to untreated *Mck*, the survival of *Mck* mice treated with any of the evaluated doses, besides 1×10^{12} vg/kg, was significantly increased (log-rank Mantel–Cox statistical test, $P < 0.05$). Compared to WT mice, only the survival of *Mck* mice treated at 2.5×10^{12} and 1×10^{12} vg/kg was significantly decreased. (**B**) BW. Statistical analyses are reported in the Supplementary Material, Table S1. (**C–E**) Longitudinal echocardiography analysis of LV SF (C) LV mass normalized to BW (D) and CO normalized to BW (E). Data are represented as mean ± SD and statistical analyses reported in the Supplementary Material, Table S1. See also Supplementary Material, Fig. S1 for mice individual LV SF and correlation analyses between dose-LV SF and dose-CO/BW. (**F**) Histological analysis of fibrosis and cell infiltrates by H&E or WGA staining. Representative imaging of the LV anterior wall. Scale bar, 50 µm. See also Supplementary Material, Figs S3 and S4 for extended fibrosis analysis.

severely altered cardiac function (16–17% LV SF). Noteworthy, this meaningful therapeutic effect was achieved at a dose 5-fold lower than the one used in the initial study (19). Here, 2.5×10^{13} vg/kg was the pivotal therapeutic dose and similarly the heterogeneity of the therapeutic outcome increased substantially in the lower dose groups (Supplementary Material, Fig. S2B).

Interestingly, a similar trend was observed for heart fibrosis. Above these pivotal doses, there were only few or no fibrotic patches and cell infiltrates in both *Mck* mice treated at 5 weeks (Fig. 1F and Supplementary Material, Fig. S3) and 7 weeks of age (Fig. 2F and Supplementary Material, Fig. S5). Mice treated at these pivotal doses or below displayed increasing amount of fibrosis, either interstitial or as patches, as revealed by hematoxylin and eosin (H&E) staining and confirmed by the labelling of extracellular matrix proteoglycans with wheat germ agglutinin (WGA) staining (Supplementary Material, Figs S4A and S6A). The relative heart surface labelled with WGA, compared between wild-type (WT) and treated *Mck* mice, confirmed this trend but showed statistical difference only at the lowest doses (Supplementary Material, Figs S4B and S6B). Furthermore, H&E revealed the subcellular disorganization of cardiomyocytes in untreated and treated *Mck* mice, in the regions of the heart sections circled with blue dotted line (Supplementary Material, Figs S3 and S5). Observations at high magnification revealed that the disorganization of the myofilaments, labelled by eosin with a typical fibrillary aspect, while the endoplasmic reticulum, labelled by hematoxylin, appeared substantially dilated. *Mck* mice treated at the pivotal therapeutic dose or above displayed few or none of these subcellular alterations, while mice treated with decreasing dose showed increasing level of alteration.

Here, the minimal therapeutic doses were identified as 1 and 2.5×10^{13} vg/kg, respectively for *Mck* mice treated upon early and advanced cardiac dysfunction. This difference is most likely explained by the rapid progression of the disease past 7 weeks and the slow expression kinetic of the vector *in vivo*. Indeed, we have shown previously that the FXN protein level reaches its peak of expression in the heart, and therefore its maximum therapeutic effect, only 10 days post-injection (19).

Vector biodistribution in heart correlated strongly with vector expression and the percentage of cardiomyocytes transduced

In order to investigate the biological significance of these pivotal doses and the underlying mechanisms of the therapeutic

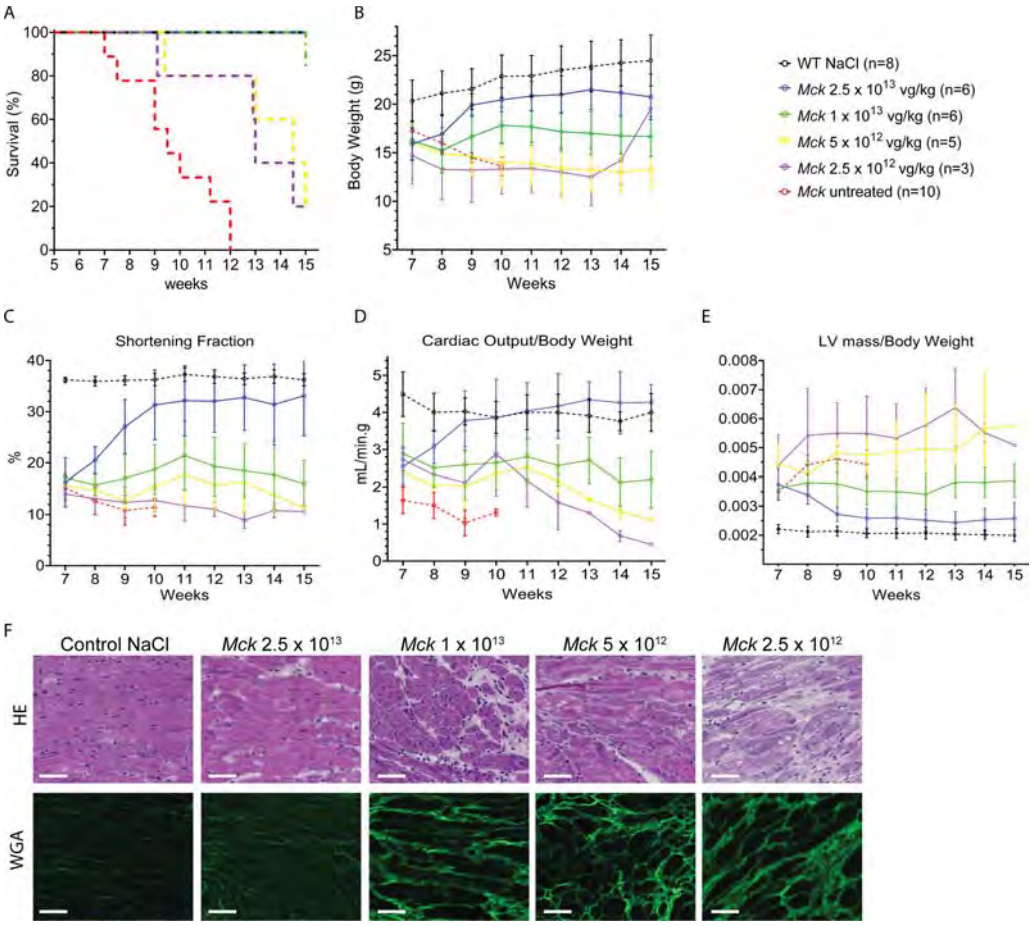

Figure 2. Dose-dependent rescue of survival, cardiac function, hypertrophy and fibrosis in *Mck* mice treated at 7 weeks of age, upon heart failure. (**A**) Survival of *Mck* mice treated with decreasing doses of AAVrh10.CAG-hFXN-HA vector from 2.5×10^{13} down to 2.5×10^{12} vg/kg. Control mice were treated with vehicle (NaCl). For untreated *Mck* mice, historical data were plotted. Compared to untreated mice, the survival of *Mck* mice treated with any of the evaluated doses, was significantly increased (log-rank Mantel–Cox statistical test, $P < 0.05$). Compared to WT mice, only the survival of *Mck* mice treated at 5×10^{12} and 2.5×10^{12} vg/kg was significantly decreased. (**B**) BW. Data are represented as mean ± SD and statistical analyses reported in the Supplementary Material, Table S2. (**C–E**) Longitudinal echocardiography analysis of LV SF (C), LV mass normalized to BW (D) and CO normalized to BW (E). Data are represented as mean ± SD and statistical analysis reported in the Supplementary Material, Table S2. See also Supplementary Material, Fig. S2 for mice individual LV SF and correlation analyses between dose-LV SF and dose-CO/BW. (**F**) Histological analysis of fibrosis and cell infiltrates by H&E or WGA staining. Representative imaging of the LV anterior wall. See also Supplementary Material, Figs S5 and S6 for extended fibrosis analysis.

effect, we first quantified the vector biodistribution and frataxin expression in the heart and then analyzed their correlation. The distribution of the VCN per diploid genome, human FXN mRNA level and protein concentration ([hFXN]) were quantified specifically at the level of the apex, middle and base of the heart. In both 5- and 7-week-old treated animals, the VCN, FXN mRNA and [hFXN] appeared to decrease proportionally with the dose administrated (Fig. 3A–C and Supplementary Material, Fig. S7A–C) but did not reach statistical significance due to the low number of mice per group and their relative heterogeneity. Thus, the relationship between dosing and VCN can be described by linear regression, but with moderate stringency (Fig. 3D and Supplementary Material, Fig. S7D).

The VCN measured at the apex, middle and base of the heart, was similar for each individual mouse, despite an apparent trend towards higher VCN in the middle of the heart (Supplementary Material, Figs S8A and S9A). In line with these results, the vector expression was very similar at these different levels, when measured by quantitative reverse-transcriptase PCR (qRT-PCR) in a subset of samples (Supplementary Material, Fig. S8B). Furthermore, the vector biodistribution and expression strongly correlated and can be described robustly by logarithmic regression (Fig. 3E–F and Supplementary Material, Fig. S7E–F). The vector pharmacokinetics, i.e. ratio [hFXN]/VCN, was very similar in 5 and 7 weeks treated mice (i.e. 705 ± 501 and 634 ± 350, respectively) and not statistically different following *t*-test analysis ($P = 0.63$). Hence, the vector pharmacokinetic appears highly predictable in the mouse heart, independently of the age of treatment or disease severity at treatment and sacrifice.

Overall, the [hFXN] ranged between 2 and 10 927 ng of FXN per mg of total protein (Supplementary Material, Tables S3 and S4). Noteworthy, the mouse FXN protein concentration ([mFXN]) is on average 147 ± 42 ng/mg in the heart of naive adult WT mice ($n = 6$), 60 ± 11 ng/mg in healthy heterozygote mice ($n = 6$) and 9 ± 3 ng/mg in *Mck* mice ($n = 6$). Thus, the levels of transgenic FXN protein ranged between 0.01–74-fold the normal endogenous level. Rescue of cardiac function was systematically associated with [hFXN] ≥ 84 ng/mg (Supplementary Material, Table S3). Importantly, these numbers correspond to average values reflecting unequal expression

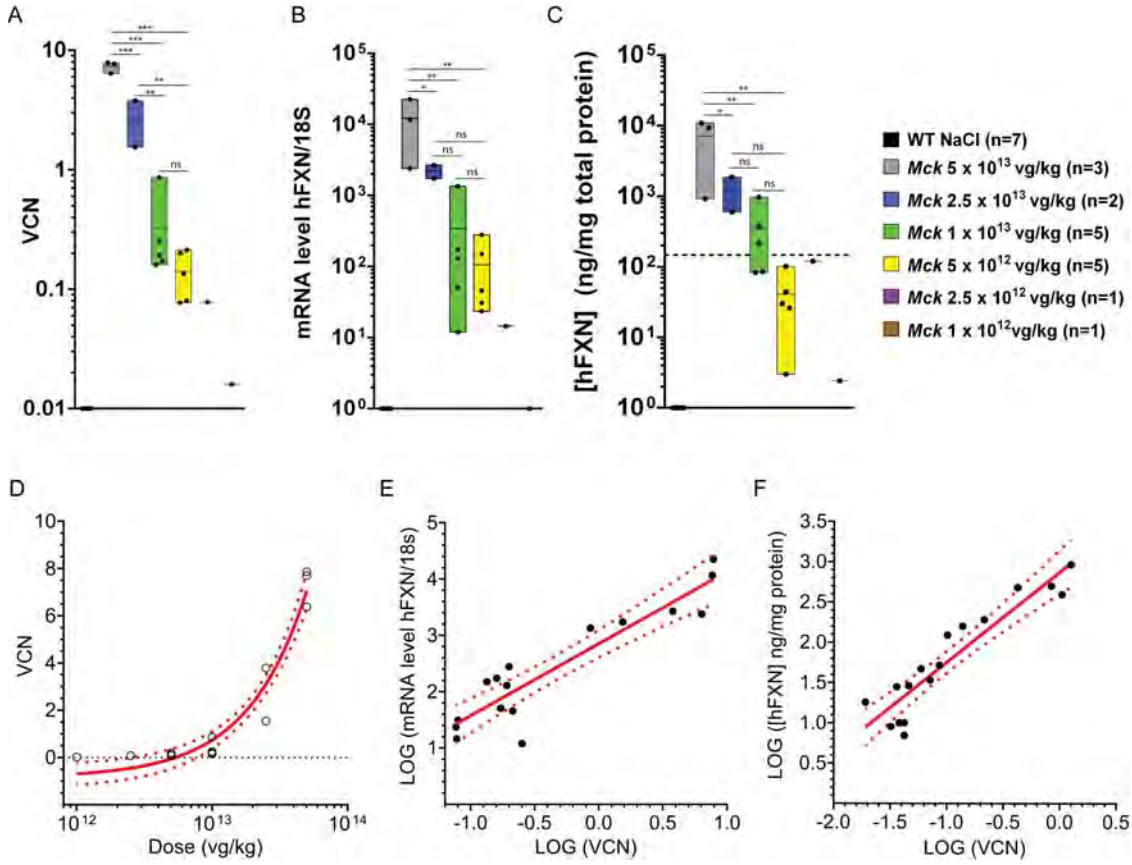

Figure 3. Analysis of vector biodistribution and pharmacokinetic in the heart of *Mck* mice treated at 5 weeks of age. (**A–C**) Vector biodistribution reported as VCN per diploid genome (A), mRNA level normalized to 18S (reported as $2^{-deltaCt} \times 10^6$) (B) and tissue concentration of human FXN protein ([hFXN]) (C). Individual values, dose group range and average level are represented. Dotted line corresponds to the minimum [hFXN] associated with full rescue of heart function. One-way analysis of variance (ANOVA) with false discovery rate (FDR) 5% statistical test: ns, non-significant; *q < 0.05; **q < 0.01; ***q < 0.0001. (**D**) Correlation analysis between dose and VCN. Spearman non-parametric test: R = 0.87, P < 0.0001. Linear regression analysis: $R^2 = 0.95$. (**E**) Correlation between vector biodistribution and mRNA level. Spearman non-parametric test: R = 0.89, P < 0.0001. Linear regression analysis of log-transformed values: $R^2 = 0.85$. (**F**) Correlation between vector biodistribution and [hFXN]. Spearman non-parametric test: R = 0.91, P < 0.0001. Linear regression analysis of log-transformed values: $R^2 = 0.72$. Individual values, best fit curve and 95% confidence intervals are plotted. See also Supplementary Material, Fig S7A–F for the similar analysis of *Mck* mice treated at 7 weeks.

of frataxin among the cardiomyocytes, some with low or no expression while others expressing high levels of FXN (Fig. 4A). Nonetheless, the [hFXN] therapeutic threshold identified here is within the physiological range and suggest that only a moderate increase in FXN is necessary while substantial overexpression (>70-fold) is not detrimental to the cardiac function or heart histology (Fig. 1C–F and Supplementary Material, Fig. S3).

To quantify the percentage of cardiomyocytes transduced and expressing the therapeutic FXN protein, heart sections were immunolabelling for both human FXN and dystrophin (Fig. 4A–B). In addition, the heart surface rescued for Fe–S enzyme activity was quantified on adjacent heart sections by histoenzymatic staining of SDH activity (Fig. 4C–D and Supplementary Material, Fig. S7G–H). As expected, the percentage of FXN positive cardiomyocyte and the cardiac surface positive for SDH activity decreased with the dose administrated (Fig. 4B and D and Supplementary Material, Fig. S7H). Importantly, the percentage of heart surface positive for SDH activity was homogenous throughout the heart volume in mice treated with the highest doses (Supplementary Material, Figs S8C and S9B). However, at lower doses, this was less homogeneous with higher SDH enzyme activity in the middle of the heart, in line with the VCN analysis (Supplementary Material, Fig. S8A). In contrast, the distribution of the SDH activity (Supplementary Material, Fig. S8D) and FXN labelling (Supplementary Material Fig. S8E) was overall very homogenous along short axis of the heart. In line with the expected rescue of Fe–S enzyme following FXN re-expression, there were strong correlations between SDH and FXN positive cardiomyocytes (Fig. 4E) and with VCN (Fig. 4F–G and Supplementary Material, Fig. S7I).

Treatment of 50% of cardiomyocytes is sufficient to obtain cardiac function correction, independently of the cardiomyopathy progression

Next, we conducted a series of correlative and regression analyses between the cardiac vector biodistribution and the heart function and morphological outcome, to identify the underlying therapeutic thresholds.

In both 5- and 7-week-old treated mice, the heart vector biodistribution correlated strongly with the efficiency of cardiac function rescue. This is illustrated by the robust correlation between VCN and LV SF, LV mass or cardiac output (Fig. 5A–C and Supplementary Material, Fig. S10A–C). In line with these results, the gene expression of cardiac biomarkers of

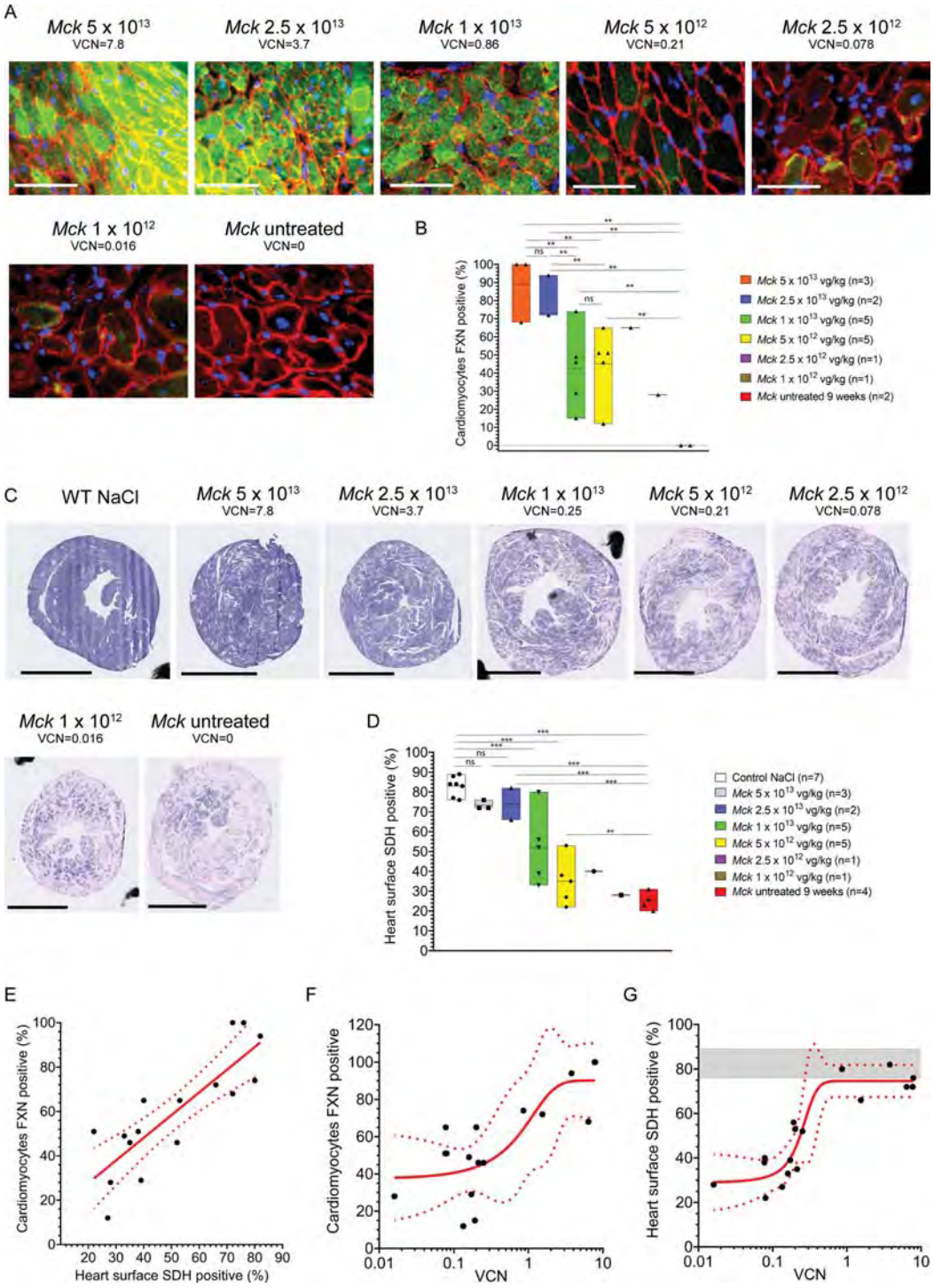

Figure 4. Cell distribution of human FXN protein and Fe–S cluster enzyme activity are correlated in the heart of *Mck* mice treated at 5 weeks. (**A**) Representative fluorescent microscopy imaging of heart tissue sections immunolabelled for dystrophin (red), human FXN (hFXN, green) and stained with 4′,6-diamidino-2-phenylindole (DAPI) (blue). Constant time of acquisition for hFXN signal (1000 ms). Scale bar, 50 µm. The corresponding dose and VCN are reported above each image. (**B**) Percentage of cardiomyocytes positive for hFXN in the LV. Individual values, dose group range and average level are represented. One-way ANOVA with FDR 5% statistical test: ns, $^{*}q < 0.05$, $^{**}q < 0.01$, $^{***}q < 0.0001$. See also **Supplementary Material, Fig. S8E** for separate quantification in septum, anterior and posterior LV walls. (**C**) Histoenzymatic staining for SDH activity on adjacent sections. Scale bar, 2.5 mm. (**D**) Quantification of the cardiac surface stained for SDH activity. Individual values, dose group range and average level are represented. One-way ANOVA with FDR 5% statistical test: ns, $^{*}q < 0.05$, $^{**}q < 0.01$, $^{***}q < 0.0001$. See also Supplementary Material, Fig. S8C for separate quantification in the apex, middle and base of the heart and **Supplementary Material, Fig. S8D** for separate quantification in septum, anterior and posterior LV walls and right ventricle (RV). (**E**) Correlation analysis between the percentage of cardiomyocytes positive for hFXN and heart surface for SDH enzymatic activity. Spearman correlation test: $R = 0.83$, $P < 0.0001$. Linear regression analysis: $R^2 = 0.70$. Individual datapoints, best fit curve and 95% confidence intervals are plotted. (**F–G**) Correlation analysis between VCN and the percentage of cardiomyocytes positive for hFXN or heart surface positive for SDH enzymatic activity. Individual datapoints, best fit curve and 95% confidence intervals are plotted. (F) Spearman correlation test: $R = 0.67$, $P = 0.0028$. Sigmoid regression analysis: $R^2 = 0.64$. (G) Spearman correlation test: $R = 0.82$, $P < 0.0001$. Sigmoid regression analysis: $R^2 = 0.87$. See also **Supplementary Material, Fig. S7G–I** for similar analysis in *Mck* mice treated at 7 weeks.

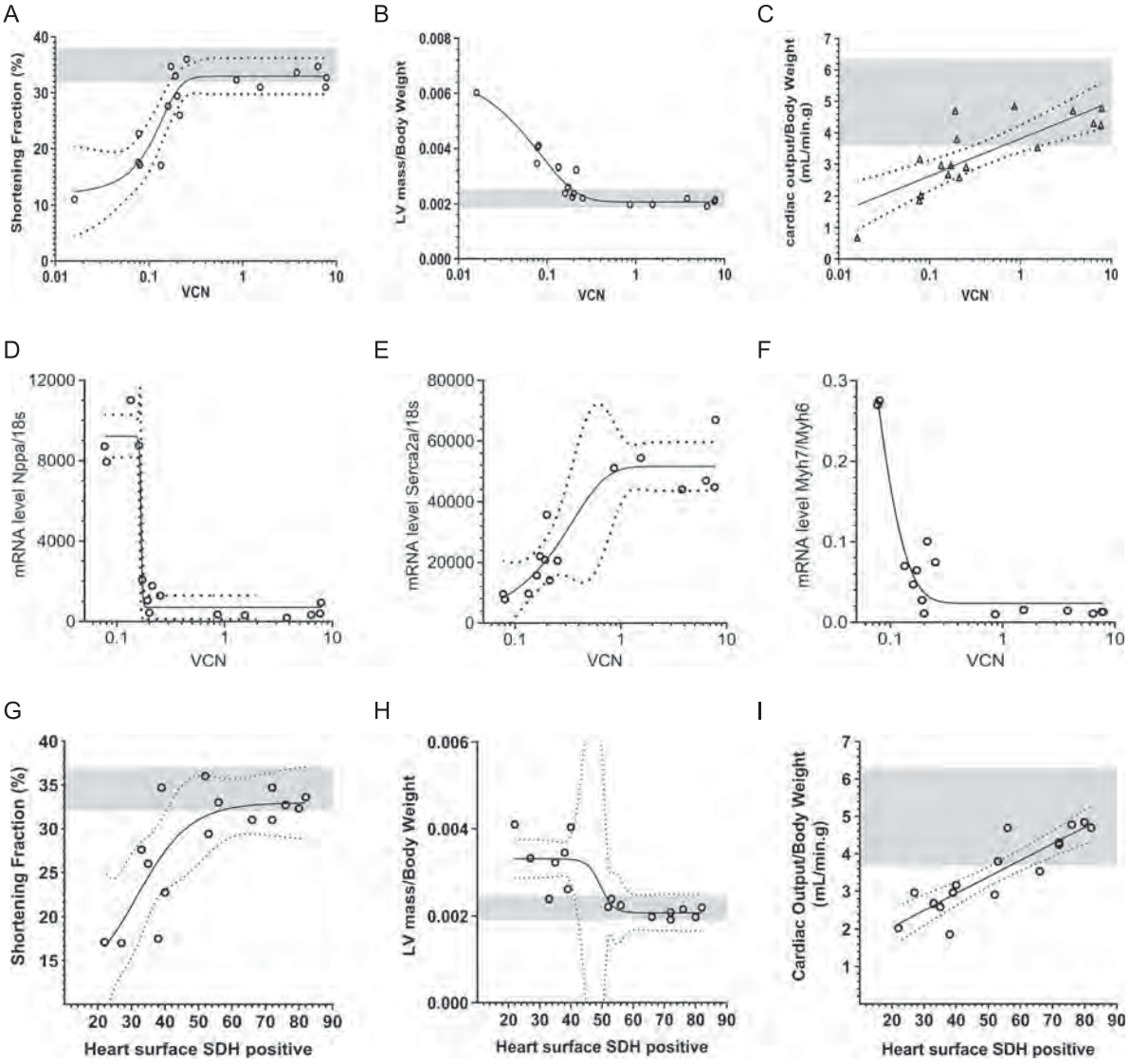

Figure 5. The rescue of the cardiac dysfunction and hypertrophy are predicted by the vector biodistribution, cell distribution of human FXN protein and rescue of Fe–S cluster enzyme activity. *Mck* mice treated at 5 weeks of age and sacrificed at 12 weeks. (**A–C**) Correlation analysis between VCN and LV SF, LV mass to BW and cardiac output normalized to BW. (A) Spearman non-parametric test: R = 0.69, P = 0.0027. Sigmoid regression analysis: $R^2 = 0.80$. (B) Spearman non-parametric test: R = −0.90, P < 0.000. Sigmoid regression analysis: $R^2 = 0.93$. (C) Spearman non-parametric test: R = 0.75, P = 0.0008. Sigmoid regression analysis: $R^2 = 0.64$. (**D–F**) Correlation analysis between VCN and gene expression of biomarkers indicative LV volume/pressure overload (Nppa), calcium handling impairment (Serca2a) and maladaptive transcriptional switch (ratio Myh7Myh6). mRNA levels are normalized to 18S and reported as $2^{-\text{deltaCt}} \times 10^6$. (D) Spearman correlation test: R = −0.81, P = 0.0004. Sigmoid regression analysis: $R^2 = 0.96$. (E) Spearman correlation test: R = 0.86, P < 0.0001. Sigmoid regression analysis: $R^2 = 0.86$. (F) Spearman correlation test: R = −0.71, P = 0.0037. Sigmoid regression analysis: $R^2 = 0.91$. (**G–I**) Correlation analysis between heart surface positive for SDH activity and LV SF, LV mass normalized to BW and cardiac output normalized to BW. (G) Spearman non-parametric test: R = 0.70, P = 0.0002. Sigmoid regression analysis: $R^2 = 0.65$. (H) Spearman non-parametric test: R = 0.88, P < 0.0001. Sigmoid regression analysis: $R^2 = 0.78$. (I) Spearman non-parametric test: R = −0.67, P = 0.0005. Sigmoid regression analysis: $R^2 = 0.67$. Individual datapoints, best fit curve and 95% confidence intervals are plotted. Grey area represents the range of normal value for control mice. See also Supplementary Material, Fig. S10 for similar analysis of *Mck* mice treated at 7 weeks.

pressure/volume overload natriuretic peptide type A (Nppa), calcium handling (Serca2a) and maladaptive transcriptional switch (ratio Myh7/Myh6) were also strongly correlated to the VCN (Fig. 5D–F). Strikingly, the VCN threshold for which complete rescue was achieved falls within the 0.2–0.4 VCN range, while partial correction is associated with VCN of 0.1–0.2. Furthermore, these thresholds were similar in 5- and 7-week-old treated *Mck* mice despite the differences in the disease progression and severity at the time of treatment.

Remarkably, the therapeutic threshold of 0.2–0.4 VCN was associated with 45–50% of cardiomyocytes positive for FXN expression (Fig. 4F) and with 45–65% of cardiomyocytes positive for SDH activity (Fig. 4G and Supplementary Material, Fig. S7I). This was independently cross-validated by the direct correlation between the rescue of SDH activity and the rescue efficiency of cardiac function and hypertrophy (Fig. 5G–I and Supplementary Material, Fig. S10D–F). Moreover, meaningful therapeutic rescue of cardiac function and survival was achieved with as little as 30–40% of cardiomyocytes treated, in both mice treated at 5 and 7 weeks. Interestingly, cardiac output appears to benefit more easily from low cardiac biodistribution and more linearly from its increase in comparison to LV SF or LV mass.

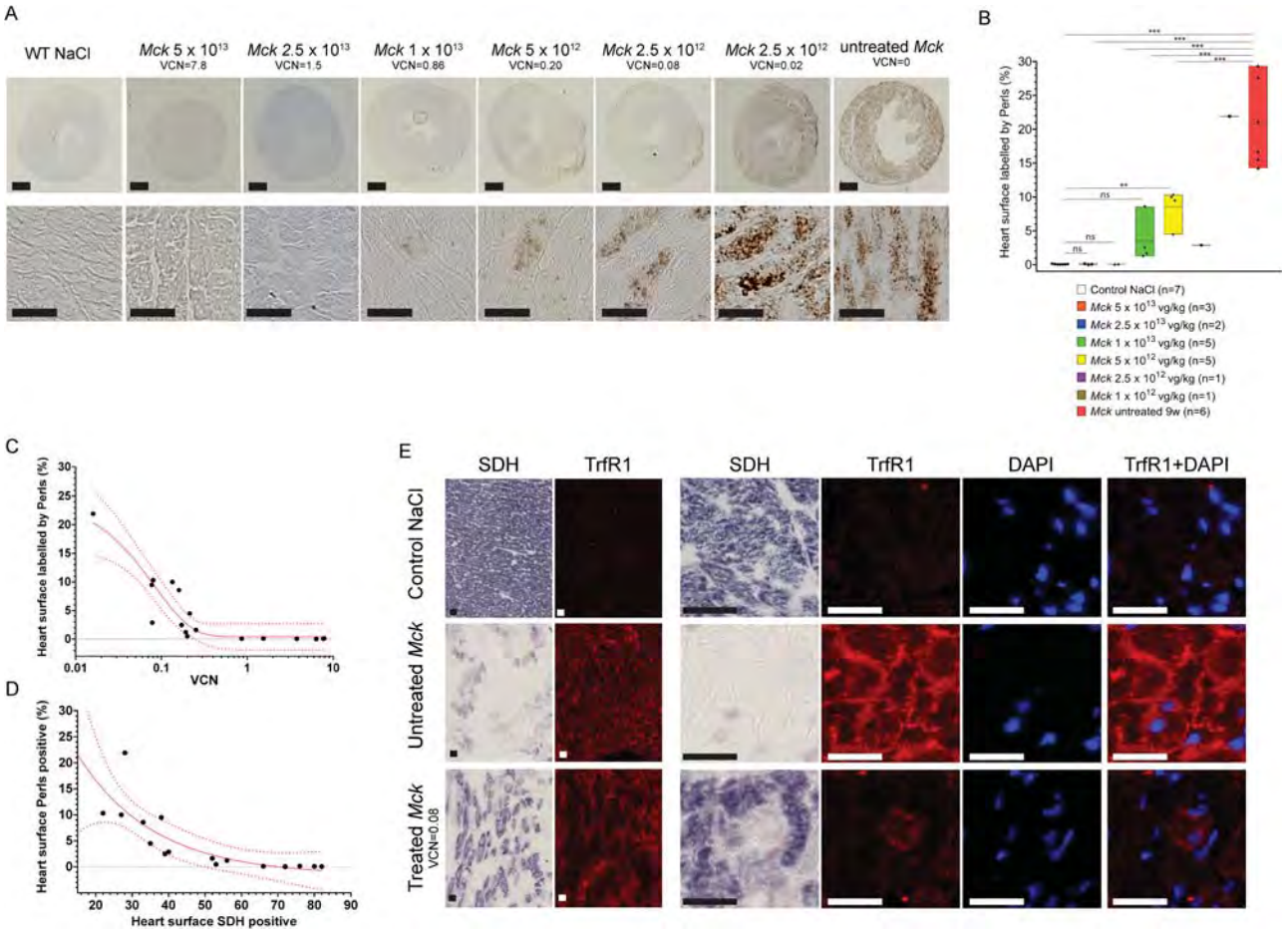

Figure 6. Rescue of iron metabolism is predicted by vector biodistribution and is mediated by cell-autonomous rescue Fe–S enzyme activity. Microscopy imaging of heart tissue sections from control and *Mck* mice treated at 5 weeks and sacrificed at 12 weeks, as well as untreated 9-week-old *Mck* mice. (**A**) DAB-enhanced Perls staining of Fe^{3+} deposits. The corresponding dose and VCN are reported above. Scale bar: upper row, 1 mm; lower row, 25 µm. (**B**) Quantification of heart surface labelled with Perls staining. Individual values, dose-group range and average level are represented. One-way ANOVA with FDR 5% statistical test: ns, $*q < 0.05$, $**q < 0.01$, $***q < 0.0001$. (**C–D**) Correlation analysis between heart surface positive for Perls staining with VCN or heart surface positive for SDH enzymatic activity. Individual datapoints, best fit curve and 95% confidence intervals are plotted. (C) Spearman non-parametric test: $R = -0.88$, $P < 0.0001$). One phase regression analysis: $R^2 = 0.81$. (D) Spearman non-parametric test: $R = -0.94$, $P < 0.0001$. One phase regression analysis: $R^2 = 0.67$. See also **Supplementary Material, Fig. S11** for similar analysis in *Mck* mice treated at 7 weeks. (**E**) Co-staining of heart frozen sections for SDH enzymatic activity and transferrin receptor 1 (TrfR1) in WT, untreated and treated *Mck* at the dose of 5×10^{12} vg/kg. Nuclear DNA labelling with DAPI. Scale bar, 25 µm. See also **Supplementary Material, Figs S12 and S13** for histological analysis of mitochondria bioenergetic and dynamic.

In summary, the cellular and molecular thresholds conditioning the therapeutics effects are independent of the severity of the cardiac dysfunction and were identified as (1) the percentage of treated cardiomyocytes, i.e. ≥50%, (2) the corresponding VCN, i.e. 0.2–0.4 and (3) moderate increase of FXN protein level, i.e. >84 ng/mg.

Cell-autonomous rescue of mitochondrial hallmarks associated with FXN deficiency

Beyond the impairment of Fe-S enzyme activity, such as SDH, secondary hallmarks of FXN deficiency are increased cellular iron uptake and deposits, as well as altered mitochondria proliferation, autophagy and bioenergetics (7,25,26). Cardiac iron deposits are detected by Perls staining and electron microscopy starting 7 weeks of age in untreated *Mck* mice (7). In 5- and 7-week-old treated *Mck* mice, the prevention and clearance of Perls positive iron deposits in cardiomyocytes appeared to be dose dependent (**Fig. 6A–B and Supplementary Material, Fig. S11A–B**). Moreover, the amount of iron deposits was inversely correlated with the VCN (**Fig. 6C and Supplementary Material, Fig. S11C**) and the rescue of SDH activity (**Fig. 6D and Supplementary Material, Fig. S11D**).

Deficiency in Fe-S biosynthesis results in a switch of the iron regulatory protein IRP1 to its Iron Response Element (IRE) form, thereby regulating protein essential for iron metabolism, such as the iron transporter TrfR1 (27). As illustrated by the immunofluorescent labelling of TrfR1 on heart sections, untreated 9-week-old *Mck* mice displayed much higher signal than WT control mice (**Fig. 6E**). High level of TrfR1 colocalized systematically with cardiomyocytes-lacking SDH activity. Furthermore, cardiomyocytes with residual SDH activity displayed low TrfR1 labelling, while SDH negative cardiomyocytes displayed variable levels of TrfR1 immunolabelling. Treated *Mck* mice displayed identical colocalization patterns, independently of the dose administered or the efficiency of cardiac function rescue (**Fig. 6E**). These first results suggested a cell-autonomous effect, i.e only cells transduced with the AAVrh.10.CAG vector, expressing the therapeutic hFXN protein and therefore rescued for SDH activity, are rescued for iron metabolism.

To confirm the cell-autonomous nature of this therapeutic effect, we have investigated the colocalization relationship between SDH enzymatic activity, mitochondrial bioenergetic and mitochondria dynamic. Impairment of mitochondria bioenergetic and NAD+/NADH metabolism was evaluated indirectly by assessing the level of pan-lysine acetylation (AcetylK) (26,28). This post-translation modification was previously shown to be substantially elevated in untreated *Mck* mice heart, particularly on mitochondrial proteins, increasing with disease progression (26). Here, this was confirmed independently by western blot analysis on total heart protein extracts from WT controls and untreated *Mck* mice, between 3 and 9 weeks of age (Supplementary Material, Fig. S12A) and by immunofluorescent labelling of heart sections from untreated 9-week-old *Mck* mice and WT control mice (Supplementary Material, Fig. S12B). Untreated *Mck* mice displayed high level of mitochondria AcetylK, as revealed by the filamentous mitochondrial network in SDH-negative cardiomyocytes. In contrast, residual SDH-positive cardiomyocytes displayed near normal level of AcetylK labelling. Treated *Mck* mice displayed the same pattern of labelling (Supplementary Material, Fig. S12B) with high AcetylK signal colocalized systematically with SDH-negative cardiomyocytes, while SDH-positive cardiomyocytes always displayed low signal levels (Supplementary Material, Fig. S12B). Strikingly, identical co-localization patterns were observed also for prohibitin (Supplementary Material, Fig. S13A), a marker of mitochondria biomass and for the autophagosome receptor Sqstm1 (Supplementary Material, Fig. S13B).

Altogether, these results demonstrate a biodistribution-dependent and cell-autonomous rescue of iron metabolism and mitochondria homeostasis in the heart, when using SDH activity as a proxy for cell expression of the hFXN therapeutic transgene.

Importantly, the cell-autonomous effects were observed systematically in all treated mice, independently of the dose, VCN, percentage of cardiomyocytes treated (FXN and SDH positive) and the level of cardiac function rescue. The direct clinical implication would be that the heart function is rescued only when enough cardiomyocytes are directly transduced and collectively generate sufficient mechanical force. This is illustrated by the mouse treated with the therapeutic pivotal dose 1×10^{13} vg/kg imaged in the Supplementary Material, Figs S12A and S13A–B. While this mouse had fully normalized cardiac function, the associated vector biodistribution was in the lower range of this dose group. Indeed, the VCN was 0.17 while this group values ranged from 0.16 to 0.86. Similarly, the percentage of heart surface positive for SDH was 39%, while this group ranged from

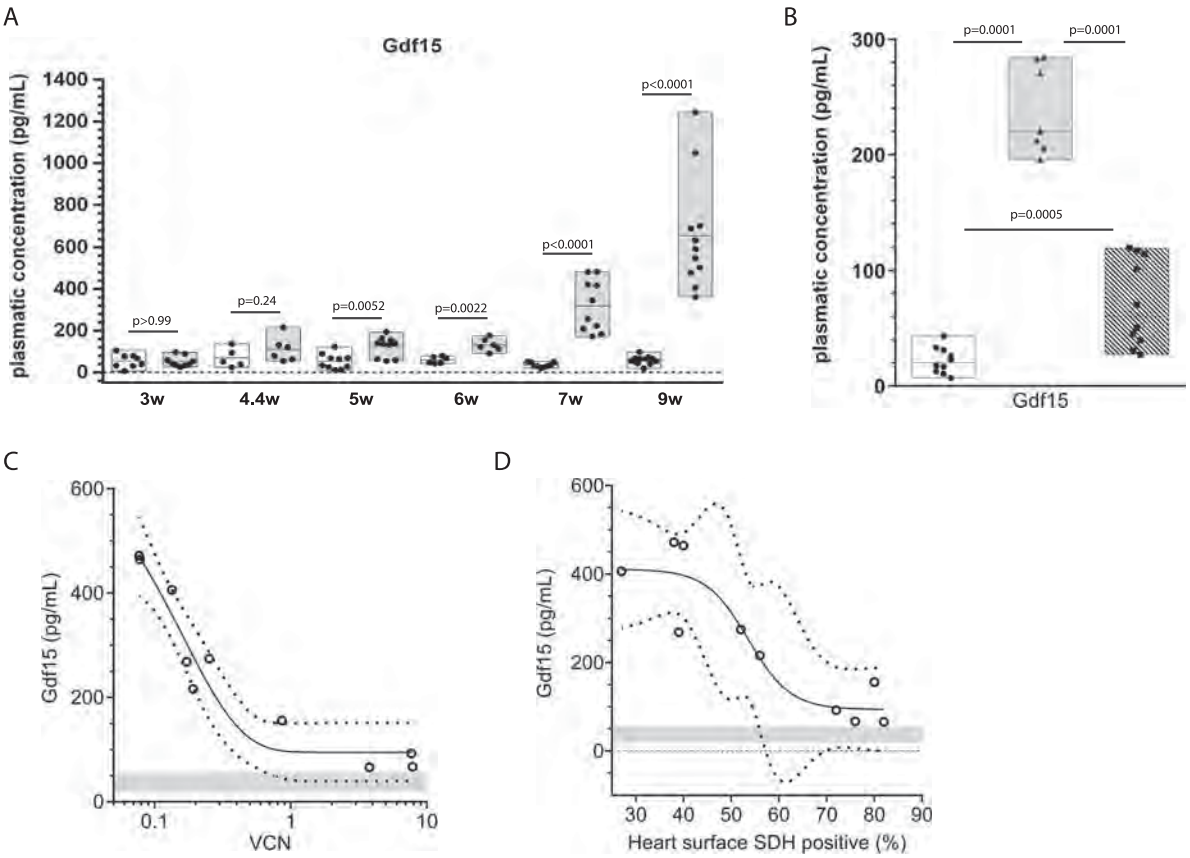

Figure 7. Gdf15 plasmatic concentration correlates with disease progression, decreases shortly after AAVrh10.CAG-hFXN-HA administration and correlates with vector biodistribution in the heart of treated *Mck* mice. (**A**) Untreated *Mck* mice (grey, $n = 6$–11) and their control littermates (white, $n = 5$–11) were sampled for plasma between 3 and 9 weeks of age. Gdf15 concentration ([Gdf15]) was measured by ELISA assay. Data are reported as individual values, group range and mean level. Mann–Whitney statistical test's *P*-values are reported. (**B**) [Gdf15] in control and *Mck* mice treated at 7 weeks and sacrificed 1 week later. Control mice injected with NaCl 0.9% (white, $n = 10$), *Mck* treated injected with 5×10^{13} vg/kg of AAVrh10.CAG-hFXN-HA (Hatched, $n = 10$) and *Mck* mice injected with NaCl 0.9% (grey, $n = 7$). Data are reported as individual values, group range and mean level. Mann–Whitney statistical test's *P*-values are reported. See also Supplementary Material, Fig. S14 for molecular analysis of vector biodistribution and expression, analysis of cardiac dysfunction biomarkers and ATF4 pathway. (**C–D**) Correlation analysis between [Gdf15] and cardiac vector biodistribution, i.e. VCN (C) or heart surface rescued for SDH activity (D). Spearman non-parametric test $R = -0.93$, $P < 0.0001$ and $R = -0.88$, $P = 0.0016$, respectively. Modelling by one-phase decay (C) and sigmoid regression (D) with best fit curve and 95% confidence intervals: $R^2 = 0.93$ and 0.86, respectively.

33 to 80%. In line with the correlation analysis reported above, this mouse illustrates nicely the cell-autonomous mechanism underlying the therapeutic rescue of cardiac gene therapy.

Dose response rescue of the integrated stress response and the GDF15 plasma concentration

Previously, the integrated stress response (ISR) was shown to be activated in the *Mck* mouse heart, increasing with disease progression (29) and rescued just 1 week after the gene therapy treatment of 7-week-old *Mck* mice (19). More recently, the ISR has been shown to be a common cellular stress response of mitochondrial failure mediated by ATF4 and results in increase gene expression and plasma level of growth differentiation factor 15 ([GDF15]) (24,30,31).

Plasmatic [GDF15] was significantly elevated in untreated *Mck* mice, as soon as 5 weeks of age, upon early LV systolic dysfunction and increased with the cardiomyopathy progression (Fig. 7A). To assess the effect of the treatment on GDF15, 7-week-old *Mck* mice were injected with 5×10^{13} vg/kg of vector and sacrificed 1 week later. Significant cardiac vector biodistribution (VCN = 2.4 ± 0.9) and expression were confirmed (Supplementary Material, Fig. S14A–B). Importantly, just 1 week after treatment, there was no or very limited rescue of the cardiac gene expression for biomarkers of pressure/volume overload, maladaptive transcriptional switch and calcium handling (Supplementary Material, Fig. S14C). In contrast, gene expression of Atf4 and its target genes, including Asns, Mthfd2, Ddit3, Trib3 and Gdf15, were substantially down-regulated 1 week after treatment (Supplementary Material, Fig. S14D). In line with these results, plasmatic [GDF15] was also partially rescued just 1 week after treatment, suggesting an early and direct effect mediated by FXN re-expression and Fe-S biosynthesis rescue. Furthermore, *Mck* mice treated with decreasing doses of vector at 5 weeks of age, displayed [Gdf15] level directly correlating with the vector biodistribution and cardiac surface rescue for SDH activity, which also support the direct and cell-autonomous relationship between FXN, Fe-S and ISR-driven expression of GDF15 (Fig. 7D–E). Thus, plasmatic [GDF15] is a direct readout of the mitochondrial stress response associated with FXN cardiac depletion in the *Mck* mouse model and potentially also in a recently developed inducible mouse model that showed similar involvement of the ISR (32). In consequence, [GDF15] could be a useful biomarker for the preclinical evaluation and development of candidate drugs in these mouse models.

Discussion

To advance the preclinical development of cardiac gene therapy for FA, we have investigated the biodistribution thresholds conditioning the partial or complete rescue of the heart function in the *Mck* mouse model. Previously, the proof-of-concept studies have been conducted in mouse models with high dose of AAV vector, resulting in >90% of cardiomyocyte transduced and >8-fold the endogenous FXN level (11,18,19). However, the same dose and biodistribution efficiency is unlikely to be replicated in adult patients, with the current vector manufacturing and delivery methods. Therefore, it appears crucial to define the minimal therapeutic threshold as amenable objectives in order to design efficiently relevant clinical administration paradigms. Here, we demonstrate that the therapeutic outcome was mainly dependent on the vector cardiac biodistribution and not so much on the cellular level of FXN protein re-expressed. Indeed, full rescue of the cardiac function and hypertrophy was achieved systematically with around half the cardiomyocytes treated throughout the heart and 0.2–0.4 VCN. Moreover, partial correction and meaningful therapeutic effects on survival and heart failure associated comorbidities were also achieved with as low as 30–40% of treated cardiomyocytes and 0.1–0.2 VCN. Surprisingly, these therapeutic thresholds are not altered by the severity of the cardiac dysfunction at the time of treatment. Furthermore, the vector pharmacokinetic was overall very reproducible and unaffected by the age or severity of cardiac and cellular dysfunction at the time of treatment or sacrifice. Although no obvious functional or histological toxicity could be observed in the heart, up to 72-fold the endogenous level, the toxic threshold and mechanism associated with FXN overexpression will have to be fully investigated to define safety guidelines.

Furthermore, we have investigated the interplay between the vector biodistribution, rescue of mitochondrial hallmarks of FXN deficiency and the progressive rescue of the cardiac function. Here, we have shown a direct and linear relationship between the percentage of cardiomyocytes positive for FXN labelling, the rescue of Fe-S enzymes activity (SDH) and the rescue of iron metabolism and mitochondria homeostasis. Altogether, our results rule out cross-correction between transduced and untransduced cardiomyocytes for the rescue of mitochondrial hallmarks of FXN deficiency and support a cell-autonomous therapeutic mechanism. Only cells transduced with the vector express FXN protein are corrected. Noteworthy, this also excludes the horizontal transfer of mitochondria or FXN protein between cardiomyocytes, as a possible therapeutic strategy. This appears as a crucial consideration for the clinical trial design of cardiac gene therapy or other similar therapeutic strategies, as their success might also depend directly on the percentage of cardiomyocytes treated throughout patients' heart, enabling sufficient mechanical force to be generated and to restore normal heart contractility.

Finally, we have investigated the ISR in relation to the vector biodistribution and the therapeutic outcome. While the mechanistic relationship between FXN deficiency and the ISR remains to be elucidated, the ISR activation has been shown in several FXN knock-out or siRNA mouse models (29,32,33), as well as *in vitro,* following FXN knock-down in human cell line (34). In the current study, GDF15, which is a target gene of the ISR and a cytokine involved in the systemic regulation of the body metabolism (35), displayed elevated cardiac gene expression and plasma concentration in untreated *Mck* mice. Strikingly, GDF15 plasma concentration increased with the cardiomyopathy progression and was rescued almost completely just 1 week after the administration of high dose of vector. While the ISR activation and GDF15 overexpression are secondary pathological events, they appear closely related to the rescue of Fe-S cluster biosynthesis and mitochondria function. Indeed, the cardiac expression of all ISR target genes measured was rescued just 1 week after treatment, before any significant correction of the cardiac phenotype at the functional or molecular levels. Hence, GDF15 could be leveraged as a valuable read-out, in these mouse models, to infer the therapeutic efficacy and cardiac biodistribution for other therapeutic agents, besides gene therapy, such as protein replacement (16) or drug targeting downstream mitochondrial dysfunction and stress (36,37). To date, there is no published data regarding [GDF15] levels in FA patients.

Overall, we have elucidated the biodistribution thresholds and the cellular mechanisms mediating the dose-dependent therapeutic effect of cardiac gene therapy in the *Mck* mouse model recapitulating FA cardiomyopathy. This provides a com-

prehensive framework for the preclinical development of FA cardiac gene therapy protocols in small and large animal model, and therefore the successful design of clinical trial. Beyond gene therapy, these therapeutic thresholds and the cell-autonomous effect are considerations that most likely apply to other therapeutic strategies for FA such as synthetic mRNA delivery (12), artificial transcription factor (11), protein replacement (15,16), RNA (13) or DNA (10) modifiers.

Materials and Methods

Detailed methods are given in the Supplementary Material information.

Animal procedures

Mck mice with a specific deletion of *Fxn* gene in cardiac and skeletal muscle were described previously (7). All animal procedures were approved by the local and national ethical committee for Animal Care and Use. Gender-balanced *Mck* mice at 5 and 7 weeks were injected intravenously with AAVrh10 vector encoding human FXN or NaCl 0.9%. Echocardiography were performed as described previously (38) by an operator blinded to genotype and treatment.

Histochemistry

The 5 µm thick frozen heart sections were stained with H&E or WGA conjugated with Alexa 488 nm, DAB 3,3′-Diaminobenzidine (DAB)-enhanced Perls labelling, SDH histoenzymatic activity or immunofluorescent labelling, as previously described (19).

Correlative DNA, RNA and protein analysis

RNA was extracted with Tri-Reagent® [Molecular Research Center, Cat. No. TR118] from heart frozen sections, 100 µm thick, sampled exclusively at the apex, middle or basis of the heart. DNA was extracted from heart samples following RNA isolation, following the manufacturer's instructions. Proteins were extracted from heart tissue section 2–3 mm thick as described previously (19). VCN per diploid genome were quantified by qPCR, gene expression by qRT-PCR as described previously (19).

Enzyme-linked immunoassay (ELISA) analysis

ELISA assay was performed in duplicate, using the SimpleStep Human Frataxin ELISA Kit (ABCAM, ab176112), Mouse Frataxin ELISA kit (ABCAM, ab199078) and Mouse GDF-15 DuoSet ELISA kit (R&Dsystems, DY6385), following manufacturer instructions.

Statistical, correlation and regression analysis

Unless otherwise specified, data are reported as mean ± standard deviation (SD). Statistical analyses were carried out using GraphPad Prism 6 (GraphPad Software, La Jolla, California, USA) and methods are described in the figure legends.

Supplementary Material

Supplementary Material is available at *HMG* online.

Acknowledgements

We thank Shankaranarayanan Pattabhiraman, Hugues Jacob, Doulay Dembele for scientific discussions.

Conflict of Interest statement. H.P. is a scientific co-founder and advisor of AAVlife SAS. B.B. is currently employed by Adverum Biotechnologies, although the work was done previous to employment. All other authors declare no competing financial interests.

Funding

Lefoulond-Delalande Foundation, Institut de France (post-doctoral research fellowships years 2013 and 2016); the Friedreich Ataxia Research Alliance (general research grant year 2014 and Keith Michael Andrus Cardiac Research Award year 2016); the French Muscular Dystrophy Association AFM-Téléthon (Research grant year 2014); AAVLIFE SAS (sponsored research agreement years 2014–2016). Grant [ANR-10-LABX-0030-INRT], a French State fund managed by the Agence Nationale de la Recherche under the frame program Investissement d'Avenir [ANR-10-IDEX-0002-02].

References

1. Pandolfo, M. (2009) Friedreich ataxia: the clinical picture. *J. Neurol.*, **256** Suppl 1, 3–8.
2. Tsou, A.Y., Paulsen, E.K., Lagedrost, S.J., Perlman, S.L., Mathews, K.D., Wilmot, G.R., Ravina, B., Koeppen, A.H. and Lynch, D.R. (2011) Mortality in Friedreich ataxia. *J. Neurol. Sci.*, **307**, 46–49.
3. Plehn, J.F., Hasbani, K., Ernst, I., Horton, K.D., Drinkard, B.E. and Di Prospero, N.A. (2018) The subclinical cardiomyopathy of Friedreich's ataxia in a pediatric population. *J. Card. Fail.*, **24**, 672–679.
4. Campuzano, V., Montermini, L., Molto, M.D., Pianese, L., Cossee, M., Cavalcanti, F., Monros, E., Rodius, F., Duclos, F., Monticelli, A. *et al.* (1996) Friedreich's ataxia: autosomal recessive disease caused by an intronic GAA triplet repeat expansion. *Science*, **271**, 1423–1427.
5. Colin, F., Martelli, A., Clemancey, M., Latour, J.M., Gambarelli, S., Zeppieri, L., Birck, C., Page, A., Puccio, H. and Ollagnier de Choudens, S. (2013) Mammalian frataxin controls sulfur production and iron entry during de novo Fe4S4 cluster assembly. *J. Am. Chem. Soc.*, **135**, 733–740.
6. Sheftel, A., Stehling, O. and Lill, R. (2010) Iron-sulfur proteins in health and disease. *Trends Endocrinol. Metab.*, **21**, 302–314.
7. Puccio, H., Simon, D., Cossee, M., Criqui-Filipe, P., Tiziano, F., Melki, J., Hindelang, C., Matyas, R., Rustin, P. and Koenig, M. (2001) Mouse models for Friedreich ataxia exhibit cardiomyopathy, sensory nerve defect and Fe–S enzyme deficiency followed by intramitochondrial iron deposits. *Nat. Genet.*, **27**, 181–186.
8. Strawser, C., Schadt, K., Hauser, L., McCormick, A., Wells, M., Larkindale, J., Lin, H. and Lynch, D.R. (2017) Pharmacological therapeutics in Friedreich ataxia: the present state. *Expert Rev. Neurother.*, **17**, 895–907.
9. Gimenez-Cassina, A., Wade-Martins, R., Gomez-Sebastian, S., Corona, J.C., Lim, F. and Diaz-Nido, J. (2011) Infectious delivery and long-term persistence of transgene expression in the brain by a 135-kb iBAC-FXN genomic DNA expression vector. *Gene Ther.*, **18**, 1015–1019.

10. Erwin, G.S., Grieshop, M.P., Ali, A., Qi, J., Lawlor, M., Kumar, D., Ahmad, I., McNally, A., Teider, N., Worringer, K. *et al.* (2017) Synthetic transcription elongation factors license transcription across repressive chromatin. *Science*, **358**, 1617–1622.
11. Chapdelaine, P., Gerard, C., Sanchez, N., Cherif, K., Rousseau, J., Ouellet, D.L., Jauvin, D. and Tremblay, J.P. (2016) Development of an AAV9 coding for a 3XFLAG-TALEfrat#8-VP64 able to increase *in vivo* the human frataxin in YG8R mice. *Gene Ther.*, **23**, 606–614.
12. Nabhan, J.F., Wood, K.M., Rao, V.P., Morin, J., Bhamidipaty, S., LaBranche, T.P., Gooch, R.L., Bozal, F., Bulawa, C.E. and Guild, B.C. (2016) Intrathecal delivery of frataxin mRNA encapsulated in lipid nanoparticles to dorsal root ganglia as a potential therapeutic for Friedreich's ataxia. *Sci. Rep.*, **6**, 20019.
13. Li, L., Matsui, M. and Corey, D.R. (2016) Activating frataxin expression by repeat-targeted nucleic acids. *Nat. Commun.*, **7**, 10606.
14. Benini, M., Fortuni, S., Condo, I., Alfedi, G., Malisan, F., Toschi, N., Serio, D., Massaro, D.S., Arcuri, G., Testi, R. *et al.* (2017) E3 ligase RNF126 directly ubiquitinates frataxin, promoting its degradation: identification of a potential therapeutic target for Friedreich ataxia. *Cell Rep.*, **18**, 2007–2017.
15. Britti, E., Delaspre, F., Feldman, A., Osborne, M., Greif, H., Tamarit, J. and Ros, J. (2018) Frataxin-deficient neurons and mice models of Friedreich ataxia are improved by TAT-MTScs-FXN treatment. *J. Cell. Mol. Med.*, **22**, 834–848.
16. Vyas, P.M., Tomamichel, W.J., Pride, P.M., Babbey, C.M., Wang, Q., Mercier, J., Martin, E.M. and Payne, R.M. (2012) A TAT-frataxin fusion protein increases lifespan and cardiac function in a conditional Friedreich's ataxia mouse model. *Hum. Mol. Genet.*, **21**, 1230–1247.
17. Zhao, H., Li, H., Hao, S., Chen, J., Wu, J., Song, C., Zhang, M., Qiao, T. and Li, K. (2017) Peptide SS-31 upregulates frataxin expression and improves the quality of mitochondria: implications in the treatment of Friedreich ataxia. *Sci. Rep.*, **7**, 9840.
18. Gerard, C., Xiao, X., Filali, M., Coulombe, Z., Arsenault, M., Couet, J., Li, J., Drolet, M.C., Chapdelaine, P., Chikh, A. *et al.* (2014) An AAV9 coding for frataxin clearly improved the symptoms and prolonged the life of Friedreich ataxia mouse models. *Mol. Ther. Methods Clin. Dev.*, **1**, 14044.
19. Perdomini, M., Belbellaa, B., Monassier, L., Reutenauer, L., Messaddeq, N., Cartier, N., Crystal, R.G., Aubourg, P. and Puccio, H. (2014) Prevention and reversal of severe mitochondrial cardiomyopathy by gene therapy in a mouse model of Friedreich's ataxia. *Nat. Med.*, **20**, 542–547.
20. Kotin, R.M. and Snyder, R.O. (2017) Manufacturing clinical grade recombinant adeno-associated virus using invertebrate cell lines. *Hum. Gene Ther.*, **28**, 350–360.
21. Deverman, B.E., Pravdo, P.L., Simpson, B.P., Kumar, S.R., Chan, K.Y., Banerjee, A., Wu, W.L., Yang, B., Huber, N., Pasca, S.P. *et al.* (2016) Cre-dependent selection yields AAV variants for widespread gene transfer to the adult brain. *Nat. Biotechnol.*, **34**, 204–209.
22. White, J.D., Thesier, D.M., Swain, J.B., Katz, M.G., Tomasulo, C., Henderson, A., Wang, L., Yarnall, C., Fargnoli, A., Sumaroka, M. *et al.* (2011) Myocardial gene delivery using molecular cardiac surgery with recombinant adeno-associated virus vectors in vivo. *Gene Ther.*, **18**, 546–552.
23. Chung, H.K., Ryu, D., Kim, K.S., Chang, J.Y., Kim, Y.K., Yi, H.S., Kang, S.G., Choi, M.J., Lee, S.E., Jung, S.B. *et al.* (2017) Growth differentiation factor 15 is a myomitokine governing systemic energy homeostasis. *J. Cell Biol.*, **216**, 149–165.
24. Khan, N.A., Nikkanen, J., Yatsuga, S., Jackson, C., Wang, L., Pradhan, S., Kivela, R., Pessia, A., Velagapudi, V. and Suomalainen, A. (2017) mTORC1 regulates mitochondrial integrated stress response and mitochondrial myopathy progression. *Cell. Metab.*, **26**, 419–428 e415.
25. Whitnall, M., Suryo Rahmanto, Y., Huang, M.L., Saletta, F., Lok, H.C., Gutierrez, L., Lazaro, F.J., Fleming, A.J., St Pierre, T.G., Mikhael, M.R. *et al.* (2012) Identification of nonferritin mitochondrial iron deposits in a mouse model of Friedreich ataxia. *Proc. Natl. Acad. Sci. U. S. A.*, **109**, 20590–20595.
26. Wagner, G.R., Pride, P.M., Babbey, C.M. and Payne, R.M. (2012) Friedreich's ataxia reveals a mechanism for coordinate regulation of oxidative metabolism via feedback inhibition of the SIRT3 deacetylase. *Hum. Mol. Genet.*, **21**, 2688–2697.
27. Wang, J. and Pantopoulos, K. (2011) Regulation of cellular iron metabolism. *Biochem. J.*, **434**, 365–381.
28. Martin, A.S., Abraham, D.M., Hershberger, K.A., Bhatt, D.P., Mao, L., Cui, H., Liu, J., Liu, X., Muehlbauer, M.J., Grimsrud, P.A. *et al.* (2017) Nicotinamide mononucleotide requires SIRT3 to improve cardiac function and bioenergetics in a Friedreich's ataxia cardiomyopathy model. *JCI Insight*, **2**, e93885.
29. Huang, M.L., Sivagurunathan, S., Ting, S., Jansson, P.J., Austin, C.J., Kelly, M., Semsarian, C., Zhang, D. and Richardson, D.R. (2013) Molecular and functional alterations in a mouse cardiac model of Friedreich ataxia: activation of the integrated stress response, eIF2alpha phosphorylation, and the induction of downstream targets. *Am. J. Pathol.*, **183**, 745–757.
30. Quiros, P.M., Prado, M.A., Zamboni, N., D'Amico, D., Williams, R.W., Finley, D., Gygi, S.P. and Auwerx, J. (2017) Multi-omics analysis identifies ATF4 as a key regulator of the mitochondrial stress response in mammals. *J. Cell Biol.*, **216**, 2027–2045.
31. Pakos-Zebrucka, K., Koryga, I., Mnich, K., Ljujic, M., Samali, A. and Gorman, A.M. (2016) The integrated stress response. *EMBO Rep.*, **17**, 1374–1395.
32. Chandran, V., Gao, K., Swarup, V., Versano, R., Dong, H., Jordan, M.C. and Geschwind, D.H. (2017) Inducible and reversible phenotypes in a novel mouse model of Friedreich's ataxia. *Elife*, **6**, e30054.
33. Martelli, A., Schmucker, S., Reutenauer, L., Mathieu, J.R., Peyssonnaux, C., Karim, Z., Puy, H., Galy, B., Hentze, M.W. and Puccio, H. (2015) Iron regulatory protein 1 sustains mitochondrial iron loading and function in frataxin deficiency. *Cell Metab.*, **21**, 311–322.
34. Lu, C. and Cortopassi, G. (2007) Frataxin knockdown causes loss of cytoplasmic iron-sulfur cluster functions, redox alterations and induction of heme transcripts. *Arch. Biochem. Biophys.*, **457**, 111–122.
35. Mullican, S.E. and Rangwala, S.M. (2018) Uniting GDF15 and GFRAL: therapeutic opportunities in obesity and beyond. *Trends Endocrinol. Metab.*, **29**, 560–570.
36. Abeti, R., Baccaro, A., Esteras, N. and Giunti, P. (2018) Novel Nrf2-inducer prevents mitochondrial defects and oxidative stress in Friedreich's ataxia models. *Front. Cell. Neurosci.*, **12**, 188.
37. Zesiewicz, T., Salemi, J.L., Perlman, S., Sullivan, K.L., Shaw, J.D., Huang, Y., Isaacs, C., Gooch, C., Lynch, D.R. and Klein, M.B. (2018) Double-blind, randomized and controlled trial of EPI-743 in Friedreich's ataxia. *Neurodegener. Dis. Manag.*, **8**, 233–242.
38. Seznec, H., Simon, D., Monassier, L., Criqui-Filipe, P., Gansmuller, A., Rustin, P., Koenig, M. and Puccio, H. (2004) Idebenone delays the onset of cardiac functional alteration without correction of Fe–S enzymes deficit in a mouse model for Friedreich ataxia. *Hum. Mol. Genet.*, **13**, 1017–1024.

Molecular Therapy
Methods & Clinical Development
Original Article

High Levels of Frataxin Overexpression Lead to Mitochondrial and Cardiac Toxicity in Mouse Models

Brahim Belbellaa,[1,2,3,4,6] Laurence Reutenauer,[1,2,3,4] Nadia Messaddeq,[1,2,3,4] Laurent Monassier,[5] and Hélène Puccio[1,2,3,4,7]

[1]Institut de Génétique et de Biologie Moléculaire et Cellulaire (IGBMC), Illkirch 67404, France; [2]Institut National de la Santé et de la Recherche Médicale, U1258, Illkirch 67404, France; [3]Centre National de la Recherche Scientifique, UMR7104, Illkirch 67404, France; [4]Université de Strasbourg, Illkirch 67404, France; [5]Laboratoire de Pharmacologie et Toxicologie NeuroCardiovasculaire EA7296, Faculté de Médecine, Strasbourg 67085, France

Friedreich ataxia (FA) is currently an incurable inherited mitochondrial disease caused by reduced levels of frataxin (FXN). Cardiac dysfunction is the main cause of premature death in FA. Adeno-associated virus (AAV)-mediated gene therapy constitutes a promising approach for FA, as demonstrated in cardiac and neurological mouse models. While the minimal therapeutic level of FXN protein to be restored and biodistribution have recently been defined for the heart, it is unclear if FXN overexpression could be harmful. Indeed, depending on the vector delivery route and dose administered, the resulting FXN protein level could reach very high levels in the heart, cerebellum, or off-target organs such as the liver. The present study demonstrates safety of FXN cardiac overexpression up to 9-fold the normal endogenous level but significant toxicity to the mitochondria and heart above 20-fold. We show gradual severity with increasing FXN overexpression, ranging from subclinical cardiotoxicity to left ventricle dysfunction. This appears to be driven by impairment of the mitochondria respiratory chain and ultrastructure, which leads to cardiomyocyte subcellular disorganization, cell death, and fibrosis. Overall, this study underlines the need, during the development of gene therapy approaches, to consider appropriate vector expression level, long-term safety, and biomarkers to monitor such events.

INTRODUCTION

Friedreich ataxia (FA) is a rare neurodegenerative disease characterized by spinocerebellar and sensory ataxia associated with hypertrophic cardiomyopathy (HCM).[1] Cardiac dysfunction is the main cause of premature death in FA patients.[2] 95% of FA patients present a homozygous (GAA) expansion within the first intron of the frataxin gene (*FXN*).[3] This pathological expansion causes the heterochromatinization of the locus leading to reduced transcription of the *FXN* gene.[4] FXN is a highly conserved mitochondrial protein regulating the biosynthesis of iron sulfur clusters (Fe-S) through an interaction with the *de novo* Fe-S complex assembly machinery.[5] Fe-S are prosthetic groups crucial for many biological functions, including the mitochondrial respiratory chain; heme, lipoid acid, and molybdenum biosynthesis; tRNA thiolation; and iron metabolism.[6–9] Frataxin deficiency leads to impaired Fe-S biogenesis, impairment of Fe-S enzymes, mitochondrial dysfunction, iron metabolism dysregulation, and eventually cellular dysfunction and death.[10,11]

The therapeutic potential of AAV-mediated *in vivo* gene therapy in preventing and rescuing mitochondrial dysfunction associated with FXN deficiency, both in cardiac and neurological tissues, has clearly been demonstrated in several mouse studies.[12–14] To successfully translate these initial proof-of-concept studies to the clinic, we undertook to define the therapeutic thresholds conditioning the rescue of the cardiac phenotype as well as the potential toxic effects associated with FXN overexpression. This first point was addressed in a recent publication describing the dose-response studies we have conducted in the cardiac *Mck* conditional knockout mouse model (or *Mck* mouse), which recapitulates most features of the FA cardiomyopathy.[10,15] We demonstrated that the therapeutic outcome of AAV-FXN gene therapy is directly and proportionally correlated with the vector biodistribution in the heart. The correction of only half the cardiomyocyte was sufficient to restore fully the cardiac morphology and function.[15] Regarding the maximum level of FXN protein expression tolerated, earlier mouse studies have reported that the constitutive overexpression of FXN in muscle and heart up to 6-fold the normal level was innocuous.[16,17] In contrast, several recent studies have

Received 30 March 2020; accepted 27 August 2020;
https://doi.org/10.1016/j.omtm.2020.08.018.

[6]Present address: Adverum Biotechnologies Inc., 800 Saginaw Drive, 94027 Redwood City, California, USA.

[7]Present address: Institut NeuroMyoGene, UMR5310 INSERM U1217, Université Claude Bernard Lyon I, Faculté de Médecine, 8 Avenue Rockefeller, 69008 Lyon, France.

Correspondence: Brahim Belbellaa, Adverum Biotechnologies Inc., 800 Saginaw Drive, 94027 Redwood City, California, USA.
E-mail: bbelbellaa@adverum.com
Correspondence: Hélène Puccio, Institut NeuroMyoGene, UMR5310 INSERM U1217, Université Claude Bernard Lyon I, Faculté de Médecine, 8 Avenue Rockefeller, 69008 Lyon, France.
E-mail: helene.puccio@inserm.fr

suggested otherwise when constitutive or induced FXN overexpression reach higher levels in yeast (>14-fold),[18] HEK293 inducible cell line (>13-fold),[19] and transgenic *Drosophila* (>9-fold).[20,21] However, the possible toxicity of similar levels of FXN overexpression were never investigated in preclinical relevant animal models (i.e., rodent or large animal models) or in the context of AAV-mediated gene therapy.

In the present study, we investigated whether *in vivo* AAV-mediated gene transfer could be detrimental in wild-type (WT) mice or frataxin-deficient *Mck* mice. We evaluated FXN overexpression *in vivo* and its functional and morphological consequences on mitochondria and the heart. FXN protein expression over 20-fold the endogenous level is toxic for the mitochondria and results in severe impairment of complexes I and II enzymatic activity, alteration of the mitochondria ultrastructure, cardiomyocyte cell death, and fibrosis leading to heart dysfunction. This was also associated with an increased mitochondria biomass in cardiomyocytes and the induction of the integrated stress response (ISR). Overexpression of frataxin up to 9-fold the endogenous level in the cardiac tissue was uneventful, suggesting that the maximum safe level of FXN overexpression is between 9- and 20-fold the normal level. Strikingly, liver overexpression of FXN > 90-fold the normal level did not result in any detectable toxicity, suggesting organs specific susceptibility to FXN overexpression in mice.

RESULTS

FXN Overexpression Leads to Impairment of Mitochondria Succinate Dehydrogenase (SDH) Activity

Previously, we conducted a dose-response study in 5-week-old *Mck* mice injected intravenously with decreasing doses of AAVRh.10-CAG-hFXN-HA vector, from 5×10^{13} down to 1×10^{12} vector genomes (vg)/kg.[15] Upon sacrifice at 12 weeks of age, the human FXN (hFXN) protein level measured in the heart by ELISA assay ranged from 2 to 10,927 ng of FXN per mg of total heart protein (ng/mg). In WT 9-week-old C57/B6J mice (n = 6), the mouse FXN protein level measured by ELISA in the heart was 147 ± 42 ng/mg. Despite more than 70-fold overexpression, the cardiac function and morphology of treated *Mck* mice was rescued. In the present study, we performed additional histological analysis on the heart tissue sections from the same *Mck* mice to further investigate the relationship between FXN overexpression in the heart and the rescue of mitochondrial metabolism (Table S1). Unexpectedly, the heart tissue sections from *Mck* mice treated at the highest dose of vector (i.e., 5×10^{13} vg/kg) displayed regions with very high level of hFXN-HA expression, where SDH enzymatic activity was systematically impaired (Figures 1A and S1). This was particularly obvious in the mouse with the highest cardiac vector biodistribution (7.68 per diploid genome on average) and protein concentration (10,927 ng/mg, or 74-fold the endogenous level) (Figure 1A, first row). No SDH impairment was observed in the cardiomyocytes expressing much lower hFXN-HA levels or neighboring these hotspots of expression. Quantification of the heart surface positive for SDH enzymatic activity in the *Mck* mice treated with the highest dose (n = 3; 73% ± 2%) in comparison to NaCl-injected WT mice (n = 7; 83% ± 4%) revealed that less than 12% of the total heart surface was affected. These hotspots were not associated with cardiomyocyte cell death, fibrosis, or cell infiltrations, as assessed by hematoxylin and eosin (H&E) and wheat germ agglutinin (WGA) staining of adjacent heart tissue sections, in comparison to untreated *Mck* mice (Figure 1B). Interestingly, the cardiomyocytes with high hFXN-HA expression and SDH activity impairment did not show any iron accumulation following Perls-DAB (3,3′-Diaminobenzidine) staining of Fe^{3+} (Figure 1C), as this would be expected following FXN deficiency and/or Fe-S biosynthesis impairment.[10,22]

Importantly, the left ventricle (LV) function of these mice did not appear substantially impaired at rest at 12 weeks of age (Figures 1D–1F and S1A–S1C). *Mck* mice treated at 5×10^{13} vg/kg displayed LV shortening fraction (SF) and cardiac blood output normalized to body weight (CO/BW) corrected to WT levels (Figures 1D and 1E), similar to *Mck* mice treated at 2.5×10^{13} vg/kg. Importantly, *Mck* mice treated at 5×10^{13} vg/kg displayed a sustained functional rescue at long term (Figures S1D–S1H) when evaluated by echocardiography until 25 weeks of age in a separate cohort of mice (n = 5; Table S1). Most likely, this is explained by the relative small proportion of cardiomyocytes and heart surface affected overall (<12%). Indeed, we showed previously that the functional rescue of the cardiac phenotype is achieved with as low as 50%–60% of heart surface corrected.[15] It is worth noting that these mice did not display significant LV hypertrophy (Figure 1F), but the LV diameters at the end systole (LV-ESD) and diastole (LV-EDD) appeared slightly higher in the mouse treated at 5×10^{13} vg/kg and expressing 74-fold the normal level of FXN (Figures S1A and S1B). Overall, these results suggested that a very high level of hFXN-HA protein in cardiomyocytes could lead to impaired mitochondrial SDH enzymatic activity but without notable iron accumulation.

Overexpression of human FXN in WT Mice Leads to Mitochondrial and Cardiac Toxicity

In order to rule out any potential confounding effects from the *Mck* mouse cardiac phenotype, we undertook to replicate these experimental conditions in WT C57/B6J mice. WT mice received 5×10^{14} vg/kg (n = 4) or 5×10^{13} vg/kg (n = 3) of the same AAVRh.10-CAG-hFXN-HA vector at 7 weeks of age (Table S1). At the 5×10^{14} vg/kg dose, we were able to replicate similar vector copy number (VCN) ($\geq$7) and hFXN-HA expression ($\geq$10,000 ng/mg) (Figures 2A–2C), as reported above in *Mck* mice treated at 5×10^{13} vg/kg. However, one-log higher of vector dose was required in WT mice to achieve the same vector biodistribution and overexpression as in *Mck* mice. This might suggest a difference of transgene expression between WT and *Mck* mice. However, no significant difference in hFXN-HA expression when normalized to the vector copy number was observed between treated WT mice (n = 7) and *Mck* mice (n = 35) (Figure S2). At the study endpoint, 21 weeks of age, all treated WT mice were alive, with normal BW growth curve (Figure 2D) and no behavioral sign of stress or suffering. At necropsy, no gross anatomical anomaly was observed at the levels of the heart, lung, liver, kidney, digestive tract, or skeletal muscles.

The consequences of hFXN overexpression on the heart histology were evaluated following H&E and WGA staining, performed on

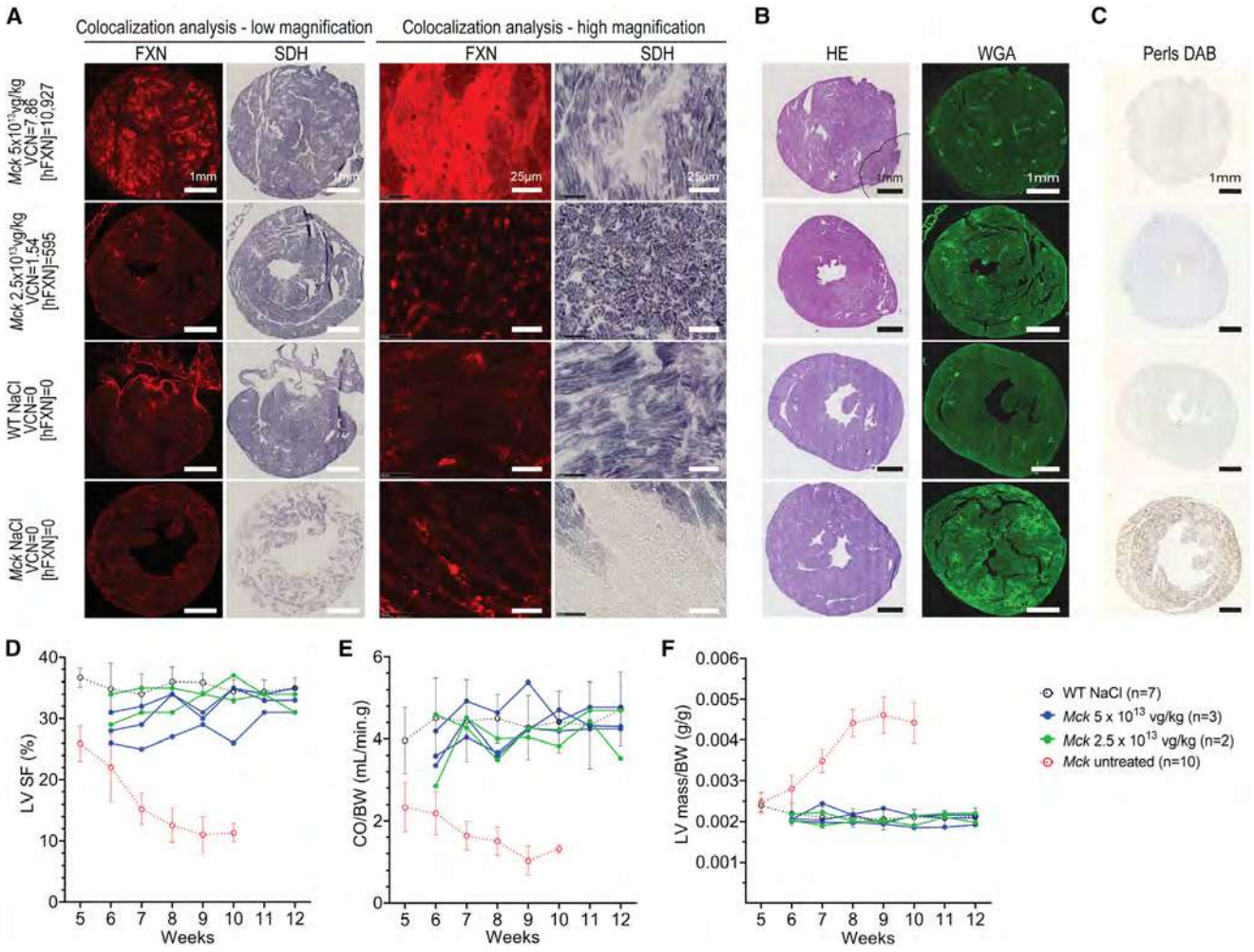

Figure 1. High Expression of FXN-HA in Cardiomyocytes Is Associated with Impaired Succinate Dehydrogenase (SDH) Enzymatic Activity despite Functional Rescue of *Mck* Mice Treated with AAVRh.10-CAG-hFXN-HA

(A–C) Histological analysis of heart tissue sections collected from the *Mck* mice treated at 5 weeks of age with the AAVRh.10-CAG-hFXN-HA vector and sacrificed at 12 weeks. Representative images are from the *Mck* mouse treated with 5×10^{13} vg/kg and expressing the highest level of hFXN-HA (10,927 ng/mg) and from another *Mck* mouse treated with 2.5×10^{13} vg/kg and with lower hFXN-HA level (695 ng/mg). For controls, heart tissue sections from 12-week-old NaCl-injected wild-type (WT) mice and 9-week-old untreated *Mck* mice were also analyzed. The corresponding vector copies per diploid genome (VCN) and tissue concentration in human FXN ([hFXN] in ng per mg of total protein) are reported. The same time exposure was used for all animals. (A) Co-staining and co-localization analysis of hFXN-HA overexpression and SDH enzymatic activity. Acquisitions of a single microscopic field at low and high magnification are shown, to compare the distribution of hFXN-HA expression hotspots and SDH activity impairment. (B) Hematoxylin and eosin (H&E) and wheat germ agglutinin (WGA) staining. (C) DAB-enhanced Perls labeling of iron deposits with methyl green counterstaining. (D–F) Longitudinal echocardiography analysis of the same *Mck* mice, represented here as individual kinetics. Data are represented as mean ± SD for WT control mice (n = 7) and untreated *Mck* mice (n = 10). For untreated *Mck* mice, historical data were plotted. Statistical analyses are reported in Table S2. (D) Left ventricle (LV) shortening fraction (SF). (E) Cardiac blood output (CO) measured at the aorta and normalized to body weight (BW). (F) LV mass normalized to BW. See also Figures S1A–S1C for the extended echocardiography analysis of this cohort of mice. See also Figures S1D–S1H for the echocardiography follow-up, until 25 weeks of age, of a second cohort of *Mck* mice treated at 5 weeks of age at 5×10^{13} vg/kg. Figure partially adapted from Belbellaa et al.[15]

adjacent heart frozen tissue sections (Figures 2E and S3). Both stains revealed and confirmed sparse fibrotic patches, but only in the animals treated at 5×10^{14} vg/kg and more visibly in the three mice with the highest transgene expression, ranging from 5,206 up to 12,773 ng/mg (i.e., 34- and 85-fold the normal FXN level, respectively) (Figure 2C). Heart tissue sections from WT mice treated at 5×10^{13} vg/kg and NaCl-injected WT mice appeared similar (Figures 2C and S3). While the overall total extent of heart fibrosis was not statistically different between NaCl-injected WT mice and WT mice treated at 5×10^{14} or 5×10^{13} vg/kg (Figure 2F), the qRT-PCR analysis of *Col1a1*, *Col3a1*, and *Tgfβ1* revealed significant increased expression of *Col1a1* and *Col3a1* in the hearts of WT mice treated at 5×10^{14} vg/kg, indicating ongoing fibrosis (Figure 2G).

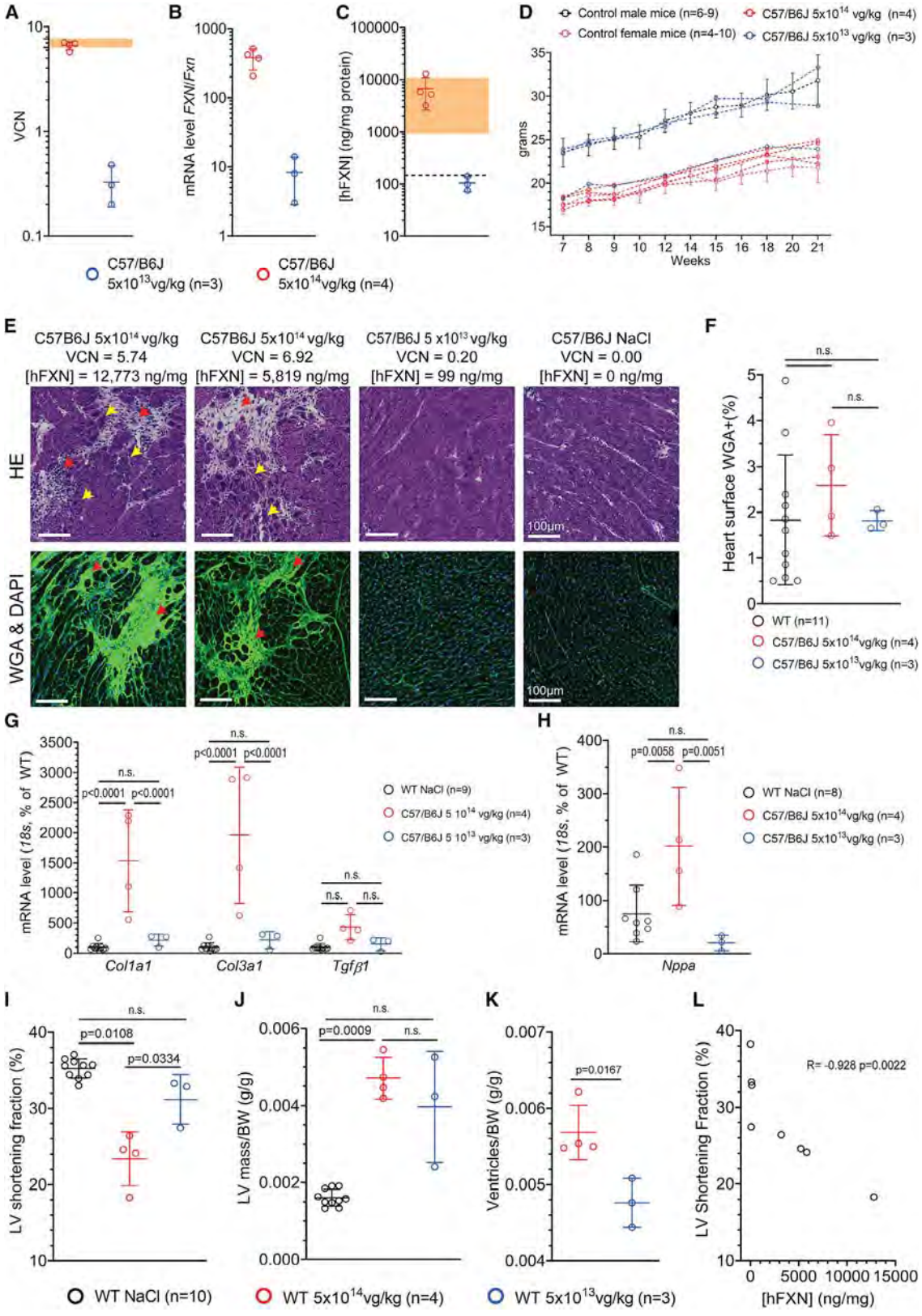

(legend on next page)

While WT mice treated at 5×10^{14} vg/kg displayed significant increased *Nppa* gene expression (Figure 1H), indicative of volume/pressure overload, none of them developed severe cardiac dysfunction at 21 weeks of age (Figures 1I–1K). Nonetheless, the three mice with the highest level of transgene expression in the 5×10^{14} vg/kg group displayed meaningful reduction of LV SF at rest (Figure 2I; Video S1) and increased heart hypertrophy (Figures 2J and 2K). Importantly, no functional or morphologic heart alteration was observed in the mice treated with vehicle or at 5×10^{13} vg/kg. The inverse correlation between hFXN-HA expression and the LV SF was statistically significant (Figure 2L).

To assess the mitochondria function in relation to the level of hFXN-HA expression, semiquantitative histoenzymatic assays were performed on adjacent heart tissue sections. We probed the activity of the respiratory chain complexes I, II, and IV (Figures 3 and S3). As reported in *Mck* mice (Figure 1A), the co-labeling and co-localization analysis of SDH enzymatic activity and hFXN-HA revealed hotspots of transgene expression where the SDH enzymatic activity was strongly reduced (Figure 3). However, the overall heart surface affected was relatively limited (Figure S3), and this was observed only in mice treated at 5×10^{14} vg/kg. SDH enzymatic activity in WT mice treated at 5×10^{13} vg/kg appeared similar to NaCl-injected WT mice (Figures 3 and S3). When quantified, the total surface positive for SDH activity was, respectively, 95.0% ± 2.1% (n = 4) and 98.5% ± 0.3% (n = 3) in mice treated at 5×10^{14} and 5×10^{13} vg/kg. Of note, the SDH staining and image acquisition and quantification were performed in batch, with all individuals from a given study processed in a single run, including untreated WT and *Mck* controls. However, there were some variations from one run to another, at different steps and especially during the image quantification, which thresholding result led to bias in the background signal. This explains the difference in WT mice values between the analysis of this cohort of mice and the one reported earlier. WT mice treated at 5×10^{14} vg/kg also displayed sparse impairment of the enzymatic activity of complex I (NADH-ubiquinone oxidoreductase [NADH]), contrary to WT mice treated at 5×10^{13} vg/kg. In contrast, the enzymatic activity of complex IV (cytochrome C oxidase [COX]) seemed unaffected in both dose groups (Figures 3 and S3). Strikingly, these results were reminiscent of what is observed in the heart of untreated *Mck* mice, in which FXN deficiency leads to the impairment of Fe-S enzymes, including SDH and NADH, but not COX, dependent on heme cofactors and not Fe-S cofactors.[23]

The consequences of FXN overexpression on the cardiomyocyte ultrastructure were also assessed by transmission electron microscopy (TEM). In contrast to WT mice treated at 5×10^{13} vg/kg or NaCl, WT mice treated at 5×10^{14} vg/kg displayed a substantial proportion of cardiomyocytes with severe alterations of their subcellular organization, with scattered and disordered myofibrils (Figure 3). Their mitochondria were swollen with sparse cristae, whose stacking is crucial for mitochondria bioenergetic efficiency.[24] The total volume occupied by mitochondria in cardiomyocytes also appeared significantly increased, suggesting altered mitochondrial proliferation or turnover. We also frequently observed the presence of electron-dense bodies inside the mitochondria matrix. These were not reminiscent of collapsed cristae or iron deposits, as commonly observed in FA patients and untreated *Mck* mouse cardiomyocytes.[10,25,26] To rule out the presence of mitochondrial iron deposits, adjacent ultrathin sections were stained with bismuth subnitrate to label iron complexed with ferritin, in the mitochondria as well as in lysosomes.[25,27–29] All WT mice displayed lysosomal labeling, as expected, since this organelle is central to ferritin turnover, but none showed mitochondrial labeling in contrast to untreated *Mck* mice (Figure 3). Collectively, these observations rule out iron accumulation as part of the cardio- and mitochondrial toxicity mechanism, which is in line with the lack of Perls labeling observed in treated *Mck* mice (Figure 1C).

To further investigate the mitochondria biomass, heart tissue sections from the same WT mice were co-labeled for SDH enzymatic activity and for prohibitin (PHB) (Figure 4A). PHB is a ubiquitous protein predominately located in the mitochondrial inner membrane,[30] which we used previously to assess mitochondria biomass.[15] In line with the above TEM observations, WT mice treated at 5×10^{14} vg/kg displayed a substantial increase of PHB labeling, but

Figure 2. High Level of FXN-HA Overexpression in the Heart of WT Mice Treated with AAVRh.10-CAG-hFXN-HA Vector Is Associated with Cardiac Fibrosis and Subclinical Impairment of Heart Function and Morphology

WT C57/B6J mice were treated at 7 weeks of age at 5×10^{14} (n = 4, red) or 5×10^{13} (n = 3, blue) vg/kg and sacrificed at 21 weeks. Unless stated otherwise, individual data points are plotted, with mean and SD. (A) qPCR quantification of the VCN in the heart. Light orange area represents the VCN range in *Mck* mice treated at 5×10^{13} vg/kg (n = 3) with the same vector from a previous study.[15] (B) qRT-PCR analysis of the transgene mRNA level normalized to mouse *Fxn* mRNA level. (C) ELISA assay quantification of hFXN-HA protein concentration ([hFXN]) in the heart, normalized to mg of total heart protein. Light orange area represents the [hFXN] range in *Mck* mice treated at 5×10^{13} vg/kg (n = 3) from a previous study and reported in Figure 1.[15] Black dotted line represents the endogenous level of FXN in untreated WT mice. (D) BW reported as individual, with males in blue and females in red. For untreated WT mice, historical data were plotted as mean ± SD. (E) Representative images from the histological analysis of adjacent heart tissue section collected from WT mice (5×10^{14}, n = 4; 5×10^{13}, n = 3) and stained with HA or WGA. Red arrows indicate fibrosis and cell infiltrates and yellow arrows indicate cardiomyocytes displaying subcellular disorganization. VCN and [hFXN] values are reported above for each animal. See also Figure S3 for the extended histological analysis. (F) Quantification of heart surface labeled with WGA. NaCl-injected WT mice sacrificed at 15 or 22 weeks of age (n = 11) were used as control. Brown-Forsythe and Welch one-way ANOVA statistical test, p values are reported with n.s. $p > 0.05$. (G–H) qRT-PCR quantification of cardiac gene expression normalized to *18S* and reported as percentage of NaCl-treated WT mice (n = 9). (G) *Col1a1*, *Col3a1*, and *Tgfβ1* mRNA level. Two-way ANOVA and FDR 5% statistical test, p values are reported with n.s. $p > 0.05$. (H) *Nppa* mRNA level. Brown-Forsythe and Welch one-way ANOVA test, p values are reported with n.s. $p > 0.05$. (I and J) Echocardiography at 21 weeks of age. For control, historical data from 21-week-old WT mice treated with NaCl are reported. Brown-Forsythe and Welch one-way ANOVA test, p values are reported with n.s. $p > 0.05$. (I) LV SF. (J) LV mass normalized to BW. (K) Heart ventricle weight measured upon necropsy at 21 weeks of age, normalized to BW. (L) Correlation analysis between [hFXN] and LV SF. Spearman non-parametric correlation coefficient and p value are reported.

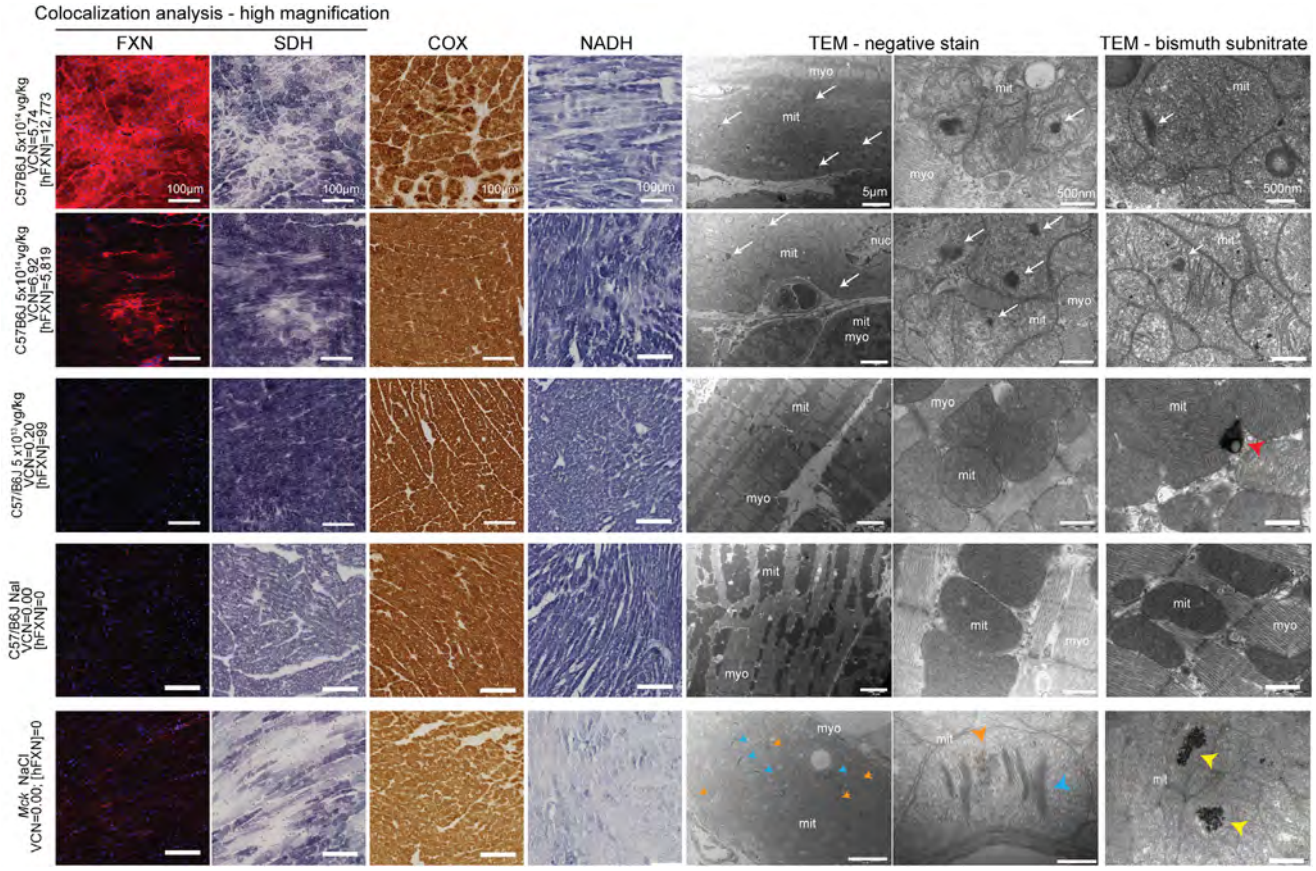

Figure 3. High Level of FXN-HA Overexpression in WT Mice Cardiomyocytes Leads to Mitochondrial Function and Structure Impairment

Representative histological observations from the correlative analysis of adjacent heart tissue sections/sample from WT mice treated at 7 weeks of age with AAVRh.10-CAG-hFXN-HA vector (5×10^{14} vg/kg, n = 4; 5×10^{13} vg/kg, n = 3) and sacrificed at 21 weeks. For controls, 21-week-old NaCl-injected WT mouse (n = 1) and 9-week-old untreated *Mck* mice (n = 2) were also analyzed. Each image series corresponds to the same individual for which dose of vector, VCN, and [hFXN] are reported. From left to right, co-staining and co-localization analysis of hFXN-HA protein expression and SDH enzymatic activity, cytochrome C oxidase (COX), and NADH-ubiquinone oxidoreductase (NADH) enzymatic activities assessed by *in situ* histoenzymatic assay are shown. Transmission electron microscopy (TEM) observations at low and high magnification of the LV myocardium is shown, following negative stain performed to assess cardiomyocyte and mitochondria ultrastructure. Finally, TEM observations of adjacent ultrathin sections at high magnification following bismuth sodium tartrate labeling of iron-ferritin complexes are shown. White arrows indicate non-iron mitochondrial electron-dense bodies, blue arrowheads indicate collapsed mitochondrial cristae, orange arrowheads indicate mitochondrial iron deposits, yellow arrowheads indicate mitochondrial iron-ferritin complex accumulation in mitochondria, and red arrowheads indicate ferritin sequestrated in the lysosome. myo, myofibrils; mito, mitochondria; nuc, nucleus. See also Figure S3 for extended histological analysis.

less than untreated *Mck* mice. In WT mice treated at 5×10^{14} vg/kg, we also observed a substantial co-localization between increased PHB labeling and reduction of SDH enzymatic activity. In contrast, WT mice treated at 5×10^{13} vg/kg appeared similar to NaCl-injected WT mice. Interestingly, WT mice treated at 5×10^{14} vg/kg also displayed increased cardiac gene expression for *Asns*, *Mthfd2*, and *Ddit3*, hallmark genes of the ISR (Figure 4C). The expression of *Fgf21* and *Gdf15*, which are downstream target genes of the ISR, were also strongly increased, although only statistically significant for *Fgf21* (Figures 4D and 4E). Interestingly, *Fgf21* and *Gdf15* have been proposed as biomarkers of mitochondria and heart dysfunction.[31,32]

Altogether, these results suggest that cardiac overexpression of hFXN-HA $\geq$ 20–30-fold the normal endogenous level is toxic for the heart and mitochondria. The mitochondria toxicity is characterized by severe alterations of the mitochondria ultrastructure and bioenergetics and the induction of ISR.

High Level of FXN Overexpression Results in Acute Cardiotoxicity and Compromised the Gene Therapy Outcome

While the study in WT mice recapitulated and confirmed the mitochondrial toxicity observed initially in *Mck* mice, it was unclear if this toxicity could also be explained by the high dose of vector administered, the resulting high number of vector copies per cell, and/or the HA tag fused to transgene (Figure 5A). To address these questions, we designed an optimized expression cassette and vector, AAVRh.10-hFXN (Figure 5B). The 5′ UTR and Kozak sequences were optimized. The h*FXN* cDNA was not codon optimized, but the HA tag was

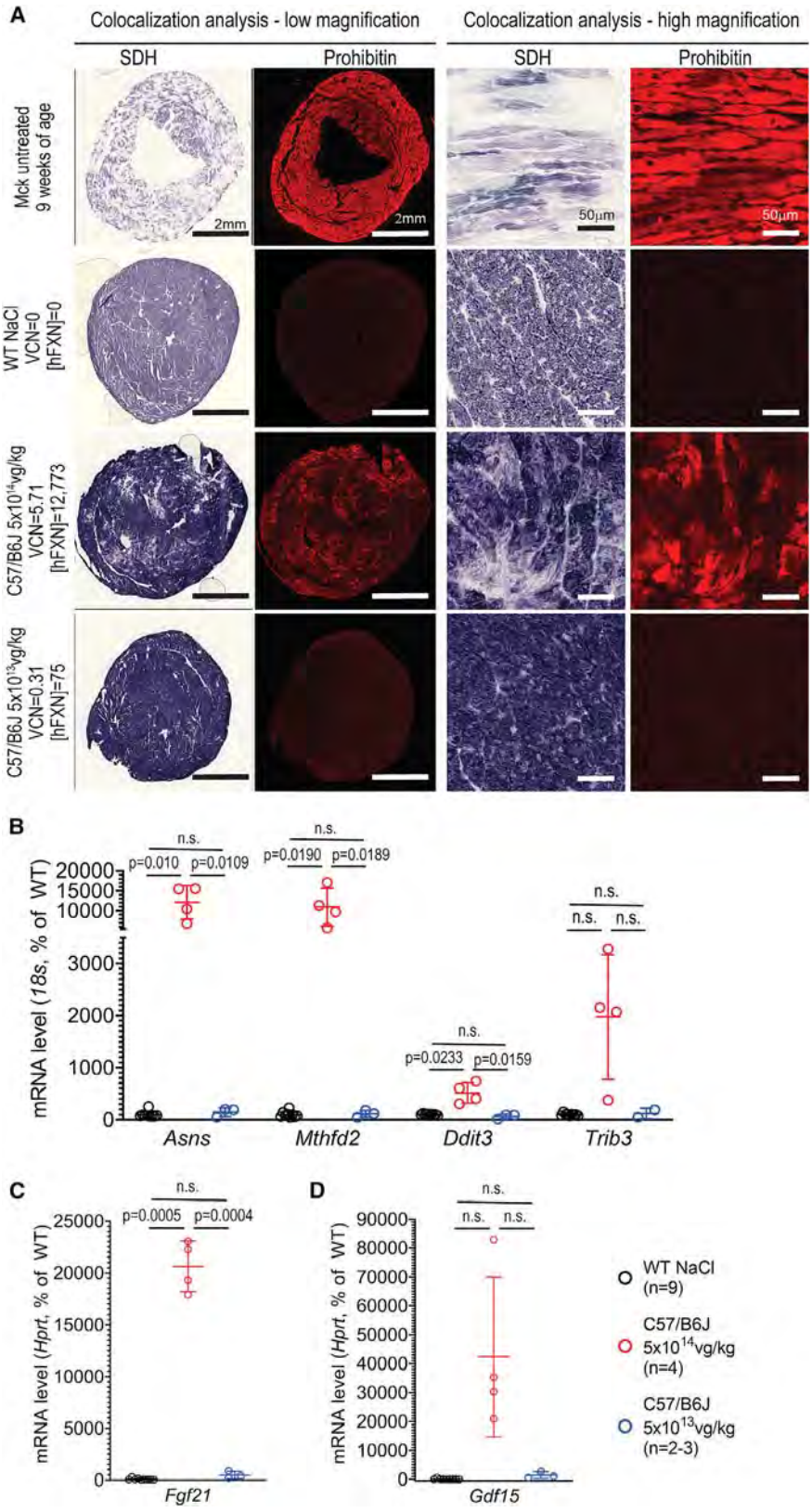

Figure 4. Cardiotoxic Overexpression of FXN-HA Is Associated with Increased Mitochondria Biomass and the Induction of the Integrated Stress Response

(A) Co-labeling and co-localization observation for prohibitin (Phb) and the enzymatic activity of SDH, on heart tissue sections from WT mice treated with AAVRh.10-hFXN-HA (5×10^{14}, n = 4; 5×10^{13}, n = 3). For controls, NaCl-injected WT and untreated *Mck* mice are represented. For each image series, the dose of vector, VCN, and [hFXN] are reported. (B-D) qRT-PCR analysis of heart mRNA levels reported to *18S* or *Hprt* (depending on the abundance of the target gene) and reported as percentage of NaCl-injected WT mice level. Individual data points are reported, with mean and SD. Brown-Forsythe and Welch ANOVA test, p values are reported with n.s. $p > 0.05$. (B) Integrated stress response (ISR) hallmark genes. (C and D) Downstream ISR-target genes encoding for secreted proteins (C) *Fgf21* and (D) *Gdf15*.

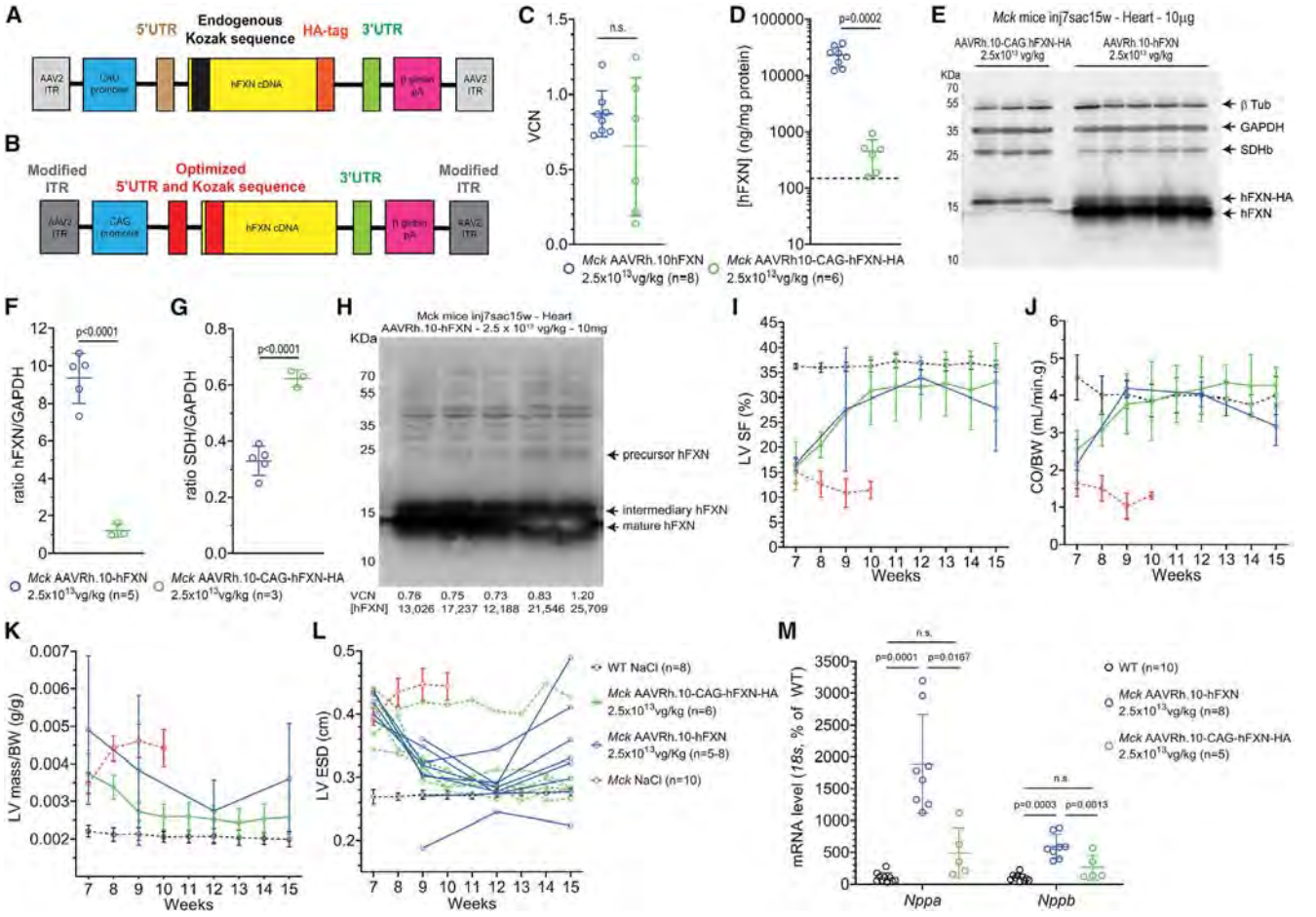

Figure 5. Cardiotoxicity FXN Overexpression Is Independent of the Dose Administered and Vector Biodistribution and Compromised the Success of Cardiac Gene Therapy in *Mck* Mouse Heart

Mck mice were treated at 7 weeks of age with the non-optimized vector AAVRh.10-CAG-hFXN-HA (n = 6) or with the optimized vector AAVRh.10-hFXN (n = 8) at 2.5×10^{13} vg/kg, followed up by echocardiography, and then sacrificed at 15 weeks of age to perform molecular analysis. NaCl-injected WT (n = 8–10) mice were used as control. (A and B) Schematic description of the vector construct for (A) the non-optimized AAVRh10-CAG-hFXN-HA vector, and (B) the optimized AAVRh.10-hFXN vector. (C) qPCR quantification of the number of VCN in the heart. Individual data points are reported, with mean and SD. Welch's t test, n.s. for $p > 0.05$. (D) ELISA assay quantification of hFXN protein concentration in the heart, normalized to mg of total heart protein. Black dotted line represents the endogenous mouse FXN level in untreated C57/B6J WT mice (i.e., 147 ± 42 ng/mg) (n = 6). Individual data points are reported, with mean and SD. Welch's t test, p values are reported. (E) Western blot (WB) analysis of total heart protein extract from *Mck* mice treated with the non-optimized vector (n = 3) or the optimized vector (n = 5). Immunoblotting against FXN, SDHb, GAPDH, and beta-tubulin (β-Tub). (F and G) WB quantification of the relative protein levels of FXN (F) and SDHb (G), normalized to GAPDH. Welch's t test, p values are reported. (H) WB analysis of FXN protein maturation, in the heart of *Mck* mice treated with the optimized vector (n = 5) and expressing up to 179-fold the normal level of FXN. The dose of vector, VCN, and [hFXN] corresponding to each sample are reported. (I–L) Longitudinal echocardiography analysis. For control, WT mice were injected with NaCl (n = 8), and historical data are plotted for NaCl-injected *Mck* mice (n = 10). Data are reported as mean ± SD. Statistical analyses are presented in Table S4. (I) LV SF. (J) CO normalized to BW. (K) LV mass normalized to BW. (L) LV end-systole diameter (LV-ESD) reported as individual kinetic for treated *Mck* mice. See also Figure S4 for LV end-diastole measurement and BW. (M) qRT-PCR quantification of the cardiac gene expression of *Nppa* and *Nppb*, normalized to *18S* and reported as percentage of NaCl-injected WT mice. Brown-Forsythe and Welch ANOVA test, p values are reported with n.s. $p > 0.05$.

removed. The same promoter and polyA sequences were used in both vectors (Figures 5A and 5B). In this third mouse study, *Mck* mice at 7 weeks old (upon heart failure) received 2.5×10^{13} vg/kg of the optimized AAVRh.10-hFXN vector (n = 8) or 2.5×10^{13} vg/kg of the non-optimized AAVRh.10-CAG-hFXN-HA vector (n = 6) and were then sacrificed at 15 weeks of age (Table S1). For controls, 7-week-old WT mice received NaCl (n = 10) or the optimized AAVRh.10-hFXN vector at doses of 2.5×10^{13} (n = 2) or 5×10^{12} vg/kg (n = 1).

When compared to the non-optimized vector, the optimized vector led to much higher levels of hFXN expression in the heart and liver despite similar VCN (Figures 5C–5F, 8A, and 8C–8E). The resulting levels of hFXN protein in the heart were on average

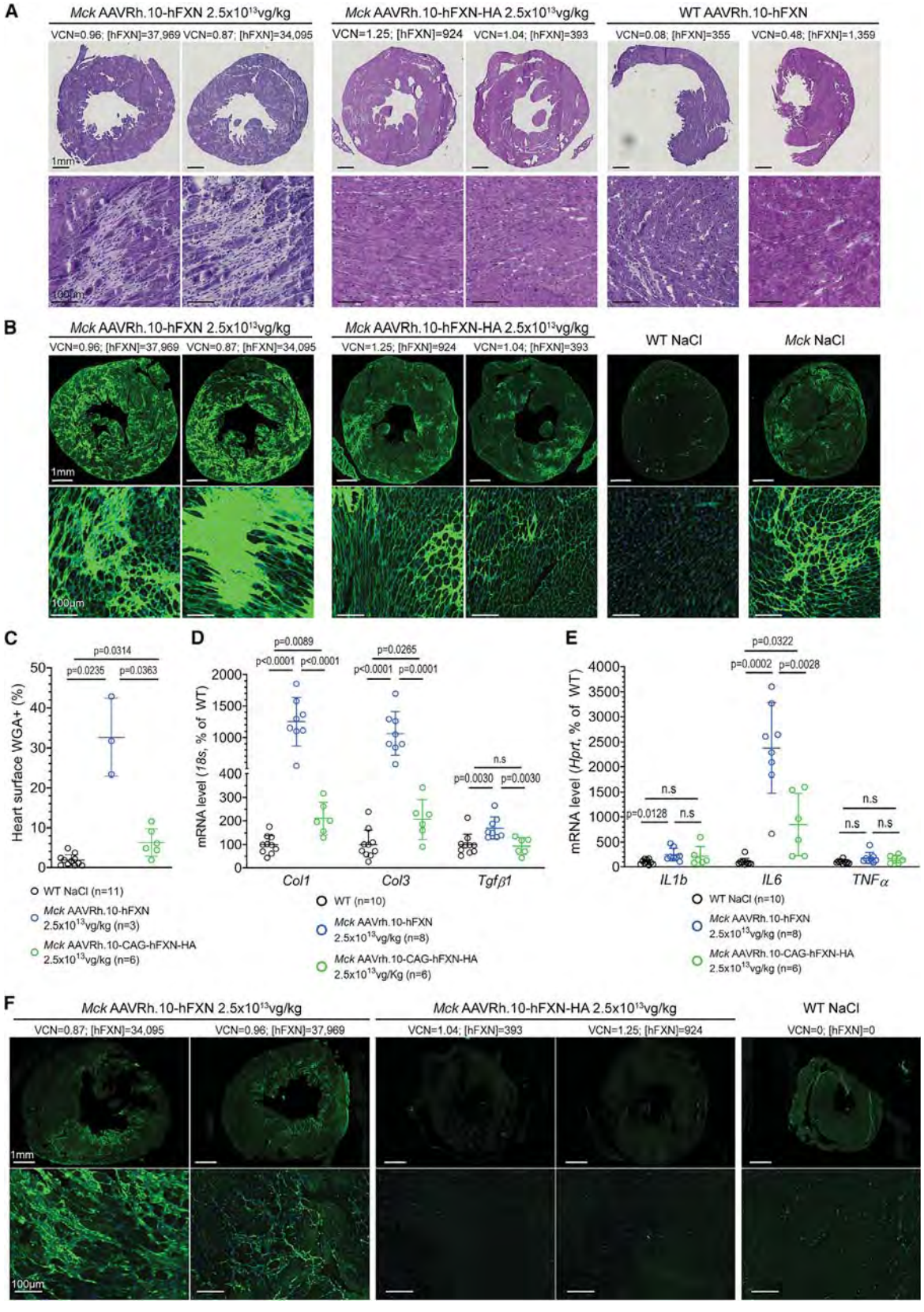

(legend on next page)

23,376 ± 9,336 ng/mg and 441 ± 276 ng/mg, respectively, corresponding to 156-fold and 2.9-fold the endogenous FXN level (Figure 5D). This large difference in expression was confirmed by western blot analysis (Figures 5E and 5F). Despite the very high overexpression in *Mck* mice treated with the optimized vector, no significant accumulation of hFXN precursor (23 kDa) was observed (Figure 5H). While we observed some accumulation of the hFXN intermediary form (19 kDa), the vast majority was processed into the mature form (14 kDa). These results suggest that the majority of the transgenic hFXN protein was targeted to the mitochondria, without severe saturation or impairment of the mitochondria import and processing capacity.[33] Of note, the biodistribution and expression of the optimized AAVRh.10-hFXN vector was also quantified in WT mice treated at 2.5×10^{13} (n = 2) or 5×10^{12} vg/kg (n = 1). The vector biodistribution was similar to *Mck* mice treated at identical doses,[15] with, respectively, 0.983 and 0.475 VCN at 2.5×10^{13} vg/kg and 0.078 VCN at 5×10^{12} vg/kg. In contrast, the vector expression was much lower compared to *Mck* mice treated with the same vector, with, respectively, 5,963 and 3,526 ng/mg at 2.5×10^{13} vg/kg and 355 ng/mg at 5×10^{12} vg/kg.

The expression normalized to the VCN of the optimized vector was 35-fold higher than the expression of the non-optimized vector in the heart of *Mck* mice (Figure S2). As mentioned above, the expression of the non-optimized AAVRh.10-CAG-hFXN-HA vector was similar in the heart of WT and *Mck* mice (Figure S2), despite the significant transcriptional and metabolic dysregulations occurring upon mouse FXN depletion.[10,12,15,34] In contrast, the expression normalized to the VCN of the optimized AAVRh.10-hFXN vector was on average 5-fold higher in the heart of *Mck* mice than in WT mice (Figure S2). This increased expression is possibly driven by the strong induction of the ISR and EIF2α phosphorylation in *Mck* mouse heart,[34] which might favorably impact the transcription and translation of the optimized expression cassette, in part through the optimized 5′ UTR and Kozak sequence. In line with this hypothesis, both vectors displayed similar VCN and transcription levels in the liver of *Mck* mice (Figures 8A and 8B), which is not depleted in FXN and does not present any functional or molecular phenotype. Nonetheless, the optimization of the 5′ UTR and Kozak sequences still resulted in a 48-fold increase of the average hFXN protein levels in the liver (Figures 8C–8E). Furthermore, the optimized AAVRh.10-hFXN vector led to much higher hFXN protein expression in the heart than liver of the same *Mck* mice (Figures 5D and 8C).

To assess the consequences of hFXN overexpression on the outcome of FA cardiac gene therapy, the cardiac function and morphology of the same *Mck* mice was assessed by echocardiography (Table S1). Longitudinal echocardiography analyses were performed from 7 to 15 weeks of age (Figures 5I–5L and S4). By 12 weeks of age, *Mck* mice treated with either vector displayed full correction of the heart function and morphology. However, mice treated with the optimized AAVRh.10-hFXN vector started deteriorating afterward, while sustained full correction was achieved in mice treated with the non-optimized AAVRh.10-CAG-hFXN-HA vector. This deterioration was characterized by a decrease of the LV SF (Figure 5I) and CO/BW (Figure 5J) and an increase of the LV mass (Figure 5K) and LV-ESD (Figure 5L). The LV-EDD was also increased but in a delayed manner compared to the other parameters measured (Figure S4A). Overall, this suggest a primary impairment of the contractile and systolic function of the LV, in line with our previous observation in WT mice treated with the non-optimized AAVRh.10-CAG-hFXN-HA (Figures 2I and 2J; Video S1). The impairment of the cardiac function in *Mck* mice treated with the optimized vector is supported by the increased gene expression of *Nppa* and *Nppb*, indicative of pressure/volume overload (Figure 5M).

Histological analysis of the heart fibrosis and cell infiltration was also performed on heart tissue sections (Figures 6A and 6B). Following H&E stain, *Mck* mice treated with the optimized vector displayed substantial heart fibrosis, distributed throughout the LV and associated with numerous cell infiltrates (Figure 6A). *Mck* mice treated with the non-optimized vector displayed a few fibrotic patches. Importantly, heart tissue sections from WT mice treated with the optimized vector at 2.5×10^{13} (n = 2) or 5×10^{12} vg/kg (n = 1) looked similar to heart tissue section from NaCl-injected WT mice (Figure 6A). This suggests the lack of intrinsic toxicity of the optimized vector. To quantify the accumulation of extracellular matrix associated with fibrosis, adjacent heart tissue sections were stained with WGA (Figure 6B). *Mck* mice treated with the non-optimized vector displayed more labeling than WT mice treated with NaCl, but at a much lower level than *Mck* mice treated with the optimized vector (Figure 6C). Furthermore, these observations were in agreement with the increased gene expression of *Col1a1*, *Col3a1*, and *Tgfβ*, which are indicative of ongoing fibrosis (Figure 6D), but also of *Il1b* and *Il6*, which are indicative of ongoing inflammatory response (Figure 6E). To further investigate the nature of these cell infiltrates, adjacent heart tissue sections were immunolabeled for cluster of differentiation 14

Figure 6. FXN Cardiotoxic Overexpression Is Associated with Acute Heart Fibrosis and Inflammation

(A) Histological analysis of fibrosis and cell infiltrates following H&E staining of heart tissue sections. Analysis of *Mck* mice treated with the AAVRh.10-hFXN (n = 8) or the AAVRh.10-hFXN-HA vector (n = 6) and WT mice treated with the AAVRh.10-hFXN vector at 2.5×10^{13} (n = 2) or 5×10^{12} (n = 1) vg/kg. The VCN and [FXN] in ng/mg are reported for each animal. (B) WGA staining of the extracellular matrix on heart tissue sections. Analysis of *Mck* mice injected with AAVRh.10-hFXN (n = 3) or AAVRh.10-CAG-hFXN-HA (n = 6) at 2.5×10^{13} vg/kg, WT mice injected with NaCl (n = 11) and untreated 9-week-old *Mck* mice (n = 6). (C) Quantification of heart surface labeled with WGA. Brown-Forsythe and Welch ANOVA test, p values are reported with n.s. $p > 0.05$. (D and E) qRT-PCR analysis of the heart mRNA level normalized to 18S and reported as percentage of NaCl-WT level. Brown-Forsythe and Welch ANOVA test, p values are reported with n.s. $p > 0.05$. (D) *Col1a1*, *Col3a1*, and *Tgfb1* mRNA levels. (E) *Il1b*, *Il6*, and *Tnfα*. (F) Representative observations at low and high magnification of heart tissue sections immunolabeled for the monocyte cell marker CD14 (same exposure time). Analysis of 15-week-old NaCl-injected mice (n = 3) and *Mck* mice treated with AAVRh.10-hFXN (n = 3) or AAVRh.10-CAG-hFXN-HA (n = 3) at 2.5×10^{13} vg/kg. See also Figure S5 for supplementary histological analysis of CD14, CD45, and CD3.

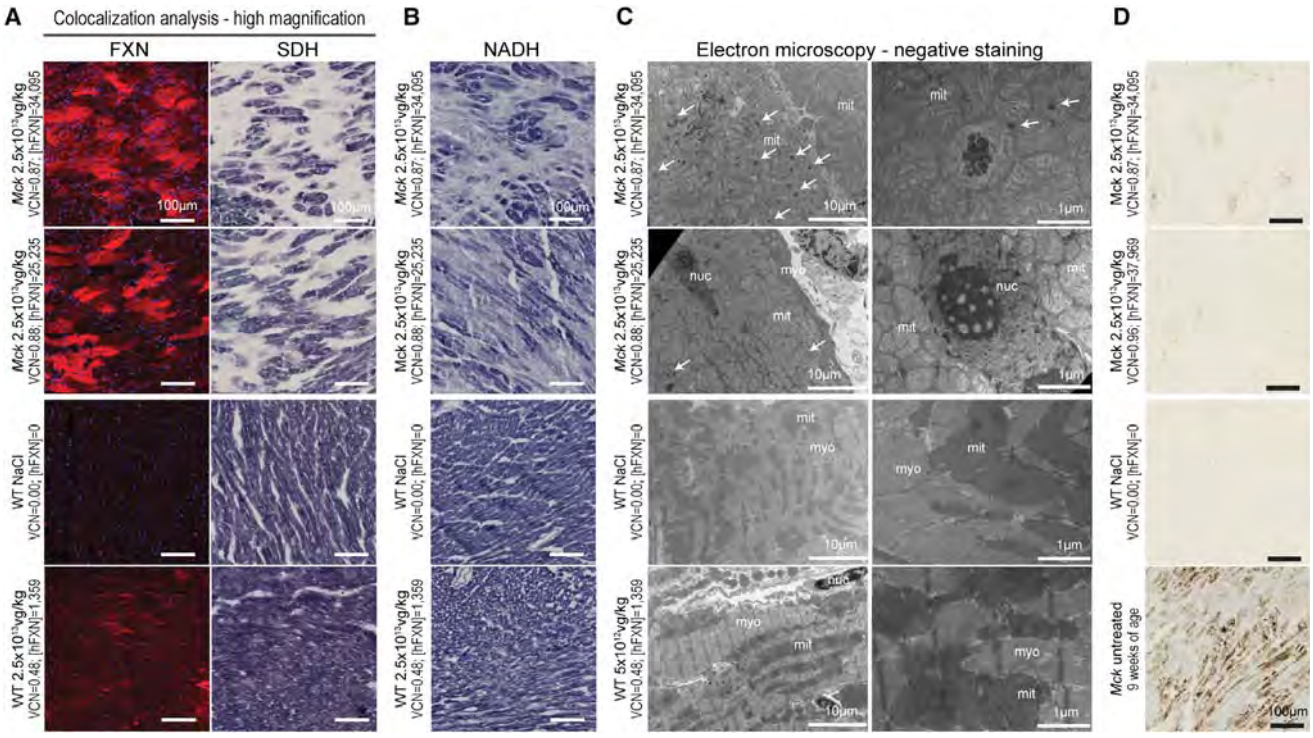

Figure 7. FXN Cardiotoxic Overexpression Is Associated with Impaired Mitochondrial Function and Ultastructure, but Not with Iron Overload

Representative histological observations from the analysis of adjacent heart tissue sections/sample collected from mice treated at 7 weeks of age with the AAVRh.10-hFXN vector and sacrificed at 15 weeks of age. Analysis of *Mck* mice treated at 2.5×10^{13} vg/kg (n = 3), WT mice treated at 2.5×10^{13} (n = 2) or 5×10^{12} vg/kg (n = 1), NaCl-injected WT mice (n = 2) and untreated 9-week-old *Mck* mice (n = 2). See also Figure S6 for low-magnification imaging. (A) Co-staining and co-localization analysis of hFXN-HA protein expression and SDH enzymatic activity, respectively, labeled by immunofluorescence and *in situ* histoenzymatic assay. (B) NADH enzymatic activities assessed by *in situ* histoenzymatic assay. (C) TEM observations at low and high magnification of the LV myocardium, following negative stain. White arrows indicate non-iron mitochondrial electron-dense bodies; myo, myofibrils; mito, mitochondria; nuc, nucleus. (D) DAB-enhanced Perls labeling of iron deposits.

(CD14), a maker of monocytes and macrophages (Figures 6F and S5A); CD45, a general marker of leukocytes including lymphocytes T, B, and monocytes (Figure S5B); and CD3, a general marker of lymphocytes including regulatory T cells and cytotoxic/natural killer (NK) T cells (Figure S5C). Spleen tissue sections were used as positive labeling controls for all these markers (Figures S5A–S5C). In line with the inflammatory and fibrotic response measured, *Mck* mice treated with the optimized vector showed extensive infiltrations of CD14+ and CD45+ cells, while mice treated with non-optimized vector showed much lower CD14+ and CD45+ labeling. Importantly, WT mice treated with the optimized vector did not show any cell infiltrates, supporting further the lack of intrinsic immunogenicity of the vector or its formulation (Figures S5A–S5C). In contrast, we were unable to identify CD3+ cell infiltrates in the heart tissue sections from animals treated with either vector, which would be expected in case of cytotoxic immune response (NK cells), as shown previously.[35,36]

The investigation of the mitochondria function in *Mck* mice treated with the optimized vector at 2.5×10^{13} vg/kg (Figures 7A, 7B, and S6A) revealed similar alterations as reported above in the *Mck* and WT mice treated with the non-optimized vector at higher doses (Figures 1A and 3). However, the severity and extent were much higher in mice treated with the optimized vector, in line with the much higher hFXN overexpression across the heart. In *Mck* mice treated with the optimized vector at 2.5×10^{13} vg/kg, co-labeling and co-localization analysis revealed numerous cardiomyocytes throughout the heart, with very high levels of FXN expression and impaired SDH enzymatic activity (Figure 7A). These hotspots of expression covered most of the heart surface (Figure S6A). In contrast, *Mck* mice treated with the non-optimized vector were rescued for SDH enzymatic activity throughout the heart, except for a few fibrotic patches (Figure S6B). Interestingly, the protein level of SDH subunit b (SDHb) was significantly decreased in the heart of the *Mck* mice treated with the optimized vector, when compared with *Mck* mice treated with the non-optimized vector (Figures 5E and 5G). Moreover, *Mck* mice treated with the optimized vector also showed impaired NADH enzymatic activity throughout the heart (Figures 7B and S6A), in line with previous observations in WT mice treated with the non-optimized vector at 5×10^{14} vg/kg (Figures 3 and S3). In contrast, the WT mouse treated with the optimized vector at 2.5×10^{13} vg/kg and expressing 9.2-fold the endogenous FXN level displayed normal SDH and NADH enzymatic activity (Figures 7A, 7B, and S6A). The second WT mouse treated similarly but overexpressing 38.7-fold the

endogenous level of FXN displayed few and sparse cardiomyocytes, with reduced SDH and NADH enzymatic activity.

To assess the cardiomyocytes and mitochondria ultrastructure following the administration of the optimized vector, samples from the LV myocardium of these same *Mck* (n = 3) and WT (n = 1) mice were collected and observed under TEM after negative staining (Figure 7C). *Mck* mice treated at 2.5×10^{13} vg/kg displayed severe alterations of cardiomyocyte subcellular organization, with scattered and disordered myofibrils and accumulation of swollen mitochondria, with very few visible cristae (Figure 7C). We also observed electron-dense bodies, inside the matrix of several mitochondria. These did not resemble collapsed cristae or iron deposits but appeared similar to what we observed in WT mice treated with the non-optimized vector at 5×10^{14} vg/kg (Figure 3). The absence of iron accumulation in the heart of these *Mck* mice was confirmed with DAB-Perls staining (Figure 7D).

Finally, we also analyzed the liver of the same *Mck* mice treated with the optimized vector at 2.5×10^{13} vg/kg to assess possible toxic effects beyond the heart. The level of hFXN protein in the liver ranged from 1,419 to 4,890 ng/mg when quantified by ELISA assay (Figure 8C). When measured in a distinct cohort of 9-week-old WT C57/B6J mice, the normal level of mouse FXN protein in the liver is 49.6 ± 7.8 ng/mg (n = 5). Thus, *Mck* mice treated with the optimized vector at 2.5×10^{13} vg/kg express up to 97-fold the endogenous level in the liver. The high expression was confirmed by western blot analysis (Figures 8D and 8E). Despite this high level of overexpression ([hFXN] = 2,565 ± 1,123 ng/mg; n = 8) and the high VCN (31 ± 10; n = 8) measured (Figures 8A–8C), the liver histology of the three mice evaluated appeared all normal following H&E staining, with no obvious sign of fibrosis or cell infiltrations (Figure 8G). The latter would have been expected if an adaptive immune response was raised against the transgene and driving the cardiotoxicity. Moreover, TEM observation of adjacent liver samples collected from the same mice (n = 3) did not reveal any obvious alterations of hepatocyte subcellular organization or alterations of mitochondria ultrastructure and/or biomass (Figure 8G). These results support further the lack of intrinsic toxicity of the AAVRh.10-hFXN vector or its formulation, when administered in *Mck* or WT mice (Figure 8G). The lack of similar mitochondrial toxicity in the liver was also supported by quantification of SDHb protein level (Figure 8F), which was similar to *Mck* mice treated with the non-optimized vector and expressing much lower levels of FXN ([hFXN] = 53 ± 14 ng/mg; n = 3). Altogether, these results support the lack of acute liver toxicity, despite very high levels of FXN overexpression, which contrast with the observed cardiotoxicity in the same mice.

DISCUSSION

Here, we showed unequivocally the cardiotoxicity of FXN overexpression when expressed >20-fold the endogenous level and its safety when expressed <9-fold. This was demonstrated in three independent studies, using two different animal models and two different AAVRh.10 vector constructs. The severity of this cardiotoxicity appeared to be proportional to the level of hFXN overexpression but also to the proportion and extent of cardiomyocytes affected throughout the heart. This led to more- or less-severe impairment of LV function and morphology, which then evolved either toward compensated heart hypertrophy or severe impairment of heart function. As demonstrated here, this cardiotoxicity might also compromise the therapeutic outcome of cardiac gene therapy for FA. The identification of this toxic threshold will help define more precisely the safe and efficient range of FXN expression for sustained correction of the FA cardiac phenotype. Our results also suggest that this toxicity might not be generalizable to all organs and/or cell types, as the mouse liver appeared to be tolerant to hFXN overexpression up to 90-fold the normal level.

The [hFXN] values and fold-overexpression numbers reported here correspond to average values reflecting unequal expression of FXN among the cardiomyocytes, some with relatively low or moderate levels and hotspots with very high levels. As shown previously,[37] the inhomogeneous distribution of the FXN expression in the heart reflects most likely the inhomogeneous diffusion of the AAV vectors throughout the cardiac vasculature and then into the parenchyma. This is most likely an inherent characteristic of AAV and intravenous administration. Nonetheless, the safe level of hFXN overexpression in the heart ($\leq$9-fold the endogenous level) is in line with previous studies conducted in yeast, mammalian cell lines, transgenic *Drosophila*, and mouse models constitutively overexpressing FXN. Collectively, these studies reported toxicity when FXN overexpression was higher than 6- to 10-fold the endogenous level[18–21,38,39] but good tolerance for lower levels.[16,17,40–43] Importantly, the current study did not investigate if the expression of the hFXN in the mouse organism would overestimate or underestimate the toxic threshold to be identified if a similar study were to be conducted with the overexpression of the mouse FXN protein. Indeed, the precursor and mature form of the mouse and hFXN present, respectively, 70% and 91% identity. Previous studies have shown that the human ortholog can complement the knockout of the mouse *Fxn* gene, through the genomic insertion and the constitutive expression of the h*Fxn* gene locus in transgenic mouse models.[16,44] These transgenic mice have a normal phenotype and lifespan, therefore suggesting that the hFXN protein has the same functionalities as its mouse ortholog. However, it remained to be shown whether the human and mouse FXN protein have the same affinity and kinetics of activation on the mouse Fe-S cluster assembly complex. It is also unclear if a large excess of FXN could stifle and impair the Fe-S cluster assembly complex and how potential difference in affinity would be impactful. As non-human primates (NHP) have closer physiology to humans and express FXN ortholog with higher identity, we expect toxicology studies conducted in NHP to be more predictive of future clinical trials in FA patients. Indeed, the FXN precursor proteins in cynomolgus and rhesus monkeys are 91% and 92% identical to the hFXN, respectively.

Our results do not support the hypothesis of a potential intrinsic toxicity of the vector construct or production lot used in these mouse

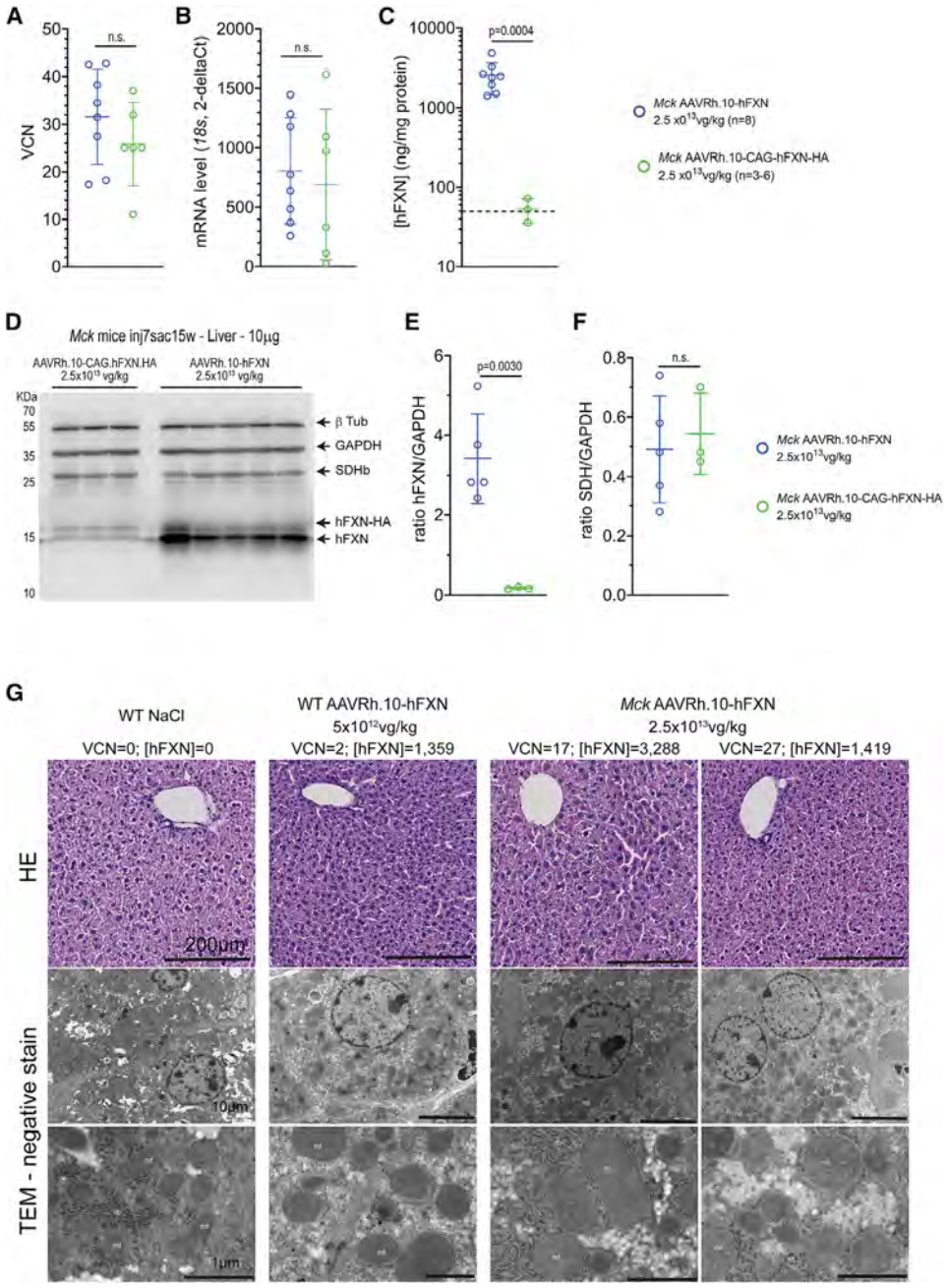

Figure 8. Liver Overexpression up to 87-Fold the Normal Level Does Not Result in Similar Cellular and Mitochondria Acute Toxicity

(A–C) The vector biodistribution and expression were assessed in the liver of *Mck* mice treated at 7 weeks of age with AAVRh.10-CAG-hFXN-HA (n = 6) or AAVRh.10-hFXN (n = 8) at 2.5×10^{13} vg/kg and sacrificed at 15 weeks of age. Individual data points are reported, with mean and SD. Welch's t test, p values are reported with n.s. $p > 0.05$. (A) qPCR analysis of VCN. (B) qRT-PCR quantification of the transgene mRNA level normalized to mouse FXN mRNA level. (C) ELISA quantification of FXN reported as ng per mg of total liver protein. Black dotted line represents the normal level of mouse FXN in WT mouse liver (i.e., 49.6 ± 7.8 ng/mg) (n = 5). (D–F) WB analysis of total liver protein extract from *Mck* mice treated with the non-optimized (n = 3) and optimized (n = 5) AAVRh.10 vector. (D) Immunoblotting against FXN, SDHb, GAPDH, and beta-Tubulin (β-Tub). (E) Relative FXN protein level normalized to GAPDH. (F) Relative SDHb protein level normalized to GAPDH. Individual data points are reported, with mean and SD. Welch's t test, p values are reported. (G) Representative histological observations of liver tissue section and ultrathin sections from *Mck* mice treated at 7 weeks of age with AAVRh.10-hFXN (n = 2–3) at 2.5×10^{13} vg/kg, WT treated with NaCl (n = 2) or with optimized AAVRh.10-hFXN at 5×10^{12} vg/kg (n = 1) and sacrificed at 15 weeks of age. The corresponding dose, VCN, and [hFXN] are reported next to each image series. Upper row, H&E staining. Lower row, TEM observations following negative stain.

studies, as WT mice injected with the same vectors did not show signs of toxicity, unless the hFXN protein level was beyond the toxic threshold. Several studies have shown cytotoxicity or genotoxicity following the administration of high-dose vector, particularly in large animal models.[45,46] Here, we have partially ruled out this possibility, as a much lower dose of the optimized AAVRh.10-hFXN vector also induced high levels of FXN expression and cardiotoxicity. In addition, previous mouse studies have shown that similar doses of vector, but with different DNA cargo, were well tolerated up to 5×10^{14} vg/kg, without noticeable cardiotoxicity at long term.[47–51] In the current study, we did not investigate the potential involvement of the innate or adaptive immune response against the vector, transgene, and/or transduced cells.[35,36,52,53] It is likely that the treated mice developed a humoral response against the capsid, including neutralizing antibodies, as shown previously in many mouse gene therapy studies.[50,51] However, the emergence of antibody against the capsid has not been shown to preclude the long-term expression of transgene or to drive cardiac inflammation but only the re-administration of the same vector.[54] Here, we did not explore the potential presence of antibodies against the transgene and, more importantly, the development of a potential cytotoxic cell response targeting the transduced cardiomyocytes. The cytotoxic immune response was shown previously to result in loss of transgene expression in animal models and patients.[35,36,52,53] In the present study, the AAVRh.10 vectors were delivered intravenously, leading to broad biodistribution and strong expression in many organs and muscles.[12,55] Therefore, we would expect a potential cytotoxic immune response to lead to cell infiltration, not only in the heart but also in all transduced organs, especially the liver, for which the AAVRh.10 capsid has the highest tropism. We will investigate these questions in future studies, as they are critical for future clinical development.

Cardiotoxic hFXN overexpression appeared to be driven by cell autonomous impairment of the mitochondria function and structure, most likely followed by cardiomyocyte cell death, heart fibrosis, and LV contractile dysfunction. Strikingly, the mitochondria toxicity affected NADH and SDH enzymatic activities but not COX. The severe ultrastructure anomalies of the mitochondria most likely contributed to their functional impairment,[24] which altogether leads to higher mitochondria biomass. These features are reminiscent of the cardiac, mitochondrial, and biochemical phenotype observed in untreated *Mck* mice and are hallmarks of FXN deficiency.[10,12,15,56] However, it is unclear if hFXN toxic overexpression was associated with or caused by (partial) impairment of Fe-S biogenesis or handling. Indeed, these two cardiac phenotypes differ from one another by the accumulation of mitochondrial iron upon FXN deficiency,[22] which was consistently not observed upon hFXN overexpressing in the three mouse studies conducted here. Indeed, cellular iron metabolism and dysregulation are mediated by IRP1, which is a cytosolic Fe-S protein.[22] These results are in line with previous overexpression studies conducted in yeast,[18] human cells,[19] and *Drosophila*,[20] where only a modest increase in labile iron was observed. Future studies will be needed to address the underlying mechanism, through time course analysis of pathological events, including exhaustive biochemical analysis of the Fe-S biosynthesis, handling, and Fe-S enzymes.

These findings would likely apply to all *in vivo* gene replacement strategies for hFXN, independently of the AAV serotype or other type of viral vector used. Besides gene replacement strategies, this would also be of concern for alternative approaches if presenting the same risk of acute hFXN tissue concentration, either due to their mechanism of action or their delivery modality. This would include synthetic mRNA,[57] FXN protein replacement,[58,59] and *in vivo* gene transfer of strong artificial transcription factors.[60,61] While the current study was focused on the heart, this mitochondrial toxicity is likely to affect other organs. The dorsal root ganglia, the spinal cord, the cerebellum, and the dentate nucleus are important targets to address the neurological symptoms and would be of particular interest for future studies. The spleen and kidney are major off-target sites for AAV vectors following intravenous delivery and should also be considered carefully. Importantly, the FXN level varies largely among these organs,[3,10] most likely along cell-type specific metabolism and abundance of mitochondria. In the present and previous studies,[14,15] we have shown that the normal mouse FXN level is 147 ng/mg in the heart, 49 ng/mg in the liver, 12–25 ng/mg in dorsal root ganglia, and 28 ng/mg in the cerebellum. Therefore, we can hypothesize a different therapeutic index for each one of these organs. To ensure the safety of future clinical trials, AAV vectors will need to be designed to manage appropriately their expression profile across these different tissues. This could be achieved with (1) synthetic weak promoter or the endogenous human frataxin promoter,[62–64] (2) vector de-targeting strategies,[65,66] and/or (3) the design of expression cassette responsive to negative cellular feedback loop. Leveraging our knowledge of the cellular response to toxic FXN overexpression might help achieve the self-regulation of the vector expression and avoid toxic overexpression. For example, the 3′ UTR sequence could be engineered to be targeted by inhibitory endogenous microRNA, specifically induced by the ISR,[67,68] or other cellular stress response such as the oxidative stress response.[69,70] In addition, specific routes of drug delivery might also present risk of high local concentration, such as intracardiac injection[71] or local delivery in the central nervous system.[72,73] Due diligence in the design of appropriate pharmacokinetic and toxicity studies, in relevant large animal models, will be crucial for the development of safe clinical therapeutic protocols. Finally, the identification of biomarkers to monitor subclinical toxicity and manage such events would be very advantageous. In this regard, the current study has identified potential candidates, including FGF21, to be explored in future studies.

In summary, the overexpression of hFXN is safe when $\leq$9-fold the normal endogenous level but cardiotoxic when greater than 20-fold. The pathological mechanism was partially elucidated and is most likely primed by the alteration of the mitochondria structure and function. Depending on the percentage of cardiomyocytes affected, this resulted in either subclinical or acute cardiotoxicity.

The toxic threshold and potential readout for toxicity identified here will support the design of robust and meaningful toxicity studies, for safer FA gene therapy clinical trials.

MATERIALS AND METHODS

Adeno-Associated Viral Vector Constructs and Production

The AAVRh.10-CAG-hFXN-HA and AAVRh.10-hFXN vectors are described in Figures 5A and 5B and encode, respectively, the human frataxin cDNA, including the mitochondrial targeting sequence, and fused or not in C-terminal to the HA tag. These vectors were produced by triple transfection method in HEK293 cells,[74] respectively, at the Vector Core at the University Hospital of Nantes (France) and the Belfer Gene Therapy Core facility at Weill Cornell Medical College. Their respective concentration was measured as 8.7×10^{13} and 1.96×10^{14} vg/mL, by qPCR. Their purity was checked with a combination of the following assay: potential protein contamination by SDS-PAGE and Coomassie Blue Staining, endotoxin contamination with Endosafe-PTS LAL (<0.5 EU/m), sterility by growth in liquid and agar-based test media (no contamination detected at 48 h), and qPCR quantification of residual DNA material from AAV Rep or Adenovirus plasmids.

Animal Procedures

WT C57/B6J mice were supplied by Charles River Laboratory, France. *Mck* mice were generated in 100% C57BL/6J background, with a conditional deletion of *Fxn* gene in cardiac and skeletal muscle (*Mck*-Cre-*Fxn*$^{L3/L}$) and genotyped, as described previously.[10] This results in the complete depletion of frataxin protein in these organs. Note that *Mck* mice develop a cardiac dysfunction at 5 weeks of age, progressively worsening into heart failure at 7 weeks of age, eventually causing their death around 10 weeks of age.[10] Housing animal facility was controlled for temperature and humidity, with a 12-h light/dark cycle and free access to water and a standard rodent chow (D03, SAFE, Villemoisson-sur-Orge, France). All animal procedures and experiments were approved by the local ethical committee for animal care and use (Com'Eth HP/2012/09/27 and 5344). They were performed in accordance with the Guide for the Care and Use of Laboratory Animals (National Institutes of Health). Five- and seven-week-old animals were anesthetized with isoflurane prior to the retro-orbital injection of vector, in 100 μL bolus. Control littermate or WT mice were injected with equivalent volume of NaCl 0.9% solution. Survival and comorbidities were evaluated daily, and BW was evaluated weekly. Echocardiography was performed with the Sonos 5500 system (Hewlett Packard) with a 15 MHz linear transducer (15L6) or with the Vevo 2100 system (Fujifilm Visualsonics) with a 25–55 MHz transducer, as described previously.[15] Briefly, echocardiography was performed under isoflurane anesthesia (0.5%–1.5%) and 0.8 mL/min O_2, to maintain the heart rhythm between 450 and 550 bpm. Historical data were used as reference for untreated *Mck* mouse survival, BW, and cardiac function

Following intraperitoneal injection of ketamine-xylazine and blood sampling, mice were perfused with cooled NaCl 0.9%, and the heart and liver were retrieved quickly.

Briefly, the apex of the heart was sampled in cryotubes and flash frozen in liquid nitrogen for subsequent DNA and RNA extraction and analysis, as described previously.[15] Two small pieces from the LV anterior wall (less than 1 mm^3) were sampled in Karnovsky's fixative and processed for TEM morphological analysis. A thin transverse section (around 2 mm thick) was cut at the middle level of the heart for protein analysis. The middle to the base of the heart was embedded in OCT and frozen in isopentane chilled with liquid nitrogen for histological analysis.

The liver medial left lobe was sampled and fixed in PBS 1× formaldehyde 10%, dehydrated, and then embedded in paraffin for histological analysis. Two small pieces from the left lateral lobe (less than 2 mm^3) were sampled and fixed in Karnovsky's fixative for transmitted electron microscopy (TEM) analysis. The remaining lobes—lateral left, medial right, lateral right, and caudate lobes—were sampled in a cryotube and flash frozen in liquid nitrogen for subsequent DNA, RNA, and protein analysis.

The spleen was fixed in PBS 1× formaldehyde 4%, embedded in OCT, and frozen in isopentane chilled with liquid nitrogen for histological analysis.

Histochemistry

Frozen sections from the heart and the spleen, and liver paraffin sections, were collected on Superfrost glass slides. For each staining, the group and number of animals analyzed is reported in the respective figure legend (1–3 tissue sections stained per animal for each histological analysis). Heart and liver tissue sections were stained with H&E. In addition, heart tissue sections were stained with WGA conjugated with Alexa 488 nm, or stained with DAB-enhanced Perls labeling, or used to perform *in situ* histoenzymatic activity assay for SDH or cytochrome C oxidase, as previously described.[15] NADH dehydrogenase *in situ* histoenzymatic activity was performed on heart tissue sections accordingly to Luna et al.[75]

Immunofluorescent labeling, with or without SDH co-labeling, was performed as described previously,[15] with the following antibodies and dilutions: frataxin (anti-FXN, 1/50, IGBMC; FXN935 and anti-HA, 1/100, Abcam, Ab9110), prohibitin (1/300, Ab28172), Sqstm1 (1/300, 2C11, H00008878-M01, Millipore). The FXN antibodies recognize both the human and mouse FXN, including the precursor, intermediate, and mature forms.

For labeling of CD3-, CD14-, and CD45-positive cells, tissue sections were fixed in 4% paraformaldehyde (PFA) for 5 min, permeabilized in PBS 1× 0.3% Triton X-100 at room temperature (RT) for 10 min, and then blocked with PBS, 1% NGS, 5% BSA, 0.2% Tween (PBS-NBT) for 30 min at RT. Subsequently, tissue sections were incubated overnight (O/N) at 4°C with the rabbit antibody against CD3 (1/100, ab16669, Abcam) or CD14 (1/100, ab183322, Abcam,) or CD45 (1/100, ab10558, Abcam) and afterward with Alexa fluor 488 nm conjugated goat anti-rabbit antibody (1/300, Molecular Probes).

Imaging of the heart, liver, and spleen tissue sections were performed with the Hamamatsu NanoZoomer 2.0 slide scanner.

Electron Microscopy Analysis

The samples were fixed with 2.5% glutaraldehyde and 2.5% PFA in cacodylate buffer (0.1 M [pH 7.4]), washed 30 min in cacodylate buffer, post-fixed with 1% osmium tetroxide in 0.1 M cacodylate buffer for 1 h at 4°C, and dehydrated through graded alcohol (50%, 70%, 90%, and 100%) and propylene oxide for 30 min each. Samples were oriented and embedded in Epon 812. Semithin sections were cut at 2 μm with the Leica Ultracut UCT ultramicrotome and stained with 1% toluidine blue and 1% sodium borate. Ultrathin sections were cut at 70 nm and contrasted with uranyl acetate and lead citrate. Electron microscopy observation and image acquisition were performed at 70 kv with the Morgagni 268D electron microscope (FEI Electron Optics, Eindhoven, the Netherlands) and equipped with the Mega View III camera (Soft Imaging System). The bismuth sodium tartrate staining of ferritin was performed as described previously.[27,76]

DNA, RNA, and Protein Analysis

DNA, RNA, and protein extraction and quantification, as well as cDNA synthesis, were performed as described previously.[15]

Briefly, absolute quantification of vector biodistribution was performed in triplicate and the qRT-PCR in duplicate, using the Quantitect Sybr Green CR kit (QIAGEN, 1037795) and the Light Cycler 480 II (Roche Biosciences). Primers were used at 0.4 μM final concentration, and their sequences are reported in Table S5. qPCR amplification program: 1 cycle, 15 min 95°C; 50 cycles, 15 s 94°C–30 s 60°C–30 s 72°C; 1 cycle for melting curve. Depending on the expression level of the target genes quantified, cDNA dilutions ranging from 1/50 to 1/2,000 were performed. As working Ct (threshold cycle) values ranged between 12 and 34 cycles, *18S* and *Hprt* were used for normalization, respectively, when the target genes required high and low cDNA dilution for the qPCR assay.

SimpleStep Human Frataxin ELISA Kit (Abcam, ab176112) and SimpleStep Mouse Frataxin ELISA kit (Abcam, ab199078) were used to quantify the heart and liver tissue concentration in human and mouse frataxin, respectively, following manufacturer instructions.

For western blot analysis, between 10 and 30 μg of total protein extract were loaded and migrated in 14% or 4%–12% SDS-PAGE gels (Novex, Nupage 4%–12% Bis-Tris Midi Gels, 26 wells). Following transfer onto nitrocellulose membranes (Amersham Protran 0.45 μm NC), Red Ponceau staining (Sigma Aldrich, P7170-1L), and blocking, the membranes were immunoblotted O/N at 4°C with the following antibodies and dilution: mouse anti-frataxin (1/10,000, 4F9, IGBMC), mouse anti-complex II 30 kDa subunit SDHb (1/10,000, 21A11AE7, Novex), mouse anti-glyceraldehyde-3-phosphate dehydrogenase (1/30,000, MAB374, Millipore), and/or mouse anti-beta-tubulin (1/10,000, IGBMC). After incubation for 2 h at 4°C with goat anti-mouse IgG H^+L (1/10,000, 115-035-146, Jackson Immunoresearch), the signal was revealed using the SuperSignal West Dura Extended Duration Substrate (ThermoSienctific, 34075) and imaged with the Amersham Imager 600 (GE Healthcare).

Statistical, Correlation, and Regression Analysis

Unless otherwise specified, data are reported as mean ± standard deviation (SD). Statistical analyses were carried out using GraphPad Prism 8.3 (GraphPad Software, La Jolla CA, USA), and methods are described in the figure legends.

SUPPLEMENTAL INFORMATION

Supplemental Information can be found online at https://doi.org/10.1016/j.omtm.2020.08.018.

AUTHOR CONTRIBUTIONS

B.B. and H.P. conceived the project. B.B. conducted and analyzed the experiments. L.R. managed mouse production. N.M. performed electron microscopy. L.M. provided logical support for echocardiography. B.B. and H.P. wrote the manuscript.

CONFLICTS OF INTEREST

H.P. is the owner of patents pertaining to cardiac and neurological gene therapy methods for the treatment of FA (WO2016150964A1, EP2950824A1, US20150313969A1, US9066966B2, and CA2900135A1) and is one of the scientific co-founders of AAVlife SAS. H.P. is an advisor and beneficiary of sponsored research agreement from Adverum Biotechnologies and Voyager Therapeutics. B.B. is currently employed by Adverum Biotechnologies, although the work was done previous to employment. H.P. and B.B. own equities in Adverum Biotechnologies. All other authors declare no competing financial interests.

ACKNOWLEDGMENTS

We thank Dr. Hugues Jacob, Karim Hnia, Nicolas Charlet-Berguerand, and Pr. Jean-Louis Mandel for scientific discussions and Dr. Wyatt Delphino and Mehdi Gasmi for critical review of the manuscript. We thank Dr. Ronald G. Crystal (Department of Genetic Medicine, Weill Cornell Medicine, NY, USA) for the production of the optimized construct and vector and Dr. Mustapha Oulad-Abdelghani for providing the 4F9 mouse monoclonal antibodies against FXN. We thank Dr. Tania Sorg, Ghina Bou-About, Josiane Hergueux, the mouse clinic institute phenotyping platform, and Dr. Luc Dupuis for logistical and technical assistance. This work was supported by the Lefoulond Delalande Foundation–Institut de France (postdoctoral research fellowships, 2016); the Friedreich Ataxia Research Alliance (Keith Michael Andrus Cardiac Research Award, 2016); the French Muscular Dystrophy Association AFM-Téléthon (research grant year 2014); and AAVLIFE SAS (sponsored research agreement years 2014–2016). This study was also supported by the grant ANR-10-LABX-0030-INRT, a French State fund managed by the Agence Nationale de la Recherche under the frame program Investissement d'Avenir ANR-10-IDEX-0002-02.

REFERENCES

1. Bürk, K. (2017). Friedreich Ataxia: current status and future prospects. Cerebellum Ataxias *4*, 4.
2. Tsou, A.Y., Paulsen, E.K., Lagedrost, S.J., Perlman, S.L., Mathews, K.D., Wilmot, G.R., Ravina, B., Koeppen, A.H., and Lynch, D.R. (2011). Mortality in Friedreich ataxia. J. Neurol. Sci. *307*, 46–49.
3. Campuzano, V., Montermini, L., Moltò, M.D., Pianese, L., Cossée, M., Cavalcanti, F., Monros, E., Rodius, F., Duclos, F., Monticelli, A., et al. (1996). Friedreich's ataxia: autosomal recessive disease caused by an intronic GAA triplet repeat expansion. Science *271*, 1423–1427.
4. Saveliev, A., Everett, C., Sharpe, T., Webster, Z., and Festenstein, R. (2003). DNA triplet repeats mediate heterochromatin-protein-1-sensitive variegated gene silencing. Nature *422*, 909–913.
5. Maio, N., Jain, A., and Rouault, T.A. (2020). Mammalian iron-sulfur cluster biogenesis: Recent insights into the roles of frataxin, acyl carrier protein and ATPase-mediated transfer to recipient proteins. Curr. Opin. Chem. Biol. *55*, 34–44.
6. Sheftel, A., Stehling, O., and Lill, R. (2010). Iron-sulfur proteins in health and disease. Trends Endocrinol. Metab. *21*, 302–314.
7. Mayr, J.A., Feichtinger, R.G., Tort, F., Ribes, A., and Sperl, W. (2014). Lipoic acid biosynthesis defects. J. Inherit. Metab. Dis. *37*, 553–563.
8. Leimkühler, S. (2017). Shared function and moonlighting proteins in molybdenum cofactor biosynthesis. Biol. Chem. *398*, 1009–1026.
9. Braymer, J.J., and Lill, R. (2017). Iron-sulfur cluster biogenesis and trafficking in mitochondria. J. Biol. Chem. *292*, 12754–12763.
10. Puccio, H., Simon, D., Cossée, M., Criqui-Filipe, P., Tiziano, F., Melki, J., Hindelang, C., Matyas, R., Rustin, P., and Koenig, M. (2001). Mouse models for Friedreich ataxia exhibit cardiomyopathy, sensory nerve defect and Fe-S enzyme deficiency followed by intramitochondrial iron deposits. Nat. Genet. *27*, 181–186.
11. Chandran, V., Gao, K., Swarup, V., Versano, R., Dong, H., Jordan, M.C., and Geschwind, D.H. (2017). Inducible and reversible phenotypes in a novel mouse model of Friedreich's Ataxia. eLife *6*, e30054.
12. Perdomini, M., Belbellaa, B., Monassier, L., Reutenauer, L., Messaddeq, N., Cartier, N., Crystal, R.G., Aubourg, P., and Puccio, H. (2014). Prevention and reversal of severe mitochondrial cardiomyopathy by gene therapy in a mouse model of Friedreich's ataxia. Nat. Med. *20*, 542–547.
13. Gérard, C., Xiao, X., Filali, M., Coulombe, Z., Arsenault, M., Couet, J., Li, J., Drolet, M.C., Chapdelaine, P., Chikh, A., and Tremblay, J.P. (2014). An AAV9 coding for frataxin clearly improved the symptoms and prolonged the life of Friedreich ataxia mouse models. Mol. Ther. Methods Clin. Dev. *1*, 14044.
14. Piguet, F., de Montigny, C., Vaucamps, N., Reutenauer, L., Eisenmann, A., and Puccio, H. (2018). Rapid and Complete Reversal of Sensory Ataxia by Gene Therapy in a Novel Model of Friedreich Ataxia. Mol. Ther. *26*, 1940–1952.
15. Belbellaa, B., Reutenauer, L., Monassier, L., and Puccio, H. (2019). Correction of half the cardiomyocytes fully rescue Friedreich ataxia mitochondrial cardiomyopathy through cell-autonomous mechanisms. Hum. Mol. Genet. *28*, 1274–1285.
16. Pook, M.A., Al-Mahdawi, S., Carroll, C.J., Cossée, M., Puccio, H., Lawrence, L., Clark, P., Lowrie, M.B., Bradley, J.L., Cooper, J.M., et al. (2001). Rescue of the Friedreich's ataxia knockout mouse by human YAC transgenesis. Neurogenetics *3*, 185–193.
17. Miranda, C.J., Santos, M.M., Ohshima, K., Tessaro, M., Sequeiros, J., and Pandolfo, M. (2004). Frataxin overexpressing mice. FEBS Lett. *572*, 281–288.
18. Wang, Y., Wang, Y., Marcus, S., and Busenlehner, L.S. (2014). The role of frataxin in fission yeast iron metabolism: implications for Friedreich's ataxia. Biochim. Biophys. Acta *1840*, 3022–3033.
19. Vannocci, T., Notario Manzano, R., Beccalli, O., Bettegazzi, B., Grohovaz, F., Cinque, G., de Riso, A., Quaroni, L., Codazzi, F., and Pastore, A. (2018). Adding a temporal dimension to the study of Friedreich's ataxia: the effect of frataxin overexpression in a human cell model. Dis. Model. Mech. *11*, dmm032706.
20. Edenharter, O., Clement, J., Schneuwly, S., and Navarro, J.A. (2017). Overexpression of Drosophila frataxin triggers cell death in an iron-dependent manner. J. Neurogenet. *31*, 189–202.
21. Navarro, J.A., Llorens, J.V., Soriano, S., Botella, J.A., Schneuwly, S., Martínez-Sebastián, M.J., and Moltó, M.D. (2011). Overexpression of human and fly frataxins in Drosophila provokes deleterious effects at biochemical, physiological and developmental levels. PLoS ONE *6*, e21017.
22. Richardson, D.R., Huang, M.L., Whitnall, M., Becker, E.M., Ponka, P., and Suryo Rahmanto, Y. (2010). The ins and outs of mitochondrial iron-loading: the metabolic defect in Friedreich's ataxia. J. Mol. Med. (Berl.) *88*, 323–329.
23. Rich, P.R., and Maréchal, A. (2010). The mitochondrial respiratory chain. Essays Biochem. *47*, 1–23.
24. Dudkina, N.V., Kouril, R., Peters, K., Braun, H.P., and Boekema, E.J. (2010). Structure and function of mitochondrial supercomplexes. Biochim. Biophys. Acta *1797*, 664–670.
25. Koeppen, A.H., Ramirez, R.L., Becker, A.B., Bjork, S.T., Levi, S., Santambrogio, P., Parsons, P.J., Kruger, P.C., Yang, K.X., Feustel, P.J., and Mazurkiewicz, J.E. (2015). The pathogenesis of cardiomyopathy in Friedreich ataxia. PLoS ONE *10*, e0116396.
26. Ward, P.G.D., Harding, I.H., Close, T.G., Corben, L.A., Delatycki, M.B., Storey, E., Georgiou-Karistianis, N., and Egan, G.F. (2019). Longitudinal evaluation of iron concentration and atrophy in the dentate nuclei in friedreich ataxia. Mov. Disord. *34*, 335–343.
27. Michael, S., Petrocine, S.V., Qian, J., Lamarche, J.B., Knutson, M.D., Garrick, M.D., and Koeppen, A.H. (2006). Iron and iron-responsive proteins in the cardiomyopathy of Friedreich's ataxia. Cerebellum *5*, 257–267.
28. Koeppen, A.H. (2011). Friedreich's ataxia: pathology, pathogenesis, and molecular genetics. J. Neurol. Sci. *303*, 1–12.
29. Arosio, P., Elia, L., and Poli, M. (2017). Ferritin, cellular iron storage and regulation. IUBMB Life *69*, 414–422.
30. Tatsuta, T., Model, K., and Langer, T. (2005). Formation of membrane-bound ring complexes by prohibitins in mitochondria. Mol. Biol. Cell *16*, 248–259.
31. Planavila, A., Redondo-Angulo, I., and Villarroya, F. (2015). FGF21 and Cardiac Physiopathology. Front. Endocrinol. (Lausanne) *6*, 133.
32. Montero, R., Yubero, D., Villarroya, J., Henares, D., Jou, C., Rodríguez, M.A., Ramos, F., Nascimento, A., Ortez, C.I., Campistol, J., et al. (2016). GDF-15 Is Elevated in Children with Mitochondrial Diseases and Is Induced by Mitochondrial Dysfunction. PLoS ONE *11*, e0148709.
33. Schmucker, S., Argentini, M., Carelle-Calmels, N., Martelli, A., and Puccio, H. (2008). The in vivo mitochondrial two-step maturation of human frataxin. Hum. Mol. Genet. *17*, 3521–3531.
34. Huang, M.L., Sivagurunathan, S., Ting, S., Jansson, P.J., Austin, C.J., Kelly, M., Semsarian, C., Zhang, D., and Richardson, D.R. (2013). Molecular and functional alterations in a mouse cardiac model of Friedreich ataxia: activation of the integrated stress response, eIF2α phosphorylation, and the induction of downstream targets. Am. J. Pathol. *183*, 745–757.
35. Manno, C.S., Pierce, G.F., Arruda, V.R., Glader, B., Ragni, M., Rasko, J.J., Ozelo, M.C., Hoots, K., Blatt, P., Konkle, B., et al. (2006). Successful transduction of liver in hemophilia by AAV-Factor IX and limitations imposed by the host immune response. Nat. Med. *12*, 342–347.
36. Mingozzi, F., Maus, M.V., Hui, D.J., Sabatino, D.E., Murphy, S.L., Rasko, J.E., Ragni, M.V., Manno, C.S., Sommer, J., Jiang, H., et al. (2007). CD8(+) T-cell responses to adeno-associated virus capsid in humans. Nat. Med. *13*, 419–422.
37. Prasad, K.M., Xu, Y., Yang, Z., Acton, S.T., and French, B.A. (2011). Robust cardiomyocyte-specific gene expression following systemic injection of AAV: in vivo gene delivery follows a Poisson distribution. Gene Ther. *18*, 43–52.
38. Vannocci, T., Dinarelli, S., Girasole, M., Pastore, A., and Longo, G. (2019). A new tool to determine the cellular metabolic landscape: nanotechnology to the study of Friedreich's ataxia. Sci. Rep. *9*, 19282.
39. Llorens, J.V., Navarro, J.A., Martínez-Sebastián, M.J., Baylies, M.K., Schneuwly, S., Botella, J.A., and Moltó, M.D. (2007). Causative role of oxidative stress in a Drosophila model of Friedreich ataxia. FASEB J. *21*, 333–344.
40. Seguin, A., Bayot, A., Dancis, A., Rogowska-Wrzesinska, A., Auchère, F., Camadro, J.M., Bulteau, A.L., and Lesuisse, E. (2009). Overexpression of the yeast frataxin

homolog (Yfh1): contrasting effects on iron-sulfur cluster assembly, heme synthesis and resistance to oxidative stress. Mitochondrion *9*, 130–138.

41. Ristow, M., Pfister, M.F., Yee, A.J., Schubert, M., Michael, L., Zhang, C.Y., Ueki, K., Michael, M.D., 2nd, Lowell, B.B., and Kahn, C.R. (2000). Frataxin activates mitochondrial energy conversion and oxidative phosphorylation. Proc. Natl. Acad. Sci. USA *97*, 12239–12243.

42. Shoichet, S.A., Bäumer, A.T., Stamenkovic, D., Sauer, H., Pfeiffer, A.F., Kahn, C.R., Müller-Wieland, D., Richter, C., and Ristow, M. (2002). Frataxin promotes antioxidant defense in a thiol-dependent manner resulting in diminished malignant transformation in vitro. Hum. Mol. Genet. *11*, 815–821.

43. Runko, A.P., Griswold, A.J., and Min, K.T. (2008). Overexpression of frataxin in the mitochondria increases resistance to oxidative stress and extends lifespan in Drosophila. FEBS Lett. *582*, 715–719.

44. Sarsero, J.P., Li, L., Holloway, T.P., Voullaire, L., Gazeas, S., Fowler, K.J., Kirby, D.M., Thorburn, D.R., Galle, A., Cheema, S., et al. (2004). Human BAC-mediated rescue of the Friedreich ataxia knockout mutation in transgenic mice. Mamm. Genome *15*, 370–382.

45. Hinderer, C., Katz, N., Buza, E.L., Dyer, C., Goode, T., Bell, P., Richman, L.K., and Wilson, J.M. (2018). Severe Toxicity in Nonhuman Primates and Piglets Following High-Dose Intravenous Administration of an Adeno-Associated Virus Vector Expressing Human SMN. Hum. Gene Ther. *29*, 285–298.

46. Nault, J.-C., Datta, S., Imbeaud, S., Franconi, A., Mallet, M., Couchy, G., Letouzé, E., Pilati, C., Verret, B., Blanc, J.F., et al. (2015). Recurrent AAV2-related insertional mutagenesis in human hepatocellular carcinomas. Nat. Genet. *47*, 1187–1193.

47. Foust, K.D., Wang, X., McGovern, V.L., Braun, L., Bevan, A.K., Haidet, A.M., Le, T.T., Morales, P.R., Rich, M.M., Burghes, A.H., and Kaspar, B.K. (2010). Rescue of the spinal muscular atrophy phenotype in a mouse model by early postnatal delivery of SMN. Nat. Biotechnol. *28*, 271–274.

48. Bočkor, L., Bortolussi, G., Iaconcig, A., Chiaruttini, G., Tiribelli, C., Giacca, M., Benvenuti, F., Zentilin, L., and Muro, A.F. (2017). Repeated AAV-mediated gene transfer by serotype switching enables long-lasting therapeutic levels of hUgt1a1 enzyme in a mouse model of Crigler-Najjar Syndrome Type I. Gene Ther. *24*, 649–660.

49. Xu, R., Jia, Y., Zygmunt, D.A., and Martin, P.T. (2019). rAAVrh74.MCK.GALGT2 Protects against Loss of Hemodynamic Function in the Aging mdx Mouse Heart. Mol. Ther. *27*, 636–649.

50. Zygmunt, D.A., Xu, R., Jia, Y., Ashbrook, A., Menke, C., Shao, G., Yoon, J.H., Hamilton, S., Pisharath, H., Bolon, B., and Martin, P.T. (2019). rAAVrh74.MCK.*GALGT2* Demonstrates Safety and Widespread Muscle Glycosylation after Intravenous Delivery in C57BL/6J Mice. Mol. Ther. Methods Clin. Dev. *15*, 305–319.

51. Manso, A.M., Hashem, S.I., Nelson, B.C., Gault, E., Soto-Hermida, A., Villarruel, E., Brambatti, M., Bogomolovas, J., Bushway, P.J., Chen, C., et al. (2020). Systemic AAV9.LAMP2B injection reverses metabolic and physiologic multiorgan dysfunction in a murine model of Danon disease. Sci. Transl. Med. *12*, eaax1744.

52. Zhu, J., Huang, X., and Yang, Y. (2009). The TLR9-MyD88 pathway is critical for adaptive immune responses to adeno-associated virus gene therapy vectors in mice. J. Clin. Invest. *119*, 2388–2398.

53. Ashley, S.N., Somanathan, S., Giles, A.R., and Wilson, J.M. (2019). TLR9 signaling mediates adaptive immunity following systemic AAV gene therapy. Cell. Immunol. *346*, 103997.

54. Leborgne, C., Barbon, E., Alexander, J.M., Hanby, H., Delignat, S., Cohen, D.M., Collaud, F., Muraleetharan, S., Lupo, D., Silverberg, J., et al. (2020). IgG-cleaving endopeptidase enables in vivo gene therapy in the presence of anti-AAV neutralizing antibodies. Nat. Med. *26*, 1096–1101.

55. Hu, C., Busuttil, R.W., and Lipshutz, G.S. (2010). RH10 provides superior transgene expression in mice when compared with natural AAV serotypes for neonatal gene therapy. J. Gene Med. *12*, 766–778.

56. Wagner, G.R., Pride, P.M., Babbey, C.M., and Payne, R.M. (2012). Friedreich's ataxia reveals a mechanism for coordinate regulation of oxidative metabolism via feedback inhibition of the SIRT3 deacetylase. Hum. Mol. Genet. *21*, 2688–2697.

57. Nabhan, J.F., Wood, K.M., Rao, V.P., Morin, J., Bhamidipaty, S., LaBranche, T.P., Gooch, R.L., Bozal, F., Bulawa, C.E., and Guild, B.C. (2016). Intrathecal delivery of frataxin mRNA encapsulated in lipid nanoparticles to dorsal root ganglia as a potential therapeutic for Friedreich's ataxia. Sci. Rep. *6*, 20019.

58. Vyas, P.M., Tomamichel, W.J., Pride, P.M., Babbey, C.M., Wang, Q., Mercier, J., Martin, E.M., and Payne, R.M. (2012). A TAT-frataxin fusion protein increases lifespan and cardiac function in a conditional Friedreich's ataxia mouse model. Hum. Mol. Genet. *21*, 1230–1247.

59. Britti, E., Delaspre, F., Feldman, A., Osborne, M., Greif, H., Tamarit, J., and Ros, J. (2018). Frataxin-deficient neurons and mice models of Friedreich ataxia are improved by TAT-MTScs-FXN treatment. J. Cell. Mol. Med. *22*, 834–848.

60. Chapdelaine, P., Gérard, C., Sanchez, N., Cherif, K., Rousseau, J., Ouellet, D.L., Jauvin, D., and Tremblay, J.P. (2016). Development of an AAV9 coding for a 3XFLAG-TALEfrat#8-VP64 able to increase in vivo the human frataxin in YG8R mice. Gene Ther. *23*, 606–614.

61. Cherif, K., Gérard, C., Rousseau, J., Ouellet, D.L., Chapdelaine, P., and Tremblay, J.P. (2018). Increased Frataxin Expression Induced in Friedreich Ataxia Cells by Platinum TALE-VP64s or Platinum TALE-SunTag. Mol. Ther. Nucleic Acids *12*, 19–32.

62. Puspasari, N., Rowley, S.M., Gordon, L., Lockhart, P.J., Ioannou, P.A., Delatycki, M.B., and Sarsero, J.P. (2011). Long range regulation of human FXN gene expression. PLoS ONE *6*, e22001.

63. Sarsero, J.P., Holloway, T.P., Li, L., Finkelstein, D.I., and Ioannou, P.A. (2014). Rescue of the Friedreich ataxia knockout mutation in transgenic mice containing an FXN-EGFP genomic reporter. PLoS ONE *9*, e93307.

64. Li, J., Li, Y., Wang, J., Gonzalez, T.J., Asokan, A., Napierala, J.S., and Napierala, M. (2020). Defining Transcription Regulatory Elements in the Human Frataxin Gene: Implications for Gene Therapy. Hum. Gene Ther. *31*, 839–851.

65. Wang, D., Li, S., Gessler, D.J., Xie, J., Zhong, L., Li, J., Tran, K., Van Vliet, K., Ren, L., Su, Q., et al. (2018). A Rationally Engineered Capsid Variant of AAV9 for Systemic CNS-Directed and Peripheral Tissue-Detargeted Gene Delivery in Neonates. Mol. Ther. Methods Clin. Dev. *9*, 234–246.

66. Xie, J., Xie, Q., Zhang, H., Ameres, S.L., Hung, J.-H., Su, Q., He, R., Mu, X., Seher Ahmed, S., Park, S., et al. (2011). MicroRNA-regulated, systemically delivered rAAV9: a step closer to CNS-restricted transgene expression. Mol. Ther. *19*, 526–535.

67. Chitnis, N.S., Pytel, D., Bobrovnikova-Marjon, E., Pant, D., Zheng, H., Maas, N.L., Frederick, B., Kushner, J.A., Chodosh, L.A., Koumenis, C., et al. (2012). miR-211 is a prosurvival microRNA that regulates chop expression in a PERK-dependent manner. Mol. Cell *48*, 353–364.

68. Ye, H., Xie, M., Xue, S., Hamri, G.C.-E., Yin, J., Zulewski, H., and Fussenegger, M. (2016). Self-adjusting synthetic gene circuit for correcting insulin resistance. Nat. Biomed. Eng. *1*, 0005.

69. Shah, N.M., Rushworth, S.A., Murray, M.Y., Bowles, K.M., and MacEwan, D.J. (2013). Understanding the role of NRF2-regulated miRNAs in human malignancies. Oncotarget *4*, 1130–1142.

70. Sun, W., Yi, Y., Xia, G., Zhao, Y., Yu, Y., Li, L., Hua, C., He, B., Yang, B., Yu, C., et al. (2019). Nrf2-miR-129-3p-mTOR Axis Controls an miRNA Regulatory Network Involved in HDACi-Induced Autophagy. Mol. Ther. *27*, 1039–1050.

71. Merentie, M., Lottonen-Raikaslehto, L., Parviainen, V., Huusko, J., Pikkarainen, S., Mendel, M., Laham-Karam, N., Kärjä, V., Rissanen, R., Hedman, M., and Ylä-Herttuala, S. (2016). Efficacy and safety of myocardial gene transfer of adenovirus, adeno-associated virus and lentivirus vectors in the mouse heart. Gene Ther. *23*, 296–305.

72. Hordeaux, J., Hinderer, C., Goode, T., Buza, E.L., Bell, P., Calcedo, R., Richman, L.K., and Wilson, J.M. (2018). Toxicology Study of Intra-Cisterna Magna Adeno-Associated Virus 9 Expressing Iduronate-2-Sulfatase in Rhesus Macaques. Mol. Ther. Methods Clin. Dev. *10*, 68–78.

73. Hordeaux, J., Hinderer, C., Goode, T., Katz, N., Buza, E.L., Bell, P., Calcedo, R., Richman, L.K., and Wilson, J.M. (2018). Toxicology Study of Intra-Cisterna Magna

Adeno-Associated Virus 9 Expressing Human Alpha-L-Iduronidase in Rhesus Macaques. Mol. Ther. Methods Clin. Dev. *10*, 79–88.

74. Rabinowitz, J.E., Rolling, F., Li, C., Conrath, H., Xiao, W., Xiao, X., and Samulski, R.J. (2002). Cross-packaging of a single adeno-associated virus (AAV) type 2 vector genome into multiple AAV serotypes enables transduction with broad specificity. J. Virol. *76*, 791–801.

75. Luna, L.G. (1992). Histopathologic Methods and Color Atlas of Special Stains and Tissue Artifacts (American Histolabs).

76. Ainsworth, S.K., and Karnovsky, M.J. (1972). An ultrastructural staining method for enhancing the size and electron opacity of ferritin in thin sections. J. Histochem. Cytochem. *20*, 225–229.

doi:10.1093/brain/awn269 Brain 2009: 132; 116–123 | 116

BRAIN
A JOURNAL OF NEUROLOGY

Visual system involvement in patients with Friedreich's ataxia

Filippo Fortuna,[1] Piero Barboni,[1,2] Rocco Liguori,[1] Maria Lucia Valentino,[1] Giacomo Savini,[3] Cinzia Gellera,[4] Caterina Mariotti,[4] Giovanni Rizzo,[1,5] Caterina Tonon,[5] David Manners,[5] Raffaele Lodi,[5] Alfredo A Sadun[6] and Valerio Carelli[1]

1 Department of Neurological Sciences, University of Bologna, Bologna, Italy
2 Studio oculistico d'Azeglio, Bologna, Italy
3 Fondazione G.B. Bietti-IRCCS, Rome, Italy
4 U.O. Biochemistry and Genetics, Fondazione IRCCS-Istituto Neurologico Nazionale 'Carlo Besta', Milan, Italy
5 Department of Clinical Medicine and Applied Biotechnology, University of Bologna, Bologna, Italy
6 Doheny Eye Institute, Keck School of Medicine, University of Southern California, USA

Correspondence to: Valerio Carelli, MD, PhD,
Dipartimento di Scienze Neurologiche,
Università di Bologna, Via Ugo Foscolo 7,
40123 Bologna, Italy
E-mail: valerio.carelli@unibo.it

Optic neuropathy is common in mitochondrial disorders, but poorly characterized in Friedreich's ataxia (FRDA), a recessive condition caused by lack of the mitochondrial protein frataxin. We investigated 26 molecularly confirmed FRDA patients by studying both anterior and posterior sections of the visual pathway using a new, integrated approach. This included visual field testing and optical coherence tomography (OCT), pattern visual evoked potentials (P-VEPs) and diffusion-weighted imaging. The latter was used to study optic radiation by calculating water apparent diffusion coefficients (ADC). All patients suffered optic nerve involvement with their disorder. Different patterns of visual field defects were observed and a variably reduced retinal nerve fiber layer thickness was seen by OCT in all cases. P-VEPs were abnormal in approximately half of the patients. Decreased visual acuity and temporal optic disc pallor were present in advanced stages of the disease, but only five patients were symptomatic. Two of these patients suffered a sudden loss of central vision, mimicking Leber's hereditary optic neuropathy (LHON), and of the other three symptomatic patients two were noted to be compound heterozygotes. ADC values of optic radiations in patients were significantly higher than controls ($P < 0.01$). Retinal nerve fiber layer thickness at OCT and P-VEPs correlated with age at onset and ICARS total score. ADC values correlated with age at onset, disease duration, GAA triplet expansion size, ICARS total score and P-VEPs. Visual pathway involvement is found consistently in FRDA, being previously underestimated, and we here document that it also involves the optic radiations. Occasional LHON-like cases may occur. However, optic neuropathy in FRDA substantially differs from classic mitochondrial optic neuropathies implying a different pathophysiology of visual system degeneration in this mitochondrial disease.

Keywords: optic neuropathy; Friedreich's Ataxia; mitochondria; OCT; frataxin

Abbreviations: ADC = apparent diffusion coefficients; DOA = dominant optic atrophy; DWI = diffusion-weighted imaging; EPI = echo planar imaging; F-ERG = flash-electroretinogram; FRDA = Friedreich's ataxia; ICARS = International Cooperative Ataxia Rating Scale; LHON = Leber's hereditary optic neuropathy; MERRF = myoclonic epilepsy, ragged-red-fibres; mtDNA = mitochondrial DNA; nt = nucleotide; OCT = optical coherence tomography; ONH = optic nerve head; PCR = polymerase chain reaction; P-VEPs = pattern visual evoked potentials; RGC = retinal ganglion cell; RNFL = retinal nerve fiber layer; ROI = regions of interest; RPE = retinal pigmented epithelium

Received May 30, 2008. Revised September 9, 2008. Accepted September 22, 2008. Advance Access publication October 18, 2008

Introduction

Friedreich's ataxia (FRDA) is the commonest form of hereditary ataxias with autosomal recessive transmission (Harding, 1993). Disease onset is usually before the age of 25 years. Clinical features include spinocerebellar and sensory ataxia with absence of deep tendon reflexes, dysarthria, hypertrophic cardiomyopathy and scoliosis (Harding, 1993). Additional clinical features may include diabetes mellitus, pes cavus, hypoacusia and optic atrophy (Harding, 1993).

The genetic defect has been located on chromosome 9q13-q21.1 and affected individuals present a GAA triplet expansion in the first intron of the *FXN* gene (Campuzano *et al.*, 1996). This expansion may reach over 1000 repeats in both alleles, the normal range being 27–36 repeats. A minority of FRDA patients are compound heterozygotes for the GAA triplet expansion and a point mutation (Campuzano *et al.*, 1996). The FRDA gene encodes a 210 amino-acid long protein called frataxin whose function is still not completely elucidated. Soon after its identification frataxin was recognized as a mitochondrial protein necessary to maintain respiratory function and mitochondrial DNA (mtDNA) in yeast (Koutnikova *et al.*, 1997; Wilson *et al.*, 1997). Frataxin is directed to the inner mitochondrial membrane and FRDA-associated mutations drastically reduce the protein amount (Campuzano *et al.*, 1997). Further studies confirmed deficient mitochondrial respiration in the heart and muscle of FRDA patients, with a specific impairment of iron-sulphur containing proteins such as complexes I, II and III and aconitase (Rotig *et al.*, 1997; Lodi *et al.*, 1999). Frataxin has been implicated in iron homeostasis (Babcock *et al.*, 1997) and hypersensitivity to oxidative stress (Wong *et al.*, 1999). However, the role of oxidative stress in the disease pathophysiology remains unclear (Seznec *et al.*, 2005). More recently, frataxin has been shown to be involved in the biosynthetic pathways related to Fe-S clusters containing enzymes (Tan *et al.*, 2003; Shan *et al.*, 2007).

Mitochondrial optic neuropathies are a relatively homogeneous group of genetic and acquired disorders characterized by the peculiar preferential involvement of the small axons serving central vision, colour vision and high spatial frequency contrast sensitivity; these fibers form the papillomacular bundle (Carelli *et al.*, 2004). Non-syndromic mitochondrial optic neuropathies essentially include Leber's hereditary optic neuropathy (LHON) and dominant optic atrophy (DOA), and present clinically as visual loss and optic nerve atrophy reflecting retinal ganglion cell (RGC) degeneration as the only or at least primary pathological feature (Carelli *et al.*, 2004). Mitochondrial optic neuropathies may also occur in more complex syndromes such as encephalomyopathies due to mtDNA mutations, i.e. Leigh syndrome and myoclonic epilepsy, ragged-red-fibers (MERRF) (Carelli *et al.*, 2006), or mitochondrial disorders due to nuclear DNA genetic defects, i.e. Charcot-Marie-Tooth 2A (mutations in mitofusin 2) (Zuchner *et al.*, 2006), deafness-dystonia-optic atrophy (Mohr-Tranebjerg) syndrome (mutations in TIMM8A) (Jin *et al.*, 1996), and complicated hereditary spastic paraplegia (mutations in paraplegin) (Casari *et al.*, 1998). The occurrence of optic atrophy in FRDA belongs to this latter group of mitochondrial disorders and this feature has been recognized but poorly characterized for a long time (Newman, 2005). The last systematic study of optic atrophy in a series of FRDA patients was based on electrophysiology by Carroll *et al.* (1980), and more recently there have been only a few case reports published (Givre *et al.*, 2000; Porter *et al.*, 2007). However, the recent revolution in mitochondrial medicine had made the study of mitochondrial optic neuropathies a hot topic that is now being intensely investigated (Carelli *et al.*, 2006), using a variety of new technical tools in ophthalmology such as optical coherence tomography (OCT) (Barboni *et al.*, 2005; Savini *et al.*, 2005).

This study aimed to characterize the pathological features of visual pathway involvement in FRDA. Twenty-six molecularly confirmed FRDA patients were evaluated by applying an integrated approach able to explore the entire visual pathway by visual fields and pattern visual evoked potentials (P-VEPs). Additionally, the anterior visual pathways (retinal ganglion cell/optic nerve system) were directly assessed by OCT, and the posterior visual pathways (optic radiations) by magnetic resonance using the diffusion-weighted imaging (DWI) technique.

Methods

Patient sample

We recruited 26 patients (18 males, mean age 32 ± 8) from 21 Italian families with genetically confirmed FRDA diagnosis, by an advertisement on the website and the newspaper of the 'Associazione Italiana per la lotta alle Sindromi Atassiche' (AISA), the Italian association of patients with ataxia. Five pairs of siblings and 16 sporadic cases were included, the sample being composed of 18 males and eight females ranging from 15 to 45 years of age. The demographic and clinical features are summarized in Table 1. The quantification of disability was performed according to the ICARS (Trouillas *et al.*, 1997), whose score progresses from 0 to 100 with the degree of disease severity. About one third of the patients were severely affected as they could not conduct activities of daily life independently, and

Table 1 Demographic and clinical features of the 26 FRDA patients

Gender (male/female)	18/8
Age (years, mean ± SD)	32 ± 8
Age of onset (years, mean ± SD)	18 ± 9
Disease duration (years, mean ± SD)	13 ± 8
Late onset (>25 years old)	27% (7/26)
ICARS TOTAL score (mean ± SD)	56 ± 24
Autonomy in daily life activities	73% (19/26)
Spinocerebellar ataxia	100% (26/26)
Wheelchair bound	54% (14/26)
Dysarthria	70% (18/26)
Hearing loss	11% (3/26)
Left ventricle hypertrophy[a]	62% (16/26)
Scoliosis	81% (21/26)
Diabetes mellitus	4% (1/26)
Idebenone treatment	54% (14/26)

a Assessed using echocardiography.
SD = standard deviation; ICARS = International Cooperative Ataxia Rating Scale.

about half were wheelchair bound. All patients had the typical features of spinocerebellar ataxia. Only one patient had diabetes and three suffered hearing loss, as inferred by previous medical reports. All participants gave their informed consent according to the Declaration of Helsinki and the study was approved by the internal review board of the Department of Neurological Sciences at the University of Bologna.

Neuro-ophthalmologic studies

Each patient had a comprehensive ophthalmologic examination, including best-corrected visual acuity measurement, slit lamp biomicroscopy, intraocular pressure measurement, and indirect ophthalmoscopy. Visual field testing by Humphrey Field Analyzer (HVF, Zeiss-Humphrey Systems, Dublin, CA, USA), retinal nerve fiber layer (RNFL) thickness measurement and optic nerve head (ONH) analysis by OCT (StratusOCT, software version 4.0.1; Carl Zeiss Meditec, Inc, Dublin, CA, USA) were carried out in all patients with a good fixation (23 out of 26).

The OCT acquisition protocols adopted were RNFL Thickness 3.4 and Fast Optic Disc, as previously reported (Barboni *et al.*, 2005; Savini *et al.*, 2005). Briefly, for each eye, we studied the mean RNFL thickness (360° measure), temporal quadrant thickness (316°–45° unit circle), superior quadrant thickness (46–135°), nasal quadrant thickness (136–225°), and inferior quadrant thickness (226–315°), all automatically calculated by OCT using the existing software. ONH evaluation consisted of six radial scans centred on the optic disc and spaced 30 degrees apart. The machine automatically defined the edge of the optic disc as the end of the retinal pigmented epithelium (RPE)/choriocapillaris and used smoothing with fit to circle to fill the gaps between scans. The examination was performed under mydriasis by an experienced operator (PB) who was masked regarding the clinical status of each subject. RNFL measurements in FRDA patients were compared to a control group matched for age and ONH size, since both factors have been found to influence RNFL thickness assessment by OCT (Barboni *et al.*, 2005; Savini *et al.*, 2005). The control group ($n = 48$, 28 males, mean age 32.9 ± 7.8) was composed of volunteers without evidence of either optic disc or retinal disease.

The neuro-physiological evaluation included P-VEPs and Flash-electroretinogram (F-ERG) performed in all patients. P-VEPs to stimulation with 31′ checks and with 15′ checks and F-ERG were recorded at least twice in order to ensure reproducibility using established methods (Ikeda, 1982).

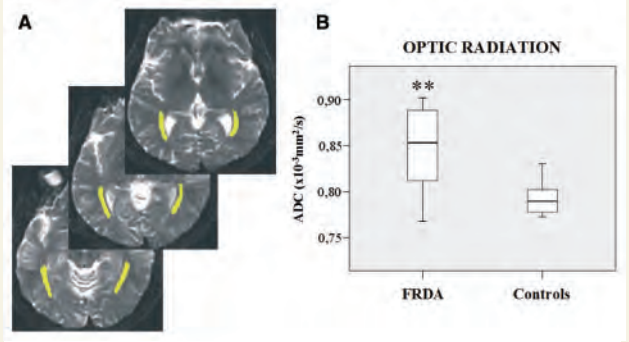

Fig. 1 (**A**) ROIs including optic radiations. (**B**) Scatter plot of optic radiations mean ADC values of FRDA patients and controls. (Each box shows the median, quartiles and extreme values; $^{**}P \leq 0.01$.)

DWI studies

We used a 1.5-T General Electrics Medical Systems (Milwaukee, Wisconsin) Signa Horizon LX whole-body scanner to study a subset of 13 FRDA patients (11 males, mean age 31 ± 8) and 18 healthy age-matched volunteers (13 males, mean age 28 ± 8). Axial DW images were obtained (slice thickness = 5 mm, inter-slice gap = 1 mm) using a single-shot echo planar imaging (EPI) sequence (matrix size = 192×192 mm) as previously reported (Nicoletti *et al.*, 2006). Orthogonal *x*, *y* and *z* diffusion encoding gradients were applied with gradient strengths corresponding to *b*-values of 900 s/mm^2. In addition, images without diffusion weighting were acquired, corresponding to $b = 0$ s/mm^2 and exhibiting T_2-contrast. The apparent diffusion coefficient (ADC) in each direction was determined pixel-wise using a least-squares fit, assuming a signal attenuation depending mono-exponentially on *b*-value. By calculating the mean of three directions, the ADC map was generated. Regions of interest (ROI) (Fig. 1A) were determined by segmentation of the left and right optic radiations (Yamamoto *et al.*, 2005) on three slice using the EPI images with $b = 0$ s/mm^2 and were copied on the ADC maps to obtain the mean ADC values.

Polymerase chain reaction amplification and sequence analysis of the FXN gene

Genomic DNA was prepared from peripheral-blood lymphocytes using standard procedures. The detection and quantification of the $(GAA)_n$ repeat size was achieved by polymerase chain reaction (PCR) amplification performed in three independent reaction mix, using different forward primers (Gellera *et al.*, 2007). Amplifications of exons 1–5A and 5B of the *FXN* gene were performed as previously described (Campuzano *et al.*, 1997). Direct sequence analysis of PCR products from patients and controls was performed by automated sequencing on an ABI PRISM 3100 Genetic Analyzer (Applera, Foster City, CA) using the BigDyeDeoxy™ Terminator Cycle Sequencing Kit (Applera) according to the manufacturer's recommendations. Nucleotides were numbered so that the first nucleotide (nt) of the first in-frame ATG codon was nucleotide +1 [GenBank cDNA reference sequence: NM_000144.3 (GI:31742514)].

Statistical analysis

For the ophthalmologic studies, one eye was chosen randomly to be considered for each patient and for each control subject. Statistical analyses were performed with SPSS 12.0. The Mann–Whitney U-test was used to evaluate differences in demographic, clinical, electrophysiological and imaging data between FRDA patients and healthy controls. Possible relations between the structural and functional ophthalmologic parameters and the onset and duration of the disease, triplet expansion of the shorter expanded allele and ICARS score were analysed using the Spearman rank test for non-parametric data. Moreover, data for correlation between the structural and functional ophthalmologic parameters were also analysed. For all analyses, only $P < 0.05$ was accepted as statistically significant.

Results

Molecular investigation

All patients recruited in this study underwent genetic analysis of the FXN gene and the triplet expansion of the minor affected

allele ranged from 200 to 1100 repetitions (mean = 435 GAA). Two patients were compound heterozygotes for the expansion and a point mutation. The first patient carried a GAA expansion of 900 triplets and a nucleotide deletion (157delC) producing a frameshift at codon 53 and the premature truncation of the protein at codon 75. The second carried a GAA expansion of 470 triplets and a 13-nt deletion at exon 3-intron three boundaries (c.381_384delTGGG+g.IVS3+1_+9delGTACCTCTT). This latter deletion eliminates the last four nucleotides of exon 3 and the first nine nucleotides of intron 3, including the splice donor site, possibility leading to an aberrantly spliced mRNA that could be unstable and rapidly degraded (Gellera *et al.*, 2007).

Neuro-ophthalmologic investigation

Two patients presented with sudden bilateral loss of central vision at 25 and 29 years of age respectively, mimicking the clinical course of LHON. They had 1100 and 850 triplets in the shorter expanded allele, respectively. One of these patients reported visual loss immediately after vigabatrin administration as antispastic; this is a drug with recognized optic nerve toxicity (Frisen *et al.*, 2003). At the time of examination, 2 and 8 years respectively after onset, the patients presented a residual visual acuity of counting fingers and fundus examination demonstrated diffuse optic disc atrophy (Fig. 2A). Furthermore, P-VEPs were absent and RNFL thickness at OCT was severely reduced compared to controls (average 49 and 33 versus 100 ± 8.9).

Concerning the remaining 24 patients, three were symptomatic with reduced visual acuity, and 21 were completely asymptomatic for visual disturbances. The three symptomatic individuals included two compound heterozygotes (900 and 470 GAA triplet expansion) and one homozygous patient with 600 GAA triplet expansion in the shorter allele and a disease duration of 24 years. This latter patient was only partially investigated because of severe nystagmus. The two compound heterozygote cases stand out from the rest of our case series and had severe ophthalmologic features, close to those suffering the LHON-like visual loss. In fact, they had consistent reduction of RNFL thickness compared to controls (average 53 and 42 versus 100 ± 8.9), bilateral involvement of central visual field with reduction of visual acuity (20/200 and 20/25 respectively) and absent P-VEPs response.

In the 21 asymptomatic patients the ophthalmoscopic investigation showed a variable optic disc appearance (Fig. 2B and C), ranging from diffuse optic disc pallor to essentially normal fundus appearance. Visual field examination showed variable patterns of impairment as reported in Fig. 3. All examined patients demonstrated one of three different common patterns of visual field defect. The first pattern represented severe visual field impairment with general and concentric reduction of sensitivity (Fig. 3A). A second pattern was characterized by a mild reduction of sensitivity and a concentric superior or inferior arcuate defect (Fig. 3B). Finally, the third pattern showed very little depression and only an isolated small paracentral area of reduced sensitivity (Fig. 3C).

OCT measurements of RNFL thicknesses showed a statistically significant reduction in the temporal (61 ± 9.6 versus 71 ± 14.4; $P = 0.006$), superior (87 ± 21.4 versus 125 ± 14.0; $P < 0.0001$), nasal (58 ± 20.9 versus 78 ± 15.6; $P = 0.0005$), inferior (98 ± 20.1 versus 126 ± 14.4; $P < 0.0001$) quadrants and the 360° average measurement (76 ± 12.0 versus 100 ± 8.9; $P < 0.0001$) in patients compared to controls (Fig. 4). Thus, all patients had a reduced number of axons, which were graduated in three categories, progressively more severe, that corresponded with the previously defined patterns of visual field defects (Figs 3D and 4).

P-VEPs 31′ were abnormal in 27 (61%) out of 44 eyes investigated (14 out of 21 patients), whereas P-VEPs 15′ were abnormal in 29 (66%) out of 44 eyes (15 out of 21 patients). Absent response was detected in four eyes at 31′ (9%) and 10 at 15′ (23%) out of the 44 eyes investigated. Eight eyes (18%) showed only decreased amplitude at 31′, whereas at 15′ showed also increased latency. F-ERG was normal in all patients. In order to include the patients with absent VEP response in the correlation analysis, we used a semi-quantitative score for latency

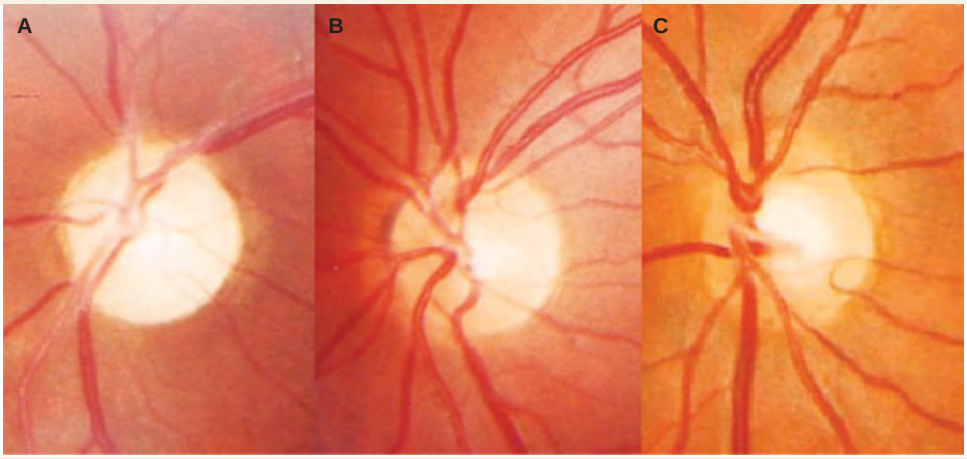

Fig. 2 Colour fundus pictures of three FRDA patients with different levels of severity of optic neuropathy. **(A)** Diffuse optic disc atrophy in a patient with a Leber-like acute and severe loss of visual acuity. (**B**) Diffuse pallor of the optic disc in a patient with intermediate pattern of RNFL thickness reduction and normal visual acuity. (**C**) Normal appearance of the optic disc in a patient with mild pattern of RNFL thickness reduction and normal visual acuity.

abnormalities (normal = 0; 1–25% increase= 1; 26–50% = 2; 51–75% = 3; 76–100% = 4; >100% = 5; absent = 6).

We then correlated functional (visual field mean deviation, P-VEPs 31′ and 15′) and anatomical (average RNFL thickness at OCT) parameters with age of onset, disease duration, GAA triplet expansion, and ICARS total score. Table 2 shows that P-VEPs and RNFL thickness were significantly correlated with age of onset and ICARS total score. None of these parameters was correlated with disease duration and the GAA triplet expansion in the 21 patients considered, having excluded the two LHON-like and the two compound heterozygote patients (Table 2). This discrepancy was possibly due to three outlier cases, two of whom carried high triplet expansion (768 and 1000 GAA) and did not present a severe ophthalmologic pathology. The opposite was observed in one case with low number of repeats (200 GAA). The correlation between the functional (visual field mean deviation, P-VEPs 31′ and 15′) and anatomical (average RNFL thickness at OCT) parameters are shown in Table 3. A significant correlation was detected between visual fields and P-VEPs, both parameters exploring the entire visual pathway.

DWI investigation

A subset of 13 patients (age 31 ± 8 years, mean ± SD) and 18 matched healthy volunteers (28 ± 8; $P = 0.3$) were studied by DWI. Water ADC values were not statistically different in corresponding right and left hemisphere ROIs in either normal subjects or patients and hence are reported as mean values. The FRDA patients had significantly higher ADC values in the optic radiations than healthy subjects ($P < 0.01$) (Table 4A and Fig. 1B). ADC values correlated with age of disease onset ($r = -0.66$, $P < 0.01$), disease duration ($r = 0.65$, $P < 0.05$), GAA triplet expansion ($r = 0.71$, $P < 0.01$), total ICARS score ($r = 0.69$, $P < 0.01$) and all neurophysiologic parameters, particularly P-VEPs-15′ latencies ($r = 0.80$, $P = 0.001$) (Table 4B). We failed to find a correlation between ADC values and average RNFL thickness or visual field from the same patients.

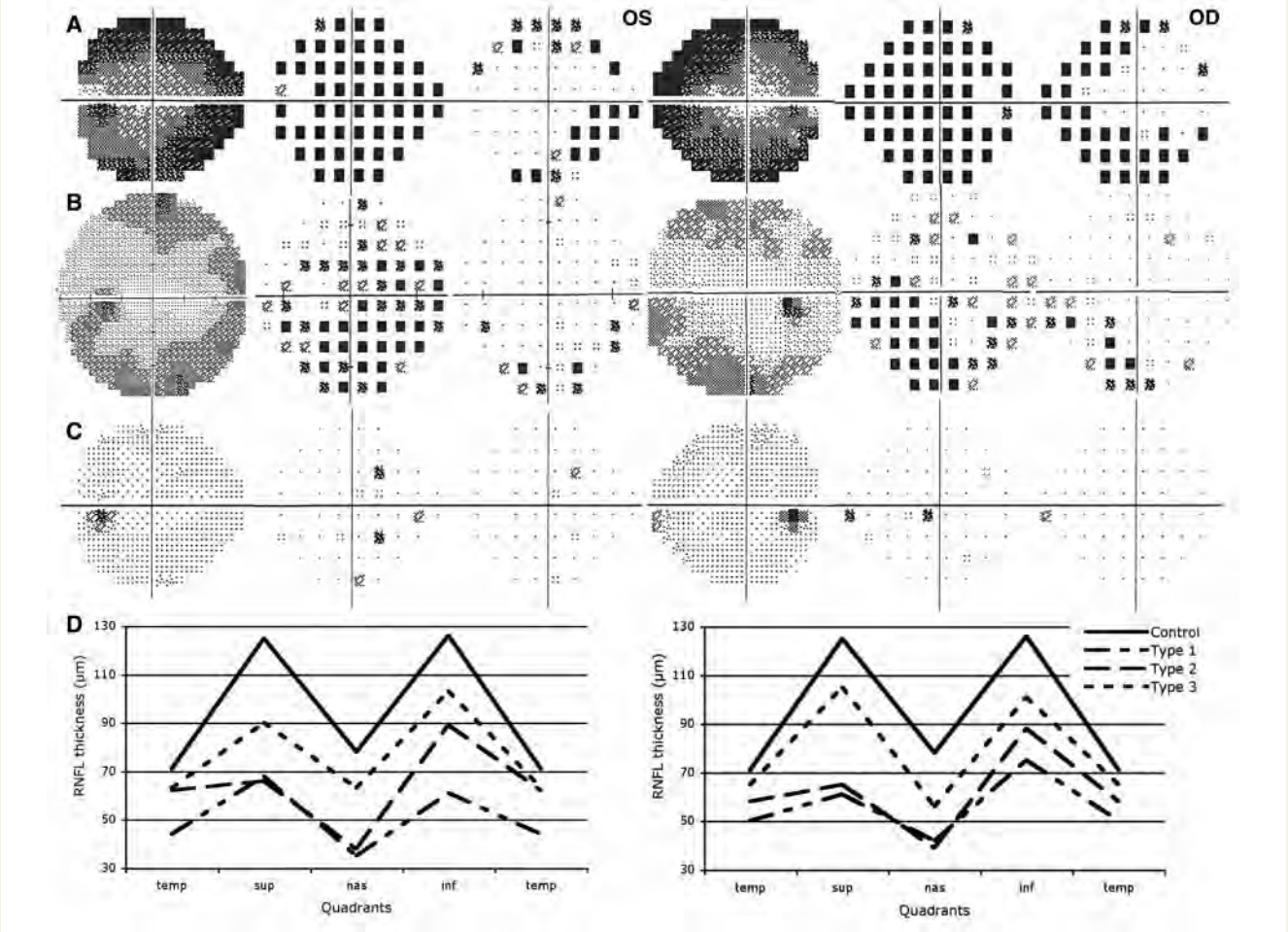

Fig. 3 Full-threshold, 24° and 30° visual field of the right eye (OD), left eye (OS) and the corresponding pattern of RNFL thickness in each quadrant at OCT. (**A**) Severe visual field impairment with general and concentric reduction of sensitivity (Type 1 in D). (**B**) Mild reduction of sensitivity and concentric inferior arcuate type defect (Type 2 in D). (**C**) Isolated area of reduced sensitivity (Type 3 in D). (**D**) The increasing reduction of RNFL thickness at OCT was graded to three types that corresponded to the visual field patterns shown in **A**–**C**. Type 1 shows diffuse and severe reduction of RNFL thickness in all quadrants. Type 2 shows diffuse RNFL reduction more marked in the superior quadrant corresponding to the inferior visual field defect. Type 3 shows diffuse but mild reduction of RNFL thickness in all quadrants.

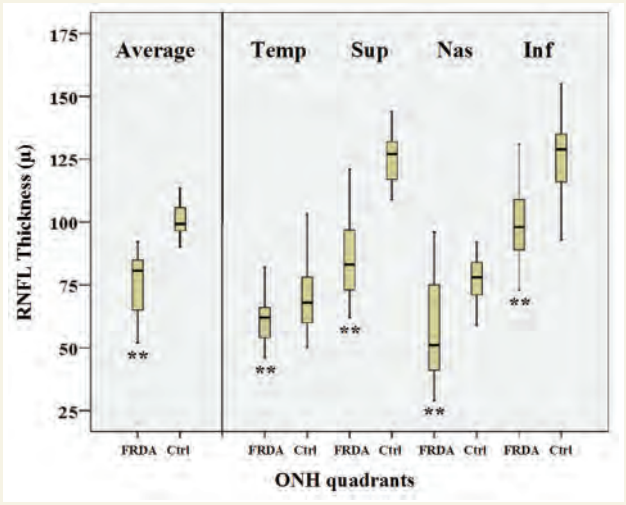

Fig. 4 RNFL thickness (average and each quadrant) of FRDA patients, having excluded the two LHON-like and the two compound heterozygote patients, compared to controls. (Each box shows the median, quartiles and extreme values; $^{**}P \leq 0.01$).

Table 2 Correlation of functional and anatomical ophthalmologic parameters with age of onset, disease duration, triplet expansion and ICARS score in the 21 FRDA patients, having excluded the two LHON-like and the two compound heterozygote cases

	Visual field (MD)	P-VEPs 31′ latency (score)	P-VEPs 15′ latency (score)	Average RNFL thickness
Age of onset				
Correlation coefficient (*r*)	0.368	–0.559	–0.575	0.568
P	0.101	**0.008**	**0.006**	**0.007**
Disease duration				
Correlation coefficient (*r*)	–0.216	0.288	0.308	–0.406
P	0.348	0.206	0.174	0.068
Triplet expansion				
Correlation coefficient (*r*)	–0.290	0.327	0.367	–0.376
P	0.202	0.148	0.101	0.093
CARS score				
Correlation coefficient (*r*)	–0.292	0.558	0.644	–0.576
P	0.199	**0.009**	**0.002**	**0.006**

MD = mean defect; P-VEP = pattern reversal visual evoked potential; RNFL = retinal nerve fibre layer; ICARS: International Cooperative Ataxia Rating Scale. Bold values indicate statistically significant values.

Table 3 Spearman correlation (*r*) between functional and anatomical ophthalmologic parameters in 21 FRDA having excluded the two LHON-like patients and the two compound heterozygote patients

	Visual Field (MD)	P-VEPs 31′ latency (score)	P-VEPs 15′ latency (score)
Average RNFL thickness			
r	0.274	–0.132	–0.252
P	0.229	0.568	0.270
Visual Field (MD)			
r		–0.613	–0.525
P		**0.003**	**0.015**

MD = mean defect; P-VEP = pattern reversal visual evoked potential; RNFL = retinal nerve fibre layer. Bold values indicate statistically significant values.

Table 4 Panel A Comparison of mean ADC values in optic radiations of FRDA patients and controls. Panel B Correlations between mean ADC values of optic radiations in FRDA patients and age at onset, disease duration, triplet expansion, ICARS score, P-VEP values, average RFNL thickness and visual field defect

	Normal controls (18)	FRDA patients (13)	*P*
Panel A: Group comparison (Mann–Whitney U-test)			
Optic radiation ADC[a] ($\times 10^{-3}$ mm^2/s) (mean ± SD)	0.79 ± 0.02	0.85 ± 0.04	**0.0016**
Panel B: Correlations (Spearman's rank test)			
Age at onset		*r* = –0.66	**0.015**
Disease duration		*r* = 0.65	**0.015**
Triplet expansion		*r* = 0.71	**0.006**
ICARS score		*r* = 0.69	**0.009**
P-VEP 31′ latency (score)[a]		*r* = 0.58	**0.038**
P-VEP 15′ latency (score)[a]		*r* = 0.80	**0.001**
Average RFNL thickness[a]		*r* = –0.49	0.10
Visual field (MD)[a]		*r* = –0.35	0.26

a Mean of left and right values.
ADC = apparent diffusion coefficient; ICARS = international cooperative ataxia rating scale; *P*-VEP = pattern reversal visual evoked potential; RNFL = retinal nerve fiber layer; MD: mean defect. Bold values indicate statistically significant values.

Discussion

Our study fills a historical gap in the clinical description of FRDA, the best studied form of hereditary ataxia, and provides novel details on visual pathway involvement and pathophysiology due to mitochondrial dysfunction. We systematically studied the visual pathway by the integrated use of different techniques, exploring the anterior visual pathways (RGCs and their axons forming the optic nerve) by OCT, the posterior pathways (optic radiation) by DWI, and both by visual fields and P-VEPs. We showed that all FRDA patients investigated presented some degree of visual pathway involvement, notwithstanding a wide range of variability in multi-systemic clinical expression. However, only in a small subset was this apparent clinically, explaining why visual impairment is underestimated in FRDA. Loss of central vision associated with poor visual acuity appears to occur late in the course of FRDA, with predilection for patients compound heterozygotes, as previously reported (Cossee *et al.*, 1999). Our findings suggest that in FRDA there exists a slowly progressive degenerative process involving both the optic nerve and the optic radiations. In a

small number of cases, all with severe diseases and large triplet expansion, a subacute/acute visual failure mimicking the mitochondrial disease LHON may overlap the slow progression of FRDA optic neuropathy.

The integrated findings with visual fields and OCT, link a functional evaluation with a technique exploring objectively the structural changes of fiber loss in the optic nerve. The present study showed a diffuse and progressive pattern of fiber loss, which initially did not result in a visual field defect (Fig. 3). The appearance of such defects, starting from the periphery and becoming increasingly severe concentrically, relates to the crossing of a threshold in terms of fiber loss. This loss, based on the defect observed, is most probably uniformly scattered over the entire RGCs pool, without the typical selectivity shown by other mitochondrial optic neuropathies, such as LHON or OPA1-related DOA where the papillomacular bundle is preferentially affected (Carelli *et al.*, 2004). The visual field and OCT data were corroborated by electrophysiology, which investigates the integrity of the entire visual pathway, from the eye to the visual cortex.

In contrast, we observed in two cases a rapid, subacute loss of vision that clearly resembled the typical pattern of LHON, with a central vision defect. Prior to their subacute loss of vision, these two patients did not complain of visual defects, though often peripheral field losses are not subjectively evident. These two cases were peculiar for having a large GAA triplet expansion (1100 and 850 repeats in the shorter allele, respectively), and in one patient a possible exogenous trigger (vigabatrin) may have played a role. The ophthalmologic features of these two acute cases were similar to other two recently reported, one of which was a compound heterozygote (Givre *et al.*, 2000; Porter *et al.*, 2007). In our study too, despite the small number of cases, the only two compound heterozygote patients were in fact most severely affected with symptomatic visual loss. This confirms the findings of Cossee *et al.* (1999) that showed the high recurrence of pale optic discs in FRDA compound heterozygote patients.

We also explored the optic radiations by DWI, evaluating the post-geniculate visual pathway separately from the pre-synaptic anterior visual pathway that was explored by OCT. DWI allows the assessment of water ADC, a measure of tissue water diffusivity. Typically, pathological processes that modify tissue integrity, as in neurodegenerative disorders, result in an increased ADC (Nicoletti *et al.*, 2006). This study demonstrates that a pathological process affects also the post-geniculate posterior visual pathway (Fig. 1). The changes revealed by DWI may relate to a degenerative process of the posterior visual pathways that is independent from the anterior visual pathways (optic nerves). The alternative explanation would entail a trans-synaptic mechanism involving first the optic nerve and only secondarily the post-geniculate radiations. However, we failed to find a correlation between ADC values and RNFL thickness, as evaluated by OCT (Table 4B), suggesting that involvement of the anterior and posterior visual pathways may be independent and asynchronous. This is further supported by the correlation found between the functional parameters visual field and P-VEPs (Table 3), both involving the evaluation of the entire visual pathway, but not with the RNFL thickness (anterior pathway).

Our current results provide new details on visual pathway involvement in FRDA, and also provide evidence that in this mitochondrial multi-systemic disorder the pattern of visual loss and the underlying pathological mechanism are clearly different from the classical clinical features that characterize the so-called non-syndromic mitochondrial optic neuropathies, such as LHON and OPA1-related DOA (Carelli *et al.*, 2004, 2006). In particular, in FRDA the papillomacular axonal system is not preferentially involved. However, under special conditions a different, rapid acute/subacute loss of vision mimicking LHON may occur, as seen in two patients from our case series, and as previously reported (Givre *et al.*, 2000; Porter *et al.*, 2007). The selectivity for the papillomacular bundle in LHON and DOA has been related to the general feature of all RGC axons, which are non-myelinated in their initial portion and myelinated after the emergence from the lamina cribrosa at the posterior pole of the ocular globe (Carelli *et al.*, 2004) and to special features of the papillomacular bundle fibers that consist of the smallest and least myelinated axons. A combination of energy failure, oxidative stress, predisposition to apoptosis and mitochondrial distribution within this axonal system is considered the pathological basis for RGC degeneration in both LHON and DOA (Carelli *et al.*, 2007). In the case of FRDA, the progressive scattered loss of RGCs strongly indicates that other pathological mechanisms and timing are at work.

The currently favoured hypothesis for the main functional role of frataxin is its involvement in the biogenesis and the chaperoning of the Fe-S cluster insertion in various enzymes (Tan *et al.*, 2003; Shan *et al.*, 2007). Alterations in frataxin may have consequences in the respiratory chain leading to bioenergetic impairment (Rötig *et al.*, 1997; Lodi *et al.*, 1999) and increased oxidative stress (Wong *et al.*, 1999), accumulation of iron (Babcock *et al.*, 1997) and thus increased sensitivity of cells to undergo apoptosis (Tan *et al.*, 2003). Most of these features are common to the non-syndromic optic neuropathies LHON and DOA, which however seem more specifically related to a defect of complex I (Carelli *et al.*, 2004; Zanna *et al.*, 2008) and involve a more specific subset of visual fibers. In FRDA complexes I, II and III are all involved, thus limiting the compensatory mechanisms, which may operate in LHON and DOA. In fact, the clinical expression is a much more severe and widespread disorder, involving the central nervous system and heart as main targets. The issue of mitochondrial transport down the long axons of spinocerebellar tracts, or along the vulnerable fibers of the optic nerve associates neurodegeneration in FRDA with other multisystemic mitochondrial disorders that involve the optic nerve such as, for example, complicated spastic paraplegia (Casari *et al.*, 1998). However, it is remarkable that despite the different pathological mechanisms that apparently involve the visual pathways in FRDA, LHON-like cases may also occur in the presence of high GAA triplet expansion (our cases) or compound heterozygosis and severe clinical expression (Givre *et al.*, 2000; Porter *et al.*, 2007). Thus, even in FRDA we have a spectrum of clinical expression that goes from the slowly progressive pattern of RGC degeneration to the rapid, more catastrophic pattern of papillomoacular RGC loss, peculiar to the non-syndromic mitochondrial optic neuropathies (Carelli *et al.*, 2004).

In conclusion, we have provided a detailed characterization of visual pathway involvement in FRDA, showing an asynchronous,

slowly progressive degeneration of both anterior and posterior visual pathways. In our series of patients we confirmed the possible occurrence of acute/subacute cases mimicking LHON. Clinically significant visual impairment is late in FRDA patients, but degeneration of these neurons must be not underestimated and should be considered in therapeutic decision making. Furthermore, the correlation of both RNFL thickness and optic radiation ADC values with ICARS suggests that OCT and DWI may become tools for evaluating disease activity and progression, possibly useful for future clinical trials in FRDA.

Acknowledgements

We are deeply indebted to all patients and their families for participating to this project. We also thank Ms Monica Lucchi for her technical help.

Funding

Fondazione Gino Galletti (grant to V.C.); the Ministry of Health (Ricerca Finalizzata 2006 to V.C.).

References

Babcock M, de Silva D, Oaks R, Davis-Kaplan S, Jiralerspong S, Montermini L, et al. Regulation of mitochondrial iron accumulation by Yfh1p, a putative homologue of frataxin. Science 1997; 276: 1709–12.

Barboni P, Savini G, Valentino ML, Montagna P, Cortelli P, De Negri AM, et al. Retinal nerve fiber layer evaluation by optical coherence tomography in Leber's hereditary optic neuropathy. Ophthalmology 2005; 112: 120–26.

Campuzano V, Montermini L, Moltò MD, Pianese L, Cossée M, Cavalcanti F, et al. Friedreich ataxia: autosomal recessive disease caused by an intronic GAA triplet repeat expansion. Science 1996; 271: 1423–7.

Campuzano V, Montermini L, Lutz Y, Cova L, Hindelang C, Jiralerspong S, et al. Frataxin is reduced in Friedreich ataxia patients and is associated with mitochondrial membranes. Hum Mol Genet 1997; 6: 1771–80.

Carelli V, Ross-Cisneros FN, Sadun AA. Mitochondrial dysfunction as a cause of optic neuropathies. Prog Retin Eye Res 2004; 23: 53–89.

Carelli V, Barboni P, Sadun AA. Mitochondrial ophthalmology. In: DiMauro S, Hirano M, Schon EA, editors. Mitochondrial medicine. Oxon, UK: Informa Healthcare; 2006. p. 105–42.

Carelli V, La Morgia C, Iommarini L, Carroccia R, Mattiazzi M, Sangiorgi S, et al. Mitochondrial optic neuropathies: how two genomes may kill the same cell type? Biosci Rep 2007; 27: 173–84.

Carroll WM, Kriss A, Baraitser M, Barrett G, Halliday AM. The incidence and nature of visual pathway involvement in Friedreich's ataxia. A clinical and visual evoked potential study of 22 patients. Brain 1980; 103: 413–34.

Casari G, De Fusco M, Ciarmatori S, Zeviani M, Mora M, Fernandez P, et al. Spastic paraplegia and OXPHOS impairment caused by mutations in paraplegin, a nuclear-encoded mitochondrial metalloprotease. Cell 1998; 93: 973–83.

Cossée M, Dürr A, Schmitt M, Dahl N, Trouillas P, Allinson P, et al. Friedreich's ataxia: point mutations and clinical presentation of compound heterozygotes. Ann Neurol 1999; 45: 200–6.

Frisen L, Malmgren K. Characterization of vigabatrin-associated optic atrophy. Acta Ophthalmol Scand 2003; 81: 466–73.

Gellera C, Castellotti B, Mariotti C, Mineri R, Seveso V, Didonato S, et al. Frataxin gene point mutations in Italian Friedreich ataxia patients. Neurogenetics 2007; 8: 289–99.

Givre SJ, Wall M, Kardon RH. Visual loss and recovery in a patient with Fridreich Ataxia. J Neuro-ophthalmol 2000; 20: 229–33.

Harding AE. Clinical features and classification of inherited ataxias. Adv Neurol 1993; 61: 1–14.

Jin H, May M, Tranebjaerg L, Kendall E, Fontán G, Jackson J, et al. A novel X-linked gene, DDP, shows mutations in families with deafness (DFN-1), dystonia, mental deficiency and blindness. Nat Genet 1996; 14: 177–80.

Koutnikova H, Campuzano V, Foury F, Dollé P, Cazzalini O, Koenig M. Studies of human, mouse and yeast homologues indicate a mitochondrial function for frataxin. Nat Genet 1997; 16: 345–51.

Ikeda H. Clinical electroretinography. In: Halliday AM, editor. Evoked potentials in clinical testing. London: Churchill Livingstone; 1982. p. 121–47.

Lodi R, Cooper JM, Bradley JL, Manners D, Styles P, Taylor DJ, et al. Deficit of in vivo mitochondrial ATP production in patients with Friedreich ataxia. Proc Natl Acad Sci USA 1999; 96: 11492–95.

Newman NJ. Optic neuropathy as a manifestation of hereditary degenerative or developmental diseases. Hereditary ataxias. In: Miller NR, Newman NJ, Biousse V, Kerrison JB, editors. Walsh and Hoyt's clinical neuroopthalmology. Baltimore: Lippincott Williams & Wilkins; 2005. p. 482–84.

Nicoletti G, Lodi R, Condino F, Tonon C, Fera F, Malucelli E, et al. Apparent diffusion coefficient measurements of the Middle Cerebellar Peduncle differentiate the Parkinson variant of MSA from PD and PSP. Brain 2006; 129: 2679–87.

Porter N, Downes SM, Fratter C, Anslow P, Nemeth AH. Catastrophic visual loss in a patient with Friedreich ataxia. Arch Ophthalmol 2007; 125: 273–74.

Rötig A, de Lonlay P, Chretien D, Foury F, Koenig M, Sidi D, et al. Aconitase and mitochondrial iron-sulphur protein deficiency in Friedreich ataxia. Nat Genet 1997; 17: 215–17.

Savini G, Barboni P, Valentino ML, Montagna P, Cortelli P, De Negri AM, et al. Retinal nerve fiber layer evaluation by optical coherence tomography in unaffected carriers with Leber's hereditary optic neuropathy mutations. Ophthalmology 2005; 112: 127–31.

Seznec H, Simon D, Bouton C, Reutenauer L, Hertzog A, Golik P, et al. Friedreich ataxia, the oxidative stress paradox. Hum Mol Genet 2005; 14: 463–74.

Shan Y, Napoli E, Cortopassi G. Mitochondrial frataxin interacts with ISD11 of the NFS1/ISCU complex and multiple mitochondrial chaperones. Hum Mol Genet 2007; 16: 929–41.

Tan G, Napoli E, Taroni F, Cortopassi G. Decreased expression of genes involved in sulfur amino acid metabolism in frataxin deficient cells. Hum Mol Genet 2003; 12: 1699–711.

Trouillas P, Takayanagi T, Hallett M, Currier RD, Subramony SH, Wessel K, et al. International Cooperative Ataxia Rating Scale for pharmacological assessment of the cerebellar syndrome. The Ataxia Neuropharmacology Committee of the World Federation of Neurology. J Neurol Sci 1997; 145: 205–11.

Wilson RB, Roof DM. Respiratory deficiency due to loss of mitochondrial DNA in yeast lacking the frataxin homologue. Nat Genet 1997; 16: 352–57.

Wong A, Yang J, Cavadini P, Gellera C, Lonnerdal B, Taroni F, et al. The Friedreich's ataxia mutation confers cellular sensitivity to oxidant stress which is rescued by chelators of iron and calcium and inhibitors of apoptosis. Hum Mol Genet 1999; 8: 425–30.

Yamamoto T, Yamada K, Nishimura T, Kinoshita S. Tractography to depict three layers of visual field trajectories to the calcarine gyri. Am J Ophthalmol 2005; 140: 781–85.

Zanna C, Ghelli A, Porcelli AM, Karbowski M, Youle RJ, Schimpf S, et al. OPA1 mutations associated with dominant optic atrophy impair oxidative phosphorylation and mitochondrial fusion. Brain 2008; 131: 352–67.

Züchner S, De Jonghe P, Jordanova A, Claeys KG, Guergueltcheva V, Cherninkova S, et al. Axonal neuropathy with optic atrophy is caused by mutations in mitofusin 2. Ann Neurol 2006; 59: 276–81.

REVIEW

HGT

Central Nervous System Therapeutic Targets in Friedreich Ataxia

Ian H. Harding,[1,2] David R. Lynch,[3,*] Arnulf H. Koeppen,[4] and Massimo Pandolfo[5]

[1]Department of Neuroscience, Central Clinical School, Monash University, Melbourne, Australia.
[2]Monash Biomedical Imaging, Monash University, Melbourne, Australia.
[3]Division of Neurology, The Children's Hospital of Philadelphia, Philadelphia, Pennsylvania, USA.
[4]Research, Neurology, and Pathology Services, Veterans Affairs Medical Center and Departments of Neurology and Pathology, Albany Medical College, Albany, New York, USA.
[5]Laboratory of Experimental Neurology, Université Libre de Bruxelles (ULB), Brussels, Belgium.
All authors contributed equally to this work.

Friedreich ataxia (FRDA) is an autosomal recessive inherited multisystem disease, characterized by marked differences in the vulnerability of neuronal systems. In general, the proprioceptive system appears to be affected early, while later in the disease, the dentate nucleus of the cerebellum and, to some degree, the corticospinal tracts degenerate. In the current era of expanding therapeutic discovery in FRDA, including progress toward novel gene therapies, a deeper and more specific consideration of potential treatment targets in the nervous system is necessary. In this work, we have re-examined the neuropathology of FRDA, recognizing new issues superimposed on classical findings, and dissected the peripheral nervous system (PNS) and central nervous system (CNS) aspects of the disease and the affected cell types. Understanding the temporal course of neuropathological changes is needed to identify areas of modifiable disease progression and the CNS and PNS locations that can be targeted at different time points. As most major targets of long-term therapy are in the CNS, this review uses multiple tools for evaluation of the importance of specific CNS locations as targets. In addition to clinical observations, the conceptualizations in this study include physiological, pathological, and imaging approaches, and animal models. We believe that this review, through analysis of a more complete set of data derived from multiple techniques, provides a comprehensive summary of therapeutic targets in FRDA.

Keywords: Friedreich ataxia, frataxin, neuroanatomy, proprioceptive system, cerebellum, corticospinal system

INTRODUCTION

Friedreich ataxia (FRDA) is an autosomal recessive inherited multisystem disease, the classical neurological features of which reflect a specific neuropathology, characterized by marked differences in the vulnerability of neuronal systems.[1,2] First described in 1863 by Nikolaus Friedreich, a German physician, the genetic cause of Friedreich's ataxia was discovered in 1996[3]: a homozygous expansion of a guanine-adenine-adenine (GAA) trinucleotide repeat in intron 1 of the frataxin gene (*FXN*), or rarely, a point mutation or large deletion in one *FXN* allele and GAA expansion in the other. Expanded GAA repeats promote chromatin condensation and disrupt *FXN* mRNA transcription, leading to markedly reduced frataxin levels in affected individuals.[4] Multiple functions have been proposed for frataxin, but the one supported by evidence is in the mitochondrial biogenesis of iron-sulfur (Fe/S) clusters.[5] Fe/S clusters are cofactors for proteins with a variety of functions that are located in all cellular compartments. In the mitochondria, these include Krebs cycle enzymes, subunits of respiratory chain complexes I, II, and III, ferrochelatase, lipoic acid synthase, and several others. The function of these proteins is impaired by frataxin deficiency, leading to lower energy production and oxidative stress due to respiratory chain dysfunction. In the cytosol, a key factor that controls iron metabolism is iron responsive element binding protein 1 (IRP1), which generally carries an Fe/S cluster in iron-rich conditions. The loss of the Fe/S cluster from IRP1 activates its function as an RNA binding protein that promotes degradation of mRNAs coding for proteins that utilize or store iron, while promoting synthesis of proteins that participate in iron

*Correspondence: David R. Lynch, Division of Neurology, Children's Hospital of Philadelphia, Room 502, Abramson CHOP, Philadelphia, PA 19104, USA. E-mail: lynchd@mail.med.upenn.edu

DOI: 10.1089/hum.2020.264

uptake. Activation of IRP1 occurs when frataxin is low, increasing iron uptake to support Fe/S cluster synthesis.[6] However, because this mechanism is defective in FRDA, it results in toxic intramitochondrial iron accumulation that further aggravates oxidative stress. This is further potentiated by secondary deficiency of peroxisome proliferator-activated receptor gamma coactivator 1 alpha (PGC1α) that impairs mitochondrial biogenesis.[7,8] However, despite notable progress in understanding frataxin function and FRDA pathogenesis, the reasons why most cells do not seem to be functionally impaired by the low frataxin levels found in FRDA patients, while other cell types are vulnerable, are not yet understood.

The neuroanatomical sequelae of FRDA are increasingly well understood. The proprioceptive system appears to be affected early, with reduced number of dorsal root ganglion (DRG) cells mediating proprioception and of their large myelinated axons in peripheral nerves, dorsal roots, and dorsal columns of the spinal cord. At the same time, the dorsal spinocerebellar tracts, relaying proprioceptive information to the cerebellum, are affected. With time, the dentate nucleus (DN) of the cerebellum and, to some degree, the corticospinal tracts degenerate. A few other central nervous system (CNS) nuclei, mostly in sensory pathways (trigeminal, auditory, and visual), atrophy in a subset of individuals. This unique pattern of lesions gives rise to a distinct clinical picture, usually identifiable even without genetic confirmation.

Insight into the genetic and biochemical basis of FRDA has led to the identification of potential therapeutic targets, launching an era of therapeutic discovery with development of many novel approaches, including gene therapy. For several reasons, such new therapies require knowledge of neuroanatomical details not commonly appreciated in clinical neurology. At the simplest level, understanding the combination of peripheral nervous system (PNS) and CNS aspects of the disease is essential for selection of drugs and vectors based on their tissue and cellular distribution. As most major targets of long-term therapy are in the CNS, such agents must reach those targets by crossing the blood–brain barrier (BBB) or by direct administration into the cerebrospinal fluid or brain parenchyma. Pharmacological targeting also requires an understanding of affected cell types, which in gene therapy influences selection of capsids and promoters. In FRDA, the neuron is traditionally viewed as the affected cell. However, glial cells (astrocytes, satellite cells, and oligodendrocytes) may contribute to the phenotype of FRDA with secondary damage. Additional targets that lie outside the BBB must also be reached by the same or different therapeutic agents, possibly requiring multiple routes of administration. Although the ongoing development of novel drug delivery systems, including advanced forms of nanotechnology, may alleviate some of these challenges, biodistribution currently limits therapeutic success in the new generation of therapies. Consequently, understanding the true neuropathology of FRDA and those areas of *modifiable* disease progression is essential.

In this work, we have re-examined the neuropathology of FRDA, recognizing new issues superimposed on classical findings. First, the neuropathology of FRDA changes over time, a concept important in defining targets at different disease stages. Some structures and pathways may change subclinically before clinical presentation, possibly during development. Subsequent pathology in these structures may be driven by secondary events no longer directly reflecting frataxin deficiency. Understanding the temporal course of neuropathological changes is needed to define which CNS and PNS locations may be successfully targeted at different time points.

This review uses multiple tools for evaluation of the importance of specific CNS locations as targets. In addition to clinical observations, the conceptualizations in this study include physiological approaches, such as the recording of evoked potentials, nerve conduction studies, and magnetoencephalography (MEG); pathological approaches, including analysis of autopsy tissue; imaging approaches, including magnetic resonance imaging (MRI); and animal models. Notably, animal data are limited in its ability to define human anatomical targets, particularly as complete *FXN* knockout (KO) is lethal to the embryo, and thus, conditional KO models have been used to study pathogenic mechanisms triggered by loss of frataxin. Although these models have been the major ones used in gene therapy in mice, they have prespecified target cells, so they cannot be used to investigate the neuroanatomical pattern of the disease. However, in selected circumstances, the failure of *FXN* KO to alter animal phenotype can provide compelling information. Mice in which *FXN* is knocked out in astrocytes later in life develop no clear neurological phenotype, possibly showing the limits of frataxin re-introduction in astrocytes in mature animals.[9] We believe that this review, through analysis of a more complete set of data derived from multiple techniques, provides a comprehensive summary of therapeutic targets in FRDA.

AFFECTED SYSTEMS IN FRDA

Proprioceptive system/somatosensory

The dorsal root ganglia (DRG) are a principal affected tissue in FRDA, and both large and small DRG neurons are affected (Fig. 1C). The underlying disease process is hypoplasia rather than atrophy,[10] although satellite cell proliferation, inflammatory infiltration, and neuronophagia continue beyond the developmental period. The proposed mechanism in the developmental failure of DRG is incompetence of the boundary cap that controls the transit of DRG axons into the dorsal spinal cord parenchyma. As an indication of the boundary cap incompetence, autopsy specimens of FRDA patients show the intrusion of CNS-derived astroglia into dorsal roots.[11] Loss and dysfunction of DRG neurons cause a great paucity of myelinated nerve

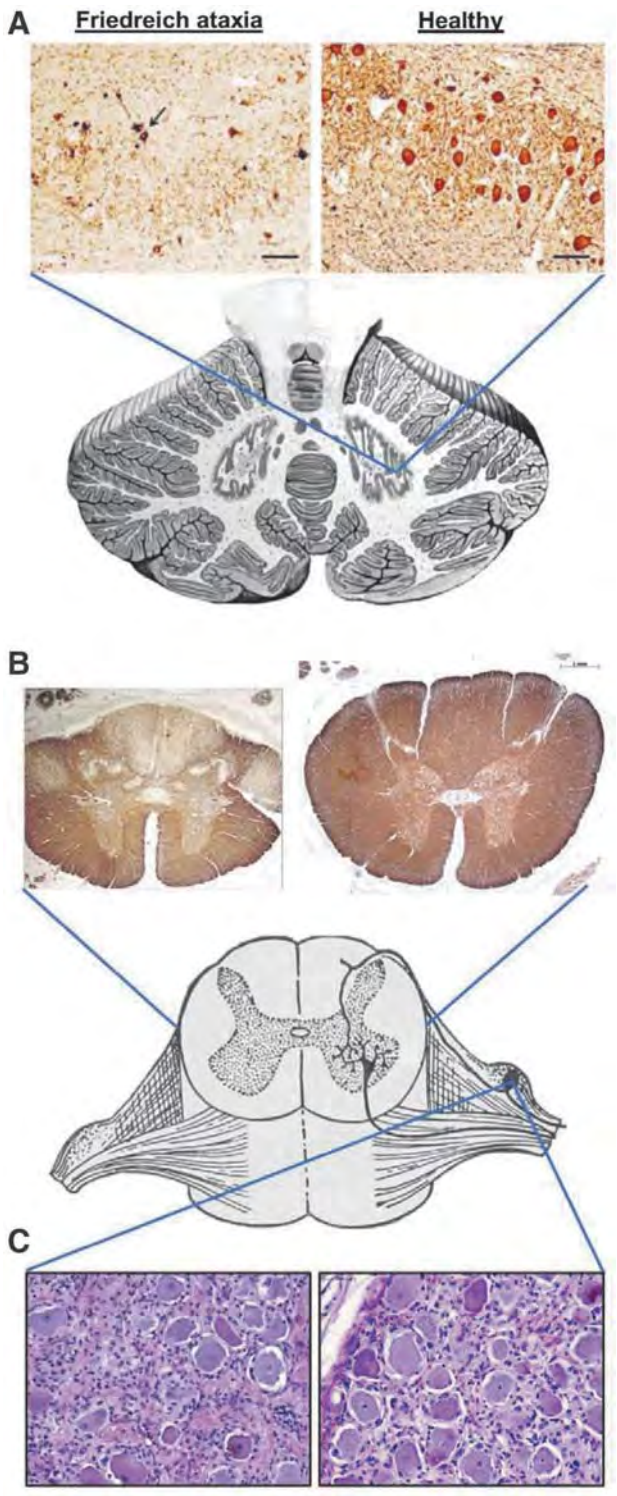

Figure 1. Key neuropathological features of Friedreich ataxia. **(A)** Dentate nucleus stained for neurons (neuron-specific enolase), showing loss of large glutaminergic neurons. The arrow indicates surviving small neurons. Reproduced with permission from Koeppen AH *et al.*(**B**) Spinal cord cross-sections stained for myelin (myelin basic protein), showing pronounced lack of myelin in the dorsal columns, dorsal spinocerebellar, and corticospinal tracts. **(C)** Dorsal root ganglion stained with hematoxylin and eosin (nuclei in dark purple and cytoplasm in pink). A reduction in the average size and number of neurons (large cells) and proliferation of satellite cells and monocytes (other nuclei) is evident.

fibers in the dorsal roots. Lack of large myelinated nerve fibers in sensory peripheral nerves is the hallmark of the sensory neuropathy in FRDA, and the proposed cause is failure of trophic support from DRG neurons.

Hypoplasia of DRG neurons also has multiple effects on fibers in the spinal cord, notably the development of the dorsal columns. During normal development, DRG are the source of most myelinated fibers in the dorsal columns that travel the long distance to secondary neurons in gracile and cuneate nuclei in the medulla oblongata. At the spinal level, short dorsal root collaterals also reach neurons in the dorsal nuclei of the thoracic and upper lumbar spinal cord. Proper development of these connections allows growth and survival of the large neurons of the dorsal nuclei. When these collaterals are sparse or absent, neurons in the dorsal nuclei undergo transneuronal degeneration, or more correctly, developmental failure.[12] The timing of such deafferentation in FRDA, however, is unknown. Autopsy data from two very young patients with FRDA showed that the neurons in the dorsal nuclei were greatly reduced in number or entirely absent.[13] It is likely that these normally rather large nerve cells failed to survive due to lack of innervation from dorsal root collaterals that normally occurs between 14 and 17 weeks of gestation.[10] Axons of the dorsal nuclei that travel in the ipsilateral dorsal spinocerebellar tracts therefore do not develop properly, and the combined lack of fibers in the dorsal columns and dorsal spinocerebellar tracts is a key neuropathological observation in all cases of FRDA (Fig. 1B).[11] Transneuronal atrophy also affects the gracile and cuneate nuclei because they lose their input from the gracile and cuneate fasciculi in the spinal cord.

As described above, changes in the spinal cord include a lack of large nerve cells in the dorsal nuclei at thoracic and upper lumbar levels. Motor neurons of the spinal cord, however, are not seriously affected by FRDA. The classical finding of loss of deep tendon reflexes in most patients with FRDA can be attributed to pathology in the sensory arm of the monosynaptic stretch reflex arc, although other sites may also mediate the early absence of reflexes. Some patients with the disease have fibrillations on electromyograms as well as electrodiagnostic evidence that muscles undergo chronic denervation.[14] Therefore, a ventral root lesion is not unexpected. Although older studies concluded that ventral (motor) roots in FRDA are normal, histograms of the anterior roots in 15 FRDA patients showed a mild shift to smaller axons, possibly representing modest anterior horn disease.[15,16]

Spinal cord changes evident on MRI include reduced volume, low cross-sectional area, and increased eccentricity (flattening), observed at all vertebral levels, with strongest effects in upper cervical and upper thoracic sections.[17–19] Changes in spinal cord morphometry are an early disease feature. One MRI study reported, in young ambulatory patients (10–35 years old; average 5.6 years

from symptom onset), a baseline decrease in spinal cord white matter integrity and thickness at the cervical level relative to controls and significant declines over 1- and 2-year longitudinal follow-ups,[20,21] implying that both atrophy and hypoplasia contribute to the smaller diameter spinal cord seen in autopsy tissues.

In terms of clinicoanatomic correlation, the lack of fibers in the dorsal columns is presumed to cause the profound deficit of joint position sense and vibratory sense in the extremities of patients with FRDA. Sensory neuropathy correlates well with the advanced changes in sensory nerves that are evident on sural nerve biopsies and autopsies.

Cerebellar system

Atrophy of DN of the cerebellum is a significant contributor to the neurological phenotype of FRDA (Fig. 1A). Clinical, neuropathological, imaging, and neurophysiological data support this concept.

Clinically, the pattern of progression of neurological impairment in FRDA shows that the perceived onset of neurological symptoms corresponds to the appearance of cerebellar ataxia, affecting gait before stance, speech, and limb coordination.[22–24] Even though proprioceptive ataxia usually precedes the appearance of cerebellar symptoms, as shown by a Romberg sign in almost all patients at the time of diagnosis,[25] it is usually mild and effectively compensated by visual control. Gait and stance worsen until patients lose the ability to walk. However, some degree of upper limb dysmetria is almost always present in recently diagnosed patients, as shown by clinical rating scales and functional tests.[22,24–26] Dysarthria may be initially absent, but most patients become dysarthric within a few years after diagnosis.[22,23,27] Upper limb dysmetria, dysarthria, and eventually dysphagia continue to worsen in all patients, contributing to increasing disability in the late stages of the disease. FRDA patients only show limited eye movement abnormalities that can be directly attributed to cerebellar pathology. Gaze-evoked nystagmus is not a feature of FRDA, despite older reports to the contrary. Instead, FRDA patients almost invariably show fixation instability with square-wave jerks (SWJs). SWJs are present in normal subjects, but their frequency and amplitude are higher in FRDA patients, often present at or appearing early after diagnosis with a tendency to worsen with time. SWJs may reflect a temporary lapse in inhibitory control of omnipause cells over saccadic burst neurons in the brain stem, which can be the consequence of cortical, basal ganglia, brainstem, or cerebellar pathology.[28] Dysmetria of saccades occurs in patients with more advanced disease. Cerebellar pathology also leads to a specific profile of cognitive dysfunction called cerebellar cognitive affective syndrome (CCAS),[29] defined by altered executive function, visuospatial cognition, emotion–affect, and language, above and beyond speech. Although cognitive disorders in FRDA are relatively subtle and less prominent than in other ataxias, and do not cause obvious functional impairment, evidence has accumulated that FRDA patients show features of CCAS,[30] the severity of which correlates with cerebellar impairment.[31]

Two additional remarks need to be made about cerebellar signs and symptoms in an FRDA patient. First, some cerebellar signs and symptoms, in particular kinetic or ''intentional'' tremor, are absent or minimal in many or most individuals with FRDA. Second, parallel corticospinal tract involvement clouds the assessment of cerebellar dysfunction in FRDA, more so in advanced disease. While early loss of ambulation more likely reflects ataxia rather than weakness or spasticity, items included in the ataxia rating scales utilized in FRDA clinical studies, such as the SARA[32,33] and the mFARS,[25,34] to assess upper limb coordination are particularly affected by weakness and slowness of movements of pyramidal origin.

Taken together, clinical data indicate progressive loss of cerebellar function in FRDA, with limited ability to pinpoint the specific sites that are affected. Early impairment of balance and gait suggests involvement of spinocerebellar tracts. Dysarthria and upper limb dysmetria point to more global cerebellar dysfunction, but do not allow distinction between cortical and DN pathology. However, the concomitant progression of cerebellar ataxia and CCAS in FRDA[31] contrasts with the dichotomy between cerebellar motor and nonmotor symptoms reported in other cerebellar pathologies where functional and anatomical studies point to a segregation between the cerebellar anterior lobe, responsible for motor functions, and the cerebellar posterior lobe, responsible for cognitive processes. These findings point to involvement of the DN, the axons of which form the dentatothalamic pathway connecting the cerebellum with many neocortical areas, affecting motor control as well as perceptual and cognitive processes.

Neuropathology confirms and aids in defining the temporal and anatomical details of cerebellar involvement in FRDA. Atrophy of the DN and its efferent myelinated dentatothalamic fibers in the superior cerebellar peduncle is a hallmark of FRDA cerebellar pathology. Importantly, DN atrophy becomes more severe as disease progresses, regardless of age of onset or length of the GAA repeat expansions,[35] confirming its progressive nature. The DN is probably entirely normal before onset of the disease, but becomes atrophied soon after the appearance of cerebellar ataxia.[15] The other nuclei, in particular the fastigial nucleus, do not appear to be affected. The DN shows loss of large glutamatergic neurons, while small, GABAergic neurons projecting to the inferior olives are preserved. Furthermore, the inferior olive in FRDA appears normal, containing normal glutamatergic (VGlutT1 and VGluT2 positive) afferents as well. Small intrinsic inhibitory GABAergic and glycinergic interneurons in the DN are also preserved, but postsynaptic contacts in the surviving large neurons are abnormal, showing loss of gephyrin and

failure to correctly position GABA and glycine receptors.[35] There is some loss of glutamatergic afferents in the DN, possibly due to loss of spinocerebellar tract and olivocerebellar (climbing) fibers that send collaterals to the DN. The cerebellar cortex is overall preserved in FRDA,[36] with normal parallel and climbing fiber contacts to Purkinje cells and no evident change in the intrinsic circuitry, although mild cerebellar cortical atrophy occurs in advanced disease. Axonal terminals of Purkinje cells, however, in the DN are abnormal, showing a characteristic abnormality called ''grumose degeneration,'' possibly as a consequence of the loss of their synaptic targets, which is also found in other conditions such as spinocerebellar ataxia type 3 and progressive supranuclear palsy. Overall, neuropathology demonstrates the progressive, degenerative nature of cerebellar pathology in FRDA as well as the severe loss of large projection neurons in the DN, confirming that they constitute a major cellular target for frataxin-restoring therapies.

Neuroimaging of the cerebellum in FRDA shows macrostructural and microstructural changes, as well as metabolic abnormalities. Overall, cerebellar atrophy is not a major feature of FRDA; some MRI studies demonstrate a mild, but significant reduction of the total cerebellar volume,[37–39] while others fail to detect any significant difference from controls.[40] There is also limited consensus on the most affected cerebellar lobules, some studies showing a wider distribution of gray matter loss to lobules V, VI, and VIII, as well as in the crus of cerebellum, posterior lobe of the vermis, in the flocculi, and in the tonsil,[38,41] others localizing it mostly to lobule IX[37] or lobule VI.[39] Atrophy of the DN is clearly detected[40,42] and progresses with disease duration.[43] Progressively increased iron content in the DN, which is physiologically iron rich, is also reported[43–46] and thought to reflect altered iron metabolism due to frataxin deficiency. However, other iron-rich brain structures are not or marginally affected in FRDA, so elevated normal iron content does not explain the DN-specific vulnerability. On the microstructural level, changes in fractional anisotropy by diffusion MRI are consistently detected in the deep cerebellar white matter and in the dentatothalamic tracts,[39,40,47–50] which appear to correlate with ataxia severity. Correspondingly, several studies detected impaired cerebellocerebral connectivity,[17,51–53] which is essentially due to atrophy of dentatothalamic fibers. Overall, imaging confirms the presence and progression of cerebellar pathology in FRDA, mostly, but not exclusively, affecting the DN, and the consequent impairment in structural and functional connectivity.

There are limited neurophysiology data supporting cerebellar dysfunction in FRDA, as this is not a functionality that is routinely explored with these techniques. Some evidence of cerebellar involvement comes from a MEG study showing impaired cortical mismatch positivity after unexpected touch stimuli in FRDA patients, a physiological correlate of change detection thought to depend on cerebellar processing of sensory information.[54] This abnormality is more severe with earlier age of onset and longer GAA repeats and does not seem to change with disease duration, suggesting that it is due to spinocerebellar tract pathology, which, as discussed in the spinal cord section, is likely to be developmental.

FRDA mouse models carrying expanded GAA repeats or systemic frataxin knockdown by RNAi also show behavioral, anatomical, and molecular evidence of cerebellar abnormalities.[8,55–58] Some parallels between such models exist at the cellular level; for example, DN pathology in $Fxn^{(GAA)230/-}$ (KIKO) mice shows loss of glutamatergic, but not GABAergic cells, matching human FRDA.[56] Although providing evidence of overall vulnerability of the cerebellum to frataxin deficiency, none of these models fully recapitulates the specific pattern of cerebellar pathology in humans.

Overall, the above presented data firmly establish the cerebellum as a target for frataxin-restoring treatments. At the cellular level, large glutamatergic projecting neurons in the DN appear to be the main target, as they are the only cell type that becomes significantly depleted. The reason for such specific vulnerability is not yet known; in particular, the connection with atrophy of the spinocerebellar tracts, the only affected afferent pathway to the cerebellum in FRDA, is unknown. Clinical features that may benefit from such treatment include truncal and limb ataxia, dysarthria, and possibly the CCAS, all major components of the neurological impairment in FRDA.

Corticospinal system

The primary motor system arises in the projection neurons in the lower levels of the cerebral cortex (layers V and VI, including the large so-called Betz cells). It projects through the internal capsule, cerebral peduncles, longitudinal fibers of the pons, pyramid, and its decussation to the lateral corticospinal tract. It synapses on the alpha motor neurons of the ventral horn that project directly to muscle.

While this is the primary motor pathway, the constituents at each of the levels of named structure are not identical. For example, a large portion of the corticospinal tract eventually synapses in the dorsal horn (controlling afferent information), and many other fibers in the internal capsule and cerebral peduncle are destined to synapse in the midbrain, pons, or medulla on cranial nerve nuclei and nuclei such as the red nucleus, pontine nuclei, or inferior olivary nucleus. Thus, relative levels of atrophy in different white matter structures could vary.

The motor and premotor cortices also show changes over the course of the disease. Evidence in FRDA for a progressive loss of the corticospinal tract and the associated cell bodies (including Betz cells) in the primary motor cortex is supported by multiple sources of data. Clinically,

this manifests with Babinski signs frequently at initial presentation.[59] In later disease, corticospinal dysfunction is present as spasticity and weakness,[60] which become prominent particularly after loss of ambulation. However, because of coexistent sensory changes, individuals are usually not hyperreflexic, even in late-onset FRDA. In such late-onset FRDA patients with retained reflexes, there is typically minimal sensory loss and progressive hyperreflexia. Some early-onset individuals have retained or increased reflexes that become more prominent over time. Another clinical consequence of corticospinal tract degeneration is the slowness of movements that develops with FRDA progression. Analysis of repetitive movements in FRDA patients shows progressive slowing, but no loss of regularity, indicating corticospinal rather than cerebellar pathology as the underlying cause (M. Pandolfo, unpublished observations). The clinical evidence suggests progression of corticospinal tract and motor cortex disease from presentation through all stages of disease.

The loss of corticospinal tracts and the relevant cell bodies in the motor cortex is supported by pathological results. There is a reduction of the size of the medullary pyramid and paucity of myelinated fibers and marked atrophy of the corticospinal tract at the level of the thoracic spinal cord. The neuropathological phenotype also includes hypoplasia or atrophy of Betz cells.[10] It is uncertain, however, how upper motor neuron loss correlates with progressive atrophy of the corticospinal tracts. Betz cells account for only a small minority of fibers in the corticospinal tracts.[10] The remainder arise from other pyramidal cells of the lower layers (V and VI) of the motor cortex. Some cell loss in this area is suggested by MRI studies that have shown cortical thinning in adult patients at the left central sulcus.[18,41,61] Prefrontal and premotor areas, however, appear to be anatomically spared in FRDA, except perhaps late in the disease. Compensatory activity in these regions has been reported in functional neuroimaging studies of motor and cognitive behavior,[39,62] indicating the potential for adaptive mechanisms to play a role in disease mitigation or expression. Finally, upper motor neurons degenerate to at least some degree in several mouse models of FRDA, although this has not been studied to a major degree.[56,63]

Physiological testing in humans with FRDA also implicates loss of the corticospinal motor pathways. Motor evoked potentials (MEPs), requiring functional integrity of the motor pathways to skeletal muscle, are delayed, prolonged, and of decreased amplitude, worsening over time.[64–67] Based on more recent studies including children, some MEP abnormalities may predate clinical presentation.[68]

How meaningful is the damage to descending motor pathways? While all data suggest that descending pathways are mildly affected at presentation and worsen over time, their exact clinical importance is difficult to assess due to pre-existing sensory abnormalities (which may both cover and in other situations magnify the loss of motor systems) and the parallel loss of the DN and other sites. Still, in mid- to late-stage individuals, progressive spasticity, weakness, and bradykinesia due to damage of the corticospinal tracts are clinically meaningful changes, making this system a target for intervention in FRDA.

Visual and auditory

Defects in the visual pathways are common in individuals with FRDA. Clinical visual loss typically appears in more advanced individuals,[69] but rare patients present with a subacute visual loss resembling Leber hereditary optic neuropathy. Visual dysfunction in such individuals can be quite severe, progressing to blindness in some. Abnormalities have been reported across both the anterior and posterior divisions of the primary visual system. The anterior system is formed by the retinal ganglion cells (RGCs) of the eye, which project to the lateral geniculate nuclei (LGN) of the thalamus through the optic nerves and tracts. The posterior division comprises neurons of the LGN that innervate the primary visual cortex through the optic radiation. Visual information subsequently cascades to other cortical areas.

Of remarkable interest is the neuronal loss in the retina. Histological assessment of six eyes obtained by autopsy revealed variable degrees of loss of RGCs, thinning of the retinal nerve fiber layer, and optic nerve atrophy. The severity of optic nerve atrophy and RGC loss has been previously reported to correlate with age of onset,[70] although this has not been consistently observed (A. Koeppen, unpublished observations). *In vivo* optical coherence tomography has confirmed thinning of the retinal nerve fiber layer.[70]

Anterior (optic tract) and posterior tracts (optic radiations) are also impacted in the disease. Using clinical, neurophysiological, and neuroimaging techniques, an observational study described a slowly progressing degenerative phenotype involving fiber loss in both the optic tract, resulting from loss of RGCs and the optic radiations. These defects correlate with impaired visual evoked potentials and the severity of ataxia.[71] Involvement of the anterior and posterior visual pathways in FRDA may be independent and asynchronous.[71] Focal gray matter atrophy has also been reported in the extrastriate cortices.[41,61] White matter macrostructural and microstructural impairments occur in the posterior forceps, including the splenium of the corpus callosum.[50,72]

Regarding the auditory system, FRDA patients commonly experience impaired speech understanding in the presence of background noise,[73,74] although hearing loss presents only in a minority of FRDA patients ($\sim$10%).[75] The auditory system consists of the spiral ganglia in the inner ear giving rise to the cochlear nerves, which

innervate the cochlear nuclei in the brainstem. Auditory signals then ascend through the lateral lemniscus to the inferior colliculus (midbrain), with a subset of axons synapsing in the superior olive (pons), before reaching the medial geniculate nuclei (MGN) of the thalamus. Finally, the MGN projects to the primary auditory cortex.

Electrophysiological evidence consistent with axonopathy in the cochlear nerve and auditory brainstem is common in individuals with FRDA, including delayed or blunted auditory brainstem responses.[54,76–78] Finally, increased latency of auditory evoked potentials has also been reported,[77,78] and gray matter atrophy of the primary auditory cortex (Heschl's gyrus and planum temporale) has been observed.[61]

Thus, multiple sites within the visual and auditory pathways may represent targets for therapy in advanced stage patients with potential for significant impact on quality of life.

Autonomic

FRDA patients often report autonomic dysfunction in multiple domains, more commonly in advanced disease. Bladder dysfunction, the symptoms of which include frequency and urgency, up to incontinence, is common with disease progression. It is likely due to degeneration of descending fibers traveling with the corticospinal tract. Nonambulatory patients frequently complain of cold, purple legs and feet, which may be a nonspecific autonomic dysfunction. One study reported sudomotor dysfunction attributed to loss of small cholinergic postganglionic fibers.[79] Increased heart rate at rest and during orthostatic challenge is the most common autonomic abnormality in FRDA patients.[80] Cardiovascular dysfunction, however, is primarily due to heart disease rather than dysautonomia.

Conceivably, therapies able to restore frataxin in the cortex and descending fiber systems may also positively affect bladder function. There is no other specific CNS therapeutic target for autonomic dysfunction in FRDA.

NON-NEURONAL AFFECTED CELL TYPES IN FRDA

Glial abnormalities also feature prominently in the neural phenotype of FRDA.[15] Proliferation of reactive microglia and astrogliosis in the dentate nuclei and infiltration of peripheral monocytes and hyperplasia of satellite cells in DRG are observed.[81–84] These glial responses reflect not only a secondary reaction to neuronal necrosis but also frataxin knockdown that has been shown to result in direct microglial activation and astrocyte pathology, producing a cytotoxic environment.[9,85–88] However, KO of frataxin in astrocytes leads to a neuroanatomical pattern distinct from human FRDA.[9] Microglial activation and inflammation have been detected in mouse models as well as in affected human structures such as the DRGs. Cell line and animal studies indicate that blocking maladaptive glial responses, and thereby reducing chronic proinflammatory secretion and oxidative stress, may mitigate non-cell autonomous neuronal death in FRDA. Interestingly, there is also some preliminary evidence of a beneficial effect of restoring frataxin in microglia.[82]

Myelinating glial cells are also implicated in FRDA. Schwann cell loss results in the progressive myelin deficit and impaired myelin repair in the dorsal roots and sensory nerves, independent of axonal degeneration.[16,89] Reduced myelination of the corticospinal tract has also been reported. These results are consistent with neuroimaging evidence of microstructural irregularities in the cerebellar peduncles, corticospinal tract, and brainstem white matter that occur independent of macrostructural atrophy.[50] In addition, reductions in white matter have been noted in the fornix, posterior thalamic radiation, forceps, inferior fronto-occipital fasciculus and inferior longitudinal fasciculus, corpus callosum, corona radiate, and corticospinal tracts.[50]

Taken together, although the pathology of FRDA is primarily neuronal, glial cells likely have important roles in non-cell autonomous mechanisms of neuronal atrophy, and other modulating or subordinate contributions to disease progression.

CONCLUSIONS

The pathogenesis of FRDA is complex. While the early loss of proprioceptive afferents remains a characteristic aspect of the pathology of FRDA, other areas such as the DN, the corticospinal system, and other nuclei do atrophy and play important roles in the neurological features of the disorder. Developing new therapies, including gene therapy, must consider this complexity, including not only which systems are affected but also *when* they become affected, and whether and when they are receptive to specific therapies, and the ability of affected areas to be physically targeted by therapy (Tables 1 and 2). The proprioceptive system, usually considered a major target for frataxin-restoring treatments, shows substantial evidence of hypoplasia and/or early developmental loss, with minimal evidence of progression over time. It seems likely that this system is not an ideal target for therapies given after early childhood. Targeting the DN of the cerebellum is likely to be most effective early in the course of the disease, when it is functionally affected, but still shows limited atrophy. The corticospinal tract degenerates over time contributing to disease progression throughout its late stages and may be considered a target. Choice of the target from the proprioceptive system, DN, corticospinal system, or other nuclei depends on the patient age, desired goal, and practical considerations of any therapy. In any case, it is very clear that for any frataxin-restoring treatment to successfully mitigate the neurological symptoms of FRDA, it must target structures that are beyond the BBB,

Table 1. *Summary of evidence reviewed in this study to identify affected structures and therapeutic targets in Friedreich ataxia*

Structure (Cell Type)	*Evidence from Autopsy*	*Evidence from Imaging*	*Evidence from Neurophysiology*	*Clinical Evidence*	*Evidence from Mouse Models*	*Potential Clinical Impact of Successful Therapy*	*Potential Biological Outcome Measures*
Dentate nucleus (glutamatergic neurons; astrocytes; microglia)	Yes	Yes	Indirect	Yes	Yes	Speech, motor, cognition, swallowing, gait	sMRI: Volume, iron dMRI: Efferent pathway (superior cerebellar peduncle) integrity
Cerebellar cortex (Purkinje and granular cells)	No	Yes	Indirect	No	Yes	motor/gait	aMRI: Volume TMS: Cerebellar brain inhibition
Motor/premotor cortex (pyramidal and Betz neurons)	Yes	Yes	Yes	Yes	Yes	Motor/gait	aMRI: Cortical thickness dMRI: Efferent pathway (corticospinal) integrity TMS: MEP
Premotor/prefrontal cortices		Yes		Yes		Cognition and motor (motor planning/ structuring)	aMRI: Cortical thickness TMS: MEP
Dorsal root ganglia	Yes		Yes	Yes	Yes	Proprioception, neuropathy, mechanoreceptors	EEG: SSEP Nerve conduction: SNAP
Spinal cord (dorsal columns, corticospinal tracts, dorsal spinocerebellar tracts, dorsal nuclei)	Yes	Yes	Indirect	Pathway only		Motor/gait, proprioception	aMRI: Cross-sectional area dMRI: dorsal pathway integrity MRS: NAA, myo-inositol EEG: SSEP
Retina (Ganglion cells)		Yes	Yes	Yes	Yes	Vision	OCT: retinal thickness EEG: VEP
Visual pathways		Yes					EEG: VEP
Auditory pathway	No; labyrinth yes	No	Yes	Yes	Not evaluated	Hearing	EEG: AEP

AEP, auditory evoked potential; aMRI, anatomical magnetic resonance imaging (T1/T2 weighted); dMRI, diffusion-weighted MRI; EEG, electroencephalogram; MEP, motor evoked potential; MRS, magnetic resonance spectroscopy; OCT, optical coherence tomography; sMRI, susceptibility-weighted MRI (including quantitative susceptibility mapping); SNAP, sensory nerve action potential; SSEP, somatosensory evoked potential; TMS, transcranial magnetic stimulation; VEP, visual evoked potential.

either by using therapeutics that are able to cross into the CNS after systemic administration or by direct dosing into the brain parenchyma or in CSF.

There remain key questions in defining target selection:

1. Most of the temporal changes have been characterized only generally. In the future, one must be able to connect pathological events more directly with clinical features.
2. This review focuses on results from different approaches in a qualitative manner. Future work must establish the relative sensitivity and temporal course of pathological, radiological, physiological, and clinical events.
3. These findings must also be used to establish the relative importance of each area in the disease phenotype, in isolation or as a component of the complete FRDA phenotype. This will allow any therapy to have a rational expectation of potential benefit when specific anatomical areas are targeted.

Table 2. *Summary of evidence reviewed in the present study to identify additional affected structures in Friedreich ataxia*

Structure	*Evidence from Autopsy*	*Evidence from Imaging*	*Evidence from Neurophysiology*	*Clinical Evidence*	*Evidence from Mouse Models*	*Potential Clinical Impact of Successful Therapy*	*Potential Biological Outcome Measures*
Thalamus	Yes	Yes	Pathway	Pathway	No	Motor/gait, cognitive, vision (LGN)	aMRI: Volume
Red nucleus	Limited	Yes	No	No	No	Motor/gait	aMRI/sMRI: Volume, iron
Brain stem and pontine nuclei	Gracile and cuneate nuclei Yes	Yes	Yes	Pathway (sensory)	No	Motor/gait, defective corneal innervation	
Spinal cord Anterior horn neurons	Yes; limited	No		Amyotrophy		Not a target. Possible evidence of late involvement	

LGN, lateral geniculate nuclei.

Overall, much has been learned about the neuropathology of FRDA. Future work should facilitate the translation of novel therapies into practice.

ACKNOWLEDGMENTS

We thank Patrick Ritschel, Jennifer Farmer, Dr. Barbara Tate, and Dr. Elisabetta Soragni of FARA for comments and assistance in preparing the article.

AUTHORS' CONTRIBUTIONS

I.H.H., D.R.L., A.H.K., and M.P. wrote the first draft and reviewed the article.

AUTHOR DISCLOSURE

No competing financial interests exist.

FUNDING INFORMATION

I.H.H. is supported by the Australian National Health and Medical Research Council (Fellowship 1106533 and Grant 1184403), Friedreich Ataxia Research Alliance (FARA), and Friedreich Ataxia Research Association (FARA Australia). D.R.L. is supported by the NIH, FDA, FARA, MDA, Reata Pharmaceutical, and Retrotope Pharmaceutical. A.H.K. is supported by FARA and M.P. is supported by FARA and FNRS (Fonds National de la Recherche Scientifique, Belgium).

REFERENCES

1. Pandolfo M. Friedreich ataxia: the clinical picture. J Neurol 2009;256 Suppl 1:3–8.
2. Cook A, Giunti P. Friedreich's ataxia: clinical features, pathogenesis and management. Br Med Bull 2017;124:19–30.
3. Campuzano V, Montermini L, Molto MD, et al. Friedreich's ataxia: autosomal recessive disease caused by an intronic GAA triplet repeat expansion. Science 1996;271:1423–1427.
4. Yandim C, Natisvili T, Festenstein R. Gene regulation and epigenetics in Friedreich's ataxia. J Neurochem 2013;126 Suppl 1:21–42.
5. Schmucker S, Martelli A, Colin F, et al. Mammalian frataxin: an essential function for cellular viability through an interaction with a preformed ISCU/NFS1/ISD11 iron-sulfur assembly complex. PLoS One 2011;6:e16199.
6. Martelli A, Schmucker S, Reutenauer L, et al. Iron regulatory protein 1 sustains mitochondrial iron loading and function in frataxin deficiency. Cell Metab 2015;21:311–323.
7. Marmolino D, Manto M, Acquaviva F, et al. PGC-1alpha down-regulation affects the antioxidant response in Friedreich's ataxia. PLoS One 2010;5: e10025.
8. Lin H, Magrane J, Rattelle A, et al. Early cerebellar deficits in mitochondrial biogenesis and respiratory chain complexes in the KIKO mouse model of Friedreich ataxia. Dis Model Mech 2017; 10:1343–1352.
9. Franco C, Genis L, Navarro JA, et al. A role for astrocytes in cerebellar deficits in frataxin deficiency: protection by insulin-like growth factor I. Mol Cell Neurosci 2017;80:100–110.
10. Koeppen AH, Becker AB, Qian J, et al. Friedreich ataxia: hypoplasia of spinal cord and dorsal root ganglia. J Neuropathol Exp Neurol 2017;76:101–108.
11. Koeppen AH, Becker AB, Qian J, et al. Friedreich ataxia: developmental failure of the dorsal root entry zone. J Neuropathol Exp Neurol 2017;76: 969–977.
12. Stavraky GW, Drake CG. An extension of the law of denervation to afferent neurones. Fed Proc 1947;6(1 Pt 2):211.
13. Quercia N, Somers GR, Halliday W, et al. Friedreich ataxia presenting as sudden cardiac death in childhood: clinical, genetic and pathological correlation, with implications for genetic testing and counselling. Neuromuscul Disord 2010;20:340–342.
14. Caruso G, Santoro L, Perretti A, et al. Friedreich's ataxia: electrophysiological and histological findings. Acta Neurol Scand 1983;67:26–40.
15. Koeppen AH, Mazurkiewicz JE. Friedreich ataxia: neuropathology revised. J Neuropathol Exp Neurol 2013;72:78–90.
16. Koeppen AH, Morral JA, Davis AN, et al. The dorsal root ganglion in Friedreich's ataxia. Acta Neuropathol 2009;118:763–776.
17. Dogan I, Romanzetti S, Didszun C, et al. Structural characteristics of the central nervous system in Friedreich ataxia: an in vivo spinal cord and brain MRI study. J Neurol Neurosurg Psychiatry 2019; 90:615–617.
18. Rezende TJR, Martinez ARM, Faber I, et al. Developmental and neurodegenerative damage in Friedreich's ataxia. Eur J Neurol 2019;26:483–489.
19. Chevis CF, da Silva CB, D'Abreu A, et al. Spinal cord atrophy correlates with disability in Friedreich's ataxia. Cerebellum 2013;12:43–47.
20. Pierre-Gilles Henry JJ, Deelchand D,Eberly L, et al. MRI and DTI in the spinal cord in Friedreich's Ataxia: 24-month follow-up. 2017 International Ataxia Research Conference, Pisa, Italy, 2017.
21. Christophe Lenglet JJ, Deelchand D, Eberly V, et al. MRI and DTI in the spinal cord in Friedreich's Ataxia: 36-month Follow-up. 2018 FARA Meeting on Biomarkers and Outcome Measures, Tampa, FL, 2018.
22. Pandolfo M. Neurologic outcomes in Friedreich ataxia: study of a single-site cohort. Neurol Genet 2020;6:e415.
23. Parkinson MH, Boesch S, Nachbauer W, et al. Clinical features of Friedreich's ataxia: classical and atypical phenotypes. J Neurochem 2013;126 Suppl 1:103–117.
24. Patel M, Isaacs CJ, Seyer L, et al. Progression of Friedreich ataxia: quantitative characterization over 5 years. Ann Clin Transl Neurol 2016;3:684–694.
25. Rummey C, Corben LA, Delatycki MB, et al. Psychometric properties of the Friedreich Ataxia Rating Scale. Neurol Genet 2019;5):371.
26. Reetz K, Dogan I, Hilgers RD, et al. Progression characteristics of the European Friedreich's Ataxia Consortium for Translational Studies (EFACTS): a 2 year cohort study. Lancet Neurol 2016;15):1346–1354.
27. Harding AE. Friedreich's ataxia: a clinical and genetic study of 90 families with an analysis of early diagnostic criteria and intrafamilial clustering of clinical features. Brain 1981;104: 589–620.
28. Lemos J, Eggenberger E. Saccadic intrusions: review and update. Curr Opin Neurol 2013;26: 59–66.
29. Schmahmann JD, Sherman JC. The cerebellar cognitive affective syndrome. Brain 1998;121 (Pt 4):561–579.
30. Selvadurai LP, Harding IH, Corben LA, et al. Cerebral abnormalities in Friedreich ataxia: a review. Neurosci Biobehav Rev 2018;84:394–406.

31. Naeije G, Rai M, Allaerts N, eta l. Cerebellar cognitive disorder parallels cerebellar motor symptoms in Friedreich ataxia. Ann Clin Transl Neurol 2020;7:1050–1054.

32. Schmitz-Hubsch T, du Montcel ST, Baliko L, et al. Scale for the assessment and rating of ataxia: development of a new clinical scale. Neurology 2006;66:1717–1720.

33. Reetz K, Dogan I, Costa AS, et al. Biological and clinical characteristics of the European Friedreich's Ataxia Consortium for Translational Studies (EFACTS) cohort: a cross-sectional analysis of baseline data. Lancet Neurol 2015;14:174–182.

34. Subramony SH, May W, Lynch D, et al. Measuring Friedreich ataxia: interrater reliability of a neurologic rating scale. Neurology 2005;64:1261–1262.

35. Koeppen AH, Ramirez RL, Becker AB, et al. Friedreich ataxia: failure of GABA-ergic and glycinergic synaptic transmission in the dentate nucleus. J Neuropathol Exp Neurol 2015;74: 166–176.

36. Koeppen AH, Davis AN, Morral JA. The cerebellar component of Friedreich's ataxia. Acta Neuropathol 2011;122:323–330.

37. Cocozza S, Costabile T, Pontillo G, et al. Cerebellum and cognition in Friedreich ataxia: a voxel-based morphometry and volumetric MRI study. J Neurol 2020;267:350–358.

38. Vavla M, Arrigoni F, Nordio A, et al. Functional and structural brain damage in Friedreich's Ataxia. Front Neurol 2018;9:747.

39. Dogan I, Tinnemann E, Romanzetti S, et al. Cognition in Friedreich's ataxia: a behavioral and multimodal imaging study. Ann Clin Transl Neurol 2016;3:572–587.

40. Lindig T, Bender B, Kumar VJ, et al. Pattern of cerebellar atrophy in Friedreich's Ataxia-using the SUIT Template. Cerebellum 2019;18:435–447.

41. Selvadurai LP, Harding IH, Corben LA, et al. Cerebral and cerebellar grey matter atrophy in Friedreich ataxia: the IMAGE-FRDA study. J Neurol 2016;263:2215–2223.

42. Harding IH, Raniga P, Delatycki MB, et al. Tissue atrophy and elevated iron concentration in the extrapyramidal motor system in Friedreich ataxia: the IMAGE-FRDA study. J Neurol Neurosurg Psychiatry 2016;87:1261–1263.

43. Ward PGD, Harding IH, Close TG, et al. Longitudinal evaluation of iron concentration and atrophy in the dentate nuclei in friedreich ataxia. Mov Disord 2019;34:335–343.

44. Waldvogel D, van Gelderen P, Hallett M. Increased iron in the dentate nucleus of patients with Friedrich's ataxia. Ann Neurol 1999;46:123–125.

45. Bonilha da Silva C, Bergo FPG, D'Abreu A, et al. Dentate nuclei T2 relaxometry is a reliable neuroimaging marker in Friedreich's ataxia. Eur J Neurol 2014;21:1131–1136.

46. Boddaert N, Le Quan Sang KH, Rotig A, et al. Selective iron chelation in Friedreich ataxia: biologic and clinical implications. Blood 2007;110: 401–408.

47. Mascalchi M, Toschi N, Giannelli M, et al. Regional cerebral disease progression in Friedreich's Ataxia: a Longitudinal Diffusion Tensor Imaging Study. J Neuroimaging 2016;26:197–200.

48. Vieira Karuta SC, Raskin S, de Carvalho Neto A, et al. Diffusion tensor imaging and tract-based spatial statistics analysis in Friedreich's ataxia patients. Parkinsonism Relat Disord 2015;21:504–508.

49. Akhlaghi H, Corben L, Georgiou-Karistianis N, et al. Superior cerebellar peduncle atrophy in Friedreich's ataxia correlates with disease symptoms. Cerebellum 2011;10:81–87.

50. Selvadurai LP, Corben LA, Delatycki MB, et al. Multiple mechanisms underpin cerebral and cerebellar white matter deficits in Friedreich ataxia: the IMAGE-FRDA study. Hum Brain Mapp 2020; 41:1920–1933.

51. Cocozza S, Costabile T, Tedeschi E, et al. Cognitive and functional connectivity alterations in Friedreich's ataxia. Ann Clin Transl Neurol 2018;5: 677–686.

52. Zalesky A, Akhlaghi H, Corben LA, et al. Cerebello-cerebral connectivity deficits in Friedreich ataxia. Brain Struct Funct 2014;219: 969–981.

53. Harding IH, Corben LA, Storey E, et al. Frontocerebellar dysfunction and dysconnectivity underlying cognition in friedreich ataxia: the IMAGE-FRDA study. Hum Brain Mapp 2016;37: 338–350.

54. Naeije G, Wens V, Bourguignon M, et al. Altered neocortical tactile but preserved auditory early change detection responses in Friedreich ataxia. Clin Neurophysiol 2019;130):1299–1310.

55. Abeti R, Brown AF, Maiolino M, et al. Calcium deregulation: novel insights to understand Friedreich's ataxia pathophysiology. Front Cell Neurosci 2018;12:264.

56. Lin H, Magrane J, Clark EM, et al. Early VGLUT1-specific parallel fiber synaptic deficits and dysregulated cerebellar circuit in the KIKO mouse model of Friedreich ataxia. Dis Model Mech 2017; 10:1529–1538.

57. McMackin MZ, Henderson CK, Cortopassi GA. Neurobehavioral deficits in the KIKO mouse model of Friedreich's ataxia. Behav Brain Res 2017;316: 183–188.

58. Chandran V, Gao K, Swarup V, et al. Inducible and reversible phenotypes in a novel mouse model of Friedreich's Ataxia. Elife 2017;6:e30054.

59. Harding AE. Early onset cerebellar ataxia with retained tendon reflexes: a clinical and genetic study of a disorder distinct from Friedreich's ataxia. J Neurol Neurosurg Psychiatry 1981;44: 503–508.

60. Milne SC, Corben LA, Yiu E, et al. Gastrocnemius and soleus spasticity and muscle length in Friedreich's ataxia. J Clin Neurosci 2016;29:29–34.

61. Harding I. Brain atrophy in Friedreich ataxia preferentially manifests in cerebellar and cerebral motor areas: Results from the ENIGMA-Ataxia consortium. 2019 International Ataxia Research Conference, Washington, DC, 2019.

62. Harding IH, Corben LA, Delatycki MB, et al. Cerebral compensation during motor function in Friedreich ataxia: the IMAGE-FRDA study. Mov Disord 2017;32:1221–1229.

63. Mercado-Ayon E, Warren N, Lynch D, Lin, H. Knockdown of frataxin leads to mitochondrial fragmentation and cerebellar degeneration in an inducible mouse model of Friedreich ataxia. 2019 International Ataxia Research Conference, Washington DC, 2019.

64. Schwenkreis P, Tegenthoff M, Witscher K, et al. Motor cortex activation by transcranial magnetic stimulation in ataxia patients depends on the genetic defect. Brain 2002;125(Pt 2):301–309.

65. Cruz Martinez A, Anciones B. Central motor conduction to upper and lower limbs after magnetic stimulation of the brain and peripheral nerve abnormalities in 20 patients with Friedreich's ataxia. Acta Neurol Scand 1992;85:323–326.

66. Mondelli M, Rossi A, Scarpini C, et al. Motor evoked potentials by magnetic stimulation in hereditary and sporadic ataxia. Electromyogr Clin Neurophysiol 1995;35:415–424.

67. Lanzillo B, Perretti A, Santoro L, et al. Evoked potentials in inherited ataxias: a multimodal electrophysiological study. Ital J Neurol Sci 1994; 15:25–37.

68. Kessler SBT, Andersen K, Schmidt A, et al. Motor evoked potential input output measures and FRDA Disease Burden. 2019 International Ataxia Research Conference, Washington, DC, 2019.

69. Hamedani AG, Hauser LA, Perlman S, et al. Longitudinal analysis of contrast acuity in Friedreich ataxia. Neurol Genet 2018;4:e250.

70. Seyer LA, Galetta K, Wilson J, et al. Analysis of the visual system in Friedreich ataxia. J Neurol 2013;260:2362–2369.

71. Fortuna F, Barboni P, Liguori R, et al. Visual system involvement in patients with Friedreich's ataxia. Brain 2009;132(Pt 1):116–123.

72. Rezende TJ, Silva CB, Yassuda CL, et al. Longitudinal magnetic resonance imaging study shows progressive pyramidal and callosal damage in Friedreich's ataxia. Mov Disord 2016;31: 70–78.

73. Rance G, Fava R, Baldock H, et al. Speech perception ability in individuals with Friedreich ataxia. Brain 2008;131(Pt 8):2002–2012.

74. Rance G, Corben L, Delatycki M. Auditory processing deficits in children with Friedreich ataxia. J Child Neurol 2012;27:1197–1203.

75. Reetz K, Dogan I, Hohenfeld C, et al. Nonataxia symptoms in Friedreich Ataxia: report from the Registry of the European Friedreich's Ataxia Consortium for Translational Studies (EFACTS). Neurology 2018;91:e917–e930.

76. Rance G, Corben L, Barker E, et al. Auditory perception in individuals with Friedreich's ataxia. Audiol Neurootol 2010;15:229–240.

77. Taylor MJ, McMenamin JB, Andermann E, et al. Electrophysiological investigation of the auditory system in Friedreich's ataxia. Can J Neurol Sci 1982;9:131–135.

78. Amantini A, Rossi L, De Scisciolo G, et al. Auditory evoked potentials (early, middle, late components) and audiological tests in Friedreich's ataxia. Electroencephalogr Clin Neurophysiol 1984;58: 37–47.

79. Takazaki KAG, Rezende TJR, Martinez ARM, et al. Sudomotor dysfunction is frequent and correlates with disability in Friedreich ataxia. Clin Neurophysiol 2018;129:2290–2295.

80. Indelicato E, Fanciulli A, Ndayisaba JP, et al. Autonomic function testing in Friedreich's ataxia. J Neurol 2018;265:2015–2022.

81. Koeppen AH, Ramirez RL, Becker AB, et al. Dorsal root ganglia in Friedreich ataxia: satellite cell proliferation and inflammation. Acta Neuropathol Commun 2016;4:46.

82. Shen Y, McMackin MZ, Shan Y, et al. Frataxin deficiency promotes excess microglial DNA damage and inflammation that is rescued by PJ34. PLoS One 2016;11:e0151026.

83. Hayashi G, Shen Y, Pedersen TL, et al. Frataxin deficiency increases cyclooxygenase 2 and prostaglandins in cell and animal models of Friedreich's ataxia. Hum Mol Genet 2014;23: 6838–6847.

84. Koeppen AH, Ramirez RL, Yu D, et al. Friedreich's ataxia causes redistribution of iron, copper, and zinc in the dentate nucleus. Cerebellum 2012;11: 845–860.

85. Loria F, Diaz-Nido J. Frataxin knockdown in human astrocytes triggers cell death and the release of factors that cause neuronal toxicity. Neurobiol Dis 2015;76:1–12.

86. Cotticelli MG, Xia S, Kaur A, et al. Identification of p38 MAPK as a novel therapeutic target for Friedreich's ataxia. Sci Rep 2018;8:5007.

87. Lu C, Schoenfeld R, Shan Y, et al. Frataxin deficiency induces Schwann cell inflammation and death. Biochim Biophys Acta 2009;1792:1052–1061.

88. Kemp KC, Cerminara N, Hares K, et al. Cytokine therapy-mediated neuroprotection in a Friedreich's ataxia mouse model. Ann Neurol 2017;81:212–226.

89. Morral JA, Davis AN, Qian J, et al. Pathology and pathogenesis of sensory neuropathy in Friedreich's ataxia. Acta Neuropathol 2010;120:97–108.

Received for publication October 5, 2020;
accepted after revision November 3, 2020.

Published online: November 25, 2020.

Molecular Therapy
Methods & Clinical Development
Original Article

In vivo overexpression of frataxin causes toxicity mediated by iron-sulfur cluster deficiency

Claudia Huichalaf,[1] Tyler L. Perfitt,[1] Anna Kuperman,[1] Renea Gooch,[1] Ramesh C. Kovi,[2] Karrie A. Brenneman,[2] Xian Chen,[3] Dinesh Hirenallur-Shanthappa,[3] Tiffany Ma,[1] Basel T. Assaf,[2] Ingrid Pardo,[2] Tania Franks,[2] Laura Monarski,[2] Ting-Wen Cheng,[1] Kevin Le,[1] Chunyan Su,[1] Suryanarayan Somanathan,[1] Laurence O. Whiteley,[2] Christine Bulawa,[1] Marko J. Pregel,[1] and Alain Martelli[1]

[1]Rare Disease Research Unit, Worldwide Research, Development and Medical, Pfizer Inc., 610 Main Street, Cambridge, MA 02139, USA; [2]Drug Safety Research and Development, Worldwide Research, Development and Medical, Pfizer Inc., Cambridge, MA 02139, USA; [3]Comparative Medicine, Worldwide Research, Development and Medical, Pfizer Inc., Cambridge, MA 02139, USA

Friedreich's ataxia is a rare disorder resulting from deficiency of frataxin, a mitochondrial protein implicated in the synthesis of iron-sulfur clusters. Preclinical studies in mice have shown that gene therapy is a promising approach to treat individuals with Friedreich's ataxia. However, a recent report provided evidence that AAVrh10-mediated overexpression of frataxin could lead to cardiotoxicity associated with mitochondrial dysfunction. While evaluating an AAV9-based frataxin gene therapy using a chicken β-actin promoter, we showed that toxic overexpression of frataxin could be reached in mouse liver and heart with doses between 1×10^{13} and 1×10^{14} vg/kg. In a mouse model of cardiac disease, these doses only corrected cardiac dysfunction partially and transiently and led to adverse findings associated with iron-sulfur cluster deficiency in liver. We demonstrated that toxicity required frataxin's primary function by using a frataxin construct bearing the N146K mutation, which impairs binding to the iron-sulfur cluster core complex. At the lowest tested dose, we observed moderate liver toxicity that was accompanied by progressive loss of transgene expression and liver regeneration. Together, our data provide insights into the toxicity of frataxin overexpression that should be considered in the development of a gene therapy approach for Friedreich's ataxia.

INTRODUCTION

Friedreich's ataxia (FRDA), the most prevalent autosomal recessive ataxia in Caucasians, is a devastating early-onset neurodegenerative disease characterized by a progressive spinocerebellar and sensory ataxia, hypertrophic cardiomyopathy, and increased incidence of diabetes.[1,2] The major FRDA-causing mutation is a GAA-repeat expansion within the first intron of the *FXN* gene, resulting in decreased transcription of the gene and a reduced amount of the encoded protein, frataxin (FXN).[3] FXN is a mitochondrial and ubiquitously expressed protein implicated in the biogenesis of iron-sulfur (Fe-S) clusters, inorganic cofactors with essential roles in various cellular functions such as mitochondrial respiration.[4] FXN is involved in the early steps of Fe-S cluster assembly within mitochondria via its binding and regulation of the Fe-S cluster core complex consisting of the cysteine desulfurase NFS1, the scaffold protein ISCU, and accessory proteins ISD11 and the mitochondrial acyl carrier protein (ACP).[5–9] Reduction of FXN level in cells causes impairment of Fe-S cluster biogenesis and reduction of the level of Fe-S cluster client proteins, leading to multiple cellular metabolic dysfunctions and ultimately cell death.[10,11]

Preclinical evaluations in cardiac and neuronal mouse models of FRDA have shown that AAV-based gene therapy is a promising therapeutic approach for the treatment of the disease.[12–15] The first gene therapy proof of concept was obtained with the intravenous injection of an AAVrh10 construct expressing HA-tagged FXN under the control of a ubiquitous chicken b-actin promoter (CAG) in a cardiac mouse model of FRDA.[12] The study showed the approach can correct the severe cardiac phenotype rapidly and efficiently. However, a recent report showed that systemic injection of high doses of the same AAVrh10-FXN construct in mice could be toxic.[16] Transgene protein levels higher than 20-fold the endogenous mouse FXN protein level were associated with cardiotoxicity characterized by mitochondrial dysfunction with impaired activities of respiratory complexes I and II.[16] In parallel, no detectable toxicity was reported in the liver of mice treated with this AAVrh10 construct despite expression up to 90-fold of the wild-type FXN protein level.[16] How and why FXN led to such toxicity in the heart of injected animals remains unclear.

Herein, we report insights into the toxicity associated with high level of FXN expression that was observed while evaluating a AAV9-based

Received 7 December 2021; accepted 4 February 2022;
https://doi.org/10.1016/j.omtm.2022.02.002.

Correspondence: Alain Martelli, PhD, Rare Disease Research Unit, Worldwide Research, Development and Medical, Pfizer Inc., 610 Main Street, Cambridge, MA, 02139, USA.
E-mail: alain.martelli@pfizer.com

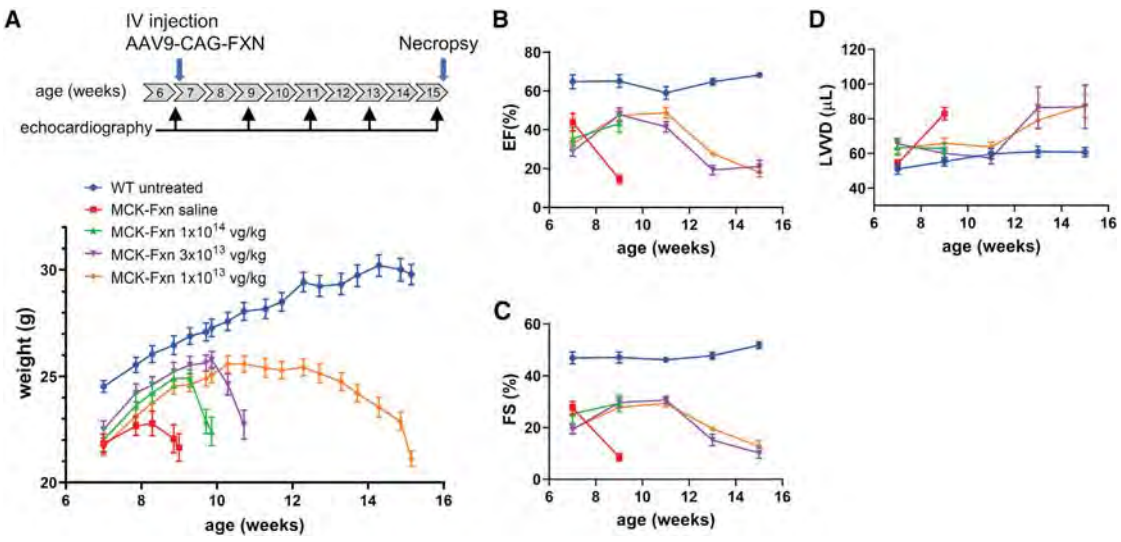

Figure 1. Transient correction of cardiac dysfunction in MCK-*Fxn* mice after AAV9-CAG-FXN administration

(A) *Upper,* Experimental time course of AAV9-CAG-FXN injection and echocardiographic measurements. *Lower,* Body weight curves obtained from WT untreated (n = 15), MCK-*Fxn* saline injected (n = 12), MCK-*Fxn* treated at 1×10^{13} vg/kg (n = 13), 3×10^{13} vg/kg (n = 13), or 1×10^{14} vg/kg (n = 12). (B–D) Echocardiographic measurements of ejection fraction (EF) (B), fractional shortening (FS) (C), and left ventricular volume at diastole (LVVD) (D). Echocardiographic data for each group and time point are provided in Table S1. All data are mean ± SEM.

gene therapy approach in mice. Specifically, we showed that with doses ranging from 1×10^{13} to 1×10^{14} vg/kg, an AAV9 construct expressing an untagged FXN under the control of a CAG promoter (AAV9-CAG-FXN) leads to high level of FXN expression and to only partial and transient correction of the cardiac function of a cardiac mouse model of FRDA. The lack of efficacy in that dose range was accompanied by weight loss and premature death in the two highest dose groups and marked adverse findings in the liver that were associated with Fe-S cluster deficiency. *In vivo* and molecular studies using constructs expressing FXN^{WT} or FXN^{N146K} point mutation showed that toxicity is driven by FXN primary function involving binding to the NFS1-ISD11-ISCU-ACP mitochondrial Fe-S cluster core complex. Furthermore, we provided evidence that even with the lowest tested dose, FXN-induced toxicity occurred in the liver but could be mitigated by liver regeneration while leading to loss of FXN transgene expression.

RESULTS

Transient improvement of cardiac function of MCK-*Fxn* mice after AAV9-CAG-FXN administration

Evaluation of AAV9-CAG-FXN was performed using the conditional cardiac mouse model of FRDA (MCK-*Fxn*), in which deletion of the endogenous mouse *Fxn* gene is triggered by a Cre recombinase under the control of the muscle creatine kinase (MCK) promoter.[10] This model reproduces key features of the disease including progressive hypertrophic cardiomyopathy, mitochondrial dysfunction, dysregulation of iron metabolism, and reduced Fe-S cluster biosynthesis.[10,12] To evaluate the ability of AAV9-CAG-FXN to correct cardiac dysfunction, we followed a similar protocol as the one reported for AAVrh10-FXN evaluation.[12] Seven-week-old MCK-*Fxn* mice were injected intravenously at a dose of 1×10^{13}, 3×10^{13}, or 1×10^{14} vg/kg. Efficacy was assessed by longitudinal weight recording and by echocardiographic analysis at baseline, 9, 11, 13, and 15 weeks of age (Figure 1A). Saline-injected MCK-*Fxn* animals were maintained up to 9 weeks of age, and then euthanized before reaching critical endpoints due to severe cardiac dysfunction. For all mice injected with AAV9-CAG-FXN, weight improvement was observed during the first 3 weeks post-injection compared with the saline group (Figure 1A) and was independent of the dose level. At about 3 weeks after injection, a significant drop in weight reaching critical loss of 10%–20% of the initial body weight was observed in animals of the 1×10^{14} vg/kg dose group (Figure 1A). All 12 mice of this group had to be euthanized between 20 days and 26 days post AAV9-CAG-FXN administration. Later, a similar weight decline was seen with the 3×10^{13} vg/kg dose group (Figure 1A). Eight of the 12 mice of this group had to be euthanized between 26 days and 30 days post-injection, one died prematurely, one was euthanized at 51 days, and two could be maintained throughout the study (57 days post-injection). All mice of the 1×10^{13} vg/kg dose group survived until the end of the study, but weight plateaued below wild-type (WT) values between 25 days and 35 days post-injection, and then progressively declined (Figure 1A). The weight curve of the 1×10^{13} vg/kg dose group was mirrored by the echocardiographic measurements showing an improvement followed by a decline of the ejection fraction (Figure 1B and Table S1), the fractional shortening (Figure 1C and Table S1), and the left ventricular end diastolic volume (Figure 1D and Table S1). Although only two mice could be maintained throughout the study, a similar trend was observed with echocardiographic data of the 3×10^{13} vg/kg dose group (Figures 1B–1D and Table S1). Before premature euthanasia, the

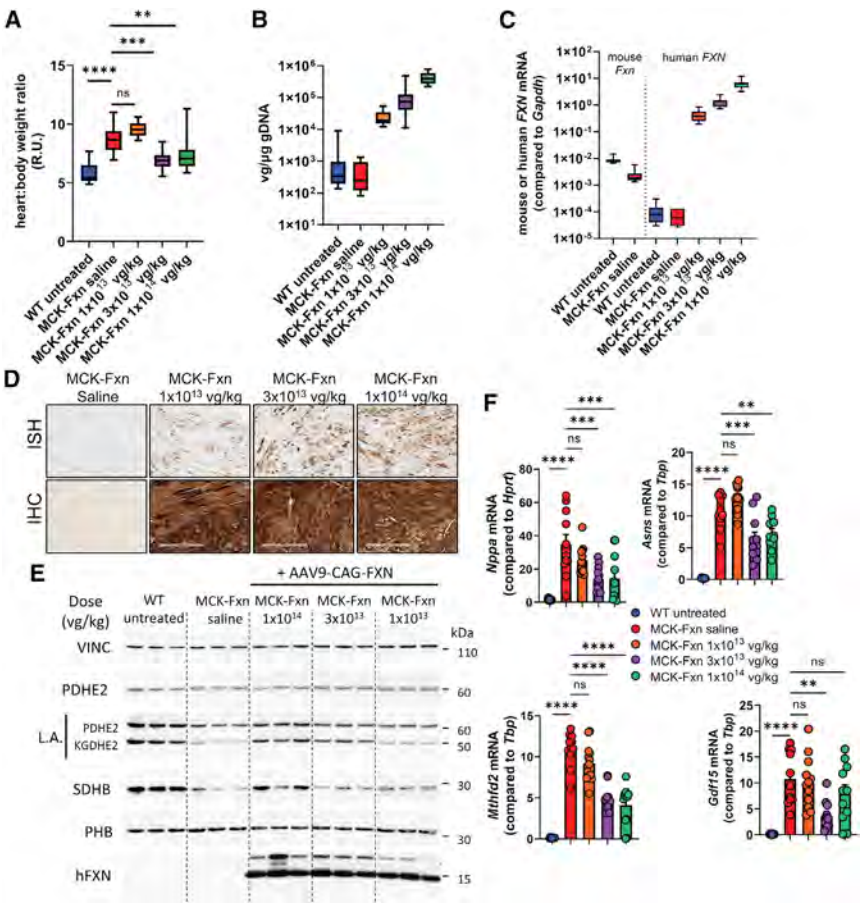

Figure 2. Time- and dose-dependent correction of MCK-*Fxn* heart phenotype after AAV9-CAG-FXN treatment

(A) Heart to body weight ratios at the time of necropsy: 57 days post-injection (dpi) for WT untreated (n = 15) and MCK-*Fxn* treated at 1×10^{13} vg/kg (n = 13), 14 dpi for MCK-*Fxn* saline group (n = 12), 26–57 dpi for MCK-*Fxn* treated at 3×10^{13} vg/kg (n = 11), and 20–26 dpi for MCK-*Fxn* treated at 1×10^{14} vg/kg (n = 12). (B) Vector genome copy (VGC) of AAV9-CAG-FXN in heart samples, as measured by ddPCR at the time of necropsy in WT untreated (n = 15), MCK-*Fxn* saline (n = 12), and MCK-*Fxn* treated at 1×10^{13} vg/kg (n = 12), 3×10^{13} vg/kg (n = 10), or 1×10^{14} vg/kg (n = 11). (C) mRNA expression of endogenous mouse *Fxn* and human *FXN* transgene in heart samples, as measured by ddPCR in WT untreated (n = 14), MCK-*Fxn* saline (n = 11), and MCK-*Fxn* treated at 1×10^{13} vg/kg (n = 13), 3×10^{13} vg/kg (n = 11), or 1×10^{14} vg/kg (n = 11). (D) Detection of *Fxn* transgene mRNA expression by *in situ* hybridization (ISH, upper panels) and human FXN protein by immunohistochemistry (IHC, lower panels) in heart sections. Scale bars, 300 µm. (E) Western blot analysis of mitochondrial and Fe-S client proteins from three mouse heart extracts from each group. Vinculin (VINC) was used as a loading control. (F) mRNA expression of cardiac dysfunction and FXN deficiency markers *Nppa*, *Asns*, *Mthfd2*, and *Gdf15* as measured by ddPCR in WT untreated (n = 15), MCK-*Fxn* saline (n = 11), and MCK-*Fxn* treated at 1×10^{13} vg/kg (n = 13), 3×10^{13} vg/kg (n = 11), or 1×10^{14} vg/kg (n = 12). All data are mean ± SEM. **p < 0.01, ***p < 0.001, ****p < 0.0001.

1×10^{14} vg/kg dose group showed similar improvement in the ejection fraction, fractional shortening, and left ventricular volume at diastole as the other injected groups at the 9-week recording (Figures 1B–1D and Table S1), suggesting cardiac function was improving at the time mice had to be euthanized.

Hearts of the different groups were collected for analyses. At necropsy, the heart to body weight ratio was calculated to estimate cardiac hypertrophy (Figure 2A). As reported for this model,[10] the heart to body weight ratio was significantly higher in saline-injected MCK-*Fxn* at 9 weeks compared with control animals (Figure 2A). This ratio was significantly lower in AAV9-CAG-FXN-injected mice of the 1×10^{14} vg/kg and 3×10^{13} vg/kg dose groups than in the saline MCK-*Fxn* group, suggesting an improvement of the cardiac hypertrophy at the time of euthanasia, which is in agreement with the echocardiographic data (Figures 1B–1D). Conversely, the heart to body weight ratio was not distinguishable from saline-injected MCK-*Fxn* mice in the 1×10^{13} vg/kg dose group at 15 weeks (Figure 2A).

Histopathological assessment was performed on heart sections after hematoxylin and eosin (H&E) staining (Table S2 and Figures S1A–S1C). Saline-injected MCK-*Fxn* mice showed minimal to moderate cardiomyocyte degeneration/necrosis with minimal to mild fibrosis. Severity of cardiomyocyte degeneration/necrosis and interstitial fibrosis decreased with increasing dose of AAV9-CAG-FXN. However, severity of findings was similar between the MCK-*Fxn* disease model and mice injected at 1×10^{14} vg/kg and 3×10^{13} vg/kg doses, whereas findings were more severe in heart sections of the 1×10^{13} vg/kg dose group. This could indicate worsening of the heart pathology with time since the lowest dose group was euthanized at 15 weeks and the MCK-*Fxn* saline group at 9 weeks of age.

Robust transduction and expression of FXN in heart of AAV9-CAG-FXN-injected MCK-*Fxn* mice

Heart samples were further analyzed by measuring vector genome copy (VGC) and transgene mRNA expression by digital droplet PCR (ddPCR). VGC values and mRNA levels showed a clear dose response (Figures 2B and 2C). At the mRNA level, *FXN* transgene expression reached ~50 fold the level of endogenous mouse *Fxn* measured in heart of untreated WT animals in the 1×10^{13} vg/kg dose group, ~160 fold in the 3×10^{13} vg/kg dose group, and ~735 fold in the 1×10^{14} vg/kg dose group (Table 1). Distribution and

Table 1. Summary of VGC and fold human *FXN* transgene mRNA expression over endogenous mouse *Fxn* mRNA expression as measured by ddPCR. Data are shown as mean ± SD.

Mouse	MCK-Fxn			WT		WT		
Transgene	FXN^{WT}			FXN^{WT}	FXN^{N146K}	FXN^{WT}		FXN^{N146K}
Dose (vg/kg)	$1E^{13}$	$3E^{13}$	$1E^{14}$	$3E^{13}$		$1E^{13}$		
Time at euthanasia								
dpi	57	26–57	20-26	21	21	35	56	56
wpi	8	3.7–8	2.8–3.7	3	3	5	8	8
Vector genome copy number (vg/µg gDNA)								
Heart	$2.4 \pm 1.3E^{+04}$	$1.2 \pm 1.4E^{+05}$	$4.4 \pm 1.8E^{+05}$	$1.1 \pm 0.3E^{+05}$	$1.1 \pm 0.7E^{+05}$	nd	$1.2 \pm 0.6E^{+04}$	$8.8 \pm 3.5E^{+03}$
Liver	$5.7 \pm 2.6E^{+05}$	$6.5 \pm 1.4E^{+06}$[b]	$2.0 \pm 0.4E^{+07}$	$7.3 \pm 1.8E^{+06}$	$7.8 \pm 5.0E^{+06}$	$4.0 \pm 1.4E^{+05}$	$5.0 \pm 2.2E^{+04}$	$1.2 \pm 0.3E^{+06}$
Fold FXN mRNA expression over mouse Fxn								
Heart	51 ± 26[a]	159 ± 57[a]	735 ± 289[a]	89 ± 25	44 ± 27	nd	8 ± 4	10 ± 5
Liver	57 ± 27	489 ± 209[b]	776 ± 292	930 ± 325	568 ± 132	109 ± 26	14 ± 16	215 ± 57

dpi: days post-injection; wpi: weeks post-injection; nd: not determined.
[a]Fold change was determined using the mean value of mouse *Fxn* expression as measured in WT untreated group.
[b]Only animals euthanized between 26 and 30 dpi were used due to loss of transgene expression in liver of animals euthanized at later time points.

expression of the *FXN* transgene was also assessed on heart sections by *in situ* hybridization (ISH) to specifically measure transgene mRNA and by immunohistochemistry (IHC) to detect human protein expression. Whereas a dose-responsive increase in ISH signal was seen (Figure 2D, upper panels), the human FXN IHC signal was high and consistent across heart sections for all dose groups (Figure 2D, lower panels), suggesting it was saturated due to high expression of FXN.

Altogether, our data indicate that doses between 1×10^{13} and 1×10^{14} vg/kg of our AAV9-CAG-FXN construct lead to broad and high expression of FXN in heart but could at best provide partial and transient correction of the cardiac dysfunction in the MCK-*Fxn* model.

AAV9-CAG-FXN injection leads to transient correction of Fe-S cluster deficit in heart of MCK-*Fxn* mice

Heart samples were further analyzed by western blot to detect levels of Fe-S cluster-dependent enzymes and activities as an indirect way to assess the integrity of Fe-S cluster biogenesis and the ability of human FXN to correct the molecular phenotype.[11,12] Puccio and collaborators identified perturbations in several Fe-S cluster-dependent proteins in cardiac tissue isolated from MCK-*Fxn* mice.[10,12] In particular, the level of succinate dehydrogenase subunit B (SDHB), a Fe-S cluster-containing subunit of mitochondrial respiratory complex II, was reduced. Furthermore, decreased activity of the Fe-S cluster-containing lipoic acid synthase resulted in low lipoic acid (LA) modification of pyruvate dehydrogenase (PDHE2) and a-ketoglutarate dehydrogenase (KGDHE2) E2 subunits. As expected, these deficiencies were observed in saline-injected MCK-*Fxn* mice (Figure 2E). In contrast, both SDHB and LA signals were improved in the 1×10^{14} vg/kg dose group (Figure 2E), in agreement with the improved cardiac function that was measured by echocardiography just prior to the premature euthanasia (Figures 2B–2D). For the 3×10^{13} vg/kg dose group, results were mixed with some improvement of the LA signal but no obvious increase in SDHB compared with the saline MCK-*Fxn* group (Figure 2E). In the 1×10^{13} vg/kg dose group, both LA and SDHB signals were indistinguishable from the saline-injected group (Figure 2E), despite the strong and distributed FXN transgene expression (Figures 2E and 2D).

We then measured the mRNA expression of markers associated with FXN deficiency in the MCK-*Fxn* model: the natriuretic peptide A gene (*Nppa*) and *Gdf15*, two markers of cardiac dysfunction, as well as *Asns* and *Mthfd2*, two genes known to be upregulated in FXN deficiency.[11,12,17] As previously reported, all genes were significantly upregulated in the saline-injected MCK-*Fxn* group at 9 weeks of age (Figure 2F). In the 3×10^{13} vg/kg and 1×10^{14} vg/kg dose groups, *Nppa*, *Asns*, and *Mthfd2* were significantly reduced compared with the saline group (Figure 2F), whereas *Gdf15* was significantly lower in the 3×10^{13} vg/kg dose group only (Figure 2F). This might reflect the fact that at the time of euthanasia, most mice of both 3×10^{13} and 1×10^{14} vg/kg dose groups showed improvement of the cardiac function as seen by echocardiography (Figures 1B–1D and Table S1). Conversely, no significant change in expression was observed in the lowest dose group compared to the saline control group, reflecting the cardiac dysfunction measured by echocardiography for this group at the end of the study (Figures 1B–1D and Table S1).

Together, our analyses of the *in vivo* and molecular heart phenotype showed that all the tested doses of AAV9-CAG-FXN had the ability to correct the cardiac dysfunction in the first weeks after injection. For the lowest 1×10^{13} vg/kg dose group, cardiac correction could not be maintained during the study. This observation of a transient effect might be explained by a progressive increase of FXN expression after AAV injection, going from efficacious levels to toxic levels. Because most mice dosed at 3×10^{13} and 1×10^{14} vg/kg were euthanized when the heart function was improving,

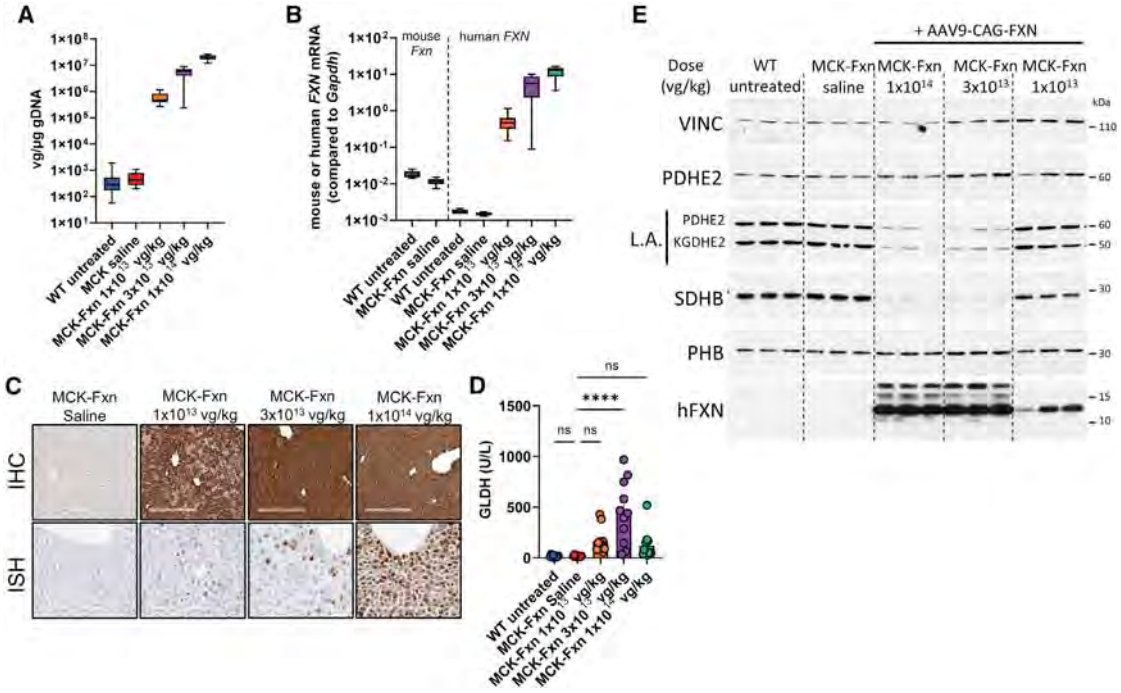

Figure 3. Mice requiring early euthanasia display liver pathology and Fe-S cluster deficiency

(A) Vector genome copy (VGC) of AAV9-CAG-FXN in liver samples, as measured by ddPCR in WT untreated (n = 15), MCK-*Fxn* saline (n = 12), and MCK-*Fxn* treated at 1×10^{13} vg/kg (n = 13), 3×10^{13} vg/kg (n = 10), or 1×10^{14} vg/kg (n = 12). (B) mRNA expression of endogenous mouse *Fxn* and human *FXN* transgene in liver extracts, as measured by ddPCR in WT untreated (n = 15), MCK-*Fxn* saline (n = 12), and MCK-*Fxn* treated at 1×10^{13} vg/kg (n = 13), 3×10^{13} vg/kg (n = 9), or 1×10^{14} vg/kg (n = 12). (C) Detection of *Fxn* transgene mRNA expression by *in situ* hybridization (ISH, upper panels) and human FXN protein by immunohistochemistry (IHC, lower panels) in liver sections. Scale bars, 200 µm (ISH), 300 µm (IHC). (D) Measurements of liver-specific glutamate dehydrogenase (GLDH) from sera taken at time of necropsy: 57 days post-injection (dpi) for WT untreated (n = 15) and MCK-*Fxn* treated at 1×10^{13} vg/kg (n = 12), 14 dpi for MCK-*Fxn* saline group (n = 10), 26–57 dpi for MCK-*Fxn* treated at 3×10^{13} vg/kg (n = 11) and 20–26 dpi for MCK-*Fxn* treated at 1×10^{14} vg/kg (n = 13). All data are mean ± SEM. ****$p < 0.0001$. (E) Western blot analysis of mitochondrial and Fe-S client proteins from three mouse liver extracts from each group. Vinculin (VINC) was used as a loading control.

we investigated the possibility that other factors than the cardiac phenotype contributed to weight loss and reduced survival in these groups.

Toxic overexpression of FXN leads to Fe-S cluster deficit in liver of MCK-*Fxn* mice

Because AAV9 has a high tropism for liver, we performed analyses on the livers of MCK-*Fxn* mice. High transduction of liver in AAV9-CAG-FXN-injected MCK-*Fxn* mice was confirmed by the measurement of VGC and transgene mRNA expression (Figures 3A and 3B). In both cases, a dose-responsive increase was observed, and the fold human *FXN* transgene mRNA expression over endogenous mouse *Fxn* mRNA level was ~57 for the 1×10^{13} vg/kg dose group, ~490 for the 3×10^{13} vg/kg dose group, and ~775 for the 1×10^{14} vg/kg dose group (Table 1). A dose-responsive increase was also seen by ISH (Figure 3C, left panels), and high FXN protein expression was detected by IHC (Figure 3C, right panels). Of note, depending on when animals were euthanized, different levels of FXN IHC staining were observed in liver samples of the 3×10^{13} vg/kg dose group (Figure S2A). The significance of this observation will be discussed in a section below.

Histopathological assessment of liver tissues indicated the presence of a significantly higher number of microscopic findings in the injected groups when compared with WT or saline-injected MCK-*Fxn* mice (Table S2 and Figures S1D–S1F). Minimal and mild single cell hepatocyte degeneration/necrosis was consistently observed in all AAV9-CAG-FXN injected groups. All three dose groups also showed minimal to mild hepatocellular hypertrophy and vacuolation that was variable in incidence and distribution. The highest incidence of hepatocyte hypertrophy was seen in the highest dose group and was centrilobular. The highest severity changes were observed in the 1×10^{14} vg/kg dose group with moderate centrilobular hepatocellular vacuolation (one mouse of 12), and in the 1×10^{13} vg/kg dose group with a marked midzonal hepatocellular necrosis (two mice of 13) (Table S2 and Figures S1D–S1F). Clinical pathology showed higher levels of aspartate aminotransferase (AST), alanine aminotransferase (ALT), and glutamate dehydrogenase (GLDH) markers in sera of all injected groups (Figures 3D and S2B). However, whereas AST and ALT were significantly higher in all groups, GLDH values were only significantly increased in the 3×10^{13} vg/kg dose group when compared with saline-injected MCK-*Fxn* mice (Figure 3D).

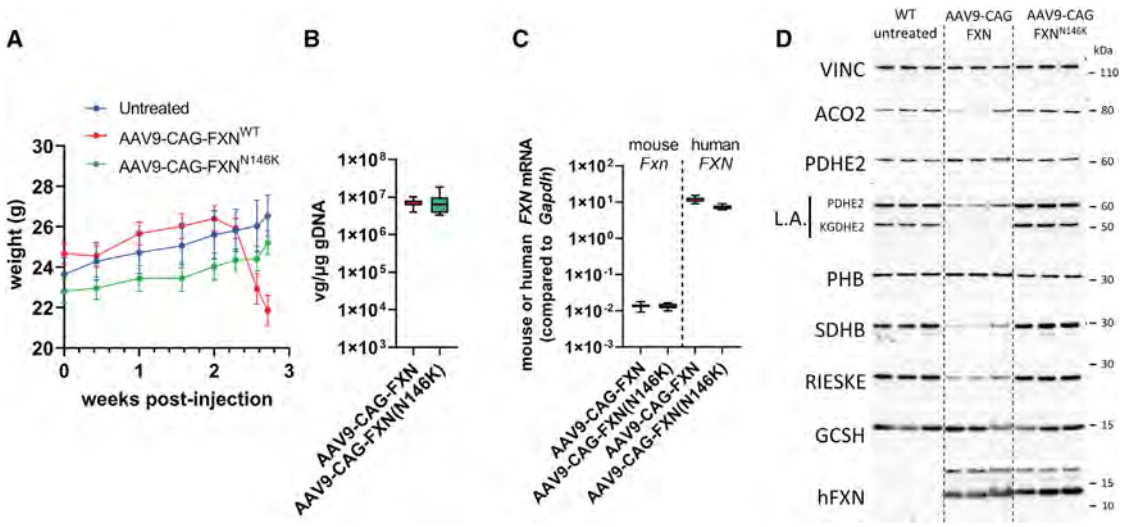

Figure 4. Toxicity associated with FXN overexpression requires FXN binding to the Fe-S cluster core complex

(A) Body weight curves obtained from WT untreated (n = 4), AAV9-CAG-FXN-injected (n = 8), and AAV9-CAG-FXN(N146K)-injected (n = 8) mice dosed at 3×10^{13} vg/kg. Necropsy was performed 3 weeks post-injection. (B) Vector genome copy (VGC) in liver samples, as measured by ddPCR in WT treated with AAV9-CAG-FXN (n = 8) or AAV9-CAG-FXN(N146K) (n = 8) at 3×10^{13} vg/kg, 3 weeks post-injection. (C) mRNA expression of endogenous mouse *Fxn* and human *FXN* transgene in liver samples, as measured by ddPCR in WT treated with AAV9-CAG-FXN (n = 8) or AAV9-CAG-FXN(N146K) (n = 8) at 3×10^{13} vg/kg, 3 weeks post-injection. (D) Western blot analysis of mitochondrial and Fe-S client proteins from three mouse liver extracts, 3 weeks post-injection. Vinculin (VINC) was used as a loading control.

We then assessed levels of Fe-S cluster client proteins and activities by western blot. Strikingly, the levels of LA and SDHB in liver were strongly impacted by AAV9-CAG-FXN transduction in the 1×10^{14} vg/kg and 3×10^{13} vg/kg dose groups when compared with WT non-injected, saline-injected MCK-*Fxn* animals or even the 1×10^{13} vg/kg dose group (Figure 3E). Mitochondrial PDHE2 and prohibitin (PHB) levels were not affected (Figure 3E), suggesting that FXN high expression in liver might trigger a specific deficit of Fe-S cluster client proteins.

Together, these data indicate that liver dysfunction could be the primary cause of body weight loss and premature death observed in the 3×10^{13} and 1×10^{14} vg/kg dose groups.

FXN overexpression-mediated toxicity correlates with FXN ability to bind the Fe-S cluster mitochondrial core complex

Belbellaa et al. showed that high overexpression of frataxin in mouse heart lowered the activity of SDH and NADH-ubiquinone oxidoreductase, two enzymes that require Fe-S clusters, whereas cytochrome *c* oxidase, a heme-dependent enzyme, was unaffected.[16] In addition to the liver phenotype in AAV9-CAG-FXN-treated MCK-*Fxn* mice described above, this suggests that overexpression of FXN could inhibit Fe-S cluster biosynthesis, and paradoxically leads to a phenotype similar to FXN depletion. To further explore this possibility, we performed additional experiments in WT mice and evaluated the levels of multiple Fe-S cluster-containing proteins. In addition, we generated a construct expressing FXN(N146K) point mutation. This mutation is found in some individuals with FRDA and has been shown to maintain FXN mitochondrial localization and folding but to impair binding to the Fe-S cluster core complex.[6,8,18–20] Furthermore, because the protein sequences of human and mouse FXN are different, in particular in the mitochondrial targeting sequence, the comparison between FXN^{WT} and FXN^{N146K} was also a way to assess whether the toxicity could be independent of the FXN function and could for instance result from an altered mitochondrial import or of peptides generated during human FXN maturation.

We first explored whether the deleterious effect of high FXN expression occurs in WT mice and showed that following intravenous injection of AAV9-CAG-FXN at 3×10^{13} vg/kg in 7-week-old WT animals, weight loss at around 3 weeks post-injection could be reproduced (Figure 4A). In contrast, injection of 7-week-old WT mice with AAV-CAG-FXN(N146K) at 3×10^{13} vg/kg had no impact on the weight curve of injected animals (Figure 4A). Tissues of the different groups were harvested 3 weeks post-injection to perform comparative analyses.

Similar VGCs were measured between animals injected with FXN^{WT} and FXN^{N146K} constructs in both liver and heart (Figures 4B and S3A). At the mRNA level, although AAV9-CAG-FXN(N146K) injected mice displayed slightly lower FXN expression compared with the FXN^{WT} construct (Figures 3B and S3B), both constructs showed mean mRNA expression levels in liver higher than the mean FXN expression measured in livers of MCK-*Fxn* injected with AAV9-CAG-FXN at the same dose. Indeed, the mean fold transgene mRNA expression over endogenous mouse *Fxn* in liver was of ~930 fold and ~568 fold for FXN^{WT} and FXN^{N146K} constructs,

respectively (Table 1). Conversely, transgene mRNA expression in heart was higher in MCK-*Fxn* animals than in WT mice, although VGC values were similar between groups (Table 1). This might suggest that the pathological state of MCK-*Fxn* mice could influence cardiac expression of the FXN transgene. FXN expression in both liver and heart was further confirmed by IHC showing strong and homogeneous signal in liver and an evenly distributed but patchy staining in heart (Figures S3C and S4A). Histopathological analysis of H&E sections revealed that AAV9-CAG-FXN expression was associated with an increased incidence and/or severity of centrilobular to midzonal hepatocellular hypertrophy (minimal to mild), karyocytomegaly of hepatocytes (minimal), hepatocellular lipid-like vacuolation (minimal to mild), single cell necrosis of hepatocytes (multifocal, minimal), and mononuclear/mixed cell infiltrate (multifocal, minimal) (Table S3, and Figure S5). Conversely, liver from mice injected with AAV9-CAG-FXN(N146K) was not distinguishable from non-injected controls (Table S3). No test article-related findings were seen in heart sections of these animals. Levels of GLDH were slightly but significantly elevated in AAV9-CAG-FXN-injected animals, whereas AST and ALT markers were not distinguishable from WT or AAV9-CAG-FXN(N146K)-injected mice (Figure S4B).

Western blot analysis showed that levels of LA on PDHE2 and KGDHE2 as well as of SDHB were reduced in livers of WT mice injected with AAV9-CAG-FXN (Figure 4D). The protein levels of mitochondrial aconitase (ACO2) and respiratory complex III Rieske subunit, two other mitochondrial Fe-S cluster clients, were also impaired (Figure 4D). Conversely, PDH2, PHB, and glycine cleavage system H (GCSH), which are all non-Fe-S cluster-containing mitochondrial proteins, were not affected by the AAV-mediated FXN expression (Figure 4D). Strikingly, despite similar FXN protein levels detected by western blot between FXN^{WT} and FXN^{N146K}, the introduction of the N146K point mutation could prevent all Fe-S cluster-related dysregulations observed with the FXN^{WT} construct since levels of LA, SHDB, ACO2, and Rieske were maintained (Figure 4D). In heart, neither FXN^{WT} nor FXN^{N146K} had an impact on Fe-S cluster client protein levels at this dose and time point (Figure S3D).

Together, our data demonstrate that toxicity associated with FXN overexpression is not mediated by differences between human and mouse FXN but rather by the binding of FXN to the mitochondrial Fe-S cluster core complex that leads to Fe-S cluster deficit the same way FXN depletion does.

FXN overexpression-mediated toxicity can trigger liver regeneration

As mentioned above, MCK-*Fxn* mice injected with AAV9-CAG-FXN at 3×10^{13} vg/kg led to heterogeneous phenotypes with some animals euthanized earlier than others. Further microscopic evaluation of the liver sections stained for FXN showed that whereas animals from early time points (from 26 to 30 days post-injection) displayed homogeneous FXN staining, the three animals euthanized later in the study (at 51 and 57 days post-injection) had a patchy FXN staining (Figure S2A). This observation correlated with lower VGC and lower GLDH serum levels in mice euthanized at the end of the study (Figures S2C and S2D). The decrease in FXN staining observed in liver was not observed in heart of the same animals (Figure S2E), thus indicating that variation of staining in liver was not a result of variability in AAV injection. These data suggest that a concomitant loss of transgene expression and an improvement of liver function might have occurred in surviving mice. On this basis, we hypothesized that hepatocytes expressing high levels of FXN could be lost due to FXN toxicity while being replaced by transgene non-expressing or low-expressing cells via liver regeneration.

To investigate this hypothesis, we performed additional studies by injecting 7-week-old WT mice with AAV9-CAG-FXN at 1×10^{13} vg/kg, a dose that did not have an impact on survival and allowed long-term evaluation of transgene liver expression. In a first 8-week study, a group injected with AAV9-CAG-FXN(N146K) was also included for comparison. Although no significant difference in weight between the groups was observed at the end of the study (Figure 5A), a transient decrease in weight was seen in the AAV9-CAG-FXN cohort around 3–4 weeks post-injection (Figure 5A). Both heart and liver tissues were harvested for analyses. In heart samples, no significant difference between FXN^{WT} and FXN^{N146K} constructs was measured for VGC, *FXN* mRNA, or protein expression, indicating similar doses were injected for both constructs (Figures S6A–S6C). In liver, much lower VGC, *FXN* mRNA, and protein expressions were detected in the AAV-CAG-FXN-injected animals than in the AAV-CAG-FXN(N146K) group (Figures 5B–5E). Accordingly, a patchy FXN IHC staining was obtained in the FXN^{WT} group, whereas it was more homogeneous in animals expressing the FXN^{N146K} construct (Figures 5D and S7A). Assessment of liver H&E sections indicated that FXN^{WT} expression was associated with an increased incidence and/or severity of single cell necrosis of hepatocytes, mononuclear and mixed cell infiltrates, increased mitosis, and karyo/cytomegaly of hepatocytes when compared with AAV9-CAG-FXN(N146K) administration, which was similar to non-injected controls (Table S4). Additionally, no test article-related microscopic findings were observed in the heart of injected mice.

Another cohort of 7-week-old WT mice was injected with AAV9-CAG-FXN at 1×10^{13} vg/kg and euthanized 5 weeks post-injection, a time at which mice were starting to recover weight after a transient loss (Figure 5A). Analysis of VGC and *FXN* mRNA levels in this new cohort showed intermediate values between the ones for FXN^{WT} and FXN^{N146K} constructs at 8 weeks post-injection (Figures 5B and 5C). This supports the idea that FXN^{WT} liver expression was lost over time in AAV9-CAG-FXN-injected animals. At 5 weeks post-injection, FXN staining by IHC was variable between animals with mice displaying more patchy staining than others, but overall, it was more homogeneous than the signal observed at 8 weeks post-injection (Figures 5D and S7B). A progressive decrease of transgene expression in liver was further confirmed by western blot showing a barely detectable FXN signal at 8 weeks post-injection when compared

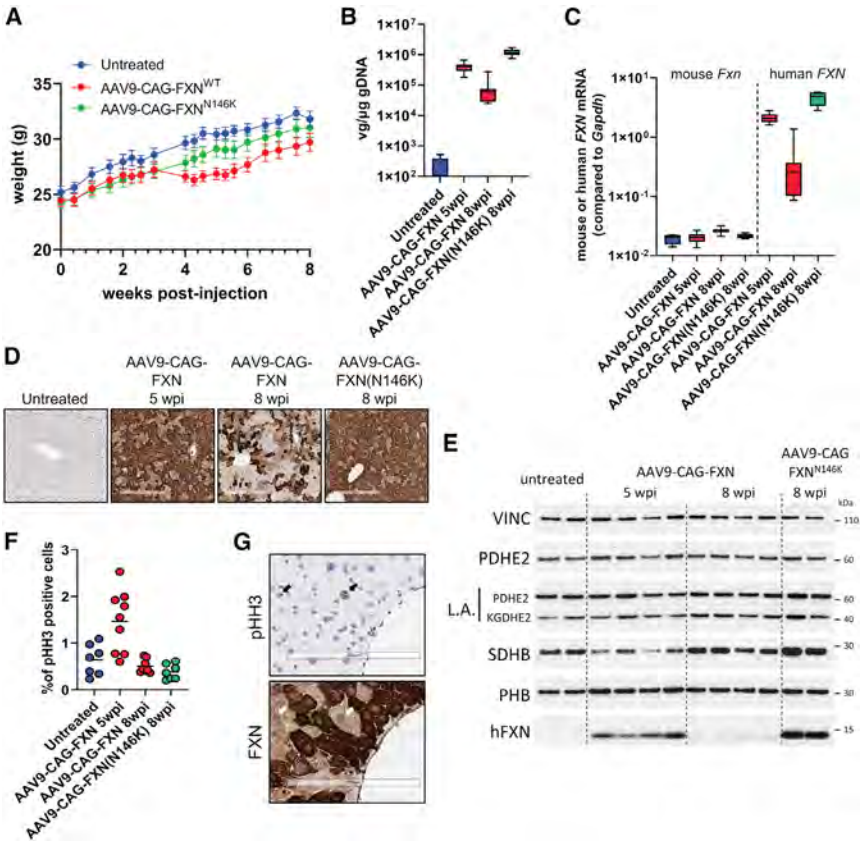

Figure 5. Recovery from moderate FXN-mediated liver toxicity correlates with loss of transgene expression and liver regeneration

(A) Body weight curves obtained from WT untreated (n = 4), AAV9-CAG-FXN-injected (n = 8), and AAV9-CAG-FXN(N146K)-injected (n = 8) mice dosed at 1×10^{13} vg/kg. Necropsy was performed 8 weeks post-injection. All data are mean SEM. (B) Vector genome copy (VGC) in liver samples, as measured by ddPCR in WT untreated (n = 4), treated with AAV9-CAG-FXN at 1×10^{13} vg/kg, 5 weeks (n = 10) or 8 weeks (n = 8) post-injection (wpi), or with AAV9-CAG-FXN(N146K) at 1×10^{13} vg/kg, 8 wpi (n = 8). (C) mRNA expression of endogenous mouse *Fxn* and human *FXN* transgene in liver samples, as measured by ddPCR in WT untreated (n = 4), treated with AAV9-CAG-FXN at 1×10^{13} vg/kg, 5 weeks (n = 10) or 8 weeks (n = 8) post-injection (wpi), or with AAV9-CAG-FXN(N146K) at 1×10^{13} vg/kg, 8 wpi (n = 8). (D) Detection of human FXN protein by immunohistochemistry in liver section from WT mice dosed with AAV9-CAG-FXN or AAV9-CAG-FXN(N146K). Necropsy was performed 5 or 8 weeks post-injection (wpi). Scale bars, 300 µm. (E) Western blot analysis of mitochondrial and Fe-S client proteins from mouse liver extracts. Necropsy was performed 5 or 8 weeks post-injection (wpi). Vinculin (VINC) was used as a loading control. (F) Quantification of percentage of phospho-histone H3 (pHH3)-positive cells in liver sections of WT untreated (n = 7), dosed with AAV9-CAG-FXN at 1×10^{13} vg/kg, 5 weeks (n = 9) or 8 weeks (n = 7) post-injection (wpi), or dosed with AAV9-CAG-FXN(N146K) at 1×10^{13} vg/kg, 8 wpi (n = 7). (G) Representative image of pHH3 IHC (upper panel) and FXN IHC (lower panel) on consecutive liver sections of WT mouse dosed with AAV9-CAG-FXN at 1×10^{13} vg/kg. Arrows indicate corresponding pHH3-positive nuclei. Scale bars, 200 µm.

with the 5-week post-injection time point or the FXN^{N146K} construct (Figure 5E). Interestingly, no deficit in LA could be detected at either 5 weeks or 8 weeks post-injection in liver extracts, and only a slight decrease of SDHB signal could be seen in some animals dosed with AAV9-CAG-FXN at 5 weeks post-injection (Figure 5E). Histopathological analysis after H&E staining revealed minimal to moderate single cell necrosis of hepatocytes, minimal increased karyocytomegaly/binucleation, mild to moderate degeneration/vacuolation of hepatocytes, and minimal to mild increased mitoses in AAV-injected animals (Table S5 and Figure S8). Markers were measured in serum samples of mice at 3, 5, and 8 weeks after injection. GLDH was highly increased in the AAV9-CAG-FXN cohort at the 5-week time point when compared with non-injected controls, and slightly increased at 8 weeks post-injection (Figure S9A). AST and ALT were not significantly different from control mice at any of the time points (Figures S9B and S9C). Furthermore, no difference in total protein, albumin (ALB), or alkaline phosphatase (ALP) levels was seen in animals at 5 weeks after dosing (Figure S9D).

Based on the increased mitoses observed in the histopathological analysis, liver cell proliferation in AAV9-CAG-FXN injected animals was further investigated by IHC of phospho-histone H3 (pHH3), a marker of cell division. The number of pHH3-positive cells was increased in AAV9-CAG-FXN-injected mice at 5 weeks post-injection, in particular in mildly to moderately affected livers as seen in the histopathological assessment (Figures 5F and S9E). Evaluation on consecutive liver sections indicated that occasional pHH3-positive cells appeared to be larger cells with lower FXN IHC signal intensity and larger round nuclei (Figure 5G), thus further suggesting that cell division occurred in favor of transgene low- or non-expressing cells.

Together, our data demonstrate that FXN-expressing cells were lost with time in animals injected with the FXN^{WT} construct because of liver injury associated with FXN toxicity. Consequently, cell proliferation was induced to regenerate the liver and restore function. Our results also confirmed the ability of the N146K mutation to mitigate most of the effects observed in liver, pointing again to the intrinsic role of FXN function in the toxic mechanism.

DISCUSSION

Our work provides insights into the toxicity associated with AAV-mediated supraphysiological expression of FXN *in vivo*. We observed toxicity in heart of MCK-*Fxn* mice treated with our lowest AAV9 tested dose, with a cardiac function that first improved and then

deteriorated 4 weeks after injection. This suggests a transition from efficacious transgene expression levels to toxic levels in heart. Surprisingly, toxicity was not observed in WT mice with a similar dose and time frame. However, *FXN* transgene mRNA levels reached in heart of MCK-*Fxn* mice were higher than the ones measured in WT mice with similar doses (see Table 1). Whereas the difference in expression could correlate with VGC differences at 1×10^{13} vg/kg, similar VGCs were obtained at 3×10^{13} vg/kg, suggesting a potential impact of the heart pathological state on transgene expression. Effect of cardiac disease on AAV9-mediated transgene expression was recently reported in a mouse model of heart ischemia.[21] Therefore, we could speculate that transgene expression is affected by the phenotype of MCK-*Fxn* mice, leading to expression above the toxicity threshold in the cardiac model that was not achieved in the WT background with the same dose. These data point to the need to consider the pathological state of target tissues in the evaluation of toxicity associated with FXN gene therapy. Another potential reason for the difference in toxicity-related outcome is that heart in MCK-*Fxn* mice relies on transduced cells to correct and maintain function, whereas in WT animals, the non-transduced wild-type cardiomyocytes could still contribute to the cardiac activity. Hence, toxicity in AAV9-transduced cells could have acute consequences on the phenotype of MCK-*Fxn* mice and subclinical consequences in WT animals. However, no histopathological microscopic findings could be seen in heart of dosed WT animals, suggesting no toxicity had occurred with the tested AAV9 doses. Taking into consideration the fold expression levels shown in Table 1, it appears that transgene mRNA expression 8-fold over mouse *Fxn* expression would be safe for the heart. This value is in agreement with the 9-fold FXN protein level threshold reported by Belbellaa et al. with AAVrh10.[16] Furthermore, the 50-fold transgene mRNA expression over mouse *Fxn* measured in MCK-*Fxn* mice is also in line with the report suggesting that cardiotoxicity could be reached over a 20-fold FXN protein expression.[16]

In addition to the cardiotoxicity, we report marked toxic effects in liver of MCK-*Fxn* and WT mice dosed with AAV9-CAG-FXN. This toxicity was either acute, leading to weight loss and early mortality, or moderate with a transient liver dysfunction and a progressive loss of transgene expression. The time component of the moderate liver toxicity is a challenge for the detection as well as for the definition of a tolerable expression level. Data obtained with the FXN^{N146K} construct could however provide some indication on the threshold between moderate and acute toxicity. Assuming the FXN N146K point mutation prevents any loss of expression with time, the 215-fold *FXN* mRNA expression over mouse *Fxn* measured in our 8-week study using 1×10^{13} vg/kg would be a condition leading to moderate toxicity. Around and above 500-fold transgene expression, our data show the liver toxicity would be acute. It is interesting that AAVrh10 that has a good tropism for liver did not show similar acute toxicity in reported experiments.[16] However, the protein transgene expression obtained with AAVrh10 reached up to 90-fold over endogenous levels, indicating that a threshold for acute toxicity might have not been attained with the tested doses. It is possible that a moderate toxicity occurred in the AAVrh10-dosed mice but might have been missed because evaluation was performed 8 weeks after AAV administration, when liver damages might have resolved after induced regeneration.[16] Additional longitudinal experiments would be required to further evaluate this type of toxicity with other capsids. For this purpose, our data show that GLDH is a better serum marker than AST, ALT, ALB, or AP to detect both the acute and moderate FXN-related liver toxicities.

Finally, we demonstrated a direct correlation between the primary function of FXN and the AAV-mediated toxicity observed *in vivo*. High expression of FXN recapitulated features observed in FXN deficiency, with a specific deficit of Fe-S cluster-dependent activities. It is possible that high amount of FXN might impair the dynamic of Fe-S cluster biosynthesis by affecting the equilibrium between different complexes involving NFS1 and ISCU. For instance, high concentration of FXN might favor the formation of the FXN-bound Fe-S core complex and might constrain ISCU and NFS1 in specific conformations, hence preventing further maturation of the nascent Fe-S cluster and/or its transfer to acceptor proteins. It is very likely that this toxic mechanism would happen in any cell type and species since the Fe-S cluster assembly is a ubiquitous process relying on the same evolutionary-conserved machinery and components. What might change between tissues or cell types is the amount of FXN that can be tolerated, based on mitochondrial metabolism or Fe-S cluster demand. Investigating the toxicity in other cells such as neurons of the dorsal root ganglion (DRG), the dentate nucleus, or the motor cortex, primarily affected neuronal cell types in FRDA, would be important to understand whether different thresholds can be identified. In the context of DRG transduction, the intrinsic toxicity of FXN overexpression reported herein should be considered in addition to the AAV-induced pathology that was recently reported.[22]

In summary, our work provides further evidence as well as mechanistic insights into the toxicity associated with FXN overexpression. We show that toxicity is intrinsic to FXN function and that multiple organs can be affected, with different levels of overexpression leading to either moderate or acute liver dysfunction. These findings call for careful design and preclinical evaluation of gene therapy approaches for FRDA, to ensure a safe and efficacious expression of the FXN transgene in the targeted tissues.

MATERIALS AND METHODS

Animal procedures

$Fxn^{flox/null}$:MCK-cre (MCK-*Fxn*) mice (strain #029720) and WT C57Bl/6 mice (strain #000664) were obtained from The Jackson Laboratory (Farmington, CT, USA) at 5 weeks of age. Animal housing facility was controlled for temperature and humidity, with a 12-h light/dark cycle and free access to water and a standard rodent chow. Seven-week-old males (MCK-*Fxn* or C57Bl/6) were anesthetized with isoflurane prior to a single intravenous injection into the orbital vein. For the MCK-*Fxn* efficacy study, doses of 1×10^{13}, 3×10^{13}, or 1×10^{14} vg/kg of AAV9-CAG-FXN^{wt} were injected.

WT C57BL/6 mice were injected at 7 weeks of age with 1×10^{13} or 3×10^{13} vg/kg of AAV9-CAG-FXN^{wt} or AAV9-CAG-FXN^{N146K} preparations. Animals were observed twice a week and body weight was recorded weekly. At the end of each study, mice were anesthetized with isoflurane, perfused with PBS, and tissues of interest were harvested. For gDNA, RNA, and protein analyses, tissues were snap frozen in liquid nitrogen. For histochemical analysis, a piece of each tissue was collected in a cassette and fixed in 10% formalin (#426-797, Thermo Fisher Scientific, Waltham, MA) for 48 h. Blood was collected from awake animals via submandibular route using a 5-mm lancet (#GR5MM Goldenrod, Braintree Scientific, Braintree, MA) or at the end of each study via cardiac puncture before PBS perfusion.

For echocardiography, mice were induced to anesthetic state using isoflurane (3%) in an induction chamber, and then anesthetic status was maintained at ~2% isoflurane during animal preparation and image acquisition. While anesthetized, an animal was transferred onto a water-circulating heated blanket to remove hair around the left lateral and ventral thoracic area using a chemical hair removal agent. After hair removal, each animal was transferred onto a heated (~34–35°C) platform for echocardiography. Transthoracic parasternal long axis B-mode and parasternal short axis M-mode images of the heart were acquired using 18–38 MHz transducer (VisualSonics MS400) in Vevo 2100 ultrasound machine to assess left ventricular (LV) structure and function. Anesthesia level was adjusted to maintain heart rate between 450 and 550 bpm during image acquisition. After image acquisition, the animal was transferred to a warm cage for recovery. Post image acquisition, images were analyzed using Vevo lab analysis software, and the following parameters were collected from image analysis: LV ejection fraction, fractional shortening, LV end diastolic and systolic volume, LV end diastolic and systolic area, LV posterior and anterior wall thickness, LV corrected mass, and heart rate.

All animal-involved procedures were reviewed and approved by Pfizer's Institutional Animal Care and Use Committee (IACUC) and conducted in an Assessment and Accreditation of Laboratory Animal Care (AAALAC) International accredited facility.

Constructs and AAV production

Codon-optimized WT and N146K human *FXN* cDNAs coding for full-length mitochondrial frataxin (Uniprot: Q16595-1) were synthesized (Genewiz, South Plainfield, NJ, USA) and cloned into an AAV plasmid between a chicken beta-actin (CAG) promoter consisting of the cytomegalovirus (CMV) enhancer, the CAG promoter sequence and a beta-globin intron, and an SV40 polyA sequence. AAV9 vectors were produced by triple transfection method in HEK293 cells.[23] Titers of AAV preparations were obtained by quantitative real-time PCR using Taqman probes targeting the human *FXN* transgene sequence. Titers were of 2.14×10^{13} vg/mL (MCK-*Fxn* study) and 3.41×10^{12} vg/mL (WT C57Bl/6 studies) for AAV9-CAG-FXN^{WT} and of 4.07×10^{12} vg/mL for AAV9-CAG-FXN^{N146K}. Quality control of AAV preparations was performed by SDS-PAGE and silver staining, analysis of DNA content on agarose gel, and evaluation of endotoxin contamination with Endosafe PTS test (<0.5 EU/m).

Histology

All mouse tissues were fixed in 10% neutral buffered formalin and processed to paraffin blocks using standard histologic procedures. Tissue sections were cut on a rotary microtome at 5 μm and mounted on SuperFrost Plus slides (#12-550-15, ThermoFisher, Waltham, MA) for H&E, IHC, and ISH.

Frataxin IHC was performed on Leica Bond RX (Leica Biosystems, Buffalo Grove, IL) using an Alexa Fluor 488-conjugated mouse monoclonal antibody directed against human frataxin (#ab156033, Abcam, Cambridge, MA). Tissue sections were baked at 60°C for 30 min, deparaffinized, and pretreated with Epitope Retrieval 2 (#AR9640, Leica Biosystems) for 20 min at 100°C. Slides were incubated in peroxide block using the Bond DAB Polymer Refine detection kit (#DS9800, Leica Biosystems) for 10 min followed by primary antibody incubation at 1 μg/mL for 30 min, and incubation with a rabbit anti-Alexa Fluor 488 secondary antibody (#A11094, Thermo Fisher Scientific) at 0.5 μg/mL for 10 min. Frataxin was detected using the anti-rabbit HRP polymer in the Bond DAB Polymer Refine detection kit for 10 min and visualized using DAB chromogen for 10 min. An Alexa Fluor 488-conjugated mouse IgG2a κ negative control antibody was also run in parallel at 1 μg/mL (#IC003G, R&D Systems, Minneapolis, MN).

pHH3 IHC was performed on Leica Bond III. Sections were baked at 60°C for 30 min, deparaffinized, and pretreated with Epitope Retrieval 2 for 20 min at 100°C. Background Buster (#NB306, Innovex Biosciences, Richmond, CA) was applied for 10 min followed by a rabbit polyclonal antibody to Phospho-Histone H3 (#9701, Cell Signaling Technology, Danvers, MA) for 15 min at 0.13 μg/mL. Slides were incubated with the Refine kit peroxide block for 10 min prior to application of the Refine Kit anti-rabbit HRP polymer for 8 min. The signal was visualized through incubation with the Refine Kit DAB chromogen for 10 min. A rabbit negative isotype control was run at the same concentration (#02-6102, ThermoFisher, Waltham, MA). All slides were counterstained with hematoxylin, dehydrated through graded ethanol and xylene, and permanently mounted with coverslips.

Frataxin ISH was performed using either the RNAScope 2.5 LSx Assay – Brown reagent kit (#322700 or #322100, Advanced Cell Diagnostics, Newark, CA) according to the manufacturer's guidelines on a Leica Bond RX (Leica Biosystems). The human frataxin probe (#814408) was designed by Advanced Cell Diagnostics. Positive control assays were performed using a mouse PPIB probe (#313918, Advanced Cell Diagnostics), and negative control assays were performed using an *Escherichia coli* DapB probe (#312038, Advanced Cell Diagnostics).

DNA, RNA, and protein analyses

Tissues were pulverized using a mortar and pestle in the presence of liquid nitrogen. A portion of pulverized tissue was transferred into an

RNAse-free 2-mL tube using a disposable smartSpatula (#Z561762 Sigma, St. Louis, MO). One stainless-steel bead (#1026563, Qiagen, Venlo, Netherlands) and 1 mL of Trizol (#5596026, Invitrogen, Carlsbad, CA) were added to each tube. Tissue was homogenized using Qiagen TissueLyser II (Frequency 25 1/s x 2 times 2.5 min). After homogenization, samples were transferred to a phasemaker tube (#A33248, Invitrogen, Carlsbad, CA). Two hundred microliters of chloroform (#BP1145, Thermo Fisher Scientific) were added to the tube and vortexed for 15 s, then incubated for 5 min at room temperature. Samples were then centrifuged at 4°C x 14,000 g for 5 min. RNA extraction was completed using PureLink RNA mini kit (#12183025, Invitrogen) according to manufacturer's instructions. First-strand cDNA was prepared from extracted RNA using iScript Reverse Transcription Supermix (#1708840, Bio-Rad, Hercules, CA). Cycling conditions for cDNA generation were 25°C for 1 min x 1, 42°C for 30 min x 1, and 85°C for 5 min x 1.

For genomic DNA extraction, pulverized tissue was resuspended in TEN Lysis buffer (0.1 M NaCl, 0.01 M Tris, pH 8.0, 0.001 M EDTA, pH 8.0, 1% SDS) and vortexed at full speed for 15 s. Seven and half microliters of Proteinase K (#25530-049, Invitrogen) were added, and samples were incubated in a Thermomixer for 3 h at 56°C x 1,000 rpm. Samples were then cooled at room temperature for 10 min. Two microliters of RNAse A (#EN0531, Thermo Fisher Scientific) were then added and incubated for 5 min at room temperature. One volume of phenol:chloroform:isoamyl alcohol (25:24:1 ratio) (#P2609, Sigma) was added and samples were vortexed for 20 s at full speed. Samples were centrifuged at 15,0000 x *g* for 5 min at room temperature. The upper aqueous phase was transferred to a new tube and gDNA was precipitated with 0.5x volume of 7.5 M NH_4OAc (#A2000, Teknova, Hollister, CA) and 3 volumes of 100% ethanol. Samples were kept at −20°C overnight and then centrifuged at 16,000 x *g* for 30 min at 4°C to pellet DNA. Pellets were washed once with cold 70% ethanol and resuspended in nuclease-free water. Genomic DNA was diluted to 10 ng/μL prior to analysis. All reactions were prepared inside an Airclean 600 PCR workstation.

ddPCR reactions were set up using dUTP-free ddPCR Supermix for Probes (#186-3024, Bio-Rad, Hercules, CA) according to manufacturer's instructions, with droplets prepared using the Auto DG droplet generator. Amplification of target cDNA or genomic DNA was performed using the following cycling conditions: 95°C for 10 min x 1, 94°C for 30 s x 40, 60°C for 1 min x 40, 98°C for 10 min x 1. Droplets were then read using a QX200 Droplet Reader and data were analyzed using Quantasoft software (Bio-Rad) following manufacturer's recommendations for quality control and analysis. The following primer/probe sets were used: primer/probe set targeting the codon-optimized cDNA of WT and N146K human *FXN* was designed and synthesized (Applied Biosystems, Sparta, NJ); mouse *Fxn* (FAM20X, Applied Biosystems, #dMmuCPE5107916); *Asns* (FAM 20X, #Mm00803785_m1, Applied Biosysems, Foster City, CA); *Nppa* (FAM 20X, #Mm01255747_g1, Applied Biosystems); *Mthfd2* (FAM 20X, #Mm00485276_m1, Applied Biosystems), and *Gdf15* (FAM 20X, #Mm00442228_m1, Applied Biosystems); *Gapdh* (HEX 20X, #dMmuCPE5195283, Bio-Rad); *Hprt* (HEX 20X, #dMmuCPE5095493, Bio-Rad); and *Tbp* (VIC 20X, #Mm00446973_m1, Applied Biosystems); mouse *Tfrc* Copy Number Reference Assay (VIC-Tamara 20X) (#4458366, Applied Biosystems).

For protein extraction, pulverized tissue was resuspended in 1X NP40 extraction buffer (50 mM Tris-HCl, pH 7.5, 150 mM NaCl and 0.2% NP-40) containing 1x Protease Inhibitor Cocktail (#04693159001, Roche, Basel, Switzerland). Samples were sonicated briefly for 8–15 rounds at 25% amplitude, 0.2 s on/0.2 s off, and then incubated on ice for 20 min. After incubation, samples were centrifuged at 10,000 x *g* for 10 min at 4°C. One volume of 2.5X protein sample buffer (PSB 5X: 100 mL contains 2.5g Tris base, 50 mL glycerol, 10g SDS and is adjusted at pH 6.8 with HCl 37%) was added directly to the tube containing the NP40 buffer and pellet. Samples were resuspended by pipetting up and down, and sonication was repeated as necessary to shear DNA and resuspend membrane proteins. Determination of protein concentration was performed using Pierce 660 nm Protein Assay Reagent (#22660, Thermo Scientific, Waltham, MA) on NP40 extracts and adjusted according to the final volumes.

Samples were run on 4%–12% NuPage Bis-Tris gels in MES Buffer (#NP0002, Thermo Fisher Scientific) using 2.5–5 μg of protein per lane. Samples were transferred onto nitrocellulose membranes using the Trans-Blot Turbo Transfer system (Bio-Rad) and blocked in TBS-T (0.05%) + 5% non-fat milk (#9999S, Cell Signaling Technology, Danvers, MA). Primary antibodies used were Anti-FXN (#ab110328, Abcam), Anti-Lipoic Acid (#437695, Calbiochem, San Diego, CA), Anti-Vinculin (#SAB4200080, Sigma), Anti-SDHB (#ab14714, Abcam), Anti-PDHE2 (#ab172617, Abcam), Anti-Prohibitin (PHB) (#ab28172, Abcam), Anti-ACO2 (#ab129069, Abcam), and Anti-GCSH (#ab192613, Abcam). Secondary antibodies used were Goat Anti-Mouse HRP (#G21040, Invitrogen) and Goat Anti-Rabbit HRP (#65-6120, Invitrogen).

Serum analysis

Serum was obtained by collecting blood in 0.8-mL MiniCollect Serum Clot Activator Tubes (#450472 Greiner Bio-One, Austria) and allowing to clot for 30 min at room temperature. Samples were centrifuged for 10 min at 10,000 rpm at 4°C. Supernatant was transferred to a new Eppendorf tube and stored at −80°C until analysis. Serum samples were analyzed in the ADVIA 1800 Chemistry System. ALT was measured using Siemens Advia Chemistry reagent (#10318168, Munich, Germany). AST was measured using Siemens Advia Chemistry reagent (#10341132), and GLDH was measured using Randox (#GL441/GL442, Crumlin, UK). GLDH was measured using an optimized standard method according to the recommendations of the Deutsche Gesellschaft für Klinische Chemie (DGKC). Alkaline phosphatase was measured using Siemens Advia Chemistry reagent (#10916067) and the bichromatic (410/478 nm) rate technique. Albumin was measured using Siemens Advia Chemistry reagent (#10211832); serum albumin quantitively binds to BCG to form albumin-BCG complex and was measured at 596/694 nm. Total

protein was measured using Siemens Advia Chemistry reagent (#10311878) reading the reaction at 545 nm.

Statistical analysis

Data were compiled and graphed using GraphPad Prism software (version 9.0.0, GraphPad Software, San Diego, CA). Statistical analyses were performed in GraphPad Prism using one-way ANOVA and Dunnett's multiple comparison test.

SUPPLEMENTAL INFORMATION

Supplemental information can be found online at https://doi.org/10.1016/j.omtm.2022.02.002.

ACKNOWLEDGMENTS

The authors would like to acknowledge Pfizer Biomedicine Design team for the generation of AAV vectors, Madhu Sirivelu and James Stejskal for clinical pathology interpretation and assays, and Joan Kristel Aguilar for performing phospho-histone H3 staining.

AUTHOR CONTRIBUTIONS

C.H., D.H-S., B.T.A., S.S., L.O.W., M.P., and A.M designed and supervised experiments, C.H., T.L.P., A.K., R.G., R.C.K., K.A.B, X.C., T.M., B.T.A., I.P., T.F., L.M, T-W.C, K.L., C.S., and A.M. conducted experiments or collected data, C.H., T.L.P., A.K., R.G., R.C.K., K.A.B., X.C., D.H-S., T.M., B.T.A., I.P., L.O.W., and A.M. analyzed and interpreted data, C.H., T.L.P., and A.M. drafted the manuscript, C.H., T.L.P., R.C.K., K.A.B., D.H-S., L.O.W., C.B., M.P., and A.M. performed critical revision of the manuscript.

DECLARATION OF INTERESTS

All authors are or were employees of Pfizer Inc. at the time of their contribution to this manuscript.

REFERENCES

1. Harding, A.E. (1981). Friedreich's ataxia: a clinical and genetic study of 90 families with an analysis of early diagnostic criteria and intrafamilial clustering of clinical features. Brain *104*, 589–620.
2. Pandolfo, M. (2009). Friedreich ataxia: the clinical picture. J. Neurol. *256*, 3–8.
3. Campuzano, V., Montermini, L., Molto, M.D., Pianese, L., Cossee, M., Cavalcanti, F., Monros, E., Rodius, F., Duclos, F., Monticelli, A., et al. (1996). Friedreich's ataxia: autosomal recessive disease caused by an intronic GAA triplet repeat expansion. Science *271*, 1423–1427.
4. Lill, R., and Freibert, S.A. (2020). Mechanisms of mitochondrial iron-sulfur protein biogenesis. Annu. Rev. Biochem. *89*, 471–499.
5. Tsai, C.L., and Barondeau, D.P. (2010). Human frataxin is an allosteric switch that activates the Fe-S cluster biosynthetic complex. Biochemistry *49*, 9132–9139.
6. Schmucker, S., Martelli, A., Colin, F., Page, A., Wattenhofer-Donze, M., Reutenauer, L., and Puccio, H. (2011). Mammalian frataxin: an essential function for cellular viability through an interaction with a preformed ISCU/NFS1/ISD11 iron-sulfur assembly complex. PLoS One *6*, e16199.
7. Colin, F., Martelli, A., Clemancey, M., Latour, J.M., Gambarelli, S., Zeppieri, L., Birck, C., Page, A., Puccio, H., and Ollagnier de Choudens, S. (2013). Mammalian frataxin controls sulfur production and iron entry during de novo Fe4S4 cluster assembly. J. Am. Chem. Soc. *135*, 733–740.
8. Fox, N.G., Yu, X., Feng, X., Bailey, H.J., Martelli, A., Nabhan, J.F., Strain-Damerell, C., Bulawa, C., Yue, W.W., and Han, S. (2019). Structure of the human frataxin-bound iron-sulfur cluster assembly complex provides insight into its activation mechanism. Nat. Commun. *10*, 2210–2217.
9. Gervason, S., Larkem, D., Mansour, A.B., Botzanowski, T., Muller, C.S., Pecqueur, L., Le Pavec, G., Delaunay-Moisan, A., Brun, O., Agramunt, J., et al. (2019). Physiologically relevant reconstitution of iron-sulfur cluster biosynthesis uncovers persulfide-processing functions of ferredoxin-2 and frataxin. Nat. Commun. *10*, 3566–3577.
10. Puccio, H., Simon, D., Cossee, M., Criqui-Filipe, P., Tiziano, F., Melki, J., Hindelang, C., Matyas, R., Rustin, P., and Koenig, M. (2001). Mouse models for Friedreich ataxia exhibit cardiomyopathy, sensory nerve defect and Fe-S enzyme deficiency followed by intramitochondrial iron deposits. Nat. Genet. *27*, 181–186.
11. Martelli, A., Schmucker, S., Reutenauer, L., Mathieu, J.R.R., Peyssonnaux, C., Karim, Z., Puy, H., Galy, B., Hentze, M.W., and Puccio, H. (2015). Iron regulatory protein 1 sustains mitochondrial iron loading and function in frataxin deficiency. Cell. Metab. *21*, 311–322.
12. Perdomini, M., Belbellaa, B., Monassier, L., Reutenauer, L., Messaddeq, N., Cartier, N., Crystal, R.G., Aubourg, P., and Puccio, H. (2014). Prevention and reversal of severe mitochondrial cardiomyopathy by gene therapy in a mouse model of Friedreich's ataxia. Nat. Med. *20*, 542–547.
13. Gerard, C., Xiao, X., Filali, M., Coulombe, Z., Arsenault, M., Couet, J., Li, J., Drolet, M.C., Chapdelaine, P., Chikh, A., and Tremblay, J.P. (2014). An AAV9 coding for frataxin clearly improved the symptoms and prolonged the life of Friedreich ataxia mouse models. Mol. Ther. Methods Clin. Dev. *1*, 14044–14054.
14. Piguet, F., de Montigny, C., Vaucamps, N., Reutenauer, L., Eisenmann, A., and Puccio, H. (2018). Rapid and complete reversal of sensory ataxia by gene therapy in a novel model of Friedreich ataxia. Mol. Ther. *26*, 1940–1952.
15. Salami, C.O., Jackson, K., Jose, C., Alyass, L., Cisse, G.I., De, B.P., Stiles, K.M., Chiuchiolo, M.J., Sondhi, D., Crystal, R.G., and Kaminsky, S.M. (2020). Stress-induced mouse model of the cardiac manifestations of Friedreich's ataxia corrected by AAV-mediated gene therapy. Hum. Gene Ther. *31*, 819–827.
16. Belbellaa, B., Reutenauer, L., Messaddeq, N., Monassier, L., and Puccio, H. (2020). High levels of frataxin overexpression lead to mitochondrial and cardiac toxicity in mouse models. Mol. Ther. Methods Clin. Dev. *19*, 120–138.
17. Belbellaa, B., Reutenauer, L., Monassier, L., and Puccio, H. (2019). Correction of half the cardiomyocytes fully rescue Friedreich Ataxia mitochondrial cardiomyopathy through cell-autonomous mechanisms. Hum. Mol. Genet. *28*, 1274–1285.
18. Gellera, C., Castellotti, B., Mariotti, C., Mineri, R., Seveso, V., Didonato, S., and Taroni, F. (2007). Frataxin gene point mutations in Italian Friedreich ataxia patients. Neurogenetics *8*, 289–299.
19. Bridwell-Rabb, J., Winn, A.M., and Barondeau, D.P. (2011). Structure-function analysis of Friedreich's ataxia mutants reveals determinants of frataxin binding and activation of the Fe-S assembly complex. Biochemistry *50*, 7265–7274.
20. Bellanda, M., Maso, L., Doni, D., Bortolus, M., De Rosa, E., Lunardi, F., Alfonsi, A., Noguera, M.E., Herrera, M.G., Santos, J., et al. (2019). Exploring iron-binding to human frataxin and to selected Friedreich ataxia mutants by means of NMR and EPR spectroscopies. BBA - Proteins Proteomics *1867*, 140254–140265.
21. Garcia-Olloqui, P., Rodriguez-Madoz, J.R., Di Scala, M., Abizanda, G., Vales, A., Olague, C., Iglesias-Garcia, O., Larequi, E., Aguado-Alvaro, L.P., Ruiz-Villalba, A., et al. (2020). Effect of heart ischemia and administration route on biodistribution and transduction efficiency of AAV9 vectors. J. Tissue Eng. Regen. Med. *14*, 123–134.
22. Hordeaux, J., Buza, E.L., Dyer, C., Goode, T., Mitchell, T.W., Richman, L., Denton, N., Hinderer, C., Katz, N., Schmid, R., et al. (2020). Adeno-associated virus-induced dorsal root ganglion pathology. Hum. Gene Ther. *31*, 808–818.
23. Grieger, J.C., Soltys, S.M., and Samulski, R.J. (2016). Production of recombinant Adeno-associated virus vectors using suspension HEK293 cells and continuous harvest of vector from the culture media for GMP FIX and FLT1 clinical vector. Mol. Ther. *24*, 287–297.

Journal of Neuropathology & Experimental Neurology Advance Access published January 12, 2017

J Neuropathol Exp Neurol
Vol. 00, No. 0, 2017, pp. 1–8
doi: 10.1093/jnen/nlw111

ORIGINAL ARTICLE

Friedreich Ataxia: Hypoplasia of Spinal Cord and Dorsal Root Ganglia

Arnulf H. Koeppen, MD, Alyssa B. Becker, BA, Jiang Qian, MD, PhD, and Paul J. Feustel, PhD

Abstract

After Friedreich's description in 1877, depletion of myelinated fibers in the dorsal columns, dorsal spinocerebellar and lateral corticospinal tracts, and neuronal loss in the dorsal nuclei of Clarke columns were considered unique and essential neuropathological features of Friedreich ataxia (FA). Lack of large neurons in dorsal root ganglia (DRG), thinning of dorsal roots (DR), and poor myelination in sensory nerves are now recognized as key components of FA. Here, we measured cross-sectional areas of the mid-thoracic spinal cord (SC) and neuronal sizes in lumbosacral DRG of 24 genetically confirmed FA cases. Mean thoracic SC areas in FA (24.17 mm^2) were significantly smaller than those in 12 normal controls (37.5 mm^2); DRG neuron perikarya in FA (1362 μm^2) were also significantly smaller than normal (2004 μm^2). DRG neuron sizes were not correlated with SC areas. The FA patients included a wide range of disease onset and duration suggesting that the SC undergoes growth arrest early and remains abnormally small throughout life. Immunohistochemistry for phosphorylated neurofilament protein, peripheral myelin protein 22, and myelin proteolipid protein confirmed chaotic transition of axons into the SC in DR entry zones. We conclude that smaller SC areas and lack of large DRG neurons indicate hypoplasia rather than atrophy in FA.

Key Words: Atrophy, Dorsal roots, Dorsal root ganglion, Friedreich ataxia, Hypoplasia, Spinal cord.

INTRODUCTION

Since Friedreich's illustration in 1877 of dorsal column degeneration in the disease that now bears his name (1), many generations of medical trainees have accepted that the most important abnormalities reside in the spinal cord. Beyond the dorsal columns, the disease also affects the dorsal spinocerebellar and lateral corticospinal tracts, and the dorsal nuclei of Clarke columns. While Friedreich was aware of thinning of the dorsal spinal roots, he wrote that dorsal root ganglia (DRG) were normal (1). Remarkably, he observed that the nerve fibers in the dorsal roots (DR) were more abundant than normal and rather thin, displaying only rare thicker fibers similar to those in the intact ventral roots. Over the ensuing years, it became clear that DRG are a critical target of the disease, and that fiber loss in the dorsal columns and neuronal atrophy of the dorsal nuclei could be secondary. The neuropathological phenotype also includes hypoplasia or atrophy of Betz cells of the motor cortex that matches the invariable degeneration of the lateral corticospinal tracts. Although the normal dentate nucleus (DN) receives sparse collaterals from mossy fibers of spinal origin, the severe lesion of the DN in Friedreich ataxia (FA) is not obviously related to the damaged spinal cord.

Irrespective of disease onset, the spinal cord in FA is thinner than normal (2), and the bony spinal canal in FA patients is abnormally narrow on plain radiographs (3). In retrospect, this old observation gains significance because of more recent measurements of magnetic resonance images (4–6). The narrow spinal canal on plain X-ray films in FA (3) must be interpreted as the result of incomplete anteroposterior and transverse enlargement of the spinal cord during growth. Therefore, thinning of the spinal cord in FA may be more appropriately termed hypoplasia, although it is likely that inflammation and invasion of DRG neurons continue to damage afferent fibers in DR (7). It is of interest that Friedreich had already proposed in 1877 that smallness of the clavae (gracile and cuneate nuclei) was developmental (1).

The neurons of DRG, satellite cells, and Schwann cells of DR and peripheral nerves derive from the neural crest (8), although boundary cap cells may also contribute to the constituents of DRG and proximal and distal processes (9). Axons deriving from DRG neurons grow into the periphery where they become sensory nerves, into the gray matter of the spinal cord, and, over remarkably long distances, into the nuclei of the dorsal columns. Histoautoradiography and immunohistochemistry have clarified the developmental steps in the complex specification of DRG neurons (10–13), but it is unknown how frataxin deficiency impacts this elaborately tooled process. Total absence of frataxin in genetically engineered mice is lethal to the embryo (14), but it must still be determined

From the Research Service, Veterans Affairs Medical Center, Albany, NY (AHK, ABB); Department of Pathology, Albany Medical College, Albany, NY (AHK, JQ); and Department of Neuroscience and Experimental Therapeutics, Albany Medical College, Albany, NY (PJF)

Send correspondence to: Arnulf H. Koeppen, MD, Research Service (151), Veterans Affairs Medical Center, 113 Holland Ave., Albany, NY 12208. E-mail: arnulf.koeppen@med.va.gov

Funding: New York State Department of Health, Albany, NY, USA; Friedreich's Ataxia Research Alliance, Downingtown, PA, and Neurochemical Research, Inc., Glenmont, NY.

Disclosure/conflict of interest: The authors have no duality or conflicts of interest to declare.

whether spinal cord and DRG development proceeds normally when frataxin is only low rather than totally absent.

It is impossible to establish from autopsy tissues of patients who succumbed to FA after years of illness how neural crest abnormalities cause hypoplasia of spinal cord and DRG. The current study used quantitative measurements to establish a possible correlation of the cross-sectional area of the thoracic spinal cord and neuronal sizes in lumbosacral DRG. The results strongly support the conclusion that these neural tissues are small because of hypoplasia rather than atrophy and that their developmental delay occurs independently.

MATERIALS AND METHODS

The table summarizes clinical and genetic data of 24 FA patients. The cases were selected from among 47 FA autopsies because the harvested tissues included thoracic spinal cord and lumbosacral DRG. One patient (FA4) with early onset and short survival was a compound heterozygote with a guanine-adenine-adenine (GAA) trinucleotide expansion of 730 on 1 allele and a deletion (c.11_12delTC) on the other allele. We considered inclusion of this patient justified because clinical features were similar to those of the other FA patients with early onset and short duration. The neuropathology was identical to a patient with long biallelic GAA expansions (FA1; GAA1, 1016; GAA2, 1016). Disease onset in 2 patients was delayed to 32 and 34 years (FA23 and FA24, Table), and their deaths occurred at 87 and 77 years, respectively. In FA23, FA was not diagnosed during life although the patient was ataxic. The diagnosis was assured, however, by characteristic neuropathology and genetic testing of DNA extracted from frozen cerebellar cortex. In homozygous FA patients, ages of onset and disease duration correlated inversely with the shorter GAA trinucleotide repeat expansion (Table). The cause of death in 19 patients was cardiomyopathy (79%). Other causes of death were cachexia (FA3), myoglobinuria and renal failure (FA16), myocardial infarction (FA17), brain hemorrhage (FA20), and coronary atherosclerosis (FA23). The hearts of all patients were available for detailed histological study, and iron-reactive inclusion in cardiomyocytes were detectable in 23 of 24 cases (96%).

Although the spinal cord in FA is thin at all levels, we elected to measure the cross-sectional areas at the midthoracic level because they change little between the second and twelfth segments (15), and long-tract disease in FA is most distinct (Fig. 1). Measurements of neuronal areas in lumbosacral rather than thoracic DRG were preferred because of the vast sensory input from legs and perineum, and the known correlation of DRG neuronal size and the extent of the innervated region (16). Transverse sections of thoracic spinal cord were embedded in paraffin, sectioned at 6-μm thickness, and stained by immunohistochemistry with an antibody to myelin basic protein (MBP). Sections of DRG were stained with hematoxylin and eosin. Twelve adult control cases with ages of death from 41 to 90 years (mean ± SD: 65 ± 15 years) were made available by the autopsy services of Veterans Affairs Medical Center in Albany, NY, and Albany Medical College. Inclusion criteria were absence of neurological disease of any kind and availability of the midthoracic spinal cord and lumbar DRG. In some older archival control cases, paraffin blocks were no longer available, and measurements of the spinal cord were made on sections stained with hematoxylin and eosin or the Luxol fast blue-periodic acid-Schiff method for myelin. In selected cases of FA and normal controls, 1.5-cm-long segments of upper lumbar spinal cord were trimmed longitudinally to represent DR entry zones. Paraffin sections were immunostained for phosphorylated neurofilament protein, peripheral myelin protein 22 (PMP22), and proteolipid protein (PLP).

Host, clonality, supplier, catalogue number, antigen retrieval method, and final protein concentration of antibodies were as follows: MBP, mouse monoclonal (IgG), Covance, Emeryville, CA; SMI-94R, 80% ethanol overnight at 4 °C, ascites fluid (protein not assayed); PMP22, rabbit polyclonal (IgG), Abcam, Cambridge, MA, ab15506, 80% ethanol overnight at 4 °C, 0.4 μg/ml; PLP, rabbit polyclonal (IgG), Abcam, ab105784, 80% ethanol overnight at 4 °C, followed by 0.01M citric acid-sodium citrate buffer (pH 6) at 95 °C for 20 minutes, 2 μg/ml; phosphorylated neurofilament protein, mouse monoclonal (IgG), Sternberger Monoclonals, Inc., Lutherville, MD (now Covance), SMI-31, 0.01 M citric acid-sodium citrate buffer (pH 6) at 95 °C for 20 min, ascites fluid (protein not assayed). A summary of the immunohistochemical procedure is available (7).

Image capture and measurements of the cross-sectional areas of the spinal cord and perikaryal area of DRG neurons were made with AxioVision software (version 4.8) (Carl Zeiss, Oberkochen, Germany). Thoracic spinal cord areas were expressed as mm^2 and neuronal areas as μm^2. Selection of DRG neurons for measurement was based on the presence of distinct nuclei and nucleoli (17). DRG exhibit a common autolytic artifact, namely, separation of the neuronal plasma membrane from the cytoplasmic borders of surrounding satellite cells. In an effort to compensate for this artifact, the measuring spline was drawn midway between satellite cells and the neuronal surface, as practiced by Ohta et al (18). To prevent duplicate measurement of DRG neurons, the specimen stage of the microscope was moved in register across the section.

Statistical Analysis

Comparison of FA patients and normal controls was by Student t-test with values expressed as mean ± SD. Correlation between thoracic spinal cord area and DRG neuronal size and GAA repeat expansion were assessed by regression. To model the thoracic spinal cord area as a function of age, we used non-linear regression (OriginPro 2016, Origin Lab Corporation, Northampton, MA) under the assumption that the area is 11.56 mm^2 at birth (19) and subsequent growth is exponential, reaching a constant fully mature size. The equation was therefore $S(t) = 11.56 + (S_{mature})\,(1-e^{-kt})$ where S is the thoracic spinal cord area as a function of time (t) in years; S_{mature} the increase in the area of the spinal cord from birth to maturity; and k the growth constant. Thoracic spinal cord areas at younger ages were obtained from the literature (15, 19) and the growth rate constant was assumed to be equal in both groups.

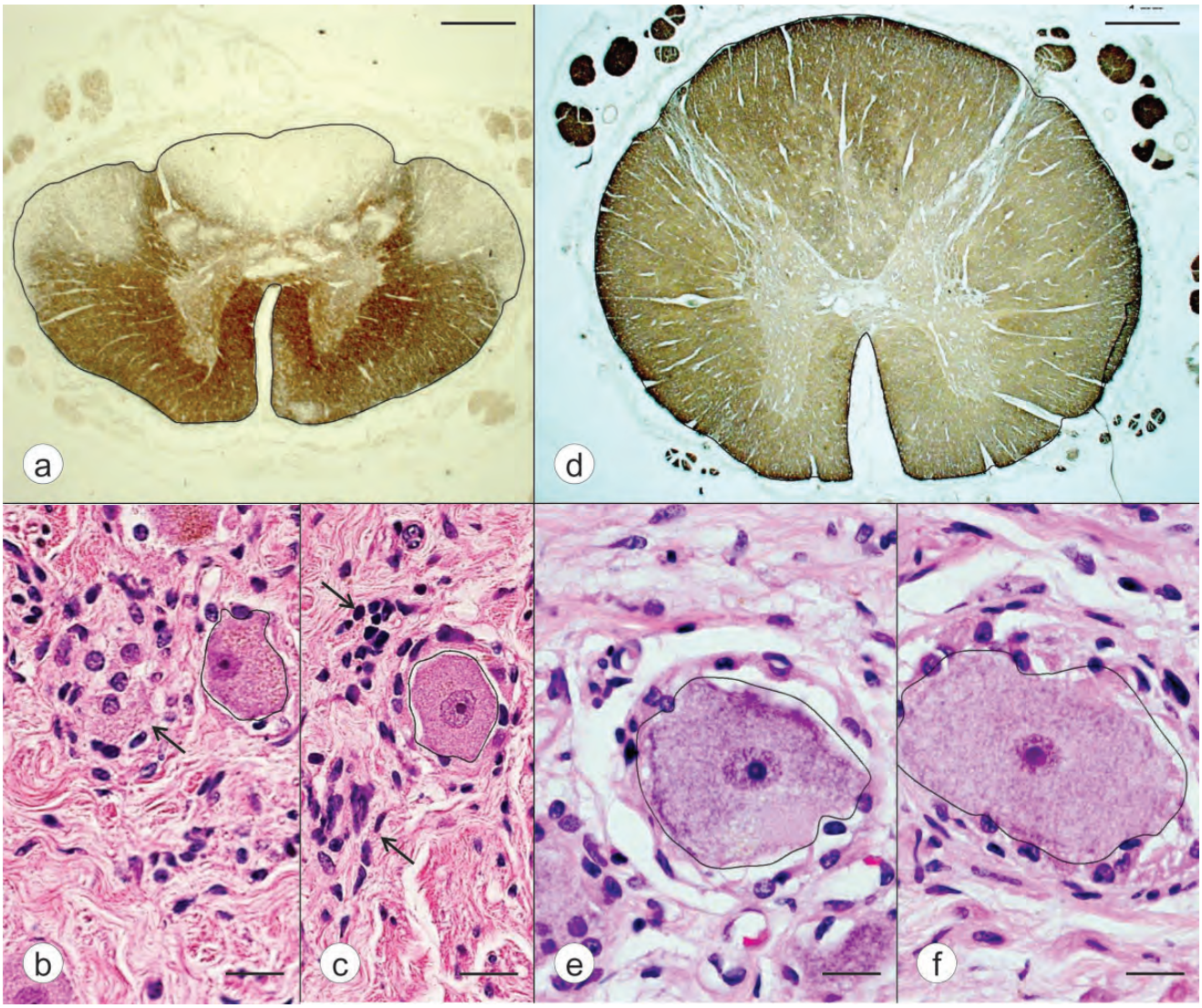

FIGURE 1. Area measurements of the thoracic spinal cord and DRG neurons. **(a–c)** FA (FA18, Table); **(d–f)** normal control (man, age of death, 62 years). **(a, d)** Immunostain of MBP; **(b, c, e, f)** hematoxylin and eosin. The transverse section of the thoracic spinal cord in FA **(a)** shows the overall reduction in size and the characteristic symmetrical loss of myelinated fibers in dorsal columns, dorsal spinocerebellar, and lateral corticospinal tracts. After outlining the limits of the spinal cord in FA **(a)** and the control **(d)** with the spline feature of the program, cross-sectional areas were measured as 19.11 and 36.53 mm^2, respectively. DRG neurons with distinctly visible nucleoli were similarly outlined and measured **(b, c, e, f)**. When the satellite layer and neuronal plasma membrane were separated due to postmortem artifact, the outline was placed midway between satellite cells and the neuron (18). In FA, neurons were generally smaller **(b, c)**. The section shown in **(c)** reveals residual nodules (arrows). In **(b)**, a neuron is undergoing active invasion by satellite cells or monocytes (arrow). Scale bars: **a, d,** 1 mm; **b, c, e, f,** 20 μm.

RESULTS

Figure 1 shows composite photomicrographs of thoracic spinal cord and DRG of an FA patient (FA18, Table) (Fig. 1a–c) and a normal control (man, age of death: 62 years) (Fig. 1d–f). The stain for MBP shows the small size of the cord and the severe symmetrical depletion of myelinated fibers in dorsal columns, dorsal spinocerebellar, and lateral corticospinal tracts (Fig. 1a). The section of the FA case also shows anteroposterior flattening of the thoracic spinal cord when compared with the normal control (Fig. 1d). Neurons in the DRG of FA (Fig. 1b, c) are generally smaller in comparison with normal DRG nerve cells (Fig. 1e, f). In FA, DRG are hypercellular, residual nodules are frequent (Fig. 1c, arrows); and a cluster of small cells suggests active invasion of a neuron by mononuclear cells, satellite cells, or both (Fig. 1b, arrow).

Figure 2 shows a composite of a DR entry zone in FA (FA22, Table) and a control case after immunohistochemical staining for phosphorylated neurofilament protein (Fig. 2a, b), PMP22 (Fig. 2c, d), and PLP (Fig. 2e, f). Reaction product of phosphorylated neurofilament protein shows transition of thin axons from the DR into the central nervous system (CNS)

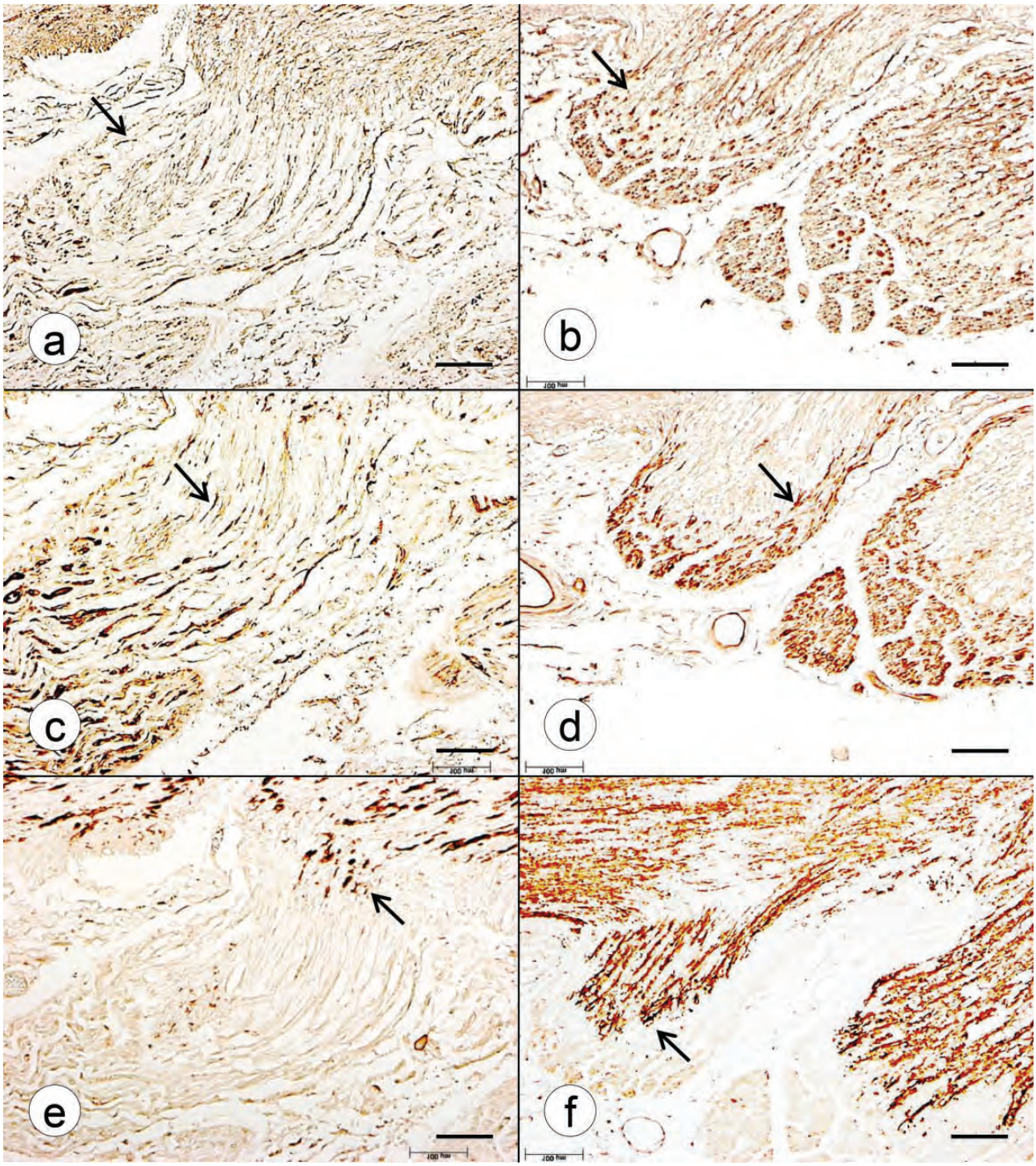

FIGURE 2. DR entry zone in FA and a normal control. **(a, c, e)** FA (FA22, Table); **(b, d, f)** normal control (woman, age of death, 42 years). Adjacent sections were immunostained with antibodies to phosphorylated neurofilament protein **(a, b)**; PMP22 **(c, d)** or PLP **(e, f)**. The cranial direction of the spinal cord is to the right. In FA, the DR contains an abundance of thin axons **(a)**, but the transition from relatively thick axons of the peripheral nervous system (PNS) to thin CNS axons is indistinct (**a,** arrow). In the normal control, the transition from PNS to CNS axons occurs over a very narrow segment of the DR (**b,** arrow), and larger axons are restricted to the PNS portion of the root. In normal DR, PMP22 immunoreactivity ends abruptly (**d,** arrow) whereas in FA, some PMP22-reactive fibers can be traced across the entire DR entry zone (**c,** arrow). In the normal control, PLP-reactive myelin sheaths begin at a considerable distance (~200 μm) before entering the spinal cord proper, and the transition to CNS myelin is sharp (**f,** arrow). In FA, PLP immunoreactivity in the CNS portion of the DR is sparse, and the transition from PNS to CNS territory is irregular (**e,** arrow). Bars: 100 μm.

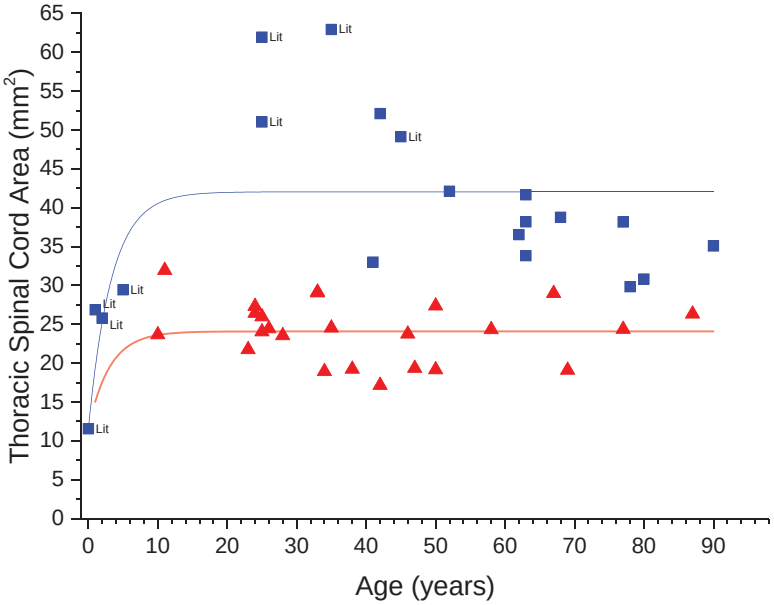

FIGURE 3. Comparison of growth curves of the thoracic spinal cord areas in FA and normal controls. Red triangles and red line, FA; blue squares and blue line, normal controls. Values taken from the literature are labeled as "Lit" (normal controls only). Curves were fitted by a non-linear regression program (OriginPro 2016) under the assumption that the thoracic spinal cord area is the same for FA and normal controls at birth, and subsequent growth is exponential until reaching a fully mature size. Thereafter, size is assumed to be constant without increasing or decreasing. The underlying equation is $S(t) = 11.56 + (S_{mature})(1-e^{-kt})$, where S is the thoracic spinal cord area as a function of time t (in years); 11.56 is the cord size in mm^2 at $t = 0$; S_{mature} is the increase in size from birth to maturity; and k is the rate constant of growth. k has units of inverse time. 1/k will be the time constant for growth and 0.693/k is the half time of growth. Both FA and normal controls show rapid growth of the spinal cord over the first 10 years of life, but FA fails to achieve normal adult dimensions. The spinal cord in FA remains hypoplastic throughout life and does not undergo progressive thinning as a function of age.

of the spinal cord in FA (Fig. 2a, arrow), but the sharp demarcation of relatively large axons in normal DR is absent (Fig. 2b, arrow). Similarly, the DR entry zone in FA lacks the abrupt ending of PMP22 (Fig. 2c, arrow), which characterizes the normal DR (Fig. 2d, arrow). Reaction product of the CNS-specific protein, PLP, mirrors the disorganized transition of PMP22-positive DR fibers in FA (Fig. 2e, arrow), and stands out against the sharply demarcated CNS myelin in the normal DR (Fig. 2f, arrow).

The adult thoracic spinal cord area in FA (death at >24 years, Table) is 23.83 ± 3.68 mm^2 (mean ± SD), which is significantly lower than the mean in normal adults (42.19 ± 10.35, including data from the literature) ($p < 0.001$) (Table). Figure 3 shows a regression analysis of thoracic spinal cord areas vs age of death (Table). The curve for FA was constructed under the assumptions that newborns destined to develop FA have the same thoracic spinal cord areas as normal newborns (11.56 mm^2 [19]) and that the area increases exponentially to a final size. The regression curve for FA shows that the spinal cord fails to achieve normal adult size and remains stable over the entire disease duration or at least does not significantly decrease in those who die at more advanced age. In normal controls, the spinal cord grows rapidly and reaches its final size at the approximate age of 25 years. The growth phase of these curves should be interpreted with caution as we have little information aside from the literature on the rate of growth of the spinal cord in normal humans, and no information at all on FA.

The nerve cell area in DRG of FA (1362 ± 442 μm^2 [mean ± SD]) is significantly lower than normal (2004 ± 233 μm^2) ($p < 0.001$). Figure 4 shows a display of the mean area of neurons in DRG of FA and normal controls plotted against the area of the thoracic spinal cord in matching specimens (FA cases from the Table). There is no correlation in FA or normal controls, implying that delayed growth of DRG neurons and spinal cord in FA proceeds independently over time. Spinal cord areas and neuronal sizes in DRG of FA patients did not correlate significantly with the GAA trinucleotide repeats on either allele (Table).

DISCUSSION

Hypoplasia or Atrophy of Spinal Cord and DRG Neurons in FA

FA is commonly called a "neurodegenerative" disease, implying that the nervous system at one time during the patient's life is normal and then undergoes "atrophy". In the absence of information about the sizes of spinal cord and DRG neurons before disease onset, these terms may no longer be justified. Length and volume of the human spinal cord increase massively between birth and maturity, and most of the accrual is due to white matter (19).

Pooling the meticulous planimetric measurements of the cross-sectional area of the thoracic spinal cord (segment VI)

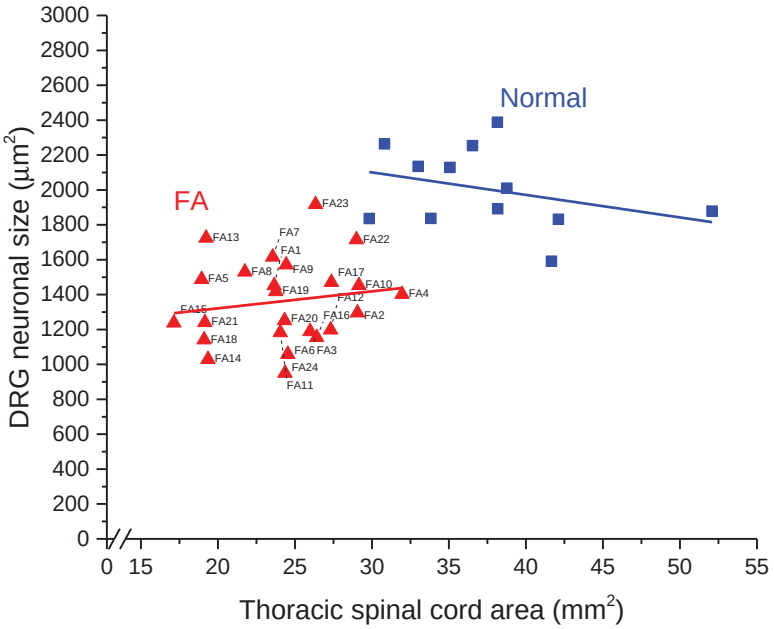

FIGURE 4. Correlation of DRG neuronal sizes and thoracic spinal cord area in FA and normal controls. Red triangles and red line, FA (labeled according to the Table); blue squares and blue line, normal controls. Spinal cord areas and mean nerve cell sizes in DRG are lower in FA than in normal controls but linear regression shows no significant correlation between DRG and spinal cord measurements. Neither slope is significantly different from zero ($p = 0.29$; $R^2 = 0.11$ for normal and $p = 0.47$; $R^2 = 0.02$ for FA).

by Stilling at the ages of 1, 2, 25, 35, and 45 years (15), the combined measurements of thoracic spinal gray and white matter in newborns (19), and measurements in this laboratory allowed the construction of a growth curve of the normal spinal cord that can be compared with FA (Fig. 3). Based on the equation shown in the legend to Figure 3 for normal spinal cords, the expected thoracic cross-sectional areas in our FA patients succumbing to early deaths (FA1 and FA4 in the Table) should be 40.5 mm^2 (death at 10 years) and 40.9 mm^2 (death at 11 years), respectively. The measurements, however, were 23.7 and 32.0 mm^2. It is likely that planimetry of camera clara or lucida drawings practiced by the earlier authors (15, 19) was less accurate than the quantitative method described here. The areas determined in the 2 rapidly fatal cases of FA by our method did not differ significantly from those in adult FA patients (Table) who died between the ages of 23 and 87. These observations support the interpretation that spinal cord enlargement in FA stops prematurely after growth at either a normal or a reduced rate, representing of hypoplasia.

The exacting measurements of neuronal diameters in the first sacral DRG of humans by Ohta et al (18) revealed rapid growth of nerve cell sizes between the ages of 0.5 and 12 years with little change thereafter into advanced age. Our measurements of neuronal areas in normal controls are not directly comparable to data published by Ohta et al due to technical differences and a less selective harvesting of lumbosacral DRG. Nevertheless, the significantly lower neuronal sizes in DRG of FA patients undergo little change between the ages of 10 and 87 years (Table). This result implies that hypoplasia also affects DRG neurons in FA. In this context, inflammatory destruction of DRG neurons (7) may be a superimposed process and ultimately less important than dysfunction due to life-long hypoplasia.

Previous systematic measurements of DR nerve fibers in FA and a comparison with ventral roots also militated against atrophy (20). Histograms published by Koeppen et al confirmed Friedreich's original report (1) that DR lacked large myelinated fibers (20). Surprisingly, the overall degree of myelination of thin DR axons was significantly higher (20).

Only 2 groups of authors have examined the transition of DR fibers from the PNS to the CNS in FA (21, 22). Hughes et al (22) traced DR fibers into the spinal cord and concluded that they reached the gray matter of the dorsal horns while few entered the dorsal columns. In contrast, Jitpimolmard et al favored regeneration of thin fibers to account for their abnormal abundance (21). Our data (Fig. 2a) support the former conclusion, i.e. that DR axons traverse the entry zone though the abrupt transition from thicker peripheral axons to thin centrally projecting fibers is absent. Several other observations suggest that a developmental abnormality of DR accounts for the fiber depletion in the spinal cord. It is likely that the disorganization of the DR entry zone reflects incorrect signaling to growing axons during development. An incidental observation in the 2 very young patients (FA1 and FA4, Table) was the presence in their DR of bizarre expansions that reacted with antibodies to S100 and glial fibrillary acidic protein (not illustrated). This observation may indicate an abnormal Schwann cell response in FA that is no longer detectable in adult cases of FA. The spinal cord areas normally occupied by the dorsal columns in FA are clearly recognizable although there is subtotal loss of myelinated fibers. Gliosis characteristically occurs in sheaf-like bundles, suggesting that DRG at one time successfully projected axons through DR and dorsal columns to

TABLE. Patient Data

No.	Sex	Age of onset (years)	Age at death (years)	Disease duration (years)	GAA1	GAA2	Spinal cord area (mm^2)	Mean neuronal area (μm^2)
FA1	M	2	10	8	1016	1016	23.66	1452
FA2	F	2	33	31	455	604	29.06	1296
FA3	F	5	25	20	800	1100	25.98	1189
FA4	M	5	11	6	730	deletion	31.96	1402
FA5	M	7	34	27	1114	1114	18.94	1488
FA6	M	7	35	28	750	1000	24.54	1058
FA7	F	8	28	20	559	709	23.56	1616
FA8	F	8	23	15	528	777	21.75	1530
FA9	F	9	26	17	690	850	24.44	1571
FA10	M	9	33	24	925	925	29.16	1453
FA11	F	10	25	15	750	850	24.05	1183
FA12	F	10	24	14	700	950	27.32	1198
FA13	M	10	38	28	249	934	19.23	1725
FA14	F	10	47	37	613	613	19.36	1029
FA15	F	11	42	31	761	990	17.15	1238
FA16	F	12	24	12	740	910	26.42	1155
FA17	M	14	50	36	400	750	27.37	1471
FA18	F	15	69	54	568	568	19.11	1141
FA19	M	16	46	30	599	599	23.76	1418
FA20	F	17	58	41	566	566	24.33	1252
FA21	F	17	50	33	512	1122	19.16	1241
FA22	F	18	67	49	621	766	28.99	1715
FA23	M	32	87	55	120	170	26.34	1917
FA24	F	34	77	43	466	841	24.36	950
Mean ± SD		12 ± 7.8	40.1 ± 20.1	28.1 ± 13.8	635 ± 222	814 ± 225	24.17 ± 3.89	1362 ± 242

Patients are listed in order of age of onset, also showing sex, age of death, disease duration, GAA1 and GAA2, thoracic spinal cord area in mm^2, and mean area of DRG neurons in μm^2.

In 12 adult locally procured controls (F, 2; M, 10), the age of death was 65 ± 15 years and ranged from 41 to 90 years. The thoracic spinal cord area in these cases is 37.3 ± 3.6 mm^2. In matching DRG, the neuronal area is 2004 ± 233 μm^2 (mean ± SD). The differences between FA and controls are significant at $p < 0.001$ (spinal cord and DRG neuronal areas). Data are expressed as mean ± SD.

F, female; FA, Friedreich ataxia; DRG, dorsal root ganglia; GAA, guanine-adenine-adenine trinucleotide expansion; M, male; SD, standard deviation.

reach the gracile and cuneate nuclei. The presence of gliosis, however, is consistent with superimposed degeneration before the spinal cord reaches its final transverse size (Fig. 3).

One of the most dramatic lesions in the spinal cord of FA is the total or subtotal lack of large nerve cells in the dorsal nuclei of Clarke columns at thoracic and upper lumbar spinal levels. While interpretable as transsynaptic degeneration, the timing of this deafferentation in FA is unknown. Even in the 2 very young patients with FA, the neurons in the dorsal nuclei were greatly reduced in number (FA1, Table) or entirely absent (FA4, Table). It is likely that these normally rather large nerve cells failed to survive due to lack of innervation from DR collaterals that normally occurs between 14 and 17.5 weeks of gestation (23).

Muscle spindle afferents make monosynaptic contacts with anterior horn cells, and areflexia is a common observation in FA. Motor neurons of the spinal cord, however, are not seriously affected by FA though ventral roots may show more numerous clusters of small fibers compared with normal ventral roots (20). There is also significant electrodiagnostic evidence that muscles undergo denervation in FA (24).

In situ hybridization of mouse embryos with digoxigenin-labeled antisense riboprobes first detects frataxin transcripts in DRG at the gestational ages of 14.5–16.5 days (25), at which time the spinal cord also shows frataxin expression. Assuming that DRG and spinal cord are similar in the human embryo, high prenatal frataxin expression may make these tissues vulnerable later in life, and the onset of developmental delay may have to be placed into prenatal life.

The Functional Consequences of Hypoplastic DRG and Spinal Cord in FA, and Therapeutic Implications

The described observations suggest that the term "onset" of FA may have to be redefined. Some parents report that their children who are ultimately affected by the disease did not develop motor skills at the same pace as their unaffected siblings. It remains to be established how clinical onset occurs on a background of neural hypoplasia. Many clinicians charged with the care of FA patients rely on the length of GAA trinucleotide repeats, and notably the shorter GAA expansion, to set a prognosis. Statistical analysis, however, reveals no correlation between the lengths of GAA trinucleotide repeats and spinal cord area or DRG neuronal size ($R^2 < 0.1$). This observation may be surprising in light of the inverse

correlation between the shorter GAA expansion and clinical onset of FA (Table). Very short GAA trinucleotide repeat expansions convey a benign course and long survival, such as in FA23 (Table), and cardiomyopathy in such cases may be entirely absent. Hypoplasia of spinal cord and DRG do not appear to conform to a gradient of GAA trinucleotide expansion. It is likely that even modest reductions of frataxin are detrimental to the development of spinal cord and DRG.

In contrast to DRG and spinal cord, thinning of the DN in FA represents true atrophy (26). The DN may remain intact in cases of rapidly fatal FA cardiomyopathy (27); and it is reasonable to correlate the onset of the cerebellar manifestations of FA with a threshold level of neuronal loss. Onset of proprioceptive and superficial sensory loss may coincide with beginning inflammatory infiltration of DRG (7). It is uncertain how upper motor neuron weakness correlates with progressive atrophy of the corticospinal tracts. Loss of Betz cells is common in FA, but these very large neurons of the frontal cortex account for only a small minority of fibers in the corticospinal tracts.

The recognition of hypoplasia in the pathogenesis of FA may redirect therapy. At this time, onset is defined by clinical criteria, and disability is quantified by one or more widely used ataxia rating scales. Clinical trials with drugs generally involve symptomatic FA patients in a specific age group. FA is an uncommon disease (28), but newborn screening for the FA mutation may be justified as the downstream effects of frataxin deficiency are better defined. The task of preventing growth arrest of spinal cord and DRG evolving between birth and maturity will differ from therapy in established FA patients. It seems reasonable to propose that drugs raising systemic frataxin levels should be used mainly for presymptomatic FA patients.

ACKNOWLEDGMENTS

We thank the families who agreed to donate autopsy tissue for FA research. Many pathologists agreed to complete detailed autopsies on FA patients though death in remote areas of the United States often made this task very difficult. The work described in this article was completed in the research laboratories of the Veterans Affairs Medical Center in Albany, NY, USA. Michigan State University, East Lansing, MI, USA made available a copy of the classic 1859 treatise on the structure of the spinal cord by Stilling (15).

REFERENCES

1. Friedreich N. Ueber Ataxie mit besonderer Berücksichtigung der hereditären Formen. Nachtrag. Virchows Arch Pathol Anat Physiol Klin Med 1877;70:140–52
2. Koeppen AH, Neuropathology of the inherited ataxias. In: Manto M-U, Pandolfo M, eds., The Cerebellum and its Disorders, Cambridge University Press, Cambridge 2002:387–405
3. Vassilopoulos D, Spengos M, Scarpalezos S. Étude radiologique de la colonne vertébrale cervicale dans certaines maladies dégénératives neurologiques. J Radiol Electrol 1977;58:183–6
4. Wessel K, Schroth G, Diener HC, et al. Significance of MRI-confirmed atrophy of the cranial spinal cord in Friedreich's ataxia. Eur Arch Psychiatry Neurol Sci 1989; 238:225–30
5. Mascalchi M, Salvi F, Piacentini S, et al. Friedreich's ataxia: MR findings involving the cervical portion of the spinal cord. AJR Am J Roentgenol 1994;163:187–91
6. Chevis CF, da Silva CB, D'Abreu A, et al. Spinal cord atrophy correlates with disability in Friedreich's ataxia. Cerebellum 2013;12:43–7
7. Koeppen AH, Ramirez RL, Becker AB, et al. Dorsal root ganglia in Friedreich ataxia: satellite cell proliferation and inflammation. Acta Neuropathol Commun 2016;4:46
8. Pannese E. The histogenesis of the spinal ganglia. Adv Anat Embryol Cell Biol 1974;47:7–97
9. Maro GS, Vermeren M, Voiculescu O, et al. Neural crest boundary cap cells constitute a source of neuronal and glial cells of the PNS. Nat Neurosci 2004;7:930–8
10. Lawson SN, Caddy KWT, Biscoe TJ. Development of rat dorsal root ganglion neurons. Cell Tissue Res 1974;153:399–413
11. Lawson SN, Biscoe TJ. Development of mouse dorsal root ganglia: an autoradiographic and quantitative study. J Neurocytol 1979;8:265–74
12. Kitao Y, Robertson B, Kudo M, et al. Neurogenesis of subpopulations of rat lumbar dorsal root ganglion neurons including neurons projecting to the dorsal column nuclei. J Comp Neurol 1996;371:249–57
13. Raible DW, Ungos JM. Specification of sensory neuron cell fate from the neural crest. Adv Exp Med Biol 2006;589:170–80
14. Cossée M, Puccio H, Gansmuller A, et al. Inactivation of the Friedreich ataxia mouse gene leads to early embryonic lethality without iron accumulation. Hum Mol Genet 2000;9:1219–26
15. Stilling B. Neue Untersuchungen ueber den Bau des Rückenmarks. Heinrich Hotop. Cassel 1859
16. Lieberman AR, Sensory ganglia. In: Landon DN, editor. The peripheral nerve. Chapman and Hall, London 1976:188-278
17. Aherne W. Some morphometric methods for the central nervous system. J Neurol Sci 1975;24:221–41
18. Ohta M, Offord K, Dyck PJ. Morphometric evaluation of first sacral ganglia of man. J Neurol Sci 1974;22:73–82
19. Lassek AM, Rasmussen GL. A quantitative study of the newborn and adult spinal cords of man. J Comp Neurol 1938;69:371–9
20. Koeppen AH, Morral JA, Davis AN, et al. The dorsal root ganglion in Friedreich's ataxia. Acta Neuropathol 2009;118:763–76
21. Jitpimolmard S, Small J, King RHM, et al. The sensory neuropathy of Friedreich's ataxia: an autopsy study of a case with prolonged survival. Acta Neuropathol 1993;86:29–35
22. Hughes JT, Brownell B, Hewer RL. The peripheral sensory pathway in Friedreich's ataxia. An examination by light and electron microscopy of the posterior nerve roots, posterior root ganglia, and peripheral sensory nerves in cases of Friedreich's ataxia. Brain 1968;91:803–18
23. Altman J, Bayer SA, Development of the Human Spinal Cord. An Interpretation Based on Experimental Studies in Animals. Oxford: Oxford University Press 2001
24. Caruso G, Santoro L, Perretti A, et al. Friedreich's ataxia: electrophysiological and histological findings. Acta Neurol Scand 1983;67:26–40
25. Jiralerspong S, Liu Y, Montermini L, et al. Frataxin shows developmentally regulated tissue-specific expression in the mouse embryo. Neurobiol Dis 1997;4:103–13
26. Koeppen AH, Ramirez RL, Becker AB, et al. Friedreich ataxia: failure of GABA-ergic and glycinergic synaptic transmission in the dentate nucleus. J Neuropathol Exp Neurol 2015;74:166–76
27. Koeppen AH, Morral JA, McComb RD, et al. The neuropathology of late-onset Friedreich's ataxia. Cerebellum 2011;10:96–103
28. Vankan P. Prevalence gradients of Friedreich's ataxia and R1b haplotype in Europe co-localize, suggesting a common Palaeolithic origin in the Franco-Cantabrian ice age refuge. J Neurochem 2013;126(suppl 1): 11–20

International Journal of Cardiology 330 (2021) 259–265

Contents lists available at ScienceDirect

International Journal of Cardiology

journal homepage: www.elsevier.com/locate/ijcard

Prognostic value of longitudinal strain and ejection fraction in Friedreich's ataxia

L. Legrand [a,c,e], C. Heuze [a], A. Diallo [d,e], M.L. Monin [b], C. Ewenczyk [b], E. Vicaut [d,e], G. Montalescot [a,c,e], R. Isnard [a,c,e], A. Durr [b], F. Pousset [a,c,e,*]

[a] Sorbonne Université, Cardiology Department, AP-HP, Pitié-Salpêtrière University Hospital, Paris, France
[b] Sorbonne Université, Institut du Cerveau et de la Moelle épinière (ICM), AP-HP, INSERM, CNRS, Pitié-Salpêtrière University Hospital, Paris, France
[c] ICAN (Institute for Cardiometabolism and Nutrition), Pitié-Salpêtrière University Hospital, Paris, France
[d] URC Lariboisière University Hospital, Paris, France
[e] ACTION (Allies in Cardiovascular Trials Initiatives and Organized Networks) Group, France

ARTICLE INFO

Article history:
Received 21 October 2020
Received in revised form 1 February 2021
Accepted 11 February 2021
Available online 14 February 2021

Keywords:
Friedreich's ataxia
Prognosis
Myocardial strain
Cardiomyopathy

ABSTRACT

Background: Friedreich's ataxia (FA) is a rare autosomal recessive mitochondrial disease most commonly due to a triplet repeat expansion guanine-adenine-adenine (GAA) in the *FXN* gene. Cardiac disease is the major cause of death, patients with reduced left ventricular ejection fraction (LVEF) having the worse prognosis. Longitudinal strain (LS) appeared to be a better predictor of outcome than LVEF in different diseases. We compared the prognostic value of LS measured from the 4 chambers view to LVEF.
Methods: From 2003 to 2017 consecutive patients with FA were included and LS analysis was retrospectively performed.
Results: We studied 140 patients, with a median age of 34 (26–41) years (Q1–Q3) with age at onset of 14 (11–19) years and GAA repeats on the shorter allele of 600 (467–783) pb. Mean LS was 19.9 ± 5.0% and LVEF 64 ± 8%. After a mean follow-up of 7.4 ± 3.9 years, 14 patients died. In univariate Cox analysis, all-cause mortality was associated with: LS (HR 0.83; 95%CI, 0.75–0.91, $p = 0.0002$), LVEF (HR 0.30; 95%CI, 0.19–0.49, $p < 0.0001$), GAA repeats on the shorter allele (HR 1.29; 95%CI, 1.10–1.51, $p = 0.002$), age at onset (HR 0.87; 95%CI, 0.77–0.98, $p = 0.018$), LVSystolic Diameter (HR 1.17; 95%CI, 1.09–1.26, $p < 0.0001$), LVMass index (HR 1.02; 95%CI, 1.00–1.04, $p = 0.027$), and LVDiastolic Diameter (HR1.12; 95%CI, 1.01–1.23, $p = 0.028$). In multivariate analysis, LVEF was the only independent predictor of mortality (HR 0.41; 95%CI, 0.23–0.74, $p = 0.0029$).
Conclusion: In FA, LS was not an independent predictor of mortality, LVEF remained the only independent predictor in the present study.

1. Introduction

Friedreich ataxia (FA) is an inherited autosomal recessive mitochondrial disorder and the most frequent inherited ataxia. It is characterized by progressive spinocerebellar ataxia, auditory and visual neuropathy, scoliosis and extra neurological effects such as diabetes, and cardiomyopathy. First symptoms often occur during adolescence or occasionally later in life. FA is in most cases caused by a homozygous guanine-adenine-adenine (GAA) trinucleotide expansion in the frataxin (*FXN)* gene, which encodes frataxin, a mitochondrial protein involved in iron metabolism [1–3]. Longer GAA expansions are associated with earlier symptom onset and increased severity of the neurologic and cardiac disease [3,4].

Cardiac disease is the major cause of premature mortality in FA: congestive heart failure and supraventricular arrhythmia are the most frequent cardiac complications [5–7]. Left ventricular ejection fraction (LVEF) has been shown to be an independent predictor of prognosis in FA [6].

Assessment of myocardial deformation using two-dimensional (2D) speckle tracking echocardiography has emerged as a method for the assessment of myocardial function. Global longitudinal strain (GLS) that reflects the longitudinal percentage deformation of all myocardial segments in the apical views has been validated as an index for global LV function [8,9]. Subtle LV dysfunction can be detected by this technique in a number of circumstances, even when LVEF is normal [10]. Furthermore, GLS appeared to be a stronger predictor of outcome compared to LVEF in different diseases, particularly in individuals with preserved

Abbreviations: ECG, electrocardiogram; FA, Friedreich's ataxia; LS, Longitudinal strain; LV, left ventricle; LVDD, left ventricular end diastolic diameter; LVEF, left ventricular ejection fraction; LVSD, left ventricular end systolic diameter; PWT, posterior wall thickness; RWT, relative wall thickness; SWT, septal wall thickness; GAA, guanine-adenine-adenine trinucleotide.

* Corresponding author at: Département de Cardiologie, Hôpital de la Pitié Salpêtrière, 47 boulevard de l'Hôpital, 75651 Paris Cedex 13, France.
E-mail address: f.pousset@aphp.fr (F. Pousset).

https://doi.org/10.1016/j.ijcard.2021.02.032
0167-5273/

ejection fraction [11]. In FA, reduced LV long axis function has been reported using Tissue Doppler imaging [12], and longitudinal strain in adult subjects with a normal LVEF [13], and has also been reported in cohorts of adults and children which included subjects with a reduced LVEF [7,14].

The objective of the present study was to compare the prognostic value of longitudinal strain and of LVEF in a large cohort of adult FA patients.

2. Methods

2.1. Population

We studied unselected genetically confirmed FA subjects evaluated from February 2003 through November 2017 in the Department of Cardiology (Pitié-Salpêtrière University Hospital, Paris, France), who had digitally-acquired baseline echocardiographic images, stored in 2D DICOM file formats to retrospectively assess myocardial strain. If a patient had several exams, the oldest was studied. The *Institut National de la Santé et de la Recherche Médicale* (INSERM) approved the study. Informed written consent was given in accordance with the law and local ethical regulations.

2.2. Outcome of interest

Follow-up data were obtained in May 2018 by clinical visits, or telephone interviews with the patient or relative, or by mail. Death, cardiac arrhythmia, heart failure and stroke were recorded. When contact with a patient or the family was not possible, the date of death was obtained from the French national registry of deaths. All-cause mortality was the endpoint.

2.3. Neurological evaluation

Neurological assessment was performed by a neurologist within three months of cardiac evaluation, and was assessed using the SARA score (Scale for the Assessment and Rating of Ataxia), a semi-quantitative scale developed to assess ataxia with values from 0 (no ataxia) to 40 (most severe ataxia) [15] and eight items assessing stance, sitting, speech disturbances, finger chase, dysmetria, nose-finger test, tremor, fast alternating hand movements, and heel-shin slide.

Cardiac evaluation-including clinical evaluation, standard 12-lead electrocardiography, and standard transthoracic echocardiography-was performed on the same day.

2.4. Electrocardiogram (ECG)

A 12-lead surface resting ECG was recorded at 25 mm/s and 10 mm/mV and analyzed blinded to the echocardiographic data by one experienced cardiologist (LL). Repolarization was considered abnormal in the presence of negative T waves (≥0.1 mV) or flat T waves in at least two leads, except V1 and V2 in the absence of bundle branch block.

2.5. Echocardiography

All studies were performed on standard commercially available echocardiographic systems (Acuson C256, *Siemens Company, Mountain view, USA*), Vivid 7 and E9 *(General Electric Company, Horten, Norway)* by the same expert cardiologist (FP) blinded to genetic data. Standard techniques were used to obtain M-mode, 2-dimensional, and Doppler measurements in accordance with the recommendations of the American Society of Echocardiography. Each measure was the mean of three measurements [16]. Left ventricular (LV) end diastolic diameter (LVDD), LV end systolic diameter (LVSD), septal wall thickness (SWT), and posterior wall thickness (PWT) were obtained in the parasternal long axis view from an M-mode acquisition. Relative wall thickness (RWT) was defined as SWT + PWT/LVDD, and a concentric remodeling pattern as RWT > 0.42 [17]. Left ventricular mass index (LVMi) was obtained from M-mode and normalized for body surface area (ASE convention). Left ventricular ejection fraction (LVEF) was calculated using the bi-plane Simpson's disk method [16]. The peak E and A waves were measured from the pulsed wave Doppler signal obtained at the mitral valve leaflet tips.

2.6. Strain analysis

We used the TOMTEC Imaging Systems (Image Arena 4.6.3, Unterschleißheim, Germany) that is independent of ultrasound machines. The reliability of TOMTEC software for the measurement of LS on digitally stored images has been validated [18,19]. Acquired images were stored in DICOM format. All analyses were performed by a single experienced cardiologist (CH) blinded to clinical, genetic, LVEF, and outcome data. Longitudinal strain (LS) assessments of the LV were performed in the apical 4 chamber view, because cine loops in 3 or 2 chamber views were not available in the oldest exams. First, the cardiac cycle with the best image quality was selected and cardiac cycles were defined by the positioning of R waves. After manual tracing of three points designated by the software in the left ventricle on an end-systolic frame, the software automatically traced the endocardial border. Segments that failed to track were manually adjusted by the operator. Any view in which two or more segments could not be tracked was not included in the analysis. Peak systolic longitudinal strain was computed automatically, generating regional data from six segments (apical, mid, proximal) and an average value for the 4 chamber view (Fig. 1).

The intra- and inter-observer variability for LS measurement was assessed in 22 participants of the study. For intra observer variability (CH), analyses were repeated blinded to the initial results on the same cardiac cycles. Inter-observer variability was tested by a second observer (LL) blinded to the results of the first observer.

2.7. Statistical analysis

Continuous variables are presented as mean and standard deviations (SD) or median (interquartile range) if appropriate. By definition, LS was a negative number, but the absolute value of LS was used in the study. To measure the strength of association between LS and the other variables, Pearson's correlation was used for normally-distributed data; in case of non-normally data, Spearman's correlation was used. Baseline characteristics of the population were compared between living and deceased people using Student's *t*-test when Gaussian distribution occurred, or Mann-Whitney tests for non-Gaussian distribution. Categorical variables are presented as numbers and percentages, and are compared using Chi-square test *p*-values, or Fisher's test *p*-values when there were few events.

Kaplan-Meier curves were constructed and compared using the log-rank test.

Associations between any death and baseline parameters were assessed by using a multivariate Cox regression model. Unadjusted and adjusted models were performed for death; we included LVEF and GLS. Candidate covariables were selected for use in the multivariable model based on previous mortality studies and the rule of number of events per variable.

The two-sided significance level was fixed at 5%. All tests were performed with SAS version 9.4 statistical software (SAS Institute Inc., Cary, NC, USA).

3. Results

3.1. Clinical characteristics of the population

We identified 156 patients with standard echocardiogram and images digitally stored in 2D DICOM file format. Among these patients

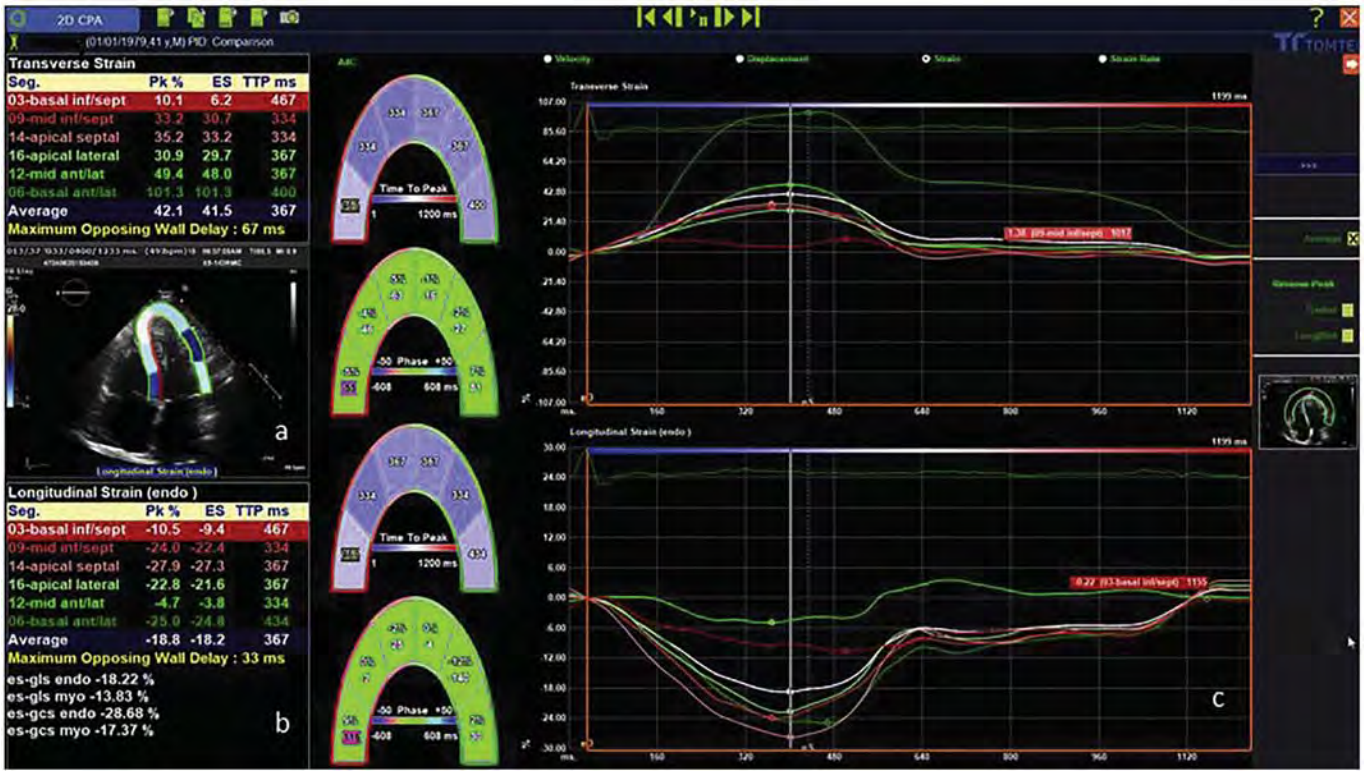

Fig. 1. Longitudinal strain (LS) measurement from 4-chamber apical view with Tomtec software(a) Example of tracking for the segments measured. (b) Peak longitudinal strain value (%) for each segment measured and the average is Longitudinal Strain (LS). (c) Peak strain in each segment is presented graphically.

140 had Longitudinal Strain (LS) and LVEF: LS was not available in 15 patients because of poor image quality (14), and persistent atrial fibrillation (1) and LVEF was not available in 1 patient. Characteristics of the 140 patients are presented in Table 1. Five patients carried point mutations in one of the two alleles. The shorter allele correlated with the larger allele ($r = 0.50$ $p < 0.0001$). As in previous studies, age at onset correlated with the length of the shorter GAA ($r = -0.56$ $p < 0.0001$) and of the longer GAA ($r = -0.42$ $p < 0.0001$), but in

Table 1
Baseline characteristics of 140 patients with Friedreich ataxia.

	Population $N = 140$	Death $N = 14$	Alive $N = 126$	p value
Age (years)	34 (2.6–41)	33 (27–39)	34 (25–41)	ns
Age at onset (years)	14 (11–19)	10 (9–12)	15 (12−21)	0.0020
Duration of symptoms (years)	16 (11−23)	19 (16–23)	15 (10−23)	0.0726
Age at onset of wheelchair use (years), $N = 109$	23 (18–29)	17 (15–24)	24 (20−30)	0.0104
GAA repeats on the shorter allele (pb)	600 (467–783)	800 (667–867)	600 (433–767)	0.0008
GAA repeats on the longer allele (pb)	867 (767–1000)	1017 (833–1100)	833 (733–1000)	0.0172
Body mass index (kg/m^2)	21.8 (19.5–23.9)	22.2 (19.1–23.8)	21.8 (19.6–23.9)	ns
Body surface area (m^2)	1.7 (1.6–1.8)	1.7 (1.5–1.8)	1.7 (1.6–1.8)	ns
Systolic blood pressure (mmHg)	117 ± 15	105 ± 14	119 ± 14	0.0018
Diastolic blood pressure (mmHg)	71 ± 9	65 ± 9	72 ± 9	0.0220
Heart rate (bpm)	77 ± 12	77 ± 14	77 ± 12	ns
Longitudinal Strain (%)	20.2 (17.2–22.7)	12.9 (8.7–20.0)	20.6 (17.7–22.8)	0.0015
LV Ejection Fraction (%)	64 (60–68)	59 (42–65)	64 (61–69)	0.0080
Septal Wall Thickness (mm)	11.4 ± 2.4	12.6 ± 2.7	11.3 ± 2.3	0.0080
Posterior Wall Thickness (mm)	10.4 ± 1.8	10.1 ± 2.4	10.5 ± 1.8	0.0661
Relative Wall Thickness	0.50 ± 0.13	0.51 ± 0.18	0.50 ± 0.12	ns
LV End Diastolic Diameter (mm)	43.8 (40.1–48.2)	46.7 (41.0–50.6)	43.5 (40.1–47.7)	ns
LV End Systolic Diameter (mm)	26.2 (23–30.4)	31.9 (25–37.6)	26.0 (22.9–29.8)	0.0213
LV Mass index (g/m^2)	99 ± 24	113 ± 27	98 ± 24	0.0250
LV Mass index male (g/m^2)	108 ± 26			
LV Mass index female(g/m^2)	91 ± 20			
Transmitral E wave (cm/s)	0.72 ± 0.15	0.70 ± 0.13	0.72 ± 0.15	ns
Transmitral A wave (cm/s)	0.52 (0.43–0.62)	0.34 (0.24–0.47)	0.53 (0.44–0.63)	0.0002
E/A ratio	1.4 (1.1–1.7)	2.1 (1.4–3.3)	1.4 (1.1–1.7)	0.0025
Left atrial area (cm^2)	15 (12–18)	15 (13−23)	15 (12–18)	ns
Previous Heart failure	4 (2.9%)	4 (28.6%)	0	<0.0001
Previous stroke	1 (0.7%)	0	1 (0.8%)	ns
Previous atrial fibrillation	9 (6.4%)	4 (28.6%)	5 (4%)	0.0061
Hypertension	11 (7.9%)	1 (7.1%)	10 (7.9%)	ns
Diabetes	7 (5%)	3 (21.4%)	4 (3.2%)	0.0222

Data are expressed as mean ± SD or median (interquartile range).

multivariate analysis the correlation was independent only for the shorter allele ($p < 0.0001$).

Nine patients (6.4%) had previous paroxysmal or persistent atrial fibrillation, 4 (2.9%) had previous symptoms of heart failure, and 1 (0.7%) had previous stroke. At baseline, there were 7 (5.0%) subjects with a diagnosis of diabetes and 11 (7.9%) with a diagnosis of hypertension. The mean SARA score was 19.5 ranging from 9 to 39 for 21 (15%) patients. At baseline, 20 (14.3%) patients were on beta-blockers, 15 (10.7%) on angiotensin converting enzyme inhibitors or angiotensin receptor blockers, 7 (6%) on oral anticoagulants (vitamin K antagonist or new oral anticoagulant), 4 (2.9%) on aspirin, 7 (5%) on amiodarone, 4 (2.9%) on diuretics, 2 (1.4%) on spironolactone, and 1 (0.7%) on digoxin.

3.2. ECG

Cardiac involvement assessed by ECG was present in 89% of the patients with abnormal repolarization, and 27/140 (19%) had a right bundle branch block (complete or incomplete).

3.3. Echocardiographic variables

Echocardiographic parameters are shown in Table 1. Left ventricular structural abnormalities, were observed with a concentric pattern assessed by a mean RWT of 0.50 ± 0.13, 105 (75%) patients had RWT >0.42. Only 14 patients had SWT or PWT ≥13 mm, and 2 patients ≥15 mm. Mean LV mass index was 99 ± 24 g/m^2: 91 ± 20 g/m^2 in 72 women and 108 ± 26 g/m^2 in 68 men; LVMI was increased in 54/140 (39%) patients: 25/68 men had a LVMI >115 g/m^2 and 29/72 women had a LVMI >95 g/m^2. Left ventricle outflow tract obstruction was not observed. Mean LVEF was 64 ± 8% and ranged from 26% to 80%.

3.4. Longitudinal strain

The intra-observer coefficient of variation (CV) for longitudinal strain was 5.8% and the inter-observer CV was 6.3%. Mean LS was 19.9 ± 5.0% and ranged from 5.9% to 31.2% (Fig. 2). No relationship was found between LS and the SARA score. LS negatively correlated with the length of the shorter GAA repeats ($r = -0.23$, $p = 0.0059$) and with the length of the longer GAA repeats ($r = -0.25$, $p = 0.0027$), but the correlation was not independent in multivariate analysis for both alleles. LS correlated with LVEF ($r = 0.31$, $p = 0.0002$) in total population and in patients with LVEF >50% ($r = 0.26$, $p = 0.003$). The 131/140 (84%) patients with LVEF>50% had a mean LVEF of 65 ± 5% and a mean LS of 20.4 ± 4.6%. The 9/140 (6%) patients with a LVEF ≤50% had a mean LVEF of 41 ± 7% and a mean LS of 12.0 ± 3.7%.

LS correlated with the echographic parameters reflecting hypertrophy: SWT ($r = -0.27$, $p = 0.001$) and LVMi ($r = -0.18$, $p = 0.034$), but no significant correlation was found with PWT, RWT, LVDD, and LVSD.

3.5. Follow up

After a mean follow up of 7.4 ± 3.9 years ranging from 0.4 to 14.7 years, 14 (10%) patients died at a mean age of 33.0 ± 7.8 years: 10 from cardiovascular origin, 4 from unknown origin. No patient was lost to follow-up. During the follow-up, atrial fibrillation occurred in 12 (8.6%) patients, heart failure in 6 (4.3%), and stroke in 2 (1.4%). No ventricular arrhythmia was reported. Patients who died during the follow up had younger age of disease onset and larger GAA repeats on the shorter allele, and they had at baseline lower LVEF and lower LS (Table 1).

3.6. Survival analysis

In the univariate Cox analysis all-cause mortality was associated with smaller LS (HR 0.83; 95%CI 0.75–0391, $p = 0.0002$) and smaller LVEF (HR 0.30; 95%CI 0.19–0.48, $p < 0.0001$). The other prognostic factors are shown in Table 2. Parameters reflecting the diastolic function, mitral peak A wave, the ratio E/A, and the left atria area were significantly associated with all-cause mortality. In multivariate Cox analysis, LVEF was the only independent factor associated with all-cause

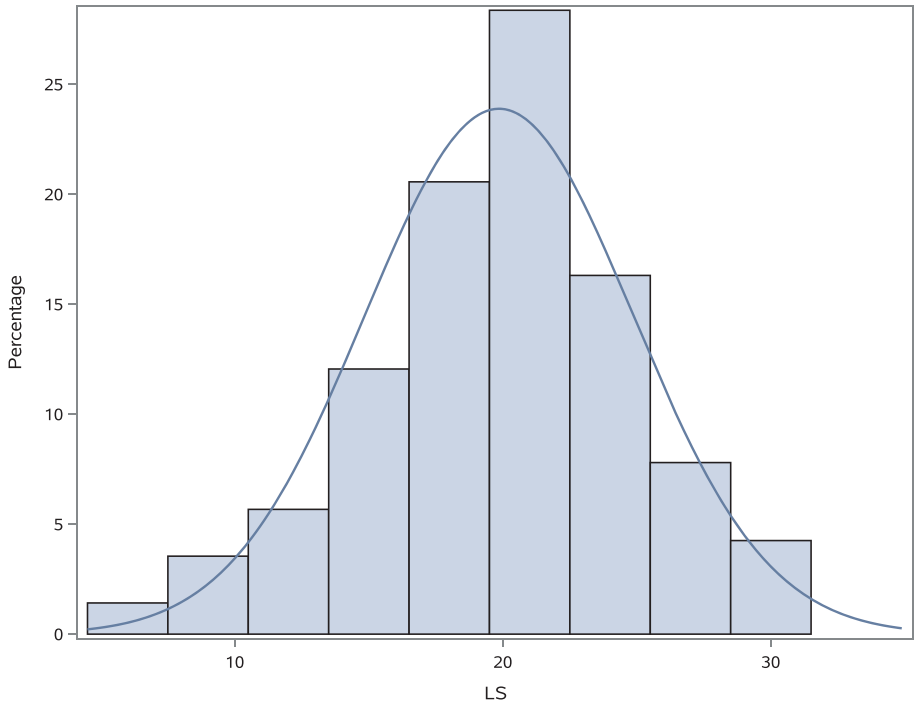

Fig. 2. Distribution of Longitudinal strain (LS) in 140 patients with Friedreich ataxia median LS = 20.2% (17.2–22.7).

Table 2
Survival analysis in 140 patients with Friedreich ataxia and factors associated with all-cause mortality.

	Univariate Cox model			Multivariate Cox model		
Variables	N	Hazard-ratio (95%CI)	*p*-value	N	Hazard ratio (95%CI)	*p*-value
Longitudinal strain (%)	140	0.83 (0.75–0.91)	0.0002	140	0.91 (0.81–1.03)	0.1375
LV ejection fraction (units = 10%)	140	0.30 (0.19–0.48)	<0.0001	140	0.41 (0.23–0.74)	0.0029
Age (years)	140	0.98 (0.93–1.04)	0.5005			
Age at onset (years)	139	0.87 (0.77–0.98)	0.0176			
GAA repeats on the shorter allele (units = 50pb)	140	1.29 (1.10–1.51)	0.0018			
LV Mass index (g/m^2)	140	1.02 (1.00–1.04)	0.0270			
Sex Female	140	1.73 (0.58–5.16)	0.3283			
Body mass index (kg/m^2)	140	0.98 (0.83–1.17)	0.8309			
Septal wall thickness (mm)	140	1.20 (0.98–1.46)	0.0844			
LV end diastolic diameter (mm)	140	1.12 (1.01–1.23)	0.0283			
LV end systolic diameter (mm)	138	1.17 (1.09–1.26)	<0.0001			
Posterior wall thickness (mm)	140	0.88 (0.65–1.19)	0.4096			
Relative wall thickness	140	0.87 (0.01–73.1)	0.9516			
Mitral E wave (cm/s)	138	0.92 (0.65–1.32)	0.6621			
Mitral A wave (cm/s)	138	0.45 (0.30–0.68)	0.0.0001			
Mitral E/A ratio	138	1.28 (1.16–1.42)	<0.0001			
Left atrial area (cm^2)	139	1.13 (1.01–1.26)	0.0333			

mortality (HR 0.41; 95%CI 0.23–0.74, $p = 0.0029$). If LVEF was not included as covariate, LS and shorter GAA were significantly associated with all-cause mortality: HR 0.87; 95%CI, 0.79–0.96 $p = 0.0066$ and HR 1.23; 95%CI, 1.04–1.45 $p = 0.0164$ respectively. If the multivariate model included the covariates LS and LVMi, only LS was associated with all-cause mortality HR 0.85; 95%CI, 0.77–0.94 $p = 0.0009$.

In this population, the optimal cut-off of LS was 15.4% and was determined based on the LS value that yielded the maximum value of Youden index. When dividing the population according to this cutoff value, 23 patients had LS ≤15.4% (11.8 ± 2.8%) and 117 patients had LS > 15.4% (21.5 ± 3.6%). Patients with LS ≤15.4% had a worse outcome ($p < 0.0001$) compared with patients with LS >15.4% (Fig. 3). When LVEF and LS were included in the multivariate analysis as subgroups (LS ≤ 15.4% and LVEF≤45%), LVEF (HR 6.35; 95%CI, 1.49–27.07, $p = 0.0125$).was associated with all-cause mortality but not LS (HR 3.40; 95%CI, 0.86–13.47, $p = 0.0821$).

Among the 131 patients with LVEF >50%, 8 deaths occurred during the mean follow up of 7.6 ± 3.8 years. LS was not different between patients who died and the others: 17.1 ± 7.8% and 20.6 ± 4.3% respectively, $p = 0.28$. In univariate Cox analysis, LS was not significantly associated with all-cause mortality: LS (HR 0.89; 95%CI, 0.79–1.02, $p = 0.0899$). Similar results were obtained when we studied the 133 patients with LVEF > 45% with 9 (6.8%) deaths observed during the follow up.

4. Discussion

This study is the first to evaluate the prognostic value of longitudinal strain (LS) assessed by two-dimensional echocardiography in a large cohort of Friedreich's ataxia adult patients. We demonstrated that LS was a strong prognostic factor in univariate analysis, but was not an independent predictor of all-cause mortality when LVEF was included in the

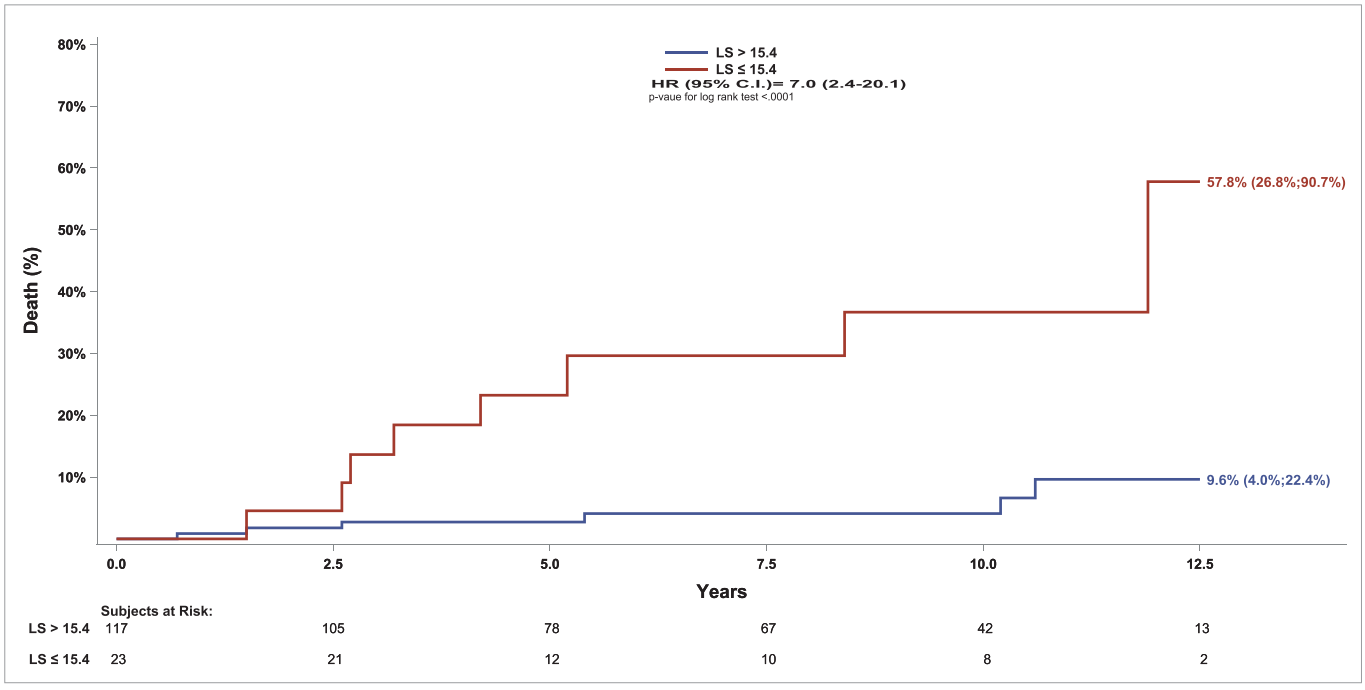

Fig. 3. Unadjusted Kaplan-Meier curve for individuals using LS cutoff in 140 patients with Friedreich ataxia.

analysis. In the present study the superiority of LVEF could be explained by the significant correlation between longitudinal strain and LVEF, and by the larger amplitude of variation of LVEF between FA patients who died and surviving patients. These results are not in accordance with previous studies where longitudinal strain appeared to provide stronger prognostic information than LVEF in different diseases [11,20]. It was especially demonstrated in individuals with preserved ejection fraction [20,21]. In the 131 FA patients with LVEF > 50%, LS tended to be associated with all-cause mortality, but too few events occurred in this group of patients to confirm the prognostic value of longitudinal strain in FA patients with preserved ejection fraction.

An important finding of this study is that LS appeared to be significantly correlated with the length of both alleles of the *FXN* gene: greater genetic severity might be associated with lower strain values. Such a relation was previously suggested by St John Sutton et al. [14] We can hypothesize that decreased longitudinal strain may reflect lack of frataxin and impaired mitochondrial function in the heart. However the weak correlation between GAA repeats and LS suggested that others factors are involved in LS value of these patients.

Cardiac remodeling is thought to represent a compensatory process to mitochondrial dysfunction in FA. In the present study, LS was weakly negatively correlated with septal wall thickness and left ventricular mass index. However the relations between myocardial hypertrophy and longitudinal strain remain unclear in the disease. It was previously reported in 27 FA children that LS was similar in patients with septal wall thickness smaller or larger than 12 mm [14].

Dedobbeleer et al. demonstrated that global longitudinal strain was reduced (15.3 ± 2.1%) in a small group of 20 FA patients with a typical concentric remodeling pattern and normal LVEF, compared to age and sex matched healthy individuals [13]. In our study, mean LS assessed in apical four chamber was lower (19.9 ± 5.0%) than the mean reference values (22.6 ± 3%) reported in healthy subjects in the European NORRE study, but remained in the normal range defined by this study [19]. Patients who died during our study had significantly lower LS and LVEF compared to the survivors: 12.9% versus 20.6% and 59% versus 64% respectively. In the MICONOS study performed in 205 FA patients, Weidemann et al. reported lower levels of longitudinal strain in FA subjects with more severe disease: −16.4 ± 2.9% in patients classed as not having a cardiomyopathy with normal LVEF of 65% and normal wall thickness (mean septal wall thickness of 0.89 cm), −15.3 ± 3.1% in patients with mild cardiomyopathy with a normal LVEF of 65% and mild hypertrophy (SWT of 1.11 cm), −13.3 ± 3.4% in patients with intermediate cardiomyopathy with normal LVEF of 65% and intermediate hypertrophy (SWT of 1.38 cm), and − 12.8 ± 3.9% in patients with severe cardiomyopathy with altered LVEF (53%) [7]. In Friedreich's ataxia, the rate and nature of progression to left ventricular dysfunction and heart failure are highly variable. Therefore longitudinal strain is likely to reflect left ventricular dysfunction, while longitudinal function is primarily involved before the alteration of LV ejection fraction. Longitudinal strain could be proposed as an early parameter to follow to detect subtle LV dysfunction in these patients.

We can speculate that in FA, longitudinal strain decreased when myocardial fibrosis appeared, as was demonstrated in hypertrophic cardiomyopathy [22]. The presence of myocardial fibrosis is likely to be an important feature during the progression of the cardiac disease and may play a role in prognosis in these patients.

This study did not provide evidence for an association between neurologic and cardiac involvement assessed by longitudinal strain.

5. Limitations

We did not assess global radial and circumferential strain analyses, because they are not sufficiently reproducible for routine clinical work, despite demonstrated utility in research studies in FA [14].

In this study, retrospective LS analysis in apical 4 chamber view was possible in only 90% of the patients for technical reasons. Longitudinal strain measurement is dependent on high quality 2D images and appropriate imaging settings, and could not be performed in all FA subjects. Strain analysis was assessed from stored DICOM images, but storing images does not significantly compromise analysis of global strain measurements [18]. LS values reported in this study cannot be assumed to apply to other echocardiographic platforms.

In this retrospective study, we were able to assess longitudinal strain in single apical 4 chambers view, because apical 2 or 3 chamber views were not available for all patients. It would have been of particular interest to study the inferolateral wall, which may be affected at an earlier stage than other walls in FA. [7]

Although there is a good correlation in diffuse process between GLS using the 3 chamber apical long axis views and single view longitudinal strain measurement [23], GLS calculated from 3 apical views should actually remain the preferred method for evaluation of longitudinal strain in FA.

6. In conclusion

Left ventricular strain analysis by 2D echocardiography speckle tracking is a simple and feasible method available in standard ultrasound machines and is now routine practice in many echocardiographic laboratories. Longitudinal strain assessed in one single view provides prognostic information, but LVEF remains a stronger prognostic factor in Friedreich's Ataxia. Moreover, serial measurements are needed to characterize the temporal course of longitudinal strain and the relationship to the evolution of LVEF. Longitudinal studies are necessary to confirm the prognostic value of global longitudinal strain in FA and to clarify the most appropriate cut-off values that predict greater risk. These additional studies could allow for definition of the role of longitudinal strain in the management of FA in clinical practice.

Biet who helped with data management and to Charlotte Lellman for English editing.

Author contributions

- Conception: F. Pousset.
- Acquisition of the data: L. Legrand, C. Heuze, F. Pousset A. Durr, C. Ewenczyk, M.L. Monin.
- Analysis and interpretation of the data: C. Heuze, A. Durr, R. Isnard, L. Legrand, M.L. Monin, and F. Pousset G Montalescot.
- Critical revision of the manuscript: All authors reviewed and revised the manuscript.
- Statistical analysis: A. Diallo, E. Vicaut.

Funding

AFAF (Association Francaise ATaxie Friedreich), France (www.afaf.fr)

Declaration of Competing Interest

L. Legrand, C. Heuze, M.L. Monin, C. Ewenczyk, R. Isnard, C. Heuze, A. Diallo, E. Vicaut, G. Montalescot, A. Durr, and F. Pousset declare that they have no potential conflicts of interest that might be relevant to this work.

Acknowledgment

The authors would like to thank all patients who participated in the study and the French Friedreich Ataxia Association (AFAF) for a grant (2016).

Special thanks go to Marie Biet who helped with data management and to Charlotte Lellman for English editing.

References

[1] A. Durr, M. Cossee, Y. Agid, et al., Clinical and genetic abnormalities in patients with Friedreich's ataxia, N. Engl. J. Med. 335 (1996) 1169–1175.

[2] V. Campuzano, L. Montermini, M.D. Molto, et al., Friedreich's ataxia: autosomal recessive disease caused by an intronic GAA triplet repeat expansion, Science 271 (1996) 1423–1427.

[3] K. Reetz, I. Dogan, A.S. Costa, et al., Biological and clinical characteristics of the European Friedreich's Ataxia Consortium for Translational Studies (EFACTS) cohort: a cross-sectional analysis of baseline data, Lancet Neurol. 14 (2015) 174–182.

[4] K. Reetz, I. Dogan, R.D. Hilgers, et al., Progression characteristics of the European Friedreich's Ataxia Consortium for Translational Studies (EFACTS): a 2 year cohort study, Lancet Neurol. 15 (2016) 1346–1354.

[5] A.Y. Tsou, E.K. Paulsen, S.J. Lagedrost, et al., Mortality in Friedreich ataxia, J. Neurol. Sci. 307 (2011) 46–49.

[6] F. Pousset, L. Legrand, M.L. Monin, et al., A 22-year follow-up study of long-term cardiac outcome and predictors of survival in Friedreich Ataxia, JAMA Neurol. 72 (2015) 1334–1341.

[7] F. Weidemann, C. Rummey, B. Bijnens, et al., The heart in Friedreich ataxia: definition of cardiomyopathy, disease severity, and correlation with neurological symptoms, Circulation 125 (2012) 1626–1634.

[8] T.H. Marwick, S.J. Shah, J.D. Thomas, Myocardial strain in the assessment of patients with heart failure: a review, JAMA Cardiol. 4 (2019) 287–294.

[9] N. D'Elia, S. Caselli, W. Kosmala, et al., Normal global longitudinal strain: an individual patient meta-analysis, JACC Cardiovasc. Imaging 13 (2020) 167–169.

[10] J. Brown, C. Jenkins, T.H. Marwick, Use of myocardial strain to assess global left ventricular function: a comparison with cardiac magnetic resonance and 3-dimensional echocardiography, Am. Heart J. 157 (2009) 102 e1–102 e5.

[11] T. Stanton, R. Leano, T.H. Marwick, Prediction of all-cause mortality from global longitudinal speckle strain: comparison with ejection fraction and wall motion scoring, Circ. Cardiovasc. Imaging 2 (2009) 356–364.

[12] P.M. Mottram, M.B. Delatycki, L. Donelan, et al., Early changes in left ventricular long-axis function in Friedreich ataxia: relation with the FXN gene mutation and cardiac structural change, J. Am. Soc. Echocardiogr. 24 (2011) 782–789.

[13] C. Dedobbeleer, M. Rai, E. Donal, et al., Normal left ventricular ejection fraction and mass but subclinical myocardial dysfunction in patients with Friedreich's ataxia, Eur. Heart J. Cardiovasc. Imaging 13 (2012) 346–352.

[14] M. St John Sutton, B. Ky, S.R. Regner, et al., Longitudinal strain in Friedreich Ataxia: a potential marker for early left ventricular dysfunction, Echocardiography 31 (2014) 50–57.

[15] C. Marelli, J. Figoni, P. Charles, et al., Annual change in Friedreich's ataxia evaluated by the Scale for the Assessment and Rating of Ataxia (SARA) is independent of disease severity, Mov. Disord. 27 (2012) 135–138.

[16] R.M. Lang, M. Bierig, R.B. Devereux, et al., Recommendations for chamber quantification: a report from the American Society of Echocardiography's Guidelines and Standards Committee and the Chamber Quantification Writing Group, developed in conjunction with the European Association of Echocardiography, a branch of the European Society of Cardiology, J. Am. Soc. Echocardiogr. 18 (2005) 1440–1463.

[17] M. Foppa, B.B. Duncan, L.E. Rohde, Echocardiography-based left ventricular mass estimation. How should we define hypertrophy? Cardiovasc. Ultrasound 3 (2005) 17.

[18] N. Risum, S. Ali, N.T. Olsen, et al., Variability of global left ventricular deformation analysis using vendor dependent and independent two-dimensional speckle-tracking software in adults, J. Am. Soc. Echocardiogr. 25 (2012) 1195–1203.

[19] T. Sugimoto, R. Dulgheru, A. Bernard, et al., Echocardiographic reference ranges for normal left ventricular 2D strain: results from the EACVI NORRE study, Eur. Heart J. Cardiovasc. Imaging 18 (2017) 833–840.

[20] K. Kalam, P. Otahal, T.H. Marwick, Prognostic implications of global LV dysfunction: a systematic review and meta-analysis of global longitudinal strain and ejection fraction, Heart 100 (2014) 1673–1680.

[21] Y.L. Hiemstra, P. Debonnaire, M. Bootsma, et al., Global longitudinal strain and left atrial volume index provide incremental prognostic value in patients with hypertrophic cardiomyopathy, Circ. Cardiovasc. Imaging 10 (2017).

[22] T.F. Haland, V.M. Almaas, N.E. Hasselberg, et al., Strain echocardiography is related to fibrosis and ventricular arrhythmias in hypertrophic cardiomyopathy, Eur. Heart J. Cardiovasc. Imaging 17 (2016) 613–621.

[23] P. Thavendiranathan, T. Negishi, M.A. Cote, et al., Single versus standard multiview assessment of global longitudinal strain for the diagnosis of cardiotoxicity during cancer therapy, JACC Cardiovasc. Imaging 11 (2018) 1109–1118.

American Journal of Cardiovascular Drugs
https://doi.org/10.1007/s40256-019-00375-z

ORIGINAL RESEARCH ARTICLE

Predictors of Left Ventricular Dysfunction in Friedreich's Ataxia in a 16-Year Observational Study

Lise Legrand[1,4] · Abdourahmane Diallo[5] · Marie-Lorraine Monin[1,2] · Claire Ewenczyk[2] · Perrine Charles[2] · Richard Isnard[1,4,5] · Eric Vicaut[5] · Gilles Montalescot[1,5] · Alexandra Durr[2,3] · Francoise Pousset[1,4,6]

Abstract

Background Friedreich's ataxia (FRDA) is a cerebellar ataxia due to GAA repeat expansions in the *FXN* gene, and in affected patients, lower left ventricular ejection fraction (LVEF) leads to poorer prognosis. We aimed to identify patients likely to develop worsening LVEF at an early stage.

Methods We included 115 FRDA patients aged 30 ± 10 years with 620 ± 238 GAA repeats on the shorter allele and disease onset of 15 ± 7 years.

Results At baseline, left ventricular (LV) hypertrophy was present in 53%, with LVEF 65 ± 7%, LV end diastolic diameter (LVEDD) 43 ± 5 mm, septal wall thickness (SWT) 11.8 ± 2.7 mm, and posterior wall thickness 11.1 ± 2.5 mm. After a mean follow-up of 13 ± 6 years, LVEF ≤ 50% was observed in 12 patients. The main determinants of LVEF ≤ 50% were GAA repeat number on the shorter allele (odds ratio [OR] 1.007, 95% confidence interval [CI] 1.003–1.012, $p = 0.002$), LVEDD (OR 1.217, 95% CI 1.058–1.399, $p = 0.006$), and SWT (OR 1.352, 95% CI 1.016–1.799, $p = 0.04$). High-risk patients were predicted 5 years before LVEF ≤ 50% occurred: area under the curve of 0.91, 95% CI 0.85–0.97. Patients with GAA repeats > 800 were categorized as high risk, patients with 500 < GAA < 800 were high risk if LVEDD was ≥ 52.6 mm and SWT was ≥ 13.3 mm, and patients with GAA < 500 were low risk if LVEDD was < 52.6 mm and SWT was < 13.3 mm.

Conclusions Echocardiographic follow-up combined with size assessment of GAA repeat expansions is a powerful tool to identify patients at high risk of developing LV systolic dysfunction up to 5 years before clinical symptoms. Further studies are mandatory to investigate if these patients would benefit from cardiac interventions.

1 Introduction

Friedreich's ataxia (FRDA) is a mitochondrial disease exhibiting cerebellar ataxia, diabetes, optic atrophy and cardiomyopathy. Onset is often around puberty and occasionally later in life, and rare cases can occur in early childhood. In the majority of cases, the disease is caused by a homozygous GAA triplet expansion in the *FXN* gene encoding frataxin, a mitochondrial protein involved in iron-sulfur cluster biosynthesis. The level of functional frataxin expressed depends on the length of the shorter GAA repeat, as a greater number of repeats correlates with a lower amount of functional frataxin [1]. Accordingly, longer GAA repeats on the shorter allele are associated with earlier symptom onset and increased severity of both neurological and cardiac disease [1–4].

No approved pharmacological treatment exists that can effectively cure or even slow down disease progression. Current therapeutic strategies aim to increase frataxin levels and/or alleviate the consequences of frataxin deficiency.

Electronic supplementary material The online version of this article (https://doi.org/10.1007/s40256-019-00375-z) contains supplementary material, which is available to authorized users.

✉ Francoise Pousset
f.pousset@aphp.fr

1 Cardiology Department, AP-HP, Pitié-Salpêtrière University Hospital, Sorbonne Université, Paris, France

2 Genetics Department, AP-HP, Pitié-Salpêtrière University Hospital, Sorbonne Université, Paris, France

3 ICM (Brain and Spine Institute), INSERM, CNRS, Pitié-Salpêtrière University Hospital, Sorbonne Université, Paris, France

4 ICAN (Institute for Cardiometabolism and Nutrition), Pitié-Salpêtrière University Hospital, Paris, France

5 ACTION (Allies in Cardiovascular Trials Initiatives and Organized Networks) Group, URC Lariboisière University Hospital, Paris, France

6 Département de Cardiologie, Hôpital de la Salpêtrière, 47 boulevard de l'Hôpital, 75651 Paris Cedex 13, France

Published online: 25 October 2019

Key Points

Friedreich's ataxia (FRDA) is an inherited ataxia that typically affects young adults, with cardiac involvement.

The most common cause of death is heart failure.

Genetic and simple echographic features may identify FRDA patients at higher risk of systolic dysfunction.

These high-risk patients could be candidates for cardiac intervention.

Research into potential pharmacological treatment for FRDA has advanced considerably in the past 2 decades; there are many potential therapeutic agents in various stages of development (http://www.curefa.org/pipeline) [5–8].

Cardiac involvement with various degrees of hypertrophy may progress to left ventricular systolic dysfunction [2]. Cardiac disease is the major cause of premature mortality in FRDA. Congestive heart failure and supraventricular arrhythmia are the most frequent cardiac complications [2, 9]. The main prognostic factor of survival was the size of the expanded GAA repeat on the shorter allele, but impaired left ventricular systolic function seems to be the most important prognostic factor over time [2, 9, 10]. However, in clinical practice, it remains difficult to identify in early disease stages, patients whose left ventricular ejection fraction (LVEF) will worsen and, especially, to pinpoint the moment at which deterioration begins. Furthermore, wheelchair-bound patients have few symptoms of heart failure, which delays the diagnosis of left ventricular dysfunction and the institution of therapy, contributing to a poor prognosis.

Our objective was to predict left ventricular systolic dysfunction in FRDA patients by studying cardiomyopathy evolution over time in a large cohort of FRDA patients, with several cardiac evaluations per patient. We aimed to identify markers that would enable the prediction of left ventricular dysfunction (LVEF $\leq$ 50%), in order to identify high-risk patients, who would require early initiation of cardiac therapy.

2 Methods

From April 27, 1990 to March 18, 2016 we enrolled and followed 142 genetically confirmed FRDA adult patients at the National Reference Center for Rare Diseases who had been referred for cardiac evaluation (Pitié-Salpêtrière University Hospital, Paris, France). One hundred and fifteen out of 142 patients with at least one cardiac follow-up visit after inclusion contributed to the studied population. The majority of the 115 patients participated in our previous study [2]. Patients underwent a mean of 4.9 ± 2.7 cardiac evaluations per patient, with a mean interval of 2.0 ± 1.1 years between visits, resulting in a total of 606 cardiac evaluations.

Informed written consent was obtained from patients in accordance with appropriate legal and ethical regulations. All patients gave their informed consent for genetic studies (Paris Necker ethics committee approval [RBM 01-29 and RBM 03-48] to AD). Some patients were included as part of a prospective European FRDA registry (European Friedreich's Ataxia Consortium for Translational Studies, ClinicalTrials.gov identifier: NCT02069509) [11, 12].

2.1 Cardiac Evaluation

Electrocardiograms (ECGs) were retrospectively interpreted, blinded from the echocardiography results. Abnormal repolarization was considered in the presence of T-wave inversions ($\geq$ 0.1 mV) or flat T waves in at least two leads except V1 or V2, in the absence of bundle branch block.

More than 90% of the transthoracic echocardiographic studies were performed by the same cardiologist, initially using a Kontron then an Acuson Sequoia C256 system, a General Electric Vivid-7, and finally a General Electric Vivid-9. Left ventricular end diastolic diameter (LVEDD) and left ventricular end systolic diameter (LVESD), end diastolic interventricular septal wall thickness (SWT), and posterior wall thickness (PWT) were measured using standard M-Mode from a parasternal long-axis view [13]. Left ventricular systolic ejection fraction (LVEF) was calculated using the bi-apical Simpson disk method [13]. Calculated morphological parameters included relative wall thickness (RWT), defined as (SWT + PWT)/LVEDD, and pathological concentric remodeling of left ventricular was defined by RWT > 0.42 [14]. Left ventricular mass (LVM) was assessed using the formula $LVM = 0.8 \times [1.04\ (LVEDD + PWT + SWT)^3 - LVEDD^3] + 0.6$ g, and was indexed to body surface area (LVMI) [13]. Doppler of mitral valve inflow was measured to obtain the ratio of early (E) to late (A) diastolic flow velocity.

As the European Society of Cardiology reported normal LVEF values as > 50%, left ventricular systolic dysfunction was defined as LVEF $\leq$ 50% [15]. As LVM in FRDA patients could remain within the normal range, left ventricular hypertrophy was defined when SWT or PWT exceeded the 95% predicted value for age and body surface area according to the Henry nomogram [2, 16, 17].

2.2 Statistical Analysis

Continuous variables are presented as mean and standard deviation (SD) and median (range quartile 1–3 [Q1–Q3]), and were compared using Student's *t* test for Gaussian distributions and Mann-Whitney tests for non-Gaussian

distributions. Categorical variables are presented as numbers and percentages, and are compared using Chi-square test *p* values, or Fisher's test *p* values when there were few events.

Since at least two cardiac evaluations were performed on every patient, we performed three logistic multivariate regressions to identify potential early prognostic factors of LVEF deterioration (LVEF ≤ 50%). For the first model, we used clinical and echocardiographic parameters at baseline; for the next model, measurements obtained 5 years before LVEF ≤ 50% were used; and for the last model, measurements obtained 3 years before LVEF ≤ 50% were assessed. Variables that significantly differed between groups with and without LVEF ≤ 50% were entered in a stepwise logistic regression model. Associations between any death and baseline parameters were assessed by using a multivariate Cox regression model with the same procedure as for the multivariate logistic regression model. For associations between any death and LVEF ≤ 50%, we constructed Kaplan-Meier curves for cumulative event-free survival. The two-sided significance level was fixed at 5%. All tests were performed with SAS version 9.4 statistical software (SAS Institute Inc., Cary, NC, USA).

3 Results

3.1 Population Baseline Characteristics

Clinical characteristics of these 115 patients at baseline (inclusion) are shown in Table 1. Mean age was 30 ± 10 years old, age at disease onset was 15 ± 7 years, and 36 patients used wheelchairs, since the mean age of 27 ± 11 years. Patients were homozygous for GAA expansions; the mean number of GAA repeats on the shorter allele was 620 ± 238 GAA repeats. Thirteen patients presented with diabetes mellitus, and eleven with hypertension. Four patients had previous atrial fibrillation, and three of four had experienced previous heart failure symptoms. In terms of medication, 23 were taking beta-blockers, three angiotensin-converting enzyme (ACE) inhibitors, three anticoagulants, and one was receiving amiodarone. At inclusion, no patients had signs of heart failure; four patients (3.5%) experienced dyspnea, 11 (9.6%) chest pain, and 12 (10.4%) palpitations.

Abnormal repolarization on ECG was observed in 90% of patients, where 81% and 9% had negative or flat T waves, respectively, in inferior (7.6%), lateral (11.4%), or both leads (78.1%). Two patients were recorded in atrial fibrillation.

At baseline, mean LVEF was 68 ± 7%; no patient had LVEF below 50%. Most patients (80.9%) displayed abnormal left ventricle morphology, with left ventricular remodeling assessed by a RWT > 0.42. Left ventricular hypertrophy was detected in 53% of FRDA patients, with septal or PWT exceeding the 95% predicted value for age and body surface area according to the Henry nomogram.

3.2 Follow-Up

3.2.1 Survival

During a mean follow-up of 13 ± 6 years (1–25 years), 16 out of 115 patients (13.9%) died (age of death 39 ± 10 years), and death occurred 10 ± 5 years after inclusion (3–18 years). Eight patients' deaths had a cardiovascular origin: six died of progressive heart failure with previous atrial fibrillation (at age 21, 27, 28, 40, 39 and 50 years) and two died of cardioembolic stroke (at age 43 and 32 years) with previous heart failure and atrial fibrillation. Two patients died of respiratory disease (at age 33 and 37 years), and one patient died from suicide (at age 28 years). For five patients (who died at age 33, 47, 49, 50, 62 years), the cause of death was unknown, but four of these five patients had previous atrial fibrillation.

Compared with those who survived, those who died had an earlier disease onset (11 ± 5 vs 16 ± 7 years, $p < 0.01$), longer GAA repeats on the shorter *FXN* allele (840 ± 193 vs 585 ± 226 repeats, $p < 0.0001$) (see the electronic supplementary material, supplementary Table S1). In multivariate analysis, the only independent predictor of death at baseline was a greater number of GAA repeats on the shorter allele: hazard ratio (HR) 1.005, 95% confidence interval (CI) 1.002–1.008, $p = 0.0003$.

3.2.2 Left Ventricular Dysfunction (LVEF ≤ 50%) Over Time

During the cardiac follow-up of 13 ± 6 years, we observed LVEF ≤ 50% in 12 out of 115 patients (10.4%); LVEF ≤ 50% occurred 7 ± 5 years after inclusion. Table 1 displays the baseline characteristics at inclusion of these 12 patients, compared to those with LVEF > 50%. They had increased GAA repeats on the shorter allele ($p = 0.0001$), earlier disease onset ($p < 0.01$), lower LVEF, which remained in the normal range (63 ± 6% vs 68 ± 7%, $p < 0.01$), and similar LVEDD (44.0 ± 3.7 mm vs 42.5 ± 4.6 mm, p = not significant). They were likely to be receiving more ACE inhibitors ($p = 0.02$) and beta-blockers ($p = 0.03$).

These 12 patients with LVEF ≤ 50% had a significantly higher mortality rate than patients with LVEF > 50% (Fig. 1) in univariate analysis (HR 8.15, 95% CI 3.00–22.14, $p < 0.0001$) and in multivariate analysis (HR 10.52, 95% CI 51.90–58.2, $p = 0.0070$) when the following covariables were forced in the model: age, sex, beta-blockers, ACE inhibitors, age at onset of disease, and heart rate.

Table 1 Clinical and echocardiographic baseline characteristics of 115 patients with Friedreich's ataxia according to altered LVEF observed during follow-up

Variable	Total $n=115$	Group LVEF ≤ 50% $n=12$	Group LVEF > 50% $n=103$	*P* value
Sex, male, *n* (%)	63 (54.8)	4 (33.3)	59 (57.3)	0.1147
Age (years)	30 ± 10	27 ± 9	31 ± 10	0.1710
Median (Q1–Q3)	29 (23–36)	25 (20–34)	29 (23–36)	
Age at onset (years)	15 ± 7	10 ± 3	16 ± 8	**0.0036**
Median (Q1–Q3)	14 (11–18)	11 (8–12)	14 (11–19)	
Age at wheelchair use (years)	27 ± 11 (36)	21 ± 10 (3)	28 ± 11 (33)	0.2955
Median (Q1–Q3)	24 (20–31)	19 (12–32)	25 (21–31)	
GAA repeats on the shorter allele	620 ± 238	864 ± 173	592 ± 229	**0.0001**
Median (Q1–Q3)	633 (467–800)	867 (800–983)	600 (467–767)	
GAA repeats on the longer allele	891 ± 239 (114)	1031 ± 164 (12)	875 ± 241 (102)	**0.0050**
Median (Q1–Q3)	867 (800–1033)	1067 (1000–1117)	867 (800–1000)	
Body mass index (kg/m^2)	21.6 ± 3.5	22.2 ± 2.9	21.6 ± 3.6	0.4153
Median (Q1–Q3)	21.5 (19.3–23.4)	22.4 (19.7–23.7)	21.2 (19.3–23.2)	
Body surface area (m^2)	1.7 ± 0.2	1.7 ± 0.1	1.7 ± 0.2	0.3267
Median (Q1–Q3)	1.7 (1.6–1.8)	1.8 (1.6–1.8)	1.7 (1.6–1.8)	
Septal wall thickness (mm)	11.8 ± 2.7	12.7 ± 2.2	11.6 ± 2.7	0.1487
Median (Q1–Q3)	11.6 (10.0–13.0)	12.0 (11.0–14.5)	11.5 (9.7–12.9)	
Posterior wall thickness (mm)	11.1 ± 2.5	11.3 ± 1.6	11.1 ± 2.6	0.4916
Median (Q1–Q3)	11.0 (9.4–12.2)	11.0 (10.0–12.6)	10.8 (9.3–12.2)	
Relative wall thickness	0.5 ± 0.1	0.6 ± 0.1	0.5 ± 0.1	0.6074
Median (Q1–Q3)	0.5 (0.4–0.6)	0.5 (0.5–0.6)	0.5 (0.4–0.6)	
LV end diastolic diameter (mm)	42.6 ± 4.5	44.0 ± 3.7	42.5 ± 4.6	0.2834
Median (Q1–Q3)	42.0 (40.0–45.5)	44.7 (40.5–46.7)	42.0 (39.0–45.0)	
LV end systolic diameter (mm)	25.0 ± 4.8 (112)	28.1 ± 5.0 (12)	24.6 ± 4.7 (100)	**0.0280**
Median (Q1–Q3)	23.9 (21.7–27.8)	29.8 (22.5–32.0)	23.7 (21.5–27.0)	
LVEF (%)	68 ± 7	63 ± 6	68 ± 7	**0.0077**
Median (Q1–Q3)	67 (63–72)	64 (60–66)	68 (63–73)	
LV mass index (g/m^2)	102 ± 31	111 ± 24	101 ± 31	0.1626
Median (Q1–Q3)	95 (82–119)	114 (89–126)	95 (80–117)	
Mitral peak early wave (cm/s)	0.7 ± 0.1 (97)	0.7 ± 0.1 (9)	0.7 ± 0.1 (88)	0.8676
Median (Q1–Q3)	0.7 (0.6–0.8)	0.7 (0.6–0.7)	0.7 (0.6–0.8)	
Mitral peak late wave (cm/s)	0.5 ± 0.25 (95)	0.4 ± 0.2 (8)	0.5 ± 0.1 (87)	**0.0219**
Median (Q1–Q3)	0.5 (0.4–0.6)	0.3 (0.3–0.4)	0.5 (0.4–0.6)	
Systolic blood pressure (mmHg)	122 ± 14 (61)	125 ± 13 (7)	121 ± 15 (54)	0.5292
Median (Q1–Q3)	120 (110–130)	120 (110–140)	120 (110–130)	
Diastolic blood pressure (mmHg)	76 ± 12 (61)	72 ± 12 (7)	76 ± 13 (54)	0.3761
Median (Q1–Q3)	70 (67–85)	70 (65–80)	71 (70–85)	
Heart rate (beats/min)	76 ± 11 (94)	85 ± 14 (9)	75 ± 10 (85)	**0.0071**
Median (Q1–Q3)	76 (70–83)	90 (78–90)	75 (70–82)	
Beta-blocker, *n* (%)	23/111 (20.7)	5/10 (50.0)	18/101 (17.8)	**0.0307**
ACE inhibitor, *n* (%)	3/114 (2.6)	2/11 (18.2)	1/103 (1.0)	**0.0242**

$P < 0.05$ are in bold

Results are presented as mean ± SD (*n*) and median (Q1–Q3) unless otherwise indicated

ACE angiotensin-converting enzyme, *LV* left ventricular, *LVEF* left ventricular ejection fraction, *Q* quartile, *SD* standard deviation

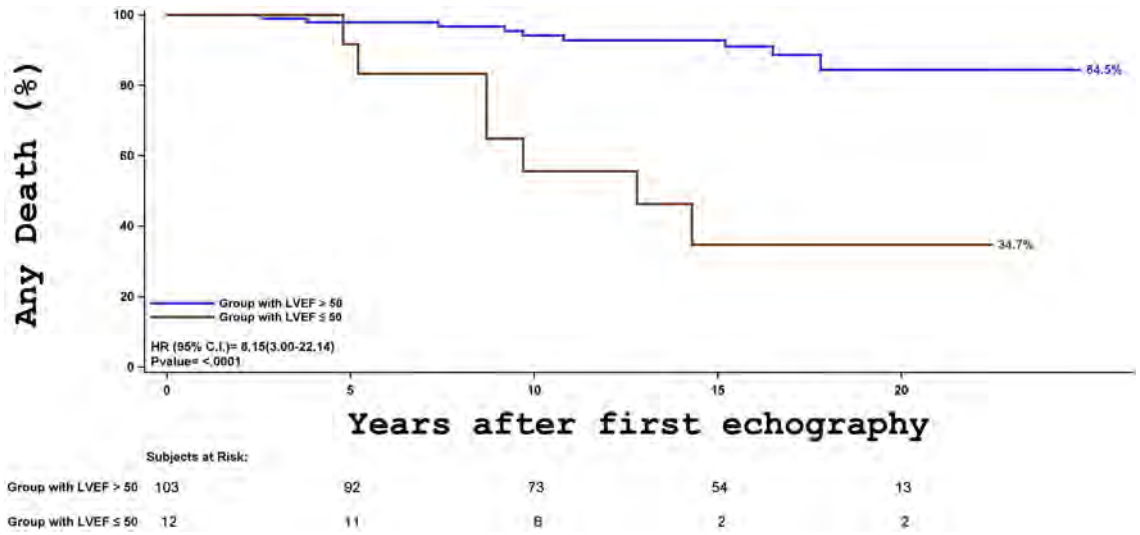

Fig. 1 Survival curves in 115 patients with Friedreich's ataxia according to altered LVEF (LVEF ≤ 50%) observed during follow-up. Patients with LVEF ≤ 50% had a lower survival than patients with preserved ejection fraction (LVEF > 50%): 34.7% vs 84.5%, respectively, $p < 0.0001$. *C.I.* confidence interval, *HR* hazard ratio, *LVEF* left ventricular ejection fraction

3.3 Prediction of LVEF ≤ 50%

When we included only baseline parameters, the independent predictive factor of LVEF ≤ 50% by multivariate logistic regression was the GAA repeat number on the shorter allele (OR 1.01, 95% CI 1.00–1.01, $p = 0.0012$), as shown in Fig. 2a. The area under the curve (AUC) was 0.83, 95% CI 0.69–0.96.

When we included baseline parameters *and* parameters collected over time, we obtained two predictive multivariate models: one model predicted LVEF ≤ 50% 3 years before observable alteration occurred (AUC 0.94, 95% CI 0.89–0.98) and the second model predicted LVEF ≤ 50% 5 years before observable alterations occurred (AUC 0.91, 95% CI 0.85–0.97). We chose the latter, since it is more effective to predict LVEF ≤ 50% as early as possible; therefore, we used it for further analysis.

Characteristics of the population 5 years before LVEF ≤ 50% occurred (the last visit before deterioration) are reported in supplementary Table S2. By stepwise multivariate logistic regression analysis, the following parameters were appointed as independent predictors of LVEF ≤ 50% (Fig. 2b): GAA repeat number on the shorter allele (OR 1.007, 95% CI 1.003–1.012, $p = 0.002$), LVEDD (OR 1.217, 95% CI 1.058–1.399, $p = 0.006$), and SWT (OR 1.352, 95% CI 1.016–1.799, $p = 0.04$).

Receiver operating characteristic (ROC) curve analysis of this predictive model was performed to assess the power to predict LVEF ≤ 50%. The AUC was calculated for combined independent predictors of LVEF ≤ 50%: the AUC was 0.8258 for GAA repeats, 0.8948 for GAA repeats and LVEDD, and 0.9135 for GAA repeats and LVEDD and SWT (Fig. 3); thus this last model was more accurate than predictions based on molecular analysis alone. By multivariate analysis, the cutoff point was 500 for GAA repeats, 52.6 mm for LVEDD and 13.3 mm for SWT (sensitivity = 91%, specificity = 85%, Youden's index = 0.76). Thus patients were categorized into the following risk groups: patients with GAA repeats > 800 were in the high-risk group; patients with 500 < GAA repeats < 800 were in the high-risk group if SWT was ≥ 13.3 mm and LVEDD was ≥ 52.6 mm; and patients with GAA repeats < 500 were in the low-risk group if SWT was < 13.3 mm and LVEDD was < 52.6 mm.

4 Discussion

We present a clinical algorithm that predicts LVEF ≤ 50% 5 years before it occurs. This algorithm relies on echocardiography data monitoring (left ventricle size and SWT), taking into account the number of GAA repeats on the shorter allele. We have previously shown that survival with FRDA was dependent on the number of expanded GAA repeats on the shorter *FXN* allele, but also on cardiac parameters [2]. In the current study, we confirmed that patients who develop left ventricular systolic dysfunction have a worse prognosis.

We demonstrated that predictive factors of left ventricular dysfunction were not the same over time, suggesting that myocardial involvement changes. At baseline, the majority of patients had left ventricle remodeling as revealed by abnormal RWT (81%), with normal LVEF, small left ventricle, and hypertrophy observed in 53%. Whereas when LVEF remained in the normal range, several more subtle changes occurred over time, such as increased left ventricular size,

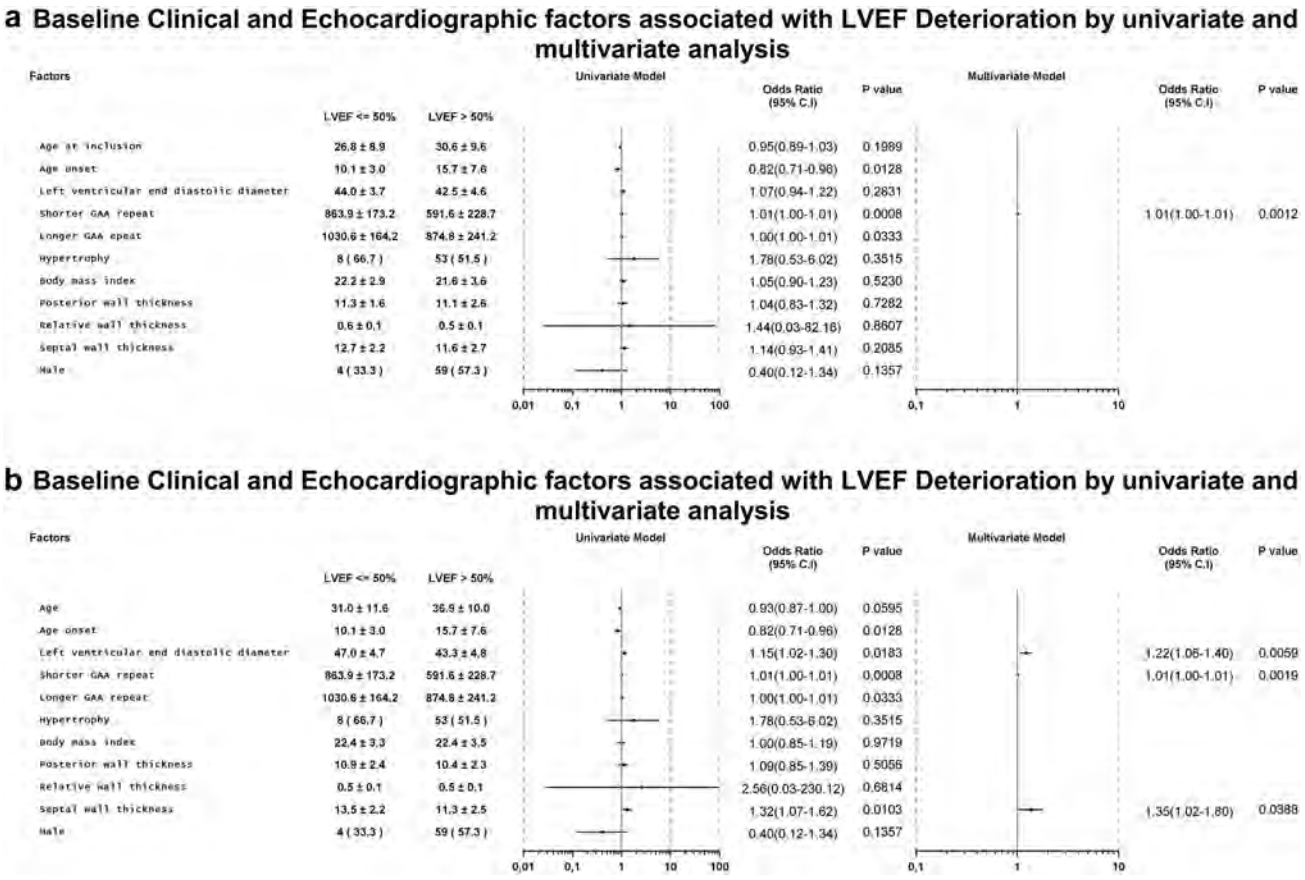

Fig. 2 **a** Determinants of decreased LVEF at baseline. By multivariate logistic regression modeling at baseline, GAA expansion on the shorter allele was the only determinant of LVEF ≤ 50%. **b** Determinants of decreased LVEF 5 years before deterioration. By multivariate logistic regression modeling 5 years before LVEF deterioration, GAA on the shorter allele, septal wall thickness and LV end diastolic diameter were independent predictors of LVEF ≤ 50%. *C.I.* confidence interval, *LV* left ventricular, *LVEF* left ventricular ejection fraction

or increased SWT. PWT tended to decrease as shown in previous studies [2, 17].

The rate and nature of progression to heart failure in individuals with FRDA are highly variable, and it has been reported that in young patients, LVEF decreased with age in a nonlinear fashion [18]. Furthermore, only some adult patients with FRDA experience systolic dysfunction, whereas ejection fraction declines slightly but remains in the normal range for others [2]. Moreover, progression to systolic dysfunction can be rapid when other influencing factors are implicated, such as arrhythmia or myocarditis. [9] McCormick et al. reported on three patients who had fewer GAA repeats but a severe cardiac phenotype leading to cardiac transplantation [19]. There is evidence of somatic instability of the GAA repeat that is tissue specific, but we do not know its role in the phenotypical expression and the severity [20]. Experts have recently proposed annual cardiac evaluation for asymptomatic FRDA patients [21]. Our results confirm that in addition to neurological evaluation, regular cardiac follow-up must be recommended when managing FRDA patients. Currently there is no specific treatment for FRDA-associated cardiomyopathy. Likewise, there are no guidelines for the introduction of ACE inhibitors, beta-blockers, or mineralocorticoid receptor antagonists in asymptomatic patients with FRDA and LVEF > 40%. To slow cardiac deterioration, ACE inhibitors and beta-blockers could be considered for genetic cardiomyopathy as soon as LVEF falls [21] and perhaps in patients identified to be at high risk of LVEF dysfunction. Additional clinically controlled studies will be necessary to evaluate the effects of preventive cardiac treatment in these high-risk FRDA patients.

4.1 Study Strengths

FRDA is a rare disease with a slow progression. The strengths of the study are the large population studied in one center over a very long time with several cardiac evaluations per patient.

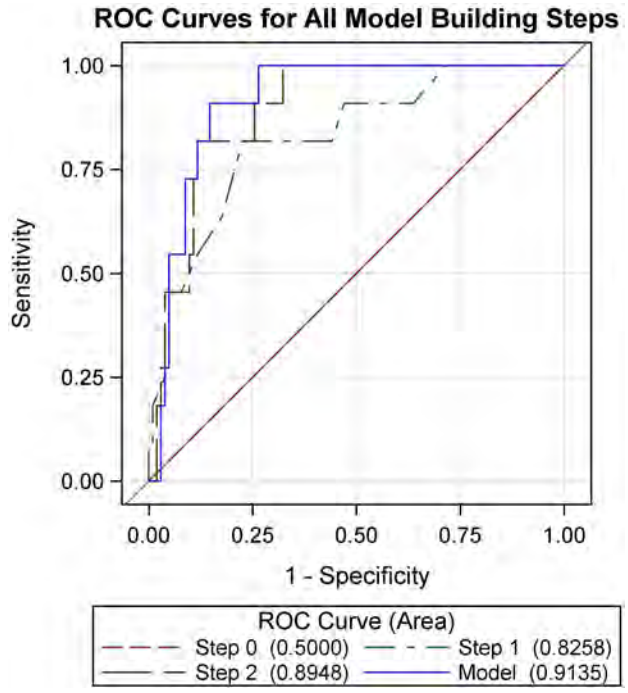

Fig. 3 ROC analysis to predict altered LVEF (LVEF ≤ 50%) in 115 patients with Friedreich's ataxia. The ROC curve for the prediction of LVEF ≤ 50% with an area under the curve of 0.8258 for the number of GAA repeats on the shorter allele alone (step 1), 0.8948 for the model including number of GAA repeats and left ventricular end diastolic diameter (step 2), and 0.9135 for the model including the number of GAA repeats, left ventricular end diastolic diameter, and septal wall thickness (model). *LVEF* left ventricular ejection fraction, *ROC* receiver operating characteristic

4.2 Study Limitations

It will be necessary to validate our predictive algorithm in another FRDA adult population.

Our study did not include severe patients of our cohort with only one cardiac evaluation. Moreover, we did not include children, specifically subjects with early onset and severe evolution, thus limiting predictive efficacy only to adults with FRDA.

Interestingly, the fact that beta-blocker and ACE inhibitor use was so much more prevalent in patients who went on to develop systolic impairment suggested that these patients were already thought to be at higher risk of doing so. Unfortunately, we were not able to follow prescription records over time, and did not assess the effects of non-cardiac or cardiac treatments on cardiomyopathy.

Unfortunately, we could not use echographic parameters measuring diastolic function, or more recent parameters, and it has been shown that subtle left ventricular dysfunction can be detected by speckle tracking imaging, even when LVEF is normal [22, 23]. Follow-up studies may evaluate the usefulness of this new technique, which could then be used to predict LVEF dysfunction. Magnetic resonance imaging (MRI) which measures myocardial fibrosis could also be useful to predict LVEF ≤ 50% in FRDA patients with cardiomyopathy and a high risk of arrhythmia [24].

Similarly, cardiac biomarkers such as high-sensitive troponin-T levels could have been of interest if they were available [10].

5 Conclusions

Simple cardiac follow-up by echocardiography taking into account the size of the expanded GAA repeat can identify patients at a higher risk of systolic dysfunction. Further studies are mandatory to confirm the validity of the prediction and to investigate whether earlier treatment of heart failure improves outcome in FRDA patients. These identified high-risk patients could benefit from future therapeutic options.

Acknowledgements The authors would like to thank all patients who participated in the study. Special thanks go to Sandra Benaich and Fabien Lesne, who helped with data handling, and Rachel Peat, for English editing.

Compliance with Ethical Standards

Funding This study was supported by FP7 (7th Framework Programme) Grant HEALTH-F2-2010-242193 from the European Commission.

Conflict of interest Lise Legrand, Abdourahmane Diallo, Marie-Lorraine Monin, Claire Ewenczyk, Perrine Charles, Richard Isnard, Eric Vicaut, Gilles Montalescot, Alexandra Durr, and Francoise Pousset declare that they have no potential conflicts of interest that might be relevant to this work.

References

1. Durr A, Cossee M, Agid Y, Campuzano V, Mignard C, Penet C, Mandel JL, Brice A, Koenig M. Clinical and genetic abnormalities in patients with Friedreich's ataxia. N Engl J Med. 1996;335(16):1169–75.
2. Pousset F, Legrand L, Monin ML, Ewenczyk C, Charles P, Komajda M, Brice A, Pandolfo M, Isnard R, Tezenas du Montcel S, Durr A. A 22-year follow-up study of long-term cardiac outcome and predictors of survival in Friedreich ataxia. JAMA Neurol. 2015;72(11):1334–41.
3. Filla A, De Michele G, Cavalcanti F, Pianese L, Monticelli A, Campanella G, Cocozza S. The relationship between trinucleotide (GAA) repeat length and clinical features in Friedreich ataxia. Am J Hum Genet. 1996;59(3):554–60.
4. Isnard R, Kalotka H, Durr A, Cossee M, Schmitt M, Pousset F, Thomas D, Brice A, Koenig M, Komajda M. Correlation between left ventricular hypertrophy and GAA trinucleotide repeat length in Friedreich's ataxia. Circulation. 1997;95(9):2247–9.
5. Tai G, Corben LA, Yiu EM, Milne SC, Delatycki MB. Progress in the treatment of Friedreich ataxia. Neurol Neurochir Pol. 2018;52(2):129–39.

6. Perdomini M, Belbellaa B, Monassier L, Reutenauer L, Messaddeq N, Cartier N, Crystal RG, Aubourg P, Puccio H. Prevention and reversal of severe mitochondrial cardiomyopathy by gene therapy in a mouse model of Friedreich's ataxia. Nat Med. 2014;20(5):542–7.
7. Piguet F, de Montigny C, Vaucamps N, Reutenauer L, Eisenmann A, Puccio H. Rapid and complete reversal of sensory ataxia by gene therapy in a novel model of Friedreich ataxia. Mol Ther. 2018;26(8):1940–52.
8. Deverman BE, Ravina BM, Bankiewicz KS, Paul SM, Sah DWY. Gene therapy for neurological disorders: progress and prospects. Nat Rev Drug Discov. 2018;17(10):767.
9. Tsou AY, Paulsen EK, Lagedrost SJ, Perlman SL, Mathews KD, Wilmot GR, Ravina B, Koeppen AH, Lynch DR. Mortality in Friedreich ataxia. J Neurol Sci. 2011;307(1–2):46–9.
10. Weidemann F, Liu D, Hu K, Florescu C, Niemann M, Herrmann S, Kramer B, Klebe S, Doppler K, Uceyler N, Ritter CO, Ertl G, Stork S. The cardiomyopathy in Friedreich's ataxia—new biomarker for staging cardiac involvement. Int J Cardiol. 2015;194:50–7.
11. Reetz K, Abbas Z, Costa AS, Gras V, Tiffin-Richards F, Mirzazade S, Holschbach B, Frank RD, Vassiliadou A, Kruger T, Eitner F, Gross T, Schulz JB, Floege J, Shah NJ. Increased cerebral water content in hemodialysis patients. PLoS One. 2015;10(3):e0122188.
12. Reetz K, Dogan I, Hilgers RD, Giunti P, Mariotti C, Durr A, Boesch S, Klopstock T, de Rivera FJ, Schols L, Klockgether T, Burk K, Rai M, Pandolfo M, Schulz JB, EFACTS Study Group. Progression characteristics of the European Friedreich's Ataxia Consortium for Translational Studies (EFACTS): a 2 year cohort study. Lancet Neurol. 2016;15(13):1346–54.
13. Lang RM, Bierig M, Devereux RB, Flachskampf FA, Foster E, Pellikka PA, Picard MH, Roman MJ, Seward J, Shanewise JS, Solomon SD, Spencer KT, Sutton MS, Stewart WJ, G. Chamber Quantification Writing Group, American Society of Echocardiography's Guidelines and Standards Committee, European Association of Echocardiography. Recommendations for chamber quantification: a report from the American Society of Echocardiography's Guidelines and Standards Committee and the Chamber Quantification Writing Group, developed in conjunction with the European Association of Echocardiography, a branch of the European Society of Cardiology. J Am Soc Echocardiogr. 2005;18(12):1440–63.
14. Foppa M, Duncan BB, Rohde LE. Echocardiography-based left ventricular mass estimation. How should we define hypertrophy. Cardiovasc Ultrasound. 2005;3:17.
15. McMurray JJ, Adamopoulos S, Anker SD, Auricchio A, Bohm M, Dickstein K, Falk V, Filippatos G, Fonseca C, Gomez-Sanchez MA, Jaarsma T, Kober L, Lip GY, Maggioni AP, Parkhomenko A, Pieske BM, Popescu BA, Ronnevik PK, Rutten FH, Schwitter J, Seferovic P, Stepinska J, Trindade PT, Voors AA, Zannad F, Zeiher A, ESC Committee for Practice Guidelines. ESC guidelines for the diagnosis and treatment of acute and chronic heart failure 2012: the Task Force for the Diagnosis and Treatment of Acute and Chronic Heart Failure 2012 of the European Society of Cardiology. Developed in collaboration with the Heart Failure Association (HFA) of the ESC. Eur Heart J. 2012;33(14):1787–847.
16. Henry WL, Gardin JM, Ware JH. Echocardiographic measurements in normal subjects from infancy to old age. Circulation. 1980;62(5):1054–61.
17. Weidemann F, Rummey C, Bijnens B, Stork S, Jasaityte R, Dhooge J, Baltabaeva A, Sutherland G, Schulz JB, Meier T, Mitochondrial Protection with Idebenone in Cardiac or Neurological Outcome (MICONOS) Study Group. The heart in Friedreich ataxia: definition of cardiomyopathy, disease severity, and correlation with neurological symptoms. Circulation. 2012;125(13):1626–34.
18. Kipps A, Alexander M, Colan SD, Gauvreau K, Smoot L, Crawford L, Darras BT, Blume ED. The longitudinal course of cardiomyopathy in Friedreich's ataxia during childhood. Pediatr Cardiol. 2009;30(3):306–10.
19. McCormick A, Shinnick J, Schadt K, Rodriguez R, Addonizio L, Hirano M, Perlman S, Lin KY, Lynch DR. Cardiac transplantation in Friedreich ataxia: extended follow-up. J Neurol Sci. 2017;375:471–3.
20. Long A, Napierala JS, Polak U, Hauser L, Koeppen AH, Lynch DR, Napierala M. Somatic instability of the expanded GAA repeats in Friedreich's ataxia. PLoS One. 2017;12(12):e0189990.
21. Corben LA, Lynch D, Pandolfo M, Schulz JB, Delatycki MB, Clinical Management Guidelines Writing Group. Consensus clinical management guidelines for Friedreich ataxia. Orphanet J Rare Dis. 2014;9:184.
22. Dedobbeleer C, Rai M, Donal E, Pandolfo M, Unger P. Normal left ventricular ejection fraction and mass but subclinical myocardial dysfunction in patients with Friedreich's ataxia. Eur Heart J Cardiovasc Imaging. 2012;13(4):346–52.
23. St John Sutton M, Ky B, Regner SR, Schadt K, Plappert T, He J, D'souza B, Lynch DR. Longitudinal strain in Friedreich ataxia: a potential marker for early left ventricular dysfunction. Echocardiography. 2014;31(1):50–7.
24. Adabag AS, Maron BJ, Appelbaum E, Harrigan CJ, Buros JL, Gibson CM, Lesser JR, Hanna CA, Udelson JE, Manning WJ, Maron MS. Occurrence and frequency of arrhythmias in hypertrophic cardiomyopathy in relation to delayed enhancement on cardiovascular magnetic resonance. J Am Coll Cardiol. 2008;51(14):1369–74.

Prevention and reversal of severe mitochondrial cardiomyopathy by gene therapy in a mouse model of Friedreich's ataxia

Morgane Perdomini[1–5,11], Brahim Belbellaa[1–5,11], Laurent Monassier[6], Laurence Reutenauer[1–5], Nadia Messaddeq[1–5], Nathalie Cartier[7], Ronald G Crystal[8], Patrick Aubourg[7,9,10] & Hélène Puccio[1–5]

Cardiac failure is the most common cause of mortality in Friedreich's ataxia (FRDA), a mitochondrial disease characterized by neurodegeneration, hypertrophic cardiomyopathy and diabetes[1–3]. FRDA is caused by reduced levels of frataxin (FXN), an essential mitochondrial protein involved in the biosynthesis of iron-sulfur (Fe-S) clusters[4–8]. Impaired mitochondrial oxidative phosphorylation, bioenergetics imbalance, deficit of Fe-S cluster enzymes and mitochondrial iron overload occur in the myocardium of individuals with FRDA[9–12]. No treatment exists as yet for FRDA cardiomyopathy[13,14]. A conditional mouse model with complete frataxin deletion in cardiac and skeletal muscle (*Mck-Cre-Fxn*$^{L3/L-}$ mice) recapitulates most features of FRDA cardiomyopathy, albeit with a more rapid and severe course[15,16]. Here we show that adeno-associated virus rh10 vector expressing human FXN injected intravenously in these mice fully prevented the onset of cardiac disease. Moreover, later administration of the frataxin-expressing vector, after the onset of heart failure, was able to completely reverse the cardiomyopathy of these mice at the functional, cellular and molecular levels within a few days. Our results demonstrate that cardiomyocytes with severe energy failure and ultrastructure disorganization can be rapidly rescued and remodeled by gene therapy and establish the preclinical proof of concept for the potential of gene therapy in treating FRDA cardiomyopathy.

Among adeno-associated virus (AAV) serotypes that efficiently target the heart, AAVrh10 is readily transported within the myocardium after intravenous injection[17,18]. We conducted a biodistribution study in wild-type (WT) mice injected intravenously with either the GFP-encoding AAVrh10-CAG-GFP vector or the frataxin-encoding AAVrh10-CAG-hFXN-HA vector. Transgene expression was robust in the heart and liver, with a substantial overexpression of human FXN (more than tenfold over that of endogenous mouse frataxin) (**Supplementary Fig. 1a–j**). In contrast, transgene expression was much lower in skeletal muscle and in the nervous system, although neurons of the dorsal root ganglia were highly positive for GFP expression all along the vertebral column as well as in their axonal projections in the posterior column of the spinal cord and in the medulla oblongata (**Supplementary Fig. 1a–j**). The tropism of AAVrh10 for heart and dorsal root ganglia, the two most affected tissues in FRDA, validates the choice of the AAVrh10 serotype for our studies.

To investigate the potential of gene therapy approaches in the treatment of the FRDA cardiomyopathy, we performed a single intravenous injection of AAVrh10-CAG-hFXN at a dose of 5.4×10^{13} vector genomes per kilogram body weight (vg kg^{-1}) into asymptomatic 3-week-old *Mck-Cre-Fxn*$^{L3/L-}$ mice (carrying a conditional allele (*L3*) allowing deletion of exon 4 of *Fxn* and the *Fxn* exon 4–deleted allele (*L–*) and a muscle creatine kinase promoter–driven *Cre* transgene), called here *Mck* mice[15] ($n = 9$) (**Supplementary Fig. 2a**). Serial echocardiographic measurements showed normal hemodynamic and morphological development in treated *Mck* mice (**Fig. 1a** and **Supplementary Tables 1–3**). *Mck* mice injected with AAVrh10-CAG-hFXN remained undistinguishable from WT mice at 35 weeks of age, demonstrating a complete prevention of cardiac disease. In contrast, untreated *Mck* mice developed, as previously demonstrated[15,16], a rapidly progressive cardiac insufficiency, with a marked decrease in left ventricle shortening fraction and cardiac output, as well as left ventricle hypertrophy associated with massive geometric remodeling (**Fig. 1a** and **Supplementary Tables 1–3**). These mice lost weight progressively and died of cardiac failure at 65 ± 10 d (9.3 ± 1.4 weeks) (**Fig. 1b** and **Supplementary Fig. 2b**).

Consistent with the development of heart failure, untreated *Mck* mice at 8 weeks of age displayed a strong increase in mRNA expression of atrial natriuretic peptide (*Nppa*) and brain natriuretic peptide (*Nppb*), two biomarkers of hemodynamic overload[19] (**Fig. 1c**). Biomarkers of hypertrophy[20] were also present, with increased

[1]Département de Médecine Translationnelle et Neurogénétique, Institut de Génétique et de Biologie Moléculaire et Cellulaire (IGBMC), Illkirch, France. [2]INSERM, U596, Illkirch, France. [3]CNRS, UMR7104, Illkirch, France. [4]Université de Strasbourg, Strasbourg, France. [5]Collège de France, Chaire de génétique humaine, Illkirch, France. [6]Laboratoire de Neurobiologie et Pharmacologie Cardiovasculaire, Fédération de Médecine Translationnelle, Faculté de Médecine, Université de Strasbourg, Strasbourg, France. [7]INSERM, U986, Le Kremlin-Bicêtre, France. [8]Department of Genetic Medicine, Weill Cornell Medical College, New York, USA. [9]University Paris-Sud, Paris, France. [10]Assistance Publique-Hôpitaux de Paris, Paris, France. [11]These authors contributed equally to this work. Correspondence should be addressed to H.P. (hpuccio@igbmc.fr) or P.A. (patrick.aubourg@inserm.fr).

Received 20 November 2013; accepted 20 February 2014; published online 6 April 2014; doi:10.1038/nm.3510

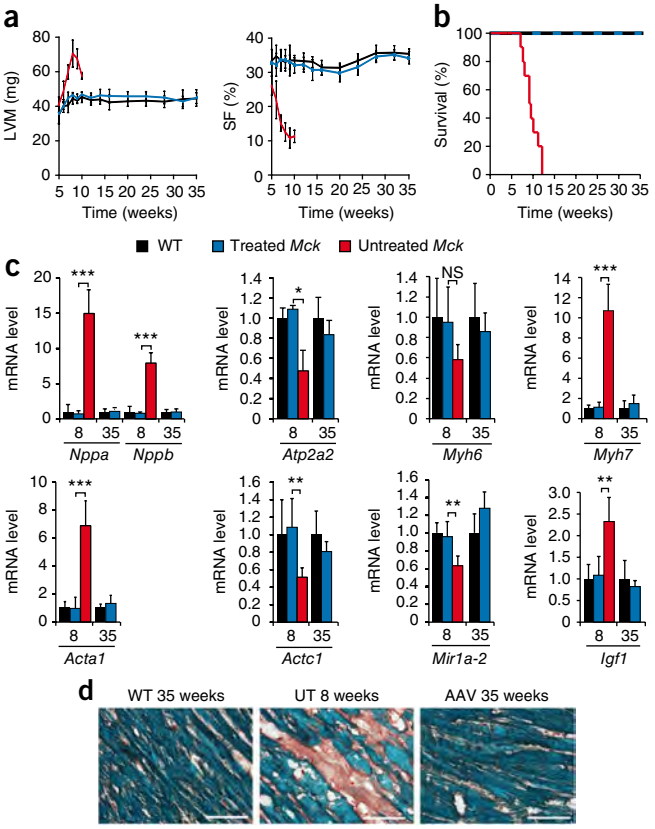

Figure 1 Treatment of asymptomatic *Mck* mice prevents the onset of cardiac failure and rescues survival. (**a**) Echocardiographic assessment of the left ventricle mass (LVM, left) and shortening fraction (SF, right) for WT ($n = 9$), treated ($n = 9$) and untreated ($n = 10$) *Mck* mice. (**b**) Survival of WT ($n = 9$), treated ($n = 9$) and untreated ($n = 10$) *Mck* mice. (**c**) Quantification of *Nppa*, *Nppb*, *Atp2a2*, *Myh6*, *Myh7*, *Acta1*, *Actc1* and *Igf1* mRNA expression and *Mir1a-2* expression in heart from WT, treated and untreated *Mck* mice at 8 and 35 weeks of age. $n = 5$ in all groups except WT mice at 35 weeks of age ($n = 4$). Data are presented as fold change relative to WT and normalized to 18S rRNA for mRNA and to *Rnu6* for *Mir1a*. (**d**) Collagen localization with Sirius red and fast green co-staining on heart cryosections from WT, untreated (UT) and treated (AAV) *Mck* mice at 8 and 35 weeks of age. Data are representative of 3 biological replicates per group with at least 6 experimental replicates. Scale bars, 50 µm. Data are represented as means ± s.d. $^*P < 0.05$; $^{**}P < 0.01$; $^{***}P < 0.001$; NS, statistically nonsignificant. For statistical comparison of three experimental groups, one-way analysis of variance (ANOVA) followed by Scheffé's *post hoc* test was used. For statistical comparison of two experimental groups, the bilateral Student's *t*-test was used.

expression of the β-myosin heavy chain (*Myh7*), skeletal muscle α-actin (*Acta1*) and the cardiac transcription factors *Gata4* and *Nkx2-5*, as well as decreased expression of α-myosin heavy chain (*Myh6*) and cardiac α-actin (*Actc1*) (**Fig. 1c**, **Supplementary Fig. 2c** and **Supplementary Data Sets**). Furthermore, untreated Mck mice showed significantly decreased expression of the microRNA (miRNA) *Mir1a-2*, a key contributor to cardiac hypertrophy[21], as well as significantly increased expression of one of its downstream targets, insulin-like growth factor-1 (*Igf1*) (**Fig. 1c**). In addition, mRNA expression of the sarcoplasmic reticulum Ca^{2+} ATPase (*Atp2a2*), a critical determinant of cardiac relaxation responsible for diastolic Ca^{2+} reuptake from the cytosol[22], was strongly decreased in untreated mice compared to WT mice (**Fig. 1c**). In contrast, we did not detect any difference in the levels of these biomarkers between treated *Mck* mice and WT littermates at 8 and 35 weeks of age (**Fig. 1c**).

Histological analysis showed myocardial degeneration with cytoplasmic vacuolization in necrotic cardiomyocytes in untreated *Mck* mice at 8 weeks of age, whereas overall heart organization was

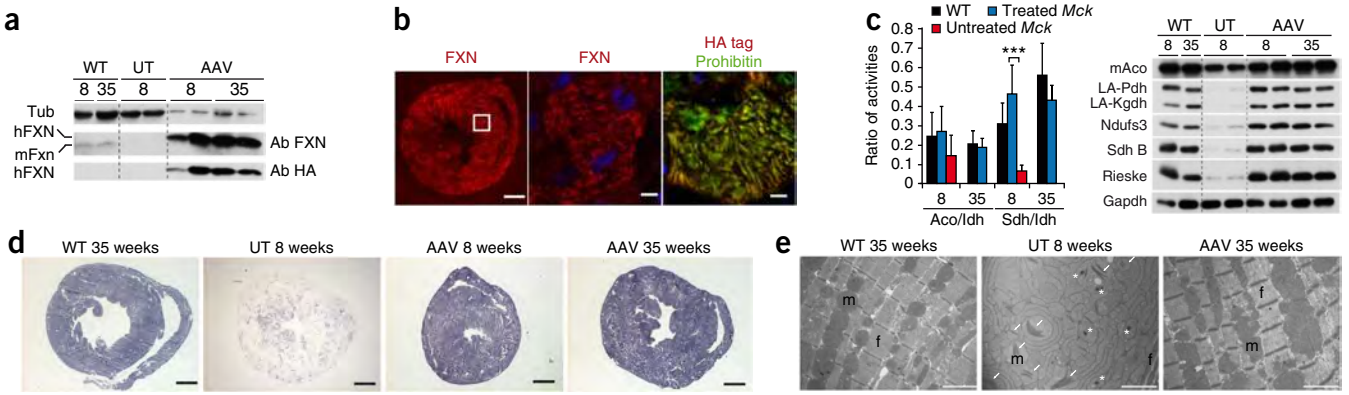

Figure 2 Expression of human FXN prevents Fe-S protein deficiency and disorganization of mitochondrial and cardiomyocyte ultrastructure in asymptomatic *Mck* mice. (**a**) Expression of mouse (mFxn) and human (hFXN) FXN protein in heart from WT, untreated (UT) and treated (AAV) *Mck* mice at 8 and 35 weeks of age. Tub, tubulin; Ab FXN, antibody targeting both mFxn and hFXN; Ab HA, antibody targeting the HA tag of hFXN. Data are representative of 5 biological replicates per group with at least 3 experimental replicates. (**b**) Left and middle, hFXN protein expression assessed by immunofluorescence in heart from 35-week-old treated *Mck* mice using antibody to FXN. Right, co-immunostaining of mitochondrial prohibitin with hFXN, using antibody to HA. Hoechst counterstain was used for DNA. Scale bars, 1 mm (left) and 5 µm (middle and right). Data are representative of 3 biological replicates per group with at least 6 experimental replicates. (**c**) Left, enzymatic activity of Aco and Sdh, normalized to that of isocitrate dehydrogenase (Idh), in heart from WT, treated and untreated *Mck* mice at 8 and 35 weeks of age. $n = 5$ per group. $^{***}P < 0.001$. For statistical comparison of three experimental groups, one-way ANOVA followed by Scheffé's *post hoc* test was used. For statistical comparison of two experimental groups, the bilateral Student's *t*-test was used. Error bars represent s.d. Right, Fe-S apoprotein expression in heart of WT, untreated and treated mice at 8 and 35 weeks of age. mAco, mitochondrial Aco; LA-Pdh, lipoic acid–bound Pdh; LA-Kgdh, lipoic acid–bound Kgdh; Sdh B: succinate dehydrogenase B subunit. (**d**) Enzymatic histochemical staining for Sdh activity (blue) on heart cryosections from WT, untreated and treated *Mck* mice at 8 or 35 weeks of age, as indicated. Scale bars, 1 mm. Data are representative of 3 biological replicates per group with at least 6 experimental replicates. (**e**) Transmission electron micrographs of cardiac muscle from WT, untreated and treated *Mck* mice at 8 or 35 weeks of age, as indicated. Asterisks indicate mitochondrial iron deposits; arrows indicate cristae. f, fiber; m, mitochondria. Scale bars, 2 µm. Data are representative of 3 biological replicates per group with at least 6 experimental replicates.

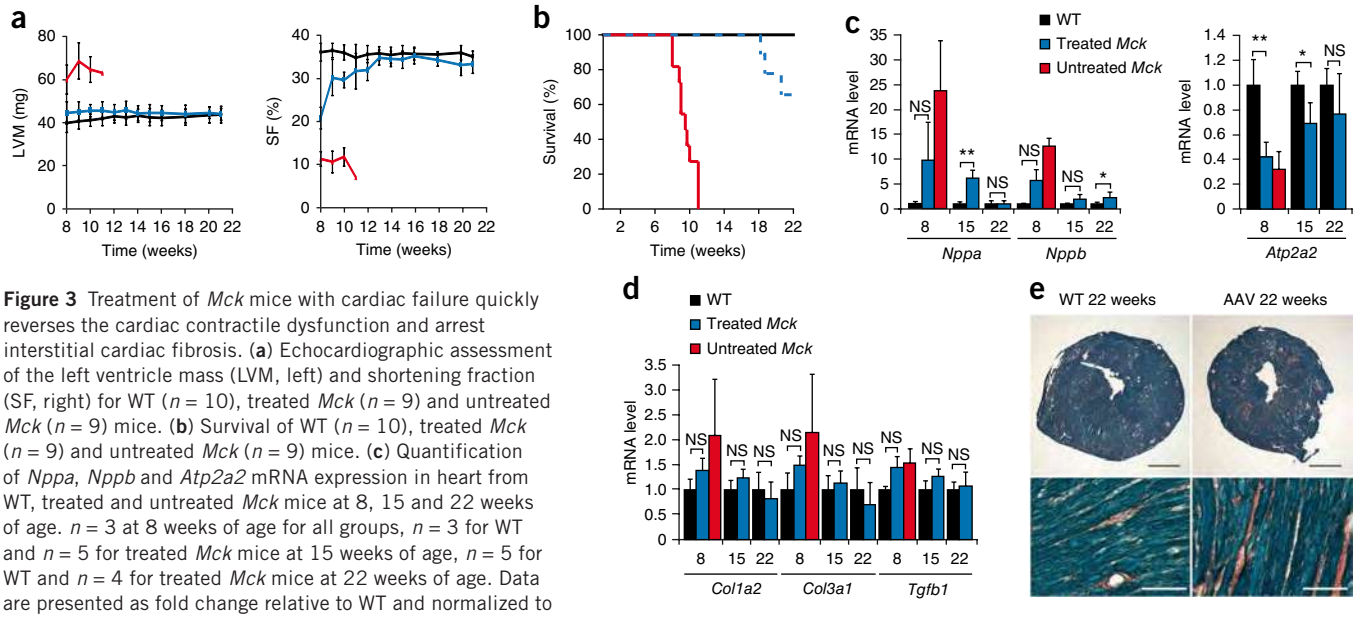

Figure 3 Treatment of *Mck* mice with cardiac failure quickly reverses the cardiac contractile dysfunction and arrest interstitial cardiac fibrosis. (**a**) Echocardiographic assessment of the left ventricle mass (LVM, left) and shortening fraction (SF, right) for WT ($n = 10$), treated *Mck* ($n = 9$) and untreated *Mck* ($n = 9$) mice. (**b**) Survival of WT ($n = 10$), treated *Mck* ($n = 9$) and untreated *Mck* ($n = 9$) mice. (**c**) Quantification of *Nppa*, *Nppb* and *Atp2a2* mRNA expression in heart from WT, treated and untreated *Mck* mice at 8, 15 and 22 weeks of age. $n = 3$ at 8 weeks of age for all groups, $n = 3$ for WT and $n = 5$ for treated *Mck* mice at 15 weeks of age, $n = 5$ for WT and $n = 4$ for treated *Mck* mice at 22 weeks of age. Data are presented as fold change relative to WT and normalized to 18S rRNA. (**d**) Quantification of collagen type 1 (*Col1a2*) and type 3 (*Col3a1*) and *Tgfb1* mRNA expression in heart from WT, treated and untreated *Mck* mice at 8, 15 and 22 weeks of age. $n = 3$ at 8 weeks of age for all groups, $n = 3$ for WT and $n = 5$ for treated *Mck* mice at 15 weeks of age, $n = 5$ for WT and $n = 4$ for treated *Mck* mice at 22 weeks of age. Data are presented as fold change relative to WT and normalized to 18S rRNA. (**e**) Collagen labeling with Sirius red and fast green co-staining on heart cryosections from WT and treated *Mck* (AAV) mice at 22 weeks of age. Observations were made at low (top; scale bars, 1 mm) and high at the level of the septum (bottom; scale bars, 50 μm) magnification. Data are representative of 6 biological replicates per group with at least 6 experimental replicates. Data are represented as means ± s.d. $^*P < 0.05$; $^{**}P < 0.01$; NS, statistically nonsignificant. For statistical comparison of three experimental groups, one-way ANOVA followed by Scheffé's *post hoc* test was used. For statistical comparison of two experimental groups, the bilateral Student's *t*-test was used.

preserved in treated *Mck* mice at 35 weeks of age (**Supplementary Fig. 2d**). Sirius red staining and the expression of collagen types I and III and transforming growth factor β1 (*Tgfb1*) indicated the absence of myocardial post-necrotic fibrosis in treated *Mck* animals, whereas there was massive interstitial fibrosis in untreated *Mck* mice at 8 weeks of age (**Fig. 1d** and **Supplementary Fig. 2c**).

Frataxin expression was robust in heart and liver in treated *Mck* mice without detectable adverse effects of frataxin overexpression. Indeed, serum biomarkers of hepatic and renal function and serum inflammatory cytokines were within the normal range, histological signs of inflammation in heart and liver were not detected and the expression of key genes involved in liver function and stress response was within the normal range (**Supplementary Figs. 1k** and **3** and **Supplementary Table 4**). Sustained overexpression of human FXN in heart was confirmed at 8 and 35 weeks of age in treated *Mck* mice, with some variation in expression levels among treated mice (**Fig. 2a** and **Supplementary Fig. 2e**). Mitochondrial import and maturation of human FXN was complete and nonsaturated, as only the intermediate and cleaved mature forms of human FXN[23] were detected in heart cell lysates (**Supplementary Fig. 2f**). Furthermore, human FXN was expressed broadly in cardiomyocyte mitochondria throughout the left and right ventricles of treated *Mck* mice (in >95% of cardiomyocytes) (**Fig. 2b**).

In line with frataxin having an essential function in regulating cellular Fe-S cluster biogenesis[6–8], FXN deficiency leads to a primary Fe-S cluster deficit, resulting in a decrease in the activity of enzymes dependent on Fe-S clusters, which leads to mitochondrial iron accumulation[15,16]. Accordingly, untreated *Mck* mice showed strong decreases in the enzymatic activities of the Fe-S cluster–dependent aconitases (Aco) and succinate dehydrogenase (Sdh), 41.3% and 79.8%, respectively, compared to WT mice at 8 weeks of age (**Fig. 2c**)[15,16]. Furthermore, untreated *Mck* mice showed a substantial reduction in the levels of the mitochondrial Fe-S proteins NADH dehydrogenase ubiquinone iron-sulfur protein 3 (Ndufs3), Sdh and Rieske (**Fig. 2c**), components of the respiratory chain complexes I, II and III, respectively, as a result of the instability of the respective Fe-S apoproteins[24]. Similarly, the levels of lipoic acid bound to α-ketoglutarate dehydrogenase (Kgdh) and to pyruvate dehydrogenase (Pdh) were decreased, suggestive of a lower activity of the Fe-S enzyme lipoic acid synthase[25] (**Fig. 2c**). In contrast, the activities and levels of mitochondrial Fe-S proteins were similar in treated *Mck* and WT littermates (**Fig. 2c**). Histoenzymatic staining of Sdh activity confirmed the correction of Fe-S biogenesis in more than 95% of cardiomyocytes throughout the heart in treated *Mck* mice (**Fig. 2d**). In line with the correction of the primary Fe-S cluster deficit, we did not observe iron accumulation or signs of cellular iron homeostasis perturbation or of an integrated stress response (either an endoplasmic reticulum stress response or a stress response related to amino acid starvation[26,27]) in the cardiac tissue of treated *Mck* mice (**Supplementary Fig. 2g–i**). Finally, cardiac sarcomere organization and mitochondria ultrastructure in treated *Mck* mice was normal as assessed by electron microscopy, whereas untreated *Mck* animals showed sparse atrophied myofibrils and massive mitochondrial proliferation with abnormal collapsed or swollen cristae and iron accumulation (**Fig. 2e** and **Supplementary Fig. 2j**). Together, these data indicate that AAVrh10-mediated human *FXN* gene transfer in asymptomatic *Mck* mice prevents the development of mitochondrial FRDA-like cardiomyopathy at the molecular, cellular and physiological levels.

To determine the therapeutic potential of a gene therapy approach when cardiac dysfunction is already present, we intravenously injected 7-week-old *Mck* mice with advanced cardiac insufficiency with a dose of 5.4×10^{13} vg kg^{-1} of AAVrh10-CAG-hFXN ($n = 9$)

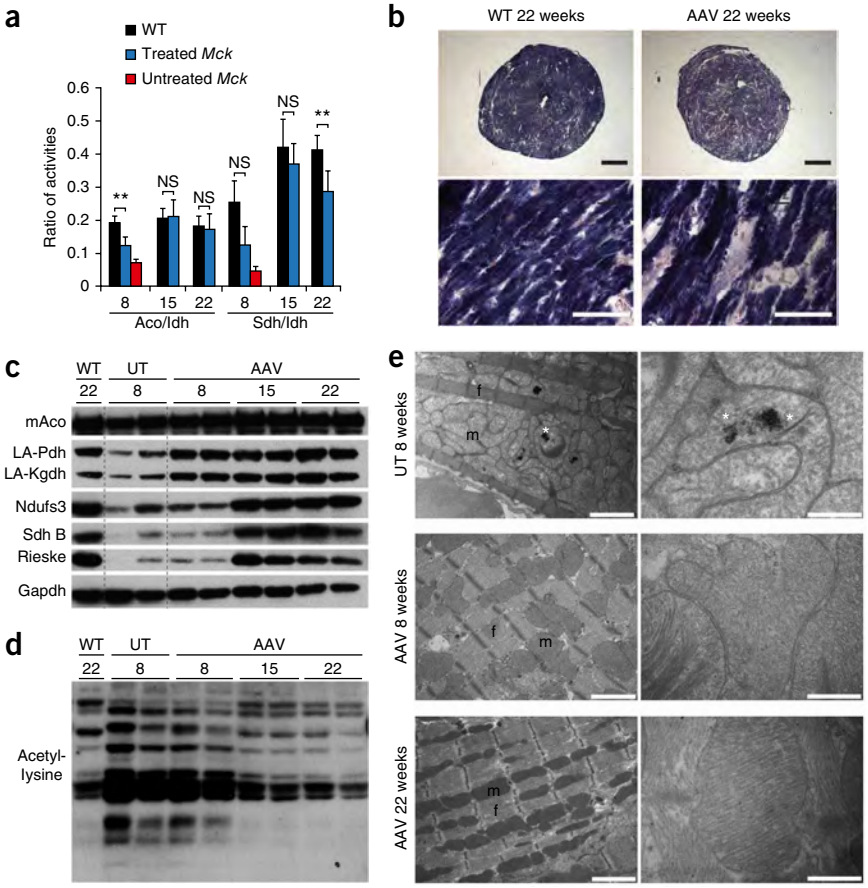

Figure 4 Treatment of *Mck* mice with cardiac failure leads to rapid correction of Fe-S deficit and of cardiac mitochondrial and sarcomere ultrastructure. (**a**) Enzymatic activity of Aco and Sdh normalized to that of isocitrate dehydrogenase (Idh), in heart from WT, treated and untreated *Mck* mice at 8, 15 and 22 weeks of age. $n = 3$ at 8 weeks of age for all groups, $n = 3$ for WT mice and $n = 5$ for *Mck* treated mice at 15 weeks of age, $n = 6$ at 22 weeks of age per group. $^{**}P < 0.01$; NS, statistically nonsignificant. For statistical comparison of three experimental groups, one-way ANOVA followed by Scheffé's *post hoc* test was used. For statistical comparison of two experimental groups, the bilateral Student's *t*-test was used. (**b**) Enzymatic histochemical staining for Sdh activity (blue) on heart cryosections from WT and treated *Mck* (AAV) mice at 22 weeks of age. Observations were made at low (top; scale bars, 1 mm) and high at the level of the septum (bottom; scale bars, 50 µm) magnification. Data are representative of 6 biological replicates per group with at least 6 experimental replicates. (**c**) Fe-S cluster apoprotein expression in heart samples from WT, untreated (UT) and treated (AAV) *Mck* mice at 8, 15 and 22 weeks of age. mAco, mitochondrial Aco; LA-Pdh, lipoic acid–bound Pdh; LA-Kgdh, lipoic acid–bound Kgdh; Sdh B, succinate dehydrogenase B subunit. (**d**) Western blot analysis for acetyl-lysine residues in heart from WT, untreated and treated *Mck* mice at 8, 15 and 22 weeks of age. (**e**) Transmission electron micrographs of heart from untreated and treated *Mck* mice at 8 and 22 weeks of age. Observations were made at low (left; scale bars, 2 µm) and high (right; scale bars, 500 nm) magnification. Asterisks indicate mitochondrial iron deposits; arrows indicate collapsed cristae. f, fiber; m, mitochondria. Data are representative of 3 biological replicates per group with at least 6 experimental replicates.

(**Supplementary Fig. 4a**). At this time point, ventricular remodeling and left ventricular systolic dysfunction were evident, with a left ventricle mass of 60 ± 4 mg (146% of WT) and shortening fraction of 15 ± 2% (44% of WT), resulting in a major decrease in cardiac output (28 ± 6 ml min^{-1}; 39% of WT) (**Supplementary Tables 1–3**). One week after vector injection, the left ventricle function of treated *Mck* mice was already significantly ($P < 0.001$) improved with shortening fraction and cardiac output reaching 21 ± 2% and 64 ml min^{-1} (58% and 66% of WT), respectively, and a decrease in left ventricle mass to 44 ± 4 mg (110% of WT) (**Fig. 3a** and **Supplementary Tables 5–7**). This rapid recovery of the cardiac phenotype correlated with strong expression and normal mitochondrial localization of human FXN in the heart at 1 week after treatment, which was sustained over 22 weeks (**Supplementary Fig. 4c–e**). In agreement with these results, evaluation of *FXN* transgene expression kinetics in WT mice showed substantial mRNA and protein levels of human FXN as soon as 3 d after injection (**Supplementary Fig. 1h**). Between 8 and 12 weeks of age, in *Mck* mice treated at 7 weeks of age, cardiac function continued to improve rapidly to reach WT values, with a complete correction of left ventricle systolic function and cardiac morphology (**Fig. 3a** and **Supplementary Tables 5–7**). The survival of treated *Mck* mice was markedly prolonged but not normal (**Fig. 3b**). Indeed, long-term analysis of *Mck* mice treated at 7 weeks of age revealed an unexpected phenotype. Despite a fully corrected cardiomyopathy, all *Mck* mice treated at 7 weeks of age lost weight at 16 weeks of age (**Supplementary Fig. 4b**) and developed severe peripheral striated muscle atrophy and kyphosis leading to the death of 3 mice between 18 and 22 weeks of age (**Fig. 3b**). Death of the treated *Mck* mice was most likely a consequence of a severe peripheral mitochondrial myopathy presenting as heterogeneous muscle fiber size, cellular infiltration and a general deficit of Fe-S cluster enzymes due to a very low level of human *FXN* transgene expression in skeletal muscle (**Supplementary Figs. 1k** and **5**). Although the *Mck* model is an appropriate model for studying FRDA cardiomyopathy, this model completely lacks FXN in skeletal muscles. This contrasts with the situation in humans with FRDA, who have residual FXN expression and do not develop overt clinical or histological signs of myopathy, although magnetic resonance spectroscopy of individuals with FRDA has demonstrated some degree of mitochondrial impairment in skeletal muscle[28].

In parallel with the rapid improvement of cardiac function, we observed a progressive normalization of the pathology-induced gene program in treated *Mck* mice (**Fig. 3c** and **Supplementary Fig. 4f**). Indeed, by 15 weeks of age (8 weeks after treatment), the expression of *Nppa* and *Nppb* decreased in treated *Mck* mice compared to mice at 8 weeks of age, suggesting normalization of the hemodynamic load. Furthermore, the hypertrophic gene program was completely normalized by 15 weeks of age, with the exception of *Acta1* and *Myh7*, whose expression remained high (**Supplementary Fig. 4f**). Likewise, the expression of *Atp2a2* progressively increased in treated

mice between 8 and 22 weeks of age, indicating that diastolic Ca^{2+} transport was probably restored (**Fig. 3c**). Notably, decreases in the mRNA expression of collagen (*Col1a2* and *Col3a1*) and *Tgfb1*, as well as decreased histological labeling of cardiac extracellular matrix, provide evidence that interstitial cardiac fibrosis was quickly arrested following treatment (**Fig. 3d**,**e**). The rare fibrotic patches in the cardiac tissue of treated mice at 22 weeks of age (**Fig. 3e**) probably already present at the time of treatment[16], and the incompletely corrected gene expression profile (**Fig. 3d**) suggest the persistence of some degree of nonprogressive fibrotic and hypertrophic scar, which, however, does not interfere with cardiac function. Rapid arrest of myocardial fibrosis would be an important advantage of this approach for its future clinical development in subjects with FRDA, in whom longitudinal myocardium strain, probably due to interstitial fibrosis, is an early index of myocardial dysfunction[3,29–31].

Finally, the progressive correction of the cardiac phenotype also correlated with progressive increases in the activities of the Fe-S proteins Aco and Sdh (**Fig. 4a**,**b**), in the levels of the Fe-S proteins Ndufs3, Sdh and Rieske, and in the lipoic acid–bound proportions of Pdh and Kgdh (**Fig. 4c**). Furthermore, there was no sign of iron deregulation in treated *Mck* mice, given the absence of cardiac iron deposits as well as the normalization in the expression of mRNA and proteins involved in cellular iron handling (**Supplementary Fig. 4g–i**). We also observed a progressive diminution of the integrated stress response in treated *Mck* mice (**Supplementary Fig. 4j**). Consistent with a rescue of mitochondrial homeostasis, the level of protein hyperacetylation, which reflects inhibition of Sirt3 deacetylase activity due to a respiratory chain defect[32], in treated *Mck* mice was similar to that in untreated *Mck* mice at 8 weeks of age, but normalized to WT levels at 15 and 22 weeks of age (**Fig. 4d**). Notably, we also observed a rapid correction of the ultrastructure of the cardiomyocytes (that is, normal sarcomere organization and a massive decrease in mitochondrial proliferation) at 1 week after treatment (**Fig. 4e**). Swollen mitochondria with parallel stacks of cristae membranes were still present 1 week after gene therapy, but at 22 weeks of age after treatment, sarcomeres and mitochondria organization showed complete recovery (**Fig. 4e**). Altogether, these data indicate that AAVrh10-hFXN treatment in symptomatic *Mck* mice results in a rapid biochemical, cellular and functional improvement leading to correction of the FRDA-like cardiomyopathy.

In summary, the rapidity of transgene expression from the AAVrh10-hFXN vector and its robust correction of cardiac parameters in a mouse model of FRDA cardiomyopathy, even when administered after the onset of heart failure, makes gene therapy using this vector an appealing potential therapeutic approach for patients with FRDA. Cardiomyocyte mitochondria responded to gene therapy correction and cardiac cells quickly recovered from their energy deficit, illustrating the highly dynamic nature of mitochondria[33]. These results also suggest that a substantial fraction of dysfunctioning frataxin-deficient cardiomyocytes are still viable after the onset of heart failure and that their phenotype can be reversed. Bioenergetics impairment is the primary cause of FRDA cardiomyopathy[9,15].

Our preclinical study paves the way for a cardiac gene therapy–based clinical trial in patients with FRDA with severe cardiomyopathy, once the dose-response efficacy of the vector as well as the delivery method and possible toxicity are tested in large animals. As suggested by the successful heart transplantation cases reported for FRDA[34], leading to an improved clinical picture, we hope that this cardiac gene therapy approach may improve the survival and quality of life in individuals with FRDA.

METHODS

Methods and any associated references are available in the online version of the paper.

Note: Any Supplementary Information and Source Data files are available in the online version of the paper.

ACKNOWLEDGMENTS

We thank A. Martelli for help in vector construction and for fruitful discussions, P. Bougnères for fruitful discussions and insightful comments on the manuscript, and V. Blouin and P. Moullier (Institut de Recherche Thérapeutique, INSERM UMR 1089) for vector production. This work was supported by the Association Française contre les Myopathies (to H.P.), the US Friedreich Ataxia Research Alliance (to H.P.), the European Community under the European Research Council (206634/ISCATAXIA; to H.P.), the Seventh Framework Programme (242193/EFACTS; to H.P.), the Association the Fondation Simone et Cino del Duca (to P.A.) and the Institut de France (to P.A.), by a personal donation from the Ledru family (to H.P.) and by a French state fund through the Agence Nationale de la Recherche under the frame programme Investissements d'Avenir labeled ANR-10-IDEX-0002-02 (ANR-10-LABX-0030-INRT). M.P. is a recipient of a PhD fellowship from the Association Française pour l'Ataxie de Friedreich.

AUTHOR CONTRIBUTIONS

M.P. injected the mice, analyzed the echocardiographic results, and performed and analyzed the molecular and biochemical experiments; B.B. performed the survival, echocardiography and histological experiments; N.M. prepared and analyzed the samples for the electron microscopy analysis; L.M. trained B.B. for echocardiography and cardiac function analysis; L.R. was responsible for mouse production; R.G.C. and N.C. provided advice for the design of the study; M.P., B.B., P.A. and H.P. designed the study; H.P. and P.A. conceived of the study and were responsible for research coordination and strategy. M.P., B.B., P.A. and H.P. wrote the manuscript. All authors discussed the results and commented on the manuscript.

COMPETING FINANCIAL INTERESTS

The authors declare competing financial interests: details are available in the online version of the paper.

1. Harding, A.E. Friedreich's ataxia: a clinical and genetic study of 90 families with an analysis of early diagnostic criteria and intrafamilial clustering of clinical features. *Brain* **104**, 589–620 (1981).
2. Tsou, A.Y. *et al.* Mortality in Friedreich ataxia. *J. Neurol. Sci.* **307**, 46–49 (2011).
3. Weidemann, F. *et al.* The heart in Friedreich ataxia: definition of cardiomyopathy, disease severity, and correlation with neurological symptoms. *Circulation* **125**, 1626–1634 (2012).
4. Campuzano, V. *et al.* Frataxin is reduced in Friedreich ataxia patients and is associated with mitochondrial membranes. *Hum. Mol. Genet.* **6**, 1771–1780 (1997).
5. Campuzano, V. *et al.* Friedreich's ataxia: autosomal recessive disease caused by an intronic GAA triplet repeat expansion. *Science* **271**, 1423–1427 (1996).
6. Tsai, C.L. & Barondeau, D.P. Human frataxin is an allosteric switch that activates the Fe-S cluster biosynthetic complex. *Biochemistry* **49**, 9132–9139 (2010).
7. Schmucker, S. *et al.* Mammalian frataxin: an essential function for cellular viability through an interaction with a preformed ISCU/NFS1/ISD11 iron-sulfur assembly complex. *PLoS ONE* **6**, e16199 (2011).
8. Colin, F. *et al.* Mammalian frataxin controls sulfur production and iron entry during *de novo* Fe_4S_4 cluster assembly. *J. Am. Chem. Soc.* **135**, 733–740 (2013).
9. Lodi, R. *et al.* Cardiac energetics are abnormal in Friedreich ataxia patients in the absence of cardiac dysfunction and hypertrophy: an *in vivo* ^{31}P magnetic resonance spectroscopy study. *Cardiovasc. Res.* **52**, 111–119 (2001).
10. Lamarche, J., Shapcott, D., Côté, M. & Lemieux, B. Cardiac iron deposits in Friedreich's ataxia. in *Handbook of Cerebellar Diseases* (ed. Lechtenberg, R.) 453–457 (CRC Press, 1993).
11. Rötig, A. *et al.* Aconitase and mitochondrial iron-sulphur protein deficiency in Friedreich ataxia. *Nat. Genet.* **17**, 215–217 (1997).
12. Michael, S. *et al.* Iron and iron-responsive proteins in the cardiomyopathy of Friedreich's ataxia. *Cerebellum* **5**, 257–267 (2006).
13. Perlman, S.L. A review of Friedreich ataxia clinical trial results. *J. Child Neurol.* **27**, 1217–1222 (2012).
14. Wilson, R.B. Therapeutic developments in Friedreich ataxia. *J. Child Neurol.* **27**, 1212–1216 (2012).
15. Puccio, H. *et al.* Mouse models for Friedreich ataxia exhibit cardiomyopathy, sensory nerve defect and Fe-S enzyme deficiency followed by intramitochondrial iron deposits. *Nat. Genet.* **27**, 181–186 (2001).

16. Seznec, H. *et al.* Idebenone delays the onset of cardiac functional alteration without correction of Fe-S enzymes deficit in a mouse model for Friedreich ataxia. *Hum. Mol. Genet.* **13**, 1017–1024 (2004).
17. Hu, C., Busuttil, R.W. & Lipshutz, G.S. RH10 provides superior transgene expression in mice when compared with natural AAV serotypes for neonatal gene therapy. *J. Gene Med.* **12**, 766–778 (2010).
18. Wang, G. *et al.* Persistent expression of biologically active anti-HER2 antibody by AAVrh.10-mediated gene transfer. *Cancer Gene Ther.* **17**, 559–570 (2010).
19. Bernardo, B.C., Weeks, K.L., Pretorius, L. & McMullen, J.R. Molecular distinction between physiological and pathological cardiac hypertrophy: experimental findings and therapeutic strategies. *Pharmacol. Ther.* **128**, 191–227 (2010).
20. Wilkins, B.J. & Molkentin, J.D. Calcium-calcineurin signaling in the regulation of cardiac hypertrophy. *Biochem. Biophys. Res. Commun.* **322**, 1178–1191 (2004).
21. Elia, L. *et al.* Reciprocal regulation of microRNA-1 and insulin-like growth factor-1 signal transduction cascade in cardiac and skeletal muscle in physiological and pathological conditions. *Circulation* **120**, 2377–2385 (2009).
22. Barry, W.H. & Bridge, J.H. Intracellular calcium homeostasis in cardiac myocytes. *Circulation* **87**, 1806–1815 (1993).
23. Schmucker, S., Argentini, M., Carelle-Calmels, N., Martelli, A. & Puccio, H. The *in vivo* mitochondrial two-step maturation of human frataxin. *Hum. Mol. Genet.* **17**, 3521–3531 (2008).
24. Guillon, B. *et al.* Frataxin deficiency causes upregulation of mitochondrial Lon and ClpP proteases and severe loss of mitochondrial Fe-S proteins. *FEBS J.* **276**, 1036–1047 (2009).
25. Navarro-Sastre, A. *et al.* A fatal mitochondrial disease is associated with defective NFU1 function in the maturation of a subset of mitochondrial Fe-S proteins. *Am. J. Hum. Genet.* **89**, 656–667 (2011).
26. Huang, M.L. *et al.* Molecular and functional alterations in a mouse cardiac model of Friedreich ataxia: activation of the integrated stress response, eIF2α phosphorylation, and the induction of downstream targets. *Am. J. Pathol.* **183**, 745–757 (2013).
27. Seznec, H. *et al.* Friedreich ataxia: the oxidative stress paradox. *Hum. Mol. Genet.* **14**, 463–474 (2005).
28. Vorgerd, M. *et al.* Mitochondrial impairment of human muscle in Friedreich ataxia in vivo. *Neuromuscul. Disord.* **10**, 430–435 (2000).
29. St John Sutton, M. *et al.* Longitudinal strain in friedreich ataxia: a potential marker for early left ventricular dysfunction. *Echocardiography* **31**, 50–57 (2014).
30. Dedobbeleer, C., Rai, M., Donal, E., Pandolfo, M. & Unger, P. Normal left ventricular ejection fraction and mass but subclinical myocardial dysfunction in patients with Friedreich's ataxia. *Eur. Heart J. Cardiovasc. Imaging* **13**, 346–352 (2012).
31. Raman, S.V. *et al.* Impaired myocardial perfusion reserve and fibrosis in Friedreich ataxia: a mitochondrial cardiomyopathy with metabolic syndrome. *Eur. Heart J.* **32**, 561–567 (2011).
32. Wagner, G.R., Pride, P.M., Babbey, C.M. & Payne, R.M. Friedreich's ataxia reveals a mechanism for coordinate regulation of oxidative metabolism via feedback inhibition of the SIRT3 deacetylase. *Hum. Mol. Genet.* **21**, 2688–2697 (2012).
33. Chan, D.C. Fusion and fission: interlinked processes critical for mitochondrial health. *Annu. Rev. Genet.* **46**, 265–287 (2012).
34. Sedlak, T.L., Chandavimol, M. & Straatman, L. Cardiac transplantation: a temporary solution for Friedreich's ataxia–induced dilated cardiomyopathy. *J. Heart Lung Transplant.* **23**, 1304–1306 (2004).

ONLINE METHODS

Adeno-associated viral vector construction and production. A human frataxin (hFXN) cDNA, including the mitochondrial targeting sequence, was fused to a hemagglutinin (HA) tag and was subcloned into a pAAV2-CAG plasmid[35] to produce pAAV2-CAG-hFXN, which included the viral inverted terminal repeat (ITR) from AAV2 and the cytomegalovirus/β-actin hybrid promoter (consisting of the enhancer from the cytomegalovirus immediate-early gene, the promoter, splice donor and intron from the chicken β-actin gene, and the splice acceptor from the rabbit β-globin gene). The AAVrh10.CAG-hFXN-HA vector was produced as previously described[36] in the Vector Core at the University Hospital of Nantes (http://www.vectors.nantes.inserm.fr). The final titers of the two batches used were 5.4×10^{12} vg ml^{-1} and 2.15×10^{13} vg ml^{-1}, respectively.

Animal procedures. Mice with a deletion of *Fxn* gene in cardiac and skeletal muscle (*Mck-Cre-Fxn*$^{L3/L-}$) (*Mck* mice) in a 100% C57BL/6J background were generated and genotyped as previously described[15]. Mice were maintained in a temperature- and humidity-controlled animal facility, with a 12-h light-dark cycle and free access to water and a standard rodent chow (D03, SAFE, Villemoisson-sur-Orge, France). Both male and female mice were used in all experiments. All animal procedures and experiments were approved by the local ethical committee (Comité d'Ethique en Expérimentation Animale IGBMC-ICS) for Animal Care and Use (Com'Eth 2011-007), and were performed in accordance with the Guide for the Care and Use of Laboratory Animals (US National Institutes of Health). For biodistribution studies, 3-week-old C57BL/6J wild-type mice were anesthetized by intraperitoneal injection of ketamine-xylazine (75 and 10 mg per kg body weight, respectively) to allow intravenous administration by retro-orbital injection of AAVrh10.CAG-FXN at a dose of 5.4×10^{13} vg kg^{-1}, and killed at 7 weeks of age (4 weeks after injection). For gene therapy studies, 3- or 7-week-old *Mck* mice were anesthetized by intraperitoneal injection of ketamine-xylazine (75 and 10 mg per kg body weight, respectively, in 3-week-old mice or 60 and 8 mg per kg body weight, respectively, in 7-week-old mice) to allow intravenous administration by retro-orbital injection of AAVrh10.CAG-FXN at a dose of 5.4×10^{13} vg kg^{-1} (from 35 to 90 µl depending on the vector concentration and the weight of the mouse). Schemes of the experimental strategy for the gene therapy studies are depicted in **Supplementary Figures 2a** and **4a**. Untreated *Mck* mice and WT littermates were injected with equivalent volumes of saline solution. Survival was evaluated daily, and mouse weight was evaluated weekly. Mouse cardiac function was evaluated under isoflurane anesthesia (1–2%) by echocardiography by an experimenter blinded to genotype and treatment regimen, as previously described[16]. Animals were killed by CO_2 inhalation at 8, 15, 22 or 35 weeks, and tissues samples for biochemical and molecular analyses were immediately frozen in liquid nitrogen. For histological analysis, mice were anesthetized by intraperitoneal injection of ketamine-xylazine and perfused with cooled saline solution. Liver and cardiac tissue were embedded in OCT Tissue Tek (Sakura Finetechnical, Torrance, California) and snap-frozen in isopentane chilled in liquid nitrogen. Samples of skeletal muscles were directly snap-frozen in isopentane chilled in liquid nitrogen. For electron microscopy analysis, small samples from the middle of the left ventricle and its apex were collected and then fixed and embedded in Epon as previously described[15].

Histopathology, enzyme histochemistry and electron microscopy. For histochemical analysis, 10-µm cryosections were stained either with H&E, Sirius red and fast green to label extracellular collagen or with DAB-enhanced Perls to label iron (Fe^{3+}) deposits[15].

Sirius red and fast green staining. Tissue sections were fixed with 10% paraformaldehyde in 0.1 M phosphate buffer (PBS), pH 7.4, for 10 min and then incubated with a saturated solution of picric acid containing 0.1% Direct red 80 (Sigma) for 2 min, washed with 0.5% glacial acetic acid solution followed by deionized water, subsequently incubated in 0.05% fast green solution for 5 min and then washed with 0.5% glacial acetic acid solution. Finally, sections were dehydrated in graded alcohols, cleared in Histosol Plus (Shandom) for 5 min and mounted using Pertex mounting medium (Histolab Products AB).

DAB-enhanced Perls iron staining. Tissue sections were fixed with 10% paraformaldehyde in 0.1 M phosphate buffer (PBS), pH 7.4, for 20 min and incubated in Perls solution (1% HCl, 1% potassium ferrocyanide) for 30 min. Staining was enhanced by incubation in a solution of 0.025% 3′-3′-diaminobenzidine tetrahydrochloride (Sigma-Aldrich) and 0.005% H_2O_2 in PBS buffer for 30 min, and then developed in the same buffer. Finally, sections were dehydrated in graded alcohols, cleared in Histosol Plus (Shandom) for 5 min and mounted using Pertex mounting medium (Histolab Products AB).

Enzyme histochemical analyses. Succinate dehydrogenase (SDH) and cytochrome *c* oxidase (COX) activities were determined on 10-µm cryostat sections of tissues, as previously described[15].

Electron microscopy analysis. Ultrathin sections (70 nm) of cardiac tissue were contrasted with uranyl acetate and lead citrate and examined with a Morgagni 268D electron microscope, as described previously[15].

Immunofluorescence and image acquisition. Cardiac and spinal cord tissue cryosections were fixed in 4% PFA for 10 min, washed and then permeabilized in methanol at −20 °C for 20 min. Sections were blocked and permeabilized at the same time with PBS containing 1% NGS, 5% BSA and 0.3% Triton X-100 for 1 h at room temperature (RT) and then washed in PBS containing 0.2% Tween, 1% BSA and 1% NGS (PBS-TBN). Subsequently, tissues were incubated overnight (O/N) at 4 °C with a rabbit polyclonal antibody against frataxin (FXN935) (1:250) (produced by the IGBMC) diluted in PBS-TBN[15]. After washing, sections were incubated for 1 h and 30 min at RT with goat anti-rabbit antibody conjugated to Alexa Fluor 488 (Molecular Probes, AB28172) diluted at 1:500 in PBS-TBN. Sections were stained with Hoechst and mounted using Aqua-Polymount mounting medium (Polysciences). For co-immunolabeling of HA tag and prohibitin, tissue sections were washed in PBS containing 0.05% Tween and then blocked O/N at 4 °C in M.O.M. Mouse Ig Blocking Reagent (Vector Laboratories, PK-2200). Sections were then incubated O/N at 4 °C with a mouse monoclonal antibody to HA tag (1:150) (Covence, clone 16B12, MMS-101P) diluted in M.O.M. diluent (Vector Laboratories). After washing, sections were incubated for 1 h at RT with goat anti-mouse antibody conjugated to Alexa Fluor 594 (1:500) (Molecular Probes, A-11037) diluted in M.O.M. diluent. Subsequently, sections were washed and blocked in PBS containing 0.3% Triton and 2% NGS for 1 h 30 min at RT, washed and incubated for 2 h at RT with rabbit polyclonal antibody to prohibitin (1:150) (Abcam, AB28172) diluted in PBS-TBN. After washing, sections were incubated for 1 h and 30 min at RT with goat anti-rabbit antibody conjugated to Alexa Fluor 488 (Molecular Probes, AB28172) diluted at 1:500 in PBS-TBN. Sections were stained with Hoechst and mounted using Aqua-Polymount mounting medium (Polysciences).

Confocal analysis was performed on a Leica TCS SP2 upright confocal microsystem with a Plan Apo CS (numerical aperture 1.4) 63× objective. Observation of whole cardiac cryosections was performed on a Leica Z16 APO A microsystem fitted with a QuanteM-S12SC camera and combined with a 2× objective (39 mm working distance). Observation of whole-brain or spinal-cord cryosections was performed on a Hamamatsu NanoZoomer 2.0 slide scanner.

Quantitative real-time PCR. Total RNA was extracted from frozen heart pulverized with a Precellys24 homogenizer (Bertin Technologies) using Trizol reagent (MRC) according to the manufacturer's protocol and was treated with DNAse I (Roche Biosciences). cDNA was generated by reverse transcription using the Transcriptor first-strand cDNA synthesis kit (Roche Biosciences) for mRNA and the Miscript II reverse transcription kit (Qiagen) for miRNA. Quantitative RT-PCR was performed using the SYBR Green I Master mix (Roche Biosciences) for mRNA and the Miscript SYBR Green PCR kit (Qiagen) for miRNA and Light Cycler 480 (Roche Biosciences) with primers described in **Supplementary Table 8**. 18S ribosomal RNA and *Rnu6* were used as internal standards for mRNA and miRNA, respectively.

Enzyme activities. The activities of the respiratory chain enzyme SDH (complex II), the citric acid cycle enzyme isocitrate dehydrogenase and mitochondrial and cytosolic aconitases were determined as described[15,37].

Immunoblot analysis. Extracts of tissues were homogenized in lysis buffer containing Tris-HCl (280 mM, pH 6.8), 10% SDS and 50% glycerol. Total protein extract (50 µg or 10 µg) was analyzed on SDS-glycine polyacrylamide gels. For frataxin detection, 50 µg of total protein was loaded for

doi:10.1038/nm.3510

wild-type and untreated *Mck* mice and 10 μg for treated *Mck* mice. Proteins were transferred to nitrocellulose membranes, blocked with 5% nonfat milk and then incubated with the following primary antibodies: polyclonal antibody to frataxin (R1250, produced by IGBMC, 1:1,000), antibody to HA (Covance, MMS-101P, 1:500), antibody to mitochondrial aconitase (R2377, produced by IGBMC, 1:20,000), antibody to Ndufs3 (Invitrogen, 439200, 1:4,000), antibody to SDH (Invitrogen, 459230, 1:4,000), antibody to Rieske (MitoSciences, MS305, 1:5,000), antibody to lipoic acid (Calbiochem, 437695, 1:5,000), antibody to transferrin receptor (Zymed Laboratories, catalog number 13-6800, 1:2,000), antibody to GAPDH (Millipore, GAPDH MAB374,1:10,000), antibody to acetyl-lysine (Cell Signaling, 9441S, 1:1,000) and monoclonal antibody to β-tubulin (2A2, produced by IGBMC, 1:1,000). Secondary antibody (goat anti-rabbit IgG (Jackson ImmunoResearch, 115-035-146) or anti-mouse IgG (Jackson ImmunoResearch, 115-035-146 and 111-035-046, respectively) coupled to peroxidase was diluted at 1:5,000 and used for detection of the reaction with Supersignal Substrate western blotting (Pierce), according to the manufacturer's instructions. Quantification was performed using GeneSnap and GeneTools software (Syngene).

Statistical analyses. All data are presented as mean ± s.d. Statistical analysis was carried out using Statview software (SAS Institute). For statistical comparison of three experimental groups, one-way analysis of variance followed by Scheffé's *post hoc* test was used. A value of $P < 0.05$ was considered significant. For statistical comparison of two experimental groups, the bilateral Student's *t*-test was used. $P < 0.05$ was considered significant, except for echocardiography, where $P < 0.01$ was considered significant. No statistical method was used to predetermine sample size. The experiments were randomized. The investigators were not blinded to allocation during experiments and outcome assessment except for echocardiography, histological and electron microscopy experiments. The inclusion criteria were the appropriate genotype. Only one WT animal in asymptomatic experiments at 35 weeks of age and one treated *Mck* animal in symptomatic experiments at 22 weeks were excluded from the qRT-PCR experiments due to biologically incoherent results.

35. Sondhi, D. *et al.* Enhanced survival of the LINCL mouse following *CLN2* gene transfer using the rh.10 rhesus macaque-derived adeno-associated virus vector. *Mol. Ther.* **15**, 481–491 (2007).
36. Rabinowitz, J.E. *et al.* Cross-packaging of a single adeno-associated virus (AAV) type 2 vector genome into multiple AAV serotypes enables transduction with broad specificity. *J. Virol.* **76**, 791–801 (2002).
37. Martelli, A. *et al.* Clinical data and characterization of the liver conditional mouse model exclude neoplasia as a non-neurological manifestation associated with Friedreich's ataxia. *Dis. Model. Mech.* **5**, 860–869 (2012).

Molecular Therapy
Original Article

Rapid and Complete Reversal of Sensory Ataxia by Gene Therapy in a Novel Model of Friedreich Ataxia

Françoise Piguet,[1,2,3,4,5] Charline de Montigny,[1,2,3,4,5] Nadège Vaucamps,[1,2,3,4] Laurence Reutenauer,[1,2,3,4] Aurélie Eisenmann,[1,2,3,4] and Hélène Puccio[1,2,3,4]

[1]Institut de Génétique et de Biologie Moléculaire et Cellulaire (IGBMC), 67404 Illkirch, France; [2]Institut National de la Santé et de la Recherche Médicale, U1258, 67404 Illkirch, France; [3]Centre National de la Recherche Scientifique, UMR7104, 67404 Illkirch, France; [4]Université de Strasbourg, 67000 Strasbourg, France

Friedreich ataxia (FA) is a rare mitochondrial disease characterized by sensory and spinocerebellar ataxia, hypertrophic cardiomyopathy, and diabetes, for which there is no treatment. FA is caused by reduced levels of frataxin (FXN), an essential mitochondrial protein involved in the biosynthesis of iron-sulfur (Fe-S) clusters. Despite significant progress in recent years, to date, there are no good models to explore and test therapeutic approaches to stop or reverse the ganglionopathy and the sensory neuropathy associated to frataxin deficiency. Here, we report a new conditional mouse model with complete frataxin deletion in parvalbumin-positive cells that recapitulate the sensory ataxia and neuropathy associated to FA, albeit with a more rapid and severe course. Interestingly, although fully dysfunctional, proprioceptive neurons can survive for many weeks without frataxin. Furthermore, we demonstrate that post-symptomatic delivery of frataxin-expressing AAV allows for rapid and complete rescue of the sensory neuropathy associated with frataxin deficiency, thus establishing the pre-clinical proof of concept for the potential of gene therapy in treating FA neuropathy.

INTRODUCTION

Friedreich ataxia (FA), the most prevalent cause of recessive hereditary ataxia, is an early-onset neurodegenerative disease characterized by progressive spinocerebellar ataxia, severe proprioceptive sensory loss, cardiomyopathy, and increase in incidence of diabetes mellitus.[1,2] Both the CNS and the peripheral nervous system (PNS) are primarily affected. Proprioceptive sensory loss in the PNS is an early feature of the disease, while the cerebellar and spinocerebellar involvement contribute to the progression of the disease.[2] The neurological symptoms are a consequence of degeneration of the large sensory neurons of the dorsal root ganglia (DRGs) and their axons, of the spinocerebellar tracts,[2–4] as well as lesions in the dentate nuclei of the cerebellum and Purkinje cells.[3,5] In addition, more recent studies provide evidence of cerebral involvement.[6] FA is associated with a shortened lifespan, with cardiac dysfunction the main cause of mortality.[7] The disease is caused by a $(GAA)_n$ expansion within the first intron of the frataxin gene (*FXN*).[8] The mutation results in heterochromatin formation[9] leading to reduced expression of frataxin (FXN), a highly conserved mitochondrial protein, involved in iron-sulfur biogenesis.[10,11] To date, there is no efficient treatment for FA.

Replenishment of frataxin either through epigenetic drugs, protein replacement, or gene therapy would be the optimal therapy for FA. Previously, we established a proof of concept for a gene therapy approach using adeno-associated virus (AAV)-expressing frataxin (AAV-FXN) to prevent and rapidly reverse the cardiomyopathy associated with FA.[12] Our study clearly demonstrated that dysfunctioning frataxin-deficient cardiomyocytes were still viable after the onset of heart failure and that their phenotype could be reversed. However, one critical question in the field is whether the ganglionopathy and sensory peripheral neuropathy reflect irreversible cell death or whether it is a consequence of neuronal dysfunction that could potentially be reversible. To address this question and with the aim of developing a gene therapy approach to tackle the neuropathology associated with FA, we developed a new neuronal conditional model of the disease. Although several mouse models of FA have already been generated, none are suited for testing gene therapy approaches for the primary sensory ataxia associated with FA. Indeed, while the GAA expansion-based models (KIKO, YG8, and YG22 models) are good models to assess the epigenetics consequence of the GAA expansion and early pathophysiological consequences of frataxin deficiency, they failed to display a robust behavioral phenotype.[13–18] Other models have been generated based on the Cre-Lox technology to knockout frataxin in specific neuronal cells; however, these models are too severe and non-specific, such as the neuronal-specific enolase (NSE) model,[19] or develop a later onset pathology and have simultaneously DRG and cerebellar ataxia with severe granule cell

Received 8 March 2018; accepted 5 May 2018;
https://doi.org/10.1016/j.ymthe.2018.05.006.

[5]These authors contributed equally to this work.

Correspondence: Hélène Puccio, IGBMC, 1 rue Laurent Fries, 67404 Illkirch, France.
E-mail: hpuccio@igbmc.fr

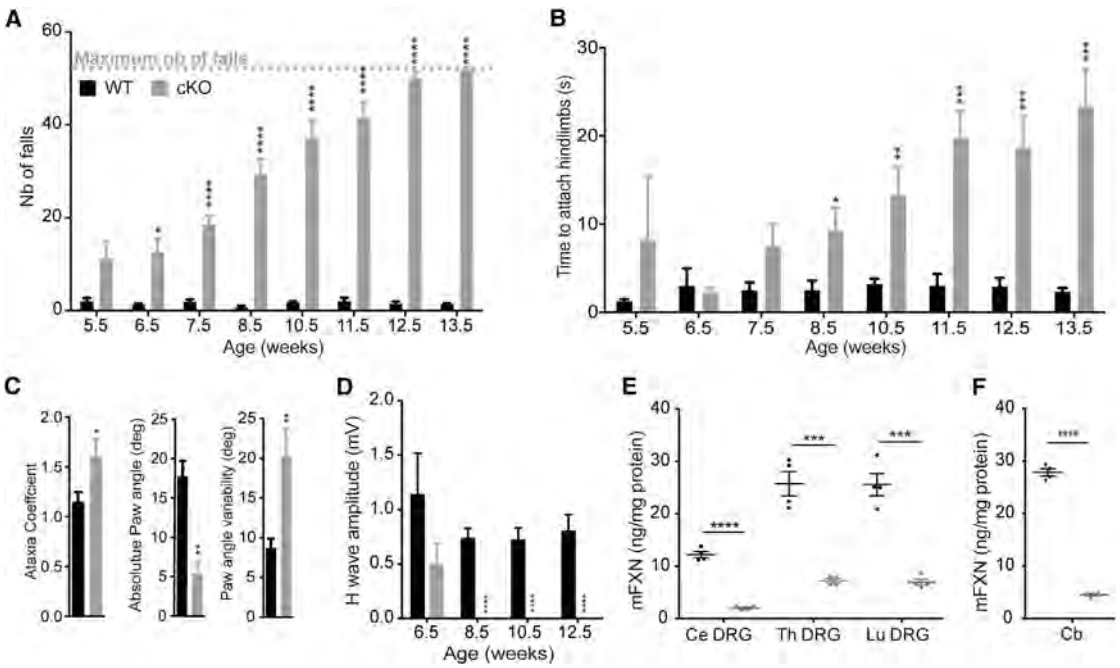

Figure 1. Impaired Behavior and Specific Loss of Sensory Wave in *Pvalb* cKO Mice Associated with Large Frataxin Depletion in DRG and Cerebellum

(A) Notched-bar test analysis, number of footfalls is represented; n = 10 WT and n = 11 *Pvalb* cKO. (B) Hanging-wire test analysis, time needed to attach hindlimbs to the string is represented; n = 10 WT and n = 11 *Pvalb* cKO. (C) Ataxia coefficient, measurement of absolute paw angle and paw angle variability after 5 s of walk on the DigitGait apparatus at 13.5 weeks of age; n = 6 WT and n = 5 *Pvalb* cKO. (D) Amplitudes of somatosensory wave (H-wave) were recorded after plantar sciatic nerve stimulation; n = 6 WT and n = 7 *Pvalb* cKO. (E and F) Mouse Frataxin expression levels evaluated by ELISA on cervical, thoracic, and lumbar DRG (E) and on cerebellum (F), in WT and *Pvalb* cKO mice at 7.5 weeks of age. n = 4. Data are represented as mean ± SEM. *p < 0.05; **p < 0.01; ***p < 0.001; ****p < 0.0001.

degeneration.[20] We thus generated a new conditional model using the $Pvalb^{tm1(Cre)Arbr/J}$ mouse line[21] to more specifically target the proprioceptive neurons. The $Pvalb^{tm1(Cre)Arbr/J}$ knockin allele has the endogenous parvalbumin promoter and enhancer elements directing Cre recombinase expression in cells expressing parvalbumin, such as proprioceptive afferent sensory neurons in the DRG, cerebellar Purkinje cell, and deep nuclei, as well as interneurons in the brain.[21]

The newly generated *Pvalb-Cre* conditional knockout (cKO) model recapitulated features of FA neuropathophysiology, in particular a ganglionopathy with sensory axonopathy, albeit with a more rapid and severe course of the disease. In addition, a cerebellar ataxia and cerebral involvement occur, but after the onset of the PNS pathology. Intravenous delivery of AAV-FXN fully prevented the onset of peripheral sensory neuropathy. Moreover, combined intravenous and intracerebral delivery AAV-FXN, after the onset of behavioral impairment, was able to reverse the phenotype of these mice at the behavioral, physiological, and cellular levels within a few days. Our results strongly demonstrate that frataxin-deficient proprioceptive neurons with severe phenotype survive for several weeks and can be rapidly and completely rescued by gene therapy in the mouse model. Thus, this study establishes the pre-clinical proof of concept for the potential of gene therapy in treating FA sensory neuropathy.

RESULTS

Pvalb cKO Mimics Neuropathophysiology Occurring in FA Patients

To induce frataxin deletion in parvalbumin-positive neurons (including the proprioceptive neurons of DRG, cerebellar deep nuclei, and Purkinje cells), we bred mice homozygous for the conditional frataxin allele ($Fxn^{L3/L3}$) with mice heterozygous for the frataxin allele carrying the *Pvalb-Cre* transgene ($Fxn^{+/L-}$; $Pvalb^{tm1(Cre)Arbr/J}$). Animals were born according to Mendelian ratio indicating no substantial embryonic lethality and displayed a normal growth until 21.5 weeks (Figure S1A). Loss of coordination in *Pvalb* cKO mice was evaluated weekly from 5.5 weeks until 13.5 weeks. *Pvalb* cKO mice developed a rapidly progressive movement disorder characterized by gait abnormality as early as 6.5 weeks of age on the notched-bar test (Figure 1A) and general coordination defects measured at 8.5 weeks of age on the wire-hanging test (Figure 1B) and on the rotarod (Figure S1B). The loss of coordination progressed over time, and *Pvalb* cKO mice showed a complete incapacity at the notched bar by 13.5 weeks of age (Figure 1A). Open field analysis did not reveal any change in general locomotor activity (Figures S1C and S1D). Digit gait analysis performed on a sub-cohort of mice at 13.5 weeks of age confirmed the ataxic gait in *Pvalb* cKO animals, with a significant increase in the ataxic coefficient, a decrease in absolute hindpaw angle, and an increase in paw angle variability (Figure 1C). On electromyographic measurements, motor-evoked

potential measurements in plantar muscle were normal (Figure S1E). In contrast, after somatosensory stimulation of the sciatic nerve, the H-wave response (sensorimotor reflex) was significantly affected at 8.5 weeks of age with a complete loss ($p < 0.0001$) (Figure 1D; Table S1), indicating that the large myelinated proprioceptive sensory neurons or their afferents are functionally defective. As a general observation, *Pvalb* cKO mice develop tremors after 8.5 weeks of age, worsening over time, and died prematurely around 21 weeks of age due to epileptic seizures. The expression of the Cre recombinase in the Purkinje cells at p40, as well as more widely throughout the cortex at 21.5 weeks, most likely contributes to the phenotype of the mice, in particular the tremors and the epileptic seizures (Figure S2; see Supplemental Results).

In agreement with the expression pattern of the *Pvalb-Cre* transgene, frataxin depletion was observed in the DRG, brain, cerebellum, and spinal cord by western blot (Figures S1F and S1G). By ELISA assay, a very strong reduction of frataxin (72%–83% reduction) was seen in the DRG of the *Pvalb* cKO compared to control (Figure 1E; Table S2), despite the fact that the proprioceptive neurons (i.e., the ones expressing the Cre recombinase) represent only 7.5% of the total cells of the DRG.[22,23] Considering that the *Pvalb* cKO are constitutive heterozygotes for the frataxin locus ($Fxn^{L3/L-}$), this demonstrates that proprioceptive neurons express 44%–66% of the total frataxin of the DRG (Table S3; Supplemental Results). Interestingly, lumbar DRG express twice as much frataxin than the cervical DRG (Figure 1E), while no clear differences was observed in different sections of the spinal cord (Figure S1G). Similarly, in the cerebellum, the Purkinje cell and the deep gray nuclei express 67% of the total frataxin expression of the cerebellum (Figure 1F; Table S3).

To determine the pathological changes associated with frataxin deficiency, histological analysis was performed on both DRG and cerebellum. The main pathological feature in the DRG was the presence of vacuoles in ~1.5% of neurons at 7.5 weeks in *Pvalb* cKO ($p = 0.0429$) (Figure 2A). No neuronal loss in the DRG was observed at 7.5 weeks of age (Figure 2B), demonstrating that the loss of somatosensory response is not a consequence of neuronal loss. At 10.5 weeks of age, although not statistically significant, a trend of 10%–15% neuronal loss in the lumbar level was observed, a tendency not further exacerbated with time (Figure 2B). Neurofilament 200 staining, a marker of proprioceptive and mechanoreceptive neurons, shows a reduction of ~30% of large myelinated neurons at 21.5 weeks in *Pvalb* cKO (Figures S3A and S3B). No neuronal loss in the cervical or thoracic DRG was observed at any time despite frataxin deletion demonstrating some specificity toward lumbar DRG (Figure S3C). In the cerebellum, abnormal localization and loss of Purkinje cells was also observed starting at 10.5 weeks of age (Figures 2C and 2D).

To further determine the pathological changes associated with the specific loss of sensory wave, ultrastructural analysis was performed on both DRG and the sciatic nerve, a mixed sensory and motor nerve. Ultrastructural analysis of DRG neurons presenting vacuoles at 7.5 weeks of age (Figure 2A, arrows) revealed signs of mitochondrial and cell degeneration. Typical features of different stages of mitophagy were observed: mitochondria starting to degenerate (Figure 2E, arrows 1), large vacuoles with membrane invagination and cytoplasmic material inside (Figure 2E, arrows 2), complete degeneration of the cell with endoplasmic reticulum (ER) dilation (Figure 2E, arrows 3). At 3.5 weeks of age, sciatic nerves of *Pvalb* cKO already displayed signs of neuropathy with degeneration affecting small caliber myelinated fibers and inner swelling tongue (Figure 2F). Such abnormalities became more frequent and severe with age. At 5.5 weeks, degenerating mitochondria were noted (Figure 2F), while by 17.5 weeks of age, clear signs of axonal loss as well as axonal shrinkage were observed, with the frequent presence of myelin debris (Figure 2F). In agreement with the lack of pathology in the thoracic and cervical DRG, analysis of radial and median nerve at 18.5 weeks did not show any abnormalities (Figure S3D).

The molecular events following frataxin depletion are iron-sulfur (Fe-S) cluster protein deficits and cellular iron dysregulation.[19,24] We initially measured SDH activity on lumbar DRG and cerebellum protein lysates by spectrophotometry; however, no difference between wild-type (WT) and *Pvalb* KO was observed (Figures S4A and S4B). Similarly, western blot analysis of the lipoic acid bound to pyruvate dehydrogenase (PDH) and α-ketoglutarate dehydrogenase (KGDH) complexes did not reveal any differences, suggesting that the Fe_4S_4-dependent lipoic acid synthase was not affected (Figures S4C and S4D). However, we hypothesized that the absence of detectable Fe-S cluster protein deficit in whole lysate of DRG and cerebellum might be a consequence of signal dilution, as proprioceptive neurons represent only 7.5% of the total cells of the DRG and Purkinje cell represents a minority of cerebellar cells (1 Purkinje cell for 778 granule neurons[25]). SDH activity was determined by histoenzymatic staining on cryostat sections of lumbar DRG and cerebellum (Figures 3A–3C). In lumbar DRG sections of *Pvalb* cKO animals, large SDH-negative neurons were observed at 8.5 weeks of age (Figure 3A, zoom). Quantification of SDH staining in DRG demonstrated a significant increase in the number of negative SDH neurons in *Pvalb* cKO animals compared to WT as early as 5.5 weeks of age (Figures 1B and S4E). Similarly, in the cerebellum, faint SDH staining was observed in *Pvalb* cKO Purkinje cells compared to control animals at 13.5 weeks of age (Figure 3C). At 18.5 weeks, Purkinje cells of Pvalb cKO animals were either SDH negative or were absent (Figure 3C), in coherence with the partial loss of Purkinje cells. We aimed at demonstrating that the SDH-negative neurons were frataxin deficient; however, due to the low levels of frataxin in DRG and cerebellum (i.e., ~30 ng FXN per mg of protein compared to ~150 ng FXN per mg of protein in the heart), we could not detect frataxin by immunohistochemistry with the available anti-frataxin antibodies. In non-neuronal FA mouse models, Fe-S cluster deficiency leads to IRP1 activation as a translational regulator leading to iron metabolism dysregulation.[19,26] In contrast with the clear iron accumulation observed in cardiomyocytes deficient for frataxin (MCK mutants; Figure S4F),[19] cerebellar Purkinje cells were negative for Perl's-enhanced iron staining at 13.5 weeks of age in *Pvalb* cKO (Figure S4G). However, upregulation of Transferrin receptor 1 (TfR1)

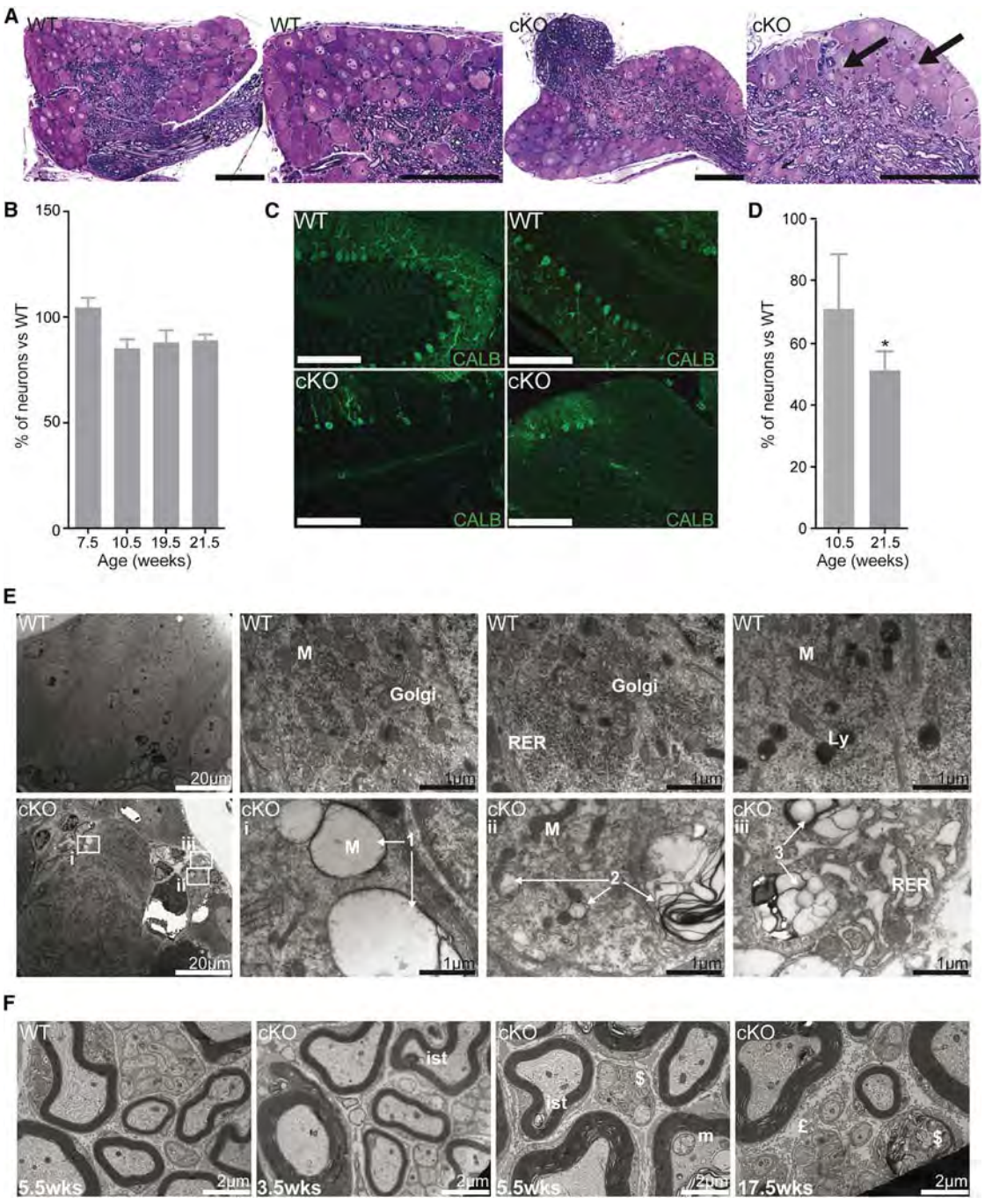

Figure 2. Neurodegeneration and Neuropathy in *Pvalb* cKO Mice

(A) Semithin sections of lumbar DRG at 7.5 weeks with arrows indicating vacuoles. n = 7,000 neurons scored. Scale bars, 100 µm. (B) Mean number of neurons per DRG normalized by DRG area in the lumbar section of the spinal cord. n = 3 or 4 mice and between 6,000 and 10,000 neurons scored per group and per age. (C) Calbindin staining on cerebellar section of control and *Pvalb* cKO mice at 21.5 weeks. Scale bars, 100 µm. (D) Purkinje cell loss in *Pvalb* cKO mice at 10.5 and 21.5 weeks assessed by scoring of Calbindin-positive cells. n = 4 mice and between 1,800 and 2,500 neurons scored per group and per age. (E) Ultrathin sections of lumbar DRG of WT and *Pvalb* cKO at 7.5 weeks with sign of cell death progression in large neurons with empty giant mitochondria (arrows 1), vacuoles (arrows 2) and with membrane invagination ending in a complete cell degeneration with dilated endoplasmic reticulum and larges vacuoles (arrows 3). M, mitochondria; Ly, lysosome; RER, rough endoplasmic reticulum. Scale bars, indicated sizes. (F) Ultrathin sections of sciatic nerves of WT and *Pvalb* cKO at 3.5, 5.5, and 17.5 weeks. ist, inner swelling tongue; £, fibrosis; m, abnormal mitochondria; $, degeneration. Scale bars, 2 µm. Data are represented as mean ± SEM. *p < 0.05.

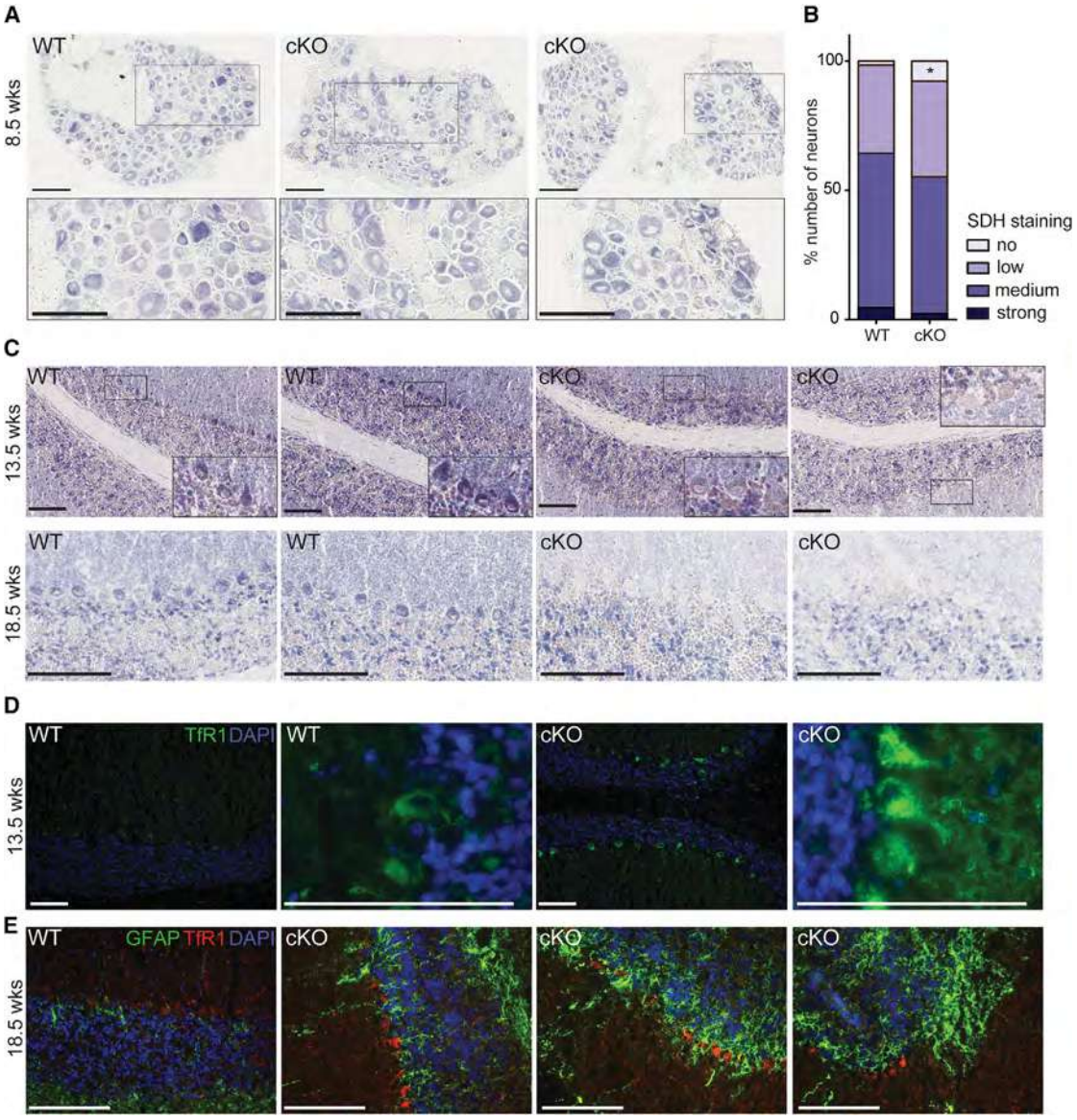

Figure 3. Fe-S Cluster Protein Deficit and Cellular Iron Metabolism Dysregulation in Some Neurons of *Pvalb* cKO Mice

(A) Representative SDH histoenzymatic activity staining in lumbar DRGs at 8.5 weeks of age WT and *Pvalb* cKO mice. Scale bars, 100 μm. (B) Scoring SDH staining intensity in lumbar DRG neurons at 5.5 weeks of age; n = 8,732 neurons counted from three WT animals and n = 11,019 neurons counted from four *Pvalb* cKO animals. *$p < 0.05$. (C) Representative SDH histoenzymatic activity staining in cerebellum at 13.5 and 18.5 weeks of age WT and *Pvalb* cKO mice with magnifications on Purkinje cells. Scale bars, 100 μm. (D) Representative images of TfR1 immunofluorescence (green) in cerebellum of WT and *Pvalb* cKO animals at 13.5 weeks of age. Scale bars, 100 μm. (E) Representative images of TfR1 (red) and GFAP (green) co-immunofluorescence in cerebellum of WT and *Pvalb* cKO animals at 18.5 weeks of age. Scale bars, 100 μm.

levels was detected in Purkinje cells in *Pvalb* cKO both at 13.5 and 18.5 weeks of age (Figures 3D and 3E), which could be a direct consequence of IRP1 activation in its iron response element (IRE) regulatory form.[26] Interestingly, the astrocyte marker GFAP signal was increased not only in the granular layer, but more particularly in the Purkinje cells and molecular layer in *Pvalb* cKO compare to controls (Figure 3E). The increase in GFAP is most likely a direct reflection of active astrogliosis coupled to Purkinje cell death.[27] All together, these results demonstrate that frataxin deficiency in neurons leads to an Fe-S cluster protein deficit and cellular iron dysregulation leading to cellular dysfunction and death.

Prevention of Progressive Loss of Sensory Defects after Treatment of Early-Symptomatic Pvalb cKO Mice

To investigate the potential of gene therapy for the treatment of the FA sensory ataxia and neuropathy, a single intravenous injection of AAV9-CAG-FXN-HA at a dose of 5×10^{13} vector genomes (vg)/kg was performed in 3.5-week-old early-symptomatic *Pvalb* cKO mice.

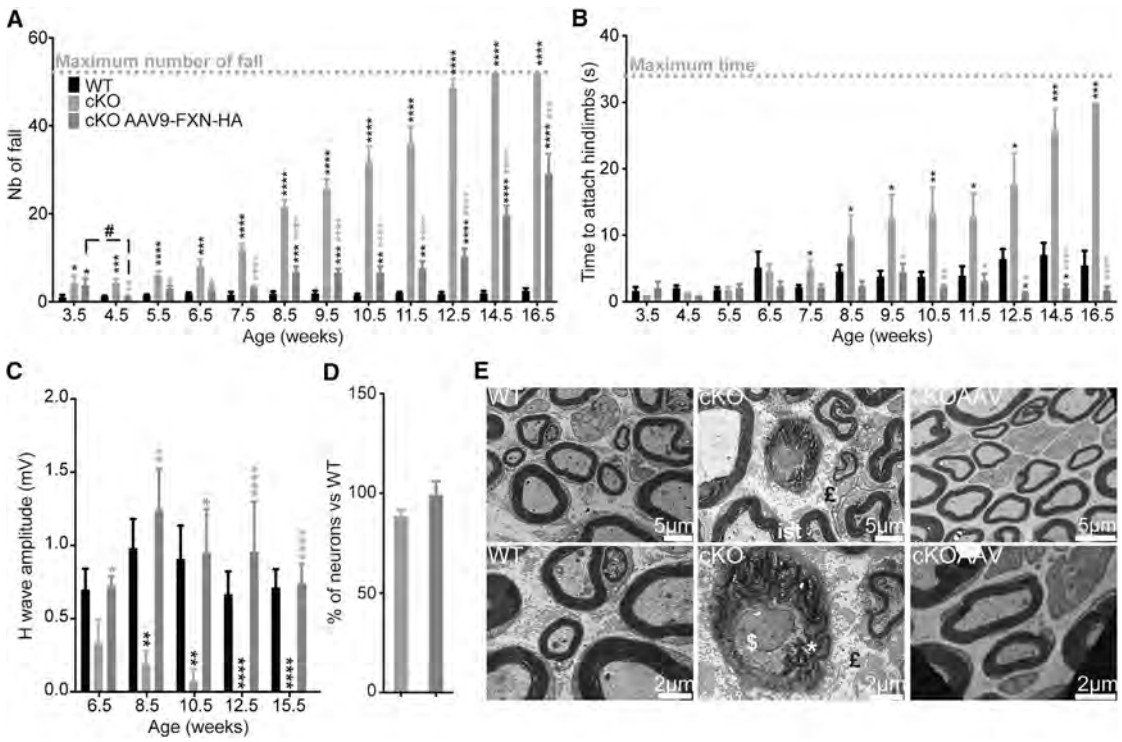

Figure 4. Evaluation of Early Symptomatic Treatment in *Pvalb* cKO Animals

(A) Notched-bar test analysis, number of footfalls is represented; n = 11 WT, n = 9 *Pvalb* cKO, and n = 9 *Pvalb* cKOAAV. (B) Hanging-wire test analysis, time needed to attach hindlimbs to the string is represented; n = 11 WT, n = 9 *Pvalb* cKO, and n = 9 *Pvalb* cKOAAV. (C) Amplitude of sensory wave (H-wave) was recorded after plantar sciatic nerve stimulation. n = 11 WT, n = 9 *Pvalb* cKO, and n = 9 *Pvalb* cKOAAV. (D) Mean number of neuron per DRG of WT and *Pvalb* (untreated and treated) was evaluated at the lumbar level of the spinal cord. n = 3 mice per group with n = 9,314 WT, n = 7,666 *Pvalb* cKO, and n = 7,610 *Pvalb* cKOAAV neurons scored. (E) Ultrathin sections of sciatic nerves of Pvalb treated at 17.5 weeks. ist, inner swelling tongue; £, fibrosis; *, myelin debris; $, degeneration. Scale bars, indicated sizes. Data are represented as mean ± SEM. *p < 0.05; **p < 0.01; ***p < 0.001; ****p < 0.0001. Black stars correspond to p value versus WT and gray stars versus untreated Pvalb cKO.

A significant coordination improvement in treated compared to untreated *Pvalb* cKO mice was observed in all tests performed (Figures 4A, 4B, and S5A). While, 1 week after treatment, a significant improvement of coordination on the notched-bar test was observed, the treated mice's performance progressively worsened starting at 8.5 weeks of age, although never to the level of untreated animals (Figure 4A). In contrast, treated *Pvalb* cKO mice remained undistinguishable from WT controls until euthanasia on the wire-hanging test (Figure 4B), showing a clear benefit on the peripheral sensory neuropathy. Consistent with the behavioral analysis, the defect in the sensorimotor reflex after sciatic nerve stimulation was completely prevented in treated *Pvalb* cKO mice (Figure 4C; Table S4).

Due to significant tremors, animals were sacrificed at 17.5 weeks of age. Biodistribution study of the AAV9-CAG-human frataxin (hFXN)-HA vector revealed a high transduction of the liver, a moderate transduction of the heart and brain, a milder transduction of the DRG, and a poor transduction of the spinal cord and cerebellum (Figure S5B). The transgenic human frataxin expression was 22 times the endogenous level in WT animals in the DRG (thoracic portion) (697 ng hFXN/mg protein) (Figure S5C). Western blot analysis showed that the majority of the transgenic human frataxin is matured and the absence of precursor accumulation (Figure S5D), as previously published.[12] Histologically, the trend in neuronal loss previously observed in *Pvalb* cKO in lumbar DRG was absent in the treated animal (Figure 4D). Furthermore, ultrastructural analysis of sciatic nerve showed no signs of degeneration, axonal loss, autophagy, or abnormal mitochondria in treated *Pvalb* cKO mice (Figure 4E), in agreement with the presence of normal somatosensory response.

AAV-hFXN Delivery Rapidly Rescues Sensory Ataxia in Late Symptomatic Pvalb Mice

While preventing the sensory ataxia is an important step, it is crucial to determine the therapeutic potential after the onset of the symptoms. Intravenous administration of AAV9-CAG-FXN-HA at a dose of 5×10^{13} vg/kg simultaneously with intracerebral deliveries of AAVrh.10-CAG-FXN-HA (1×10^{10} vg/deposit) in the striatum and the cerebellar white matter to target the CNS was performed post-symptomatically at 7.5 weeks of age. A complete correction of the peripheral fine coordination measured by the wire-hanging test was observed 1 week after treatment, which sustains overtime up to euthanasia (Figure 5A). On the notched-bar test, treated *Pvalb* cKO mice show a clear stabilization of the phenotype until 9.5 weeks of age then developed a progressive worsening of the phenotype

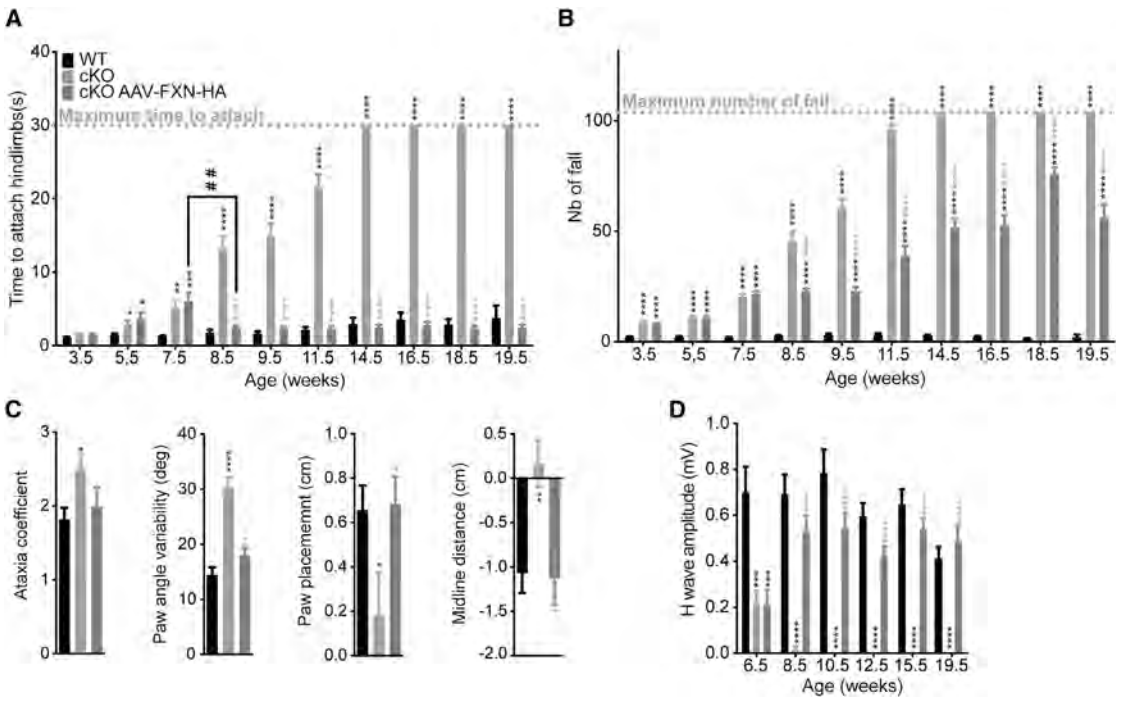

Figure 5. Rapid Correction of Neurological Phenotype after Post-symptomatic Treatment of *Pvalb* cKO Animals

(A) Hanging-wire test analysis, time needed to attach hindlimbs to the string is represented; n = 26 WT, n = 29 *Pvalb* cKO, and n = 32 *Pvalb* cKOAAV. (B) Notched-bar test analysis, number of footfalls is represented; n = 26 WT, n = 29 *Pvalb* cKO, and n = 32 *Pvalb* cKOAAV. (C) Ataxia coefficient, paw angle variability, paw placement, and midline distance measured after 2.5 s of walk on the DigitGait apparatus at 17.5 weeks of age; n = 8 WT, n = 6 *Pvalb* cKO, and n = 8 *Pvalb* cKOAAV. (D) Amplitude of sensory wave (H-wave) was recorded after plantar sciatic nerve stimulation; n = 26 WT, n = 29 *Pvalb* cKO, and n = 32 *Pvalb* cKOAAV. Data are represented as mean ± SEM. *p < 0.05; **p < 0.01; ***p < 0.001; ****p < 0.0001. Black stars correspond to p value versus WT and gray stars versus untreated Pvalb cKO.

(Figure 5B), as it was also observed on the rotarod (Figure S6A). Evaluation of the gait at 17.5 weeks of age by DigitGait analysis showed a complete correction of several parameters in the treated *Pvalb* cKO animals, including the ataxic coefficient, the paw angle variability, the paw placement, and the midline distance (Figure 5C). Concomitantly with the improvement of coordination and the ataxic phenotype, *Pvalb* cKO mice displayed a complete reversion of sensorimotor reflexes (Figure 5D; Table S5), with H-wave amplitudes within the normal range. Due to significant tremors, to avoid losing the animals of epileptic seizures and for ethical reasons, most animals were sacrificed at 18.5 weeks of age for histological and molecular analyses, with a few animals kept until 22.5 weeks for ultrastructural analysis.

Biodistribution study of the AAV-CAG-hFXN-HA vectors (both AAV9 and AAVrh10) reveals a high transduction of brain (cortex, cerebellum), a moderate transduction of brainstem in accordance with the intraparenchymal delivery of AAVrh.10, a milder transduction of the DRG, and quite poor transduction of the spinal cord (Figure S6B). Compared to what has been shown in pre-symptomatic treatment, DRG transduction is milder, in accordance with tropism and different transduction, depending on the age of delivery.[28] In agreement with the biodistribution of the vector, a widespread expression of hFXN-HA in the brain surrounding the injection site, especially in Purkinje cells and in striatum as well as in DRG neurons, was observed in the treated animals (Figures 6A–6D and S6C). Transgenic hFXN concentration was quantified by ELISA at 39.9 ng hFXN/mg protein in the DRG, corresponding to ~1.5 times the endogenous level, and at 176.3 ng hFXN/mg protein in the cerebellum, corresponding to 6 times the endogenous level (Figure S6D).

At 8.5 weeks of age, 1 week after treatment, the number of SDH-negative neurons in the DRG of treated *Pvalb* cKO animals did not differ from that of untreated animals (Figure 6E), despite the clear functional rescue at the physiological level. However, the trend in neuronal loss previously observed in lumbar DRG was absent in the treated animal, suggesting a protection against neuron loss at 18.5 weeks (Figure 6F). Moreover, ultrastructural analysis of the sciatic nerve of treated *Pvalb* mice at 22.5 weeks of age revealed a complete normal morphology with the absence of degeneration, axonal loss, autophagy, and abnormal mitochondria (Figure 6G), suggesting a complete regeneration of the sensory axonopathy. Interestingly, 1 week post-treatment, a clear process of regeneration (clearance of myelin debris, axon regrowth, and remyelination) was observed in treated animals (Figure S7A) with the nerve structure almost completely normal 2 weeks post-treatment (Figure S7B). All together, these results demonstrate a rapid and complete correction of the sensory neuropathy associated with frataxin deficiency by intravenous treatment using AAV9.

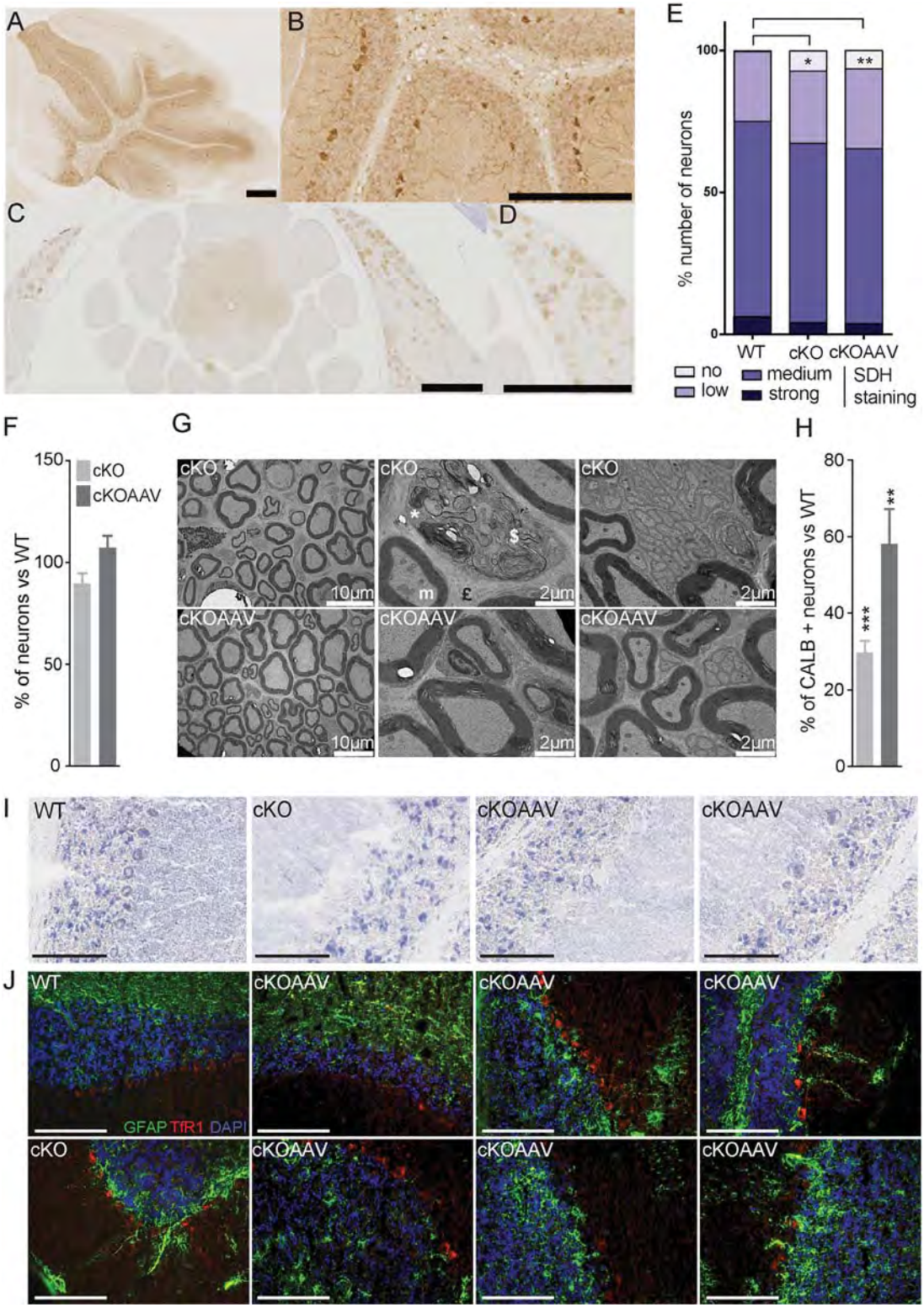

(legend on next page)

At 18.5 weeks, a significant prevention of Purkinje cell loss in the cerebellum occurred in treated animals (Figure 6H), although this was lobule dependent (Figure S6E), probably reflecting the non-homogeneous biodistribution of the vector (Figure S6C). A partial rescue of SDH-positive Purkinje cell was observed at 18.5 weeks in the treated animals (Figure 6I). Indeed, while in the cerebellum of untreated *Pvalb* cKO, few surviving Purkinje cells could be observed (all SDH negative); in treated animals, while the Purkinje cells appeared to be mostly preserved, the SDH staining varied from dark staining similar to the Purkinje cell of WT animals to SDH-negative staining, suggesting only a partial rescue. Similarly, the TfR1 and GFAP upregulation were partially corrected in treated animals, with some Purkinje cells presenting TfR1 and GFAP expression similar to WT Purkinje cells while other Purkinje cells (although less common) show various intermediate profiles of TfR1 and GFAP overexpression (Figure 6J). This is in agreement with the non-homogeneous biodistribution of the vector in the cerebellum.

DISCUSSION

Here, we report the generation of a new conditional mouse model for the ganglionopathy and sensory neuropathy associated with frataxin deficiency followed by the proof of concept of a gene therapy approach for the neuronal symptoms of FA. The new *Pvalb* cKO model developed a progressive loss of coordination and gait abnormalities, with a specific early onset of sensory defects followed by a cerebellar ataxia.

Through the characterization of this new model, several important findings were uncovered that might be of particular interest regarding the neuropathophysiology and cellular specificity in FA. One question that is still left unanswered in the field is the tissue specificity of the disease, and in particular why the large proprioceptive neurons are early and specifically affected compared to other neuronal populations, such as the nociceptive or mechanoreceptor neurons, for example. Quantitative measurements of frataxin by ELISA demonstrated not only more expression of frataxin in lumbar and thoracic DRGs than cervical DRGs, but more interestingly that proprioceptive neurons express 44%–66% of total frataxin protein of the DRGs, despite representing only 7.5% of total cell. Why would proprioceptive neurons express such high levels of frataxin compared to other cell types in the DRG is not known, but this may account partially for their higher vulnerability and premature loss in FA.[29] While it is technically impossible to measure sensorimotor reflexes in upper limbs due to the short length of the paw in mice, no signs of degeneration nor neuronal loss could be found in the radial or median nerve nor in thoracic and cervical DRG despite depletion of frataxin expression, suggesting that as in patients, the phenotype proceeds from lumbar to cervical region.[29] However, as the model exhibits premature death at 20 weeks due to epileptic seizures most likely as a consequence of frataxin depletion in cortical interneurons, it is not known whether degeneration of cervical DRG could occur with aging of the mice. Importantly, we showed that sensorimotor dysfunction by electrophysiology was an early event in the disease. While this is difficult to translate into human, the mouse model demonstrates that proprioceptive neurons completely deficient for frataxin can survive at least 7.5 weeks (as deletion occur around E17.5) and probably even more than 10 weeks of age, despite being dysfunctional early after frataxin deficiency. Considering that Schwann cells are not depleted for frataxin in the current model, our results demonstrate that proprioceptive neuronal dysfunction and pathology can occur in a cell-autonomous manner. However, it is likely that Schwann cells participate in the pathology in human, as low frataxin occurs in all tissues. Interestingly frataxin-deficient Purkinje cells in the cerebellum survive less time than frataxin-deficient proprioceptive neurons in DRG. While the reason for this difference is not known, the fact that the peripheral nervous system is regeneration competent might explain the better resistance of proprioceptive neurons to cell death. This resistance of proprioceptive neurons is a crucial point for therapeutical approaches for the sensory neuropathy, as most patients present a severe loss of proprioception at the time of the diagnosis, and the presence of proprioceptive neurons is not known. Finally, frataxin depletion in neurons, as in cardiac tissues, leads to an Fe-S cluster protein deficit, a secondary iron dysmetabolism, and mitochondrial defects before loss of cell. Whether iron accumulates in the nervous system is still under debate in the field, and recently iron accumulation was detected in cortical neurons of CRISPR-Cas9 frataxin-deficient mice.[30] In the present model, we did not detect any iron accumulation, probably because of the time course of the events. Indeed, iron accumulation in the CNS was shown to be a late event following frataxin deficiency.[30] Therefore, although the iron importer TfR1 is increased in the frataxin-deficient Purkinje cell, the neurons are lost most likely prior to sufficient iron accumulation to be detected by 3,3′-diaminobenzidine (DAB)-enhanced Perl's. In conclusion, the *Pvalb* cKO animals mimic several features of FA patients even if more severe on certain aspects and with a non-specific cerebral component due to full

Figure 6. Molecular and Histological Improvements after Post-symptomatic Treatment

(A–D) Representative images of FXN-HA expression in DRG and spinal cord (A and B) and cerebellum (C and D) of AAV-treated animals at 18.5 weeks. Scale bar, 100 μm. (E) Scoring of lumbar DRG neurons depending on the SDH staining intensity at 8.5 weeks of age; n = 6,574 neurons counted from two WT animals, n = 5,971 neurons counted from three *Pvalb* cKO animals, and n = 5,239 neurons counted from three *Pvalb* cKOAAV animals. (F) Mean number of neuron per DRG of WT and *Pvalb* cKO (untreated and treated) was evaluated at the lumbar level of the spinal cord; n = 6 mice with n = 13,375 WT, n = 11,581 *Pvalb* cKO, and n = 16,891 *Pvalb* cKOAAV neurons scored. (G) Ultrathin sections of sciatic nerves of 22.5-week *Pvalb* cKOAAV mice. £, fibrosis; m, abnormal mitochondria; *, myelin debris; $, degeneration. Scale bars, indicated sizes. (H) Mean number of Purkinje cell number in total in the cerebellum of WT and *Pvalb* cKO-treated and -untreated mice; n = 6 mice per group. (I) Representative SDH histoenzymatic staining of WT, untreated and treated *Pvalb* cKO animals in cerebellum at 18.5 weeks of age. Scale bars, 100 μm. (J) Representative images of TfR1 (red) and GFAP (green) co-immunofluorescence in cerebellum of WT, untreated, and treated *Pvalb* cKO animals at 18.5 weeks of age. Scale bars, 100 μm. Data are represented as mean ± SEM. *$p < 0.05$; **$p < 0.01$; ***$p < 0.001$. Black stars correspond to p value versus WT.

frataxin deficiency in cortical interneurons. In contrast to previously described models,[18] this new model has the advantage of having a specific proprioceptive phenotype from birth until 8 weeks of age and then develops a cerebellar ataxia with loss of frataxin in Purkinje cell and deep cerebellar nuclei.

Furthermore, our results demonstrate the capacity of intravenous AAV-hFXN delivery at a late symptomatic stage to rapidly and completely rescue the sensory neuropathy associated with frataxin deficiency. Importantly, our results suggest that dysfunctional frataxin-deficient proprioceptive neurons are in majority still alive for several weeks despite their severely affected nerve structure, and their phenotype can be completely reversed, demonstrating high plasticity. Furthermore, the rapidity of the rescue (1 week after treatment) demonstrates that little frataxin is needed to permit the neurons to regenerate and fully recover their nerve structure. This is in contrast to the recently published results from the doxycycling-inducible systemic knockdown of frataxin, which show only partial correction of the ganglionopathy and a mild improvement of axonal neuropathy after 8 weeks of frataxin rescue.[31] In addition, through intraparenchymal AAVrh10-hFXN delivery, we demonstrate a partial rescue and prevention of Purkinje cell loss. The partial rescue is mainly due to the limited diffusion of the virus and the consecutive transduction of Purkinje cells, which correlates with the correction of SDH activity as well as TfR1 and GFAP dysregulation. The absence of full transduction of the Purkinje cells as well the cortical interneurons is most likely responsible for the tremors and epileptic attacks in the treated *Pvalb* cKO.

In conclusion, our results demonstrate the strong potential of AAV delivery to restore frataxin expression in DRG and rescue the ganglionopathy and sensory neuropathy associated to frataxin deficiency, even in severely affected animals. While this is encouraging for the development of a therapeutic approach in clinical settings, the FA neuropathology in humans is complex, and the status of proprioceptive neurons in FA patients in the early stages of the disease remains to be determined. Mice still developed a cerebral phenotype; however, this is not a phenotype occurring in FA patients, although it is important to target the Purkinje cell and the dentate nucleus in the cerebellum of FA patients. To improve the therapeutical approach, it would be of interest to optimize overall brain transduction, especially the cerebellum, with new generation of AAV vectors with an optimized capsid, such as the newly described PHPeB vectors.[32]

MATERIALS AND METHODS

Animals

Mice carrying the conditional allele for the frataxin gene ($Fxn^{L3/L3}$) as described previously[19] were mated with B6;129P2-$Pvalb^{tm1(Cre)Arbr/J}$ (https://www.jax.org/strain/008069; Jackson Laboratory, Maine, USA)[21] in order to generate $Fxn^{L3/L-}$; $Pvalb^{tm1(Cre)Arbr/J}$ (named *Pvalb* cKO thereafter) and the $Fxn^{+/L3}$ mice used as controls. To monitor tissue specificity and temporal expression of Cre recombinase activity, B6;129P2-$Pvalb^{tm1(Cre)Arbr/J}$ mice were mated with a reporter B6;129S4-$Gt(ROSA)26Sor^{tm1Sor}$/J (https://www.jax.org/strain/003309).[33] Animals were maintained in a temperature- and humidity-controlled animal facility with a 12-hr light-dark cycle and free access to water and a standard rodent chow (D03, SAFE, Villemoisson-sur-Orge, France) and supplement after 7.5 weeks of age with jellified food (gel diet A03 SAFE or Dietgel 76A clear H20). All animal procedures were approved by the local ethical committee (C2EA-17, agreements 604 and 2852) and were performed in accordance with the Guide for the Care and the Use of Laboratory Animals (US NIH).

For early symptomatic studies, 3.5-week-old mice were anesthetized by intraperitoneal (i.p.) injection with ketamine and xylazine (130/13 mg/kg) to allow retro-orbital intravenous administration of AAV9-CAG-FXN-HA at a dose of 5×10^{13} vg/kg. Untreated *Pvalb* cKO and WT mice were injected with equivalent volumes of saline solution. For late symptomatic studies, 7.5-week-old mice were anesthetized by i.p. injection with ketamine and xylazine (130/13 mg/kg), positioned on the stereotactic frame (David Kopf Instruments, Tujunga, USA) and injected bilaterally in the striatum and in the white matter of the cerebellum with an AAVrh.10-CAG-FXN-HA at a dose of 1×10^{10} vg/deposit (Table S6). Injections were done using a 30G blunt needle attached to a 10 µL Hamilton syringe (Hamilton, USA) at a rate of 0.2 µL/min. Animals were then intravenously injected with AAV9-CAG-FXN-HA at a dose of 5×10^{13} vg/kg. To avoid suffering, animals received an injection of buprecare (0.3 mg/kg) before waking up (Animal Care, France). Untreated *Pvalb* cKO and WT mice were injected with equivalent volumes of saline solution. Animals were monitored daily after the surgery. The combination of AAV serotypes used was based on published[34] and preliminary tests. Pre-symptomatic AAVrh.10-CAG-FXN-HA IV delivery at a dose of 5×10^{13} vg/kg, did not prevent the onset sensory ataxia in Pvalb cKO animals measured by electromyogram (EMG) (data not shown). Furthermore, comparison of intraparenchymal delivery of AAVrh10-GFP and AAV9-GFP demonstrated better neuronal transduction efficiency for AAVrh10 (data not shown).

The AAV vectors were the same as the ones used in the previous gene therapy study[12] with final titers of 8.5×10^{13} vg/mL for the AAV9-CAG-hFXN-HA and 5.5×10^{13} vg/mL for the AAVrh.10-CAG-hFXN-HA.

Behavioral Analysis

Behavioral experiments were conducted to evaluate motor and muscular function. Coordination was evaluated using the notched-bar test (scored number of falls of the upper or lower limbs) and the wire-hanging test (scored the time needed by animal to attach their hindlimbs) as previously described[35] but without training. General motor capacities were tested using the accelerating rotarod LE8200 (Bioseb, France), and open field activity was measured on the photocell actimeter LE8811 (Bioseb, France), as previously described (https://www.mousephenotype.org/). Animals were scored weekly for each test from 3.5 weeks of age until euthanasia, in the following order: wire-hanging test, notched-bar test, rotarod, and open field. Gait analysis was performed at 13.5 weeks or at 18.5 weeks of age using a DigitGait Apparatus (Mouse Specific, Boston, USA), as described previously.[36] The paws of the mice were captured by video

during treadmill locomotion at a speed of 21 cm/s for at least 5 s of proper gait, and analysis was performed using the DigitGait Analyzer software (Mouse Specific, Boston, USA).

Electromyogram analyses were performed using the Natus UltraProS100 apparatus (Mag2Health, France). Mice were anesthetized using i.p. injection with ketamine/xylazine (130/13 mg/kg). Animals were maintained at 37°C during the whole experiment until wakeup. Latency and amplitude of M and H-waves were recorded in the plantar hindpaw muscle after sciatic nerve stimulation (0.1 ms and 8 mA intensity). An additional recording of the M-wave was performed in the gastrocnemius muscle. Measurements were performed every 2 weeks starting at 3.5 weeks of age.

Histology

For histological analyses, mice were killed by i.p. injection of ketamine-xylazine (300/13 mg/kg) and perfused with 10 mL of PBS. Various tissues were dissected and either fixed in paraformaldehyde (PFA) and embedded in paraffin or directly embedded in Shandon Cryomatrix embedding resin (Thermo Fisher Scientific) and snap-frozen in isopentane chilled on dry ice. For spinal cord and DRG analysis, prior to the paraffin embedding, the column was decalcified in EDTA 0.34 M (pH 7.4) for 14 days, and the spinal cord was divided into cervical, thoracic, and lumbar levels. DRG neurons were scored on paraffin sections (5 μm) stained with H&E. The number of neurons was normalized by the area of the DRG section. DAB-enhanced Perl's iron staining was performed on 8-μm tissue cryosections as previously described.[12] β-galactosidase staining was performed on 10-μm cryopreserved sections with a protocol adapted from Sanes et al.[37]

HA immunodetection was performed on paraffin sections using Vectastain ABC kit followed by DAB enhancement according to manufacturer's protocol (Vector Labs), with slight modification, including epitope unmasking in 10 mM Tris, 1 mM EDTA, 0.1% Tween 20 (pH 8.75) for 45 min at 95°C, and images acquired on a Hamamatsu NanoZoomer 2.0 slide scanner. Succinate dehydrogenase (SDH) activity was determined on 8-μm cryosections of tissues, as previously described[19] with adapted incubation time with the substrate solution (25 min for the DRG sections, 30 min for the brain sections). Images were acquired using the Hamamatsu NanoZoomer 2.0 slide scanner. DRG neurons were then scored on the intensity of the SDH signal: strong, medium, low, and no SDH staining. All experiments were performed blindly.

Calbindin, MBP, and Neurofilament 200-kDa (NF-200) immunofluorescences were performed on paraffin sections according to previous protocols.[38,39]

TfR1 and GFAP immunofluorescence single labeling or co-labeling were performed on 8-μm 4% PFA fixed cryosections. Sections were mounted using ProLong Gold antifade reagent (Invitrogen), and images were recorded with a Leica DM4000B-M microscope equipped with a Coolsnap HQ2 camera and Micromanager software (see Table S7 for antibodies dilutions and references).

For electron microscopy analysis, animals were perfused with 5 mL of PBS and 10 mL 4% PFA in saline, and tissues were fixed in 2.5% PFA/2.5% glutaraldehyde in cacodylate buffer, and samples were processed as previously described.[12,19]

Molecular Biology

Mice were killed by i.p. injection of ketamine-xylazine (300 mg/kg; 30 mg/kg), and samples for biochemical and molecular analyses were immediately frozen in liquid nitrogen. Protein extractions and western blot were performed as previously described.[12] Twelve micrograms of proteins were loaded on the gels, and the membranes were incubated with the different antibodies (Table S7) detected with SuperSignal West Pico chemiluminescent substrate (Thermo Fisher Scientific) or SuperSignal West Femto maximum sensitivity substrate (for frataxin detection). Chemiluminescent images were acquired on the Amersham Imager 600 (GE Healthcare Life Sciences). The activity of the respiratory chain enzyme SDH (complex II) was determined as previously described.[19,40] Mouse and human frataxin were quantified in DRG (cervical, thoracic, and lumbar) and cerebellum extracts using the mouse frataxin ELISA and human frataxin ELISA kits (Abcam, ab199078, and Abcam, ab176112, respectively) according to the manufacturer's protocol.

Vector Genome Copy Number was measured by qPCR on extracted genomic DNA from DRG, spinal cord (cervical, thoracic, and lumbar levels), brain, cerebellum, heart, and liver using the Light Cycler 480 SYBR Green I Master (Roche, France). The results (vector genome copy number per cell) were expressed as n-fold differences in the transgene sequence copy number relative to the *Adck3* gene copy as internal standard (number of viral genome copy for 2N genome).

Statistical Analyses

All data are presented as mean ± SEM. Statistical analysis was carried out using GraphPad Prism software (La Jolla, USA). Student's t tests were used to compare group, and a value of $p < 0.05$ was considered as significant.

SUPPLEMENTAL INFORMATION

Supplemental Information includes Supplemental Results, seven figures, and seven tables and can be found with this article online at https://doi.org/10.1016/j.ymthe.2018.05.006.

AUTHOR CONTRIBUTIONS

Conceptualization, F.P., C.d.M., H.P.; Methodology, F.P., C.d.M., H.P.; Investigation, F.P., C.d.M., N.V., A.E.; Resources, L.R.; Writing – Original Draft, F.P., C.d.M., H.P.; Writing – Review & Editing, F.P., C.d.M., H.P.; Funding Acquisition, H.P.; Supervision, H.P.; F.P. and C.d.M. contributed equally to the study.

CONFLICTS OF INTEREST

H.P. is scientific consultant to Voyager Therapeutics. All other authors declare no competing financial interests.

ACKNOWLEDGMENTS

We thank Nadia Messaddeq from the IGBMC imaging platform for EM analysis and Véronique Blouin (Institut de Recherche Thérapeutique, INSERM UMR 1089) for vector production. This work was supported by the US Friedreich Ataxia Research Alliance (to H.P.) and a personal donation from the Lurton family (to H.P.). C.d.M. is a recipient of a 4th year PhD fellowship from the Association Française pour l'Ataxie de Friedreich. This study was supported by the grant ANR-10-LABX-0030-INRT, a French State fund managed by the Agence Nationale de la Recherche under the frame program Investissement d'Avenir ANR-10-IDEX-0002-02.

REFERENCES

1. Harding, A.E. (1981). Friedreich's ataxia: a clinical and genetic study of 90 families with an analysis of early diagnostic criteria and intrafamilial clustering of clinical features. Brain *104*, 589–620.
2. Pandolfo, M. (2009). Friedreich ataxia: the clinical picture. J. Neurol. *256* (*Suppl 1*), 3–8.
3. Koeppen, A.H., and Mazurkiewicz, J.E. (2013). Friedreich ataxia: neuropathology revised. J. Neuropathol. Exp. Neurol. *72*, 78–90.
4. Koeppen, A.H., Ramirez, R.L., Becker, A.B., and Mazurkiewicz, J.E. (2016). Dorsal root ganglia in Friedreich ataxia: satellite cell proliferation and inflammation. Acta Neuropathol. Commun. *4*, 46.
5. Kemp, K.C., Cook, A.J., Redondo, J., Kurian, K.M., Scolding, N.J., and Wilkins, A. (2016). Purkinje cell injury, structural plasticity and fusion in patients with Friedreich's ataxia. Acta Neuropathol. Commun. *4*, 53.
6. Selvadurai, L.P., Harding, I.H., Corben, L.A., and Georgiou-Karistianis, N. (2018). Cerebral abnormalities in Friedreich ataxia: A review. Neurosci. Biobehav. Rev. *84*, 394–406.
7. Tsou, A.Y., Paulsen, E.K., Lagedrost, S.J., Perlman, S.L., Mathews, K.D., Wilmot, G.R., Ravina, B., Koeppen, A.H., and Lynch, D.R. (2011). Mortality in Friedreich ataxia. J. Neurol. Sci. *307*, 46–49.
8. Campuzano, V., Montermini, L., Molto, M.D., Pianese, L., Cossee, M., Cavalcanti, F., Monros, E., Rodius, F., Duclos, F., Monticelli, A., et al. (1996). Friedreich's ataxia: autosomal recessive disease caused by an intronic GAA triplet repeat expansion. Science *271*, 1423–1427.
9. Kumari, D., and Usdin, K. (2012). Is Friedreich ataxia an epigenetic disorder? Clin. Epigenetics *4*, 2.
10. Schmucker, S., Martelli, A., Colin, F., Page, A., Wattenhofer-Donzé, M., Reutenauer, L., and Puccio, H. (2011). Mammalian frataxin: an essential function for cellular viability through an interaction with a preformed ISCU/NFS1/ISD11 iron-sulfur assembly complex. PLoS ONE *6*, e16199.
11. Colin, F., Martelli, A., Clémancey, M., Latour, J.M., Gambarelli, S., Zeppieri, L., Birck, C., Page, A., Puccio, H., and Ollagnier de Choudens, S. (2013). Mammalian frataxin controls sulfur production and iron entry during de novo Fe4S4 cluster assembly. J. Am. Chem. Soc. *135*, 733–740.
12. Perdomini, M., Belbellaa, B., Monassier, L., Reutenauer, L., Messaddeq, N., Cartier, N., Crystal, R.G., Aubourg, P., and Puccio, H. (2014). Prevention and reversal of severe mitochondrial cardiomyopathy by gene therapy in a mouse model of Friedreich's ataxia. Nat. Med. *20*, 542–547.
13. Miranda, C.J., Santos, M.M., Ohshima, K., Smith, J., Li, L., Bunting, M., Cossée, M., Koenig, M., Sequeiros, J., Kaplan, J., and Pandolfo, M. (2002). Frataxin knockin mouse. FEBS Lett. *512*, 291–297.
14. Pook, M.A., Al-Mahdawi, S., Carroll, C.J., Cossée, M., Puccio, H., Lawrence, L., Clark, P., Lowrie, M.B., Bradley, J.L., Cooper, J.M., et al. (2001). Rescue of the Friedreich's ataxia knockout mouse by human YAC transgenesis. Neurogenetics *3*, 185–193.
15. Al-Mahdawi, S., Pinto, R.M., Ruddle, P., Carroll, C., Webster, Z., and Pook, M. (2004). GAA repeat instability in Friedreich ataxia YAC transgenic mice. Genomics *84*, 301–310.
16. Al-Mahdawi, S., Pinto, R.M., Varshney, D., Lawrence, L., Lowrie, M.B., Hughes, S., Webster, Z., Blake, J., Cooper, J.M., King, R., and Pook, M.A. (2006). GAA repeat expansion mutation mouse models of Friedreich ataxia exhibit oxidative stress leading to progressive neuronal and cardiac pathology. Genomics *88*, 580–590.
17. Anjomani Virmouni, S., Ezzatizadeh, V., Sandi, C., Sandi, M., Al-Mahdawi, S., Chutake, Y., and Pook, M.A. (2015). A novel GAA-repeat-expansion-based mouse model of Friedreich's ataxia. Dis. Model. Mech. *8*, 225–235.
18. Perdomini, M., Hick, A., Puccio, H., and Pook, M.A. (2013). Animal and cellular models of Friedreich ataxia. J. Neurochem. *126* (*Suppl 1*), 65–79.
19. Puccio, H., Simon, D., Cossée, M., Criqui-Filipe, P., Tiziano, F., Melki, J., Hindelang, C., Matyas, R., Rustin, P., and Koenig, M. (2001). Mouse models for Friedreich ataxia exhibit cardiomyopathy, sensory nerve defect and Fe-S enzyme deficiency followed by intramitochondrial iron deposits. Nat. Genet. *27*, 181–186.
20. Simon, D., Seznec, H., Gansmuller, A., Carelle, N., Weber, P., Metzger, D., Rustin, P., Koenig, M., and Puccio, H. (2004). Friedreich ataxia mouse models with progressive cerebellar and sensory ataxia reveal autophagic neurodegeneration in dorsal root ganglia. J. Neurosci. *24*, 1987–1995.
21. Hippenmeyer, S., Vrieseling, E., Sigrist, M., Portmann, T., Laengle, C., Ladle, D.R., and Arber, S. (2005). A developmental switch in the response of DRG neurons to ETS transcription factor signaling. PLoS Biol. *3*, e159.
22. Marmigère, F., and Ernfors, P. (2007). Specification and connectivity of neuronal subtypes in the sensory lineage. Nat. Rev. Neurosci. *8*, 114–127.
23. Zacharová, G., and Paleček, J. (2009). Parvalbumin and TRPV1 receptor expression in dorsal root ganglion neurons after acute peripheral inflammation. Physiol. Res. *58*, 305–309.
24. Rötig, A., de Lonlay, P., Chretien, D., Foury, F., Koenig, M., Sidi, D., Munnich, A., and Rustin, P. (1997). Aconitase and mitochondrial iron-sulphur protein deficiency in Friedreich ataxia. Nat. Genet. *17*, 215–217.
25. Lange, W. (1975). Cell number and cell density in the cerebellar cortex of man and some other mammals. Cell Tissue Res. *157*, 115–124.
26. Martelli, A., Schmucker, S., Reutenauer, L., Mathieu, J.R.R., Peyssonnaux, C., Karim, Z., Puy, H., Galy, B., Hentze, M.W., and Puccio, H. (2015). Iron regulatory protein 1 sustains mitochondrial iron loading and function in frataxin deficiency. Cell Metab. *21*, 311–323.
27. Eng, L.F., and Ghirnikar, R.S. (1994). GFAP and astrogliosis. Brain Pathol. *4*, 229–237.
28. Bostick, B., Ghosh, A., Yue, Y., Long, C., and Duan, D. (2007). Systemic AAV-9 transduction in mice is influenced by animal age but not by the route of administration. Gene Ther. *14*, 1605–1609.
29. Koeppen, A.H., Morral, J.A., Davis, A.N., Qian, J., Petrocine, S.V., Knutson, M.D., Gibson, W.M., Cusack, M.J., and Li, D. (2009). The dorsal root ganglion in Friedreich's ataxia. Acta Neuropathol. *118*, 763–776.
30. Chen, K., Ho, T.S.Y., Lin, G., Tan, K.L., Rasband, M.N., and Bellen, H.J. (2016). Loss of Frataxin activates the iron/sphingolipid/PDK1/Mef2 pathway in mammals. eLife *5*, 1–14.
31. Chandran, V., Gao, K., Swarup, V., Versano, R., Dong, H., Jordan, M.C., and Geschwind, D.H. (2017). Inducible and reversible phenotypes in a novel mouse model of Friedreich's Ataxia. eLife *6*, 1–41.
32. Chan, K.Y., Jang, M.J., Yoo, B.B., Greenbaum, A., Ravi, N., Wu, W.L., Sánchez-Guardado, L., Lois, C., Mazmanian, S.K., Deverman, B.E., and Gradinaru, V. (2017). Engineered AAVs for efficient noninvasive gene delivery to the central and peripheral nervous systems. Nat. Neurosci. *20*, 1172–1179.
33. Soriano, P. (1999). Generalized lacZ expression with the ROSA26 Cre reporter strain. Nat. Genet. *21*, 70–71.
34. Piguet, F., Sondhi, D., Piraud, M., Fouquet, F., Hackett, N.R., Ahouansou, O., Vanier, M.T., Bieche, I., Aubourg, P., Crystal, R.G., et al. (2012). Correction of brain oligodendrocytes by AAVrh.10 intracerebral gene therapy in metachromatic leukodystrophy mice. Hum. Gene Ther. *23*, 903–914.
35. Arbogast, T., Raveau, M., Chevalier, C., Nalesso, V., Dembele, D., Jacobs, H., Wendling, O., Roux, M., Duchon, A., and Herault, Y. (2015). Deletion of the App-Runx1 region in mice models human partial monosomy 21. Dis. Model. Mech. *8*, 623–634.

36. Wooley, C.M., Sher, R.B., Kale, A., Frankel, W.N., Cox, G.A., and Seburn, K.L. (2005). Gait analysis detects early changes in transgenic SOD1(G93A) mice. Muscle Nerve *32*, 43–50.

37. Sanes, J.R., Rubenstein, J.L., and Nicolas, J.F. (1986). Use of a recombinant retrovirus to study post-implantation cell lineage in mouse embryos. EMBO J. *5*, 3133–3142.

38. Sevin, C., Benraiss, A., Van Dam, D., Bonnin, D., Nagels, G., Verot, L., Laurendeau, I., Vidaud, M., Gieselmann, V., Vanier, M., et al. (2006). Intracerebral adeno-associated virus-mediated gene transfer in rapidly progressive forms of metachromatic leukodystrophy. Hum. Mol. Genet. *15*, 53–64.

39. Bolino, A., Piguet, F., Alberizzi, V., Pellegatta, M., Rivellini, C., Guerrero-Valero, M., Noseda, R., Brombin, C., Nonis, A., D'Adamo, P., et al. (2016). Niacin-mediated Tace activation ameliorates CMT neuropathies with focal hypermyelination. EMBO Mol. Med. *8*, 1438–1454.

40. Martelli, A., Friedman, L.S., Reutenauer, L., Messaddeq, N., Perlman, S.L., Lynch, D.R., Fedosov, K., Schulz, J.B., Pandolfo, M., and Puccio, H. (2012). Clinical data and characterization of the liver conditional mouse model exclude neoplasia as a non-neurological manifestation associated with Friedreich's ataxia. Dis. Model. Mech. *5*, 860–869.

EClinicalMedicine 18 (2020) 100213

Contents lists available at ScienceDirect

EClinicalMedicine

journal homepage: https://www.journals.elsevier.com/eclinicalmedicine

Research Paper

Predictors of loss of ambulation in Friedreich's ataxia

Christian Rummey[a,*], Jennifer M. Farmer[b], David R. Lynch[c]

[a] Clinical Data Science GmbH, Missionsstrasse 12, CH-4055 Basel, Switzerland
[b] Friedreich's Ataxia Research Alliance, Downingtown, PA, United States
[c] Children's Hospital of Philadelphia, Philadelphia, PA, United States

ARTICLE INFO

Article History:
Received 11 October 2019
Revised 7 November 2019
Accepted 11 November 2019
Available online xxx

Keywords:
Gait
Balance
Cerebellar ataxia
Friedreich's ataxia
Loss of ambulation

ABSTRACT

Background: Friedreich's ataxia (FRDA) is a characterized by progressive loss of coordination and balance leading to loss of ambulation (LoA) in nearly all affected individuals. While transition to becoming fully wheelchair bound is a critical milestone in the disease course, it presents a particularly challenging prediction, mostly due to variability in inter- and intra-subject severity and progression. For these reasons, LoA or potential surrogates have been impractical as outcomes in clinical trials.
Methods: We studied progressive features leading to LoA in participants enrolled into the Friedreich's Ataxia Clinical Outcome Measures Study (FA-COMS), a natural history study with currently 4606 yearly follow up visits in 1021 patients. Loss of specific functions related to walking and standing of the neurological Friedreich Ataxia Rating Scale (FARS) exams were evaluated using time to event methods. To account for different severities, patients were stratified by age of disease onset.
Findings: Early onset FRDA patients (<15y of age) typically become fully wheelchair dependent at a median of 11.5y (25th, 75th percentiles 8.6y, 16.2y) after the onset of first symptoms. Further time to loss of function analyses revealed a unique pattern of function loss, in particular in stance/balance items of the FARS exam. Each step in this typical sequence predicts future risk of LoA and can be used to rank patients in their individual progression.
Interpretation: We propose a stratification paradigm for time to LoA in FRDA. Concurrently, each step in a sequence of events represents a surrogate measure for future LoA. This will facilitate patient selection and stratification in clinical trials, and potentially enable study of LoA as a direct clinical outcome.
Funding: This work was funded by the Friedreich's Ataxia Research alliance (FARA), www.curefa.org.

1. Introduction

Friedreich's ataxia (FRDA), an autosomal recessive disorder associated with progressive neurodegeneration and cardiomyopathy resulting from a deficiency of the protein frataxin, a mitochondrial protein involved in iron sulfur cluster synthesis. Clinical experience shows that most individuals with FRDA are wheelchair bound within 15y of presentation. A variety of therapies are in development to ameliorate mitochondrial dysfunction associated with frataxin deficiency or to increase cellular frataxin levels, thus addressing the primary cause of FRDA. While several agents based on these approaches have reached late stage trials, no treatment is approved for FRDA.

One of the most difficult aspects of therapeutic development for FRDA is the identification of sensitive, meaningful clinical measures of the disease. Most clinical trials employ tools based on neurological exams or performance measures that quantify simple neurologic tasks. Such measures, like the Friedreich Ataxia Rating Scale (FARS) [1,2], the modified FARS (mFARS) [3], and the Scale for Assessment and Rating of Ataxia (SARA) [4] have been characterized in large natural history studies [5–7], and many of their overall properties are known. However, such measures are problematic due to their relative insensitivity to change over brief time periods (e.g. less than one year), their susceptibility to floor and ceiling effects as well as practice effects. Also, a clinically meaningful difference is inherently difficult to determine. In general, individual items of such scales are not necessarily related to activities with direct clinical meaning for patients, leading to indirect approaches for assessment of the clinical significance of specific changes.

One alternative for identifying meaningful change in FRDA would be to focus on a key clinical feature that can be reliably measured and observed and then use specific predictors of that event as indicators of clinical progression. In FRDA, loss of ambulation (LoA) provides such a benchmark, as it can be uniformly characterized from natural history data, and its clinical meaning is clear. In the present study, we applied this approach to the large natural history dataset from the Friedreich's

* Corresponding author.
E-mail address: christian@clindata.science (C. Rummey).

https://doi.org/10.1016/j.eclinm.2019.11.006

Research in context

Evidence before this study

Predictors of progression in Friedreich's Ataxia have been characterized in two large natural history studies (FA-COMS and EFACTS), and in addition in numerous smaller cohort studies. Such studies generally address progression of scaled neurologic exams, outcome measures without any direct clinical benefit. In clinical reports, the time of loss of ambulation - a measure with intrinsic clinical meaning - has been documented and estimated, but only on much smaller sample sizes.

Added value of this study

Given the rarity Friedreich's ataxia, cohort studies are often limited in size and restricted to specialized centres. In combination with the inherent variability of disease severity and progression, results are often descriptive for the specific cohort, rather than representative of the population.
More precise estimates of LoA and manner to stratify ambulant patients are important, because most sensitive outcome measures currently focus on this phase of the disease. In addition, the results here meet the criterion of having direct meaning to patients, thus providing a more relevant measure for registration level clinical trials.

Implications of all the available evidence

To best of our knowledge, no statistical estimates of the time to LoA in Friedreich's Ataxia exist; such estimations became feasible only through the large size and duration of the FA-COMS study. The present results show, that LoA is in principle viable as a direct outcome in clinical studies of Friedreich's ataxia, given proper stratification and design. The use of standing and balance tests as potential surrogate markers can increase sensitivity of the outcome.

Ataxia Clinical Outcome Measures Study (FA-COMS) [8], attempting to estimate the time to LoA in FRDA based on disease onset and other stratifiers. In addition, on the basis of available measures, we sought to evaluate individual assessments that could reveal a sequence of functional loss before patients become fully wheelchair bound and use such information to define a more precise model of LoA. Understanding these events might provide tools to use LoA in long-term studies either as an outcome measure or a patient selection and stratification tool.

2. Methods

2.1. Participants

Participants were enrolled and followed in the FA-COMS study on a continuous basis as described previously [7,9,10] between October 2003 and April 2019. Serial yearly evaluations were conducted at one of 12 sites: Children's Hospital of Philadelphia, University of California Los Angeles, Murdoch Children's Research Institute (Melbourne), Emory University, University of South Florida, University of Iowa, University of Florida, University of Chicago, Sick Kids Hospital (Toronto), University of Minnesota, Ohio State University and University of Rochester.

2.2. Measures analysed

The complete set of evaluations in FA-COMS have been presented previously [7] with the salient data for the present study being demographics, medical history, FARS functional disease staging (FDS) [1] and specifically the items from the upright stability sub score of the FARS neurological exam [3].

FDS is derived from an ordinal 1−6 score, graded in units of 0.5 linked by descriptors to ambulation status and overall function (5 = wheel chair bound) [1]. Values are physician determined by overall evaluation of the patient, with a score of 5 being given if a participant is unable to walk either at the visits or in daily life. The FARS-E/Upright stability sub score of the FARS neurological exam includes nine items that are ordinally scored [3]: there are six items that assess the ability to stand in different positions: with feet apart (E2A, eyes closed: E2B), with feet together (E3A, eyes closed: E3B), in tandem (E4) and on dominant foot (E5). The three other items examine sitting posture (E1), tandem walk (E6) and gait (E7). A detailed description of the FDS, the complete item set and the sub score structure of the FARS exams is provided in Supplementary Figure 1.

For the six stance items in particular (as described, E2A, B; E3A, B; E4; E5), scoring is based on the time a participant can stand in a given position. A participant who can stand greater than 60s is scored 0. Participants able to stand less than 60s in a position are given a score based on the average of 3 trials, i.e. $<$60s, $<$45s, $<$30s and $<$15s are scored 1, 2, 3, or 4 points respectively. Sitting and walking items (E1, E6, E7) in the FARS E sub score are not scored based on time, but by investigator judgment from normal (score 0) to unable (maximum score), with mild/moderate/sever impairment in-between.

We defined LoA by attainment of a maximum score 5 on item E7 (unable to walk even with assistance, wheelchair bound), and analogously loss of function as the attainment of the maximum score in a specific item for the first time. In statistical terms, the outcomes of these scales are not monotonous, as required for the time to event analyses we conducted. However, the transition to full wheelchair dependence in FRDA is a slow process even in the most severely affected patients. Marked variability in performance during this period leads to patients intermittently improving from maximum walking or stance scores. All this makes a clear definition of LoA complex, when monotony is a requirement. On the other hand, as no substantial or even persistent recovery can be expected, our conservative definition of loss of function at the first time a maximum score is reached is both clinically useful and suffices statistical requirements.

For the time to event analyses we used disease duration in years as the temporal variable, which better correlates with progression than age. Disease duration in FRDA is defined as the time from onset of the disease [2,6,11], i.e. the age in years when the first symptoms of FRDA were noticed by the patient. As shown below, the time of diagnosis (i.e. disease duration at diagnosis) is of special interest in this context and was added as an additional parameter to the time to event analyses.

All available visits from FA-COMS were used, as long as the visit had a complete FARS-E sub scale and FDS available (1026 participants, 4606 visits).

2.3. Statistical analysis

In addition to demographic parameters, we report follow up times in the study by identifying active patients (i.e. having at least one follow up visit within the last 2y), number of patients without follow up visit, and median [IQR] of follow up time in patients with follow-up.

We conducted time to event analyses for the time from disease onset to loss of specific functions related to standing/walking. The use of traditional Kaplan Meyer estimates in natural history studies is challenging, due to two conditions. First, events are occurring in between yearly scheduled visits and exact times are unknown or cannot be strictly defined. Second, the times of events that have already occurred before enrolment are unknown and ignoring these events for obtaining an population estimate (as opposed to a study sample estimate) results in substantial bias due to left truncation [12,13]. We

tried to overcome both these conditions by using the Turnbull estimator [14], a generalization of the Kaplan−Meier estimator allowing for interval-censored data [15,16], including left-censoring (i.e. participants enrolled when non-ambulatory). The Turnbull method has proven useful in similar analyses [17].

For the interval censored analyses, we used the last ambulatory visit (or last visit where the maximum score was not yet obtained) and the first non-ambulatory visit (first visit with maximum score in an item) as left and right edge of the intervals. Patients already non-ambulatory at enrolment were left-censored, i.e. a time of duration = 0 (reflecting age of symptom onset) was used as the left edge. To evaluate a potential bias on the results, either by left censoring *or* truncation, all time to event estimates were also computed without left-censored observations. Time to event results are reported as median (25th, 75th percentile).

To demonstrate the features of our proposed stratification, we additionally calculated the risk of losing ambulation in the ambulant population, using traditional Kaplan Meyer analysis and the Cox proportional hazards model.

To account for differences disease severities, patients were stratified into groups of disease onset <15y, 15−24y and >24y in all analyses.

2.4. Ethical approval

This study is a retrospective analysis of data from the FA-COMS study and thus exempt from ethics approval.

3. Results

Demographic characteristics and the analyses of follow up times of the cohort are summarized in Table 1.

The FA-COMS study has minimal enrolment criteria [8] and recruits a diverse cohort, including individuals with well-established disease who were non-ambulatory at enrolment, as well as a large number of newly diagnosed, ambulatory individuals with early onset. When stratified by age of onset (<15y, 15−24y, >24y), the groups were similar in sex and presence or absence of point mutations (Table 1). We also present the cohort by different temporal aspects of disease, i.e. the baseline status of measures, mirroring the censoring status in the analyses: Enrolled non-ambulatory (left-censored), LoA during follow up (interval censored) and ambulatory at last visit (right censored). This is reflected in age and duration differences between these three groups.

Overall, within the stratification groups disease severity (age of symptom onset and GAA1 repeat length) was sufficiently balanced among the temporally separated subgroups, ensuring adequate patient coverage of the overall disease course of interest. Of note, in the early and intermediate onset groups (<15y and 15−24y), the subgroup of patients enrolled non-ambulatory was also the most genetically severe (highest GAA1 repeat length).

Balanced above all severity groups and temporal strata, slightly less than 30% of patients in FA-COMS do not follow up, usually reflecting travel related difficulties in returning to the examination site [7,10]. Within the three severity subgroups, follow up times were longest in the groups with observed events, and shortest in groups that were ambulatory at last visit.

Baseline distributions for all items in the FARS E/upright stability sub score are shown in Fig. 1. Stance items in FARS E show distinct bimodal distributions (Fig. 1(A)), i.e. patients score either minimal (light green) or maximal score (dark green), with very few observations in-between. Only the first three stance tests (E2A, B; E3A) can be performed by a relevant number of patients [3]; few participants can perform the three more difficult items, i.e. stand with feet together/eyes closed, in tandem stance or on the dominant foot alone (items E3B, E4 and E5). A more detailed investigation showed that participants who could perform all these three tests at baseline were by trend diagnosed early in the disease or carried point mutations (data not shown).

In contrast to the six stance items, walking and sitting items in the FARS E sub score showed a different type of distributions indicating a more gradual functional loss during disease progression (Fig. 1(B)).

Table 1
Baseline demographics and follow up characteristics by onset group, and ambulation status during enrolment and follow up time.

	Onset <15y			Onset 15−24y			Onset >24y		
Status	Enrolled non-amb.	LoA during follow up	Amb. at last visit	Enrolled non-amb.	LoA during follow up	Amb. at last visit	Enrolled non-amb.	LoA during follow up	Amb. at last visit
N	231	147	325	52	44	115	18	20	69
(%)	(32.9)	(20.9)	(46.2)	(24.6)	(20.9)	(54.5)	(16.8)	(18.7)	(64.4)
Sex = *m* (%)	112 (48.5)	87 (59.2)	161 (49.5)	25 (48.1)	12 (27.3)	66 (57.4)	8 (44.4)	8 (40.0)	29 (42.0)
Age of symptom onset	9 [6, 11]	7 [5, 10]	8 [5, 12]	16 [15, 18]	18 [16, 18]	18 [16, 20]	28 [27, 33]	31 [28, 40]	34 [28, 40]
Age at diagnosis[a]	12 [9, 15]	11 [8, 13]	12 [9, 14]	20 [18, 24]	21 [19, 25]	22 [18, 26]	42 [35, 52]	36 [34, 46]	42 [33, 48]
GAA1 repeat length[b]	770 [690, 892]	748 [630, 848]	733 [633, 820]	600 [500, 750]	475 [385, 632]	466 [344, 566]	325 [200, 333]	300 [192, 419]	188 [128, 327]
Point mutation /other	13 (5.6)	7 (4.8)	21 (6.5)	3 (5.8)	1 (2.3)	6 (5.2)	0 (0.0)	0 (0.0)	5 (7.2)
Diseased uration	19 [12, 26]	5 [4, 9]	5 [3, 7]	25 [19, 31]	13 [8, 20]	8 [4, 13]	28 [24, 33]	17 [13, 18]	10 [7, 15]
Age	27 [21, 34]	14 [11, 17]	14 [11, 17]	43 [34, 49]	31 [26, 37]	26 [23, 32]	59 [52, 62]	50 [44, 59]	45 [41, 53]
Active in study[c]	88 (38.1)	106 (72.1)	194 (59.7)	22 (42.3)	32 (72.7)	62 (53.9)	6 (33.3)	9 (45.0)	29 (42.0)
No follow up visit (%)	71 (30.7)	–	91 (28.0)	12 (23.1)	–	35 (30.4)	6 (33.3)	–	20 (29.0)
Follow up time (y, SD)[d]	6 [3, 10]	10 [6, 12]	3 [1, 6]	6 [3, 10]	12 [8, 14]	5 [2, 8]	7 [5, 10]	8 [4, 12]	6 [3, 10]

Data are median [IQR] or *n* (%).
[a] Missing for *n* = 14.
[b] Excluding point mutations; 47 participants without data.
[c] At least one visit within the last 2y.
[d] Excluding inactive participants.

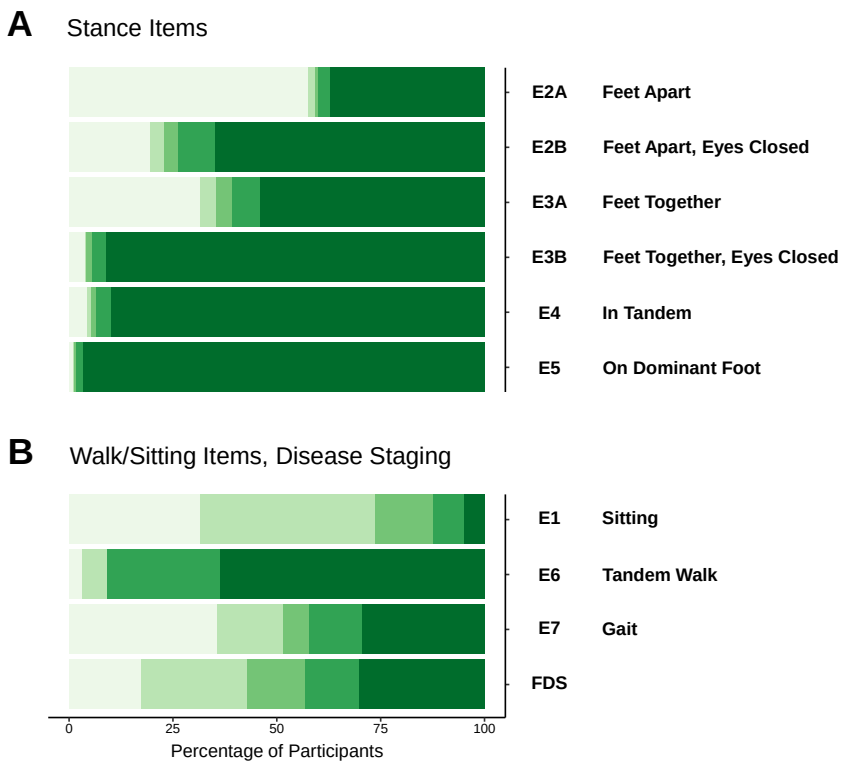

Fig. 1. FARS E item results at enrolment (baseline). Bars are coloured from minimal (light green) to maximum (dark green) item score, respectively: (A) stance items. (B) items measuring walking, sitting and FRDA Disease Staging (FDS).

For item E1 (sitting posture) most participants stay on little/no disability for a long period of time, and only a few participants lose the ability to sit completely. On the other hand, tandem walk (E6) seems to be lost earliest, similar to standing performance. The remaining two items in Fig. 1(B), E7/gait and FDS are both items with clear definitions of LoA. Their distributions are balanced, reflecting the character of the cohort. As noted above, for the definitive definition of LoA we chose E7/gait over FDS, since the former focuses on walking alone, and has clearer definitions for this capability compared to FDS, which is evaluating the overall patient status.

3.1. Disease duration at loss of ambulation, by onset group

We then used the Turnbull estimator to calculate disease duration at LoA (score 5 in E7/gait) by onset group (Fig. 2 and Table 2). In early onset FA (onset <15y of age) during the follow up time 148 participants experienced LoA at a median duration of 11.5y (25th, 75th percentiles 8.6y, 16.2y).

In this analysis, 33% of the observations were left-censored (n = 232), and when these were excluded the median duration was 2.9 years longer, indicating substantial truncation bias. Compared to the early onset group (<15y), Turnbull estimates for LoA in later onset groups were markedly higher (18.3y for 15–24y, 23.5y for >24y) and fewer events were observed during the follow up time (42 and 21, respectively). The high uncertainty of these results is also reflected in the 25th and 75th percentiles (Table 2), implicating less steep survival curves. Truncation biases in non-left censored analyses were also higher.

Analogous loss of function analyses were now conducted for all stance related items and time of FRDA diagnosis in the early onset group (<15y, Fig. 3; Table 2). In each of these analyses, we used data from all patients, left censoring the observations when a function was already lost at baseline. Patients with missing time of diagnosis were left censored in the respective analysis (n = 14, 3%). These results show that stance functions are lost step by step, in the specific order. The sequence E2B, E3A and E2A delineates that first the capability to stand with eyes closed is lost, followed by stance with eyes open, feet together and eventually with feet apart, before LoA occurs (as defined by loss of E7/gait red curve in Fig. 3).

For the most severe subgroup (onset <15y), disease duration estimates (Table 2) were well separated for E2B (stand with feet apart, eyes closed, 4.1y), E3A (stand with feet together, 5.8y) and E2A (stand with feet apart, 9.3y). In each of these cases, a high number of observed events (151, 174 and 180, respectively) strengthen these analyses, as did small truncation biases in the non-left censored analyses. In contrast, the capabilities to perform items E5, E4 and E3B were lost in 92% or more of participants already at enrolment and only very few events could be observed during the follow up time. Especially for these three analyses, this resulted also in large truncation biases in the non-left censored analyses. We do not assume these estimates as reliable (see discussion).

Remarkably, our results indicate that time at FRDA diagnosis occurs at a median time of 3y (1y, 5y), which by disease duration is located between the two groups of stance items. As visible in the survival curves for early onset (<15y, Fig. 3), 91 (13%) participants were diagnosed before or at the time of symptom onset (FRDA diagnosis is collected with yearly precision only).

To clarify further the sequence of function loss, we examined the pattern of stance function abilities in all patients at baseline. The pattern matched the sequence suggested by the time to event analyses in 96% of the patients, independent of their onset group. Loss of E2B is followed by E3A, then E2A and eventually LoA. Overall, 31 of 720 ambulatory patients (4%) did do not follow the general rule, and only 8 (1%) non-ambulant participants had some stance function remaining (see Supplementary Table 1).

In corresponding time to functional loss analyses, later onset groups (15–24y and >24y) followed the pattern of the early onset group (Supplementary Table 2. and Supplementary Figure 2.). The number of observed events were lower, leading to less precise

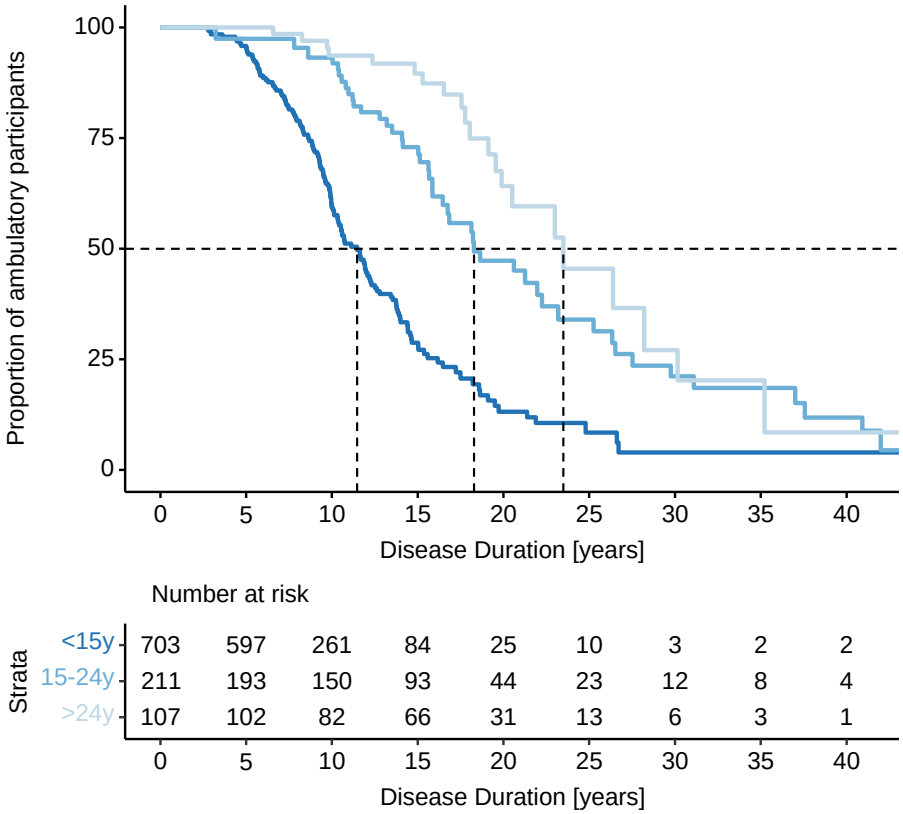

Fig. 2. Estimated proportion of ambulant participants over disease duration. Vertical dotted lines indicate the median disease duration at LoA by onset group.

estimates. Due to the uncertainties, which reflect of a lower number of patients and a higher variability, all subsequent analyses are directed to the early onset group (<15y) only.

3.2. Stance functions predict future risk of losing ambulation (onset <15y)

If this loss of function always occurs in the same order (preceding LoA), locating patients on the specific step in this sequence should facilitate a more precise estimate of individual time to LoA. Therefore, we used all ambulatory patients at baseline (onset <15y, *N* = 381), *stratified* by their stance ability (into four groups) and conducted a traditional Kaplan Meyer type analysis (using right-censoring only) for *time in study* to LoA. Ambulatory patients without a follow visit (*n* = 91, 28%, Table 1) were excluded from this analysis.

Of note, observations in this analysis are independent but are used in a different way than in the previous epidemiological analyses (see discussion). Results are summarized in Table 3 and Fig. 4. Participants at Step 0 showed a median time to LoA of 10.3 years (8.3, 11.5). At Steps 1 to 3, these times were 6.1 years (4.8, 8.9), 5.8 years (4.1, 7.3) and 2.0 years (1.2, 3.2), respectively. Thus, after five years, the risk of losing ambulation for participants on Step 0 to 3 was 9%, 39%, 43%, and 90%. After two years, only the highest risk group (Step 3) showed notable risk of losing ambulation (44%, Table 3).

For exploratory statistical comparison, we estimated pairwise hazard ratios for these four groups using a cox-proportional hazards

Table 2
Estimates for LoA by onset group, and for loss of function of FARS E Items (for onset <15y). Items are arranged by median duration, including to the analysis of diagnosis of FRDA.

Onset subgroup	Item	Description	Median duration [y]	25, 75 percentiles	*N*	Observed events	Left censored [%]	Truncation bias[a] [y]
Loss of ambulation, stratified by onset group								
<15y	E7	LoA/gait	11.5	8.6, 16.2	703	148	33	2.9
15–24y	E7	LoA/gait	18.3	14.1, 27.5	211	45	25	7.0
>24y	E7	LoA/gait	23.5	18.0, 30.1	107	21	17	4.7
Loss of stance functions in the FARS E sub score, early onset group (<15y)								
<15y	E5	Stance dominant foot	0.2	0.2, 0.2	703	14	97	7.3
<15y	E4	Stance, tandem	0.9	0.2, 2.0	703	46	92	4.8
<15y	E3B	Stance feet together, eyes closed	1.2	0.5, 1.5	703	40	93	2.9
<15y	–	Diagnosis of FRDA	3.0	1.0, 5.0	703	688	2	–
<15y	E2B	Stance feet apart, eyes closed	4.1	2.5, 6.1	703	151	68	2.2
<15y	E3A	Stance, feet together	5.8	3.6, 8.7	703	174	58	2.4
<15y	E2A	Stance, feet apart	9.3	6.7, 12.2	703	180	39	1.5
<15y	FDS	Disease stage	11.1	8.7, 15.6	703	149	33	3.3
<15y	E7	LoA/gait	11.5	8.6, 16.2	703	148	33	2.9

[a] Difference between analyses all item-results were floored, e.g. 2.33 or 2.66 were set to 2; the highest number indicates maximum disability ('unable').

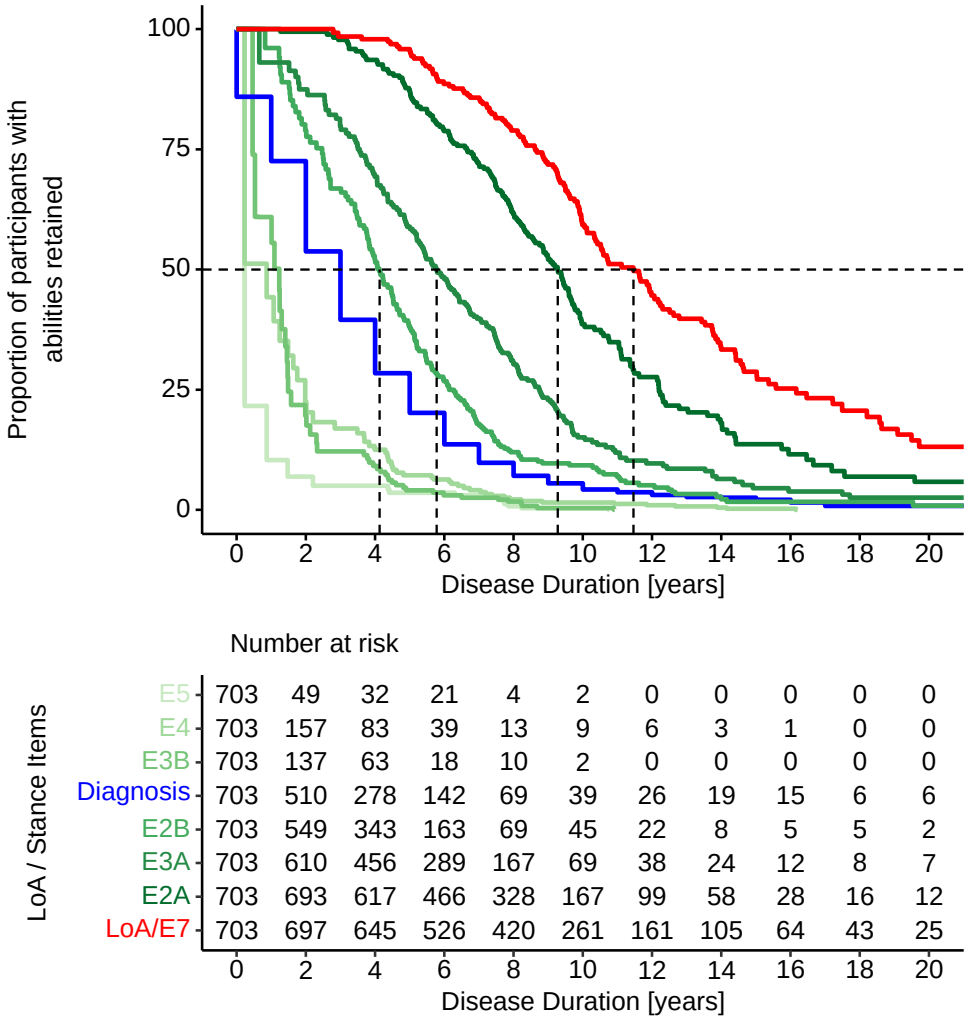

Fig. 3. Sequence of events prior to LoA in participants with early onset FRDA (<15y of age): E5, E4 and E3B are lost prior to diagnosis (blue line), followed by E2B, E3A, E2A and eventually LoA (E7, red line). See Fig. 1 for item coding.

model. The differences in hazards ratios between consecutive groups were highly significant (p-value < 0.001) for all comparisons except for Step 2 vs Step 1 ($p = 0.0522$, Table 3).

3.3. Estimation of power/sample sizes in a study measuring time to loss of ambulation

The previous analyses provide event rates that can be converted into sample size estimates for prototypic studies using LoA as an outcome measure. The power of a survival analyses is dependent on the number of events occurring. Assuming that an equal number of subjects from Step 2 and Step 3 were enrolled for a study duration of 2 years, the combined event rate would be (44 + 7) /2 = 25.5 (Table 3). When further assuming a treatment effect of slowing down the decline by 50%, the study would require 257 participants per study group for 80% power. In contrast, when selecting only participants at step 3, the overall event rate of 44% after 2y leads to 149 patients/group necessary for 80% power.

Table 3
Kaplan Meyer analysis for time from enrolment to LoA, stratified by stance capability at baseline (onset <15y).

Stance capability (hierarchical)		Median [y]	25, 75 percentiles	*N*	Observed events	Non-ambulatory after 2y, 5y [%]	Hazard ratio* (95%CI)	*p*-value*
Step 0	Can stand w. feet apart, eyes closed (E2B)	10.3	8.3, 11.5	174	44	0, 9	–	–
Step 1	Can stand w. feet together, eyes open (E3A)	6.1	4.8, 8.9	80	30	0, 39	3.5 (2.1, 5.8)	<0.0001
Step 2	Can stand w. feet apart, eyes open (E2A)	5.8	4.1, 7.3	98	49	7, 43	1.6 (0.9, 2.4)	0.0522
Step 3	Lost ability to stand with feet apart, eyes open (E2A)	2.0	1.2, 3.2	29	24	44, 90	5.0 (3.0, 8.4)	<0.0001

* Compared to previous group.

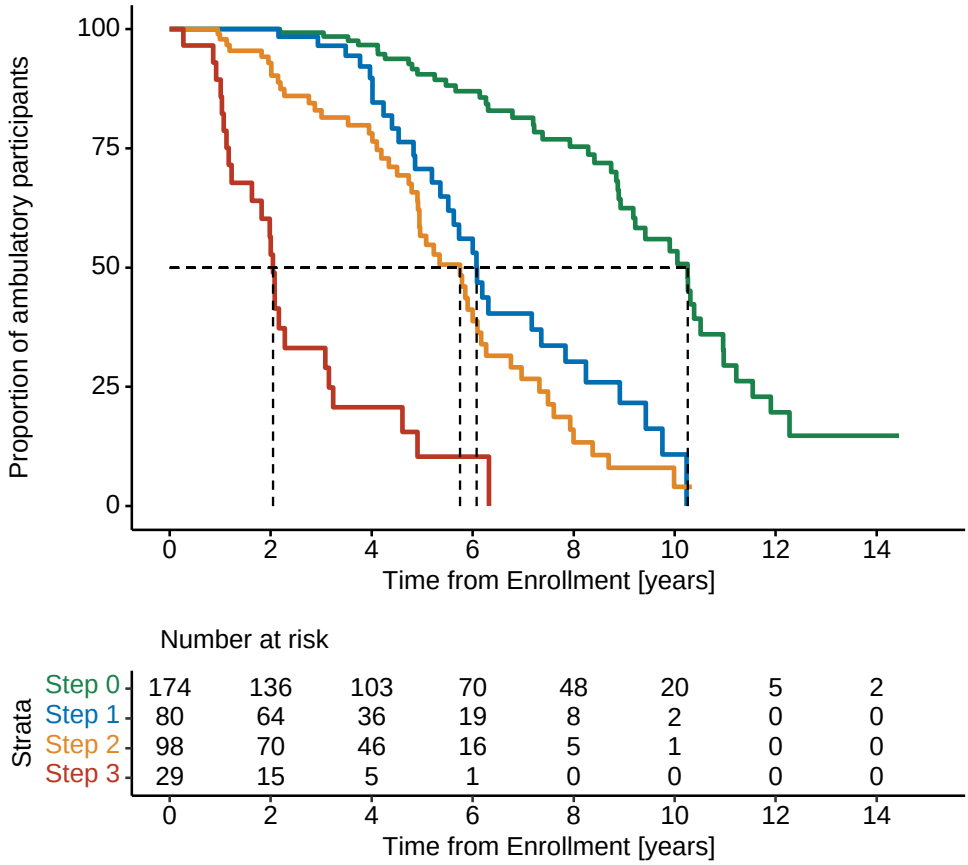

Fig. 4. Kaplan Meyer analysis for Time from Enrolment in FA-COMS to LoA, stratified by ability to stand at baseline (onset <15y).

4. Discussion

In the present study we have examined functional features in FRDA that can be used to estimate the time to LoA. As in other progressive diseases LoA in FRDA is not an acute event, but a slow, gradual transition reflected in the loss of a series of specific functions. We have shown that progression can be characterized and quantified by upright stability tasks. Moreover, these processes happen in a timely, more condensed manner in early onset patients, but similarly albeit with more variability in later onset FRDA.

Although balanced demographic results show that the FA-COMS cohort covers a broad range of disease severity and many temporal stages of FRDA progression, calculating a population estimate for LoA in FRDA is a challenging and to some extent questionable task, due to inherent disease diversity and the difficulty of defining an exact event (and the time thereof). Also, the need for left censoring of observations from participants where only a somewhat arbitrary time of enrolment is known adds concern. Especially in the later onset groups, the available methodology to estimate LoA is limited and our results must be treated with caution.

To add to the overall perspective, differential analyses of follow up time indicate the presence of a substantial number of young, still ambulatory participants at their current last visit. These observations, while contribute to the richness of the FA-COMS study in general, in our analysis lead to additional censoring, of special concern when participants have no follow up visit (which occurs for varying reasons). There will also be loss of follow up due to disease progression and eventually death, but as these events happen after LoA, they are not influential here. Follow up time however may impact results of the later onset cohorts (especially onset >24y). Late onset FRDA is under-diagnosed and lack of available participants leads to weak coverage of later disease duration in our analysis. The leads to potentially too severe results in this subgroup. Clinically, a substantial percentage of late onset FRDA patients (usually those presenting after age 35) remain ambulatory even with a normal life span.

On the other hand, the FA-COMS is the largest natural history study in FRDA. We have observed a high number of LoA events (147, 44 and 20 in respective subgroups) and our estimate of 11.5 years of disease duration for participants with an onset <15y is in line with both clinical experience and published results [18–20]. In addition, we provide the methodology to calculate further refined estimates in the future.

Furthermore, thorough investigation of all items within the upright stability sub score of the neurological FARS exam showed that specifically the stepwise loss of stance measures defines important milestones. The distributions of these functions point to the fact that stance functions might be lost over a comparatively brief period of time, as opposed to investigator rated assessments of lower limb function, providing them an event like character, ideal for time to event like analyses.

We have shown previously [3], that three out of six standing functions in FARS E, namely stand on dominant foot (E5), tandem stance (E4) and stance with feet together eyes closed (E3B) are lost early in the disease. Since (at least in FA-COMS) this typically happens before diagnosis, and the sequence of those events cannot be clearly established by time to event analyses, the Turnbull estimates for these functions are tainted with significant uncertainty. These functions are probably lost during or even before the first symptoms of the disease occur. The remaining three stance items, however, change only after diagnosis and their sequence can be well characterized in all onset groups. Functional loss starts with E2B/stance feet apart eyes closed, followed by stance feet together (E3A) and eventually normal stance (E2A).

An interesting perspective is provided by the fact that diagnosis typically happens in between function loss of both groups of items.

This suggests that loss of items E3B, E4 and E5 occurs during the period in which symptoms are not usually apparent to patients, physicians or both. It might indicate that the loss of the first three of these functions is be involved in patients' perceptions that lead affected individuals to eventual diagnosis. Anatomically, the events occurring in the pre-symptomatic period may reflect loss of proprioceptive neurons, as their loss is early and correlates with genetic severity, not clinical severity. In addition, a modest degree of metabolic myopathy might appear during this time, based on its early detection with metabolic testing. Consequently, the present findings match the evolving idea that progression in FRDA results from changes in the CNS (dentate nucleus, motor cortex) rather than ongoing loss of dorsal root ganglion neurons.

There are a variety of applications of the present work. In FRDA, a relatively slow progression combines with high intra- and inter-subject variability, which complicates patient selection for clinical trials. Having clearly defined steps before LoA will help select patients with more clearly defined risks of progression (i.e. LoA) and allow clinical trials to focus on walking. On the other hand, studies looking at earlier phases of the disease could select patients at lower risk for LoA, avoiding ceiling effects observed with the mFARS in studies using more advanced patients. Within previously used outcome measures the best available tool for covering the complete disease picture is FDS, which focuses on walking abilities but lacks clearly defined tests or measurable abilities, increasing variability and reversibility. The present approach provides alternatives to use of disease FDS in the earliest components of the disease.

Our approach to stratify patients based on upright stability item scores for the first time allows calculation of representative event rates for LoA, which then can be used to calculate sample sizes for *feasible* clinical trials using LoA as a specific outcome. The resulting study sizes are generally similar in magnitude to those from use of other measures in FRDA (greater than 100 patients in a 2-year study) [6,7], but the recognition of LoA as a specific, clinically relevant endpoint suggests that it may now be useful as a primary outcome measure in specific situations.

Of note, this type of stratification can reduce variability in subgroups, but the use of more sophisticated recruitment strategies in clinical studies might eventually require higher numbers of patients for optimal sensitivity than those available. In this context, as LoA undoubtedly constitutes a clinically significant milestone, our analysis adds clinical meaning to the loss (or retainment) of mFARS upright stability items. Therefore, they constitute milestones with value as clinical outcome measures themselves, rather than simply stratification elements. Composite endpoints, e.g. "number of steps lost" have been used in similar situations [21] and could also help to further reduce sample sizes. Furthermore, the observation that the same basis of LoA is followed in later onset patients might allow for those to be included in principle if needed, though with a loss of sensitivity in assessment of LoA.

Similarly, use of LoA as an outcome measure might be augmented by assessment of ambulatory devices and the transition between them. At present it is not clear that transitions between ambulatory devices are sufficiently systematic or sequential to facilitate their use in either patient stratification or clinical outcome. Further studies could investigate these transitions in conjunction with standing capacities.

Several limitations to the present study are apparent. First, we use an investigator driven test for the definition of LoA and a more clearly defined measure, e.g. "ability to walk 10 m without support" might help adding more precision. On the other hand, this also would not help to overcome the effects of day to day variability in FRDA, and the stance items used for stratification/prediction are clearly defined tests. Including additional measures, like lower extremity coordination (FARS C) might help to further refine our model. They correlate well with the FARS E sub score and are retained at least in early non-ambulatory patients [3].

Second, we used age of onset as an index of overall disease severity. This patient reported number is confounded by recall bias, particularly in older individuals. Biological markers such as shorter GAA repeat length or tissue frataxin levels could replace age of onset in this analysis, but those markers also carry intrinsic difficulties related to their sensitivity.

Third, FRDA is a disease of substantial day to day variability, not all of which is minimized in natural history studies. This will influence the precision of the estimates, which might be much better in clinical trial situations. In addition, the yearly visit interval is longer than the interval between visits in typical clinical trials, which will further improve the precision.

Eventually, our survival analyses do not account for the dependency of individual events. While in all analyses we strictly use independent observations, in the epidemiological analyses similar data is used multiple times to estimate different endpoints; thus, our analysis of LoA stratified by stance capability ignores the hierarchical nature of function loss. These conditions will require future, more detailed statistical analyses. Within those limitations however, the exceptionally high number of patients in our study should corroborate the reliability of our point estimates.

Data sharing

All data used in this study was collected during the FA Clinical Outcome Measures Study, (FA-COMS), registered at clinicaltrials.gov (NCT03090789). This database, including relevant study information and is part of the Friedreich's Ataxia Integrated Clinical Database (FA-ICD), which is available on appropriate request at The Data Collaboration Centre (DCC) of the Critical Path Institute (C-Path).

Declaration of Competing Interest

CR reports personal fees from FARA during the conduct of the study. JMF is an employee of FARA. DRL reports grants from FARA during the conduct of the study, grants from REATA, TAKEDA and the FDA outside of the submitted work.

Acknowledgments

Louise A. Corben, Martin B. Delatycki, S. H. Subramony, Khalaf Bushara, Chris Gomez, Chad Hoyle, Grace Yoon, Katherine Mathews, George Wilmot, Theresa Zesiewicz, Susan Perlman are acknowledged for participation in the FA-COMs study and collecting data from the patients which was used for this analysis.

Funding

This work was funded by the Friedreich's Ataxia Research alliance (FARA), www.curefa.org. The FA-COMS Study is conducted within the Collaborative Clinical Research Network in Friedreich's Ataxia (CCRN in FA), which is funded by FARA, the Cure FA Foundation and the Hamilton & Finneran Family Foundations. For more information see http://curefa.org/clinical-trials/clinical-trials-active-enrolling/clinical-outcome-measures-in-friedreich-s-ataxia-a-natural-history-study.

JF is an employee of FARA and serves as coordinator of the CCRN in FA and was involved in the study design, interpretation and writing of this manuscript.

Supplementary materials

Supplementary material associated with this article can be found in the online version at doi:10.1016/j.eclinm.2019.11.006.

References

1. Subramony SH, May W, Lynch D, et al. Measuring Friedreich ataxia: interrater reliability of a neurologic rating scale. Neurology 2005;64:1261–2.
2. Lynch DR, Farmer JM, Tsou AY, et al. Measuring Friedreich ataxia: complementary features of examination and performance measures. Neurology 2006;66:1711–6.
3. Rummey C, Corben LA, Delatycki MB, et al. Psychometric properties of the friedreich's ataxia rating scale. Neurol Genet 2019;5:e371.
4. Schmitz-Hübsch T, du Montcel ST, Baliko L, et al. Scale for the assessment and rating of ataxia: development of a new clinical scale. Neurology 2006;66:1717–20.
5. Reetz K, Dogan I, Costa AS, et al. Biological and clinical characteristics of the European Friedreich's ataxia consortium for translational studies (EFACTS) cohort: a cross-sectional analysis of baseline data. Lancet Neurol 2015;14:174–82.
6. Reetz K, Dogan I, Hilgers R-D, et al. Progression characteristics of the european friedreich's ataxia consortium for translational studies (EFACTS): a 2 year cohort study. Lancet Neurol 2016;15:1346–54.
7. Patel M, Isaacs CJ, Seyer L, et al. Progression of Friedreich ataxia: quantitative characterization over 5 years. Ann Clin Transl Neurol 2016;3:684–94.
8. FA Clinical Outcome Measures (FA-COMS). https://clinicaltrials.gov/ct2/show/NCT03090789.
9. Regner SR, Wilcox NS, Friedman LS, et al. Friedreich ataxia clinical outcome measures: natural history evaluation in 410 participants. J Child Neurol 2012;27:1152–8.
10. Friedman LS, Farmer JM, Perlman S, et al. Measuring the rate of progression in Friedreich ataxia: implications for clinical trial design. Mov Disord 2010;25:426–32.
11. Bürk K, Mälzig U, Wolf S, et al. Comparison of three clinical rating scales in Friedreich ataxia (FRDA). Mov Disord 2009;24:1779–84.
12. Cain KC, Harlow SD, Little RJ, et al. Bias due to left truncation and left censoring in longitudinal studies of developmental and disease processes. Am J Epidemiol 2011;173:1078–84.
13. Applebaum KM, Malloy EJ, Eisen EA. Left truncation, susceptibility, and bias in occupational cohort studies. Epidemiology 2011;22:599–606.
14. Turnbull BW. The empirical distribution with arbitrarily grouped and censored data. J R Stat Soc B 1976;38:290–5.
15. Giolo SR. Turnbull's nonparametric estimator for interval-censored data. Tech Rep 2004;10.
16. Anderson-Bergman C. icenReg: regression models for interval censored data in R. J Stat Softw 2017;81. doi: 10.18637/jss.v081.i12.
17. Koeks Z, Bladen CL, Salgado D, et al. Clinical outcomes in Duchenne muscular dystrophy: a study of 5345 patients from the treat-NMD DMD global database. J Neuromuscul Dis 2017;4:293–306.
18. Harding AE. Friedreich's ataxia: a clinical and genetic study of 90 families with an analysis of early diagnostic criteria and intrafamilial clustering of clinical features. Brain J Neurol 1981;104:589–620.
19. Dürr A, Cossee M, Agid Y, et al. Clinical and genetic abnormalities in patients with Friedreich's ataxia. N Engl J Med 1996;335:1169–75.
20. La Pean A, Jeffries N, Grow C, Ravina B, Di Prospero NA. Predictors of progression in patients with Friedreich ataxia. Mov Disord 2008;23:2026–32.
21. Mayer OH, Leinonen M, Rummey C, Meier T, Buyse GM. Efficacy of idebenone to preserve respiratory function above clinically meaningful thresholds for forced vital capacity (FVC) in patients with Duchenne muscular dystrophy. J Neuromuscul Dis 2017;4:189–98.

J Neurol (2013) 260:2362–2369
DOI 10.1007/s00415-013-6978-z

ORIGINAL COMMUNICATION

Analysis of the visual system in Friedreich ataxia

Lauren A. Seyer · Kristin Galetta · James Wilson · Reiko Sakai · Susan Perlman · Katherine Mathews · George R. Wilmot · Christopher M. Gomez · Bernard Ravina · Theresa Zesiewicz · Khalaf O. Bushara · S. H. Subramony · Tetsuo Ashizawa · Martin B. Delatycki · Alicia Brocht · Laura J. Balcer · David R. Lynch

Received: 4 February 2013 / Revised: 20 May 2013 / Accepted: 25 May 2013 / Published online: 18 June 2013

Abstract To use optical coherence tomography (OCT) and contrast letter acuity to characterize vision loss in Friedreich ataxia (FRDA). High- and low-contrast letter acuity and neurological measures were assessed in 507 patients with FRDA. In addition, OCT was performed on 63 FRDA patients to evaluate retinal nerve fiber layer (RNFL) and macular thickness. Both OCT and acuity measures were analyzed in relation to genetic severity, neurologic function, and other disease features. High- and low-contrast letter acuity was significantly predicted by age and GAA repeat length, and highly correlated with neurological outcomes. When tested by OCT, 52.7 % of eyes ($n = 110$) had RNFL thickness values below the fifth percentile for age-matched controls. RNFL thickness was significantly lowest for those with worse scores on the Friedreich ataxia rating scale (FARS), worse performance measure composite Z_2 scores, and lower scores for high- and low-contrast acuity. In linear regression analysis, GAA repeat length and age independently predicted RNFL thickness. In a subcohort of participants, 21 % of eyes from adult subjects ($n = 29$ eyes) had macular thickness values below the first percentile for age-matched controls, suggesting that macular abnormalities can also be present in FRDA. Low-contrast acuity and RNFL thickness capture visual and neurologic function in FRDA, and reflect genetic severity and disease progression independently.

L. A. Seyer · K. Galetta · J. Wilson · R. Sakai · L. J. Balcer · D. R. Lynch
Departments of Neurology, Ophthalmology and Epidemiology, University of Pennsylvania Medical School, Philadelphia, PA, USA

L. A. Seyer · D. R. Lynch
Department of Pediatrics, University of Pennsylvania Medical School, Philadelphia, PA, USA

L. A. Seyer (✉) · D. R. Lynch
Divisions of Neurology and Pediatrics, Children's Hospital of Philadelphia, Abramson Research Center Room 502, Philadelphia, PA 19104, USA
e-mail: SeyerL@email.chop.edu

S. Perlman
Department of Neurology, University of California Los Angeles, Los Angeles, CA, USA

K. Mathews
Department of Neurology, University of Iowa, Iowa, IA, USA

G. R. Wilmot
Department of Neurology, Emory University, Atlanta, GA, USA

C. M. Gomez
Department of Neurology, University of Chicago, Chicago, IL, USA

B. Ravina · A. Brocht
Department of Neurology, University of Rochester, Rochester, NY, USA

T. Zesiewicz
Department of Neurology, University of South Florida, Tampa, FL, USA

K. O. Bushara
Department of Neurology, University of Minnesota, Minneapolis, MN, USA

S. H. Subramony · T. Ashizawa
Department of Neurology, University of Florida, Gainesville, FL, USA

M. B. Delatycki
Department of Neurology, Murdoch Children's Research Institute, Melbourne, Australia

This suggests that such measures are useful markers of neurologic progression in FRDA.

Keywords Friedreich ataxia · Optical coherence tomography · Neurology

Introduction

Friedreich ataxia (FRDA) is an autosomal recessive neurological disorder resulting from mutations of the *FXN* (frataxin) gene [1]. With a prevalence of 1 in 50,000 in European populations [1], it is the most common inherited ataxia. Of patients with FRDA, 97 % have an expanded GAA triplet repeat in the first intron of both alleles, while the remaining 3 % carry an expanded GAA repeat on one allele and a point mutation on the other [2–5]. This leads to decreased mRNA transcription and a deficiency of the protein frataxin. Frataxin deficiency ultimately leads to the features of FRDA, including ataxia, areflexia, loss of sensation and proprioception, and dysarthria [1, 6–9]. Individuals with FRDA can also develop cardiomyopathy, scoliosis, diabetes mellitus, hypoacusis, and urinary dysfunction [1, 8, 9].

Though visual symptoms are not always recognized in FRDA, both afferent and efferent visual abnormalities may be found. Oculomotor findings associated with Friedreich ataxia include square wave jerks and difficulty with fixation [10]. Clinical or subclinical optic neuropathy is found in approximately two-thirds of people with FRDA, although severe visual loss is uncommon [11]. Visual field defects range from severe visual field impairment to isolated regions of reduced sensitivity [11]. Still, a few individuals have rapid visual loss, similar to that observed in Leber's hereditary optic neuropathy [12, 13].

As in other optic neuropathies, anatomic features of the retina can be evaluated with optical coherence tomography (OCT), a non-invasive, high resolution technique that uses near infrared light to quantify the thickness of the retinal nerve fiber layer (RNFL, the ganglion cell axons comprising the optic nerves, chiasm, and tracts) [14–17]. OCT can also image the ganglion cell and photoreceptor layers in the macular area, fovea, and optic disc, and has been used to examine various diseases of the retina and optic nerve, including optic neuritis, glaucoma, and multiple sclerosis [16, 18–21]. In multiple sclerosis, OCT reveals a decrease in RNFL thickness even in individuals who did not experience episodes of acute optic neuritis, suggesting that this technique can be useful in detecting anatomic abnormalities associated with subclinical visual loss, as is frequently found in FRDA [16].

Because of the highly quantifiable nature of visual function using measures such as low-contrast letter acuity (LCLA) and the highly reproducible results obtained through OCT in other conditions, such measures of visual function are attractive outcome measures for intervention studies in FRDA for detection of subclinical and clinically significant changes. The current study examined a large cohort of individuals with Friedreich ataxia using LCLA and a subcohort with OCT, and assessed the relation of these measures to visual and neurologic abilities in FRDA.

Methods

Friedreich ataxia clinical outcome measure study cohort

Five hundred and seven subjects participating in the Friedreich Ataxia—Clinical Outcome Measures Study (FA-COMS) were evaluated at 1 of 12 sites. Data collected as part of this study included medical history and several quantitative measures: (1) visual function testing using high- and low-contrast vision charts, (2) timed 25-foot walk (T25FW), (3) timed 9-hole peg test (9HPT), and (4) the Friedreich ataxia rating scale (FARS), a quantified neurological exam used in the evaluation of FRDA. The T25FW, 9HPT, and FARS were performed according to protocols described previously [22–24]. Genetic confirmation was obtained via commercial or research testing. De-identified data were extracted from the most recent evaluation. In a subset of patients, frataxin protein levels in buccal cells and whole blood were available, as well as homeostatic model assessment–insulin resistance (HOMA-IR) values from fasting insulin and glucose levels [25, 26].

Contrast letter acuity testing was performed using retro-illuminated vision charts. High-contrast acuity was tested both monocularly and binocularly. Binocular low-contrast letter acuity testing was performed using the 2.5 and 1.25 % Low-Contrast Sloan Letter Charts (LCSLC) at a distance of 2 m (Precision Vision, LaSalle, IL, USA), based on a protocol used to measure visual dysfunction in MS and FRDA [15, 27]. A total binocular visual acuity score was computed using the single high-contrast chart and the 2.5 and 1.25 % LCSLC (score out of a total of 210 letters). Subjects used their standard refractive correction for distance. Visual function testing was performed by trained technicians.

Optical coherence tomography

OCT was performed on both eyes of FRDA patients to evaluate RNFL and macular thickness. Medical history was reviewed before testing, and none of the subjects who underwent OCT testing had underlying ophthalmological disease present, such as cataract and optic neuropathy, according to their most recent clinical evaluations. For each eye, the OCT protocol adopted was the fast RNFL thickness scan, performed using the *STRATUS* OCT 3 with OCT 4.0

software (Carl Zeiss Meditec, Inc., Dublin, CA, USA). This protocol was used for all RNFL imaging, and was performed by trained technicians. Quadrant thickness for each eye was also measured using the Fast RNFL Thickness Scan as described previously [28]. Average RNFL thickness was compared to a control population consisting of individuals evaluated at the University of Pennsylvania and other sites ($n = 533$). To evaluate macular thickness, macular cube 200×200 scans were also performed on a subset of the population using *CIRRUS* OCT (Carl Zeiss Meditec, Inc., Dublin, CA, USA), which uses spectral domain rather than time domain technology to produce higher resolution images at a higher speed than *STRATUS* OCT.

Statistics

Summary statistics, correlations and linear regressions were calculated using STATA 12.0 (Stata; StataCorp LP, College Station, TX, USA). Visual acuity and OCT were separately compared with measures of visual and neurological function in FRDA as well as age and GAA repeat lengths. All calculations use the length of the shorter GAA repeat. In addition, monocular and binocular visual acuity scores were compared across the cohort to assess for binocular summation.

Results

FA-COMS Cohort

The FA-COMS cohort ($n = 507$) was 49 % female with mean age of 28.1 years (range 7–78). Mean length of the shorter GAA allele was 608 repeats, with 16 people carrying point mutations in conjunction with a single expanded allele. Mean age of onset was 13.8 years. The average FARS neurological exam score was 68.2, which typically corresponds to an individual ambulating with substantial difficulty. Levels of frataxin protein in buccal cells in this cohort had an average of 22.8 % of average frataxin levels in controls ($n = 188$) (Table 1).

Upon assessment with high-contrast vision charts, subjects read an average of 53.6 out of 70 letters with the right eye, 53.0 out of 70 letters with the left eye, and 58.1 out of 70 letters with both eyes (a Snellen visual acuity equivalent of 20/20) (Table 1). Thus, FRDA patients had minimal loss of central acuity, even though binocular visual acuity was slightly worse than in control subjects tested similarly and in an analogous cohort of subjects with multiple sclerosis [16, 27]. Additionally, 2 % of individuals ($n = 10$) had better monocular vision than binocular vision, which was not significantly predicted by age ($p = 0.77$) or by GAA repeat length ($p = 0.76$) accounting for sex. In addition, 29.2 % of individuals in this cohort had inter-eye differences in visual acuity of at least one acuity equivalent on a high-contrast vision chart (one line = five letters), while only 8.3 % had inter-eye differences of at least two acuity equivalents.

In general, letter acuity results reflected disease severity as assessed by genetic, temporal, neurological and biochemical measures. Scores from the binocular high- and low-contrast charts inversely correlated with GAA repeat length and length of disease duration. These scores and the total binocular score also were predicted independently by GAA repeat length and age in linear regression models

Table 1 Demographics

	FA-COMS Cohort ($n = 507$)	OCT Cohort ($n = 63$)
Age (years)	28.1 ± 15.2 (7–78)	28.2 ± 15.9 (8–67)
GAA repeat length	608 ± 246	588 ± 218
Subjects with point mutations	16	3
Age of onset (years)	13.8 ± 9.6	15.0 ± 10.6
Disease duration (years)	14.4 ± 10.5	13.3 ± 10.0
Sex (% female)	49	55
FARS score	68.2 ± 21.4	64.8 ± 20.3
High contrast visual acuity	58.1/70 ± 10.9	61.4/70 ± 10.7
Overall Snellen Ssore	20/20	20/20
Avg. 2.5 % LCSLC	29.4/70 ± 15.6	32.6/70 ± 14.0
Avg 1.25 % LCSLC	20.5/70 ± 13.9	24.0/70 ± 13.5
Hypertrophic cardiomyopathy (%)	54.0	38.8
Scoliosis (%)	78.7	89.8
Diabetes (%)	6.0	4.1
Hearing Loss (%)	15.7	4.1
Frataxin level, buccal cell (% control)	22.8 ± 19.4	26.8 ± 20.5
HOMA value (nL value <2.0)	4.0 ($n = 32$)	3.5 ($n = 21$)

Demographics from the Friedreich Ataxia—Clinical Outcomes Measures (FA-COMS) study ($n = 507$) and from the subcohort evaluated using optical coherence tomography (OCT) ($n = 63$)

Table 2 Correlations of letter acuity and OCT scores with disease features

	Binocular high contrast	2.5 % LCSLC	1.25 % LCSLC	Total low contrast	Total bin. acuity	RNFL thickness
GAA repeat length	−0.25*	−0.23*	−0.22*	−0.23*	−0.25*	−0.39**
Disease duration	−0.28*	−0.38*	−0.37*	−0.39*	−0.38*	−0.52*
FARS score	−0.50*	−0.64*	−0.65*	−0.66*	−0.66*	−0.72*
Z_2 score	−0.45*	−0.62*	−0.63*	−0.64*	−0.63*	−0.62*
Age of onset	0.17*	0.18*	0.18*	0.18*	0.19*	0.39***
RNFL thickness	0.52*	0.55*	0.51*	0.54*	0.57*	

Data presented as the correlation coefficient with significance value designated. In the cross-sectional FA-COMS population, letter acuity results reflected disease severity as assesed by multiple measures. All visual acuity scores correlated with GAA repeat length and length of disease duration. Visual acuity scores more strongly correlated with the FARS exam and Z_2 composite score including timed 9HPT and T25FW. Similarly, RNFL thickness correlated with GAA repeat length and disease duration, with the strongest correlations with the FARS exam and Z_2 score. All visual acuity scores correlated strongly with RNFL thickness

* $p < 0.001$, ** $p = 0.004$, *** $p = 0.003$

Table 3 Linear regression analysis of visual function and RNFL thickness

	Binocular high con.	2.5 % LCSLC	1.25 % LCSLC	Total bin. acuity	RNFL thickness
GAA repeat length	−0.02 ± 0.002*	−0.03 ± 0.003*	−0.02 ± 0.003*	−0.07 ± 0.01*	−0.04 ± 0.01*
Age	−0.23 ± 0.03*	−0.40 ± 0.05*	−0.33 ± 0.05*	−0.96 ± 0.12*	−0.37 ± 0.14**
Sex	0.73 ± 0.91	0.67 ± 1.33	0.02 ± 1.20	1.43 ± 3.12	1.08 ± 3.30
Overall model	*	*	*	*	***
R^2	0.14	0.16	0.14	0.18	0.26

Visual acuity scores and RNFL thickness were all significantly and independently predicted by GAA repeat length and age in linear regression models accounting for sex. This suggests that visual acuity and RNFL thickness reflect both temporal disease progression and genetic severity. Data are presented as a regression coefficient and standard deviation, with statistical significance indicated

* $p < 0.001$, ** $p = 0.013$, *** $p = 0.002$

accounting for sex (Tables 2, 3). Visual acuity scores also reflected neurological function. Performance on the binocular high- and low-contrast charts, and the total binocular score, inversely correlated with the FARS exam score and the Z_2 score summary measure of 9HPT and the T25FW (Table 2).

Visual acuity testing also reflected biochemical data in linear regression models. Scores on the binocular high- and low-contrast charts were significantly predicted by frataxin protein levels obtained from buccal cells ($p = 0.007$, $p = 0.005$, and $p = 0.001$, respectively) accounting for age and sex (Table 4).

Finally, visual dysfunction as assessed by total binocular acuity score was associated with specific related clinical phenomena. The presence of diabetes ($p < 0.001$), hearing loss ($p < 0.001$), and hypertrophic cardiomyopathy ($p < 0.001$) predicted total binocular acuity and LCSLC performance after accounting for GAA repeat length, age, and sex (Table 4). In contrast, the presence of scoliosis did not significantly predict any visual measure (data not shown). Additionally, the presence of a point mutation ($n = 16$) did not significantly predict visual acuity in linear regression models accounting for disease duration and sex (Table 5).

As an alternative method of evaluation, we explored the effect of distinct variables on the likelihood of having abnormal visual acuity, defined by a binocular visual acuity of worse than 20/32. In this population, 10.1 % of the cohort ($n = 51$) had a Snellen acuity score of <20/32. Increasing age ($p < 0.001$) and GAA repeat length ($p < 0.001$) independently predicted reduced visual acuity beyond 20/32 accounting for sex. This was also significantly predicted by the presence of hearing loss ($p < 0.001$) accounting for age, GAA repeat length, and sex. Presence of diabetes predicted reduced visual acuity; however, this did not reach significance ($p = 0.019$). Scoliosis and hypertrophic cardiomyopathy did not significantly predict visual acuity below 20/32 in models accounting for age, GAA repeat length, and sex. Similarly, frataxin protein levels did not predict reduced visual acuity in models accounting for age and sex. The presence of a point mutation also did not significantly predict acuity below 20/32 when accounting for length of disease duration and sex.

OCT cohort

A subgroup of patients with FRDA from the primary site were evaluated with OCT ($n = 63$). All except three were

Table 4 Effect of frataxin level, presence of diabetes, hearing loss, or cardiomyopathy on visual acuity

	Regression coefficients of total binocular acuity score			
Frataxin (BC)	0.47 ± 0.14*			
Diabetes		−24.68 ± 7.06*		
Hearing Loss			−25.28 ± 4.53**	
HCM				−10.59 ± 3.66***
GAA Repeat		−0.07 ± 0.01**	−0.06 ± 0.01**	−0.07 ± 0.01**
Age	−0.75 ± 0.17**	−0.97 ± 0.12**	−0.85 ± 0.12**	−1.13 ± 0.13**
Sex	1.18 ± 5.16	2.71 ± 3.17	−0.27 ± 3.14	1.10 ± 3.25
Overall Model	<0.001	<0.001	<0.001	<0.001
R^2	0.11	0.22	0.25	0.21

Linear regression models were constructed to evaluate the ability of frataxin level, presence of diabetes, hearing loss, or cardiomyopathy to predict visual function scores, accounting for age, sex, and (except for frataxin level) GAA repeat length. Binocular acuity score was significantly predicted by frataxin protein level in a model accounting for age and sex and was also significantly and independently predicted by the presence of diabetes, hypertrophic cardiomyopathy (HCM), and hearing loss in models also accounting for GAA repeat length, age, and sex. Data are presented as the regression coefficient and standard deviation, with statistical significance indicated

* $p = 0.001$, ** $p < 0.001$, *** $p = 0.004$

Table 5 Effect of point mutations on visual function

	Binocular High Con.	2.5 % LCSLC	1.25 % LCSLC	Total bin. acuity
Presence of point mutation	−4.45 ± 2.63	−0.49 ± 3.74	−1.78 ± 3.37	−6.72 ± 8.85
Disease duration	−0.33 ± 0.04*	−0.60 ± 0.06*	−0.51 ± 0.06*	−1.44 ± 0.15*
Sex	1.06 ± 0.93	0.88 ± 1.33	0.16 ± 1.20	2.10 ± 3.14
Overall model	*	*	*	*
R^2	0.12	0.17	0.15	0.17

Linear regression models were constructed to assess the effect of point mutations on visual loss, accounting for sex and disease duration. The presence of a point mutation ($n = 16$ out of 507) did not significantly predict visual acuity on high or low contrast vision charts. Data are presented as a regression coefficient and standard deviation, with statistical significance indicated

* $p < 0.001$

homozygous for GAA expansions in the *FXN* gene; the remaining three subjects, from separate kindreds, were compound heterozygotes with one GAA repeat expansion and a point mutation on the other allele. Two of these individuals had a point mutation presumed to affect RNA splicing (165 + 5 G > C) [29]. The third carried the missense mutation G130 V (Table 1) [3]. In six of the 63 individuals evaluated, OCT could not be performed because of severe visual loss, fixation instability, or ptosis. Thus, all calculations involving the OCT cohort were performed using data from the 57 evaluable subjects. Of these, we obtained usable data for a total of 110 eyes due to eye movements or ptosis in a few individuals.

The average RNFL thickness in this cohort was 85.3 ± 13.9 μm, below the fifth percentile for age-matched controls (104.0 ± 11.5 μm). Considered separately, 52.7 % of eyes ($n = 110$) had RNFL thickness below the fifth percentile for age-matched controls. When the quadrants of each eye were assessed separately, the mean inferior, nasal, and temporal quadrant average thickness values were normal, above the fifth percentile for age-matched controls; however, 32 % of eyes were below the fifth percentile in the inferior quadrant, and 25 % of eyes were below the fifth percentile in each the nasal and temporal quadrants. The mean superior quadrant thickness in this cohort was abnormally thin, with RNFL values at the fifth percentile when compared with age-matched controls, and 51 % of individual eyes below the fifth percentile.

We then determined the disease-related factors associated with OCT values. When comparing RNFL thickness with measures of visual acuity, all vision scores correlated with RNFL thickness (Table 2). In linear regression analysis, all acuity scores also predicted RNFL thickness in models accounting for sex and GAA repeat length (Table 6). RNFL thickness correlated with GAA repeat length, FARS exam score, disease duration, Z_2 score, and age of onset (Table 2). In linear regression analysis, GAA repeat length and age both predicted RNFL thickness in models accounting for sex (Table 3), showing that RNFL thickness reflects both temporal disease progression and genetic severity. Z_2 score ($p < 0.001$) also significantly predicted average RNFL thickness accounting for age, sex,

Table 6 Relation of RNFL to visual function, GAA repeat length, and sex of subjects with FRDA

	Regression coefficients of RNFL thickness		
Binocular high-contrast acuity	0.56 ± 0.12*		
Total binocular acuity		0.18 ± 0.05*	
Total low-contrast acuity			0.22 ± 0.07*
GAA repeat length	−0.02 ± 0.01	−0.02 ± 0.01	−0.02 ± 0.01
Sex	−2.22 ± 3.29	−0.02 ± 3.1	0.99 ± 3.20
Overall model	**	**	**
R^2	0.32	0.34	0.31

In linear regression analysis, visual acuity scores predicted RNFL thickness in models accounting for sex and GAA repeat length. Data are presented as regression coefficient ± standard deviation, with statistical significance indicated

* $p = 0.001$, ** $p < 0.001$

Table 7 Relation of RNFL to neurologic function

	Regression coefficients of RNFL thickness
Z_2 Score	−5.35 ± 1.3 ($p < 0.001$)
GAA repeat length	−0.02 ± 0.01 (0.082)
Age	−0.01 ± 0.15 (0.96)
Sex	1.42 ± 2.97 (0.63)
Overall model	<0.001
R^2	0.46

Z_2 score, the summary measure including the timed 9-hole peg test (9HPT) and 25-foot walk (T25FW), significantly predicted average RNFL thickness in a linear regression model accounting for age, sex, and GAA repeat length. Data are presented as a regression coefficient and standard deviation, followed by significance in *parentheses*

Table 8 Correlations of macular thickness values with RNFL thickness and neurological function

	Cube volume	Cube average thickness
Disease duration	−0.34 (0.31)	−0.33 (0.32)
FARS score	−0.15 (0.66)	−0.16 (0.65)
RNFL thickness	0.04 (0.91)	0.04 (0.92)

Measures of macular thickness correlated with disease duration; however, these data did not reach significance. Macular thickness did not strongly correlate with the FARS neurological exam. Measured in ten individuals, the correlations between macular thickness and RNFL thickness were low and also did not reach significance. Data are presented as the *r* value followed by significance in *parentheses*

and GAA repeat length (Table 7). This suggests that RNFL thickness reflects neurologic abilities even beyond GAA repeat length. In contrast, average RNFL thickness was not predicted by insulin resistance in linear regressions accounting for age, sex, and GAA repeat length, or by frataxin protein levels accounting for age and sex. In addition, the presence of scoliosis, hearing loss, diabetes, and hypertrophic cardiomyopathy do not show significant relationships with average RNFL thickness (data not shown).

Additionally, we performed parallel OCT with the *CIRRUS* protocol to evaluate macular anatomy more precisely. RNFL thickness measured by *STRATUS* OCT and *CIRRUS* OCT correlated well ($r = 0.92$; $p = 0.003$). In subjects evaluated for macular thickness using the *CIRRUS* OCT ($n = 23$), the average central subfield thickness was 249 μm, average cube volume was 10.0 mm^3, and cube average thickness in this cohort was 277.4 μm in the evaluable subjects ($n = 16$). A total of 20.7 % of eyes from adult subjects ($n = 29$ eyes) had cube volume and average thickness below the first percentile. Measures of macular thickness correlated with disease duration; however, these data did not reach significance (Table 8). When macular thickness was compared to RNFL thickness as measured by *STRATUS* OCT 3 ($n = 10$ individuals), the correlations between average cube volume and average cube average thickness and RNFL thickness were low and did not reach significance (Table 8).

Discussion

The present study demonstrates that visual measures predict neurologic function in Friedreich ataxia, allowing the use of such measures for long-term assessment of disease progression. Visual function, particularly low-contrast vision, reflected neurologic function, a finding which matches those in smaller studies [27]. Similarly, RNFL thickness correlated highly with visual and neurological function. Genetic severity and age, both representative of disease severity, also independently predicted OCT and low-contrast acuity. Interestingly, correlations of OCT were even slightly higher with neurologic function than with visual function, showing that OCT may ultimately be useful as a level four anatomic biomarker of structural neuronal loss in FRDA in clinical drug trials designed to test efficacy. Alternatively, the correlations between RNFL thickness and visual acuity may be lowered by floor and ceiling effects of acuity testing. Still, low-contrast acuity and OCT can serve as functional and anatomic measures of neurologic progression in FRDA in intervention studies.

The data from this cohort, consistent with previous studies, show that visual loss in FRDA follows a specific pattern. Low-contrast acuity was better associated with neurologic severity, age and genetic severity than high-contrast acuity, suggesting loss of peripheral fields more

than central fields. Similarly, only a minority of patients had central acuities in the abnormal range, predicted by older age and longer GAA repeat length. Thus central vision is spared early in the disease but eventually can be lost in a small subset of the FRDA population. These possible differences between central and peripheral acuity suggest that visual field testing might specifically be useful in Friedreich ataxia, as has been performed in previous studies; however, such testing is substantially confounded because FRDA causes impairment of the hand movements needed to effectively participate in automated visual field testing. This limits the utility of visual field testing as a vision specific measure in FRDA. High-contrast scores were almost always better binocularly than with either eye alone, reflecting binocular summation. Thus, efferent dysfunction, which should affect binocular vision but not monocular vision, is not a major cause of functional vision loss in FRDA.

Furthermore, the pattern of RNFL loss in FRDA is distinctive. While the RNFL for all quadrants were affected in FRDA, the superior quadrant was somewhat more affected. In other mitochondrial diseases, the temporal quadrant seems to be affected by disease processes to a larger extent than other quadrants. The optic neuropathy in FRDA is likely to involve different disease mechanisms, leading to slightly different areas of selective vulnerability.

The relative symmetry between eyes shows the bilateral nature of dysfunction in FRDA. Perhaps in conjunction with the occipital lobe abnormalities that can occur in FRDA, the dominant cause of visual dysfunction in FRDA is a symmetric optic neuropathy affecting peripheral more than central visual fields. However, this presumptive peripheral optic neuropathy is not reflected in a corresponding loss of visual acuity. If the underlying RNFL thinning present in FRDA spares central vision, this may explain the average visual acuity of 20/20 across this cohort.

While correlations between scores on visual tests and neurologic and genetic severity were high, they did not approach unity, suggesting that other factors affect visual loss in FRDA. Although increased GAA repeat length predicts increasing visual loss, the presence of hearing loss also predicted visual function independent of genetic severity or age. This is most likely explained by the presence of modifying factors exacerbating the triad of optic neuropathy, hearing loss and diabetes, matching associations from studies performed before genetic testing was available. The presence of scoliosis did not predict acuity, suggesting independent factors altering their course in FRDA. Reduced visual function in FRDA has also been associated with the presence of point mutations. We could not confirm this connection; however, this may be attributed to the small number of individuals in this cohort with point mutations (3 %). It is possible that point mutations are associated with more severe vision loss, especially for individuals with more severe mutations such as those with exon deletions or disruption of frataxin function, such as 493 C > T (R165C) or 165 + 5 G > C, a mutation which is predicted to disrupt normal gene splicing [4].

A surprising aspect of the present work is the amount of functional and anatomic loss across this broad cohort in a disorder that is not typically associated with dominant visual symptomatology. Visual acuity is abnormal compared to control subjects tested similarly, and are roughly the same as the low-contrast acuity observed in individuals with MS tested by an identical protocol [16, 27]. In multiple sclerosis, OCT has identified decreased RNFL thickness even in individuals who did not experience episodes of acute optic neuritis; this correlates with visual acuity scores [16]. In contrast, in the present FRDA cohort, RNFL thinning did not correspond to a proportionate loss of visual acuity. This suggests that the slow loss of retinal axons in FRDA could be mitigated by compensatory central or peripheral mechanisms.

Several individuals in this FRDA cohort showed abnormal macular anatomy, suggesting that FRDA may affect macular cells as well as ganglion cell axons in selected subjects. Macular changes could reflect the presence of retinal neuronopathy as well as axonopathy in FRDA. Alternatively, macular loss could result from a primary dying back from injured axons with eventual loss of cell bodies. Interestingly, previous research using electroretinography has not detected substantial retinal abnormalities in FRDA, and the loss of low-contrast and peripheral visual field with preservation of high-contrast vision is not suggestive of a primary macular disease [30]. The present data suggest that macular features may be a component of the most advanced FRDA visual loss, and could clinically affect vision only in the most severely affected patients. Still, identification of macular abnormalities is crucial for understanding the limitations of regenerative capacities in FRDA.

Future studies focusing on more clearly defining the extent of macular loss and its clinical implications will be important in this field. In addition, a large longitudinal study of RNFL thickness will be helpful to determine the rate of change in this population as compared to normal controls. The high correlation between RNFL measurements obtained with *STRATUS* OCT and *CIRRUS* OCT suggests that the more advanced instrument, *CIRRUS* OCT, can be solely and reliably utilized in future studies as a level four outcome measure.

Acknowledgments This study was funded by grants awarded by the Friedreich Ataxia Research Alliance (FARA), the Muscular Dystrophy Association (MDA), and the National Eye Institute (NEI).

Conflicts of interest This study was sponsored by the Friedreich Ataxia Research Alliance (FARA), the Muscular Dystrophy Association (MDA), and the National Eye Institute (NEI). Ms. Seyer, Ms.

Galetta, Mr. Wilson, Ms. Sakai, Dr. Gomez, Dr. Ashizawa, and Dr. Bushara report no disclosures. Dr. Perlman obtains salary support from clinical billing of insurance companies for treatment patients and from several research grants- FARA/MDA subcontract grant for Clinical Outcome Measures in FA; National Ataxia Foundation (NAF); Huntingtons Disease Society of America; and the CHDI Foundation, Inc. Dr. Mathews receives research support from PTC Therapeutics as a clinical trial site. She receives research support from the CDC, the NIH, Parent Project Muscular Dystrophy (PPMD), and FARA. Dr. Wilmot receives a consultant fee from Santhera Pharmaceuticals for serving on the Data Safety Monitoring Board for trials involving the drug idebenone. He also receives grant funding from FARA. Dr. Ravina is currently employed at Biogen-Idec. Dr. Zesiewicz is supported by grants from FARA, the NAF, Pfizer, Baxter, and the Bobby Allison Ataxia Research Center. She receives funds for speaking engagements by TEVA Pharmaceuticals and GE Healthcare. Dr. Subramony is a member of the Speaker's Bureau for Athena Diagnostics and receives honoraria for such speaking engagements. He receives research support from the NAF. Dr. Delatycki receives support from the National Health and Medical Research Council in Australia, and FARA. He has a Healthscope Pathology consultancy. Ms. Brocht receives FARA salary support. Dr. Balcer is supported by grants from the NEI, National Multiple Sclerosis Society, NIH, NINDS, DAD's Foundation, and FARA. She also holds consultancies at Biogen-Idec, Vaccinex, and Accorda. Dr. Lynch is supported by grants from the NIH, MDA/FARA (Clinical research network in Friedreich ataxia), the Trisomy 21 program of the Children's Hospital of Philadelphia, Penwest Pharmaceuticals, and Edison Pharmaceuticals. He is a FARA board member and holds consultancies at Apopharma and Athena Diagnostics. He also holds an NMDA receptor encephalitis patent.

Ethical standard All protocols were approved by the Institutional Review Board at the Children's Hospital of Philadelphia and other sites. Informed consent was obtained before participation.

References

1. Lynch DR, Farmer JM, Balcer LJ, Wilson RB (2002) Friedreich ataxia: effects of genetic understanding on clinical evaluation and therapy. Arch Neurol 59:743–747
2. Schulz JB, Denmer T, Schols L et al (2000) Oxidative stress in patients with Friedreich ataxia. Neurology 55:1719–1721
3. Bidichandani SI, Ashizawa T, Patel PI (1997) Atypical Friedreich ataxia caused by compound heterozygosity for a novel missense mutation and the GAA triple-repeat expansion. Am J Hum Genet 60:1251–1256
4. Cossee M, Durr A, Schmitt M et al (1999) Friedreich's ataxia: point mutations and clinical presentation of compound heterozygotes. Ann Neurol 45:200–206
5. Monros E, Molto MD, Martinez F et al (1997) Phenotype correlation and intergenerational dynamics of the Friedreich ataxia GAA trinucleotide repeat. Am J Hum Genet 61:101–110
6. Babady NE, Carelle N, Wells RD et al (2007) Advancements in the pathophysiology of Friedreich's ataxia and new prospects for treatments. Molec Genet Metabolism 92:23–35
7. Cooper JM, Schapira AH (2003) Friedreich's ataxia: disease mechanisms, antioxidant and coenzyme Q10 therapy. BioFactors 18:163–171
8. Harding AE (1981) Friedreich's ataxia: a clinical and genetic study of 90 families with an analysis of early diagnostic criteria and intrafamilial clustering of clinical features. Brain 104: 589–620
9. Pandolfo M (1999) Molecular pathogenesis of Friedreich ataxia. Arch Neurol 56:1201–1208
10. Fahey MC, Cremer PD, Aw ST et al (2008) Vestibular, saccadic and fixation abnormalities in genetically confirmed Friedreich ataxia. Brain 131:1035–1045
11. Fortuna F, Barboni P, Liguori R et al (2009) Visual system involvement in patients with Friedreich's ataxia. Brain 132(part 1):116–123
12. Newman NJ, Biousse V (2004) Hereditary optic neuropathies. Eye 18:1144–1160
13. Carelli V, Ross-Cisneros FN, Sadun AA (2002) Optic nerve degeneration and mitochondrial dysfunction: genetic and acquired optic neuropathies. Neurochem Int 40:573–584
14. Teesalu P, Tuulonen A, Airaksinen PJ (2000) Optical coherence tomography and localized defects of the retinal nerve fiber layer. Acta Ophthalmol Scand 78:49–52
15. Syc SB, Warner CV, Hiremath GS et al (2010) Reproducibility of high-resolution optical coherence tomography in multiple sclerosis. Mult Scler 0:1–11
16. Fisher JB, Jacobs DA, Markowitz CE et al (2006) Relation of visual function to retinal nerve fiber layer thickness in multiple sclerosis. Ophthalmology 113(2):324–332
17. Cettomai D, Pulicken M, Gordon-Lipkin E et al (2008) Reproducibility of optical coherence tomography in multiple sclerosis. Arch Neurol 65:1218–1222
18. Kanamori A, Nakamura M, Escano MF et al (2003) Evaluation of the glaucomatous damage on retinal nerve fiber layer thickness measured by optical coherence tomography. Am J Ophthalmol 135:513–520
19. Talman LS, Bisker ER, Sackel DJ et al (2010) Longitudinal study of vision and retinal nerve fiber layer thickness in multiple sclerosis. Ann Neurol. 67:749–760
20. Trip SA, Schlottmann PG, Jones SJ et al (2005) Retinal nerve fiber layer axonal loss and visual dysfunction in optic neuritis. Ann Neurol 58(3):383–391
21. Costello F, Coupland S, Hodge W et al (2006) Quantifying axonal loss after optic neuritis with optical coherence tomography. Ann Neurol 59(6):963–969
22. Lynch DR, Farmer JM, Tsou AY et al (2006) Measuring Friedreich ataxia: complementary features of examination performance measures. Neurology 66:1711–1716
23. Subramony SH, May W, Lynch D et al (2005) Cooperative ataxia group. measuring Friedreich ataxia: interrater reliability of a neurologic rating scale. Neurology 64:1261–1262
24. Friedman LS, Farmer JM, Perlman S et al (2010) Measuring the rate of progression in Friedreich ataxia: implications for clinical trial design. Mov Disord 25:426–432
25. Deutsch EC, Santani AB, Perlman SL et al (2010) A rapid, noninvasive immunoassay for frataxin: utility in assessment of Friedreich ataxia. Mol. Gen. Metab. 101:238–245
26. Matthews DR, Hosker JP, Rudenski AS et al (1985) Homeostasis model assessment: insulin resistance and beta-cell function from fasting plasma glucose and insulin concentrations in man. Diabetologia 28(7):412–419
27. Lynch DR, Farmer JM, Rochestie D, Balcer LJ (2002) Contrast letter acuity as a measure of visual dysfunction in patients with Friedreich ataxia. J Neuroophthalmol 22:270–274
28. Ratchford JN, Quigg ME, Conger A et al (2009) Optical coherence tomography helps differentiate neuromyelitis optica and MS optic neuropathies. Neurology 73:302–308
29. McCormack ML, Guttmann RP, Schumann M et al (2000) Frataxin point mutations in two patients with Friedreich's ataxia and unusual clinical features. J Neurol Neurosurg Psychiatry 68:661–664
30. Pinto F, Amantini A, deScisciolo G et al (1988) Visual involvement in Friedreich's ataxia: pERG and VEP study. Eur Neurol 28(5):246–251